Geofluids

Geothermal Systems: Interdisciplinary Approaches for an Effective Exploration

Lead Guest Editor: Domenico Montanari
Guest Editors: Matteo Lupi and Philippe Calcagno

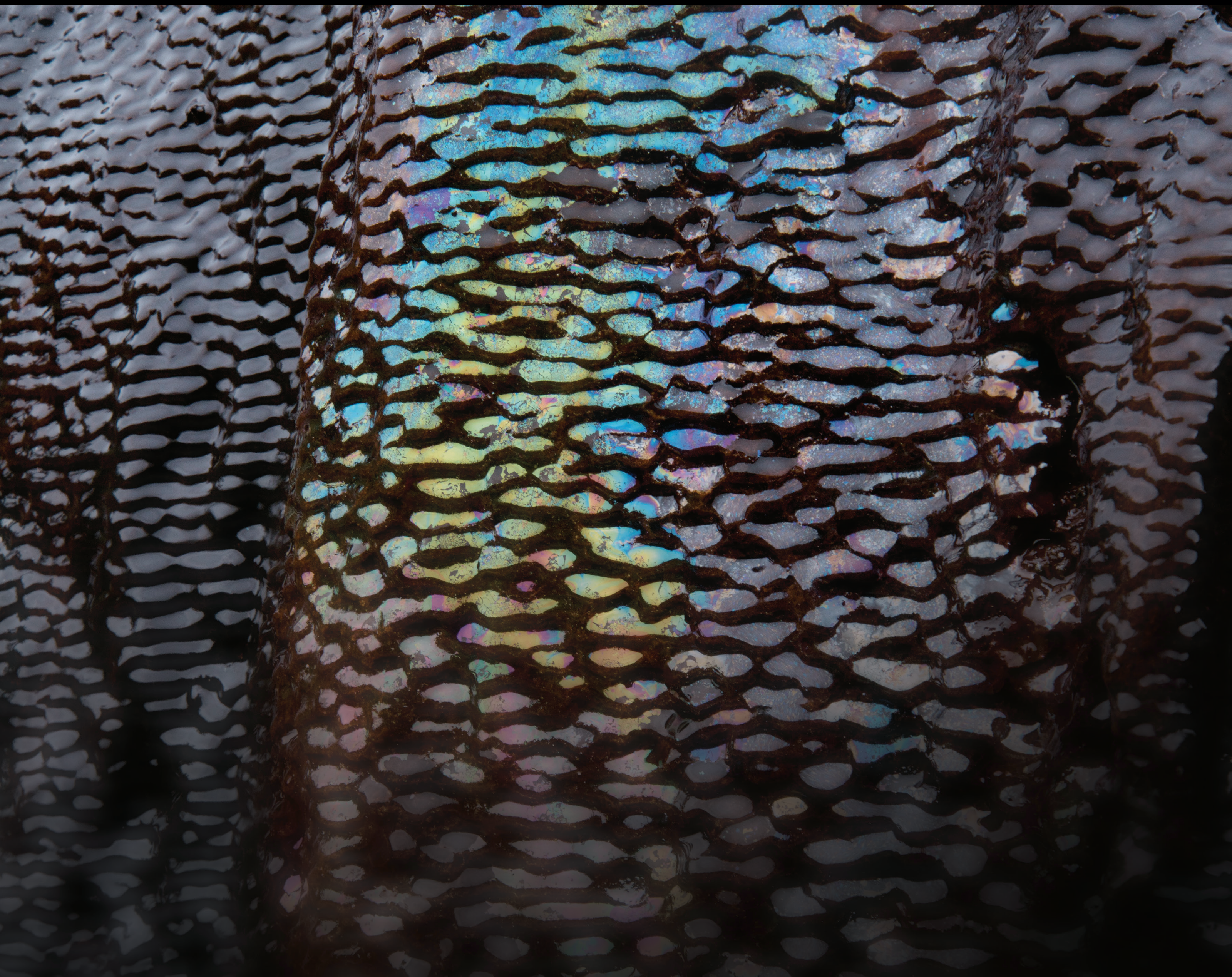

Geothermal Systems: Interdisciplinary Approaches for an Effective Exploration

Geofluids

Geothermal Systems: Interdisciplinary Approaches for an Effective Exploration

Lead Guest Editor: Domenico Montanari
Guest Editors: Matteo Lupi and Philippe Calcagno

Editorial Board

Contents

Hindawi
Geofluids
Volume 2019, Article ID 9895659, 3 pages
https://doi.org/10.1155/2019/9895659

Editorial

Geothermal Systems: Interdisciplinary Approaches for an Effective Exploration

Domenico Montanari [1] **Matteo Lupi** [2] **and Philippe Calcagno** [3]

[1] National Research Council of Italy (CNR), Florence, Italy
[2] Department of Earth Sciences, University of Geneva, Geneva, Switzerland
[3] Georesources Division, BRGM, Orléans, France

Correspondence should be addressed to Domenico Montanari; domenico.montanari@igg.cnr.it

Received 7 February 2019; Accepted 7 February 2019; Published 18 June 2019

The main goal of geothermal exploration is to identify favourable reservoirs that may be exploited for energy extraction. While drilling is the only direct method to access the subsurface structure of a given system (and its physical state), various techniques have been developed to investigate the targeted reservoir before drilling [1]. The most reliable methods for investigating geological structures at depth are geological field observations, structural geology, exhumed analogues, and geophysical methods. Parameters such as temperature or permeability can be inferred mainly from hydrogeological, geochemical, petrographic, or geophysical investigations. The information retrieved from each of these methods is a piece of a complex puzzle. Gathering and combining these pieces is the key for a comprehensive interpretation of the investigated system [2–8]. That is why, as much as possible, data coming from various disciplines are combined to enhance the understanding of a geothermal area. A multifaceted workflow is the most envisaged approach to understand the dynamics driving fluid flow at depth. However, the more data are available the more complex is the interpretation. This is because geothermal systems are characterized by the interaction of complex nonlinear physical process.

Despite the difficulties, geothermal exploration is increasingly focusing on the extensive integration of multidisciplinary data. This combined approach is leading to a new and reliable exploration and assessment process, able to determine a significant risk reduction. Furthermore, production technology is constantly evolving. Recent technological developments have significantly improved plant efficiency and performance creating new targets for exploration and revised approaches to focus them better.

This special issue contains 13 studies focusing on the interplay between different exploration approaches, reservoir characterization, and numerical models implemented throughout the various phases of geothermal exploration until the definition of the exploitation strategy.

One of the papers F. F. Amanda et al. of this special issue addresses the potential of geothermal resources beneath calderas by means of melt inclusion analysis. F. F. Amanda et al. studied the interaction between crustal fluids in the exploited reservoirs investigating the Miocene Fukano Caldera, NE Japan. The authors pointed out the total amount of fluids stored in the magmatic reservoir fuelling the ongoing geothermal system. This led to an estimation of the available electric energy equivalent of about 45 GW over 30 years of power generation.

One of the tools to guide geothermal exploration are favourability maps that can help to target promising areas. In that scope, A. Santilano et al. developed a methodology for geopressured geothermal resource, an unconventional system in sedimentary basins. Their analysis is based on the use of geological and hydrothermal 3D models to cross several parameters that play a role in the detection of prospective zones. The approach is demonstrated in the central part of Italy, on the Adriatic coast.

J. M. Marques et al. adopt an interdisciplinary approach to investigate the Chaves geothermal system in Northern Portugal. This setting is characterized by low temperatures and an abundant emission of carbon dioxide. Geochemical analyses of sampled fluids pointed out an upper mantellic origin of the sampled CO_2 emissions. J. M. Marques et al. combined these observations with geophysical studies to better describe the geothermal processes occurring at depth.

M. Zentilli et al. present a study about the past and present day hydrology and genesis of some fascinating saline springs that are claimed to be the most northerly on Earth, in the Canadian Arctic Archipelago. This paper reviews and updates descriptive features of the perennial springs and compares their mineralogy, geochemistry, and geology to some vein array which is interpreted as a hydrothermal predecessor of the springs. Authors suggest that the perennial springs are related to deep plumbing systems established by expulsion of overpressured fluids from salt structures (diapirs) at depth. The conduit system was finally proposed as a viable analogue environment for the establishment of microbial life in similar situations on other planets.

L. R. Pastoriza et al. present the results of a structural field study addressing tectonic elements in the Negros geothermal field, Philippine archipelago, providing a valuable example highlighting the importance of careful structural analysis in geothermal exploration. This work illustrates how a strongly field-based geological approach can inform exploration and eventual development strategies for drilling, even at the early stages of the field exploration (i.e., even prior to drilling), becoming certainly powerful when integrated with geochemical, geophysical, and hydrological data.

B. Walter et al. integrated structural interpretation of remote sensing images, field work, and geochemistry to determine the role of the different regional structural features that may control different fluid outflow zones, as well as the nature and the source of the different fluids along a rift zone in western Uganda. This study therefore documents the complexity of a composite hydrogeological system hosted by a major rift-bounding fault system, to the recognition of structural intersections as prime targets for exploration of fault-controlled geothermal systems.

C. Dezayes et al. focused on the paleocirculation at the Hercynian basement/sedimentary cover interface. The main purpose was to understand the behavior of the fracture-fault network and the origin of the hydrothermal fluids by means of a multidisciplinary approach based on the study of fracture-fault network orientation, mineral fillings, and fluid origins.

Remaining in the Upper Rhine Graben study area, J. Freymark et al. used a data-based 3D structural model of the central Upper Rhine Graben for 3D coupled simulations of fluid and heat transport. To assess the influence of the main faults bordering the graben on the hydraulic and the deep thermal field, the authors carried out a sensitivity analysis on fault width and permeability, evaluating the implications for the deep temperature distribution.

In their paper, T. Mackowski et al. discuss the importance of seismic methods during the geothermal exploration phase. In particular, the seismic interpretation provides not only information about the geometry of the geothermal reservoir but also relevant petrophysical figures such as porosity. The authors rely on a case study in the central part of Poland, already known for its geothermal potential and exploitation, to demonstrate the benefits of seismic survey.

R. de Franco et al. illustrate the use a synthetic seismic reflection modelling approach to investigate the structure of a geothermal system characterized by supercritical fluids. Specifically, the authors provide an interpreted image of the debated K-horizon at the Larderello-Travale geothermal field, Italy, by integrating geological and geophysical data. R. de Franco et al. use two geophysical models to study numerically the seismic response of the K-horizon. Their investigation points out that a "physically perturbed layer" best explains the reflectivity signals observed on the active reflection seismic profiles imaging the K-horizon.

M. Osvald et al. investigate the field of possible technologies for the exploitation of metal-bearing geological formations with geothermal potential at depths of 3–4 km or deeper. The authors describe laboratory leaching experiments aimed at quantifying the relative rates and magnitudes of metal release and seeing how these vary with different fluids. The results are intended to use for upscaling to reservoir scale and calculate likely dissolved loads achievable, given reaction rates and solubility of the various elements involved. In this study, the first steps were described to ensure the sustainability of the proposed technology: in the frame of the coproduction of energy and metals that would be possible and could be optimized according to market demands in the future.

Fluid scaling is an important issue that can hamper geothermal use. A. Varga et al. study the matter by combining geology, mineralogy, and chemistry to analyse the process leading to carbonate scaling in a zone of the Pannonian basin in Hungary. They break down the causes of the phenomenon and proposes a multifactor explanation that could be used in other areas, especially during exploration to assess the potential risk of cementation related to the geothermal fluid.

F. Li et al. developed a numerical optimization of the exploitation parameters through a 1D-3D fluid and heat transport model based on existing well data. They assessed energy production in a geothermal doublet in eastern Tianjin (China) to make the production as sustainable as possible, preventing the resource from heat breakthrough. Even if this work focuses on the exploitation, it can also help to forecast the location of wells to develop a geothermal sector.

Conflicts of Interest

The editors declare that they have no conflicts of interest regarding the publication of this special issue.

Domenico Montanari
Matteo Lupi
Philippe Calcagno

References

[1] Ó. G. Flóvenz, G. P. Hersir, K. Sæmundsson, H. Ármannsson, and Þ. Friðriksson, "7.03 - Geothermal Energy Exploration Techniques," in *Comprehensive Renewable Energy*, A. Sayigh, Ed., vol. 7, pp. 51–95, Elsevier, Oxford, 2012.

[2] P. Calcagno, "3D GeoModelling for a democratic geothermal interpretation," in *Proceedings of World Geothermal Congress 2015 (WGC2015)*, pp. 19–25, Melbourne, Australia, April 2015.

[3] P. Calcagno, C. Baujard, L. Guillou-Frottier, A. Dagallier, and A. Genter, "Estimation of the deep geothermal potential within the Tertiary Limagne basin (French Massif Central): an integrated 3D geological and thermal approach," *Geothermics*, vol. 51, pp. 496–508, 2014.

[4] S. Higuchi, J. Nishijima, and Y. Fujimitsu, "Integration of geothermal exploration data and numerical simulation data using GIS in a hot spring area," *Procedia Earth and Planetary Science*, vol. 6, pp. 177–186, 2013.

[5] D. Montanari, A. Minissale, M. Doveri et al., "Geothermal resources within carbonate reservoirs in western Sicily (Italy): a review," *Earth-Science Reviews*, vol. 169, pp. 180–201, 2017.

[6] Y. Noorollahi, R. Itoi, H. Fujii, and T. Tanaka, "GIS integration model for geothermal exploration and well siting," *Geothermics*, vol. 37, no. 2, pp. 107–131, 2008.

[7] L. Shako and J. Mutua, "Geo-scientific data integration to evaluate geothermal potential using GIS," in *Proceedings, Kenya Geothermal Conference, Kenyatta International Conference Centre*, p. 7, Nairobi, 2011.

[8] J. D. Witter and N. Phillips, "Integrated 3D geophysical inversion and geological modelling for improved geothermal exploration and drillhole targeting," *GRC Transactions*, vol. 36, pp. 831–834, 2012.

Hindawi
Geofluids
Volume 2019, Article ID 9502904, 33 pages
https://doi.org/10.1155/2019/9502904

Research Article

Paleo-Hydrothermal Predecessor to Perennial Spring Activity in Thick Permafrost in the Canadian High Arctic, and Its Relation to Deep Salt Structures: Expedition Fiord, Axel Heiberg Island, Nunavut

Marcos Zentilli,[1] Christopher R. Omelon,[2] Jacob Hanley,[3] and Darren LeFort[3]

[1]*Department of Earth Sciences, Dalhousie University, Halifax, Nova Scotia, Canada*
[2]*Department of Geology, University of Kansas, Lawrence, Kansas, USA*
[3]*Department of Geology, Saint Mary's University, Halifax, Nova Scotia, Canada*

Correspondence should be addressed to Marcos Zentilli; zentilli@dal.ca

Received 8 June 2018; Accepted 10 October 2018; Published 2 June 2019

Academic Editor: Domenico Montanari

It is surprising to encounter active saline spring activity at a constant 6°C temperature year-round not far away from the North Pole, at latitude 79°24′N, where the permafrost is ca. 600 m thick and average annual temperature is -15°C. These perennial springs in Expedition Fiord, Queen Elizabeth Islands, Canadian Arctic Archipelago, had previously been explained as a recent, periglacial process. However, the discovery near White Glacier (79°26.66′N; 90°42.20′W; 350 m.a.s.l.) of a network of veins of hydrothermal origin with a similar mineralogy to travertine precipitates formed by the springs suggests that their fluids have much deeper circulation and are related to evaporite structures (salt diapirs) that underlie the area. The relatively high minimum trapping temperature of the fluid inclusions (avg. ~200 ± 45°C, 1σ) in carbonate and quartz in the vein array, and in quartz veins west of the site, explains a local thermal anomaly detected through low-temperature thermochronology. This paper reviews and updates descriptive features of the perennial springs in Expedition Fiord and compares their mineralogy, geochemistry, and geology to the vein array by White Glacier, which is interpreted as a hydrothermal predecessor of the springs. The perennial springs in Axel Heiberg Island are known for half a century and have been extensively described in the literature. Discharging spring waters are hypersaline (1-4 molal NaCl; ~5 to 19 wt% NaCl) and precipitate Fe-sulfides, sulfates, carbonates, and halides with acicular and banded textures representing discharge pulsations. At several sites, waters and sediments by spring outlets host microbial communities that are supported by carbon- and energy-rich reduced substrates including sulfur and methane. They have been studied as possible analogs for life-supporting environments in Mars. The vein array at White Glacier consists of steep to subhorizontal veins, mineralized fractures, and breccias within a gossan area of ca. 350×50 m. The host rock is altered diabase and a chaotic matrix-supported breccia composed of limestone, sandstone, and anhydrite-gypsum. Mineralization consists of brown calcite (pseudomorph after aragonite) in radial aggregates as linings of fractures and cavities, with transparent, sparry calcite and quartz at the centre of larger cavities. Abundant sulfides pyrite and marcasite and minor chalcopyrite, sphalerite, and galena occur in masses and veins, much like in base metal deposits known as Mississippi Valley Type; their weathering is responsible for brown Fe oxides forming a gossan. Epidote and chlorite rim veins where the host rock is Fe- and Mg-rich diabase. The banded carbonate textures with organic matter and sulfides are reminiscent of textures observed in mineral precipitates forming in the active springs at Colour Peak Diapir. Very small fluid inclusions (5-10 μm) in two generations of vein calcite (hexagonal, early brown calcite we denominate "cal1" lining vein walls; white-orange sparry calcite "cal2" infilling veins) have bulk salinities that transition between an early, high-salinity end-member brine (up to ~20 wt% NaCl equivalent) to a later, low-salinity end-member fluid (nearly pure water) and show large fluctuations in salinity with time. Inclusions that occupy secondary planes and also growth zones in the later calcite infilling (deemed primary) have T_h ranging from 100°C to 300°C ($n = 120$, average~200°C; independent of salinity), 2 orders of magnitude higher than average discharging water temperatures of 6°C at Colour Peak Diapir. Carbon isotope composition ($\delta^{13}C_{VPDB}$) of the White Glacier vein array carbonates ranges from approximately -20 to -30‰, like carbonates formed by the degradation of petroleum, whereas carbonates at Colour Peak Diapir springs have a value of -10‰. Oxygen isotope composition ($\delta^{18}O_{VSMOW}$) of vein carbonates ranges from -0.3‰ to +3.5‰, compatible with a coeval fluid at 250°C with a composition from -3.5‰ to -7.0‰. These data are consistent with carbonates having precipitated from mixtures of heated formational waters and high-latitude meteoric waters. In contrast, the $\delta^{18}O_{VSMOW}$ value for carbonates at Colour Peak Diapir springs is +10‰, derived from high-latitude meteoric waters at 6°C. The sulfur isotope ($\delta^{34}S_{VCDT}$) composition of Fe-sulfides at the perennial springs is +19.2‰, similar to the $\delta^{34}S_{VCDT}$ of Carboniferous-age sulfate of the diapirs and consistent with low-temperature microbial reduction of finite (closed-system) sulfate. The $\delta^{34}S_{VCDT}$ values of Fe-sulfides in the vein array range from -2.7‰ to +16.4‰, possibly reflecting higher formation temperatures involving reduction of sulfate by organics. We suggest that the similar setting, mineralogical compositions, and textures between the hydrothermal vein array and the active Colour Peak Diapir springs imply a kinship. We suggest that overpressured basinal fluids expelled from the sedimentary package and deforming salt bodies at depth during regional compressional tectonic deformation ca. 50 million years ago (Eocene) during what is known as the Eurekan Orogeny created (by hydrofracturing) the vein array at White Glacier (and probably other similar ones), and the network of conduits created continued to be a pathway around salt bodies for deeply circulating fluids to this day. Fluid inclusion data suggest that the ancient conduit system was at one point too hot to support life but may have been since colonized by microorganisms as the system cooled. Thermochronology data suggest that the hydrologic system cooled to temperatures possibly sustaining life about 10 million years ago, making it since then a viable analogue environment for the establishment of microbial life in similar situations on other planets.

1. Introduction

The presence in a polar region of active saline springs at constant ca. 6°C temperature year-round, where average temperature is -15°C [1] and continuous permafrost is 600 m thick, is astonishing. This is the case in western Axel Heiberg Island (Figure 1), Queen Elizabeth Islands, Canadian Arctic Archipelago, at latitude 79°24′N (e.g. [2–4]). The perennial springs (hereforth PSS) are situated in the periphery of evaporite diapirs (bodies of salt, anhydrite, and gypsum) that underlie the Expedition Fiord area (Figures 2 and 3(a)) and have risen over time as a ductile solid from their ultimate source in beds at ca. 10 km depth in the Sverdrup sedimentary basin (Figure 1; e.g., [5, 6]). The springs have been attributed to Quaternary periglacial processes (e.g., [7]). However, during a regional study of the uplift and thermal history of the archipelago using apatite fission-track thermochronology [8–10], it was noticed that the area where the PSS occur at the head of Expedition Fiord cooled to ca. 100°C between 20 and 30 million years later than the rest of the region (Figure 4). This realization led to a search for evidence for the pervasive circulation of warm fluids in the area in the form of veins with minerals amenable to fluid inclusion studies. In 2006, a network or array of mineral veins of hydrothermal origin was identified adjacent to White Glacier (Figures 2 and 3(b)). The White Glacier vein array (hereforth WGVA) is accompanied by a colourful gossan arising from the weathering of base metal (Fe, Cu, Zn, and Pb) sulfides and is the subject of this paper. We first update the descriptive features of the local PSS and then compare the WGVA with the prominent Colour Peak Diapir, ~13.7 km distant (Figures 2 and 3(a)), and two other PSS at Expedition Diapir and Wolf Diapir in terms of mineralogy, fluid inclusion systematics, and geochemistry, including stable O, C, and S isotope compositions. Based on the above studies and the literature, we conclude that the PSS have a kinship with the WGVA and the latter owes its existence to focussed expulsion of overpressured, hot, basinal fluids from an evaporite-dominated basement during tectonic compression known as the Eurekan Orogeny predominantly during the Eocene [11, 12]. The WGVA thus may represent the establishment of a plumbing system that has been later exploited by the PSS. The WGVA also is evidence for a regional metallogenic process that may have formed mineral concentrations elsewhere.

Permafrost at high latitudes is traditionally considered to effectively separate groundwater flow systems into two zones: a shallow, supra-permafrost zone that is active during summer months when air temperatures exceed 0°C and a sub-permafrost region that is hydrologically disconnected from the Earth's surface [13]. The impervious nature of continuous permafrost means that such systems are poorly understood [14]; having a window into the subsurface through groundwater spring activity, therefore, provides a rare opportunity to further our understanding of hydrologic activity in polar environments, to explore life beneath permafrost, and to improve our appreciation of the potential for bioavailable water and subsurface life to exist on other planets such as Mars [15–18]. The update of data on these anomalous polar springs and new interpretation of their process is a contribution to the understanding of geothermal systems in salt-dominated terrains.

2. Geological Setting

The perennial springs and WGVA lie within a relatively small area of the extensive (1000 km by 350 km) Sverdrup Basin (Figure 1), which contains a thickness of over 13 km of sedimentary and volcanic rocks ranging in age from Carboniferous to Tertiary [19]. The basin has been extensively explored for petroleum [20], although the wells in the eastern Sverdrup Basin have been disappointing and are more likely to produce gas than oil, due to the intervention of tectonism and the thermal effects of igneous intrusions [21]. The geology of the Expedition Fiord area (Figure 2) was initially mapped during the Jacobsen-McGill Arctic Research Expedition (1959-1962), among others by Tozer [22], Thorsteinsson and Tozer [23], and Fricker [24]. The evaporite diapirs were described by Hoen [25, 26]. A new map of the area including both Expedition Fiord and Strand Fiord was produced by Harrison and Jackson [27] and salt-induced structures reinterpreted by Jackson and Harrison [6]; their latter paper provides a valuable geological introduction to this study. The oldest rock unit exposed in the

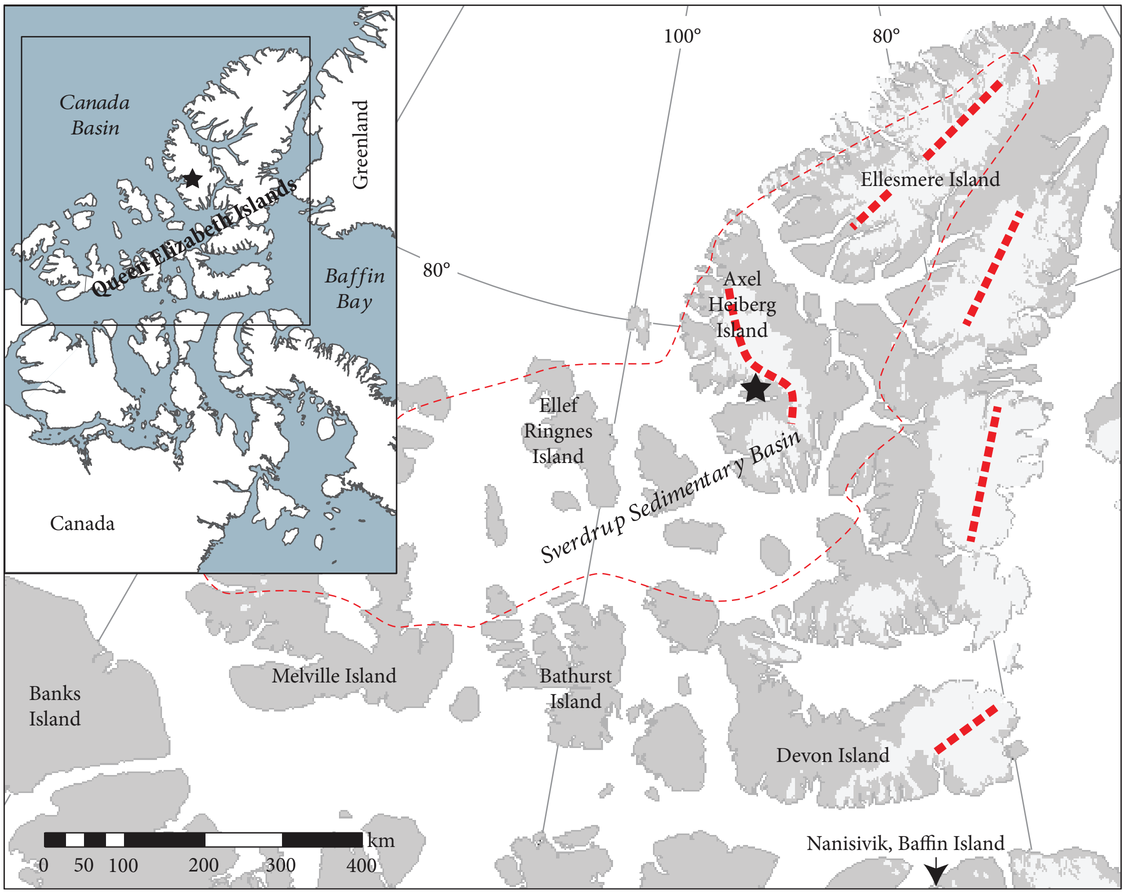

Figure 1: Location map of the White Glacier site (star) in Axel Heiberg Island, Queen Elizabeth Islands, Canadian Arctic Archipelago. Icefields are light grey, generally capping 1500–2000 m high mountains (dotted lines). The dashed line outlines the Sverdrup Basin with a thickness of up to 12 km of Paleozoic to Paleogene sedimentary and volcanic rocks, including Carboniferous salt beds at depth and diapiric salt-anhydrite-gypsum structures that reach the surface.

immediate area is allochthonous gypsum and anhydrite of the Otto Fiord Fm. of Lower Carboniferous age (in red in Figure 2), contained in diapiric bodies [5]. Ductile salt and evaporites rose and intruded the thick (12-15 km) sedimentary succession of the Sverdrup Basin [5]. The oldest exposed stratified rocks are Upper Permian to Middle Jurassic marine sandstones and shales, overlain by Jurassic to Cretaceous sandstones and limestones. The Mesozoic succession contains extensive volcanic units of basalt and sets of intrusive sills and dikes of diabase (intrusive basalt) of middle Cretaceous age (^{40}Ar-^{39}Ar dates from 129 to 80 Ma; [28]). The evaporite diapirs also contain rafts of diabase (Figure 2). Further afield are Cenozoic sediments of Paleocene to Eocene age, some disrupted by the mechanically intrusive evaporite diapirs, which may be actively rising [29]. Quaternary deposits consist of glacial and fluvial gravels and sands.

2.1. Eurekan Orogeny. The Paleozoic to Paleocene strata of the Sverdrup Basin were folded during the Paleogene Eurekan Orogeny into irregular synclines and anticlines with wavelengths of ca. 5 to 10 km. Distorted ramparts of diapiric anhydrite crop out in the cores of tight anticlines, and wider synclinal basins separate the diapiric walls. The most prominent faults are N-S, east-verging thrust faults that are interpreted by Jackson and Harrison [6] to be rooted in an evaporite canopy (extruded subhorizontal salt-anhydrite sheet) at depth. Important is a thrust fault south of Thompson Glacier at the head of Expedition River (rightmost side of Figure 2), which places Upper Permian rocks (Blind Fiord Fm.) and Carboniferous evaporite over Jurassic and Cretaceous strata. In addition, there are intermediate faults north of Expedition Diapir and Colour Peak Diapir, and the WGVA site is located at the intersection of a major WNW fault and a diabase intrusion of Cretaceous age (Figure 2). Minor faults and shattered zones (not indicated in Figure 2) abound around the evaporite diapirs, especially where ductility contrasts exist, such as between mafic igneous rocks and sedimentary rocks.

2.2. Wall and Basin Structure. Evaporite diapirs are conspicuous features in the Expedition Fiord area [25, 26]; they are clustered and irregular in shape, some forming walls and slivers [27]. Three clusters are identified in the local area from west to east: Colour Peak Diapir, Expedition Diapir (Gypsum Hill – Little Matterhorn Diapir), and a sliver east of Thompson Glacier (Figure 2). Early workers called the complexly folded region intermixed with encroaching diapirs a "wall-and-basin structure" (WABS; [30]). Schwerdtner and

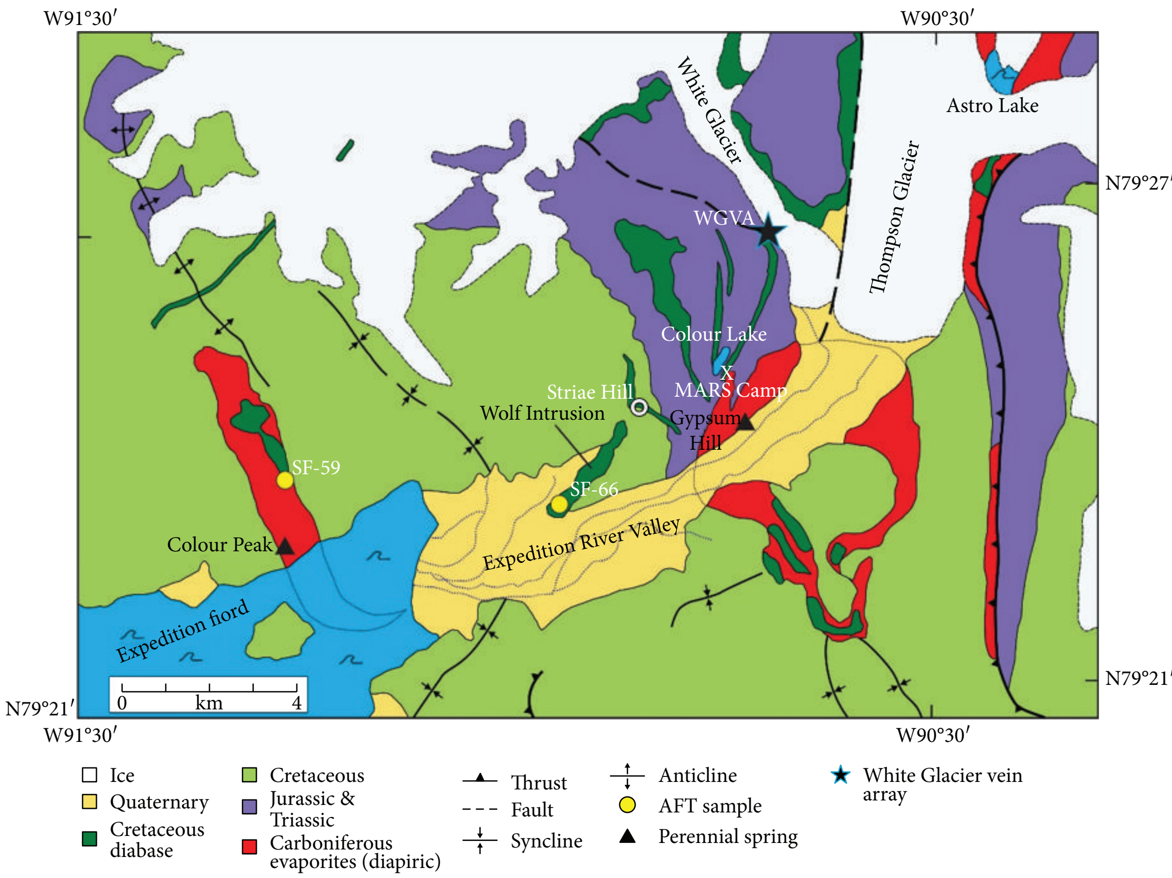

Figure 2: Generalized geological map showing the location of the White Glacier vein array site (black star) in relation to perennial springs (black triangles) and evaporite diapirs (red); purple and light green units are predominantly sedimentary strata of Mesozoic age; igneous mafic sills and dikes are dark green. Location of apatite fission track samples in Wolf Intrusion and Colour Peak marked as filled yellow circles. Fluid inclusion Striae Hill sample marked by white ring. MARS Camp (McGill Arctic Research Station - X) was used as field base. Geology modified from Harrison and Jackson [27].

Van Kranendonk [31] described this feature as "crooked walls of diapiric anhydrite contained in folded clastic rocks." The diapirs occupy the cores of narrow polygonal to oval anticlines. Jackson and Harrison [6] proposed that this restricted WABS province resulted from the development of a coalescing layer or canopy of evaporite rocks during the early Cretaceous; these evaporitic rocks would have plastically spread laterally and formed at depth the roots of now-exposed secondary diapirs created during compression, thrusting, and folding in the Paleogene (mainly Eocene) Eurekan Orogeny.

2.3. Diapirs and Springs. At the surface, the diapirs are composed of anhydrite with a carapace of porous gypsum with blocks of anhydrite, but they are known to have halite at depth from exploration drilling [32] and the presence of exposed halite at Stolz Diapir, located on southeastern Axel Heiberg Island [31]. Despite their susceptibility to erosion and the fact that they disrupt Quaternary deposits, their positive topographic relief (Figure 2) suggests continuing growth, which is being evaluated with satellite interferometry [29]. The position of perennial spring activity adjacent to or within evaporite structures led Nassichuk and Davies [32] to suggest an essential relationship between them.

2.4. Glaciers. The highlands of Expedition Fiord host the Müller Ice Cap, the largest on Axel Heiberg Island, crowning the Princess Margaret Range (2210 m.a.s.l.), ca. 40 km north of the area shown in Figure 2. One of the large outlet glaciers descending from it is the Thompson Glacier (Figure 2), spanning ~34 km in length and ~3 km wide in the ablation area. It dams several lakes, including Astro Lake (upper right corner of Figure 2) and Phantom Lake (2 km east of Astro Lake, outside Figure 2), and meets the White Glacier terminus at 80 m.a.s.l. (cf. [33]). White Glacier is a valley glacier occupying 38.5 km^2, extending from an elevation of 80 m at its present terminus to its source on the mountains to the west at ca. 1782 m.a.s.l.; ice thickness exceeds 400 m in the deepest basins, and the glacier has thinned by approximately 20 m in the vicinity of the WGVA outcrop since 1960 [34]. Glacial activity has resulted in the carving of steep walls into Triassic-Jurassic sedimentary rocks, which in combination with contemporary thinning has exposed the array of hydrothermal veins described here.

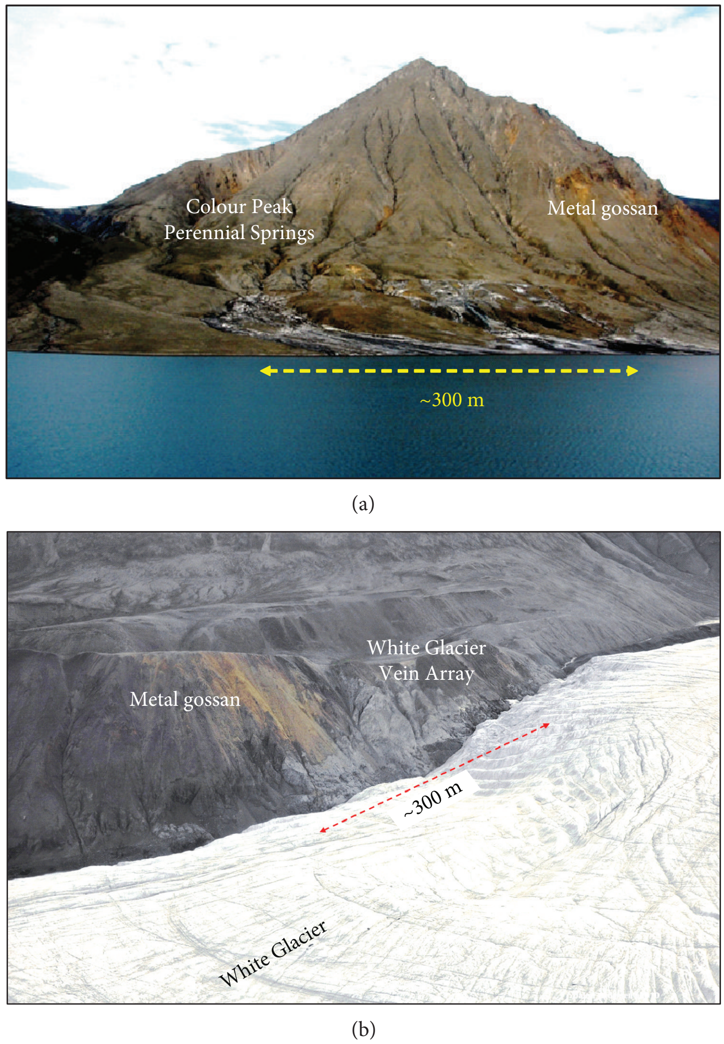

Figure 3: (a) Aerial view of travertine deposits at Colour Peak perennial springs (CPS), northern shore of Expedition Fiord, that emit brines at 6°C year-round. The 560 m hill is gypsum and anhydrite, but the colourful gossan denotes weathered iron sulfides associated with rafts of igneous mafic rocks. (b) Aerial view of the whitish vein array (WGVA) on the steep flank of White Glacier, also associated with a gossan (photo by Dale Andersen). Note the similar scale of the two phenomena.

3. Procedures

3.1. Field Work. Foot traverses by M.Z. were undertaken (2006) in the search for any evidence of hydrothermal activity that might help explain the anomalous thermal history results of the area (Table 1). A NE-trending ridge 2 to 3 km NE of the McGill Arctic Research Station (MARS camp, Figure 2), composed of diabase, shows evidence of alteration and gossans derived from oxidation of iron sulfides; the hydrothermal development described here (Figure 3(b)) was found at the intersection of the rusty ridge with White Glacier, which also coincides with the trace of a prominent fault or shear zone (Figure 2). Samples representing the various styles of mineralization were collected (2006, 2009) and prepared as double-polished thin sections (Dalhousie University). Carbonate deposits and fine-grained sediments associated with perennial spring discharge at Colour Peak Diapir (CPS) were collected by C.O. (2011, 2012). Carbonates were prepared as double-polished thin sections (Department of Earth Sciences, Western University); sediments were stored in native spring waters in air-tight serum vials capped with rubber stoppers until analysis.

3.2. Electron Microprobe. Wavelength-dispersive spectroscopic (WDS) electron microprobe analysis (EMP) on WGVA thin sections was completed at the R. MacKay Microprobe Laboratory (Department of Earth Sciences, Dalhousie University) using a JEOL 8200 microprobe operated at an accelerating voltage of 15 kV and a beam current of 20 nA and using a focussed beam (10 s on peak and 10 s off peak counting times; spot size < 1 μm). Qualitative energy-dispersive spectroscopy (EDS) was used initially for confirmation of optical microscopic phase identification.

3.3. X-Ray Fluorescence Mapping. Thin sections from both WGVA and CPS were analyzed by C.O. for trace elements by X-ray fluorescence mapping (μ-XFM) using synchrotron radiation (Advanced Photon Source, Argonne National

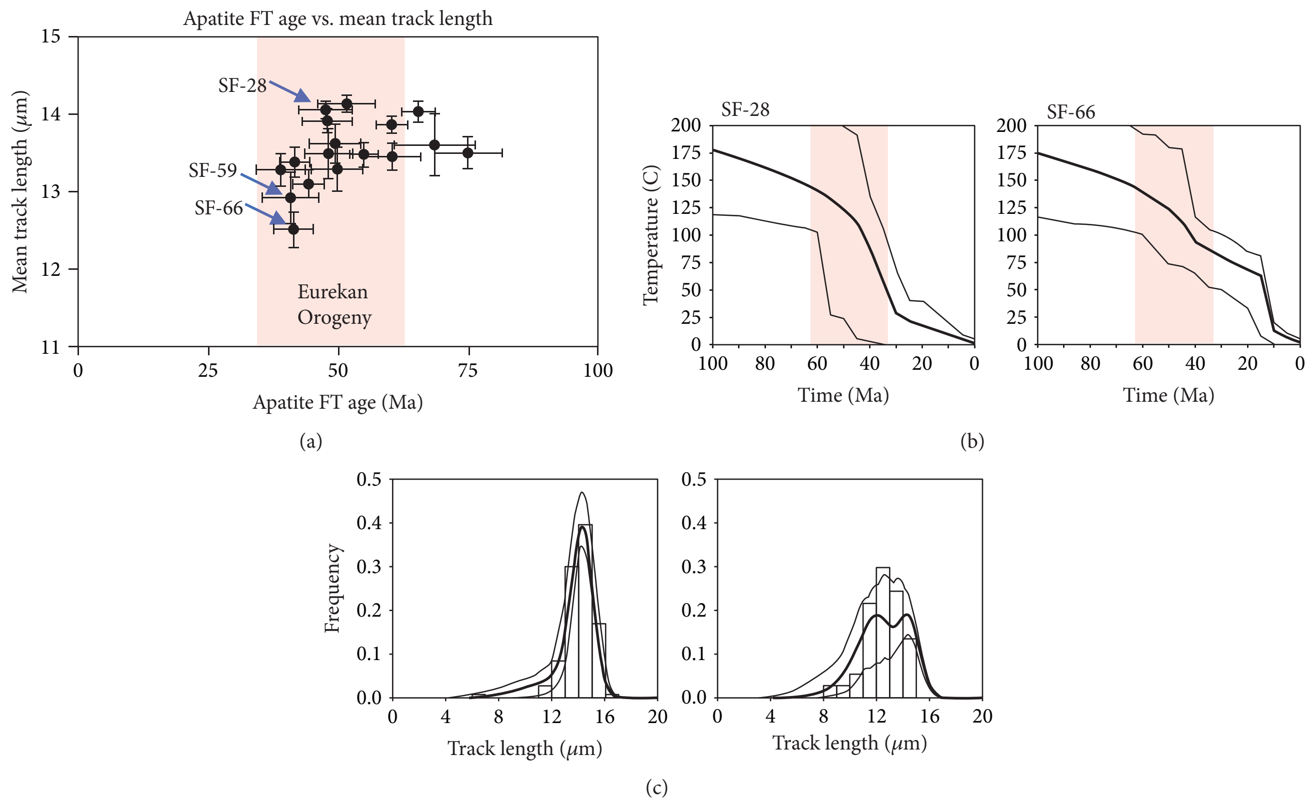

FIGURE 4: (a) Plot of Apatite Fission Track Age vs. Mean Track Length for samples in the Expedition Fiord area. Note the extreme position in the plot of samples FT-59 and FT-66, from within the area of PSS (see Figure 2). (b, c) Monte Carlo inverse thermal history models for Sverdrup Basin AFT samples using AFTINV [82, 83]. The internally consistent models are compatible with the interpretation that whereas rocks now at the surface in the Princess Margaret Range (60 km to the northeast of Expedition Fiord) cooled rapidly after the Eurekan Orogeny (62 to 33 Ma), rocks in the area of the PSS maintained temperatures of up to 75°C until the Miocene. Note: all models were done using the annealing model of [48]. The middle panels show the upper and lower bounds of time-temperature solution space explored by the 250-300 acceptable model solutions (defined by a K-S goodness of fit statistic) as well as the exponential mean solution, or preferred model (thicker line). The lower panels show the measured length histograms and the exponential mean probability distributions, as well as the upper and lower bounds of the model distributions in the solution set (note that the upper and lower bounds themselves are not solutions). 5 My time steps were used, with new populations of unannealed tracks introduced at 1 My intervals. See text for discussion. Data summary in Table 1.

Laboratory). Incident X-rays passed through a Si 111 monochromator on an insertion device (ID) at 13.5 keV to excite elements up to Pb. The incident beam was focussed to 5 μm × 5 μm using a Kirkpatrick-Baez mirror assembly. Spatially resolved XFM analyses were conducted over specific regions of interest in the samples, which were mounted 45° to the incident beam. The fluorescence X-rays were measured using a 12-element Canberra Ge (Li) detector. The fluorescence X-ray intensity was normalized by the intensity of the incident X-ray beam, and spectral analysis of the fluorescence spectrum of each pixel used to produce two-dimensional maps for each element analyzed.

3.4. Scanning Electron Microscopy. Thin sections and sediments from CPS were analyzed by C.O. by scanning electron microscopy (SEM) at the Western Nanofabrication Facility (Western University) using a LEO (Zeiss) 1540XB FIB/SEM with secondary electron (SE), backscattered electron (BSE), and in-lens detectors. Thin sections were coated with ~5 nm osmium metal, whereas sediments were initially washed in ddH_2O and air-dried before coating with osmium. Samples were imaged at 1-2 keV at a working distance of 4-6 mm. Areas targeted for focussed ion beam (FIB) milling were coarse-milled at 10 nA followed by polishing at 1 nA using Ge at 30 keV. Sediments were also examined by transmission electron microscopy (TEM) at the Biotron (Western University) using a Philips EM 300 TEM. Samples were imaged as wet mounts on carbon-coated Cu grids at 80 keV.

3.5. Confocal Raman Spectroscopy. Confocal laser Raman microspectroscopy (LRM) was used to determine the composition of carbonate minerals, specifically to differentiate between aragonite and calcite polymorphs. LRM analysis was performed by J.H. using a Horiba Jobin-Yvon LabRam HR system at Saint Mary's University. The instrument is equipped with a 100 mW 532 nm Nd-YAG diode laser (Toptica Photonics) and a Synapse charge-coupled device (CCD; Horiba Jobin-Yvon) detector. Pure silicon was used as a frequency calibration standard. Spectra were collected using an 80 μm confocal hole diameter, and a 600-groove/mm grating (spectral resolution of approximately ±2 cm^{-1}). Spectra were

Table 1: Apatite fission track data used for Figure 4.

		Age data								Length data		
Sample number	Grains counted	Rho_s	N_s	Rho_i	N_i	χ^2	Rho_d	N_d	Age ± error (Ma, 1σ)	No. of tracks	Mean ± error (μm, 2σ)	Std. dev. (μm)
ft03-038 SF-16	28	0.168	196	0.423	495	98	1.093	5701	75.0 ± 6.6	49	13.50 ± 0.41	1.43
ft03-041 SF-20	25	0.073	127	0.294	509	100	1.093	5701	47.9 ± 4.8	55	13.91 ± 0.31	1.16
ft03-042 SF-23	25	0.062	126	0.242	489	100	1.093	5701	49.4 ± 5.0	37	13.62 ± 0.49	1.48
ft03-046 SF-27	28	0.101	115	0.379	428	100	1.093	5701	51.6 ± 5.5	57	14.13 ± 0.21	0.79
ft03-047 SF-28	27	0.092	113	0.372	457	81	1.093	5701	47.5 ± 5.2	107	14.05 ± 0.23	1.2
ft03-048 SF-30	25	0.153	159	0.487	505	99	1.093	5701	60.4 ± 5.5	129	13.45 ± 0.33	1.88
ft03-052 SF-36	26	0.911	1299	2.65	3777	1.3	1.093	5701	65.4 ± 3.2	148	14.03 ± 0.25	0.11
ft03-055 SF-41	24	1.101	665	3.5	2114	22	1.093	5701	60.3 ± 3.0	140	13.86 ± 0.22	1.29
ft03-059 SF-47	28	0.712	563	2.49	1967	24	1.093	5701	54.9 ± 2.7	118	13.47 ± 0.32	1.77
ft03-063 SF-51	23	0.167	136	0.667	543	98	1.093	5701	48.1 ± 4.7	25	13.49 ± 0.64	1.54
ft03-067 SF-66	29	0.177	157	0.823	729	39	1.093	5701	41.4 ± 3.8	37	12.51 ± 0.45	1.36
ft04-009 SF-59	28	0.063	67	0.297	315	99	1.093	5701	40.8 ± 5.5	25	12.92 ± 0.65	1.57

A summary of the age and track length data for the Strand Fiord region. Ages reported are the central age [139]. Samples with a chi-square probability greater than 5 pass the chi-square test at the 95% confidence level (i.e., appear to be composed of one age population). N_s, N_i, and N_d are the number of spontaneous, induced, and flux dosimeter (CN-5) tracks, respectively. Rho_s, Rho_i, Rho_d are the density of spontaneous, induced, and dosimeter tracks, respectively ($\times 10^6/cm^2$). A value of 352.5 ± 7.1 (CN-5) was used for the zeta factor. Age error estimates are at the 67% (1σ) confidence level. Mean length error estimates are at the 95% (2σ) confidence level. Alexander M. Grist, Analyst.

collected using an accumulation of three, 50-60-second acquisitions with a laser spot size of ~1-2 micron at 100% laser power (~2.15 mW at sample surface). Spectra from different carbonate types were compared to those in Raman spectral libraries [35].

3.6. Fluid Inclusion Microthermometry. Fluid inclusion microthermometry and imaging was completed by J.H. and D.L. using a Linkham FTIR600 heating-freezing stage mounted on an Olympus BX51 microscope (Department of Geology, Saint Mary's University). Stage calibration was carried out using synthetic fluid inclusion standards containing pure CO_2 (melting at -56.6°C) and pure, critical-density H_2O (melting at 0°C and homogenizing at 374.1°C). Uncertainties for these measurements are ±0.2°C when a heating rate of 1°C/min is used. Final ice melting temperatures were used to calculate salinities [36] and isochoric data were determined using the SOWAT software package [37, 38].

3.7. Stable Isotopes. Pyrite, quartz, and carbonates from vein margins and infillings of the WGVA were sampled using a ~0.5 mm tungsten carbide drill bit to produce powders. These powders were analyzed at Queen's University Facility for Isotope Research (QFIR; Kingston, Ontario). Carbonates were reacted on a gas bench coupled to a Thermo Finnigan Delta Plus XP Isotope Ratio Mass Spectrometer (also using continuous flow). Oxygen from quartz was extracted using a conventional bromine pentafluoride extraction line, with the isotopes measured on a Finnigan Mat 252 Isotope Ratio Mass Spectrometer. Analytical uncertainties on the analyses are ±0.3‰ for O in silicates and ±0.2‰ for C and O in carbonates (K. Klassen, personal communication). Values are reported in the δ notation in units of per mil (‰) relative to Pee Dee Belemnite (VPDB) and Vienna Standard Mean Ocean Water (VSMOW), respectively. Stable sulfur isotope measurements were obtained using a Carlo Erba NCS 2500 elemental analyzer coupled to a Finnigan MAT 252 mass spectrometer with a Finnigan MAT Conflo 11. One sample of pyrite from the Colour Peak perennial springs was also analyzed. Values are reported in the δ notation in units of per mil (‰) relative to standard Vienna Canyon Diablo Troilite (VCDT). Replicate $\delta^{34}S_{VCDT}$ analyses are reproducible to within ±0.3‰ (K. Klassen, personal communication).

3.8. Trace Elements. Trace elements in carbonates were determined by J.H. using laser ablation inductively coupled plasma mass spectrometry (LA-ICP-MS) at the Swiss Federal Institute of Technology (ETH Zurich). Aerosols were generated using a GEOLAS (now Coherent Inc.) 193 nm ArF excimer laser [39]. Aerosols were generated using a pulsed (10 Hz) laser beam with an energy-homogenized beam profile at a fluence of 15 J·cm^{-2} (80-90 mJ output energy) [40]. An Ar-He gas mixture (He 1.15 L/min; Ar 0.8 L/min) carried sample aerosols into an ELAN 6100 quadrupole ICP-MS using similar conditions as Pettke et al. [41]. Oxide production rates were maintained below 0.3%. Mass spectrometer dwell time was set to 10 ms for all masses measured. Quantification of trace element concentrations was performed using the software SILLS [42]. The standard reference glass 610 from NIST was used to calibrate analyte sensitivities. Stoichiometric Ca (40 wt %) was used as the internal standard value as carbonates were determined to be ~$CaCO_3$ with minor impurities (<0.4 wt % total Fe + Mg + Mn).

Table 2: Summary data of the major geochemical parameters of waters collected from spring outflows (Gypsum Hill Springs, Colour Peak Springs, and Wolf Springs) and associated hydrologic measurements. Given that numerous spring outlets exist at Expedition Diapir and Colour Peak Diapir, geochemical data shown here represent the average of previously reported results. Concentrations of cations and anions are expressed in mol/kg. Q at Expedition Diapir and Colour Peak represent the sum of all outlets, whereas only one outlet exists at Wolf Diapir. N.D. = not determined. Data collected since 1997 (C.R. Omelon, MSc thesis); Pollard et al. [3]; Omelon et al. [55, 56]; Perrault et al. [64]; Niederberger et al. [63], Lay et al. [60]; Battler et al. [57].

	Expedition Diapir (GHS)	Colour Peak Diapir (CPS)	Wolf Diapir (WS)
Q (L/s)	10-15	20–25	4-5
T (°C)	6.3	6.1	-2.0
pH	7.4	6.1	5.8
ORP (mV)	-283	-312	-171
DO (%)	0.4	0.2	0.5
Salinity (%)	8	16	24
Na^+	1.15	2.01	3.28
Ca^{2+}	0.05	0.08	0.03
Mg^{2+}	0.004	0.011	0.012
K^+	0.002	0.005	0.004
Fe^{2+}	3.1×10^{-6}	1.4×10^{-5}	1.1×10^{-5}
NH_4^+	5.7×10^{-5}	2.2×10^{-4}	5.5×10^{-5}
Cl^-	1.11	2.02	3.05
SO_4^{2-}	0.09	0.08	0.11
NO_3^-	0.0014	0.0002	0.0004
HCO_3^-	0.0009	0.003	0.0005
HS^-	0.0006	6.9×10^{-5}	1.7×10^{-5}

3.9. Fission Track Thermochronology. The fission-track low-temperature thermochronological method as applied in this study at Dalhousie University has been fully explained in Grist and Zentilli [43] and references therein. It is based on the measured density and length distribution of linear tracks of crystal damage produced during spontaneous fission of trace amounts of ^{238}U. In monotonically cooling systems, track densities provide a measure of age with respect to the closure temperature, which for apatite (a U-bearing calcium phosphate) is ca. 100°C over geologically meaningful time periods on the order of 10-100 Ma. Assuming a geothermal gradient of 30°C/km, this corresponds to a burial depth of 4-5 km. It is this temperature-dependent behaviour between 60°C and ~130°C (the partial-annealing zone or PAZ) that allows the apatite FT method to be used as a low-temperature thermochronometer. Reviews of the method, its application to geological problems, and the development of FT thermal models have been provided by Wagner and Van den Haute

[44], Ravenhurst and Donelick [45], Gallagher et al. [46], and Gleadow and Brown [47]. All models were done using the Laslett et al. [48] annealing model; for the modelling, the accepted initial reduction in mean length to 15 μm was introduced (i.e., [49]). Data are shown in Figure 4 and Table 1.

4. Review of the Perennial Springs (PSS)

Examples of perennial groundwater discharge in the Canadian high Arctic have been documented at eight locations on Axel Heiberg Island [50, 51] and two on Ellesmere Island [52, 53]. While those on Ellesmere Island are linked to subglacial hydrology and geologic faults, saline perennial discharge having received the most attention occurs marginal to or near large evaporite diapirs [27] on Axel Heiberg Island, including those in Expedition Fiord (Gypsum Hill Springs, GHS; 79°24′16″N; 90°43′52″W; 98 m.a.s.l.) and Colour Peak Diapir (CPS; 79°22′51″N; 91°16′09″W; 3 m.a.s.l.) (Figures 2 and 3(a)) and nearby Strand Fiord Wolf Diapir (WS; 79°4′ 36″N; 90°12′39″W; 132 m.a.sl.), not shown in Figure 2. Waters discharge either through numerous outlets or a single point source at constant rates and temperatures [3, 51], despite a mean annual air temperature of -15°C [1] and a lowest measured temperature of –54.6°C at a nearby weather station (Eureka, Nunavut, 1979) and measured permafrost thickness of 400–600 m [54].

Discharging spring waters are hypersaline, ranging from ~1 to 4 molal NaCl (4.7-18.9 wt% NaCl) [55, 56] (Table 2). Minerals including sulfates, carbonates, and halides have been documented in association with spring discharge, which form by a variety of disequilibrium processes including evapoconcentration and CO_2 degassing [55–58]. Icings (sheet-like masses of layered ice) form in distal areas during winter months when air and water temperatures are lowest, as well as carbonate and sulfate minerals thought to precipitate by freezing fractionation [51, 59]. At several sites, waters and sediments near spring outlets host microbial communities that are supported by carbon- and energy-rich reduced substrates including sulfur and methane [60–65]. The source and activity of spring discharge at Expedition Fiord (CPS, GHS) has been generally interpreted to represent recent phenomena related to periglacial processes [7], but this model cannot account for activity at Wolf Spring, which is located south of Strand Fiord south of the area shown in Figure 2 [57].

Andersen et al. [7, 50, 66] proposed a qualitative and quantitative model for the PSS that envisioned a relatively surficial circulation of fluids, with recharge from Astro and Phantom Lakes, which are located on the eastern flank of Thompson Glacier, ~397 m above the outlet of the springs (upper right corner, Figure 2; Phantom Lake is located east of Astro Lake, just outside the map in Figure 2). The above authors assumed that the deep subsurface salt layer acts as a reservoir and conduit of water. Seasonally, the lakes drain partially (1-2%) and the water would circulate to the PSS through faults, such as the ones mapped in the area (Figures 2 and 3). Water would flow below the surface at a depth of 600-700 m via an evaporite layer, returning to the surface through the piercement structures associated with the springs. Below the surface, the water would attain the geothermal temperature (they assumed a geothermal gradient of 37.3°C/km after [54]). As it flows upward, the brines would lose heat to the surrounding permafrost.

This study brings a new perspective to the interpretation and significance of the PSS.

5. Results

5.1. Perennial Springs at Colour Peak Diapir (CPS). Confirmed perennial spring activity is observed at three locations on western Axel Heiberg Island, two of which (Colour Peak and Gypsum Hill) are shown in Figure 2. They are among the most poleward perennial springs on Earth and are the only known example of cold, nonvolcanic springs in a region dominated by continuous permafrost. The two spring sites proximal to the hydrothermal development in Expedition Fiord are located adjacent to Colour Peak Diapir (CPS) and Expedition Diapir (GHS), with the springs at Wolf Diapir (WS) occurring ~60 km to the south.

Table 2 summarizes and compares the main geochemical and hydrological characteristics of these perennial springs. Groundwater emerges from either a single outlet or numerous seeps and springs (~40 at GHS, ~30 at CPS; [57]) resulting in total site discharge flow rates of 4–25 L/s. Discharge temperatures range from~ -6°C to ~ +6°C, but a review of past work suggests that outlet temperatures have remained constant (±2°C). The outlet waters have varying pH (5.8–7.4) but with high reducing potential (-171 to -312 mV) and low dissolved oxygen (0.2–0.5%). While concentrations of ionic constituents vary between sites, the waters are all Na-Cl-type brines (8-24% NaCl) with minor concentrations of Ca^{2+}, Mg^{2+}, K^{+}, SO_4^{2-}, NO_3^{-}, and HCO_3^{-}. Low concentrations of Fe^{2+}, NH_4^{+}, and HS^{-} have been measured in the discharging waters.

A notable aspect that differentiates the CPS from GHS is elevated P_{CO2} in waters at CPS, which results in the oversaturation and subsequent precipitation of calcite (travertine) by CO_2 degassing [55]. Travertine precipitation (Figure 5(a)) in narrow valleys form channels, which were initially described as being composed of alternating light (calcite spar) and dark (anhedral microcrystalline calcite combined with organic matter and noncarbonate minerals) laminae enriched in Fe, S, Na, and Si (Figure 5(b), [55]). Synchrotron radiation-based μ-XFM mapping across several of these micritic laminae (Figure 6) confirm the presence of Fe but also detect smaller concentrations of Mn, Zn, Cu, and Ni. A closer inspection of laminae within the calcite fabric by SEM shows two kinds of micritic fabrics: microcrystalline FeS grains and abrupt boundary layers (Figures 5(c)–5(f)). FIB-SEM imaging of a region encompassing both micritic fabrics reveal trapped gas bubbles associated with cavitating brines, FeS grains embedded within the calcite matrix, and the boundary layer (Figures 5(g)–5(j)). These microcrystalline FeS grains are similar in morphology to fine-grained sediment collected at spring outlets that are composed of small (0.1 μM) aggregates of FeS microcrystals (Figures 5(k) and 5(l)).

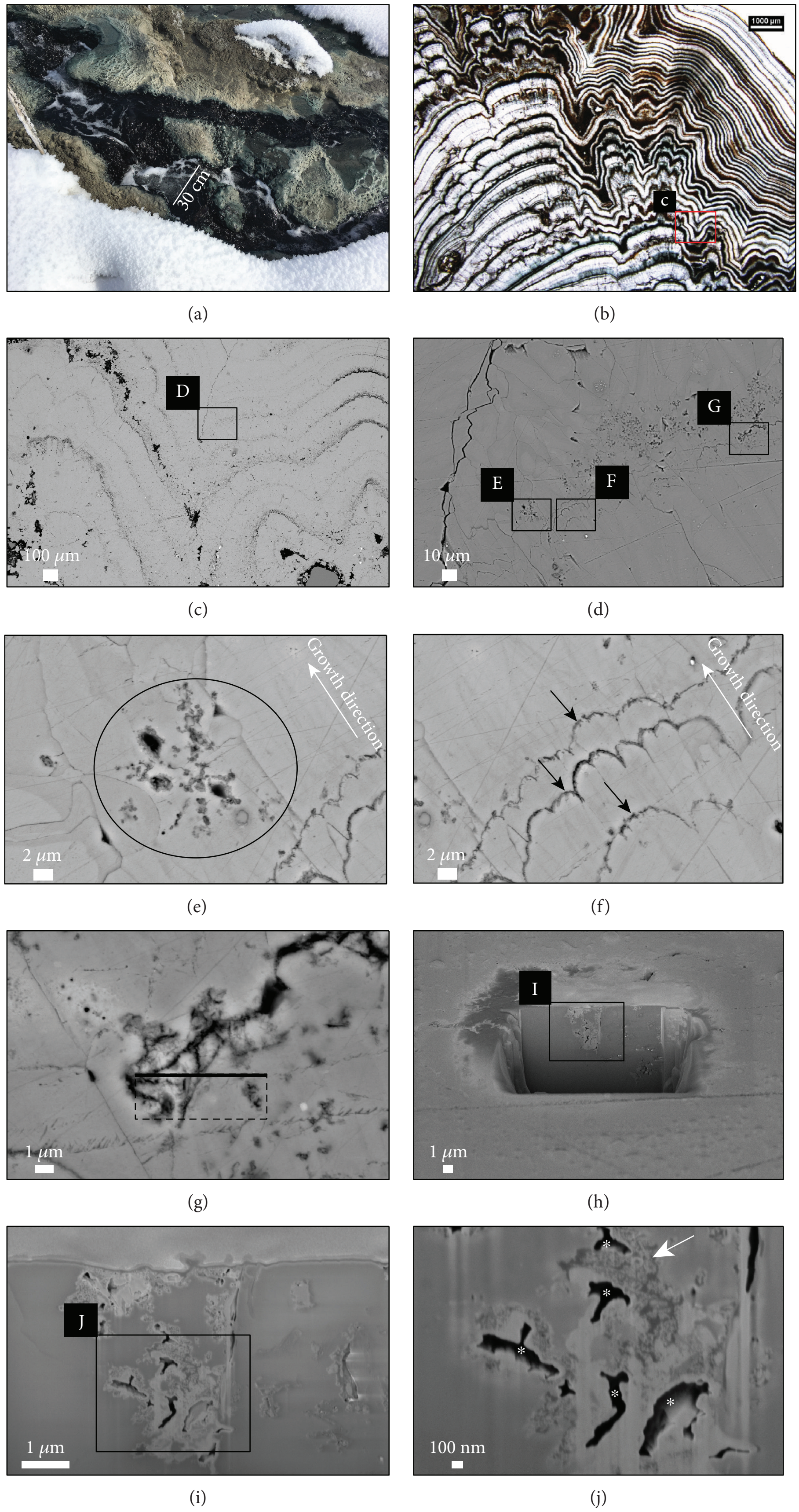

Figure 5: Continued.

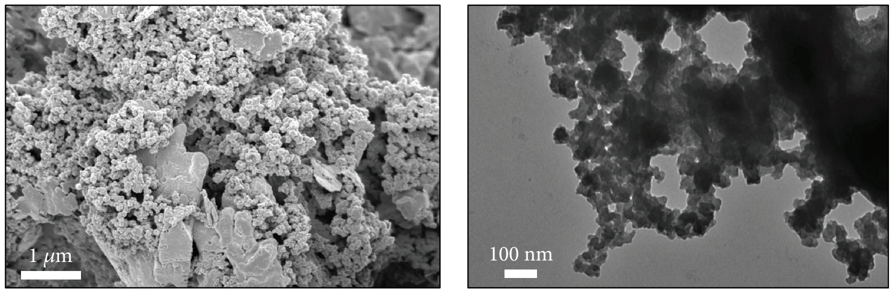

(k) (l)

Figure 5: (a) Example of channel-forming travertine at CPS. Photo taken May 2018; channel bounded by snow. (b) Double-polished thin section of channel travertine overhang showing laminated fabric. (c) SEM-BSD micrograph of area shown in (b). (d) SEM-BSD micrograph of area shown in (c). (e, f) SEM-BSD micrographs of areas shown in (d) showing two types of micritic fabrics: (e) microcrystalline grains embedded within calcite (circle) and (f) abrupt boundary layers (arrows). (g) SEM-BSD micrograph of area shown in (d). Dashed square shows area milled in (h) with thick bar showing milled face. (h) SEM in-lens micrograph of FIB-milled face shown in (g). (i) SEM in-lens micrograph of area shown in (h). (j) SEM-SE micrograph of area shown in (i). Note trapped gas inclusions (asterisks) and microcrystalline grains (arrow) within the calcite matrix. (k) SEM in-lens micrograph of aggregates of microcrystalline FeS grains intermixed with surficial sediments from a CPS outflow. (l) TEM micrograph of microcrystalline FeS aggregates from a CPS outflow. Note morphological similarities to microcrystalline grains in (j).

While it was previously suggested that Fe-rich laminations result from precipitation of iron oxyhydroxides [e.g., $Fe\,(OH)_3 \cdot nH_2O$; [55]], the combination of (1) accumulation of metals including Zn, Cu, and Ni; (2) morphological similarities between sediments observed in micritic laminate and spring outlets; and (3) the apparent absence of bacteria and/or biofilms in association with these sediments suggests that they are allochthonous. It is hypothesized that these sediments form as a by-product of subsurface sulfate-reducing bacteria that are subsequently entrained by groundwater and carried to the surface, where they accumulate in shallow outlet pools and are washed downstream and incorporated into the calcite fabric as micritic laminae during pulses of higher groundwater discharge.

5.2. Geological and Mineralogical Characteristics of the White Glacier vein array (WGVA). The WGVA forms a conspicuous brown gossan exposed on a steep western flank confining White Glacier (79°26.66′N; 90°42.20′W; 350 m.a.s.l.), covering an area of more than 350 × 50 m and a range of elevation of ca. 50 m (Figures 3(b) and 7(a)). The veins are likely to be present as well under the glacier. The WGVA includes veins, mineralized breccias, and carbonate masses with a variety of structures (Figure 7). The host rocks are a dark grey chaotic mass of tight, matrix-supported angular breccia with angular fragments of sandstone, siltstone, shale, argillaceous limestone, dolomitic limestone, anhydrite, and gypsum of sizes predominantly <10 cm; the rock is reminiscent of fault breccia. According to the geological map, these beds belong to the Lower Jurassic "Savik beds" and the Upper Jurassic Awingak Formation [27], but the rocks are a jumbled mass, like clastic deposits near advancing salt allochthons described as off-diapir debris flows [6, 67]. These breccias match the description of anomalous, commonly overpressured rubble (termed "gumbo" in the Gulf of Mexico), found beneath allochthonous salt sheets and canopies in petroleum basins (e.g., [68, 69]).

Across from the mineralized zone, there is a wide band of highly sheared and broken-up rusty diabase (a conspicuous gossan), along an extensive Cretaceous diabase sill that can be followed for ca. 4 km along a steep ridge as far as Colour Lake, which lies adjacent to the MARS camp, near Gypsum Hill (Figure 2).

Mineralization consists predominantly of calcite, but textural and crystal habit evidence indicates that the earliest generation of Ca carbonate (cal1) originally crystallized as the polymorph aragonite (*c.f.* [70]). However, the aragonite composition is not preserved and has reverted to calcite on the basis of Raman spectroscopic measurements that show none of the characteristic vibrations for aragonite ($142\,cm^{-1}$, $162\,cm^{-1}$, $190\,cm^{-1}$, $211\,cm^{-1}$, and $701\,cm^{-1}$) and, despite crystal habit, the three dominant vibration lines for calcite are present ($156\,cm^{-1}$, $281\,cm^{-1}$, and $712\,cm^{-1}$) in cal1. Minor quartz, locally barite and abundant iron sulfides pyrite and marcasite (orthorhombic dimorph *of* pyrite), with minor pyrrhotite, chalcopyrite, sphalerite, and galena are present. All the structures suggest "open-space filling" with minimal replacement, reminiscent of epithermal and epigenetic deposits formed at shallow depths. Epidote and chlorite are common where the veins intersect diabase from the mafic dike (Figure 7(c)), and clay minerals are visible in thin sections. The early generation of brown calcite (cal1; after aragonite) occurs in crustified veins, generally as acicular crystals lining fractures, or in radial crystal aggregates filling cavities or around rock fragments (Figure 7(d)). A second generation of calcite (white-orange, sparry; cal2) forms massive infillings with minor quartz, in the central parts of some veins (Figures 7(b) and 7(d)). Locally, there are clear crystals of Iceland spar of up to 10 cm in size. A common structure of calcite is banded "zebra rock" consisting of acicular calcite layers alternating with darker, cm-thick black, carbon-rich sedimentary laminae (Figures 7(e)–7(g)). The laminae are generally subhorizontal but locally contorted, showing variable inclined or vertical orientations in single exposures

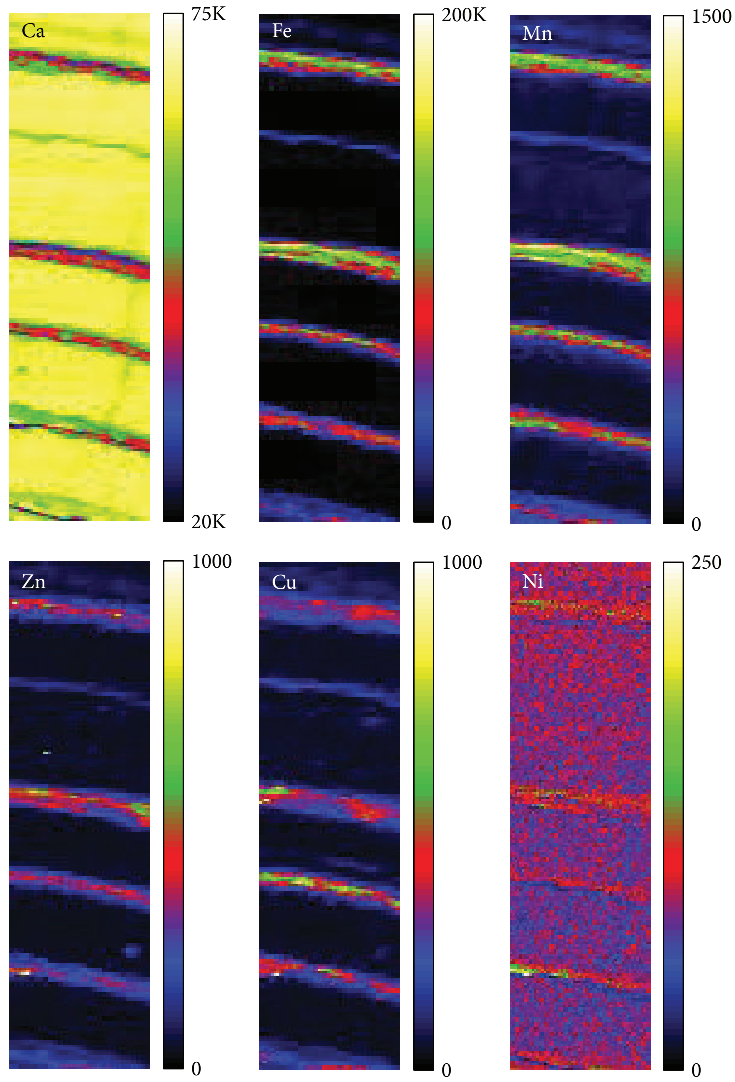

Figure 6: μ-XFM of laminated calcite forming in CPS discharge at Colour Peak Diapir. Qualitative concentrations shown as intensities in counts per second from low (black) to high (white). Intensity ranges denoted by scale bars for each element. The vertical scale of each map is 500 μm.

(Figure 7(f)), probably tectonically disrupted. Sulfides occur in darker laminae within the aggregates, in veins and as botryoidal aggregates filling large open cavities (Figures 7(g) and 7(h)). Sulfides visible in hand sample are pyrite and marcasite.

Under the reflected light microscope, pyrite occurs as subhedral to euhedral crystals of highly variable grain size (<1 mm to >1 cm), locally with cataclastic structure (Figures 8(a) and 8(b)). Marcasite was distinguished from pyrite by its conspicuous anisotropy and its commonly rosette or tabular habit, but in many samples both minerals occur together in rosettes, or plumose structures (Figures 8(c) and 8(d)) with alternating marcasite- and pyrite-rich bands. Some marcasite shows only faint anisotropy. Anhedral pyrite shows considerable porosity and minor remnant anisotropy, which may be the result of conversion from marcasite [71]; it probably crystallized as marcasite and was converted to pyrite in response to hydrothermal heating. Rare grains of galena, sphalerite (Figure 8(e)) and chalcopyrite, pyrrhotite, and arsenopyrite are observed as minute crystals hosted in early brown carbonate (cal1), locally close to the margins of the veins, within them or in the adjacent host. Pyrite framboids (5-8 μm in diameter and made of cubic or octahedral pyrite microlites of 1-2 μm) occur within black (organic-carbon rich) bands within laminated carbonate (Figure 8(f)). Some framboid aggregates appear to have partially recrystallized into euhedral pyrite (Figure 8(g)) but retain internal porosity filled with impurities.

Under the electron microprobe, pyrite (30 spot analyses) and marcasite (11 spot analyses) are compositionally indistinguishable and show a range of impurities, from below detection to maximum (in wt %) as follows: Mn (avg. 0.11%; max. 1.22%), Ni (avg. 0.03%; max. 0.23%), Co

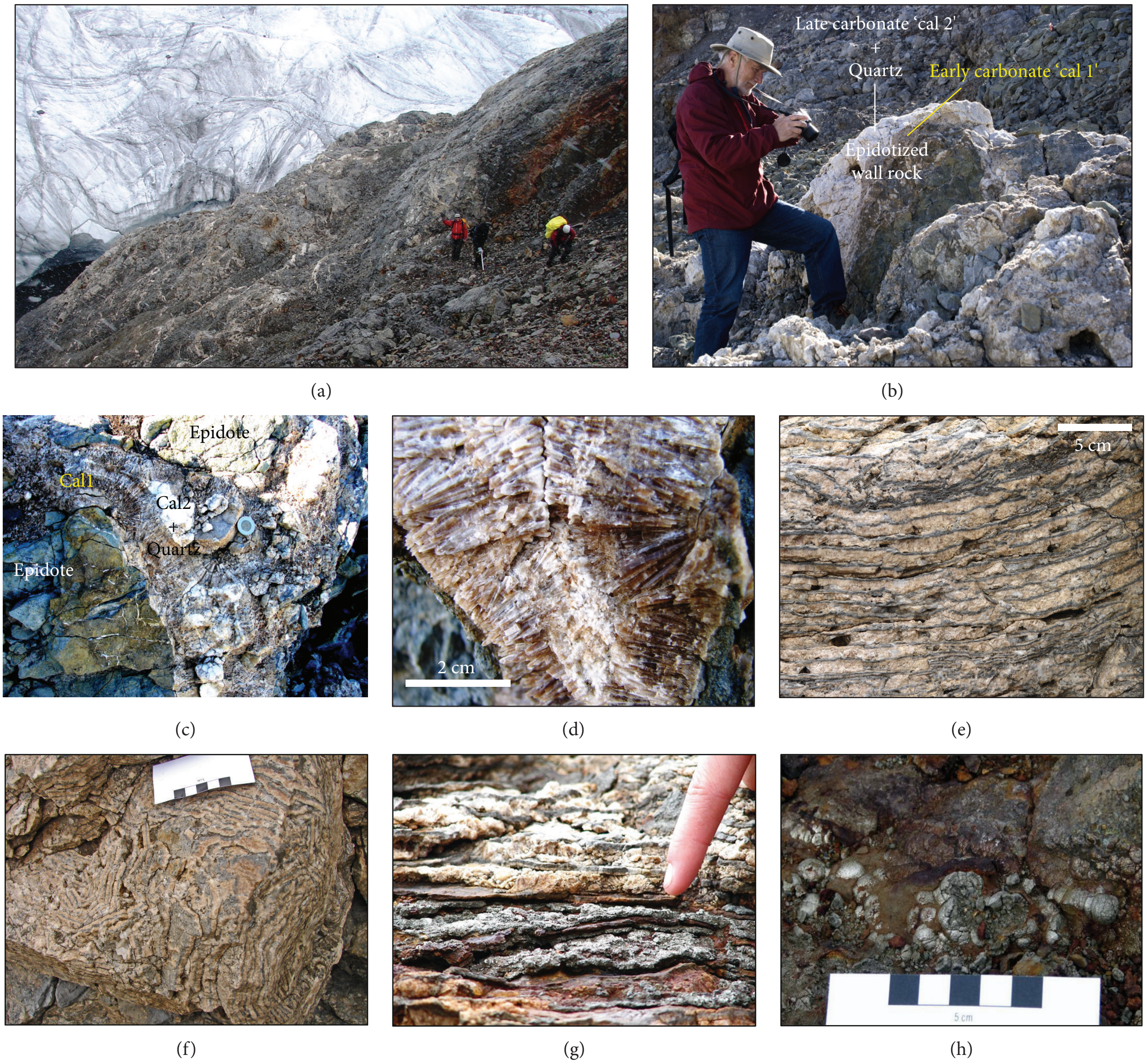

Figure 7: Outcrop-scale features of the WGVA site. (a) Partial overview of the site showing metal gossan (upper left) and hydrothermal veining in wallrock. (b) Outcrop within the exposure in (a) containing zoned calcite-quartz vein hosted in partial epidotized wallrock showing the relative size of vein structures (M. Zentilli for scale). (c) Individual vein showing early brown carbonate ("cal1") crystals symmetrically lining wallrock contacts, with a vuggy infilling white (sparry) calcite ("cal2") and quartz. Epidotized wallrock containing minor secondary vein splays occurs in the vein selvage. (d) Enlarged view of vein showing early brown carbonate crystals radiating from vein margins symmetrically towards the vein centre containing euhedral terminations and open space in this example. (e) "Zebra" texture showing alternating layers of carbonate- and sulfide-rich hydrothermal mineralization (white-tan) with wall-rock septae (grey). (f) Contorted "zebra" texture indicating post-crystallization deformation. (g) Enlarged view of sulfide-rich host rock layers separated by hydrothermal carbonate. (h) Botryoidal masses of pyrite-marcasite.

(<0.04%), Pb (avg. 0.06%; max. 0.26%), Cd (avg. 0.04%; max. 0.29%), Zn (avg. 0.01%; max. 0.08%), Cu (avg. 0.01%; max. 0.08%), Ag (avg. 0.002%; max. 0.02%), and As (avg. 0.003%; max 0.053%). Traces of Au were detected in some sulfide analyses but remain unconfirmed. Visibly zoned crystals ($n = 7$) were analyzed at their centres and margins; while no consistent compositional patterns were detected, on average the centres have one order of magnitude more As, Mn, and Ni and are depleted in Cd. Apart from carbonates, qualitative evidence for the presence of titanite, barite, and other sulphates was found, as well as Fe and Ti oxides with varying amounts of Mn.

Pyrite framboids are difficult to analyze because the microprobe beam is larger than the microlites, and low-density interstitial material (possibly organic matter or volatile minerals) contaminates the analyses, and totals are low; thus, the results are only qualitative. Prominent impurities in framboid analyses ($n = 7$) are Mn (avg. 0.15%; max. 0.60%), Pb (avg. 0.123%; max. 0.158%), Ni (avg. 0.09%; max. 0.19%), Cd (avg. 0.014%; max. 0.044%), Zn (avg.

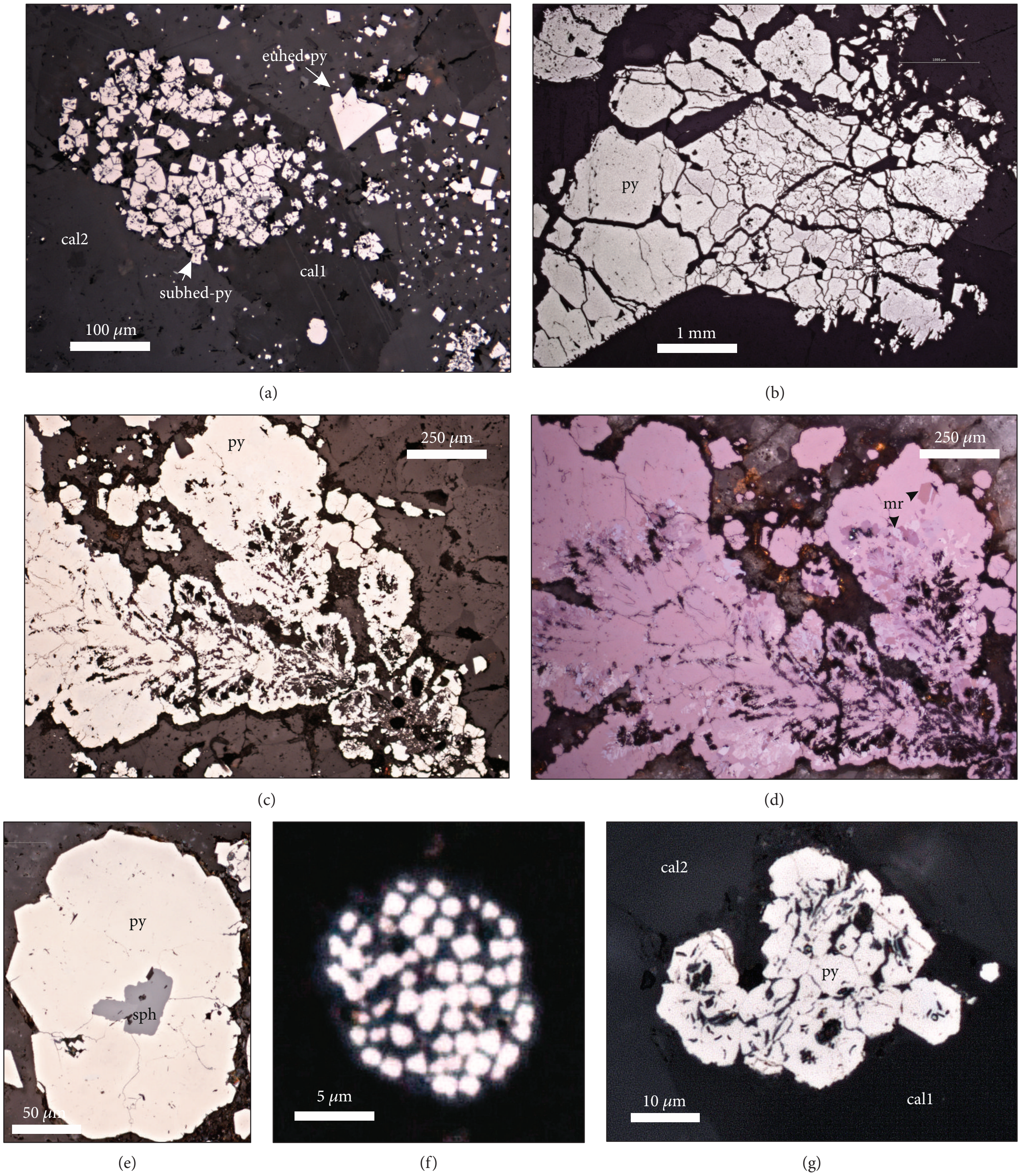

Figure 8: Reflected light photomicrographs summarizing textural and compositional characteristics of sulfides in vein margins associated with vein carbonates and laminated sedimentary wall rocks. (a) Recrystallized (former framboids) subhedral pyrite (subhed-py) in early brown carbonate ("cal 1") surrounded in later carbonate ("cal 2") containing euhedral pyrite (euhed-py). (b) Cataclastic pyrite in wall rock. (c-d) Plumose, porous, pyrite-marcasite intergrowths showing massive domains of pyrite alternating with polycrystalline domains of marcasite. (d) Same area as (c) but in crossed nicols to emphasize anisotropy of marcasite; enclosed dark material is calcite. Dark areas within pyrite-marcasite intergrowths are porosity. (e) Subhedral pyrite polycrystalline aggregate with sphalerite core. (f) Pyrite framboid in black layer of "zebra" rock (Figure 7(g)). (g) Recrystallised pyrite (former framboid) along vein-wallrock margin enclosed within early brown carbonate domain ("cal 1").

Table 3: Selected trace element concentrations from paleospring carbonates.

Ablation #	[1]Phase	Fe_2O_3 *wt.%*	MnO *wt.%*	MgO *wt.%*	Sr *μg/g*	Ba *μg/g*	La *μg/g*	Ce *μg/g*	Yb *μg/g*	Lu *μg/g*	Pb *μg/g*	Zn *μg/g*	Cu *μg/g*	Sr/Ca	[2]La_N/Yb_N
10au20e03.xl	cal2	0.034	0.361	0.023	341	0.50	0.71	1.30	0.04	b.d.l.	0.35	b.d.l.	0.10	0.0262	1.48
10au20e04.xl	cal2	0.025	0.493	0.014	125	0.53	b.d.l.	b.d.l.	b.d.l.	b.d.l.	0.15	0.21	b.d.l.	0.0096	-
10au20e05.xl	cal2	0.025	0.517	0.014	116	b.d.l.	b.d.l.	b.d.l.	b.d.l.	b.d.l.	0.33	0.16	0.06	0.0089	-
10au20e07.xl	cal2	0.011	0.287	0.011	29	0.96	2.08	2.20	0.08	0.01	0.17	b.d.l.	b.d.l.	0.0023	2.02
10au20e08.xl	cal2	0.032	0.347	0.023	252	0.41	0.66	0.86	b.d.l.	b.d.l.	1.14	b.d.l.	b.d.l.	0.0193	-
10au20e09.xl	cal2	0.034	0.377	0.021	483	2.54	0.72	1.22	0.04	0.01	0.41	0.13	b.d.l.	0.0370	1.33
10au20e10.xl	cal2	0.029	0.314	0.016	406	1.54	0.61	1.04	b.d.l.	b.d.l.	0.19	b.d.l.	0.12	0.0311	-
10au20f03.xl	cal2	0.010	0.321	0.031	349	9.31	0.62	0.98	b.d.l.	b.d.l.	0.71	0.64	0.13	0.0268	-
10au20f04.xl	cal2	0.011	0.424	0.042	175	12.00	0.27	0.41	b.d.l.	b.d.l.	1.22	0.75	0.15	0.0134	-
10au20f06.xl	cal2	0.008	0.340	0.038	214	6.96	0.49	0.69	b.d.l.	b.d.l.	6.74	2.66	0.56	0.0164	-
10au20f07.xl	cal2	0.011	0.368	0.033	224	8.21	0.54	0.74	b.d.l.	b.d.l.	0.56	0.43	b.d.l.	0.0172	-
10au20f08.xl	cal2	0.009	0.409	0.036	122	2.24	0.27	0.27	b.d.l.	b.d.l.	0.12	b.d.l.	b.d.l.	0.0093	-
10au20f09.xl	cal2	0.011	0.418	0.048	264	1.50	0.48	0.52	b.d.l.	b.d.l.	0.49	b.d.l.	0.62	0.0202	-
10au20f10.xl	cal2	0.006	0.419	0.038	265	19.82	0.59	0.67	b.d.l.	b.d.l.	3.43	b.d.l.	b.d.l.	0.0203	-
10au20f11.xl	cal2	0.014	0.413	0.044	265	17.53	0.23	0.52	b.d.l.	b.d.l.	3.51	2.04	b.d.l.	0.0203	-
10au20f12.xl	cal2	0.012	0.421	0.056	323	45.67	0.88	1.10	0.12	b.d.l.	0.38	0.36	0.21	0.0248	0.53
10au20f13.xl	cal2	0.010	0.446	0.036	56	b.d.l.	0.08	0.06	b.d.l.	b.d.l.	0.37	0.49	b.d.l.	0.0043	-
10au20f14.xl	cal2	0.011	0.462	0.038	50	b.d.l.	0.01	0.04	b.d.l.	b.d.l.	0.08	b.d.l.	b.d.l.	0.0038	-
10au20d03.xl	cal2	0.009	0.410	0.169	203	2.80	0.04	0.07	b.d.l.	0.02	0.44	b.d.l.	b.d.l.	0.0156	-
10au20d04.xl	cal2	0.012	0.450	0.164	222	15.34	0.08	b.d.l.	b.d.l.	b.d.l.	2.01	2.07	b.d.l.	0.0170	-
10au20d05.xl	cal2	0.012	0.417	0.140	214	19.37	b.d.l.	0.15	b.d.l.	b.d.l.	3.03	b.d.l.	b.d.l.	0.0164	-
10au20d06.xl	cal2	0.011	0.480	0.151	248	13.11	0.04	0.10	0.14	0.02	2.22	0.80	0.25	0.0190	0.02
10au20d07.xl	cal1	0.010	0.268	0.066	925	774.59	0.33	0.55	0.17	0.02	0.12	b.d.l.	0.46	0.0709	0.14
10au20d08.xl	cal1	0.010	0.313	0.076	940	606.54	0.34	0.68	0.16	b.d.l.	6.13	2.58	0.40	0.0721	0.16
10au20d09.xl	cal1	0.010	0.299	0.082	990	767.47	0.31	0.64	0.11	0.01	4.42	1.28	0.67	0.0759	0.20
10au20d10.xl	cal1	0.008	0.246	0.052	868	527.30	0.27	0.59	b.d.l.	b.d.l.	5.28	1.28	0.68	0.0666	-
10au20d11.xl	cal1	0.009	0.286	0.063	905	546.52	0.31	0.64	0.16	0.01	1.24	0.56	0.26	0.0694	0.14
10au20d12.xl	cal1	0.008	0.260	0.052	867	556.46	0.32	0.56	0.16	0.02	0.43	0.69	0.42	0.0665	0.15
10au20d13.xl	cal1	0.009	0.287	0.059	937	556.73	0.27	0.66	0.08	0.01	0.68	0.98	0.26	0.0719	0.25
10au20d14.xl	cal1	0.009	0.242	0.055	893	578.83	0.32	0.51	0.09	0.02	0.76	1.00	0.43	0.0685	0.25
10au20d15.xl	cal1	0.010	0.251	0.059	926	621.45	0.32	0.63	0.12	0.02	0.50	0.88	0.53	0.0710	0.20
10au20d16.xl	cal1	0.009	0.269	0.081	846	583.22	0.26	0.67	0.14	0.01	1.00	2.48	0.55	0.0649	0.13

Notes: [1]cal 2 = white/orange infilling sparry calcite; cal 1 = brown calcite lining vein wall; [2]REE normalized to PAAS.

0.006%; max. 0.021%), Cu (avg. 0.009%; max. 0.034%), and As (avg. 0.0175%; max. 0.053%).

One crystal of pyrrhotite was encountered with 0.06% Cu. One arsenopyrite grain was encountered that showed detectable Pb, Co, Ni, Zn, and Ag.

5.2.1. Trace Elements in Carbonate. Selected trace elements in cal1 and cal2 are listed in Table 3. Early brown acicular calcite has a hexagonal crystal form and elevated Sr, Ba, and Mg compared to sparry white-orange calcite. If abundant in the associated fluid, these ions are known to stabilize aragonite [72], which may have reverted to calcite as the hydrothermal fluid became diluted with time or warmer (*c.f.* [73]). Strontium and Ba are variable in concentration but reach concentrations as high as ~1000 ppm and ~770 ppm, respectively, with Sr and Ba showing a positive correlation, consistent with their precipitation from a fluid derived from dissolution of marine carbonates. In the absence of secondary dolomitization, lower Sr values emphasize meteoric water dilution. LREE/HREE ratios (e.g., PAAS normalized La/Yb) are $\ll 1$ for carbonate analyses with Sr > 800 ppm, also diagnostic of hydrothermal carbonate precipitated from seawater or a fluid that interacted with, or dissolved, marine carbonate (*c.f.*, [70]). Elevated concentrations of Ba likely indicate that small inclusions of the mineral witherite ($BaCO_3$) are present as such high concentrations would not be present as dissolved Ba in the Ca-carbonate structure. Elevated concentrations of Pb, Zn, and Cu are likely not dissolved concentrations but rather indicate the presence of very small particles of included, coprecipitated or secondary sulfide minerals (e.g., galena, sphalerite, and chalcopyrite). Petrographic observation of trace quantities of these sulfides within veins and host

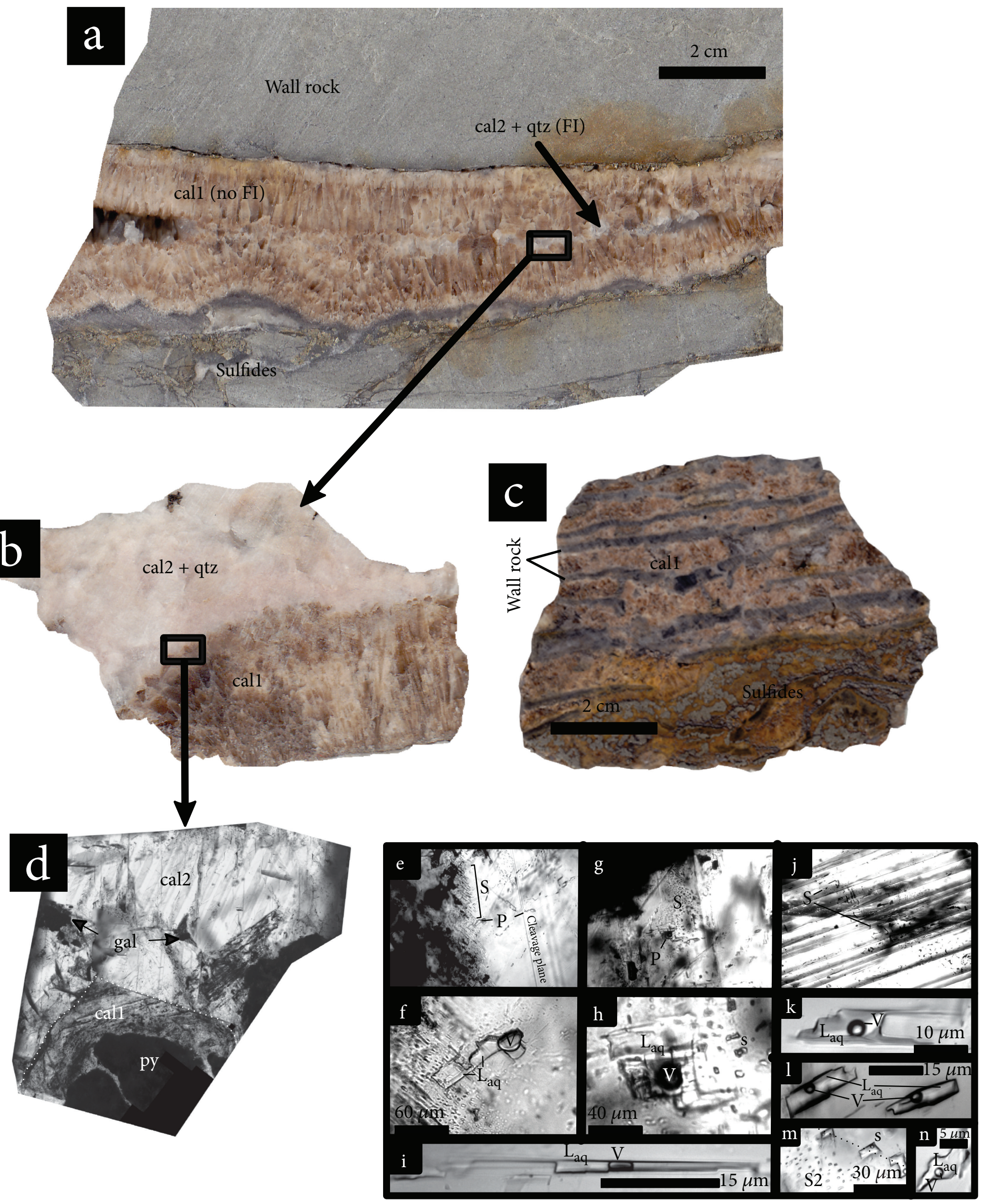

FIGURE 9: Petrographic characteristics of carbonate-quartz veins (WGVA). (a) Complete vein cross section (hand sample) showing early brown, comb-textured (acicular, hexagonal) carbonate lining vein wall (cal1), later white, massive, sparry carbonate and quartz (cal2 + qtz), and sulfide-mineralized wallrock. (b) Enlarged view of the contact between cal1 and cal2 generations where euhedral crystals of cal1 contact cal2. (c) Banded ("zebra") texture showing alternating layers consisting of sulfide-mineralized wall rock laminae and cal2. (d) Thin-section photomicrograph (transmitted light) showing the paragenetic sequence of early pyrite (py) surrounded in zoned, euhedral brown carbonate (cal1), followed by massive white-orange carbonate (cal2) infilling and late galena infilling fractures and pits in cal2. (e-h) Transmitted light (ppl) photomicrographs (at 20°C) showing large primary ("P") two-phase ($L_{aq} + V$) inclusions and planes of much smaller secondary ("S") two-phase ($L_{aq} + V$) inclusions in cal2. Images (f) and (h) show more highly magnified areas of the central parts of images (e) and (g), respectively. (i) Transmitted light (ppl) photomicrograph (at 20°C) of a long, rectangular primary two-phase ($L_{aq} + V$) inclusion in cal2. (j) Transmitted light (ppl) photomicrograph (at 20°C) of a planar trail of secondary inclusions cross-cutting cal2 cleavage planes. (k-l) Secondary fluid inclusions in cal2 containing two phases ($L_{aq} + V$) at 20°C. (m) Transmitted light (ppl) photomicrograph (at 20°C) of an irregularly shaped secondary two-phase inclusion ($L_{aq} + V$) in cal1. (n) Transmitted light (ppl) photomicrograph (at 20°C) shows two types of secondary inclusion morphologies in cal2: rectangular to irregular two-phase inclusions ("S") and later ("S2") rectangular two-phase inclusions with rounded edges. The latter inclusions tend to show lower T_h values (see text for description).

Table 4: Microthermometric data for paleocarbonate-hosted fluid inclusions from Striae Hill and White Glacier.

FIA	Stage	Location	Sample	Origin	T_m^{ice} (°C)	Salinity	T_h (°C)	FIA	Stage	Location	Sample	Origin	T_m^{ice} (°C)	Salinity	T_h (°C)
A	cal2	Striae Hill	SF05-3E	S	-0.7	1.2	n.m.	O	cal2	White Glacier	SF07-1	S	-9.8	13.8	146.9
A	cal2	Striae Hill	SF05-3E	S	-1.0	1.7	n.m.	O	cal2	White Glacier	SF07-1	S	-10.9	14.9	135.8
A	cal2	Striae Hill	SF05-3E	S	-0.6	1.1	n.m.	O	cal2	White Glacier	SF07-1	S	-9.4	13.3	178.6
A	cal2	Striae Hill	SF05-3E	S	-0.8	1.4	n.m.	P	cal2	White Glacier	SF07-1	S	-11.6	15.6	251.2
A	cal2	Striae Hill	SF05-3E	S	-0.7	1.2	n.m.	P	cal2	White Glacier	SF07-1	S	-9.1	13.0	192.5
A	cal2	Striae Hill	SF05-3E	S	-0.4	0.7	n.m.	Q	cal2	White Glacier	SF07-1	S	-7.8	11.5	192
A	cal2	Striae Hill	SF05-3E	S	-0.7	1.2	n.m.	Q	cal2	White Glacier	SF07-1	S	-5.2	8.1	228.1
A	cal2	Striae Hill	SF05-3E	S	-0.6	1.1	n.m.	Q	cal2	White Glacier	SF07-1	S	-5.2	8.1	167.8
A	cal2	Striae Hill	SF05-3E	S	-1.1	1.9	252.4	Q	cal2	White Glacier	SF07-1	S	-4.6	7.3	172.4
A	cal2	Striae Hill	SF05-3E	S	-0.9	1.6	155.6	Q	cal2	White Glacier	SF07-1	S	-1.8	3.0	192.7
A	cal2	Striae Hill	SF05-3E	S	-0.5	0.9	295.5	Q	cal2	White Glacier	SF07-1	S	-6.1	9.3	205.9
A	cal2	Striae Hill	SF05-3E	S	-0.5	0.9	270	R	cal2	White Glacier	SF07-1	S	-3	4.9	194.1
A	cal2	Striae Hill	SF05-3E	S	-1.0	1.7	n.m.	R	cal2	White Glacier	SF07-1	S	-1.9	3.2	220.6
A	cal2	Striae Hill	SF05-3E	S	-1.0	1.7	238.8	R	cal2	White Glacier	SF07-1	S	-5.2	8.1	232.9
A	cal2	Striae Hill	SF05-3E	S	-1.1	1.9	238.3	S	cal2	White Glacier	SF07-1	S	-1.3	2.2	202.2
B	cal2	Striae Hill	SF05-3E	P	-7.3	10.8	152.5	T	cal2	White Glacier	SF07-1	S	-0.2	0.2	232.8
C	cal2	Striae Hill	SF05-3E	S	-0.8	1.4	n.m.	T	cal2	White Glacier	SF07-1	S	-0.3	0.4	249.4
C	cal2	Striae Hill	SF05-3E	S	-0.6	1.1	n.m.	T	cal2	White Glacier	SF07-1	S	-0.3	0.5	250.2
D	cal2	Striae Hill	SF05-3E	S	-1.1	1.9	253.1	T	cal2	White Glacier	SF07-1	S	-0.3	0.4	224.6
D	cal2	Striae Hill	SF05-3E	S	-1.0	1.7	238.9	U	cal2	White Glacier	SF07-1	S	-0.2	0.2	199.7
D	cal2	Striae Hill	SF05-3E	S	-0.9	1.6	155.4	U	cal2	White Glacier	SF07-1	S	-0.2	0.2	174.6
E	cal2	Striae Hill	SF05-3E	S	-0.5	0.9	270.2	U	cal2	White Glacier	SF07-1	S	-0.3	0.4	163.2
E	cal2	Striae Hill	SF05-3E	S	-0.5	0.9	296.1	U	cal2	White Glacier	SF07-1	S	-0.3	0.4	155.3
F	cal2	Striae Hill	SF05-3E	P	-7.3	10.8	152.9	U	cal2	White Glacier	SF07-1	S	-0.3	0.5	111.5
G	cal2	White Glacier	SF07-1	P	-10.7	14.7	n.m.	V	cal2	White Glacier	SF07-1	S	-1.2	2.1	247.2
G	cal2	White Glacier	SF07-1	P	-7.2	10.7	n.m.	W	cal2	White Glacier	SF07-1	P	-11.5	15.4	155.7
G	cal2	White Glacier	SF07-1	P	-13.8	17.6	n.m.	W	cal2	White Glacier	SF07-1	P	-11.5	15.4	159.5
G	cal2	White Glacier	SF07-1	P	-11.5	15.5	231.5	X	cal2	White Glacier	SF07-1	P	-11.7	15.6	217.1
G	cal2	White Glacier	SF07-1	P	-11.5	15.5	156.1	X	cal2	White Glacier	SF07-1	P	-11.5	15.5	230.8
G	cal2	White Glacier	SF07-1	P	-11.4	15.4	159.7	X	cal2	White Glacier	SF07-1	P	-11.5	15.4	262.2
H	cal2	White Glacier	SF07-1	S	-1.1	1.9	n.m.	Y	cal2	White Glacier	SF07-1	P	-11.5	15.5	216.3
I	cal2	White Glacier	SF07-1	P	-10.1	14.0	n.m.	Y	cal2	White Glacier	SF07-1	P	-11.5	15.5	n.m.
I	cal2	White Glacier	SF07-1	P	-11.4	15.4	n.m.	Y	cal2	White Glacier	SF07-1	P	-11.5	15.5	n.m.
I	cal2	White Glacier	SF07-1	P	-11.5	15.5	262.8	Y	cal2	White Glacier	SF07-1	P	-11.5	15.5	n.m.
J	cal2	White Glacier	SF07-1	S	0.0	0.0	n.m.	Y	cal2	White Glacier	SF07-1	P	-11.5	15.5	n.m.

Table 4: Continued.

FIA	Stage	Location	Sample	Origin	T_m^{ice} (°C)	Salinity	T_h (°C)	FIA	Stage	Location	Sample	Origin	T_m^{ice} (°C)	Salinity	T_h (°C)
J	cal2	White Glacier	SF07-1	S	-0.2	0.4	n.m.	Y	cal2	White Glacier	SF07-1	P	-16.8	20.1	n.m.
J	cal2	White Glacier	SF07-1	S	0.0	0.0	177.2	Z	cal2	White Glacier	SF07-4	S	0.0	0.0	182.4
J	cal2	White Glacier	SF07-1	S	-0.1	0.2	233	Z	cal2	White Glacier	SF07-4	S	-0.3	0.5	112.1
J	cal2	White Glacier	SF07-1	S	-0.2	0.4	225.3	Z	cal2	White Glacier	SF07-4	S	-0.1	0.2	200.9
J	cal2	White Glacier	SF07-1	S	-0.1	0.2	174.9	Z	cal2	White Glacier	SF07-4	S	-1.3	2.2	n.m.
J	cal2	White Glacier	SF07-1	S	-1.2	2.1	246.9	Z	cal2	White Glacier	SF07-4	S	-0.1	0.2	n.m.
J	cal2	White Glacier	SF07-1	S	-0.3	0.5	250	Z	cal2	White Glacier	SF07-4	S	-1.0	1.7	n.m.
J	cal2	White Glacier	SF07-1	S	0.0	0.0	176.4	Z	cal2	White Glacier	SF07-4	S	-0.5	0.9	n.m.
K	cal2	White Glacier	SF07-1	S	-0.7	1.2	n.m.	Z	cal2	White Glacier	SF07-4	S	-1.3	2.2	n.m.
K	cal2	White Glacier	SF07-1	S	-1.4	2.4	n.m.	Z	cal2	White Glacier	SF07-4	S	-2.3	3.9	n.m.
K	cal2	White Glacier	SF07-1	S	-0.2	0.4	249.8	Z	cal2	White Glacier	SF07-4	S	-0.1	0.2	n.m.
K	cal2	White Glacier	SF07-1	S	-0.2	0.4	155.3	AA	cal2	White Glacier	SF07-4	P	-11.5	15.5	n.m.
K	cal2	White Glacier	SF07-1	S	-0.2	0.4	163.7	AA	cal2	White Glacier	SF07-4	P	-11.5	15.5	n.m.
L	cal2	White Glacier	SF07-1	S	-5.8	8.9	192.1	AA	cal2	White Glacier	SF07-4	P	-9.9	13.7	n.m.
L	cal2	White Glacier	SF07-1	S	-5.7	8.8	189.4	BB	cal1	White Glacier	SF07-1	S	n.m.	n.m.	308.2
L	cal2	White Glacier	SF07-1	S	-5.8	8.9	158.5	BB	cal1	White Glacier	SF07-1	S	n.m.	n.m.	297.9
M	cal2	White Glacier	SF07-1	S2	-3.3	5.4	125.3	BB	cal1	White Glacier	SF07-1	S	n.m.	n.m.	290.8
N	cal2	White Glacier	SF07-1	S	-3.3	5.4	144.5	CC	cal1	White Glacier	SF07-1	S	-8.3	12.1	264.8
N	cal2	White Glacier	SF07-1	S	-1.2	2.1	144	CC	cal1	White Glacier	SF07-1	S	-8.3	12.1	270.6
N	cal2	White Glacier	SF07-1	S	-2.2	3.7	137.6	DD	cal1	White Glacier	SF07-1	S	-16.9	19.8	215
N	cal2	White Glacier	SF07-1	S	-0.4	0.7	166.2	EE	cal1	White Glacier	SF07-1	S	-1.4	2.4	137.4
O	cal2	White Glacier	SF07-1	S	-9.5	13.4	193.3	EE	cal1	White Glacier	SF07-1	S	-1.2	2.1	208.4
O	cal2	White Glacier	SF07-1	S	-9.3	13.2	149.1	EE	cal1	White Glacier	SF07-1	S	-0.9	1.6	158.8
O	cal2	White Glacier	SF07-1	S	-9.5	13.4	164.3	EE	cal1	White Glacier	SF07-1	S	-1.1	1.9	175.6
O	cal2	White Glacier	SF07-1	S	-10.4	14.4	126.5	EE	cal1	White Glacier	SF07-1	S	-0.6	1.1	162.1

Notes: Salinity reported in wt% NaCl equivalent. FIA = fluid inclusion assemblage; S/S2 = secondary origin; P = primary; T_m^{ice} = final ice melting T; Th = homogenization T (L + V to L); n.m. = not measured.

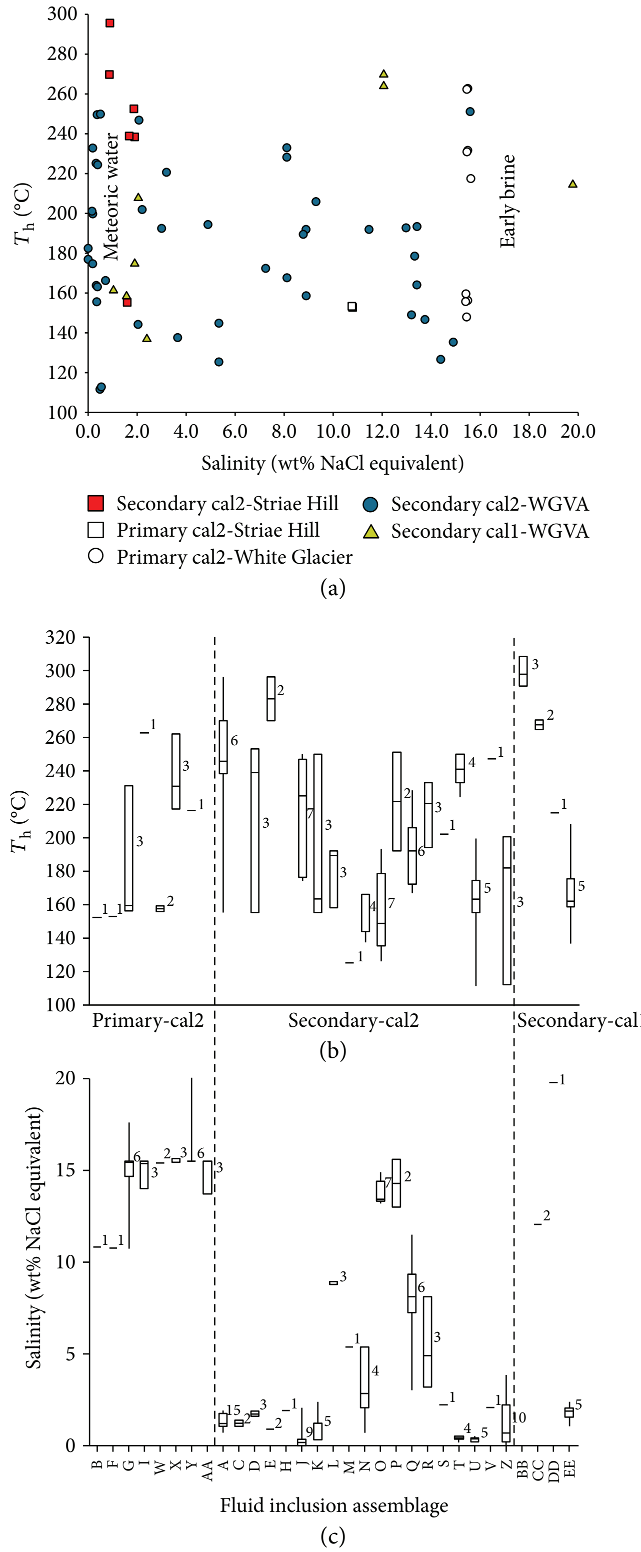

Figure 10: Microthermometric data for primary and secondary fluid inclusions in carbonates from the paleosprings (WGVA and Striae Hill sites). (a) Summary of all data (T_h vs. bulk salinity) for primary and secondary inclusions in carbonates from WGVA and Striae Hill sites. Note the lack of correlation between T and salinity, and the continuum in bulk salinity from a high-salinity brine in the earliest inclusions to variable salinity fluid (brine to meteoric range) in secondary inclusions. (b-c) Box-whisker plots summarizing microthermometry data for primary and secondary inclusions organized by fluid inclusion assemblage. Numbers next to box-whisker markers indicate the number of inclusions in each measured assemblage. Single assemblages can show up to a ~150°C intra-assemblage range in homogenization by vapour bubble disappearance, attributed to post-entrapment modification (leakage, necking down).

Table 5: Stable S-O-C analyses of mineral separates from modern spring/paleospring, and [1]calculated water $\delta^{18}O$.

Sample	Setting	Mineral phase		Measured (mineral ‰)			Calculated (fluid ‰)	
			$\delta^{34}S_{VCDT}$	$\delta^{18}O_{VSMOW}$	$\delta^{13}C_{VPDB}$	$\delta^{18}O_{H2O}$	$\delta^{18}O_{H2O}$	$\delta^{18}O_{H2O}$
						6°C	150°C	300°C
SF-10	Paleospring	Pyrite	-2.7	-	-	-	-	-
SF-14	Paleospring	Pyrite	1.7	-	-	-	-	-
SF-14	Paleospring	Pyrite	16.4	-	-	-	-	-
SF-15	Paleospring	Pyrite	11.4	-	-	-	-	-
COS1	Modern spring	Pyrite	19.2	-	-	-	-	-
SF-14	Paleospring	Drusy quartz vein infill	-	-3.2	-	-	-18.5	-10.0
SF-14	Paleospring	White massive carbonate infill (cal2)	-	-5.0	-21.9	-	-17.5	-10.6
SF-15	Paleospring	White massive carbonate infill (cal2)	-	-0.3	-20.6	-	-12.8	-5.9
SF-17	Paleospring	White massive carbonate infill (cal2)	-	3.2	-23.8	-	-9.4	-2.4
SF-17b	Paleospring	White massive carbonate infill (cal2)	-	0.8	-8.4	-	-11.7	-4.8
SF-14	Paleospring	Orange massive carbonate infill (cal2)	-	1.5	-22.5	-	-11.0	-4.1
SF-10	Paleospring	Brown bladed carbonate lining (cal1)	-	2.1	-29.5	-	-8.0	-1.6
SF-14	Paleospring	Brown bladed carbonate lining (cal1)	-	2.8	-29.2	-	-7.3	-0.9
SF-14	Paleospring	Brown bladed carbonate lining (cal1)	-	1.4	-31.2	-	-8.7	-2.3
SF-15	Paleospring	Brown bladed carbonate lining (cal1)	-	2.6	-30.4	-	-7.5	-1.1
SF-17	Paleospring	Brown bladed carbonate lining (cal1)	-	3.5	-27.3	-	-6.6	-0.2
COC1	Modern spring	Carbonate from modern spring	-	10.0	-10.6	-22.1	-	-

[1]Fractionation equations: calcite-H_2O [140], aragonite-H_2O [141], and quartz-H_2O [142].

rock margins or along host rock-vein contacts are in support of carbonate-sulfide coprecipitation.

5.2.2. Fluid Inclusion Petrography and Microthermometry. Carbonates from representative vein specimens (discrete veins, and "zebra" texture) from the WGVA were examined for fluid inclusions. The vein samples selected for study (e.g., Figures 9(a)–9(c)) contain an early generation of zoned, brown- to tan-coloured, acicular, hexagonal early brown calcite (as cal1) that grew inward from fracture walls to create a symmetrical open-space filling layer on the walls, and a later generation of white to orange massive, polycrystalline to euhedral, terminated "sparry" white-orange calcite (cal2) that infills the central vein cavities lined by terminated crystals of cal1. Quartz is also present, but rare, occurring as a massive, polycrystalline infilling within an even later cavity intergrown with cal2. No differences in the petrographic characteristics (inclusion origins, morphologies) of fluid inclusions from the White Glacier and Striae Hill study areas are observed. The infilling cal2 generation contains primary and secondary inclusions. Both generations of calcite postdate an early generation of base metal sulfide mineralization, with zoned cal1 coating, and infilling fractures within pyrite-marcasite (Figure 9(d)). Trace amounts of secondary galena, pyrite, and sphalerite grew synchronous to, or after, cal2. Primary inclusions in cal2 (Figures 9(e)–9(i)) are rare, up to 80 μm in longest dimension, and have a variety of morphologies, ranging from complex, rectangular to rhombic (Figures 9(f)–9(h)) to long, rectangular (tube-like) in shape (Figure 9(i)). The primary inclusions (type "P") occur in isolated assemblages of up to ~10 inclusions within clear domains of calcite. Secondary inclusions are smaller, and at least two different types are recognized. Type "S" inclusions (up to 30 μm; averaging ~15 μm) (Figures 9(e)–9h, 9(k), and 9(l)) show morphologies ranging from amoeboid, subangular, through rectangular to rhombic, some occurring in planar arrays that cross-cut calcite grain boundaries and cleavage planes. Type "S2" inclusions are less abundant, very small (<4 μm), and have consistently rectangular to rhombic morphologies (Figure 9(m)). The wall-lining cal1 generation contains only irregularly shaped secondary inclusions (Figure 9(n)). In both cal1 and cal2 generations, all inclusion types are two-phase at room T, containing an aqueous liquid (L_{aq}) and a vapour bubble (V), with L : V ratios varying from ~85 : 15 to 90 : 10. Fluid inclusions in the late quartz are too small to investigate (<5 μm, and obscured by a lack of transparency in the quartz) but appear to be two-phase L_{aq} + V.

Table 4 and Figures 10(a)–10(c) summarize microthermometric and calculated salinity data for inclusions in representative secondary fluid inclusion assemblages (FIA) within cal1 and primary and secondary assemblages within cal2. A total of 120 fluid inclusions were measured. In some FIA, only partial microthermometric data could be obtained owing to difficulties in accurately observing ice melting or final homogenization. Primary fluid inclusions show final ice melting (T_m^{ice}; $n = 25$ from two sites) between -7.2°C and -16.8°C, corresponding to bulk salinity between 10.7 and 20.1 wt% NaCl equivalent. Average bulk salinity for primary inclusions is 15.0 wt% $NaCl_{eq}$. Total homogenization (T_h) of primary inclusions occurred by vapour bubble disappearance ($L_{aq} + V \rightarrow L_{aq}$), between 153°C and 293°C (average = 196°C; $n = 12$). Secondary type "S" fluid inclusions show a typically much wider range in final ice melting (T_m^{ice})

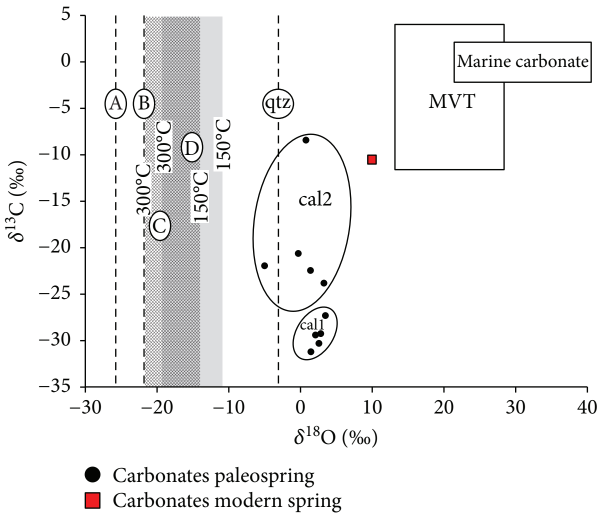

Figure 11: Plot of stable C (‰, relative to VPDB) and O (‰, relative to VSMOW) isotope data for carbonates (cal1 and cal2) from paleospring hydrothermal veins (black circles) and modern carbonate precipitate (red square). Line A is the O isotope composition of meteoric water in the study area (constrained using lat-long-elevation data; using the OIPC3.1 calculator, University of Utah). Line B is the composition of water that would be in equilibrium with modern carbonate at the springs at a mean temperature of 6°C. Fields "C" and "D" are the predicted compositional ranges for carbonates and quartz, respectively, expected if the paleospring hydrothermal veins crystallized at T between 150 and 300°C from meteoric water (based on T_h values from fluid inclusions and utilizing fractionation expressions from [140], [calcite-H_2O], [141] [aragonite-H_2O], and [142] [quartz-H_2O]).

between 0°C and -16.9°C, corresponding to bulk salinity from 0 to 19.8 wt% NaCl equivalent. However, high-salinity secondary inclusions are rare, and the average salinity for secondary inclusions is much lower (3.7 wt% $NaCl_{eq.}$; $n = 91$). The range in T_h for secondary inclusions is similar to that for primary inclusions, between 112°C and 308°C (average = 203°C; $n = 73$). Overall, there are no discernable differences in salinity or T_h data between secondary inclusions in cal1 or cal2. This, combined with the near complete lack of very high-salinity secondary inclusions in cal1 (as is typical of primary inclusions in cal2), suggests that secondary inclusions in cal1 and cal2 contain the same fluids. Figure 10(a) ($n = 10$ primary, 68 secondary) shows no correlation between T_h salinity data but illustrates a continuum of inclusion salinities from primary inclusions with consistently highest salinities, through a wide range in secondary inclusion salinity approaching and including ~ pure water. There is relatively little intra-FIA variability in inclusion salinity with only a small number of FIA showing anomalously high- or low-salinity inclusions (Figure 10(b)); given the range in inter-FIA salinity observed in secondary inclusions, anomalously high- or low-salinity inclusions within single assemblages may reflect incorrect assignment for some inclusions within larger groups to a given FIA. Compared to the salinity data, T_h data (Figure 10(c)) shows consistently large intra-FIA variability, up to a ~150°C variation in single FIA. It was noted that stretching of inclusions during heating experiments had a negligible effect on T_h; repeated heating experiments on single inclusions showed no more than a ~1°C increase in T_h even after holding T above T_h for 1 hour before repeat measurements. Petrographic scrutiny of inclusions before microthermometry was performed to exclude any inclusions showing obvious evidence of necking down. However, in the absence of any detectable visual evidence for post-entrapment modification, the effect of inclusion leakage and necking down remains likely given the range in T_h in some FIA. Variability in T_h must therefore reflect post-entrapment leakage or necking down (that could not be detected optically) or real variations in trapping conditions (T or P).

Sparry white calcite contains high-salinity primary inclusion assemblages with individual inclusion salinities ranging from 10.8 to 20 wt% NaCl and T_h values between 153°C and 263°C. Secondary inclusion groups show a wider variation in salinity from 15.6 wt% to as low as ~0 wt% $NaCl_{eq}$ (within measurement uncertainty of ±0.2°C, equivalent to salinity uncertainty of <0.2 wt% $NaCl_{eq.}$) and T_h values between 112°C and 251°C. Importantly, the transition to lower salinities from primary to secondary inclusions suggests overall dilution with time, though fluctuations in salinity during secondary inclusion entrapment appear large (i.e., Figure 10(c), secondary inclusions in cal1 and cal2).

5.2.3. Stable Isotopes. Oxygen and carbon isotope values in carbonate generation cal1 (Table 5, Figure 11) range from +1.4‰ to +3.5‰ ($\delta^{18}O_{VSMOW}$) and -22.5‰ to -31.2‰ ($\delta^{13}C_{VPDB}$), respectively. These data are similar to that for cal2 ($\delta^{18}O_{VSMOW} = -0.3$‰ to +3.2‰, and $\delta^{13}C_{VPDB} = -8.4$ ‰ to -23.8‰). Drusy quartz coeval with cal2 has $\delta^{18}O_{VSMOW} = -3.2$‰. In comparison, the modern (active) spring carbonate has significantly higher isotope ratios ($\delta^{18}O_{VSMOW} = +10.0$‰ and $\delta^{13}C_{VPDB} = -10.6$‰). The isotope composition of the modern spring carbonate lies close to the compositional range for post-mineralization pore- and fracture-filling calcite in MVT deposits in the Canadian Arctic (Figure 11; [74, 75]). With respect to O isotopes, at a $T = 6$°C (mean annual spring discharge T), we calculate a value of $\delta^{18}O_{VSMOW} = -22.1$‰ (line "B" in Figure 11) for the aqueous solution in equilibrium with the carbonate, slightly higher than the composition of high-latitude meteoric water (i.e., melt water) for the study area (-26‰; OIPC3.1 calculator, University of Utah; line "B" in Figure 11). Over a temperature range from 150 to 300°C (based on primary fluid inclusion T_h) and using a meteoric water composition of $\delta^{18}O_{VSMOW} = -26$‰ (negligible change in study area latitude beginning in the Eocene-Miocene when the paleosprings at WGVA are assumed to have been active), calculated values of $\delta^{18}O_{VSMOW}$ the carbonate and quartz expected to precipitate from that water range from -22‰ to -14‰ and -19.5‰ to -11‰, respectively (fields "C" and "D" in Figure 11). Note that these ranges represent maximum values since T_h values are minimum fluid inclusion (host mineral precipitation) T_s minimum fluid inclusion entrapment temperatures. Importantly, these values are *at least* ~6‰ lower than the measured mineral compositions. Estimated $\delta^{18}O_{VSMOW}$ values for fluid in equilibrium with cal2 are lower than for cal1 (Table 5) assuming cal1 precipitated at a similar or higher T than cal2. Consistent with the fluid inclusion salinity data, these results suggest that the hydrothermal minerals did not precipitate from heated meteoric water but rather from a *mixture* of meteoric water and a saline fluid phase, with a larger proportion of meteoric water in the mixture at the time of precipitation of the late carbonate-quartz infilling. Thus, while modern springs show a predominance of meteoric water, the paleosprings formed from mixtures of meteoric water and basinal-type brine, with fluctuations from a dominant brine to dominant meteoric water influence with time. This transition is consistent with fluid inclusion data, showing decreasing salinity from primary to secondary inclusions, approaching ~pure water in many inclusion assemblages.

The strongly depleted nature of carbon isotopes for the WGVA vein carbonates ($\delta^{13}C_{VPDB}$ in cal1 ranges from -22.5‰ to -31.2‰, and that in cal2 ranges from -8.4‰ to -23.8‰) likely reflects a dissolved carbonate source related to oxidation or thermal degradation of organic matter. A shift to higher $\delta^{13}C_{VPDB}$ values from cal1 to cal2 is observed, consistent with the shift from higher to lower values of calculated $\delta^{18}O_{VSMOW}$ for the fluid, resulting from a combination of progressive dilution by meteoric water and/or decreasing equilibration T.

Values of $\delta^{34}S_{VCDT}$ in pyrite(-marcasite) in the vein margins of the WGVA are variable (-2.7 to +16.4‰) with the highest value approaching that for Carboniferous-age evaporite diapir sulfate [76]. The wide range in $\delta^{34}S_{VCDT}$, combined with textural evidence for recrystallization of pyrite framboids, and likely thermal and compositional fluctuations in the hydrothermal system with time suggest that S isotope systematics of the WGVA reflect a combination of preserved low-temperature microbial sulfate reduction and higher-temperature reduction of sulfate by organic compounds (*c.f.* in MVT systems; [77]).

6. Discussion

6.1. Justification for an Alternative Model. The surficial model by Andersen et al. [7], which envisaged recharge from glacial lakes and near-surface circulation through evaporites and permafrost (see Section 4), was justifiable with the data available, but the younger thermal history detected by thermochronology suggested that the PSS phenomenon might have a deeper, internal energy connection. The apatite fission track dating method (Figure 4) constrains not the age, but the geological time when rocks cooled for the last time below ca. 100°C (corresponding to a depth of 3 to 4 km under normal geothermal gradients) and allows for modelling compatible time-temperature histories (e.g., [78]). Regionally, rocks now exposed at the surface cooled to temperatures below 100°C during uplift and exhumation due to the rise of mountains on Axel Heiberg Island and Ellesmere Island (Figures 4(a) and 4(b)) between ca. 62 and 33 Ma (Paleogene; [79]) caused by tectonic collision with Greenland (e.g., [5, 80]). In contrast, rocks in the Expedition Fiord area of Axel Heiberg Island (Figure 4(c)) cooled 10 to 20 My later [9, 81].

Two samples are clearly anomalous (Figure 4(a)): (1) sample SF-66, collected at the surface of the Cretaceous age gabbro Wolf Intrusion (Figure 2) between Colour Peak Diapir and White Glacier, and (2) sample SF-59, collected in a raft of gabbro intrusive within the Colour Peak Diapir (Figure 2). Their apatite fission track ages are younger than most regional samples, and their mean track length is the shortest measured in surface rocks in this area (Figure 4(a); Table 1). These characteristics suggest that, relative to other rocks, they remained within the crust for a longer time at a higher temperature. Figures 4(b) and 4(c) depict the result of Monte Carlo inverse thermal history models for two representative samples, including that from the Wolf Intrusion (SF-66) and another (SF-28) from near the summit of the Princess Margaret Range, ca. 60 km to the northeast (79.7°N; 88.5°W; 2467 m.a.s.l.). Both internally consistent cooling models used the AFTINV annealing model [48, 82, 83]. The model in Figure 4(c) is compatible with the interpretation that the rocks now at the surface in the region of the Wolf Intrusion (sample SF-66, Figure 2) could have maintained temperatures of up to ca. 75°C until the Miocene (ca. 15 Ma) and cooled since. Acceptable model solutions involving heating at higher temperatures for shorter time periods may also be compatible with the data (Figure 4(c)).

6.2. Comparison of PSS and WGVA. The active PSS in Expedition Fiord and the high-temperature veins in WGVA have many geological similarities that suggest a kinship, calling for a modification of the previous interpretations that the PSS are merely recent periglacial phenomena (e.g., [7, 50]).

6.2.1. Location. The PSS are in proximity (marginal) to anhydrite-gypsum diapiric structures, in zones that are characterized by faulting and brecciation. They are close to sea level or at the level of local rivers. The WGVA are not so close (~1-3 km) to mapped evaporite diapirs (Figure 2), but the brecciated evaporitic host rocks exposed and the proximity to large faults, which are probably rooted in diapirs at depth as suggested by geological cross sections by Jackson and Harrison [84], make it likely that a portion of their postulated evaporite salt canopy structure exists in the subsurface.

6.2.2. Size. The exposed plumbing systems (Figure 3) are comparable in areal size: PSS at Colour Peak Diapir and Gypsum Hill Diapir are 250×200 m and 400×50 m, respectively, but it is probable that they extend underneath Expedition Fiord and the Expedition River valley. The WGVA has exposures of more than 300×50 m but also extends under the glacier. Its visible vertical extent is 100 m or more; an unknown volume has been eroded.

6.2.3. Structures and Textures. The plumbing system at the WGVA consists of predominantly vertical, vein-like conduits lined by radial aggregates; however, both the WGVA and the PSS at Colour Peak Diapir exhibit banding, cyclic laminae at the mm scale in the PSS and mm to cm scale in the WGVA. The WGVA veins are crustified, often symmetrical, with acicular or fibrous crystals growing perpendicular to the margins, and some have large sparry (clear) crystals in the centre. The cyclicity in both implies the action of recurring pulses of mineral-laden fluids, which is the likely cause for laminated fabrics in the PSS mineral precipitates at Colour Peak Diapir. Sulfides occur in the WGVA within microfractures in the host rocks and as botryoidal aggregates in former open spaces up to decimetre scale.

6.2.4. Mineralogy. Both systems are mineralogically similar. The predominant mineral in both the PSS at Colour Peak Diapir and the WGVA is calcium carbonate in the form of calcite; laminated fabrics at Colour Peak Diapir contain mixtures of carbonate and micritic laminae with organic matter [55] and metal enrichments in Fe, Mn, Zn, Cu, and Ni. In addition to a predominance of calcite ($CaCO_3$), other phases identified in the PSS are halite (NaCl), ikaite ($CaCO_3{\cdot}6H_2O$), gypsum ($CaSO_4{\cdot}2H_2O$), thenardite (Na_2SO_4), mirabilite ($Na_2SO_4{\cdot}10H_2O$), and elemental sulfur (S°), which form in association with spring discharge [55–57]. The calcite in the WGVA shows signs of recrystallization judging from its mineral habit (orthorhombic blades and pseudo-hexagonal prisms resulting from twinning); therefore, it probably crystallized originally as aragonite. The pseudomorphs, however, yield calcite Raman spectra. Sulphates are also present as anhydrite ($CaSO_4$), gypsum, and barite ($BaSO_4$) but in the host breccias, not in the veins. The Fe- and Mg-rich mafic igneous host rocks of the WGVA contain epidote and chlorite as alteration of magmatic silicates, and the bulk of the Fe sulfides (marcasite and pyrite) occur within or near the mafic rocks, suggesting that they supplied the iron. However, the "zebra" banded carbonates rich in organic matter contain sulfides in the form of framboids and botryoidal aggregates. Sulfide (pyrite) microcrystalline aggregates similar to framboids are also observed within the banded mineral precipitates of the PSS at Colour Peak Diapir (Figure 5); the presence of hydrogen sulfide in discharging waters suggests microbial sulfate reduction, which is confirmed by sulfur isotope data of micritic sediments (see below). Chalcopyrite, sphalerite, galena, pyrrhotite, and arsenopyrite have so far been observed only in the WGVA and especially in the proximity of mafic igneous rocks.

6.2.5. Fluid Chemistry. A direct comparison of the chemistry of the rocks in the PSS and WGVA is not possible because the sampling and methodologies utilized were different. However, the fluids within the former can be compared with the inclusion fluids in the latter. The salinity of the brines in the PSS is bimodal, some yielding relatively low salinity fluids between 8 and 9% and others higher-salinity fluids of 16-17%; similarly, there is evidence for two different types of fluids in the fluid inclusions in the WGVA, 1.5% and 16% NaCl equivalent. The inclusion data in the WGVA suggest a progressive dilution with time from a ~20 wt% NaCl brine end-member down to ~pure (meteoric) water with evidence of large variability in salinity during progressive trapping of secondary inclusions. In comparison, the modern springs in the PSS show a variability in salinity from location to location from ~4.7 to 18.9 wt% NaCl equivalent [57] supporting the kinship between both systems. In both systems, chlorine is the most abundant halogen, and Ca and Na are the most abundant alkalis, reflecting the spatial association with evaporites, also manifest by the presence of sulfate. More internally consistent work needs to be done to confirm the comparisons made here.

6.2.6. Metals. Iron is the predominant metal sulfide in both systems, with 35 to 100 ppm sulfide (presumably as Fe sulfide) in the PSS precipitates [57], although the surfacing brines are not enriched in Fe (2 ppm; [60, 63]). In the WGVA, the sulfide content is extremely variable, from traces to 100%. The geochemical analyses of heavy mineral concentrates contain 32% Fe, 0.2% Mn, and small amounts of Ag (0.2 ppm), Cu (9 ppm), Pb (3 ppm), Zn (13 ppm), and Ba (430 ppm). These values are like those detected in 3 rock samples from a gossan in a raft of diabase adjacent to the PSS Colour Peak Diapir.

6.2.7. Stable Isotopes. Oxygen isotopes: the $\delta^{18}O_{VSMOW}$ value of the PSS hypersaline fluids is +10‰, thus dominantly high-latitude meteoric water but with a very minor non-meteoric (brine) component. Recalculation of the water composition that would be in equilibrium with the perennial spring carbonate at ~6°C (Figure 11, Table 5) gives a $\delta^{18}O_{VSMOW}$ value of -22.1‰ (similar to -26‰ for modern meteoric water in the study area; constrained using lat-long-elevation data using the OIPC3.1 calculator, University of Utah) suggesting a greater meteoric water contribution to the existing spring carbonates than in the current circulating fluid. The $\delta^{18}O_{VSMOW}$ values in the early brown (cal1) and later (cal2) carbonates at the WGVA range from -0.3‰ to +3.5‰, which based on fluid inclusion minimum trapping temperatures (~150-300°C), constrain minimum $\delta^{18}O_{VSMOW}$ values for coeval fluid between -0.2‰ and -8.7‰. This range in fluid $\delta^{18}O_{VSMOW}$ is explained through mixing of high-latitude meteoric water and a heated saline formational water or basinal brine.

Sulfur isotopes: ($\delta^{34}S_{VCDT}$) in the PSS at Colour Peak Diapir is +19.2‰ (sulfide separated from laminated carbonate-organic matter deposits) consistent with microbial sulfate reduction. In the WGVA, they range from -2.7‰ to +16.4‰, having a more ambiguous origin but likely preserving either low-temperature microbial sulfate reduction or higher-temperature reduction of sulfate by organics. The sulfur isotope systematics may have been somewhat altered by surface weathering, and more research is needed to confirm that the range in values for sulfides from the WGVA are not modified.

Carbon isotopes: $\delta^{13}C_{VPDB}$ in the PSS-laminated carbonate at Colour Peak Diapir is -10‰, suggesting an organic carbon component reflected in the measured isotope composition. The $\delta^{13}C_{VPDB}$ values in carbonates in the WGVA are -20.6 to -31.2‰, compatible with an origin from degradation of petroleum at depth. Specifically, the highly negative $\delta^{13}C_{VPDB}$ values associated with early cal1 are consistent with sourcing of hydrothermal carbonate from fluids that oxidized organic matter. Increasing $\delta^{13}C_{VPDB}$ with time approaches the same value as the PSS carbonate and nearer to the compositional field for post-ore carbonates filling pore spaces in host rocks from major MVT deposits in the Arctic of Canada [74, 75].

6.2.8. Temperature. As indicated above, the temperature of the PSS at Colour Peak Diapir is rather invariable at ~6°C [55]. The fluid inclusions in the WGVA indicate that the fluids had temperatures from 100°C to 300°C (Figures 10(a) and 10(b)). This higher temperature is compatible with the presence of epidote adjacent to the veins, requiring temperatures between ~200°C and 350°C to crystallize from hydrothermal fluids [85, 86]. It is unclear whether the fluids at depth in the PSS have warm temperatures and equilibrate with the surrounding permafrost to result in a temperature of ca. 6°C as suggested by Andersen et al. [7] or if they presently circulate to greater depths, as they must have done in the past to account for the fluid inclusion data. The inclusion data do not portray any correlation between T_h and salinity across the large continuous range in salinity observed. This can be interpreted in 2 ways: (a) maintenance of fluid T (i.e., between approximately 150°C and 250°C) during progressive dilution (unlikely because it would require the low-salinity fluid to be heated before mixing) or (b) a cooling trend from early high salinity to low salinity, if P decreased from quasi-lithostatic to hydrostatic conditions (i.e., if we correct T_h for P); exhumation of the system may have contributed to this transition. This second explanation agrees with stable isotope data (showing increasing amounts of likely meteoric water requiring a more open system to allow incursion and mixing).

6.3. Framboidal Pyrite. Framboidal pyrite has been observed in the WGVA (Figures 9(f) and 9(g)), and Fe-sulfide microlite-like constituents of framboids are observed in micritic layers in banded carbonate in the PSS at Colour Peak Diapir (Figure 5). The origin of framboidal pyrite has been debated since first described from ores in sedimentary strata by Schneiderhöhn [87] who described them as "mineralized bacteria," although subsequent research demonstrated that they can form in purely inorganic systems. Nevertheless, experimental work shows they generally form at temperatures below 100°C in environments where bacteria are present. Wilson et al. [88] argued for bacterial growth of framboids within liquid petroleum at depths of several km, based on textural evidence and sulfur isotopes, and recently Lin et al. [89] demonstrated that framboids can grow rapidly where anaerobic oxidation of methane is coupled with microbial sulfate reduction. The spherical shape of framboid aggregates has been ascribed to colloidal phenomena, or to the replacement of minute vacuoles, but their formation has proven extremely difficult in the absence of organic matter [90]. The presence of organic matter enhances the chemical formation of pyrite combining metals and biologically produced hydrogen sulfide [90]. Wilkin and Barnes [91] explain the growth of framboids in four consecutive stages: (1) nucleation and growth of initial iron monosulfide microcrystals, (2) reaction of the microcrystals to greigite (Fe_3S_4) or mackinawite (Fe_9S_8), (3) aggregation of uniformly sized greigite microcrystals, i.e., framboid growth, and (4) replacement of greigite framboids by pyrite or marcasite. Some of the microcrystalline Fe-sulfide textures observed in the PSS at Colour Peak Diapir (Figure 5(k)) illustrate this sulfide evolution. Vietti et al. [92] found that framboids grew readily within sulfidic microbial biofilms by bacterial degradation of organic matter. If there is continued influx of Fe, the originally spheroidal aggregates of microlites progressively recrystallize into idiomorphic (cubic or octahedral) crystals; this recrystallization is prevented if the framboids are isolated from new input of Fe, as within a biofilm, petroleum, or an enclosing mineral [93, 94]. Pyrite framboids formed during catastrophic dysoxic events in sedimentary basins [95] and in methane seeps associated with gypsum, where biogenic activity is possible [89]. Despite controversy, some authors are persuaded that pyrite framboids are associated with bacterial activity (e.g., [96, 97]). Both low-grade metamorphism and fluid-rich diagenesis can lead to framboid recrystallization and formation of aggregates with framboidal cores and euhedral edges [98]. Heating above 150°C makes marcasite revert to pyrite [49, 99, 100].

The presence of pyrite with microlites similar to those in framboids in the PSS at Colour Peak Diapir is a possible sign of anoxic reduction during the flow of hydrocarbons (methane) and/or microbial activity, which would explain the preliminary sulfur isotope signature. The presence of framboidal pyrite in the WGVA is suggestive of interaction with hydrocarbons at depth but also of microbial activity when marcasite was also the stable phase of Fe sulfide, probably at temperatures below 100°C. The evidence for recrystallization of framboids and the reversion of marcasite to pyrite indicate subsequent heating.

6.4. "Zebra" Textures. The "zebra"-textured veins at WGVA (Figures 7(e)–7(g)) were formed by "open space filling" and have similar mineralogy and texture to subvertical veins in the area, within diabase or brecciated sedimentary rocks. The term "zebra" texture has been applied to arrays of subparallel veins in base metal ore deposits or dolomitized carbonate masses, where there is light and dark banding that reminds of a zebra coat. They have bilateral symmetry about a central mineral band (C) with repetition of sulfide and/or gangue mineralogy in the following form: A B C B A, where A, B, and C represent different mineral phases or different generations of a single mineral phase (*c.f.* [101–103]). Originally, sedimentological and diagenetic evidence led early authors to describe their formation immediately below the sediment-water interface as "diagenetic crystallization rhythmites." However, the early-diagenetic interpretation has been rejected as a general model, since various types of zebra veins have been described in various geological environments. For instance, in the Nanisivik Pb-Zn-Ag deposit located on northwest Baffin Island (lower right in Figure 1), zebra vein arrays very similar to those at WGVA were interpreted to have formed by pulses of basinal fluids, later than lithification of the host sediments at temperatures more than 200°C [104, 105]. Recent workers (e.g., [106]) interpret zebra veins in a Mississippi Valley Type base metal deposit in the Andes as having formed as sheet cavity networks developed by extensional fracturing in deep subsurface environments such as the filling of subhorizontal tension fractures formed during thrusting. Under these conditions, the most effective mechanism to generate subparallel tension fractures is fluid overpressure and episodic hydraulic fracturing (e.g., [107–109]),

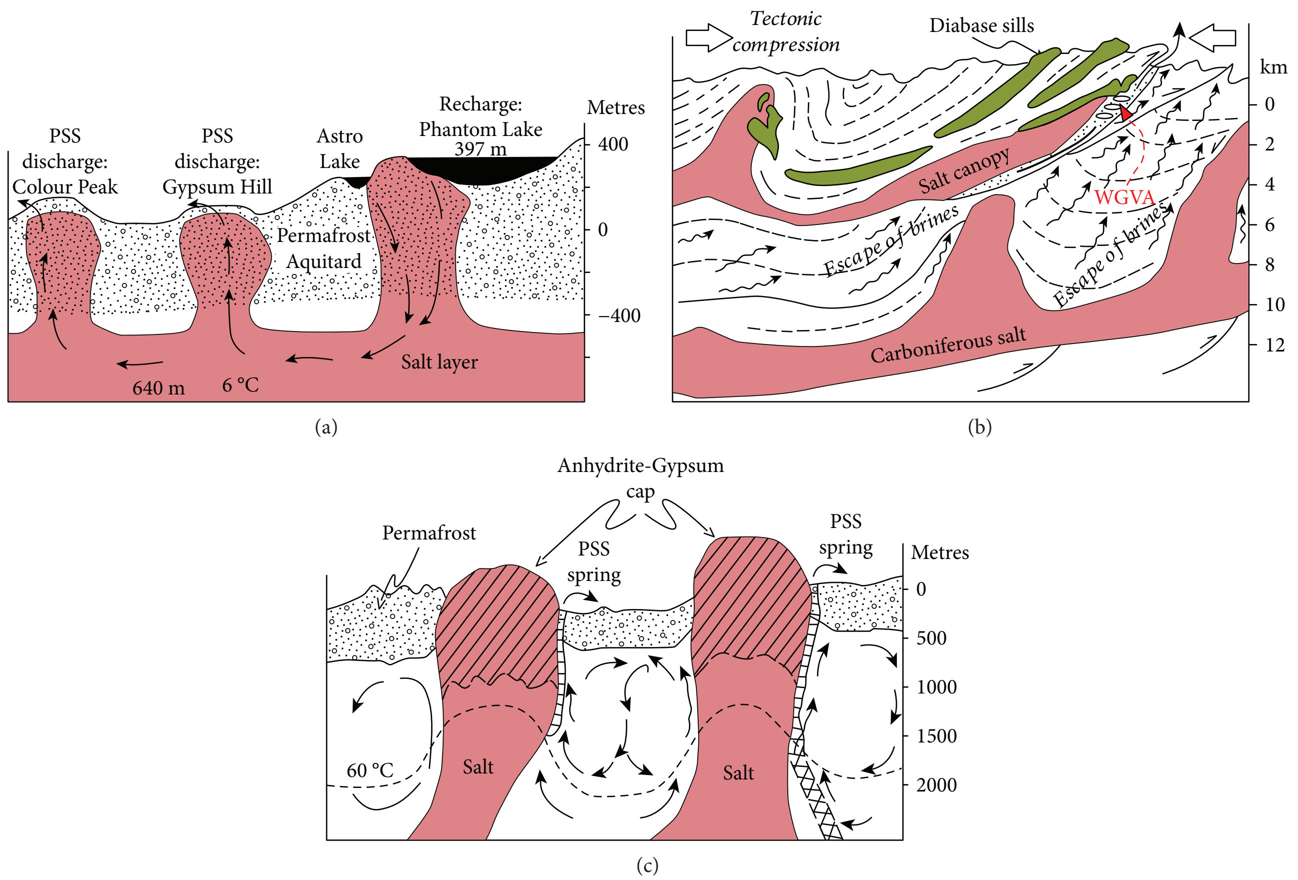

Figure 12: (a) Model for the perennial springs (PSS) as first published by Andersen et al. [7] with fluid recharge from glacial lakes through permeable evaporite (salt) diapirs, shallow circulation, and continuous escape. (b) Proposed model for White Glacier vein array (WGVA). Overpressured hot basinal fluids expelled episodically through faults from under the salt canopy during tectonic compression of the Eurekan Orogeny (hypothetical subsurface structure modified from [6]). (c) Proposed hypothetical model for the perennial springs, where fluids have a mixed origin and escape marginally to evaporite (salt-anhydrite-gypsum) diapirs through plumbing systems established during tectonic deformation (b). Not to scale. See text for discussion including description of lithologies.

repeated cycles of hydraulic fracturing and healing like the mechanism responsible for banded veins referred to as "crack-seal" veins (e.g., [110]). The generation of episodic basin dewatering of overpressured fluids in sedimentary basins with evaporites is a common phenomenon, especially if enhanced by compressive tectonics [111–113], but also due to rapid compaction [114] and in the environment of salt dome cap rocks [115]. Finally, Warren [69] discusses the common development of geopressured fluids in the environment of salt canopies similar to the one underlying Expedition Fiord as defined by Jackson and Harrison [6]. An alternative hypothesis for the formation of zebra textures relates them to force of crystallization during diagenesis or mineral replacement (e.g., [102, 116]), but we consider these interpretations not applicable to the WGVA.

Similar "zebra" textures in the PSS at Colour Peak Diapir (Figure 5(b)) at a millimeter scale were formed by a different process, since they are obviously formed at or near the surface by successive pulses of expelled fluid. It is likely that at depth in the PSS (and analogous WGVA) the conduits are lined with similarly banded, crustified mineral coatings. Drilling will be necessary to better understand their nature.

6.5. Towards a Deeply Circulating Model for the PSS. The similarities between the PSS and WGVA make it likely that both systems have some genetic kinship. Pollard et al. [3] considered it unlikely that meteoric or surface water could be the source of the brines in the PSS, yet the hypothetical model by Andersen et al. [7, 50, 66] (Figure 12(a)) envisaged relatively surficial circulation of fluids, with recharge from Astro and Phantom Lakes, which are located on the eastern flank of Thompson Glacier, ~397 m above the outlet of the springs (upper right corner of Figure 2). Andersen et al. [7] assumed (Figure 12(a)) that the deep subsurface salt layer acts as a "reservoir and conduit" of water. Seasonally, the lakes drain partially (1-2%) and the water would circulate to the PSS through faults, such as the ones mapped in the area (Figure 2). Water would flow below the surface at a depth of 600 to 700 m via an evaporite layer, returning to the surface through the piercement structures associated with the springs. Below the surface, the water would attain the geothermal temperature (they assumed a geothermal gradient of 37.3°C/km after [54]). As they flow upward, the brines would lose heat to the surrounding permafrost.

The Andersen et al. [7, 50, 66] model is problematic. Firstly, evaporites (salt, anhydrite, and gypsum) in the near-surface are among the most impermeable rocks in nature. Powers et al. [117] and Holt and Powers [118] have argued that it is virtually impossible for meteoric water to penetrate evaporitic rocks; under similar conditions in salt (halite), water would take 3 to 30 million years to advance 1 m, in anhydrite 300,000 years [119]. Even in active salt springs around salt diapirs in semi-desert Iran, Zarei and Raeisi [120] assume that surface recharge cannot penetrate more than 10 m. A further problem is that if halite is present, it is difficult to maintain permeability, because porosity becomes occluded [121]. Peripheral fracturing can lead to focussed fluid flow (e.g., [69]), but the geological map and cross sections (Figure 2; [6, 27]) show that there is no likely shallow continuous body of evaporite between Astro Lake and Colour Peak Diapir, a distance of ~20 km. More likely evaporites act as impervious barriers, and any circulation would be peripheral and focussed by them. The surficial water flow model is unlikely considering the independence of PSS brine flow temperature and wide air temperature variations between winter and summer at this latitude. Evaporite-focussed fluid leakage was postulated by Keen [122] to explain heat flow anomalies above salt diapirs in offshore Nova Scotia. Although salt conducts heat many times more effectively than other sediments, Keen [122] concluded that conduction alone could not explain the anomaly, and advective heat from escaping warm fluids was required; for the model, she assumed that the aquifer temperature would be 150°C, hence definitely did not consider surficial seawater. Evans et al. [123] have explained the mechanisms responsible for advection of fluids near salt domes, and Warren [69] discusses the flow of warm brines peripheral to evaporite diapir regions where salt canopies have developed. In the Expedition Fiord area, the evidence is compatible with models in which the PSS fluids migrate upward from considerable depth following previously developed plumbing systems marginal to evaporite bodies (Figure 12(c)), either by vein arrays such as those at WGVA or brecciation typical of the margins of displaced allochthonous salt masses [69]. The involvement of hydrocarbons in the reactions leading to precipitation of minerals including carbonates and sulfides in the above systems further suggests a connection with petroleum seeps, difficult to ascribe to surface recharge, especially in a polar region with thick permafrost. Liquid and gaseous hydrocarbons are present in fluid inclusions (Zentilli, unpublished data) in the Colour Peak Diapir (Figure 1), and deep wells drilled on salt-cored anticlines indicate the presence of adequate source rocks [21].

The apatite fission track data suggest that the rocks now at the surface in Axel Heiberg Island outside the area of the WGVA were at temperatures of ca. 100°C in the Eocene (Figure 4(b) and [8]). Based on industrial thermal data (156 deep wells) and coalification gradients, during the Paleogene the geothermal gradient in this region is estimated to have been 28 ± 9 mK/m [124], which translates into 2.7 to 5.3 km (avge. 3.6 km) of erosion. Since in the area of the PSS and WGVA the thermal regime was anomalous due to fluid advection, it is problematic to be certain of its paleogeothermal gradient. However, the apatite FT models are compatible with rocks now at the surface having been at temperatures of ca. 75°C (with large uncertainty, Figure 4(c)) until the Miocene, and one can estimate between of 0.5-2 km of exhumation until the veins were exposed by glacial erosion. The WGVA is located near the bottom bedrock of the White Glacier valley; hence, much of the mineralized zone may have been eroded. It is problematic to assess how much pre-glacial erosion has taken place in the Expedition Fiord area. When mountains in Axel Heiberg Island were rising in the Eocene, the climate was warm and humid, leading to the formation of forests (e.g., [10]), and it is unlikely that large glaciers occupied the region through the Miocene, so ensuing erosion was probably due to fluvial incision and exhumation related to landsliding of steep slopes (John Gosse, personal communication). The Late Miocene through Pliocene appears to have been a time of net deposition in the Canadian Arctic, resulting in the infilling of preexisting valleys or grabens, and extensive depositional surfaces until 2.7 Ma [125–127]. Those surfaces were subsequently incised, perhaps initially by streams, but more significantly by warm-based outlet glaciers [128] and independent valley glacier systems. While erosion by valley and outlet glaciers through unconsolidated sediment is likely to have been rapid, even bedrock has been incised by more than 80 m/Myr [129] to form fiords. However, under cold-based glaciers which occupied many summit plateaus in Arctic Canada, subglacial erosion can be negligible, as indicated by the survival of moss under cold-based glaciers for more than 5 ka [130, 131].

The fluid inclusions indicate the carbonate and sulfide minerals in the veins crystallized from more than one pulse of hot fluids with temperatures between 100°C and 300°C, and strong swings in pressure can be ascertained. The veins and zebra textures were formed in open spaces, which at a depth of a few km could only have been present if the fluids were at lithostatic pressure plus the tensional strength of the rocks [107]. The environment in which the WGVA developed is one of evolving allochthonous evaporite, with a large salt canopy at depth [6]. The region underwent strong compression during the Paleogene Eurekan Orogeny (Figure 12(b)). The zebra textures described at the WGVA are like zebra textures developed in compressive tectonic environments associated with thrusting in fluid overpressured zones (e.g., [106]). The host rocks of the WGVA are fractured mafic igneous rocks physically intermixed with a breccia or conglomerate that has some similarities with "gumbo" found in association with displaced allochthonous salt masses in various basins rich in evaporites in Oman, the Gulf of Mexico, offshore Angola and Brazil; these brecciated rocks are characteristically strongly overpressured when intersected by drilling [69].

Although overpressures may develop under autochthonous and evolving allochthonous layers of salt by simple compaction [132, 133], in some instances it leads to the generation of metallic ore deposits [114]; compressional tectonics can intensify them (Oliver, 1986; [112]). The Eurekan Orogeny (Paleogene) in the Sverdrup Basin resulted from collision of Greenland with the Canadian Arctic Archipelago [134] and led to the formation of high mountains (Figure 1) by stacking. Most thrust faults are rooted in salt, and a particular case is the formation of the folded wall-and-basin structure province that underlies Expedition Fiord, caused by shortening during the Eurekan Orogeny.

We suggest (Figure 12(b)) that during the Eurekan Orogeny, overpressures were generated under the shifting salt canopy of Jackson and Harrison [6], and successive pulses of hot fluids were expelled, which developed, by hydraulic fracturing, the veins and subparallel zebra rocks of the WGVA in a local tensional (dilatant) environment. It is a characteristic of overpressuring in this environment to reach a point where the effective pressure overtakes the lithostatic pressure and tensional strength of the rocks [107], and a fracture (and a "fracking" earthquake) ensues. Once sufficient volume has been created (dilation) to accommodate the fluid or let it escape, the fluid pressure drops. However, localized pressure drop has little effect on the first-order cause of the tectonic compression, so the pressure builds up again until a new "fracking" event occurs. A sudden pressure drop, combined with decreasing fluid salinity and temperature resulting from mixing of brine and meteoric water, is an optimal mechanism to reduce aqueous CO_2 solubility [135, 136]. These processes would precipitate carbonate on the walls of the recently created cavities and fractures followed by quartz precipitates forming the later cavity infilling textures (after carbonate) observed in the veins. However, fluid inclusion observations do not support boiling/CO_2 unmixing as a process that took place in the veins. Thus, while pressure fluctuations sufficient to cause fracture formation are mandatory, these pressure fluctuations were not sufficient enough to cause boiling/unmixing. Fluid mixing and cooling were likely important for vein mineral precipitation.

The fluids expelled from the overpressured zones contain small amounts of Cu, Zn, and Pb, which are typical in Mississippi Valley Type (MVT) deposits associated with salt diapirs [115, 137]. The precipitation as sulfides requires the presence of sulfur as dissolved sulfate from the evaporites, and some reduction mechanism to generate hydrogen sulfide. An ideal redox reaction would be the oxidation of organic matter that would be resident in porous sedimentary rocks as petroleum (oil or gas) and the concomitant reduction of dissolved sulfate. Microbial reduction could be a contributing factor, and probably was. The base metal sulfides are generally in veins marginal to the larger carbonate veins, very often in the mafic igneous rocks. The presence of pyrite-marcasite seems to coincide with the presence of mafic igneous rocks rich in Fe (magnetic when fresh). Hence, it is possible that some of the base metals are extracted from the altered diabase and that oxidation of magnetite is accompanied by reduction of sulfate. The fluid expulsion phenomenon was of regional proportions, and if it led to the formation of the WGVA, it is likely to have formed other similar mineralized sites, and this possibility seems confirmed by the presence of gossans in the vicinity of many diapirs in Axel Heiberg Island (e.g., [138]).

The kinship between the WGVA and the modern PSS is further supported by the fluid inclusion data, which suggest a progressive dilution with time from a ~20 wt% NaCl brine down to ~pure water, with a spread of data right across this range. Therefore, we propose that the PSS are exploiting a plumbing system established during the formation of the WGVA (Figure 12(c)).

7. Conclusions

(1) A carbonate vein array with metal sulfides recognized on the western boundary of White Glacier (WGVA) is interpreted to be the remnants of a hydrothermal system developed during the Eurekan Orogeny. Hydraulic fracturing by overpressured fluids led to brecciation of rocks and formation of carbonate veins in dilatant zones peripheral to allochthonous evaporite masses; brecciation of the host rocks may have developed earlier, during displacement of the salt canopies and diapirs (see Section 5.2). Processes envisaged are similar to those leading to the genesis of base metal deposits know as Mississippi Valley Type (MVT) deposits.

(2) Initially, the WGVA was formed by hot fluids with a minimum temperature of 150°C to 300°C and having high salinity, in successive pulses with wild pressure changes related to hydraulic fracturing, and later was invaded by dilute fluids of lower temperatures. The depth of emplacement can be estimated to have been a minimum of 0.5 km.

(3) The pervasive advection of hot fluids in the Expedition Fiord region explains the anomaly detected by apatite fission track thermochronology which suggested that the rocks now at the surface cooled below 100°C in the Miocene, ca. 20 My later than similar rocks regionally in Axel Heiberg Island and Ellesmere Island. Hydrothermal activity initiated in the Eocene continued for a long time with involvement of cooler, more dilute fluids, extending to this day.

(4) Perennial springs (PSS) on Axel Heiberg Island that discharge waters at constant temperatures irrespective of air temperature in an area with ca. 600 m of permafrost are not surficial, periglacial phenomena as previously interpreted, but are instead related to deep plumbing systems established by expulsion of overpressured fluids from under plastically displacing impermeable salt structures during tectonic, compressive deformation and thrust faulting in the Paleogene Eurekan Orogeny.

(5) Microbial activity and the involvement of hydrocarbons throughout the history of the WGVA is supported by mineralogy and stable isotope data. If this spring activity has lasted for ca. 10 My as suggested, it could have allowed for isolated evolution of microorganisms since the brines cooled sufficiently to permit their survival. Future work, preferably supported by deep drilling both at the WGVA and PSS, will determine the presence and diversity of microorganisms in these deep subsurface environments.

Data Availability

All data discussed in paper are in 4 tables. Any other data available on request.

Conflicts of Interest

The authors declare that they have no conflicts of interest.

Acknowledgments

The authors acknowledge support from the Natural Sciences and Engineering Research Council of Canada (NSERC) through grants to M. Zentilli, J. Hanley, and W. Pollard, and an NSERC PDF to C. Omelon. Additional funding for student research was provided by the Department of Indian and Northern Affairs Northern Scientific Training Program and McGill University's Centre for Climate and Global Change. Field work was supported by the McGill Arctic Research Station (MARS) (c/o Wayne Pollard, without whose support and encouragement this research would have been impossible), the Canadian Space Agency (c/o Gordon Osisnki), the Geological Survey of Canada, and the Polar Continental Shelf Program (c/o Marie-Claude Williamson, Party Chief 2003). We are grateful to Marie-Claude Williamson, with whom the first author first visited the perennial springs, subject of this paper. We thank Alexander (Sandy) Grist for apatite fission-track data and time-temperature modelling, Yawooz Kettanah for fluid inclusion microthermometry from one sample, Dale T. Andersen for stimulating discussions and field photos; John Gosse for advice on the Cenozoic erosion of the study region, Laura Thomson for educating us about glaciers, and Randolph Corney for drafting. We are also grateful to Todd Simpson and Tim Goldhawk of the Western Nanofabrication Facility for technical expertise. This research used resources of the Advanced Photon Source, a U.S. Department of Energy (DOE) Office of Science User Facility operated for the DOE Office of Science by Argonne National Laboratory under Contract No. DE-AC02-06CH11357. Data was collected at the X-Ray Science Division at the Advanced Photon Source, Argonne National Laboratory; we thank the Sector 20 beamline staff for their support of this research.

References

[1] P. T. Doran, C. P. McKay, W. P. Adams, M. C. English, R. A. Wharton, and M. A. Meyer, "Climate forcing and thermal feedback of residual lake-ice covers in the high Arctic," *Limnology and Oceanography*, vol. 41, no. 5, pp. 839–848, 1996.

[2] R. E. Beschel, "Sulphur springs at Gypsum Hill," *Preliminary. report 1961-1962. Axel Heiberg Island Research Report*, McGill University, Montréal, QC, USA, 1963.

[3] W. Pollard, C. Omelon, D. Andersen, and C. McKay, "Perennial spring occurrence in the Expedition Fiord area of western Axel Heiberg Island, Canadian High Arctic," *Canadian Journal of Earth Sciences*, vol. 36, no. 1, pp. 105–120, 1999.

[4] W. H. Pollard, T. Haltigin, L. Whyte et al., "Overview of analogue science activities at the McGill Arctic Research Station, Axel Heiberg Island, Canadian High Arctic," *Planetary and Space Science*, vol. 57, pp. 646–659, 2009.

[5] G. R. Davies and W. W. Nassichuk, "Carboniferous and Permian history of the Sverdrup Basin, Arctic Islands," in *Geology of the Innuitian Orogen and Arctic Platform of Canada and Greenland*, H. P. Trettin, Ed., pp. 345–367, Geological Survey of Canada, Ottawa, Canada, 1991.

[6] M. P. A. Jackson and J. C. Harrison, "An allochthonous salt canopy on Axel Heiberg Island, Sverdrup Basin, Arctic Canada," *Geology*, vol. 34, no. 12, pp. 1045–1048, 2006.

[7] D. T. Andersen, W. H. Pollard, C. P. McKay, and J. Heldmann, "Cold springs in permafrost on Earth and Mars," *Journal of Geophysical Research*, vol. 107, no. E3, 2002.

[8] D. C. Arne, A. M. Grist, M. Zentilli, M. Collins, A. Embry, and T. Gentzis, "Cooling of the Sverdrup Basin during tertiary basin inversion: implications for hydrocarbon exploration," *Basin Research*, vol. 14, no. 2, pp. 183–205, 2002.

[9] M. Zentilli, A. M. Grist, and M.-C. Williamson, "Paleothermal effects of salt diapirs detected by apatite fission track thermochronology," in *Abstracts of the European Conference on Thermochronology, Bremen, Germany*, vol. 49, p. 35, Schriftenreihe der Deutschen Gesellschaft für Geowissenschaften, 2006.

[10] M. Zentilli, A. M. Grist, and M.-C. Williamson, "The Stolz Thrust and its connection with the Eocene Metasequoia Fossil Forest of Axel Heiberg Island, Canadian Arctic Archipelago: Apatite Fission Track Evidence. Abstract," in *Proceedings from the 11th International Conference on Thermochronometry*, pp. 280–282, Anchorage, Alaska, September 2008.

[11] A. V. Okulitch and H. P. Trettin, "Late Cretaceous. Early Tertiary deformation, Arctic Islands," in *Geology of the Innutian Orogen and Arctic Platform of Canada and Greenland*, H. P. Trettin, Ed., pp. 467–489, Geological Survey of Canada, Geology of Canada, No. 3, 1991.

[12] B. D. Ricketts and R. A. Stephenson, "The demise of Sverdrup Basin: Late Cretaceous-Paleogene sequence stratigraphy and forward modeling," *SEPM Journal of Sedimentary Research*, vol. 64B, no. 516, p. 530, 1994.

[13] Department of Energy, Mines and Resources Canada, *The National Atlas of Canada; Natural Resources Canada, Geomatics Canada, MCR Series no. 4177, 1995*, Department of Energy, Mines and Resources Canada, Ottawa, Canada, 1995.

[14] M. J. van der Ploeg, S. Haldorsen, A. Leijnse, and M. Heim, "Subpermafrost groundwater systems: dealing with virtual reality while having virtually no data," *Journal of Hydrology*, vol. 475, pp. 42–52, 2012.

[15] R. Barbieri and N. Stivaletta, "Continental evaporites and the search for evidence of life on Mars," *Geological Journal*, vol. 46, no. 6, pp. 513–524, 2011.

[16] A. S. McEwen, L. Ojha, C. M. Dundas et al., "Seasonal flows on warm Martian slopes," *Science*, vol. 333, no. 6043, pp. 740–743, 2011.

[17] J. D. Rummel, D. W. Beaty, M. A. Jones et al., "A new analysis of Mars "special regions": findings of the second MEPAG Special Regions Science Analysis Group (SR-SAG2)," *Astrobiology*, vol. 14, no. 11, pp. 887–968, 2014.

[18] J. R. Michalski, J. Cuadros, P. B. Niles, J. Parnell, A. D. Rogers, and S. P. Wright, "Groundwater activity on Mars and implications for a deep biosphere," vol. 6, no. 2, pp. 133–138, 2013.

[19] A. Embry and B. Beauchamp, "Sverdrup Basin," in *Sedimentary Basins of the World*, A. D. Miall, Ed., pp. 451–471, Elsevier, 2008.

[20] Z. Chen, K. G. Osadetz, A. F. Embry, H. Gao, and P. K. Hannigan, "Petroleum potential in western Sverdrup Basin, Canadian Arctic Archipelago," *Bulletin of Canadian Petroleum Geology*, vol. 48, no. 4, pp. 323–338, 2000.

[21] S. F. Jones, H. Wielens, M. C. Williamson, and M. Zentilli, "Impact of magmatism on petroleum systems in the Sverdrup Basin, Canadian Arctic Islands, Nunavut: a numerical modelling study," *Journal of Petroleum Geology*, vol. 30, no. 3, pp. 237–256, 2007.

[22] E. T. Tozer, *Mesozoic and Tertiary Stratigraphy, Western Ellesmere Island and Axel Heiberg Island, District of Franklin (Preliminary Account)*, Department of Mines and Technical Surveys, 1963.

[23] R. Thorsteinsson and E. T. Tozer, *Geology western Queen Elizabeth Islands, district of Franklin*, Geological survey of Canada, 1964, Map 1142A, scale 1:506,880.

[24] P. E. Fricker, *Geology of the Expedition Area: Western Central Axel Heiberg Island; Canadian Arctic Archipelago; Jacobsen-McGill Arctic Research Expedition 1959–1962*, McGill University, 1963.

[25] E. W. Hoen, *The Anhydrite Diapirs and Structure of Central Western Axel Heiberg Island: Canadian Arctic Archipelago, [M.S. thesis]*, McGill University, Montreal, Canada, 1962.

[26] E. W. Hoen, *The Anhydrite Diapirs of Central Western Axel Heiberg Island. Jacobsen-McGill Arctic Research Expedition 1959-1962 Research Reports, Geology, No. 2*, McGill University, Montreal, 1964.

[27] J. C. Harrison and M. P. Jackson, "Geology, Strand fiord-expedition fiord area, western Axel Heiberg Island, Nunavut," in *Geological survey of Canada, Map 2157A, scale 1:100 000*, Geological Survey of Canada, Ottawa, Canada, 2010.

[28] M. Villeneuve and M. C. Williamson, "40Ar-39Ar dating of mafic magmatism from the Sverdrup Basin Magmatic Province," in *Proceedings of the Fourth International Conference on Arctic Margins. Dartmouth, Nova Scotia, Canada 2003*, pp. 206–216, Anchorage, Alaska, 2006.

[29] P. Budkewitsch, W. Pollard, and M. Zentilli, *Youngest Hills in Axel Heiberg Island, Canadian Arctic Archipelago: Are the Salt Domes Rising?*, Geological Association of Canada Meeting, Ottawa, Canada, 2011.

[30] J. T. van Berkel, W. M. Schwerdtner, and J. G. Torrance, "Wall-and-basin structure: an intriguing tectonic prototype in the central Sverdrup Basin, Canadian Arctic Archipelago," *Bulletin of Canadian Petroleum Geology*, vol. 32, no. 4, pp. 343–358, 1984.

[31] W. M. Schwerdtner and M. Van Kranendonk, "Structure of Stolz Diapir – a well-exposed salt dome on Axel Heiberg Island, Canadian Arctic Archipelago," *Bulletin of Canadian Petroleum Geology*, vol. 32, no. 2, pp. 237–241, 1984.

[32] W. W. Nassichuk and G. R. Davies, "Biostratigraphy and sedimentology of the Otto Fiord Foration – a major Mississippian-Pennsylvanian evaporite unit of subaqueous origin in the Canadian Arctic Archipelago," *Geological Survey of Canada*, vol. 286, article 1087, 1980.

[33] L. I. Thomson and L. Copland, "White Glacier 2014, Axel Heiberg Island, Nunavut: mapped using structure from motion methods," *Journal of Maps*, vol. 12, no. 5, pp. 1063–1071, 2016.

[34] L. I. Thomson, M. Zempf, L. Copland, G. Cogley, and M. Ecclestone, "Comparison of geodetic and glaciological mass budgets for White Glacier, Axel Heiberg Island, Canada," *Journal of Glaciology*, vol. 63, no. 237, pp. 55–66, 2016.

[35] B. Lafuente, R. T. Downs, H. Yang, and N. Stone, "The power of databases: the RRUFF project," in *Highlights in Mineralogical Crystallography*, T. Armbruster and R. M. Danisi, Eds., pp. 1–30, W. De Gruyter, Berlin, Germany, 2015.

[36] R. J. Bodnar and M. O. Vityk, "Interpretation of Microthermometric Data for H2O-NaCl Fluid Inclusions," in *Fluid Inclusions in Minerals: Methods and Application*, B. Vivo and M. L. Frezzotti, Eds., Pontignsno-Siena, 1994117130.

[37] T. Driesner and C. A. Heinrich, "The system H_2O–NaCl. Part I: correlation formulae for phase relations in temperature–pressure–composition space from 0 to 1000°C, 0 to 5000 bar, and 0 to 1 X_{NaCl}," *Geochimica et Cosmochimica Acta*, vol. 71, no. 20, pp. 4880–4901, 2007.

[38] T. Driesner, "The system H_2O–NaCl. Part II: correlations for molar volume, enthalpy, and isobaric heat capacity from 0 to 1000°C, 1 to 5000 bar, and 0 to 1 X_{NaCl}," *Geochimica et Cosmochimica Acta*, vol. 71, no. 20, pp. 4902–4919, 2007.

[39] D. Günther and C. A. Heinrich, "Enhanced sensitivity in laser ablation-ICP mass spectrometry using helium-argon mixtures as aerosol carrier," *Journal of Analytical Atomic Spectrometry*, vol. 14, no. 9, pp. 1363–1368, 1999.

[40] D. Günther, R. Frischknecht, C. A. Heinrich, and H. J. Kahlert, "Capabilities of an argon fluoride 193 nm excimer laser for laser ablation inductively coupled plasma mass spectometry microanalysis of geological materials," *Journal of Analytical Atomic Spectrometry*, vol. 12, no. 9, pp. 939–944, 1997.

[41] T. Pettke, W. E. Halter, J. D. Webster, M. Aigner-Torres, and C. A. Heinrich, "Accurate quantification of melt inclusion chemistry by LA-ICPMS: a comparison with EMP and SIMS and advantages and possible limitations of these methods," *Lithos*, vol. 78, no. 4, pp. 333–361, 2004.

[42] M. Guillong, D. L. Meier, M. M. Allan, C. A. Heinrich, and B. W. Yardley, "Appendix A6: SILLS: a MATLAB-based program for the reduction of laser ablation ICP-MS data of homogeneous materials and inclusions," *Mineralogical Association of Canada Short Course Series*, vol. 40, pp. 328–333, 2008.

[43] A. M. Grist and M. Zentilli, "The thermal history of the Nares Strait, Kane Basin, and Smith Sound region in Canada and Greenland: constraints from apatite fission-track and (U Th Sm)/He dating," *Canadian Journal of Earth Sciences*, vol. 42, no. 9, pp. 1547–1569, 2005.

[44] G. Wagner and P. Van den Haute, *Fission Track Dating*, Kluwer Academic Publishers, Dordrecht, 1992, reprinted by Ferdinand Enke Verlag Thc Netherlands.

[45] C. E. Ravenhurst and R. A. Donelick, "Fission track thermochronology," in *Short Course Handbook on Low Temperature Thermochronology*, M. Zentilli and P. H. Reynolds, Eds., pp. 21–42, Mineralogical Association of Canada, Wolfville, Nova Scotia, Canada, 1992.

[46] K. Gallagher, R. Brown, and C. Johnson, "Fission track analysis and its applications to geological problems," *Annual Review of Earth and Planetary Sciences*, vol. 26, no. 1, pp. 519–572, 1998.

[47] A. J. Gleadow and R. W. Brown, "Fission-track thermochronology and the long-term denudational response to tectonics," in *Geomorphology and global tectonics*, M. J.

Summerfield, Ed., pp. 57–75, Wiley, New York, NY, USA, 2000.

[48] G. M. Laslett, P. F. Green, I. R. Duddy, and A. J. W. Gleadow, "Thermal annealing of fission tracks in apatite 2. A quantitative analysis," *Chemical Geology: Isotope Geoscience Section*, vol. 65, no. 1, pp. 1–13, 1987.

[49] P. Vrolijk, R. A. Donelick, J. Queng, and M. Cloos, "Testing models of fission track annealing in apatite in a simple thermal setting: site 800, leg 129," in *Proceedings of the Ocean Drilling Program, Scientific Results*, vol. 129, pp. 169–176, Ocean Drilling Program College Station, TX, USA, 1992.

[50] D. T. Andersen, W. H. Pollard, and C. P. McKay, "The perennial springs of Axel Heiberg Island as an analogue for groundwater discharge on Mars," in *9th International Conference on Permafrost*, vol. 2, pp. 2140–2145, Fairbanks, Alaska, 2008.

[51] W. H. Pollard, "Icing processes associated with High Arctic perennial springs, Axel Heiberg Island, Nunavut, Canada," *Permafrost and Periglacial Processes*, vol. 16, no. 1, pp. 51–68, 2005.

[52] S. E. Grasby, C. C. Allen, T. G. Longazo, J. T. Lisle, D. W. Griffin, and B. Beauchamp, "Supraglacial sulfur springs and associated biological activity in the Canadian High Arctic—signs of life beneath the ice," *Astrobiology*, vol. 3, no. 3, pp. 583–596, 2003.

[53] S. E. Grasby, B. C. Proemse, and B. Beauchamp, "Deep groundwater circulation through the High Arctic cryosphere forms Mars-like gullies," *Geology*, vol. 42, no. 8, pp. 651–654, 2014.

[54] A. E. Taylor and A. S. Judge, *Canadian Geothermal Data Collection-Northern Wells 1975*, Energy MaRC, Earth Physics Branch, Ottawa, 1978.

[55] C. R. Omelon, W. H. Pollard, and D. T. Andersen, "A geochemical evaluation of perennial spring activity and associated mineral precipitates at Expedition Fjord, Axel Heiberg Island, Canadian High Arctic," *Applied Geochemistry*, vol. 21, no. 1, pp. 1–15, 2006.

[56] C. R. Omelon, W. H. Pollard, and G. M. Marion, "Seasonal formation of ikaite ($CaCO_3 \cdot 6H_2O$) in saline spring discharge at Expedition Fiord, Canadian High Arctic: assessing conditional constraints for natural crystal growth," *Geochimica et Cosmochimica Acta*, vol. 65, no. 9, pp. 1429–1437, 2001.

[57] M. M. Battler, G. R. Osinski, and N. R. Banerjee, "Mineralogy of saline perennial cold springs on Axel Heiberg Island, Nunavut, Canada and implications for spring deposits on Mars," *Icarus*, vol. 224, no. 2, pp. 364–381, 2013.

[58] S. E. Grasby, "Naturally precipitating vaterite (μ-CaCO3) spheres - unusual carbonates formed in an extreme environment," *Geochimica et Cosmochimica Acta*, vol. 67, no. 9, pp. 1659–1666, 2003.

[59] W. H. Pollard and V. Everdingen, "R.O. 1992. Formation of seasonal ice bodies," *Periglacial Geomorphology, Proceedings of the 22nd Annual Binghamton Symposium in Geomorphology*, pp. 281–304, John Wiley & Sons, Chichester, UK.

[60] C.-Y. Lay, N. C. Mykytczuk, T. D. Niederberger, C. Martineau, C. W. Greer, and L. G. Whyte, "Microbial diversity and activity in hypersaline high Arctic spring channels," *Extremophiles*, vol. 16, no. 2, pp. 177–191, 2012.

[61] C.-Y. Lay, N. C. S. Mykytczuk, É. Yergeau, G. Lamarche-Gagnon, C. W. Greer, and L. G. Whyte, "Defining the functional potential and active community members of a sediment microbial community in a high-Arctic hypersaline subzero spring," *Applied and Environmental Microbiology*, vol. 79, no. 12, pp. 3637–3648, 2013.

[62] T. D. Niederberger, N. N. Perreault, J. R. Lawrence et al., "Novel sulfur-oxidizing streamers thriving in perennial cold saline springs of the Canadian high Arctic," *Environmental Microbiology*, vol. 11, no. 3, pp. 616–629, 2009.

[63] T. D. Niederberger, N. N. Perreault, S. Tille et al., "Microbial characterization of a subzero, hypersaline methane seep in the Canadian High Arctic," *The ISME Journal*, vol. 4, no. 10, pp. 1326–1339, 2010.

[64] N. N. Perreault, D. T. Andersen, W. H. Pollard, C. W. Greer, and L. G. Whyte, "Characterization of the prokaryotic diversity in cold saline perennial springs of the Canadian High Arctic," *Applied and Environmental Microbiology*, vol. 73, no. 5, pp. 1532–1543, 2007.

[65] N. N. Perreault, C. W. Greer, D. T. Andersen et al., "Heterotrophic and autotrophic microbial populations in cold perennial springs of the high Arctic," *Applied and Environmental Microbiology*, vol. 74, no. 22, pp. 6898–6907, 2008.

[66] D. T. Andersen, C. P. McKay, W. H. Pollard, and J. Heldmann, "Correction to "Cold springs in permafrost on Earth and Mars"," *Journal of Geophysical Research*, vol. 110, no. E4, article E04007, 2005.

[67] M. R. Hudec and M. P. Jackson, "Interaction between spreading salt canopies and their peripheral thrust systems," *Journal of Structural Geology*, vol. 31, no. 10, pp. 1114–1129, 2009.

[68] T. E. Hearon, M. G. Rowan, T. F. Lawton, P. T. Hannah, and K. A. Giles, "Geology and tectonics of Neoproterozoic salt diapirs and salt sheets in the eastern Willouran Ranges, South Australia," *Basin Research*, vol. 27, no. 2, pp. 183–207, 2015.

[69] J. K. Warren, "Salt usually seals, but sometimes leaks: implications for mine and cavern stabilities in the short and long term," *Earth-Science Reviews*, vol. 165, pp. 302–341, 2017.

[70] T. Pichler and J. Veizer, "The precipitation of aragonite from shallow water hydrothermal fluids in a coral reef, Tutum Bay, Ambitle Island, Papua New Guinea," *Chemical Geology*, vol. 207, no. 1-2, pp. 31–45, 2004.

[71] J. B. Murowchick, "Marcasite inversion and the petrographic determination of pyrite ancestry," *Economic Geology*, vol. 87, no. 4, pp. 1141–1152, 1992.

[72] P. R. L. Browne, "Aragonite deposited from Broadlands geothermal drillhole water," *New Zealand Journal of Geology and Geophysics*, vol. 16, no. 4, pp. 927–933, 1973.

[73] L. A. Casella, E. Griesshaber, X. Yin et al., "Experimental diagenesis: insights into aragonite to calcite transformation of Arctica islandica shells by hydrothermal treatment," *Biogeosciences*, vol. 14, no. 6, pp. 1461–1492, 2017.

[74] F. Ghazban, H. P. Schwarcz, and D. C. Ford, "Carbon and sulfur isotope evidence for in situ reduction of sulfate, Nanisivik lead-zinc deposits, Northwest Territories, Baffin Island, Canada," *Economic Geology*, vol. 85, no. 2, pp. 360–375, 1990.

[75] M. M. Savard, G. Chi, T. Sami, A. E. Williams-Jones, and K. Leigh, "Fluid inclusion and carbon, oxygen, and strontium isotope study of the Polaris Mississippi Valley-type Zn–Pb deposit, Canadian Arctic Archipelago: implications for ore genesis," *Mineralium Deposita*, vol. 35, pp. 495–510, 2000.

[76] G. E. Claypool, W. T. Holser, I. R. Kaplan, H. Sakai, and I. Zak, "The age curves of sulfur and oxygen isotopes in marine sulfate and their mutual interpretation," *Chemical Geology*, vol. 28, pp. 199–260, 1980.

[77] H. Ohmoto and R. O. Rye, "Isotopes of sulfur and carbon," *Geochemistry of Hydrothermal Ore Deposits*, H. L. Barnes, Ed., pp. 509–567, 1979.

[78] P. W. Reiners, T. A. Ehlers, and P. K. Zeitler, "Past, present, and future of thermochronology," *Reviews in Mineralogy and Geochemistry*, vol. 58, no. 1, pp. 1–18, 2005.

[79] J. C. Harrison, U. Mayr, D. H. McNeil et al., "Correlation of Cenozoic sequences of the Canadian *Arctic* region and Greenland; implications for the tectonic history of northern North America," *Bulletin of Canadian Petroleum Geology*, vol. 47, no. 3, pp. 223–254, 1999.

[80] W. R. Roest and S. P. Srivastava, "Sea-floor spreading in the Labrador Sea: a new reconstruction," *Geology*, vol. 17, no. 11, pp. 1000–1003, 1989.

[81] R. Buckley, A. M. Grist, and M. Zentilli, *Application of the (U-Th-Sm)/He in Apatite: Assessing the Paleothermal Effect of Salt Structures on Sverdrup Basin Rocks*, vol. 45, Atlantic Geology, Axel Heiberg Island, Nunavut, 2009.

[82] D. I. Issler, *An Inverse Model for Extracting Thermal Histories from Apatite Fission Track Data: Instructions and Software for the Windows 95 Environment*, Geological Survey of Canada, 1996, Open File Report, 2325.

[83] S. D. Willett, "Inverse modeling of annealing of fission tracks in apatite; 1, a controlled random search method," *American Journal of Science*, vol. 297, no. 10, pp. 939–969, 1997.

[84] A. M. Grist and M. Zentilli, "Preliminary apatite fission track thermal history modelling of the Nares region of eastern Ellesmere Island and northwestern Greenland," *Polarforschung*, vol. 74, no. 1–3, pp. 113–127, 2006.

[85] J. W. Hedenquist, E. Izaw, A. Arribas, and N. C. White, *Epithermal Gold Deposits: Styles, Characteristics, and Exploration*, Society of Resource Geology, Japan, Tokyo, 1996, Special publication no. 1.

[86] M. H. Reed, "Hydrothermal alteration and its relationship to ore fluid composition," in *Geochemistry of Hydrothermal Ore Deposits*, H. L. Barnes, Ed., pp. 303–366, Wiley, New York, NY, USA, 1997.

[87] H. Schneiderhöhn, "Chalkographische untersuchung des mansfelder kupferschiefers," *Neues Jahrbuch für Mineralogie, Geologie und Paläontologie*, vol. 47, pp. 1–38, 1923.

[88] N. S. Wilson, M. Zentilli, and B. Spiro, "A sulfur, carbon, oxygen, and strontium isotope study of the volcanic-hosted El Soldado manto-type copper deposit, Chile: the essential role of bacteria and petroleum," *Economic Geology*, vol. 98, no. 1, pp. 163–174, 2003.

[89] Z. Lin, X. Sun, J. Peckmann et al., "How sulfate-driven anaerobic oxidation of methane affects the sulfur isotopic composition of pyrite: a SIMS study from the South China Sea," *Chemical Geology*, vol. 440, pp. 26–41, 2016.

[90] Z. Sawlowicz, "Pyrite framboids and their development: a new conceptual mechanism," *Geologische Rundschau*, vol. 82, no. 1, pp. 148–156, 1993.

[91] R. T. Wilkin and H. L. Barnes, "Pyrite formation by reactions of iron monosulfides with dissolved inorganic and organic sulfur species," *Geochimica et Cosmochimica Acta*, vol. 60, no. 21, pp. 4167–4179, 1996.

[92] L. A. Vietti, J. V. Bailey, D. L. Fox, and R. R. Rogers, "Rapid formation of framboidal sulfides on bone surfaces from a simulated marine carcass fall," *PALAIOS*, vol. 30, no. 4, pp. 327–334, 2015.

[93] M. Farrand, "Framboidal sulphides precipitated synthetically," *Mineralium Deposita*, vol. 5, no. 3, pp. 237–247, 1970.

[94] P. Ramdohr, *The Ore Minerals and Their Intergrowths*, Pergamon Press Ltd., Oxford, England, 2nd edition, 1980.

[95] W. Shen, Y. Lin, L. Xu, J. Li, Y. Wu, and Y. Sun, "Pyrite framboids in the Permian–Triassic boundary section at Meishan, China: evidence for dysoxic deposition," *Palaeogeography, Palaeoclimatology, Palaeoecology*, vol. 253, no. 3-4, pp. 323–331, 2007.

[96] R. L. Folk, "Nannobacteria and the formation of framboidal pyrite: textural evidence," *Journal of Earth System Science*, vol. 114, no. 3, pp. 369–374, 2008.

[97] B. Cavalazzi, R. Barbieri, S. L. Cady et al., "Iron-framboids in the hydrocarbon-related Middle Devonian Hollard Mound of the Anti-Atlas mountain range in Morocco: Evidence of potential microbial biosignatures," *Sedimentary Geology*, vol. 263-264, pp. 183–193, 2012.

[98] J. R. Craig, F. M. Vokes, and T. N. Solberg, "Pyrite: physical and chemical textures," *Mineralium Deposita*, vol. 34, no. 1, pp. 82–101, 1998.

[99] G. Kullerud, "Sulfide studies," in *Researches in Geochemistry*, P. H. Adleson, Ed., pp. 286–321, Wiley, New York, NY, USA, 2 edition, 1967.

[100] F. M. Vokes, "The metamorphism of pyrite and pyritic ores: an overview," *Mineralogical Magazine*, vol. 57, no. 386, pp. 3–18, 1993.

[101] L. Fontboté and G. C. Amstutz, "Facies and sequence analysis of diagenetic crystallization rhythmites in strata-bound Pb-Zn-(Ba-F-) deposits in the Triassic of Central and Southern Europe," in *Mineral Deposits of the Alps and of the Alpine Epoch in Europe*, Springer, Berlin, Heidelberg, 1983.

[102] U. Kelka, M. Veveakis, D. Koehn, and N. Beaudoin, "Zebra rocks: compaction waves create ore deposits," *Scientific Reports*, vol. 7, no. 1, article 14260, 2017.

[103] M. W. Wallace, R. A. Both, S. M. Ruano, P. Fenoll Hach-Ali, and T. Lees, "Zebra textures from carbonate-hosted sulfide deposits; sheet cavity networks produced by fracture and solution enlargement," *Economic Geology*, vol. 89, no. 5, pp. 1183–1191, 1994.

[104] D. C. Arne and S. A. Kissin, "The significance of "diagenetic crystallization rhythmites" at the Nanisivik Pb-Zn-Ag deposit, Baffin Island, Canada," *Mineralium Deposita*, vol. 24, no. 3, pp. 230–232, 1989.

[105] D. C. Arne, L. W. Curtis, and S. A. Kissin, "Internal zonation in a carbonate-hosted Zn-Pb-Ag deposit, Nanisivik, Baffin Island. Canada," *Economic Geology*, vol. 86, no. 4, pp. 699–717, 1991.

[106] V. Badoux, R. Moritz, and L. Fontboté, "The Mississippi Valley-type Zn-Pb deposit of San Vicente, Central Peru: an Andean syntectonic deposit," in *Mineral Deposits at the Beginning of the 21st Century, Proceedings of the 6th Biennial SGA Meeting, Krakow, Poland*, pp. 191–195, Balkema Rotterdam, August 2001.

[107] M. King Hubbert and W. W. Rubey, "Role of fluid pressure in mechanics of overthrust faulting: I. mechanics of fluid-filled porous solids and its application to overthrust faulting," *Geological Society of America Bulletin*, vol. 70, no. 2, pp. 115–166, 1959.

[108] W. J. Phillips, "Hydraulic fracturing and mineralization," *Journal of the Geological Society*, vol. 128, no. 4, pp. 337–359, 1972.

[109] D. T. Secor, "Role of fluid pressure in jointing," *American Journal of Science*, vol. 263, no. 8, pp. 633–646, 1965.

[110] J. G. Ramsay, "The crack–seal mechanism of rock deformation," *Nature*, vol. 284, no. 5752, pp. 135–139, 1980.

[111] L. M. Cathles and A. T. Smith, "Thermal constraints on the formation of Mississippi Valley-type lead-zinc deposits and their implications for episodic basin dewatering and deposit genesis," *Economic Geology*, vol. 78, no. 5, pp. 983–1002, 1983.

[112] R. J. Ryan, A. M. Grist, and M. Zentilli, "The Paleozoic Maritimes Basin of Eastern Canada: metallogenetic implications of a fission track study," in *Short Course Handbook on Low Temperature Thermochronology*, M. Zentilli and P. H. Reynolds, Eds., pp. 141–155, Mineralogical Association of Canada, Wolfville, Nova Scotia, Canada, 1992.

[113] J. M. Sharp, "Energy and momentum transport model of the Ouachita basin and its possible impact on formation of economic mineral deposits," *Economic Geology*, vol. 73, no. 6, pp. 1057–1068, 1978.

[114] C. E. Ravenhurst and M. Zentilli, "A model for the evolution of hot (>200 C) overpressured brines under an evaporite seal: the Fundy/Magdalen Carboniferous Basin of Atlantic Canada and its associated Pb-Zn-Ba deposits," in *Sedimentary Basins and Basin Forming Mechanisms, Canadian Society of Petroleum Geologists*, T. Tankard and C. Beaumont, Eds., vol. 12, pp. 335–350, Memoir, 1987.

[115] W. S. Hallager, M. R. Ulrich, J. R. Kyle, P. E. Price, and W. A. Gose, "Evidence for episodic basin dewatering in salt-dome cap rocks," *Geology*, vol. 18, no. 8, pp. 716–719, 1990.

[116] M. W. Wallace and A. V. S. Hood, "Zebra textures in carbonate rocks: fractures produced by the force of crystallization during mineral replacement," *Sedimentary Geology*, vol. 368, pp. 58–67, 2018.

[117] D. W. Powers, R. H. Vreeland, and W. D. Rosenzweig, "Biogeology: how old are bacteria from the Permian age?," *Nature*, vol. 411, no. 6834, pp. 155-156, 2001.

[118] R. M. Holt and D. W. Powers, "Synsedimentary dissolution pipes and the isolation of ancient bacteria and cellulose," *GSA Bulletin*, vol. 123, no. 7-8, pp. 1513–1523, 2011.

[119] R. L. Beauheim and R. M. Roberts, "Hydrology and hydraulic properties of a bedded evaporite formation," *Journal of Hydrology*, vol. 259, no. 1–4, pp. 66–88, 2002.

[120] M. Zarei and E. Raeisi, "Karst development and hydrogeology of Konarsiah salt diapir, south of Iran," *Carbonates and Evaporites*, vol. 25, no. 3, pp. 217–229, 2010.

[121] E. Casas and T. K. Lowenstein, "Diagenesis of saline pan halite; comparison of petrographic features of modern, Quaternary and Permian halites," *Journal of sedimentary Research*, vol. 59, no. 5, pp. 724–739, 1989.

[122] C. E. Keen, "Salt diapirs and thermal maturity," *Bulletin of Canadian Petroleum Geology*, vol. 31, no. 2, pp. 101–108, 1983.

[123] D. G. Evans, J. A. Nunn, and J. S. Hanor, "Mechanisms driving groundwater flow near salt domes," *Geophysical Research Letters*, vol. 18, no. 5, pp. 927–930, 1991.

[124] J. A. Majorowicz and A. F. Embry, "Present heat flow and paleo-geothermal regime in the Canadian Arctic margin: analysis of industrial thermal data and coalification gradients," *Tectonophysics*, vol. 291, no. 1–4, pp. 141–159, 1998.

[125] J. G. Fyles, L. V. Hills, J. V. Matthews Jr. et al., "Ballast Brook and Beaufort formations (Late Tertiary) on northern Banks Island, Arctic Canada," *Quaternary International*, vol. 22-23, pp. 141–171, 1994.

[126] A. J. Hidy, J. C. Gosse, D. G. Froese, J. D. Bond, and D. H. Rood, "A latest Pliocene age for the earliest and most extensive Cordilleran Ice Sheet in northwestern Canada," *Quaternary Science Reviews*, vol. 61, pp. 77–84, 2013.

[127] N. Rybczynski, J. C. Gosse, C. R. Harington, R. A. Wogelius, A. J. Hidy, and M. Buckley, "Mid-Pliocene warm-period deposits in the High Arctic yield insight into camel evolution," *Nature Communications*, vol. 4, no. 1, article 1550, 2013.

[128] J. England, N. Atkinson, J. Bednarski, A. S. Dyke, D. A. Hodgson, and C. Ó. Cofaigh, "The Innuitian Ice Sheet: configuration, dynamics and chronology," *Quaternary Science Reviews*, vol. 25, no. 7-8, pp. 689–703, 2006.

[129] J. K. Staiger, J. C. Gosse, J. V. Johnson et al., "Quaternary relief generation by polythermal glacier ice," *Earth Surface Processes and Landforms*, vol. 30, no. 9, pp. 1145–1159, 2005.

[130] A. Margreth, A. S. Dyke, J. C. Gosse, and A. M. Telka, "Neoglacial ice expansion and late Holocene cold-based ice cap dynamics on Cumberland Peninsula, Baffin Island, Arctic Canada," *Quaternary Science Reviews*, vol. 91, pp. 242–256, 2014.

[131] A. Margreth, J. C. Gosse, and A. S. Dyke, "Quantification of subaerial and episodic subglacial erosion rates on high latitude upland plateaus: Cumberland Peninsula, Baffin Island, Arctic Canada," *Quaternary Science Reviews*, vol. 133, pp. 108–129, 2016.

[132] S. C. Stover, S. Ge, P. Weimer, and B. C. McBride, "The effects of salt evolution, structural development, and fault propagation on Late Mesozoic-Cenozoic oil migration: a two-dimensional fluid-flow study along a megaregional profile in the northern Gulf of Mexico Basin," *AAPG Bulletin*, vol. 85, no. 11, pp. 1945–1966, 2001.

[133] M. J. Osborne and R. E. Swarbrick, "Mechanisms for generating overpressure in sedimentary basins: A reevaluation," *AAPG bulletin*, vol. 81, no. 6, pp. 1023–1041, 1997.

[134] G. N. Oakey and R. Stephenson, "Crustal structure of the Innuitian region of Arctic Canada and Greenland from gravity modelling: implications for the Palaeogene Eurekan orogen," *Geophysical Journal International*, vol. 173, no. 3, pp. 1039–1063, 2008.

[135] J. B. Fein and J. V. Walther, "Calcite solubility in supercritical CO_2-H_2O fluids," *Geochimica et Cosmochimica Acta*, vol. 51, no. 6, pp. 1665–1673, 1987.

[136] J. R. Kyle and J. A. Saunders, *Metallic deposits in the Gulf Coast Basin of southern North America: Diverse mineralization styles in a young sedimentary basin*, Society and Economy Geologists, Littleton, CO, USA, Special Publication #4, 1996.

[137] J. R. Kyle and J. A. Saunders, "Metallic deposits in the Gulf Coast Basin of southern North America: Diverse mineralization styles in a young sedimentary basin," in *Proceedings, Society and Economy Geol., Intern. Conf. on Carbonate-hosted Lead-Zinc Deposits*, pp. 218–229, 1996.

[138] M.-C. Williamson, Ed., *Environmental and Economic Significance of Gossans*, Geological Survey of Canada, 2015, Open File 7718.

[139] R. F. Galbraith and G. M. Laslett, "Statistical models for mixed fission track ages," *Nuclear Tracks and Radiation Measurements*, vol. 21, no. 4, pp. 459–470, 1993.

[140] J. R. O'Neil, R. N. Clayton, and T. K. Mayeda, "Oxygen isotope fractionation in divalent metal carbonates," *The Journal of Chemical Physics*, vol. 51, no. 12, pp. 5547–5558, 1969.

[141] Y. F. Zheng, "Oxygen isotope fractionation in carbonate and sulfate minerals," *Geochemical Journal*, vol. 33, no. 2, pp. 109–126, 1999.

[142] R. N. Clayton, J. R. O'Neil, and T. K. Mayeda, "Oxygen isotope exchange between quartz and water," *Journal of Geophysical Research*, vol. 77, no. 17, pp. 3057–3067, 1972.

Hindawi
Geofluids
Volume 2019, Article ID 4863814, 21 pages
https://doi.org/10.1155/2019/4863814

Research Article

Cements, Waters, and Scales: An Integrated Study of the Szeged Geothermal Systems (SE Hungary) to Characterize Natural Environmental Conditions of the Thermal Aquifer

Andrea Varga[1] **Gábor Bozsó,**[1] **István Garaguly,**[1] **Béla Raucsik,**[1] **Attila Bencsik,**[1,2] **and Balázs Kóbor**[1]

[1] *Department of Mineralogy, Geochemistry and Petrology, University of Szeged, H-6722, Hungary*
[2] *Geothermal Service Provider Ltd, H-6724, Hungary*

Correspondence should be addressed to Andrea Varga; raucsikvarga@geo.u-szeged.hu

Received 2 July 2018; Revised 19 December 2018; Accepted 17 January 2019; Published 24 April 2019

Guest Editor: Philippe Calcagno

The study area, Pannonian Basin (Central Europe), is characterized by high heat flow and presence of low-enthalpy geothermal waters. In the Szeged Geothermal Systems (Hungary), having Miocene to Pliocene sandstone aquifers with dominantly Na–HCO_3-type thermal water, unwanted carbonate scaling was observed. An integrated approach consisting of host rock and scale mineralogical and petrographic analyses as well as water chemistry led to a better understanding of the characteristic natural (geogenic) environmental conditions of the geothermal aquifers and to highlight their technical importance. Analyses of the reservoir sandstones showed that they are mineralogically immature mixed carbonate-siliciclastic rocks with significant macroporosity. Detrital carbonate grains such as dolomite and limestone fragments appear as important framework components (up to ~20–25%). During water–rock interactions, they could serve as a potential source of the calcium and bicarbonate ions, contributing to the elevated scaling potential. Therefore, this sandstone aquifer cannot be considered as a conventional siliciclastic reservoir. In mudrocks, a significant amount of organic matter also occurs, triggering CO_2 producing reactions. Correspondingly, framboidal pyrite and ferroan calcite are the main cement minerals in all of the studied sandstone samples which can suggest that calcite saturation state of the thermal fluid is close to equilibrium in oxygen-depleted pore water. Analysis of the dominant carbonate crystals in the scale can suggest that growth of the feather dendrites of low-Mg calcite was probably driven by rapid CO_2 degassing of CO_2-rich thermal water under far-from-equilibrium conditions. Based on hydrogeochemical data and related indices for scaling and corrosion ability, the produced bicarbonate-rich (up to 3180 mg/l) thermal water has a significant potential for carbonate scaling which supports the aforementioned statement. Taking into consideration our present knowledge of geological setting of the studied geothermal systems, temporal changes in chemical composition and temperature of the thermal water during the heating period can indicate upwelling fluids from a deep aquifer. Regarding the pre-Neogene basement, hydrologic contact with a Triassic carbonate aquifer might be reflected in the observed chemical features such as decreased total dissolved solids and increased bicarbonate content with high scale-forming ability. The proposed upflow of basin-derived water could be channeled by Neogene to Quaternary fault zones, including compaction effects creating fault systems above the elevated basement high. The results may help to understand the cause of the high carbonate scale precipitation rates in geothermal systems tapping sandstone aquifers.

1. Introduction

Geothermal systems are often characterized by the interaction of complex processes as discussed elsewhere [1]. Therefore, geothermal exploration is increasingly focusing on the extensive integration of multidisciplinary data from production technology to hydrogeochemistry and geological researches [1–8]. Unfortunately, many geothermal installations (e.g., hydrothermal cascade systems) face important operational challenges such as unwanted scaling accompanying the exploitation of high-temperature waters with high salinity and gas content from deep wells [6]. General characteristics of scales depend on natural conditions (e.g., geological setting, reservoir type, physicochemical properties, and hydrogeological and hydrochemical features) as well as man-made ones (e.g., well depth, flow rate, operating pressure, substrate material, and effects of biological processes) [5–8].

As a scale component, calcium carbonate ($CaCO_3$, aragonite, and/or calcite) precipitation is widespread in low- to moderate-enthalpy geothermal facilities tapping deep limestone and dolomite aquifers [6, 7]. Although the aquifers of the Szeged Geothermal Systems (SE Hungary, Great Hungarian Plain) are traditionally considered being siliciclastic ones (mainly very fine- to fine-grained sandstones) with dominantly Na–HCO_3-type thermal water [3, 9], relatively high carbonate scale deposition rates have been observed especially in the pipes between the production wells and their buffer tanks [7]. In Szeged, construction of a new district-heating geothermal system is in progress (Figure 1; wells H–1 and H–2), so a better characterization of the geothermal reservoir is essential to understand the water–rock interactions in this region.

Recently, some papers reported the man-made (technical/operational) effects of the district-heating geothermal systems in Szeged [2–4, 7]. Additionally, hydrogeological and hydrochemical conditions in the Great Hungarian Plain were extensively studied applying state-of-the-art geochemical methods [9–18]. Mineralogical and micropetrographic features of the Miocene–Pliocene geothermal reservoir sandstones in the study area and the related information about scaling potential, however, have not received much attention in the literature.

In this study, we include site-specific data from mineralogical and petrographic analyses of sandstone and mudrock samples collected from the H–1 exploration well (Figure 1) to describe characteristic natural (geogenic) environmental conditions of the geothermal aquifers and to highlight their technical importance. Furthermore, corresponding to an unconventional approach of the reservoir sandstone–thermal water–scale ternary system, mineralogical and petrographic features of the scales are also described to gain some information about operational processes. In order to a better characterization of the site-specific water–rock interactions, this paper presents general hydrogeochemical characteristics (e.g., temperature, pH, and concentrations of dissolved solids) and scaling properties of the thermal water from production wells operating in Szeged. The results may help to understand the cause of the high carbonate scale precipitation rates in geothermal systems tapping sandstone aquifers. It is important to note, however, that it is beyond the scope of this manuscript to discuss the man-made influences (e.g., nucleation/crystal growth mechanisms vs. corrosion processes, fluid–solid interaction modelling) in detail. This is addressed in previous separate papers and ongoing projects of other research teams [2–5, 7, 8].

2. Background

2.1. Szeged Geothermal Systems. Numerous studies demonstrated that geothermal waters in South Eastern Hungary (Pannonian Basin, Central Europe) are mainly found at a depth of 0.8–2.4 km with surface temperatures of 40–98°C and are Na–HCO_3-type with some dissolved gases (especially CH_4 and CO_2) and total dissolved solids (TDS) of 2–4 g/l. Generally, they are sourced from Upper Miocene to Pliocene sedimentary units (sandstones, clays, and clayey marls) [3–5, 9, 14, 19].

Szeged, located in the southern part of the Great Hungarian Plain, has one of the largest operating geothermal systems in Hungary where two cascade systems (downtown of Szeged and Újszeged district) are supplying heat to several large communal buildings (Figure 1). Annual thermal water production is ~300,000–320,000 m^3. The use of geothermal energy has a long history in Szeged where thermal water is also used for medical purposes and balneotherapy at the famous spas such as "Anna Fürdő" (Anna well; 52°C, depth: 944 m, date of drilling: 1927; TDS: 2809 mg/l) and "Napfényfürdő Aquapolis" (Dóra I well, 70°C, depth: 1551 m, date of drilling: 1958; Dóra II well, 80°C, depth: 1706 m; TDS: 3169 mg/l) [3, 4, 19].

Based on published data [3, 4], both heating systems are supplied by own well (production well pump pressure: 5–8 bar) producing fluid with a temperature of 92–95°C (TDS: 2500–3000 mg/l). In downtown of Szeged (Figure 1), the production well (B-415) is 1999 m deep and is screened between 1727 and 1914 m. In Újszeged, the production well (B-748) is 1937 m deep and is screened between 1733 and 1878 m. The well's pumps directly transfer the thermal water into the buffer tanks where degassing takes place (~1 bar). In order to maintain the reservoir pressure and to dispose the heat-depleted fluid in an environment-friendly manner, thermal water is reinjected into the underground layers through 2 reinjection wells at each location (total depth of the reinjection wells B-745, B-746, B-747, and B-748 is 1396 m, 1750 m, 1740 m, and 1225 m, respectively).

The abovementioned two thermal circles supply ~80% of the buildings (e.g., clinics, department buildings, and dormitories) of the University of Szeged and certain buildings of the local government (e.g., Medical Clinic No. 1, Szeged Swimming Pool). These systems replace a quantity of natural gas of 2.9 million m^3 in a year with a capacity of 8.9 MW_{th} and reduce the emission of CO_2 by approximately 5,900 t, representing a factor conducive to health in urban areas. Thanks to this the University of Szeged reached 19th place on the appreciated World Ranking List of Green Universities [3, 4].

2.2. Geological Setting. The Neogene–Quaternary Pannonian Basin is a large, approximately 600 km from east to west and 500 km from north to south, rift-related extensional basin system in Central Europe, overlying Paleogene basins and Cretaceous folds and thrusts of the greater Alpine fold belt. As a back-arc basin, its opening was controlled by different tectonic processes and the extension was manifested through a set of low angle normal and strike–slip faults resulting in formation of several depressions that are separated by uplifted basement blocks [20–25]. One of these basement highs is the so-called Algyő High between the Szeged and Makó Troughs (Figure 2(a)). The Szeged area setting is above the Algyő High whose structure is still under debate so its

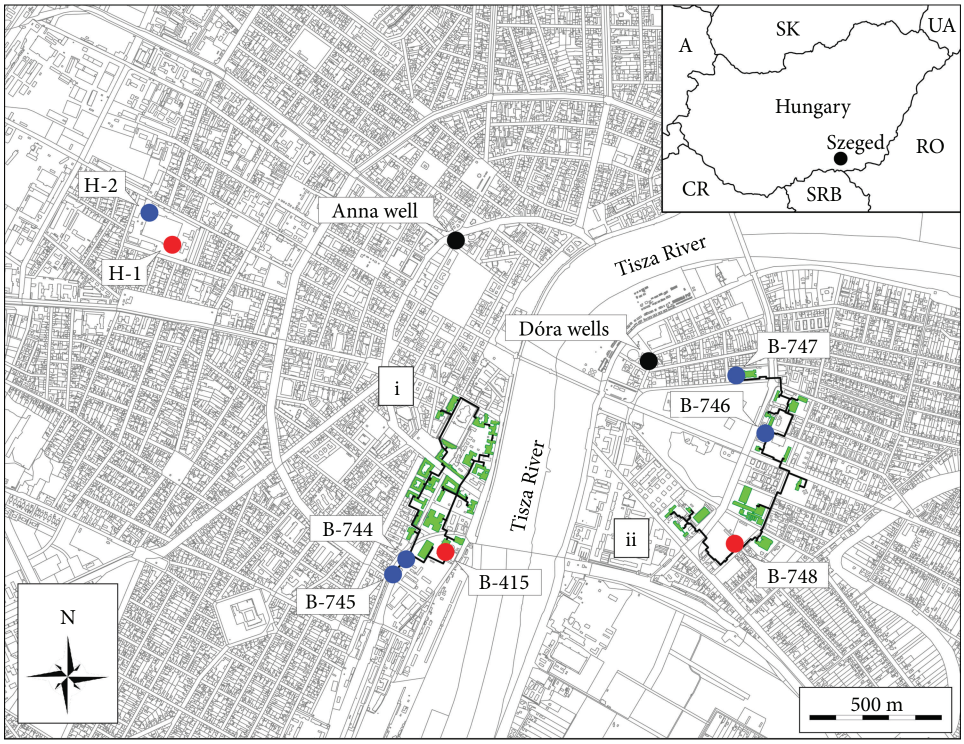

Figure 1: Geothermal cascade systems in Szeged (SE Hungary, Central Europe) together with locations of thermal production and reinjection wells (red and blue filled circles, respectively). (i) Geothermal cascade system in downtown of Szeged. (ii) Geothermal cascade system in Újszeged district. Mineralogical and petrographic rock characterization was carried out on core samples from the H–1 exploration well.

stratigraphic subdivision is not known in a satisfactory manner [22–25]. Traditionally, the pre-Cenozoic basement of the study area belongs to the Codru nappe system, Tisza mega-unit [22, 23]. Alternatively, crystalline basement parts of the Algyő High were included into the Biharia nappe system, Dacia mega-unit [24, 25]. According to the latter interpretation, there is an Alpine shear zone (Codru/Biharia buried contact) within the Algyő basement block (Figure 2(b)).

The Algyő High is made up by metamorphic rocks (e.g., gneisses, mica schists, and amphibolites) with complex internal structure, Upper Paleozoic to Lower Triassic siliciclastic formations as well as Middle Triassic shallow marine mudrocks and carbonates (Figure 3). In the local lithostratigraphy, the Anisian–Ladinian carbonate rocks are classified as Szeged Dolomite Formation which is characterized by a brecciated dark gray dolomite sequence in complicated structural positions [23, 26, 27]. These sediments were deposited on a huge ramp system on the southern margin of the European continental plate and the northern shelf of the Tethys and were completely dolomitized by either fabric-preserving or fabric-destructive processes during multiple dolomitization episodes. Rocks of this formation serve as good aquifers and hydrocarbon reservoirs in this region of Hungary with significant hydrocarbon production [27].

The high relief topographic undulations of the basement were covered by the marine waters of the Paratethys during the Miocene (i.e., 20–10 Ma) and gave way to closely spaced but profoundly different depositional environments [28–30]. It has traditionally been believed that the Pannonian Basin was disconnected from the evaporitic basins of the Paratethys, but massive Badenian (13.8 Ma) evaporites (halite together with sulphates), suggesting oversaturated brine at the bottom water, were recently discovered in the Great Hungarian Plain. Different proposed scenarios could explain how the supposedly brackish Sarmatian could have been hyper or normal saline locally in this area [31].

The Pannonian Basin most likely became an isolated brackish lake ca. 10 Ma ago and the so-called Lake Pannon persisted for about 7–8 Myr. During the Late Miocene and Early Pliocene, the paleo-Danube and paleo-Tisza Rivers progressively filled it with clastic material sourced by the surrounding mountain chains, creating one of the thickest Neogene nonmarine sedimentary sequences in Europe [28]. The central and deepest (average thickness: 2–3 km, locally up to ~7 km) depression of the Pannonian Basin is the Great Hungarian Plain, including the studied Szeged area (Figure 2), where the majority of the sediments accumulated [28–30, 32]. Based on recent calculations [33], the water depth of the lake was more than 1000 m in the deepest subbasins.

Sediments arriving from the Alpine–Carpathian source area were partly accumulated on the flat-lying morphological shelf of the Lake Pannon, whereas their other portions were passing through to the slope and deposited on the deep basin floor [28–30, 33]. The coeval sedimentation reflects the deposition of diachronous and laterally variable formations (Figure 4). Lithostratigraphically, the Endrőd Marl is a distal mudstone and the overlying Szolnok Formation includes deep-water turbidite sandstones, deposited at the toe of slope and in the basin floor. The Algyő Formation is mostly silty mudstone, deposited on the slope, whereas the Újfalu

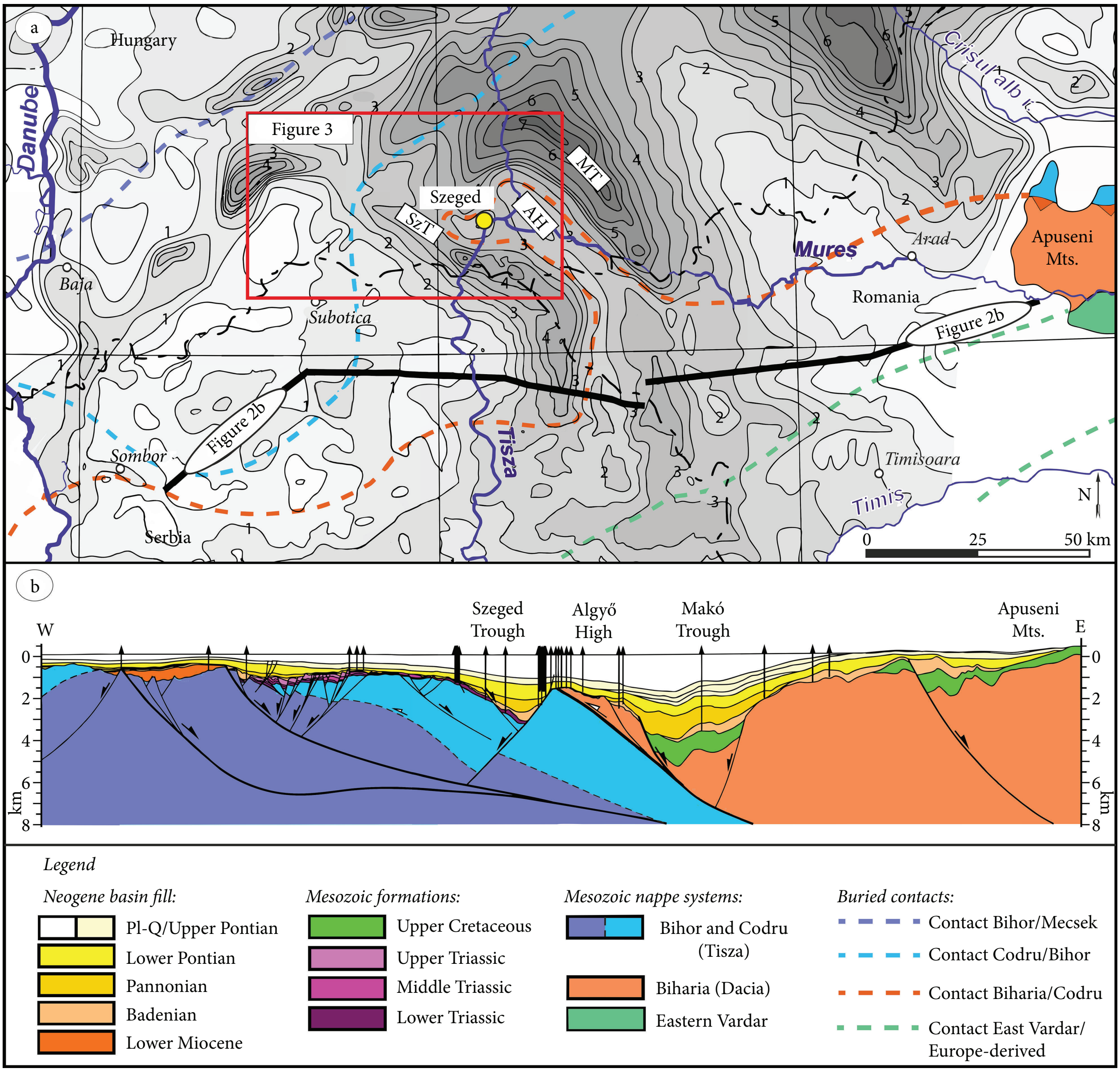

Figure 2: Generalized basement map together with a schematic cross section of the southern Pannonian Basin, showing the stratigraphic and structural relationships [24, 25]. (a) Structural map of the pre-Neogene basement of the Pannonian Basin in SE Hungary and neighboring Serbia and Romania. Isoline numbers are in kilometers. Abbreviations: SzT = Szeged Trough; AH = Algyő High; MT = Makó Trough. (b) WSW–ENE regional transect over the southern part of the Pannonian Basin (Serbia and Romania). The location of the interpreted seismic sections is displayed in (a). Note: the cross section is 4 times vertically exaggerated.

Formation represents the stacked deltaic lobes overlain by alluvial deposits of the Zagyva Formation [28–30, 32]. According to a most recently published article [33], the significant compaction associated with lateral variations of the Neogene sediment thicknesses has created nontectonic normal fault offsets and folds.

The presence of low-enthalpy geothermal waters in the region is thought to be due to high heat flow occurring after the Miocene extension which caused thinning of the lithosphere. During the Neogene extension, the heat flow rate increased from ca. 30 mW/m^2 to 110 mW/m^2. The temperature gradient calculated in wells around Szeged is 67°C/km in the upper successions of the basin (<3000 m) [15, 34, 35].

2.3. Hydrogeological and Hydrogeochemical Overview. Hydrodynamically, corresponding to the recognized pore pressure zones, the Pannonian Basin can be subdivided into two principal flow regimes: (i) an upper, gravity-driven, and unconfined flow system; and (ii) a lower, overpressured (up to 40 MPa over the hydrostatic pressure), and confined regime [10, 11, 19]. The most significant characteristic of the zone of transition between the overpressured and normally pressured hydraulic regimes is its widely variable depth between 200 and 1700 m. The transition between the potential fields of the unconfined and confined zones may be gradual in the deep troughs or stepwise abrupt. The latter changes are associated with

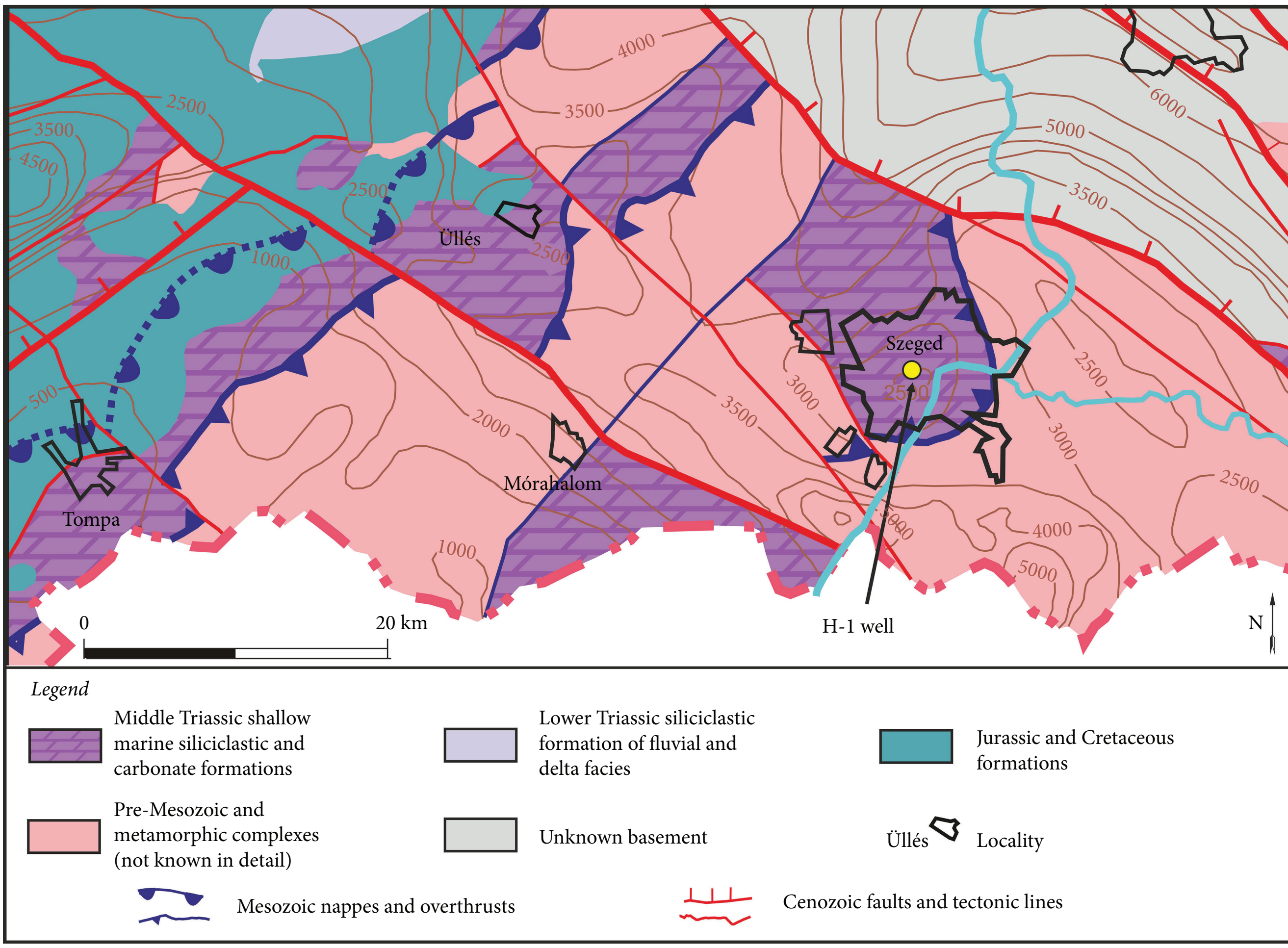

FIGURE 3: Generalized geological map of the pre-Cenozoic basement of the Szeged area, belonging to the Codru nappe system (Tisza mega-unit), and its surroundings [23, 26, 27]. Isoline numbers are in meters. The close vicinity of the town Szeged (study area) has a nearly basement-high position. Reservoir rock characterization was carried out on core samples from the well H–1-penetrated Miocene to Pliocene deposits above the basement.

basement highs and their flanks. It is important to note that the flow's vertical component is uniformly upwards in the overpressured zone [10, 11, 13].

Inside the sedimentary basin, structural discontinuities, such as faults and fracture zones, and probably also high-permeability sedimentary windows, are preferential pathways of hydraulic pressure dissipation and fluid migration from the confined zone to the unconfined regime. Therefore, the overpressured zone is in hydraulic connection with the upper, gravity-driven zone [11]. Additionally, a strong hydraulic relationship between the pre-Cenozoic basement and the overlying Neogene sequences was also suggested by several authors [12, 33, 36]. Evidences based on cement stratigraphic and diagenetic observations [12, 37] and seismic studies focusing on conductive faults that crosscut the aforementioned formations were also presented [36, 38]. These faults could serve as migration pathways for basement-derived saline waters [36] as well as for hydrocarbons [33, 37].

The subsurface of the Great Hungarian Plain has been subdivided into six regional hydrostratigraphic units which are the followings: pre-Neogene aquiclude, pre-Pannonian aquifer, Endrőd aquitard, Szolnok aquifer, Algyő aquitard with aquifer lenses, and Great Plain (Nagyalföld) aquifer [9, 11]. The Szolnok aquifer, corresponding to the Szolnok Formation (Figure 4), is a cyclic alternation of consolidated sandstones, siltstones, and clayey marl beds, whereas the Great Plain aquifer is dominated by unconsolidated sands and coarse clastics, belonging to the Újfalu and Zagyva Formations. The entire porous and permeable framework of the Great Hungarian Plain can be considered as a regional and cross-formational hydraulic continuum [10, 11]. Even though several studies demonstrated hydraulic connection between the main flow regimes, detailed information about water exchange between the basement and the upper aquifers, and in particular, their fault-related hydrochemical evolution, is almost lacking in the study area.

Despite the aforementioned hydraulic continuum, the Pannonian Basin is regarded as a large nonuniform multilayer flow system (Figure 5) in the relevant hydrogeochemical studies [9, 15–18]. Based on chemical considerations,

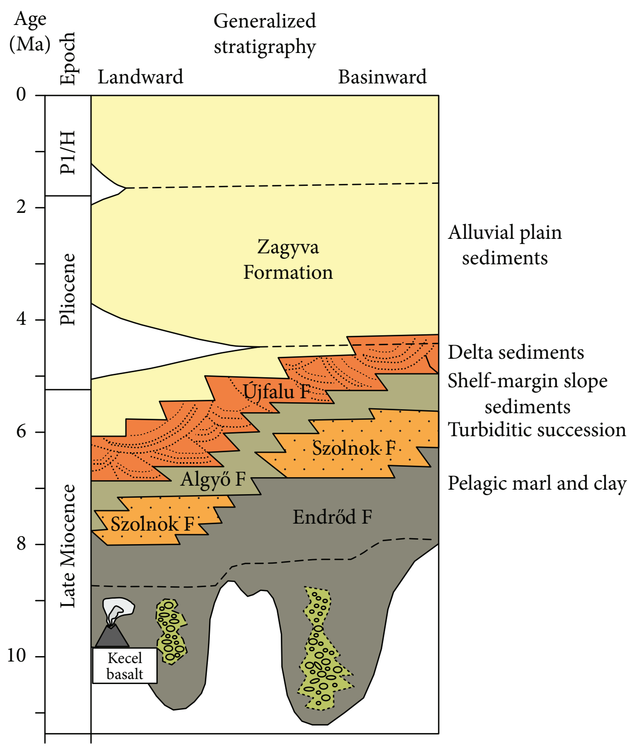

FIGURE 4: Chrono- and lithostratigraphy of the Miocene–Holocene deposits in the study area simplified after Sztanó et al. [29]. Abbreviations: Pl = Pleistocene; H = Holocene.

including isotopes, and spatial variability of the dissolved components, distinct water bodies were identified. Within the Pannonian (Late Miocene) sediments, corresponding to the Szolnok aquifer and Algyő aquifer lenses, groundwaters are practically stagnant with Na–Cl- to Na–HCO_3-type geochemistry (>2500 m; TDS > 6 g/l) [9, 14, 15]. Pannonian/-Pontian boundary was considered as the bottom of a regional flow system [15]. Sodium–HCO_3-type formation waters of paleometeoric/meteoric origin are present within the Late Miocene to Pliocene sediments, corresponding to the Újfalu and Zagyva aquifers. Waters in the deepest positions, however, are mixtures of paleometeoric waters and deep waters squeezed out from the thick sequence of the fine-grained Pannonian sediments (Algyő aquitard), underlying the Újfalu thermal water aquifer [15–18]. The Pleistocene to Holocene terrestrial sediments, depending on the dominant grain size fraction, contain Na–HCO_3-type (fine-grained layers) and Ca/Mg–HCO_3-type (coarse-grained beds) waters [15, 16].

It is important to note that the abovementioned Na–HCO_3-type waters contain large amounts of dissolved organic matter (e.g., humic substances, methane, and short-chain aliphatic acid anions). In the study area, different polycyclic aromatic hydrocarbons (PAHs) are characteristic of the waters warmer than 65°C [15, 17]. On the other hand, the Great Hungarian Plain is the principal conventional petroleum producing area in Hungary where basement highs and also the Neogene basin fills have a proven economic value. Furthermore, a large number of hydrocarbon accumulations were reported from turbidite beds of the Miocene Szolnok Formation all over the basin, mostly in structural traps above basement highs [29, 39].

3. Materials and Methods

3.1. Sampling and Methodology. For reservoir rock characterization, core samples from the H–1 exploration well (Figure 1) were examined for general lithology and sedimentary structures. The deep well was drilled as a thermal water exploration well in 2017. The available 3 core sections from the well were sampled from the depth interval between 1620 and 1800 meters below sea level, corresponding to the Újfalu and Algyő Formations, and were taken for detailed mineralogical (X-ray powder diffractometry, XRPD) and petrographic studies (Figure S1). Micropetrographic investigation was done on 20 thin sections impregnated with blue-dyed epoxy resin at the Department of Mineralogy, Geochemistry and Petrology, University of Szeged. In order to distinguish calcite, dolomite, and their ferroan variants, the thin sections were stained with alizarin red-S and potassium ferricyanide as described by Dickson [40]. Additionally, on selected sandstone samples, cathodoluminescence (CL) microscopy was also carried out by a Reliotron VII type cold CL device operating at 8–10 kV and 0.6 mA.

In order to discuss fluid (thermal water/gases) versus solid (reservoir rock/scale) interactions, general hydrochemical data (e.g., fluid chemistry, gas content, T, and pH) from available reports of the two geothermal facilities were used. Thermal waters were recovered from pipes at or close to the wellhead. The concentrations of each dissolved component in the water and the phenol index were determined as it is stated in the Hungarian Standards, under numbers MSZ 1484-3:2006 and MSZ 1484-1:2009, respectively. The measurements were made at an accredited laboratory, namely, Aqualabor Ltd (Szeged), using a PerkinElmer Optima 8000 ICP-OES device. As a first step, Langelier and Ryznar Stability Indices (LSI and RSI, respectively) [41] were also calculated for each wells together with the time-related pattern for the heating system in Újszeged district to determine the scaling and corrosion conditions of the thermal waters in general. In the geothermal cascade system of Újszeged district, hydrochemical records were made in the heating period of 2017–2018 (from 10/15/2017 to 04/15/2018).

In this paper, the LSI and RSI are used to determine the basic scaling ability and scaling/corrosion potential of thermal water, respectively. Both indices are calculated from the carbonate equilibrium based on the temperature, pH, TDS, alkalinity (which is nearly equal with the concentration of HCO_3^- in this chemical state of systems) values, as well as the concentration of calcium ion (Ca^{2+}). If the LSI is less than zero, the water is unsaturated with respect to calcium carbonate, so scaling is not possible (LSI = 0 in equilibrium). On the other hand, scale can precipitate if the LSI is higher than zero, corresponding to the supersaturated conditions. With the increase of LSI value, the scaling potential increases. The RSI refers to both scaling and corrosion. If it is less than 6.2, scale

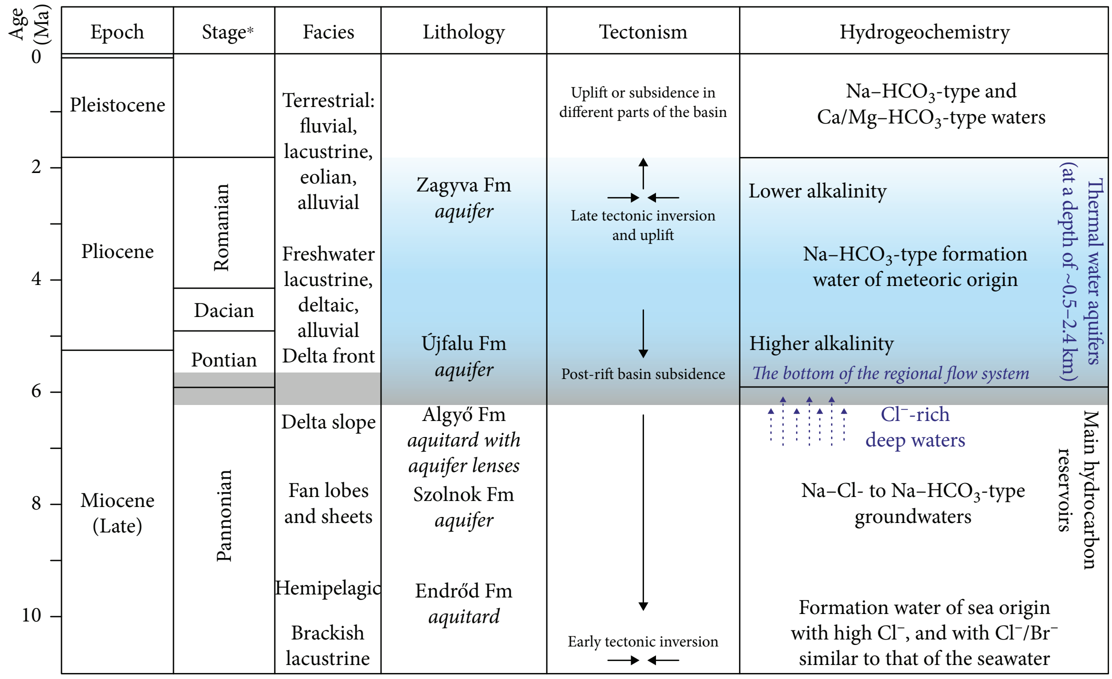

FIGURE 5: Summarized geological and geochemical information for the studied aquifers [9, 14–18, 25, 28–30]. Thermal water aquifers are indicated by a blue bar. Gray rectangle indicates the estimated bottom of a regional flow system (Pannonian/Pontian boundary) [9]. Note: hydrogeochemical interpretations do not reflect the deposition of diachronous and laterally variable formations. Additionally, the Pannonian Basin is regarded as a nonuniform multilayer flow system in this conception. Abbreviation: Fm = Formation. *Central Paratethys [25].

will form but corrosion cannot happen, whereas if it is more than 6.8, the water is aggressive [41].

Selected and representative scale-fragment samples from both study sites were investigated via mineralogical and petrographic methods. A total number of 20 mineral precipitates were collected for this study. Scales were sampled from different sections of the geothermal cascade system in Újszeged district, suffering from problems with accumulation of carbonate material formed inside pipes (substrate material: carbon steel, standard number St37.0), especially near the buffer tank (samples G-03 and G-04), and inside production facilities such as interior surfaces of buffer tank, water filtration systems (coarse: 3 mm; fine: 80 μm), and pumps (e.g., pump gland, pump blades, and filters; substrate material: acid-proof steel, alloying elements: Cr, Ni; standard number MSZ KO33) in the engine room (samples G-05–G-09, G-11, G-23–G-30). Regarding the other cascade system (downtown), scale samples were recovered from pipes between the wellhead and the buffer tank (sample G-10). The carbonate scale samples were embedded in epoxy resin, cut, and polished at the Department of Mineralogy, Geochemistry and Petrology, University of Szeged, to obtain standard petrographic thin sections.

In order to provide a more detailed petrography, besides the standard thin section microscopy, fluorescence and CL (as described above) microscopy were also carried out. Micropetrography and fluorescence microscopy was performed using an Olympus BX-41 microscope equipped with a high-pressure Hg lamp and filter sets for blue-violet (400–440 nm) and ultraviolet (360–370 nm) excitation. Additionally, bulk mineralogical composition of representative scale samples was also determined using XRPD described below in detail.

3.2. Methodology of XRPD Measurements for Rock and Scale Characterization. Determination of the bulk mineralogical composition and characterization of the separated <2 μm grain size (clay) fraction of 10 core samples from the well H–1 were made by XRPD. Homogeneous rock chips were grounded and pulverized in an agate mortar (<2 min grinding time per sample). Bulk mineralogy of the fabric-selected and powdered scale samples, corresponding to the macroscopic features (e.g., color, zonation), was also determined. About 10 grams of representative scale samples was dissolved in diluted acetic acid (10 vol%, for 24 h at room temperature) in order to characterize the insoluble residue. The representative samples were measured by a Rigaku Ultima IV X-ray diffractometer using a rotating sample holder (instrumental parameters: Bragg-Brentano geometry, CuKα radiation, graphite monochromator, proportional counter, divergence, and detector slits of 2/3° at 50 kV/40 mA from 3 to 70°2θ with goniometer step rate 1°/min and step width 0.05°) at the Department of Mineralogy, Geochemistry and Petrology, University of Szeged. The qualitative evaluation of the XRPD spectra was made by Rigaku PDXL 1.8 software using the ICDD (PDF2010) database. Semiquantitative mineralogical composition was determined based on the reference intensity ratio (RIR) method. Composition of carbonate minerals was estimated using empirical curve between d_{104} values and composition in the calcite–dolomite solid solution series [42]. Domain (crystallite) size of the scale-forming material was calculated

Table 1: Mineralogical composition of the studied bulk rock samples and separated clay fractions.

	Major components (~mass%)	Minor components (~mass%)
Sand-rich samples (bulk)	q (20–50), 10A (10–60), dol (5–20)	cal (tr–10), 14A (5–10), kf (tr), pl (tr–10), 7A (tr)
Pelitic samples (bulk)	10A (10–60), q (20–40), 7A (tr–20), 14A (tr–20), dol (5–30), pl (tr–20)	cal (tr–10), kf (tr), pyr (tr)
Sand-rich samples (clay fraction)	10A (30–70), chl (20–60)	7A (5–10), sm (tr–10), q (tr), cal (tr), dol (tr)
Pelitic samples (clay fraction)	10A (40–80), chl (10–40), 7A (5–20)	sm (5–10), q (tr), cal (tr), dol (tr), pyr (tr)

Abbreviations: 14A = 14 Ångström phase (chlorite±vermiculite±smectite); 10A = 10 Ångström phase (illite±mica); 7A = 7 Ångström phase (kaolinite); cal = calcite; chl = chlorite; dol = dolomite; kf = K-feldspar; pl = plagioclase feldspar; pyr = pyrite; q = quartz; sm = smectite±highly swelling mixed-layer illite/smectite; tr = trace amount.

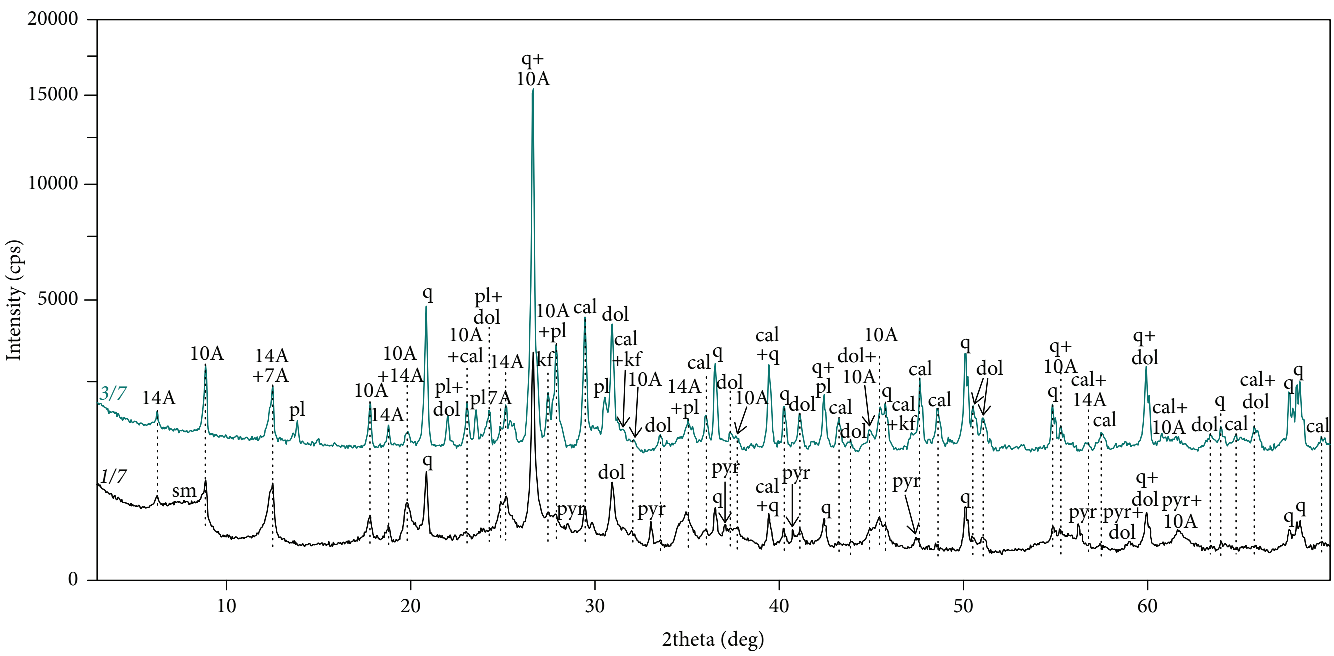

Figure 6: Typical XRPD patterns of representative bulk rock samples (sample 3/7: sandstone; sample 1/7: pyrite-bearing mudrock). Abbreviations: 14A = 14 Ångström phase (chlorite±vermiculite±smectite); 10A = 10 Ångström phase (illite±mica); 7A = 7 Ångström phase (kaolinite); cal = calcite; dol = dolomite; kf = K-feldspar; pl = plagioclase feldspar; pyr = pyrite; q = quartz; sm = smectite±highly swelling mixed-layer illite/smectite.

by the Scherrer equation after removing the instrumental broadening [43]. The diffractograms made on samples of insoluble residue do not give evaluable peaks, suggesting a predominance of amorphous (or short range ordered) phases with undetermined composition. Consequently, no further discussion related to them is provided in this study.

Grain size separation for clay fraction analysis was achieved by repeated ultrasonic deflocculation and gravitational settling using Stokes' law. Highly oriented XRPD slides with 3 mg/cm^2 density were prepared by repeated sedimentation of the separated clay fraction on a standard glass sample holder. Both air-dried and ethylene glycol-solvated preparations were scanned at 45 kV/35 mA, from 2 to 50°2θ with goniometer step rate 1°/min and step width 0.1°. Subsequently, the mounts were treated at 350 and 550°C and measured immediately after storage in a desiccator. Semiquantitative composition of the clay fraction was estimated following Moore and Reynolds' recommendation [44].

4. Results and Discussion

4.1. Core Description, Mineralogy, and Petrography. Using a hand lens together with a chart for visual estimation of grain size, the studied core samples can be subdivided into two groups, namely, sand-rich samples (very fine- to fine-grained sandstones) and pelitic ones (mudrocks); rare coal seams also occur (Figures S1 and S2). The mineralogical composition of the studied reservoir rock groups is summarized in Table 1. Based on the bulk mineralogy (Table S1), mudrocks can be classified as siltstone, clayey marl, dolomitic marl, claystone (dolomitic and calcareous), and coal-bearing shale. In the lower part of well H–1

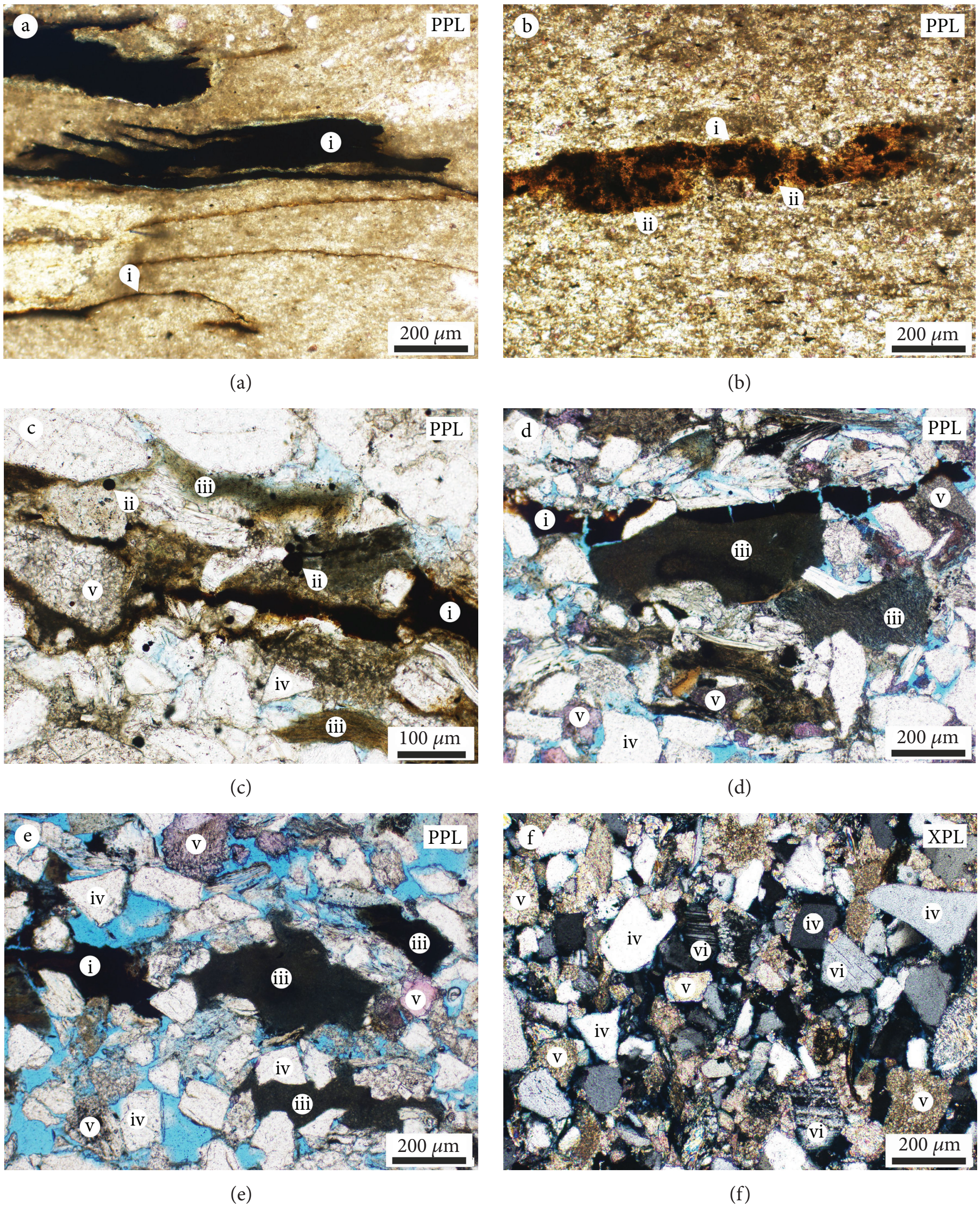

(a) (b) (c) (d) (e) (f)

Figure 7: Micropetrographic characteristics of the studied mudrock and sandstone samples (a: 1/7; b: 1/10; c–e: 1/4; f: 1/3). (a, b) Textural features of the marl samples, including oriented organic matter fragments (i). Note enrichment of framboidal pyrites (ii, "black spots") in a close relationship with organic matter. (c–f) Silt- to sand-sized detrital grains together with organic matter (i) seams and reworked mudrock (iii) fragments in sandstones. Intergranular pores are filled by blue epoxy resin. Dominant framework grains: quartz (iv), carbonate lithics (v), and plagioclase feldspar (vi). Abbreviations: PPL = plane polarized light; XPL = crossed polars.

(~1700 m), the mudrocks contain a sparse macrofauna (thin shells of *Paradacna abichi*, Sándor Gulyás pers. comm.), reflecting brackish water and delta slope depositional facies (Figure S3).

The mineralogical composition of the bulk rock samples is quite similar, but some differences appear in the relative abundances of the phases (Figure 6). Generally, quartz, 10 Å phases (illite±mica), and dolomite are the major components, whereas plagioclase (probably albitic), calcite, 14 Å phases (chlorite±vermiculite±smectite or highly smectitic mixed-layer phase), 7 Å phase (kaolinite), and K-feldspar are proved to be minor constituents. Some samples have extremely high amount of 10 Å phases (illite±mica; up to 50–60%) while others are very rich in carbonate minerals (calcite+dolomite ≈ 30–40%) or plagioclase feldspar (10–20%). A single core sample (sample 1/7; Table S1) has a unique mineralogical character; it contains kaolinite as major constituent and has detectable pyrite content.

In order to determine the stoichiometry of the trigonal carbonate minerals, d_{104} spacing was investigated on the bulk XRPD pattern of the samples. In the case of the calcite, the d_{104} shows a rather uniform distribution with a value of

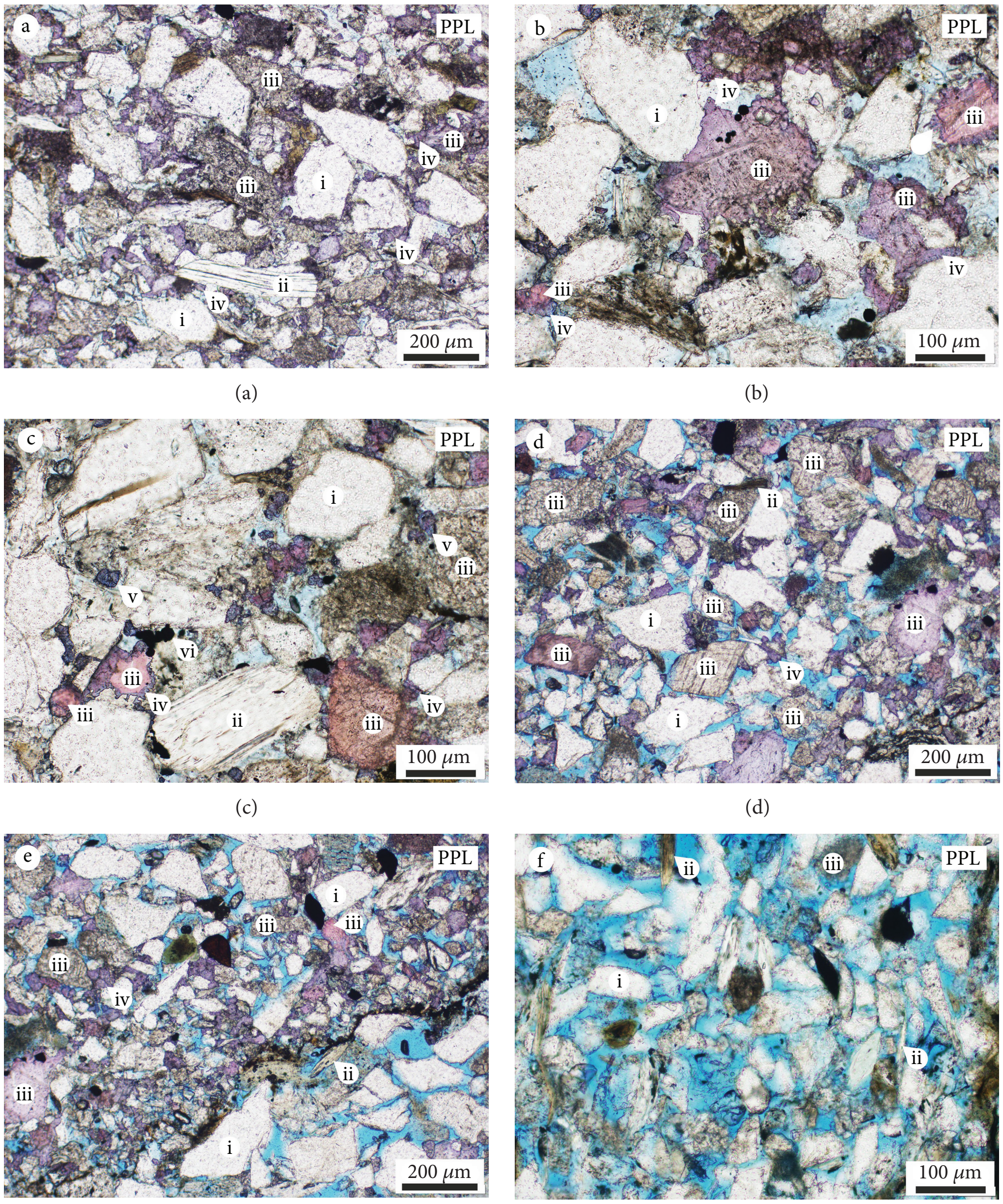

(a) (b) (c) (d) (e) (f)

Figure 8: Micropetrographic characteristics of the studied sandstone and siltstone samples. (a–e) Pervasive to patchy cemented sandstones (a–c: 1/2; d and e: 1/4; f: 3/3). Well-cemented zones can grade to poorly cemented zones over distances of a few tens of micrometers. Pores are filled by blue epoxy resin. Dominant framework grains: quartz (i), micas (ii), and carbonate lithics (iii, note: limestone clasts and detrital calcite crystals show red or pinkish color after staining but dolomite is unstained); dominant cements: Fe calcite (iv), ankerite (v), and framboidal pyrite aggregates (vi). (f) Poorly cemented sandy siltstone sample with locally high (~20–25%) porosity. Abbreviation: PPL = plane polarized light.

3.030 ± 0.001 Å ($n = 10$) which indicates a near stoichiometric composition with a < 2–3% (molar) $MgCO_3$ content. The d_{104} values of the dolomite in the studied sediments similarly show near stoichiometric composition (2.888 ± 0.002 Å; $n = 10$) with a few percent Mg^{2+} deficiency (Table S2).

Regarding the clay fraction, the samples are predominated by illite±white mica. Nevertheless, the 14 Å phase is a significant component of the clay fraction. It can be determined as chlorite due to its behavior after solvation with ethylene glycol and subsequent heat treatments. The kaolinite is generally a minor component, but two pelitic samples are relatively enriched in kaolinite (10–20%), suggesting K-feldspar hydrolysis. On the other hand, a highly expanding phase can be identified as smectite with ~17 Å base reflection, but a more accurate characterization and quantification cannot be achieved because of its diffuse peaks suggest poor crystallinity in most of the samples. Nevertheless, it is proved a minor constituent of the analyzed clay fractions with a proportion of up to 5–10%. Trace amounts of quartz, calcite, and dolomite were detected in all analyzed samples as well (Figure S4).

The most striking micropetrographic feature of the mudrock samples is the common presence of sedimentary organic matter together with densely packed, spherical (framboidal) aggregates of tiny pyrite crystals (Figure 7). Petrographic analysis of the stained thin sections showed that the moderately to well-sorted sandstone samples are mineralogically immature. They are mixed carbonate-siliciclastic rocks and are composed of variable amounts of mono- and polycrystalline quartz grains, fresh to weakly altered feldspars (plagioclase and K-feldspar), micas (muscovite, biotite), chlorite, clays, and carbonate lithic grains (Figures 7 and 8). Metamorphic and volcanic rock fragments also appear in an inconsiderable amount. Detrital carbonate grains such as dolomite, limestone, and rare bioclast (e.g., bivalve shell) fragments are important components (~10–25%). Moreover, there are some accessory minerals such as zircon, tourmaline, rutile, garnet, and opaque grains. The polymictic and highly immature clast composition reflects the importance of local provenance (e.g., recycled detritus derived from erosion of intrabasinal basement highs) during the deposition of the Újfalu and Algyő sediments. Some previous studies [32, 37] have also shown carbonate (dolomite, limestone) source components in the underlying Upper Miocene formations (Szolnok and Endrőd).

It is noteworthy that in the studied core sections, a significant macroporosity (~5–25%) was observed in the sandstone and sandy siltstone samples; however, cementation can be pervasive locally. Reduced intergranular porosity is the most abundant type (Figures 7 and 8). No evidence of enlarged/oversized intergranular pores was found. Nevertheless, intragranular secondary porosity can also be found within partly leached feldspars. This result is consistent with the previous observations, suggesting that the effective porosity of the Pannonian reservoir sandstones can reach 22–25% [19, 37].

The aforementioned mineralogical data reflect that kaolinite as a clay-mineral cement phase could occasionally form by feldspar alteration related to influx of meteoric water [12, 19, 37]; nevertheless, it is a minor component. Early diagenetic nonluminescent carbonate with variable iron content is the dominant cement in all of the studied siltstone and sandstone samples. Additionally, framboidal pyrite cement predated calcite precipitation also occurs. Carbonate staining reveals that most of the examined samples consist of ferroan calcite (Fe calcite) cements, showing mauve color, in a highly irregular distribution. Only a few pore-filling carbonate crystals show bluish color after staining, indicating the presence of minor amount of ferroan dolomite and/or ankerite as euhedral (rhomb-shaped) to subhedral crystals (Figure 8). Detrital carbonate grains serve as nuclei for calcite cement in most of the sandstones. The size of the cement crystals is controlled in part by the fabric of carbonate mineral in the detrital grains. Thus, micritic limestone/dolomite grains have microcrystalline calcite overgrowths in the first layer of cement, and crystals become larger away from the grains. On the other hand, single detrital crystals of spar have sparry overgrowths. Based on a previous study [37], ferroan calcite which is most probably one of the first authigenic phases formed is the volumetrically most significant cement type in the underlying Szolnok sandstone samples from the Algyő High.

During shallow burial diagenesis, pore waters undergo systematic changes [45]. When pore waters become significantly depleted in dissolved oxygen (<0.5 ml/l), a suboxic geochemical zone (including nitrate, manganese, and iron reduction subzones, successively) prevails. Additionally, in marine/brackish sediments, where the pore waters contain dissolved sulfate and are devoid of dissolved oxygen, bacterial sulfate reduction (BSR) can operate at shallow depths below the water–sediment interface to depths of a few hundred meters [32, 45, 46]. In the presence of reactive iron (e.g., Fe-bearing detrital minerals: biotite, chlorite; rock fragments), the precipitation of Fe sulfide as early diagenetic cement phase (i.e., framboidal aggregates of pyrite crystals) is a common process. Additionally, increased pore water alkalinity is recorded from organic-rich deposits influenced by BSR and pyrite formation [32, 45]. When pore waters are devoid of dissolved sulfide, excess Fe^{2+} can be incorporated into the carbonate lattice, forming ferroan calcite and/or ferroan dolomite/ankerite cement phases [45]. Consequently, the pore waters become significantly depleted in dissolved Fe^{2+} and sulfide.

4.2. Thermal Water Chemistry. Regarding thermal water sampling and major hydrochemical parameters, data for production and reinjection wells are listed in Table 2. All waters represent Na–HCO_3-type waters with variable TDS contents, ranging from 1670 to 6350 mg/l. The investigated production wells exhibit high TDS (5430 and 6350 mg/l, respectively), whereas the reinjection wells show lower TDS (<4640 mg/l). Sodium ion is the predominant cation, ranging from 450 to 1450 mg/l. The HCO_3^- is the predominant anion, ranging from 1010 to 3180 mg/l; Cl^- is the second highest anion, ranging from 27 to 420 mg/l. Only groundwaters of the production wells exhibit measurable SO_4^{2-} content (70 and 44 mg/l, respectively), whereas dissolved and/or gaseous sulfide (HS^-, S^{2-} and H_2S, respectively) content was not detected. Additionally, pH values range from 7.3 to 8.5 and the produced waters often show high dissolved organic matter (phenol index: 1852–2040 μg/l) and gas contents (total methane: 809–958 l/m^3; CO_2: 167–199 l/m^3).

Content of low to moderate amounts of alkaline earth metals (Ca^{2+}: up to 11.2 mg/l, Mg^{2+}: up to 3.5 mg/l), chloride ion (up to 420 mg/l), and sulfate ion (up to 70 mg/l) reflects the presence of carbonate dissolution and also indicates brackish water in the pores [45, 46]. The total Fe content in the thermal waters is relatively low (<2.2 mg/l), especially groundwaters of the production wells exhibit negligible (<0.39 mg/l) Fe content. Note that changes in thermal water chemistry such as decreasing alkaline earth metal concentrations together with increasing Fe content during system operational processes are purely related to man-made environmental conditions (e.g., carbonate scaling, corrosion, and biological processes). It is beyond the scope of this paper to discuss these technical influences in detail.

Table 2: General hydrochemical properties of the investigated production (p) and reinjection (r) wells. Data for famous spas in Szeged are also shown for comparison.

Well ID	B–415 p	B–748 p	B–744 r	B–745 r	B–746 r	B–747 r	Anna well	Dóra II well
Bottom depth (m)	1999	1937	1396	1750	1740	1225	944	1706
Depth of screens (m)	1727–1914	1733–1878	1112–1381	1636–1741	1519–1710	1012–1150	n.d.	n.d.
Number of filtered sections	6	3	5	3	3	4	n.d.	n.d.
Effluent water temperature(°C)	79.8	76.9	55.7	75.6	64.5	54.9	52	80
Water yield (m^3/h)	39	54	56	35	78	72	n.d.	n.d.
Dissolved ions (mg/l)								
Na^+	1450	1420	1270	870	830	450	350	830
K^+	18.2	19.5	15.3	10.8	8.5	3.4	2.2	8.3
Li^+	0.24	0.26	0.15	0.16	0.12	0.02	n.d.	0.13
NH_4^+	20.8	23.3	15.2	17.6	18.0	3.0	1.7	49.0
Ca^{2+}	10.1	11.2	1.5	5.0	6.5	6.4	2.1	8.9
Mg^{2+}	3.2	3.5	1.2	1.7	1.9	2.8	1.7	2.9
Fe (total)	0.39	0.07	0.17	2.20	0.96	1.69	0.17	0.35
Cl^-	420	350	245	27	40	123	35	44
Br^-	3.20	6.30	3.20	0.32	0.22	0.33	n.d.	0.26
I^-	3.20	3.10	1.90	0.11	0.09	0.12	0.08	0.15
F^-	2.90	2.30	2.00	3.00	4.00	1.38	1.20	2.60
SO_4^{2-}	70	44	<10	<10	<10	<10	<10	25
HCO_3^-	2870	3180	2500	2370	2280	1010	810	2196
TDS (mg/l)	5430	6350	4640	3480	3210	1670	2809	3169
pH	8.3	7.3	8.5	7.5	8.2	7.8	7.8	n.d.
Phenol index (μg/l)	1852	2040	1600	1740	273	<5	n.d.	n.d.
Total methane (l/m^3)	958	809	303	106	84	16	n.d.	n.d.
CO_2 (l/m^3)	167	199	5	72	38	<1	n.d.	n.d.
LSI	1.66	0.7	0.58	0.42	1.04	0.36	−0.51	—
RSI	4.98	5.9	7.34	6.65	6.12	7.07	8.82	—

Abbreviations: n.d. = no data; TDS = total dissolved solids; LSI = Langelier Stability Index; RSI = Ryznar Stability Index [41].

Table 3: Temporal changes of selected hydrochemical parameters in the geothermal system of Újszeged district (well B–748).

Date	Water yield (m^3/h)	Temperature (°C)	pH	TDS (mg/l)	HCO_3^- (mg/l)	Ca^{2+} (mg/l)	LSI	RSI
19.10.2017	5	34.6	7.75	4272	2501	6.66	0.10	7.55
20.10.2017	25	52.9	8.24	4100	3184	9.25	1.17	5.90
21.10.2017	35	74.5	8.43	4360	2251	8.32	1.53	5.38
22.10.2017	45	79.4	8.15	4340	2135	8.29	1.30	5.55
24.10.2017	55	71.7	8.43	4070	2147	8.02	1.45	5.54
26.10.2017	60	74.8	8.32	3980	2251	7.88	1.40	5.52
23.01.2018	62	91.4	8.21	3417	2561	6.90	1.56	5.09
01.03.2018	70	92.6	8.32	3405	2808	6.80	1.73	4.86
11.04.2018	54	91.6	8.32	3340	2697	6.00	1.64	5.03

Abbreviations: TDS = total dissolved solids; LSI = Langelier Stability Index; RSI = Ryznar Stability Index [41].

Interestingly, both production wells of the Szeged Geothermal Systems have relatively high-salinity thermal waters (TDS > 5 g/l) which support their scaling potential. Based on the hydrostratigraphic position of the targeted Újfalu aquifer, these values are significantly higher than the expected ones (2–4 g/l). Obviously, all of the screened layers between ~1700 and 1900 m produce thermal water with moderate to high scaling ability because of the high bicarbonate concentration (up to 3180 mg/l) and relatively high TDS values (up to 6350 mg/l). Based on LSI results, except for Anna well, waters tend to be scale forming. On the other hand, RSI values range from ~5 to 9 (Table 2). For production wells of the studied cascade systems, relatively low RSI values (<6.2) also reflect that scale will form, whereas RSI

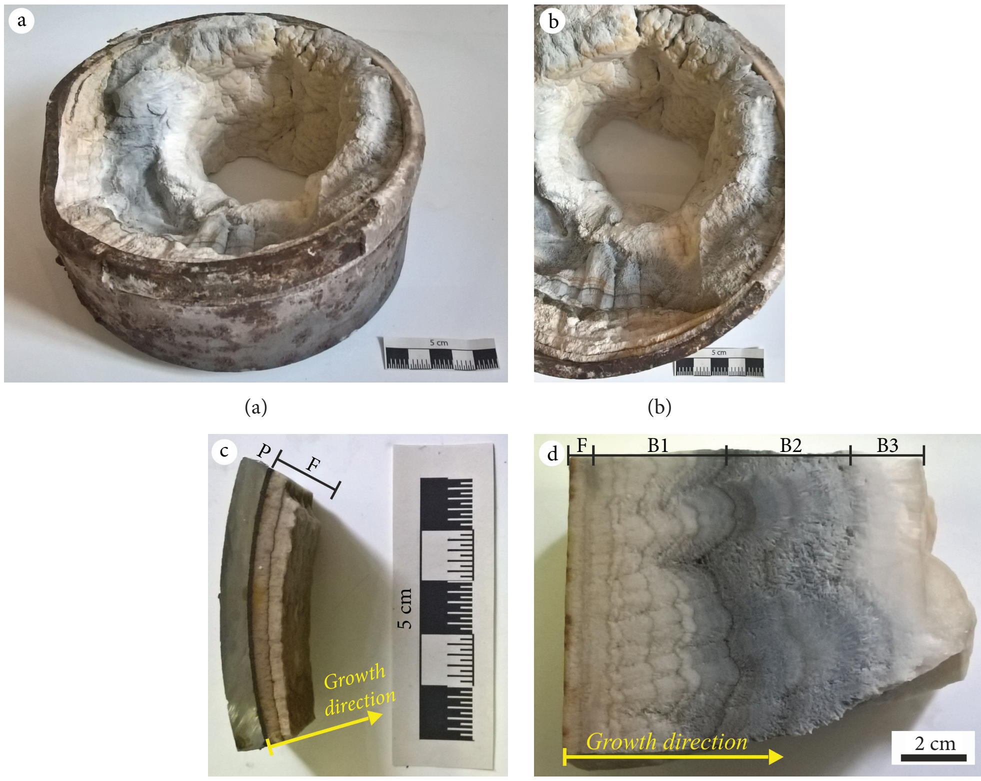

(a) (b) (c) (d)

Figure 9: Thick carbonate scale samples from the Újszeged geothermal cascade system sampled from a pipe between the production well and the buffer tank. (a, b) Macroscopic images of the sample G-03 (total length of the scale bar: 5 cm). (c) Outer part of the sample G-03, showing a fibrous (F) morphology. Substrate material (pipe, P): carbon steel. (d) Inner part of the sample G-03, showing a complex morphology with fibrous (F) to botryoidal (B1 to B3) zones. Note: B1/B2 boundary (an intermittent brownish stained layer) separates seasonal (annual) operational rhythms. Fine lamination represents effects related to the periodical (weekly or daily) operational phases.

data for two reinjection wells together with the value for Anna well indicate an aggressive water, so corrosion could be significant. Relatively high chloride content (up to 420 mg/l), as a corrosive constituent, could also promote steel corrosion and the products may constitute an attractive crystallization substrate for carbonate scales [6–8]. Results of a case study, however, indicate that strongly reducing redox conditions at pH ~6, high sulfide, chloride, and gaseous CO_2 contents together with high thermal fluid temperatures (>100°C in the aquifer) is necessary to promote efficient and rapid steel corrosion [6].

According to the temporal measurements data for the heating system of Újszeged, a decreasing tendency of TDS with some fluctuating pattern of the bicarbonate content is recognizable (Table 3) which suggests a diluted recharge of the thermal water aquifers in the screened sections. It is known for a long time now that meteoric flushing probably occurs downwards into the Szolnok Formation above the Algyő High where overlying Algyő Formation is sand dominated; additionally, synsedimentary faults can also act as pathways of fluid migration [11, 33, 37]. Therefore, it is possible that the aforementioned features reflect a contribution of meteoric water and/or might suggest a relationship with the lower TDS values of the reinjected waters (Table 2), corresponding to the man-made environmental conditions and disturbed natural hydrogeochemical equilibria.

Based on the short-term data in 2017, there is no significant correlation between the water yield and the water chemistry. Nevertheless, water sampled immediately after the off season (Table 3, first line) has the highest RSI value (7.55) that reflects to the high corrosion potential of the stagnant water in the production well. Contrarily in 2018, after ~3–4 months of operation, the TDS decreased (~15%), meanwhile the bicarbonate content fluctuated with some net increase (~10%). Additionally, a significant increase of thermal water temperature (from ~75 to ~90°C) was also observed. These features could reflect a high-temperature bicarbonate-rich water recharge from deeper aquifers (e.g., Triassic dolomite aquifers in the study area), corresponding to an open geochemical system. It is important to note that both calculated indices are in the range of calcite scale precipitation during the studied heating period. Furthermore, in 2018, low RSI data (RSI < 5.5 [41]) indicate that heavy scale will form which can also support a change of hydrogeochemical conditions during the heating season.

4.3. Mineralogical and Petrographic Characterization of the Scale Material with Genetic Aspects. The studied white to

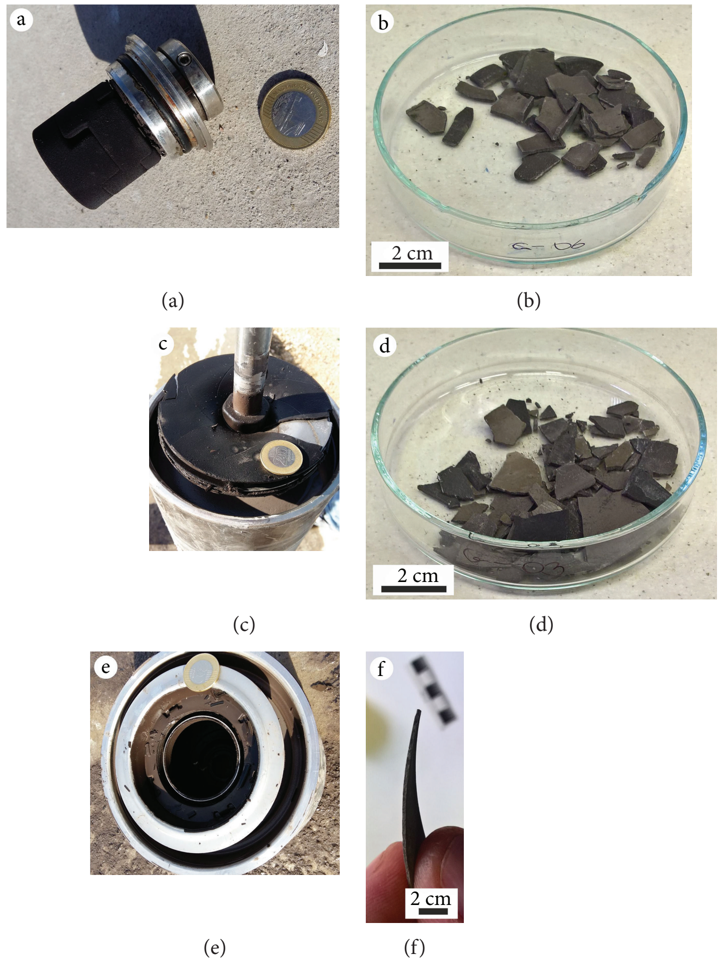

Figure 10: Scales from the Újszeged geothermal cascade system sampled in the engine room (interior surfaces of pumps). (a, b) Pump gland (sample G-06). (c, d) The last blade of the pump (sample G-08). (e, f) The first blade of the pump (sample G-09). Note: a coin (diameter: 28.3 mm) is shown to provide scale.

grayish white-colored scale samples of up to 8 cm thickness in pipes between the Újszeged production well and the buffer tank represent mineral precipitations up to 2 years, leading to a problematic reduction of inner diameters (Figure 9). They show compact (F, B1, and B3) and porous (B2) layers and thin macroscopic zonation of highly variable thicknesses, representing seasonal (annual) rhythmic growth patterns and event-like effects related to the periodical operational phases. These layers frequently show irregular, spherical boundaries and botryoidal-like textures (Figures 9 and S5). In the downtown system, the thick (up to 3 cm) annual scale sample from the pipe between the production well and the buffer tank shows very similar characteristics (Figure S6). On the other hand, dominantly dark-colored scales from facilities (e.g., filters and pumps) in the engine room are typically thin (mm (range)), laminated, and fibrous deposits (Figure 10).

Mineralogically, all the studied representative scale samples show a uniform Mg calcite composition with $d_{104} = 3.012 - 3.016$ Å, regardless of differences in color and morphology (Figure 11). According to the characteristic of the calcite 104 reflection, a 6–7% (molar) $MgCO_3$ content and a 500–600 Å domain size can be estimated.

Microscopically, the thick calcite scale samples show a typical sequence of fine zones characterized by distinct fabrics and photoluminescent features. The generalized sequence typically begins with a thin (0.5 to 5 mm) compact lamina composed of limpid, tightly packed fibrous or bladed crystals (F zone; Figures 12 and S6). Raggedness of the pipe surface serves as nuclei for the first tiny crystal, corresponding to the wall crystallization mechanism [8], and the following fibrous structure is probably the result of the limited growth competition [47]. Under CL microscope, this lamina is generally nonluminescent or shows a very dull, orange luminescence (Figure S6, b and c), suggesting reductive conditions during crystallization.

In the studied samples, the aforementioned first lamina is followed by several thicker zones (B1 to B3 zones; Figures 9 and 12). The scale in these zones is formed largely of complex calcite crystals that grew through the gradual addition of small subcrystals and are characterized by multiple level of

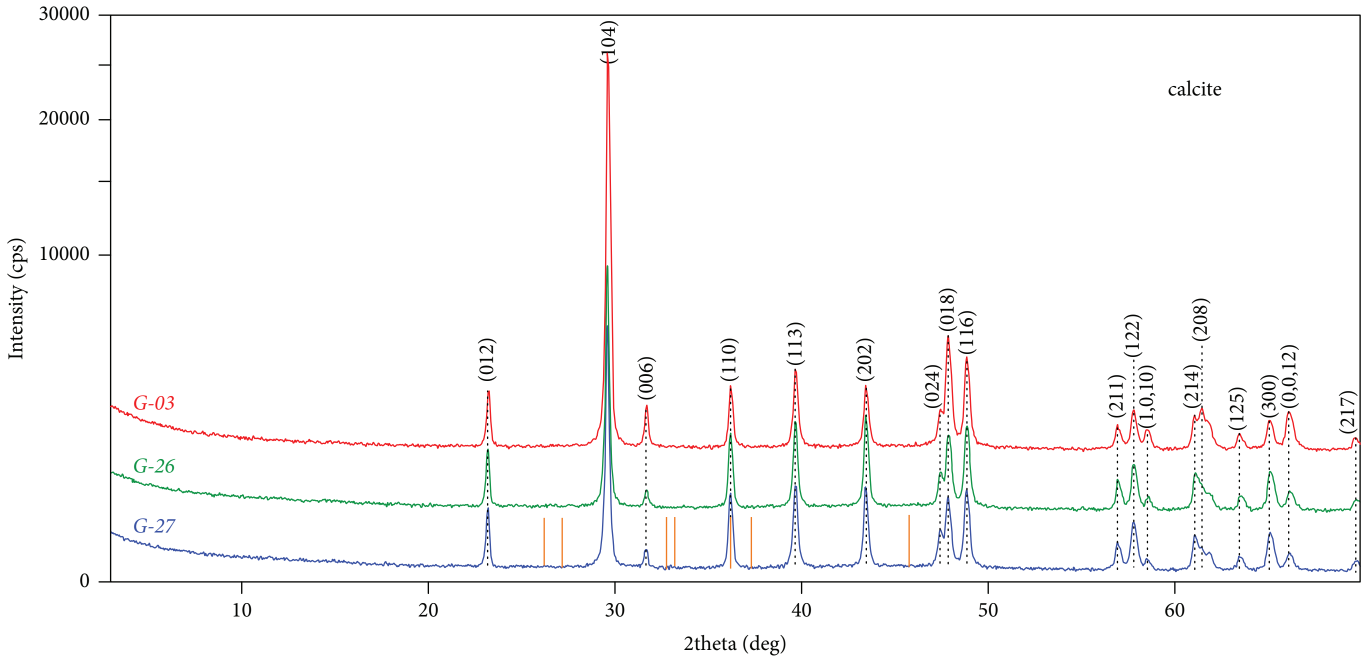

Figure 11: Typical XRPD patterns of representative scale samples (G-03: thick white scale, B1 zone; G-26 and G-27: thin dark brown scales formed inside pumps). Numbers in brackets at the peaks refer Miller indices. Orange lines indicate the diagnostic peaks of aragonite [44]. Note: aragonite (or another mineral phase) was not detected in the studied samples.

branching, corresponding to the feather dendrites which are types of noncrystallographic ones (with patterns that do not conform to the crystallographic directions [48, 49]). Branches radiate outward and upward from the main branch and have an upward-widening character. Therefore, the inner surface of the scale displays a botryoidal-like texture (Figures 12 and S5–7). Consequently, the morphology of the studied dendrite crystals with their distinctive feather-like branching habit was controlled by the competition for growth space with neighboring crystals [47–49]. The zones of the dendritic and feather-like calcite generation generally display a dull bright orange luminescence under CL (Figure S7). Interestingly, some bushes in these zones have a relatively high internal porosity (Figure 12(e)) because of the branches are arranged in a somewhat looser network. In this part of the calcite scale, detrital minerals (mainly quartz, mica, and feldspar) also occur (Figure S8).

In the case of the thick scale sample from the Újszeged geothermal cascade system, representing two years of precipitation, the petrographic features in the sequence show seasonal (annual) repetition, and the sample can be subdivided into two main parts bounded by an intermittent brownish stained and bright luminescent biofilm (B1/B2 boundary; Figures 12(c) and 12(d)). Based on the relative thicknesses of the annual zones (Figure 9(d)), a slightly increasing depositional rate can be suggested in the last heating season. This result is in accordance with the change of hydrogeochemical conditions discussed above. Additionally, the main structural zones can be subdivided into several subzones, depending mainly on the man-made environment related to the periodical (monthly/weekly or daily) operational phases. The boundary between these subzones is frequently represented by thin (few tens of micrometers) dark films without recognizable inner structure. Under CL, these films often show a bright red luminescence and have slight green fluorescence under violet–blue excitation, likely due to their organic content.

As far as the thin (~0.8–1.0 mm), dark-colored scales precipitated on the facilities in the engine room are concerned, they display a relatively simple microtexture (Figure 13). They are composed of more or less limpid, but frequently turbid, tightly packed fibrous to bladed crystals. Additionally, porous dendritic texture was also observed. Two or three subzones can be distinguished in the thin scales with dark biofilm layers. Biofilms can exert either a passive or active function with respect to scale-forming processes [8]; however, it is out of scope to discuss their potential effects in detail.

The observed petrographic and photoluminescent features of the generalized growth zones can reflect to the seasonal (probably monthly/weekly) variability in geochemical parameters such as redox potential, pH, and contamination by organic matter (e.g., biofilm forming). Manganese and Fe concentrations are the most important controlling factors in the cathodoluminescence of carbonates, and these elements have different redox potentials; therefore, the CL of carbonates can be useful for determining redox conditions during the carbonate precipitation [50, 51]. As described above, in the initial stages of the scale precipitation, generally, limpid crystals were formed which are nonluminescent or show dull red CL, suggesting slightly reductive conditions. The later-precipitated cement overgrowths (feather dendrites), showing a brighter luminescence, indicate abundant Mn^{2+} content of the calcite crystals but unequivocally suggest that oxygen level was too high (>0.5 ml/l) to allow significant

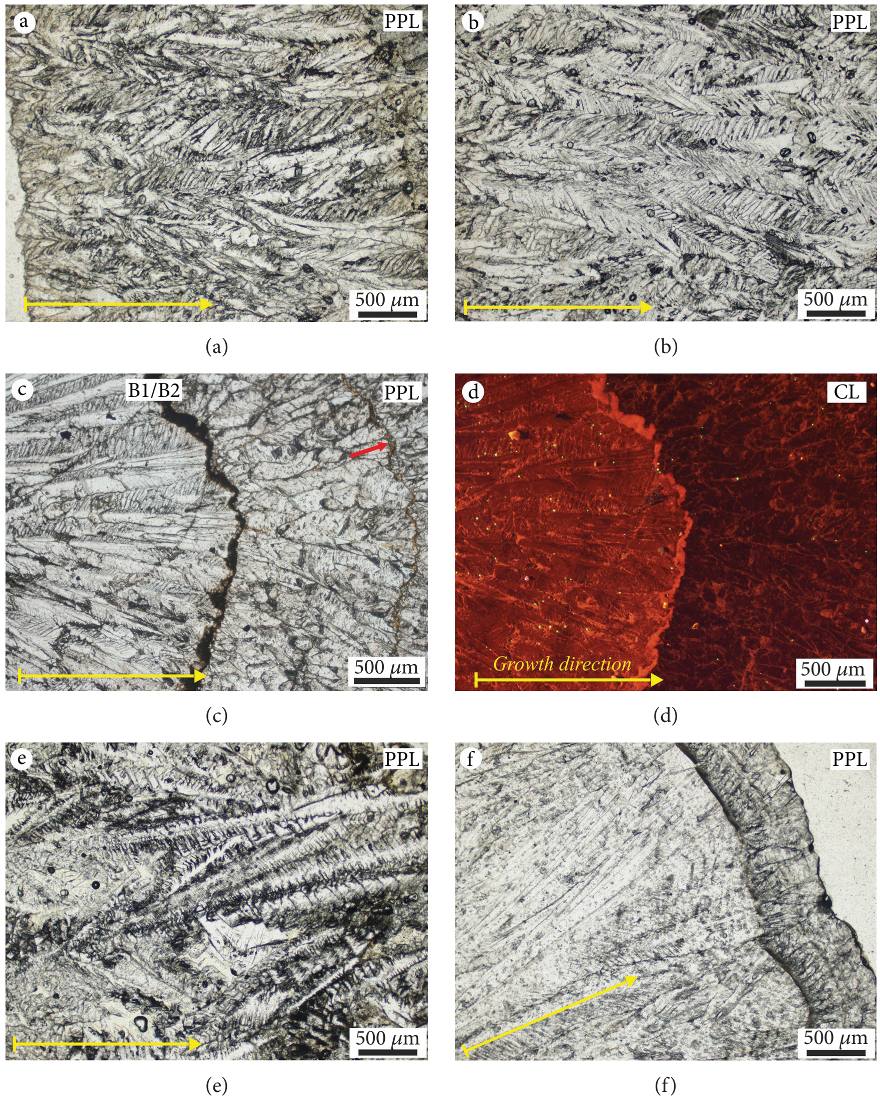

(a) (b) (c) (d) (e) (f)

Figure 12: Inner structure of the thick carbonate scale (inner part of the sample G-03). The growth direction is marked by yellow arrows. (a) The scale precipitation begins with a thin (<500 μm) compact lamina composed of limpid, tightly packed fibrous or bladed crystals (F zone), following a relatively compact dendritic–botryoidal zone (B1 zone). (b) Dendritic and feather-like calcite generation in the B1 zone. (c, d) Spherical growth zones made up of dendritic and bladed crystals and subdivided by a thin, bright luminescent film. Note: B1/B2 boundary (an intermittent brownish stained layer) separates annual operational rhythms. Red arrow indicates a very thin brownish stained layer without luminescence. (e) Feather-like dendrites in the porous B2 zone. (f) Contact of a limpid, tightly packed zone, made up of fibrous crystals and a fine, tightly packed zone with turbid crystals in the compact B3 zone. Abbreviations: PPL = plane polarized light; CL = cathodoluminescence.

Fe^{2+} to exist in aqueous solution which would quench the luminescence. It is important to note that some ingress of oxygen is possible in the buffer tank where degassing takes place (open system).

According to the previous papers [7, 48, 49], dendritic crystal growth has been attributed to the combined effects of parameters such as temperature, the presence of various (inorganic/organic) impurities, or the supercooling of a fluid, leading to high levels of supersaturation and subsequent rapid precipitation. Such crystals form through both abiotic and biotic processes (e.g., the presence of microbes and their associated biofilms). Crystal growth can be very rapid: calcite dendrites can be produced in the laboratory in 2 min [48]. For $CaCO_3$ dendrites, high levels of supersaturation induced by rapid degassing of CO_2 from fluids with high pCO_2 have commonly been the inferred conditions for dendritic crystal growth [48, 49].

Calcite dendrite crystals are important components of calcite travertine that forms around many hot springs (e.g., Iceland, Kenya, and New Zealand) [48]. Their natural waters are of Na–Ca–HCO_3 composition (temperature: 60–99°C; pH: 6.7–9.0) with varying Mg^{2+}, SO_4^{2-}, and Cl^- content. Dendritic calcite precipitation was driven by rapid CO_2 degassing of CO_2-rich thermal water that is highly supersaturated with respect to $CaCO_3$ at the time of precipitation. Furthermore, dissolved Mg could have a role in crystal morphogenesis resulted

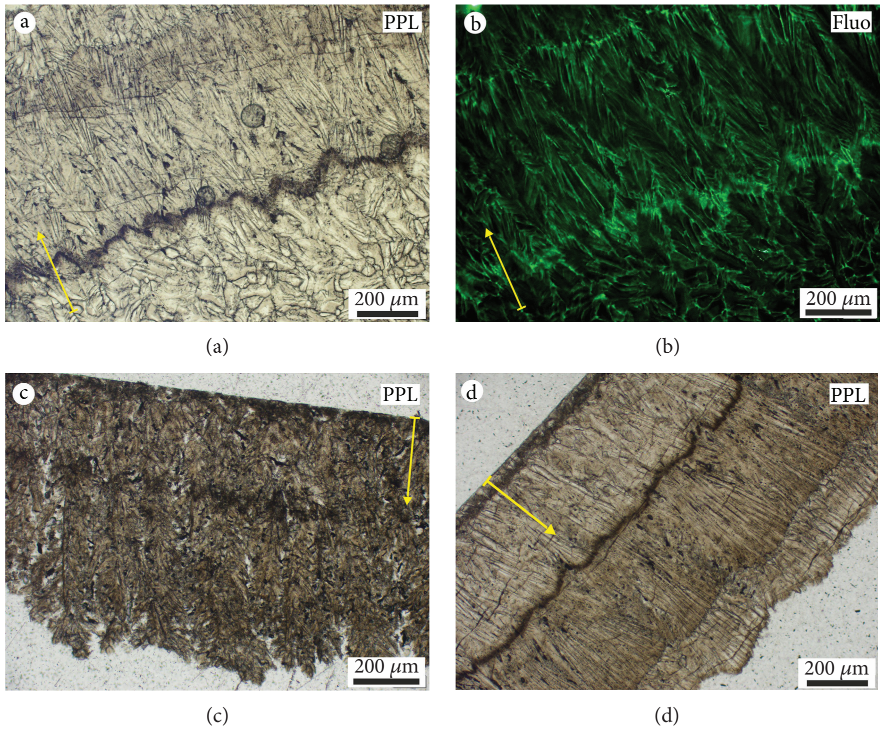

Figure 13: Inner structure of the thin carbonate scales. The growth direction is marked by yellow arrows. (a, b) Contact zone between two distinct growth zones, divided by an organic-rich, greenish fluorescent zone (sample G-06). (c) Thin dendritic carbonate scale sampled from the surface of a pump filter (sample G-07). (d) Thin fibrous and bladed carbonate scale sampled from the surface of a pump filter (sample G-08). Abbreviations: PPL = plane polarized light; Fluo = fluorescence.

in a wider range of crystal morphologies, and a change from single crystals to crystallite aggregates (precipitation of polycrystals) [48, 49]. This explanation also seems applicable to the calcite dendrites in the studied scales. Similar to the thermal spring systems, available mineralogical and micropetrographic evidences suggest that the feather dendrites of low-Mg calcite were precipitated following rapid CO_2 degassing of CO_2-rich (CO_2: 200–300 g/m^3; HCO_3^-: up to 3180 mg/l) thermal waters in the pipes close to the buffer tank where CO_2 degassing was at its maximum in the studied systems.

Calcite crystal morphogenesis has commonly been linked to a "driving force" (e.g., increasing degree of supersaturation and/or supercooling) which is a conceptual measure of the distance of the growth conditions from equilibrium conditions [49]. It is important to note that dendrites are commonly precipitated under far-from-equilibrium conditions [49, 52], a fact that must be recognized in the interpretation of other analytical data such as stable isotope compositions. Additionally, on natural hot water, travertine precipitation clear evidence of low-temperature (~13–51°C) nonequilibrium feather calcite crystallization caused by high rate of CO_2 degassing was also presented [52]. Micropetrographic analyses of the calcite dendrite crystals from scales strongly suggest that this phenomenon is equally true in both natural and man-made environments.

4.4. Water–Rock Interactions versus Thermal Water Quality. The key factors controlling porosity and permeability in reservoir sandstones are depositional characteristics such as grain size and sorting and diagenetic features such as cements and compaction-reduced primary and/or secondary porosity. Among the abovementioned factors, the distribution of mineral cements in aquifers is critical to the spatial variation of porosity and, therefore, permeability. On the other hand, dominant cement types can provide fruitful information about water-rock interactions regarding natural equilibrium conditions [32, 45, 46]. Our petrographic analysis revealed that pyrite and, finally, carbonate (dominantly Fe calcite) cements are the main diagenetic minerals in the studied geothermal reservoir rocks. The identified cement phases reveal that calcite and dolomite saturation states of thermal fluids are close to equilibrium in an oxygen-depleted aquifer [45]. This statement is supported by the nonluminescent (Fe-bearing) Mg calcite precipitation during the initial stage of the scale formation as described above.

Generally, the main sources of ions (calcium, magnesium, and bicarbonate) for carbonate cements are seawater, bioclasts, and carbonate lithic fragments [45]. In the studied Upper Miocene to Pliocene reservoir rocks, detrital carbonate grains are ubiquitous. Additionally, oxidation of local concentrations of organic matter in mudrocks, producing CO_2 during early diagenesis [45, 46], can trigger carbonate precipitation as well. Framboidal pyrite aggregates reflect that the ancient pore water contained appreciable amounts of dissolved sulfate, so bacterial sulfate reduction could operate during early diagenesis, occurring a considerable increase in alkalinity [32, 45]. In essence, the thermal water quality with a relatively high scaling potential in the study area reflects natural (geogen) environmental conditions in a mixed carbonate-siliciclastic system (instead of the pure end-member of siliciclastic aquifers).

The study area (e.g., the close vicinity of the town Szeged) has a nearly basement-high position (Figures 2 and 3). Uplifted basement highs in the Pannonian Basin have played an important role in the hydrologic history of the subbasins, providing conduits for fluid migration during basin evolution [11, 12, 37]. Temporal changes in chemistry and temperature of the produced thermal water during the heating season suggest the upflow of thermal water from an underlying aquifer. This water is characterized by somewhat decreased TDS and increased bicarbonate content, and it is important to note that both calculated indices (LSI and RSI) suggest a slightly increased scale-forming ability (Table 3). These chemical features might reflect to the hydrologic connection with a deep carbonate aquifer, such as the Triassic Szeged Dolomite Formation, which has basin-wide occurrences in the pre-Neogene basement [26, 27]. Additionally, previous modelling results suggest that the fractured basement highs in the Pannonian Basin govern heat transfer and fluid flow like a "hydrogeothermal chimney," resulting positive temperature anomaly at the top of the highs [13]. Continuous and/or temporal upflow of the basin-derived water is probably channeled by inherited extensional structures, neotectonic fault zones, and nontectonic faults above the Algyő High, as it was suggested by several authors in similar geological settings [33, 36].

5. Conclusions

In the Szeged Geothermal Systems (Hungary), having sandstone aquifers with dominantly Na–HCO_3-type thermal water, relatively high scale deposition rates have been observed. Analyses of the reservoir sandstones showed that they are mineralogically immature mixed carbonate-siliciclastic rocks with significant macroporosity. Their mineralogical composition shows rather high compositional variety but it is predominated by quartz, illite±mica, and dolomite, whereas plagioclase, calcite, chlorite, smectite, kaolinite, and K-feldspar are generally minor constituents. Interestingly, detrital carbonate grains appear as important framework components (up to ~20–25%). During water–rock interactions, they could serve as a potential source of the calcium and bicarbonate ions, contributing to the elevated scaling potential. Therefore, this sandstone aquifer cannot be considered as a conventional siliciclastic reservoir. Additionally, in accompanying mudrocks with heterogeneous composition, a significant amount of organic matter also occurs, triggering CO_2 producing reactions such as bacterial sulfate reduction in an early diagenetic system. Correspondingly, framboidal pyrite and ferroan calcite are the main cement minerals in all of the studied sandstone samples which can suggest that calcite saturation state of the thermal fluid is close to equilibrium in oxygen-depleted pore water.

Analysis of the dominant carbonate crystals in the scale can suggest that growth of the feather dendrites of low-Mg calcite was probably driven by rapid CO_2 degassing of CO_2-rich thermal water under far-from-equilibrium conditions, similarly to the hot spring systems (e.g., Iceland, Kenya, and New Zealand) [48]. Based on hydrogeochemical data and related indices for scaling and corrosion ability, the produced bicarbonate-rich thermal water has a significant potential for carbonate scaling which supports the aforementioned statement.

Taking into consideration our present knowledge of geological setting of the studied geothermal systems, the adjacent position to the Algyő High has crucial importance in the hydrologic system. First of all, temporal changes in chemical composition and temperature of the thermal water during the heating period can indicate upwelling fluids from a deep aquifer. Regarding the pre-Neogene basement, hydrologic contact with a Triassic carbonate aquifer (Szeged Dolomite Formation) might be reflected in the observed chemical features such as decreased TDS and increased bicarbonate content with high scale-forming ability. The proposed upflow of basin-derived water could be channeled by Neogene to Quaternary fault zones, including compaction effects creating fault systems above the elevated basement high.

Note that man-made influences also play a crucial role with regard to scale formation. For an advanced understanding of the controlling technical processes, therefore, further specific studies are needed in the future.

Data Availability

The hydrochemical, mineralogical, and petrographic data used to support the findings of this study are included within the article.

Conflicts of Interest

The authors declare that there is no conflict of interest regarding the publication of this paper.

Acknowledgments

The authors are thankful for the hydrochemical data and the scale and rock samples from the geothermal heating systems operating in Szeged owned by the Geothermal Service Provider Ltd., Hungary. This research was financially supported by the Economy Development and Innovation Operative Programme (GINOP-2.1.1-15-2016-00970). Regarding sandstone reservoir characterization, this research was also supported by the National Research, Development and Innovation Fund of Hungary (project Number K 108375).

Supplementary Materials

Supplementary Materials Figure S1: schematic lithologic logs of the investigated core sections (well H–1, Szeged, Hungary), showing the position of the studied samples. Figure S2: typical lithologic characters of the analyzed core sections (core diameter: 76 mm). (a) Alternating fine-grained sandstones and siltstones with disseminated pyrite (brown spots), core #3. (b) Alternating very fine-grained sandstones and mudrocks, core #3. (c) Coal-bearing claystones, core #1.

Figure S3: bivalve shells in a clayey marl sample, core #2. Note: the presence of thin shells of *Paradacna abichi* (arrow) reflects a delta slope depositional facies. Figure S4: typical XRPD patterns (<2 μm fraction, highly oriented mount) of the studied core samples (sample 1/8). Abbreviations: ad: air-dry; eg: ethylene glycol solvated; 350: heat-treated at 350°C; 550: heat-treated at 550°C; cal: calcite; chl: chlorite; dol: dolomite; ill±mu: illite±muscovite; k: kaolinite; q: quartz; sm: smectite±highly swelling mixed-layer illite/smectite. Figure S5: scanned overview images of a thin section prepared from the thick calcite scale (inner part of the sample G-03), showing a complex morphology with fibrous (F) to botryoidal (B1 to B3) zones. Note: B1/B2 boundary (an intermittent brownish stained layer) separates seasonal (annual) operational rhythms. Fine lamination represents effects related to the periodical (weekly or daily) operation phases. The growth direction is marked by a yellow arrow. Abbreviations: PPL = plane polarized light; XPL = crossed polars. Figure S6: the studied annual scale sample (sample G-10) from the downtown geothermal cascade system sampled from a pipe between the production well and the buffer tank. (a) The calcite scale shows complex microscopic zonation of highly variable thicknesses. (b) and (c) Limpid, fibrous growth zone followed by a later zone composed of turbid dendritic skeletal crystals. Note that the carbonate precipitation began with the thin, limpid, and nonluminescent lamina (left) and was followed by a thick, luminescent, and more porous lamina with siliciclastic contamination (right). Abbreviations: PPL = plane polarized light; CL = cathodoluminescence. Figure S7: dendritic crystal growth during scale formation (sample G-10, downtown system). (a) and (b) Feather-like dendrites characterized by multiple level of branching. (c) and (d) Contact of a turbid zone, made up of dendritic crystals with bright CL and a limpid, tightly packed zone with dull luminescence. Abbreviations: PPL = plane polarized light; CL = cathodoluminescence. Figure S8: detrital minerals in the porous scale (sample G-03, B2 zone): muscovite (i), quartz (ii), and feldspar (iii). Abbreviations: PPL = plane polarized light; XPL = crossed polars; CL = cathodoluminescence. Table S1: mineralogical composition of the studied bulk rock samples and separated clay fractions. Abbreviations: 14A = 14 Ångström phase (chlorite±vermiculite±smectite); 10A = 10 Ångström phase (illite ±mica); 7A = 7 Ångström phase (kaolinite); cal = calcite; chl = chlorite; dol = dolomite; sm = smectite±highly swelling mixed-layer illite/smectite; k = kaolinite; kf = K-feldspar; pl = plagioclase feldspar; pyr = pyrite; q = quartz; tr = trace amount. Table S2: measured d_{104} values and estimated composition of calcite and dolomite of the studied bulk rock samples. *(Supplementary Materials)*

References

[1] B. Norden, Ed., “Geothermal energy utilization in low-enthalpy sedimentary environments,” in *Scientific Technical Report STR11/06*, Deutsches GeoForschungsZentrum GFZ, Potsdam, 2011.

[2] J. Szanyi and B. Kovács, “Utilization of geothermal systems in South-East Hungary,” *Geothermics*, vol. 39, no. 4, pp. 357–364, 2010.

[3] J. Szanyi, T. Medgyes, B. Kóbor, and E. Pál-Molnár, *Technologies of Injection into Sandstone Reservoirs: Best Practices, Case Studies*, GeoLitera Publishing House, Szeged, Hungary, 2015.

[4] T. Marković, A. Batres, I. Bobovečki et al., “Summary report on the evaluation case studies (D.5.3.1),” in *Interreg Danube Transnational Programme*, DARLINGe, 2018.

[5] M. Osvald, G. Maróti, B. Pap, and J. Szanyi, “Biofilm forming bacteria during thermal water reinjection,” *Geofluids*, vol. 2017, Article ID 9231056, 7 pages, 2017.

[6] R. Boch, A. Leis, E. Haslinger et al., “Scale-fragment formation impairing geothermal energy production: interacting H_2S corrosion and $CaCO_3$ crystal growth,” *Geothermal Energy*, vol. 5, no. 1, 2017.

[7] R. Boch, J. Szanyi, A. Leis et al., “Geothermal carbonate scaling: forensic studies applying high-resolution geochemical methods,” in *European Geothermal Congress 2016 Strasbourg*, France, 2016.

[8] R. Boch, A. Leis, A. Mindszenty et al., “Scaling forensics: evaluating geothermal production conditions from scales as chemical-sedimentary archives,” in *German Geothermal Congress GGC 2017 Munich*, Germany, 2017.

[9] I. Varsányi, L. Ó. Kovács, and A. Bálint, “Hydraulic conclusions from chemical considerations: groundwater in sedimentary environments in the central part of the Pannonian Basin, Hungary,” *Hydrogeology Journal*, vol. 23, no. 3, pp. 423–435, 2015.

[10] J. Tóth, “Hydraulic continuity in large sedimentary basins,” *Hydrogeology Journal*, vol. 3, no. 4, pp. 4–16, 1995.

[11] J. Tóth and I. Almási, “Interpretation of observed fluid potential patterns in a deep sedimentary basin under tectonic compression: Hungarian Great Plain, Pannonian basin,” *Geofluids*, vol. 1, no. 1, 36 pages, 2001.

[12] A. Juhász, T. M. Tóth, K. Ramseyer, and A. Matter, “Connected fluid evolution in fractured crystalline basement and overlying sediments, Pannonian Basin, SE Hungary,” *Chemical Geology*, vol. 182, no. 2-4, pp. 91–120, 2002.

[13] I. Vass, T. M. Tóth, J. Szanyi, and B. Kovács, “Hybrid numerical modelling of fluid and heat transport between the overpressured and gravitational flow systems of the Pannonian Basin,” *Geothermics*, vol. 72, pp. 268–276, 2018.

[14] K. Korim, “Geological aspects of thermal water occurrences in Hungary,” *Geothermics*, vol. 1, no. 3, pp. 96–102, 1972.

[15] I. Varsányi, J.-M. Matray, and L. Ó. Kovács, “Geochemistry of formation waters in the Pannonian Basin (Southeast Hungary),” *Chemical Geology*, vol. 140, no. 1-2, pp. 89–106, 1997.

[16] I. Varsányi, J.-M. Matray, and L. Ó. Kovács, “Hydrogeochemistry in two adjacent areas in the Pannonian Basin (South-east-Hungary),” *Chemical Geology*, vol. 156, no. 1-4, pp. 25–39, 1999.

[17] I. Varsányi, L. Ó. Kovács, Z. Kárpáti, and J.-M. Matray, “Carbon forms in formation waters from the Pannonian Basin, Hungary,” *Chemical Geology*, vol. 189, no. 3-4, pp. 165–182, 2002.

[18] I. Varsányi and L. Ó. Kovács, “Origin, chemical and isotopic evolution of formation water in geopressured zones in the Pannonian Basin, Hungary,” *Chemical Geology*, vol. 264, no. 1-4, pp. 187–196, 2009.

[19] M. Osvald, J. Szanyi, T. Medgyes, B. Kóbor, and A. Csanádi, “Geothermal energy developments in the district heating of Szeged,” *European Geologists*, vol. 43, pp. 30–33, 2017.

[20] G. Tari, P. Dövényi, I. Dunkl et al., "Lithospheric structure of the Pannonian Basin derived from seismic, gravity and geothermal data," *Geological Society, London, Special Publications*, vol. 156, no. 1, pp. 215–250, 1999.

[21] G. Tari and F. Horváth, "Alpine evolution and hydrocarbon geology of the Pannonian Basin: an overview," in *The Carpathians and Their Foreland: Geology and Hydrocarbon Resources*, J. Golonka and F. J. Picha, Eds., vol. 84, pp. 605–618, AAPG Memoir, 2006.

[22] J. Haas and C. Péró, "Mesozoic evolution of the Tisza Mega-unit," *International Journal of Earth Sciences*, vol. 93, no. 2, pp. 297–313, 2004.

[23] J. Haas, T. Budai, L. Csontos, L. Fodor, and G. Konrád, *Pre-Cenozoic Geological Map of Hungary 1:500 000*, Hungarian Geological Institute, 2010.

[24] S. M. Schmid, D. Bernoulli, B. Fügenschuh et al., "The Alpine-Carpathian-Dinaridic orogenic system: correlation and evolution of tectonic units," *Swiss Journal of Geosciences*, vol. 101, no. 1, pp. 139–183, 2008.

[25] L. Matenco and D. Radivojević, "On the formation and evolution of the Pannonian Basin: constraints derived from the structure of the junction area between the Carpathians and Dinarides," *Tectonics*, vol. 31, no. 6, 2012.

[26] I. Garaguly, B. Raucsik, A. Varga, and F. Schubert, "Középső-triász dolomitok képződésének története és töréses deformációja a Szegedi-medence területén," *Földtani Közlöny*, vol. 147, no. 1, p. 39, 2017.

[27] I. Garaguly, A. Varga, B. Raucsik, F. Schubert, G. Czuppon, and R. Frei, "Pervasive early diagenetic dolomitization, subsequent hydrothermal alteration, and late stage hydrocarbon accumulation in a Middle Triassic carbonate sequence (Szeged Basin, SE Hungary)," *Marine and Petroleum Geology*, vol. 98, pp. 270–290, 2018.

[28] I. Magyar, D. Radivojević, O. Sztanó, R. Synak, K. Ujszászi, and M. Pócsik, "Progradation of the paleo-Danube shelf margin across the Pannonian Basin during the Late Miocene and Early Pliocene," *Global and Planetary Change*, vol. 103, pp. 168–173, 2013.

[29] O. Sztanó, P. Szafián, I. Magyar et al., "Aggradation and progradation controlled clinothems and deep-water sand delivery model in the Neogene Lake Pannon, Makó Trough, Pannonian Basin, SE Hungary," *Global and Planetary Change*, vol. 103, pp. 149–167, 2013.

[30] G. Juhász, G. Pogácsás, I. Magyar, and P. Hatalyák, "The Alpar canyon system in the Pannonian Basin, Hungary – its morphology, infill and development," *Global and Planetary Change*, vol. 103, pp. 174–192, 2013.

[31] K. Báldi, F. Velledits, S. Ćorić, V. Lemberkovics, K. Lőrincz, and M. Shevelev, "Discovery of the Badenian evaporites inside the Carpathian arc: implications for global climate change and Paratethys salinity," *Geologica Carpathica*, vol. 68, no. 3, pp. 193–206, 2017.

[32] A. Varga, V. Baranyi, B. Raucsik, and F. Schubert, "Az Endrődi Formáció kőzettani és palinológiai vizsgálata a Hódmezővásárhely–I fúrásban (Makói-árok) — őskörnyezeti és diagenezis-történeti értékelés," *Földtani Közlöny*, vol. 147, no. 1, p. 61, 2017.

[33] A. Balázs, I. Magyar, L. Matenco, O. Sztanó, L. Tőkés, and F. Horváth, "Morphology of a large paleo-lake: analysis of compaction in the Miocene-Quaternary Pannonian Basin," *Global and Planetary Change*, vol. 171, pp. 134–147, 2018.

[34] P. Dövényi and F. Horváth, "A review of temperature, thermal conductivity, and heat flow data from the Pannonian basin," in *The Pannonian Basin: A Study in Basin Evolution*, L. H. Royden and F. Horváth, Eds., vol. 45, pp. 195–233, AAPG Memoir, 1988.

[35] L. Lenkey, P. Dövényi, F. Horváth, and S. A. P. L. Cloetingh, "Geothermics of the Pannonian Basin, and its bearing on the neotectonics," *EGU Stephan Mueller Special Publication Series*, vol. 3, pp. 29–40, 2002.

[36] S. Simon, J. Mádl-Szőnyi, I. Müller, and G. Pogácsás, "Conceptual model for surface salinization in an overpressured and a superimposed gravity-flow field, Lake Kelemenszék area, Hungary," *Hydrogeology Journal*, vol. 19, no. 3, pp. 701–717, 2011.

[37] J. Mátyás, *Diagenesis and Porosity Evolution of Neogene Reservoir Sandstones in the Pannonian Basin (Southeast Hungary)*, University of Bern, Institute of Geological Sciences, 1994.

[38] J. Pigott and D. Radivojevic, "Seismic stratigraphy based chronostratigraphy (SSBC) of the Serbian Banat Region of the Pannonian Basin," *Open Geosciences*, vol. 2, no. 4, 2010.

[39] B. Badics and I. Vető, "Source rocks and petroleum systems in the Hungarian part of the Pannonian Basin: the potential for shale gas and shale oil plays," *Marine and Petroleum Geology*, vol. 31, no. 1, pp. 53–69, 2012.

[40] J. A. D. Dickson, "Carbonate identification and genesis as revealed by staining," *SEPM Journal of Sedimentary Research*, vol. Vol. 36, 1966.

[41] E. Hoseinzadeh, A. Yusefzadeh, N. Rahimi, and H. Khorsandi, "Evaluation of corrosion and scaling potential of a water treatment plant," *Archives of Hygiene Sciences*, vol. 2, pp. 41–47, 2013.

[42] F. Zhang, H. Xu, H. Konishi, and E. E. Roden, "A relationship between d_{104} value and composition in the calcite–disordered dolomite solid-solution series," *American Mineralogist*, vol. 95, no. 11-12, pp. 1650–1656, 2010.

[43] H. P. Klug and L. E. Alexander, *X-Ray Diffraction Procedures*, Wiley and Sons, London, United Kingdom, 1962.

[44] D. M. Moore and R. C. Reynolds, *X-Ray Diffraction and the Identification and Analysis of Clay Minerals*, Oxford University Press, Oxford, United Kingdom, 1997.

[45] S. Morad, "Carbonate cementation in sandstones: distribution patterns and geochemical evolution," in *Carbonate Cementation in Sandstones*, S. Morad, Ed., vol. 26, pp. 1–26, Special Publications of the International Association of Sedimentologists, 1988.

[46] C. A. J. Appelo and D. Postma, *Geochemistry, Groundwater and Pollution, Second Edition*, CRC Press, 2009, fourth corrected reprint.

[47] P. D. Bons, M. A. Elburg, and E. Gomez-Rivas, "A review of the formation of tectonic veins and their microstructures," *Journal of Structural Geology*, vol. 43, pp. 33–62, 2012.

[48] B. Jones, R. W. Renaut, R. B. Owen, and H. Torfason, "Growth patterns and implications of complex dendrites in calcite travertines from Lysuholl, Snaefellsnes, Iceland," *Sedimentology*, vol. 52, pp. 1277–1301, 2005.

[49] B. Jones, "Review of aragonite and calcite crystal morphogenesis in thermal spring systems," *Sedimentary Geology*, vol. 354, pp. 9–23, 2017.

[50] M. Pagel, V. Barbin, P. Blanc, and D. Ohnenstetter, *Cathodoluminescence in Geosciences*, Springer, Heidelberg, Germany, 2010.

[51] E. E. Hiatt and P. K. Pufahl, "Cathodoluminescence petrography of carbonate rocks: a review of applications for understanding diagenesis, reservoir quality, and pore system evolution," *Mineralogical Association of Canada Short Course*, vol. 45, pp. 75–96, 2014.

[52] S. Kele, M. Özkul, I. Fórizs et al., "Stable isotope geochemical study of Pamukkale travertines: new evidences of low-temperature non-equilibrium calcite-water fractionation," *Sedimentary Geology*, vol. 238, no. 1-2, pp. 191–212, 2011.

Hindawi
Geofluids
Volume 2019, Article ID 3052806, 11 pages
https://doi.org/10.1155/2019/3052806

Research Article

Seismic Methods in Geothermal Water Resource Exploration: Case Study from Łódź Trough, Central Part of Poland

Tomasz Maćkowski, Anna Sowiżdżał, and Anna Wachowicz-Pyzik

Department of Fossil Fuels, Faculty of Geology, Geophysics and Environment Protection, AGH University of Science and Technology, Al. A. Mickiewicza 30, 30-059 Kraków, Poland

Correspondence should be addressed to Anna Wachowicz-Pyzik; amwachow@agh.edu.pl

Received 10 July 2018; Revised 16 October 2018; Accepted 5 November 2018; Published 31 March 2019

Guest Editor: Philippe Calcagno

The geothermal waters constitute a specific type of water resources, very important from the point of view of their thermal energy potential. This potential, when utilized, supplies an ecological and renewable energy, which, after effective development, brings many environmental, social, and industrial benefits. The key element of any geothermal investment is the proper location of geothermal installation, which would guarantee the relevant hydrogeothermal parameters of the water intake. Hence, many studies and analyses are carried out in order to characterize the reservoir parameters, including the integrated geophysical methods. For decades, the geophysical surveys have been the trusty recognition methods of geological structure and petrophysical parameters of rock formations. Thus, they are widely applied by petroleum industry in exploration of conventional and unconventional (shale gas/oil, tight gas) hydrocarbon deposits. Advances in geophysical methods extended their applicability to many other scientific and industrial branches as, e.g., the seismic survey used in studies of geothermal aquifers. The following paper presents the opportunities provided by seismic methods applied to studies of geothermal resources in the central Poland where the geothermal waters are reservoired in both the Lower Cretaceous and the Lower Jurassic sedimentary successions. The presented results are obtained from a network of seismic profiles. An important advantage of the seismic survey is that they may support the selection of an optimal location of geothermal investment and determination of the geometry of geothermal aquifer. Furthermore, the application of geophysical methods can significantly contribute to the reduction of estimation error of groundwater reservoir temperature.

1. Introduction

Studies on conditions within the geothermal aquifers have been carried out in Poland since the 1980s, when the regional studies have been initiated at the Institute of Fossil Fuels of the Faculty of Geology, Geophysics and Environment Protection, AGH University of Science and Technology, in Kraków. The Research and Development (R&D) project was focused on utilization of geothermal waters from the Lower Jurassic reservoir in the Polish Lowlands and Mesozoic and Paleogene-Neogene reservoirs in the Carpathians. Together with the basic studies, dealing mostly with the estimation of geothermal resources, the development projects were run. This resulted in the construction of first geothermal installation in Poland, in the Podhale region, in 1994 [1, 2]. Recently, 6 district heating plants, 10 health resorts, and 13 recreation centers operate in Poland [3]. They are mostly located in the area of the Polish Lowlands, which appears to be the largest domestic geothermal province (Figure 1).

The geothermal conditions in Poland are relatively well-recognized at regional scale. The comprehensive information about domestic geothermal resources is provided by the series of geothermal atlases, which include the Polish Lowlands, the Carpathians, and the Carpathian Foredeep [5–9]. These areas are favorable not only for utilization of hydrogeothermal resources, first of all for heat generation, but also for balneotherapy, recreation, and other purposes. Generally, the geothermal waters in Poland are suitable for binary, electricity, and heat generation systems [10], which indicates

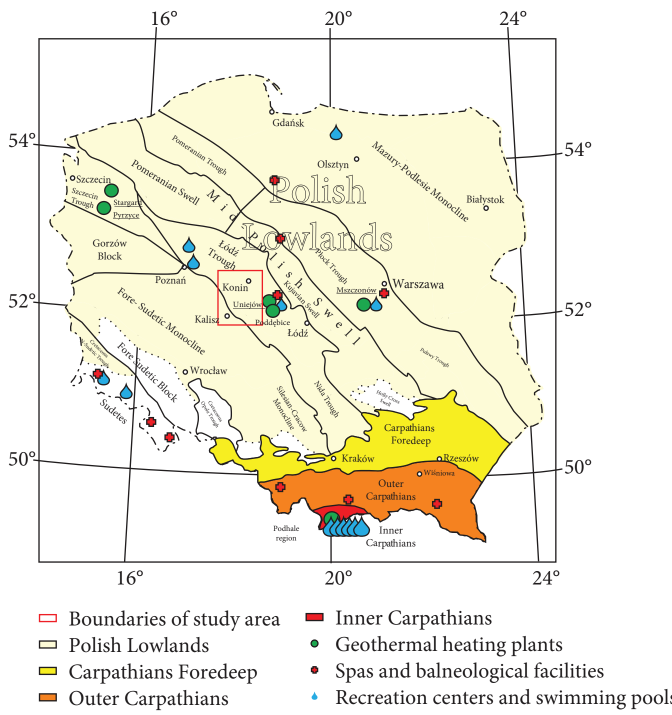

Figure 1: Geological regional division of Poland without Cenozoic cover with location of geothermal installations (after [4], modified).

the utilization of low-temperature geothermal resources for electric power generation. This technology is recently unused in Poland. In the last years, the research projects have been run, concerning the utilization of hot, dry rock (HDR) energy potential using the enhanced geothermal systems (EGS) [11].

The obvious profits resulting from operation of the existing geothermal installations together with promising results of many R&D projects do not stimulate the progress in geothermal energy utilization, which is still rather low in Poland. This is the joint effect of high capital costs and competitiveness of other resources of renewable energy. The high costs are incurred mostly by drilling of new wells or reconstruction and adaptation of the existing wells. Moreover, the important negative factor is the high geological risk incurred by the potential investor. Taking into account the previous experience, it is obvious that many interesting geothermal projects have not been implemented due to geological risk related to the first well drilling and other hydrogeothermal conditions than expected in the project [12].

From the investor's point of view, the crucial parameters controlling the economic effectiveness of geothermal investments are as follows: the temperature and the discharge dependent on petrophysical properties of reservoir rocks. Also, the content of total dissolved solids (TDS), which increases with the depth of groundwater horizons and directly affecting the drilling costs is important. The higher TDS increases the viscosity of reservoir fluids, which deteriorates the productivity of the system and, indirectly, triggers some other negative phenomena such as, e.g., clogging of the wellbore walls. Unfortunately, the deep-seated geothermal reservoirs of most favorable high temperatures show also the high TDS values, which make the efficiency lower [5, 13].

For many years, the seismic survey has been widely applied to recognition of geological structure of the bedrocks and to exploration of conventional and unconventional hydrocarbon accumulations (shale gas/oil and tight gas). In the case of geothermal energy utilization, the possible application of geophysical methods not only in the exploration of geothermal reservoirs but also directly for the purposes of geothermics is important [12, 14, 15]. The seismic methods can be successfully used in verification of potential geothermal reservoirs, providing the credible seismic image of exploration targets. However, the costs of comprehensive seismic survey are high, which strongly limits their applicability.

The seismic survey is still rather rarely applied in Polish Geothermal research. Before 2001, only one such project was completed when the Skoczów-Wadowice-Sucha 2D seismic survey was extended for additional profiles, thanks to the agreement between the petroleum industry and the Institute of Fossil Fuels, AGH University of Science and Technology, signed in 1987. The results of these studies were then used in positioning of the Biały Dunajec PAN-1, Poronin PAN-1, and Nowy Targ PIG-1 wells located in Carpathians, southernmost Poland. Later on, in the years 2001–2002, one of the Polish geophysical companies completed the seismic survey for the Geotermia Podhalańska Co.—the operator of a geothermal heat plant in the Podhale region [16]. Some seismic and magnetotelluric surveys were run for geothermal purposes in the Polish Lowlands (central Poland, [17]) and in the Sudetes [18].

In order to reduce the costs of field seismic survey, the reprocessing of archival seismic data is commonly applied. Such datasets originating from hydrocarbon exploration projects [16] were widely used in various R&D studies recently run in Poland (see, e.g., [5–9]).

Considering the progress in available interpretation software, the more detailed reprocessing of archival data is possible even if quality of source data is low. The reinterpretation not only provides the new information about geological setting of the project area but also enables the researchers to obtain more accurate geometry of the reservoir and more detailed image of its heterogeneity (location of faults, unconformities, etc.). Particularly valuable for potential investors is the opportunity of evaluation of geothermal parameters from the results of seismic survey, which reduces high geological risk of the investment [19].

1.1. Low-Temperature Geothermal Resources in Poland. In Poland, the geothermal resources are accumulated in four main hydrogeothermal provinces: the Polish Lowlands, the Carpathians, the Carpathian Foredeep, and the Sudetes. Unfortunately, these are mostly the low-temperature resources of wellhead temperatures below 100°C.

The Polish Lowlands is the largest hydrogeothermal province in Poland. The geothermal resources are hosted in the Mesozoic sedimentary formations, among which the most prospective are the Lower Jurassic and Lower Cretaceous aquifers. Local accumulations are known also from the Middle/Upper Jurassic and the Triassic sedimentary successions, but these formations show much lower geothermal potential. This distribution of geothermal resources is confirmed by parameters of currently operating geothermal heating plants, which utilize the waters from the Lower Jurassic (Pyrzyce, Stargard) and the Lower Cretaceous (Uniejów, Mszczonów, and Poddębice) aquifers [1].

The Podhale region is a "geothermal gemstone" in Poland. Here, the oldest and the largest geothermal heating installation has been in operation since the 1990s. Geothermal water is produced from three wells of permissible discharge of 960 m^3/h at a temperature of 80–86°C. The reservoir rocks are the Middle Triassic limestones and dolomites [3].

In the remaining part of the Carpathians, complicated geological settings result in low discharge of production wells and in recharge problems of geothermal reservoirs, which increase the geological risk of location of geothermal installations. However, the premises to consider the geothermal investments exist in some areas (e.g., Wiśniowa).

The geological setting of the Carpathian Foredeep is less complicated. Here, the geothermal waters are reservoired in both the Devonian and the Carboniferous carbonate sequences (in the western part) and in the Middle Jurassic sandstones (in the eastern part), as well as in the Upper Jurassic carbonates and the Upper Cretaceous (Cenomanian) sandstones (in the central part of the foredeep) [8, 20]. The highest potential discharges (over 200 m^3/h) were determined just in the Cenomanian aquifer. This is a unique value because in the most part of the foredeep and in most of its geothermal aquifers, the estimated discharges are from several to a dozen of m^3/h (never exceeding 60 m^3/h), which brings development problems of geothermal resources utilized for heating purposes [12].

The studies were carried out in the central part of the Polish Lowlands. The research area has been located in the Łódź Trough, between Kalisz and Konin towns (Figure 1). Apart from the aforementioned Podhale region, the central part of the Polish Lowlands is the most prospective area for large-scale utilization of geothermal waters in Poland. Recently, the geothermal installations operate in nearby Uniejów and Poddębice, where geothermal heating plants were constructed.

In Poddębice, the construction of geothermal district heating plant was commissioned in 2012. Geothermal aquifer is hosted by the Lower Cretaceous sandstones at the depth 1.95–2.06 km b.g.l. The geothermal district heating (geoDH) of 10 MWth geothermal capacity is based on 68°C water (maximum ca. 250 m^3/h, TDS 0.4 g/L). Since 2014, the plant supplies some public buildings, school, hospital (and its rehabilitation part), and several multifamily houses. Some part of water stream is sent to a swimming pool [3, 21].

In Uniejów, the geoDH has been operating since 2001. Geothermal aquifer is hosted by the Lower Cretaceous sandstones at the depth 1.9–2.1 km b.g.l. The maximum discharge from one production well is 33.4 L/s of 68°C water while TDS are ca. 6–8 g/L. The exploitation system includes also two injection wells. The total installed capacity of the plant is 7.4 MWth including 3.2 MWth from geothermal, 1.8 MWth from biomass boiler, and reserve 2.4 MWth from fuel oil peak boilers. Since 2008, a part of geothermal water has been used in geothermal spa and recreation center "Termy Uniejów" for pools and curative treatments (ca. 8.4 L/s of 42°C water; ca. 1 MWth, 7.7 TJ). The center is also heated by geothermal energy. Some amount of spent water (ca. 5.6 L/s, 28°C) is then used to heat up a lawn of football playground (ca. 1 MWth, 8.7 TJ) and walking paths. In 2012, Uniejów received a formal status of health resort thanks to curative geothermal water [3, 21].

In 2015 in Konin, new borehole dedicated for geothermal purposes was made. The water temperature of the Lower Jurassic aquifer confirmed very good thermal conditions of the region like high temperature at the level of 95°C. Currently, the borehole is at the initial stage; the high efficiency is expected [21]. Other towns in the region plan to utilize the geothermal resources [19].

1.2. Geological Background. The research area is located in the Łódź Trough, which is a central part of the Polish Lowlands (Figure 1). The origin of the Łódź Trough, which is an asymmetric tectonic palaeoform, is ascribed to the Laramide transpression of the Polish Basin, which triggered the inversional rearrangement of its axial part [22]. From southwest, the Łódź Trough borders with the Fore-Sudetic Monocline and from northeast with the Mid-Polish Swell (Figure 1). Tectonic character of its southwestern border is documented by a deep-rooted Poznań-Kalisz dislocation zone and related the Mesozoic tectonic graben, which was formed in the Late Triassic and at the Triassic/Jurassic turn [23]. Moreover, locally tectonic character is manifested by

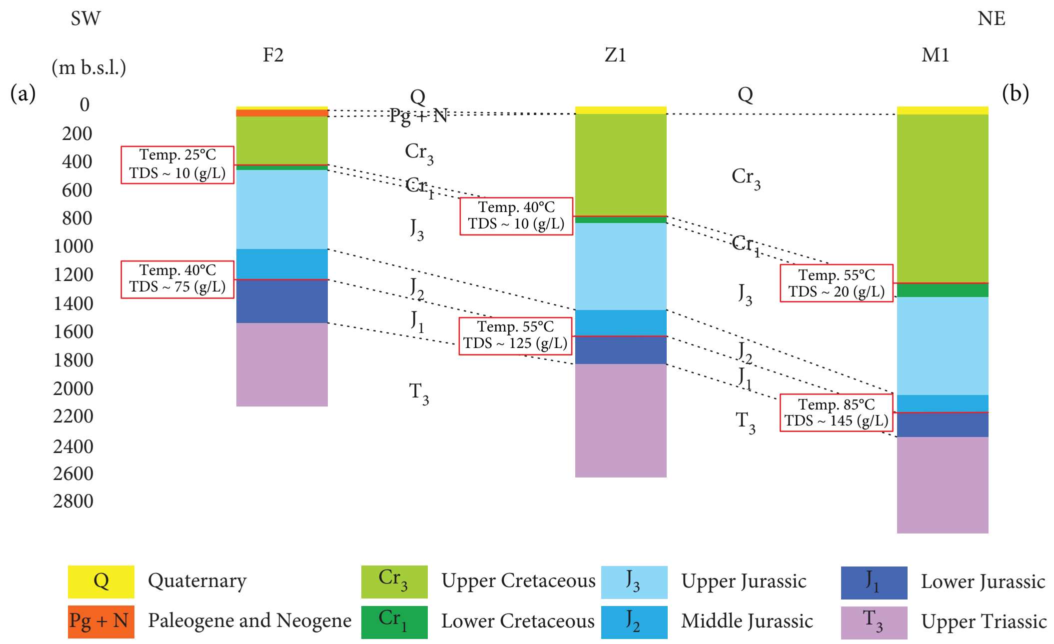

FIGURE 2: Geological correlation of deep boreholes in the research area (along the green dotted line in Figure 3).

the deposition of the Lower Jurassic strata as documented thickness increase measured in the F2 well (Figure 2), located in the marginal part of the graben. The sub-Cenozoic surface of the Łódź Trough comprises both the Permian and Mesozoic rocks.

The intensive subsidence in the Cretaceous of the Łódź Trough manifested by significant thickness of the Cretaceous sediments, which attained the maximum value in Poland—3000 m in the vicinity of Turek town [24]. In the research area, thickness of the Cretaceous succession varies from 379.5 m in the F2 well to over 1200 m in the M1 well (Figure 2).

In the research area, the Cretaceous sediments in the top part of the sequence, lithology comprises mostly gaizes (F2 well) followed by limestones, marly limestones, and glauconitic limestones (Z1 well). In the bottom part of the succession, marls and fine-grained sandstones (Z1 well) with limestones and sands (M1 well) are common.

The Jurassic sediments in the central part of the Łódź Trough varies in thickness from 0.25 to over 3000 m [25]. In the research area, the thickness of Jurassic succession varies from 997 m in the M1 well to 1082 m in the F2 well.

In the research area, the Jurassic deposits begin with calcareous claystones, grey marls, grey limestones, and marly limestones (Z1 well) as well as fine-grained sandstones (F2 well). In the bottom part of the sequence, the Jurassic strata is represented by sandstones and grey claystones interbedded with mudstones (Z1 and M1 wells). The Zechstein sequence comprises four cyclothems: Werra (PZ1), Stassfurt (PZ2), Leine (PZ3), and Aller (PZ4). In the northern part of the research area (vicinity of Turek town), the Zechstein rock salts form the salt structure [26, 27]. The geothermal water horizons in the research area (Lower Cretaceous and Lower Jurassic horizons) are recharged mostly by the subcrops of the Cretaceous sediments directly beneath the Quaternary strata. The southeastern part of the Łódź Trough forms a recharge zone of the Cretaceous aquifer whereas the opposite side of the trough is a discharge zone [5]. In the Łódź Trough, the recharge proceeds from both the Mid-Polish Swell and the Fore-Sudetic Monocline, as evidenced by the change of groundwater chemistry, i.e., the TDS contents increasing from the peripheries to the center of the structure [25, 28].

The TDS values for the Lower Cretaceous reservoirs range between 0 g/L and 100 g/L. In most of the Łódź Trough area, the TDS value is below 2 g/L but locally reaches over 100 g/L especially in the eastern part. For the Lower Jurassic reservoirs, the TDS value is higher and ranges between 0 and 250 g/L, locally even above 270 g/L [12]. In the research area, the TDS values for the Lower Cretaceous reservoirs range between ca. 10 g/L in the F2 and Z1 wells and ca. 20 g/L in the M1 well. For the Lower Jurassic, values are higher and increase from ca. 75 g/L in the F2 well up to ca. 145 g/L in the M1 well (Figure 2).

The water temperature in the top of the Lower Cretaceous reservoir is quite high and ranges from 40°C in the marginal part up to ca. 70°C in the northeast of Konin town. For the top of the Lower Jurassic aquifer, the water temperature is higher and reaches over 100°C in the axial part of the structure [12]. In the research area, the water temperature in the top of the Lower Cretaceous aquifer ranges between 25°C (F2 well) and 55°C (M1 well). For the top of the Lower Jurassic reservoir, temperature values range between 40°C (F2 well) and 85°C (M1 well) (Figure 2).

The porosity values for majority of the Lower Cretaceous reservoir in the Łódź Trough reach over 15%. The increase in porosity value is observed along the southern border of the trough and in the southern part reaching a maximum value at a level of 30%. Higher values are characterized by the Lower Jurassic deposits for which the porosity value achieves 20% in the predominating area of the trough. The maximum value reaches 30% northeast of Konin town. The lowest values around 10% characterize the southern part of the trough, south of Łódź town [12, 21]. In the case of the research area, the porosity of the Lower Cretaceous reservoir ranges from ca. 22% in the F2 well to 17% in the M1 well. In the case of the Lower Jurassic, the values range from 15% in the F2 well to 14% in the M1 well.

Petrophysical parameters of the Lower Cretaceous and Lower Jurassic aquifers indicate high potential discharge of wells in the area of Łódź Trough, which ranges from a few to over 400 m^3/h for the Lower Cretaceous and from 50 to 500 m^3/h for the Lower Jurassic reservoirs. In the research area, the potential discharge of wells in the Lower Cretaceous aquifer reaches from about few to 50 m^3/h, while in the Lower Jurassic reservoir ranges from 50 to 100 m^3/h [12].

1.3. Materials and Methods. The seismic survey run in the research area comprised several projects, which have been run since the 1970s and have provided seismic sections of highly variable data quality (Figure 3). In the 1970s, several profiles have been completed, of general NW-SE and SW-NE directions. The seismic signals were recorded with 24-channel end-on spread and significant offset, which reduced the recording of waves reflected from shallow boundaries, particularly those in the Lower Cretaceous geothermal aquifer. Seismic waves were generated by explosions of dynamite charges with shot spacing 100 m and geophone spacing 50 m. The later seismic projects were run in the 1980s with the number of channels raised to 48 and with the shot spacing reduced to 50 m, which improved the maximum fold to 24.

The archival seismic records from the years 1970s and 1980s showed very high levels of noise due to low folds and poor seismic data processing methods. Many seismic sections revealed distortion of reflections; hence, the dislocation zones cannot be discerned from fictitious deformations of reflections.

The low vertical resolution of seismic records causes the lack of the proper gradation of amplitudes related to the diversity of reflection coefficients. In an extremal case, too low dominant frequency and too narrow band of elementary signal lead to the appearance of reflections which result from the interference of lateral signal oscillations, not from the contrast of acoustic impedance.

The newest seismic surveys in the research area were completed in the late 1990s, using the regular grid of profiles with the split spread and 240 recording channels. The shot spacing was 50 m, the geophone spacing was 25 m, and the fold was 60. Seismic waves were generated with the vibrators using the frequency range 8–80 Hz.

The newest seismic sections provided high imaging quality due to significant progress in data acquisition and processing methodology. Hence, the stratigraphic interpretations of the reflections became possible together with the location of boundaries of geothermal aquifers and deep faults cutting through the Zechstein and Mesozoic rocks [18, 19]. Improvement of data resolution disclosed the wedge pinch-outs caused by disappearance of the Lower Cretaceous geothermal aquifer in the southwestern part of the research area.

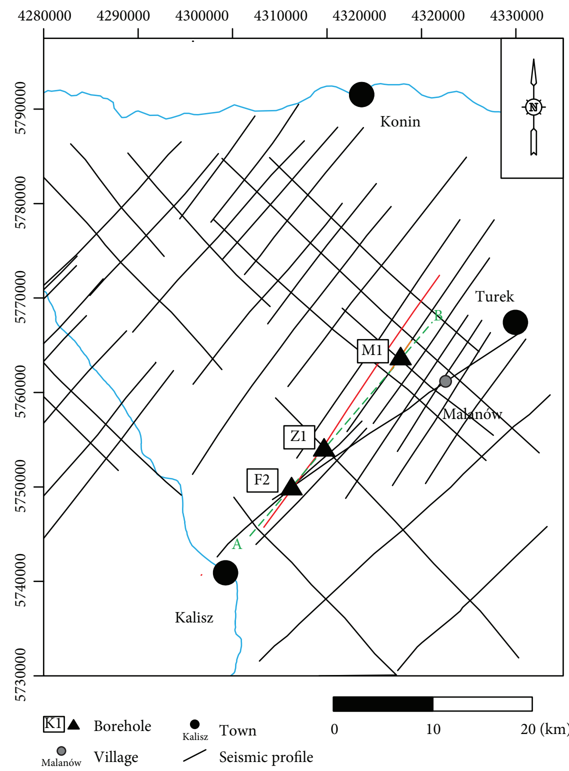

Figure 3: Map of the research area with location of deep wells and seismic profiles (correlated deep wells, along the green dotted line, are shown in Figure 2; orange part of the profile is shown in Figure 4; red line profile is shown in Figure 5).

The geological interpretation of all archival datasets required the reprocessing of the oldest records in order to adjust these seismic images to the newest profiles by increasing the vertical resolution of the sections and by elimination of the noise and the fictitious deformations of the reflections. Data processing was carried out using the scheme and procedures well-known from the literature (see, e.g., [29]).

The seismic image was influenced mostly by the stacking velocity analyses and the residual statics corrections. Many iterations were run in the stacking velocity analysis/residual statics corrections cycle, which provided stable static solution and stacking velocity. Significant influence of residual statics on seismic image appeared in the areas of tectonic disturbances and local velocity anomalies where remarkable improvements were obtained in comparison to archival processing. Before stack, a typical preprocessing was performed and spike deconvolution was applied in order to increase the resolution, followed by scaling of traces in a wide time gate. After stacking, the finite-difference time migration was applied together with the spectral whitening and the procedures increasing the signal-to-noise ratio, as F-X deconvolution and frequency filtration.

The reprocessing resulted in significant improvement of the oldest seismic profiles by elimination of noise, increase of vertical resolution, and correction of reflection continuity. The fictitious reflection deformations and the disruptions of reflections were rejected, which suggested the presence of dislocations in the Mesozoic and Zechstein complexes. The seismic images were unified at the crossings of old (coming from the 1980s) and newest (recorded in the 1990s) sections. However, the problem of reflection inconsistency at the section crossings has remained unsolved, particularly in the zones where data quality was deteriorated due to the presence of the Jurassic carbonate reefs [18].

For detailed analysis of reservoir geometry, the seismic profiles located in the research area were geologically interpreted. Interpretation includes the thickness and depth diversification and identification of the occurrence and direction of dislocations.

Seismic methods also allow assessing the variability of petrophysical parameters of geothermal reservoirs, in particular the porosity value. For this purpose, the seismic inversion procedures, on which the distribution of acoustic impedance is estimated, are used [30]. For the weakly clayey sandstones and limestones, this basic seismic parameter strongly correlates with porosity, which allows for a reliable assessment of it and further optimization of the water intake. More advanced methods of seismic inversion (before stack) determine the elastic impedance and are used to estimate the clayey degree, which allow to determination of the reservoir and the variability continuity of the permeability in terms of quality [15, 31].

1.4. Geological Identification of Seismic Reflections. The stratigraphic identification of seismic reflections in time sections was based upon the stratigraphic interpretations of well-logs, the checkshot data, and the synthetic seismograms, which were correlated with the true seismic traces at the well sites (Figure 4) [32].

The most credible synthetic seismogram was prepared for the newest M1 well spud in the central part of the research area. In this well, high-quality density (RHOB) and acoustic (DT) logs were recorded, which provided the basis for calculations of distribution of seismic reflection coefficient values.

Within the Upper Cretaceous succession, the high-amplitude reflections were absent from the synthetic seismogram and from the true seismic section. The first reflection with distinct positive amplitude was identified as the top surface of the Upper Albian strata located at in the bottom part of the Upper Cretaceous succession, immediately above the Lower Cretaceous sequence. The top surface of that sequence (Cr_1) correlates well with the negative amplitude of an interfered reflection, similarly to the top surface of the Portlandian (J_3p), which is correlated with the positive amplitude. The top surface of the Oxfordian sequence is marked by weak positive amplitude due to low contrast of acoustic impedance at the Kimmeridgian/Oxfordian (J_3km/J_3o) boundary. On the contrary, the boundary of the Upper Jurassic carbonates and Middle Jurassic clastics (J_2) is seismically distinct and recorded by reflection with negative peak.

The true Lower Jurassic (J_1to) and Upper Triassic (T_3re: Rhaetian and T_3k: Keuper) reflections show very low correlation with the synthetic seismogram. This can be explained by local deterioration of data quality beneath the Oxfordian reefs. The regional, marker seismic reflections related to the top surfaces of the Middle Muschelkalk (T_2m) and the Middle Bunter Sandstone (T_2p) quite well correspond to

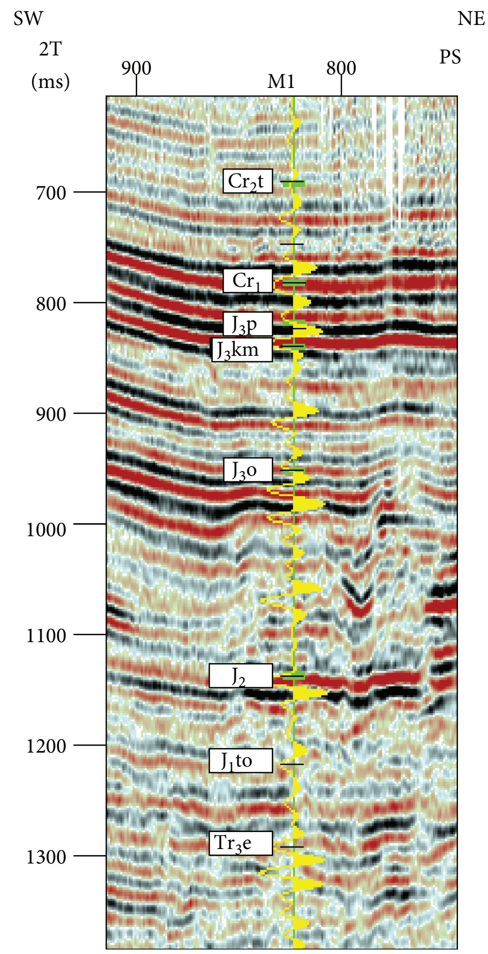

Figure 4: Correlation of synthetic seismogram (yellow trace) for M1 well with the true seismic section (red and black colour—negative and positive true seismic reflections, respectively) in the Lower Cretaceous and Lower Jurassic geothermal reservoir intervals (orange part of line in Figure 3). Explanations of seismic horizons: Cr_2t: top of the Turonian; Cr_1: top of the Lower Cretaceous; J_3p: top of the Portlandian; J_3km: top of the Kimmeridgian; J_3o: top of the Oxfordian; J_2: top of the Middle Jurassic; J_1to: top of the Lower Jurassic (Toarcian); T_3re: top of the Triassic (Rhaetian).

reflections in the synthetic seismogram. Hence, their correlation is not problematic.

The top surface of the Zechstein sequence is represented by weak reflection of negative amplitude located at the boundary of the Lower Triassic strata and the Youngest Halite (Na4) of the PZ4/Aller cyclothem. This reflection is poorly marked in the seismic record from the vicinity of the M1 well but is better visible towards the southwest, in the zone of the F2 and Z1 wells. The bottom surface of the Zechstein (top of the Upper Rotliegend: P_1) is marked by negative reflection.

1.5. Time-Depth Conversion of Seismic Data. The key problem of seismic data conversion from time to depth domain is the recognition and preparation of a model of propagation velocity of seismic waves in the geological medium. Errors in velocity estimations provide the erroneous estimations of depth to particular layers, which, in turn, affect the planning and the execution of drilling operations for the purposes of geothermal installations.

In the case of 2D seismic datasets, common problem is the discrepancy of depths to particular reflectors at the section crossings if the models are generated separately for specific seismic sections. This problem was solved by application of 3D variant of velocity model construction for a set of seismic profiles.

The insufficient number of well-log data precluded the elaboration of credible maps of average and interval seismic wave velocities from the checkshot data for the 3D model. Moreover, the statistical dependences of the changes of interval velocities with the depth could not be determined in particular lithostratigraphic units. Hence, the solution of the problem was sought using the velocities determined from the surface seismic surveys. At the stage of seismic data processing, these are the stacking velocity or the velocities determined from various seismic data inversions. Commonly used are two methods: the coherency inversion and the tomographic inversion [33]. Although less credible than the inversion methods, the conversion of stacking velocity to interval velocities using the Dix formula is popular [34]. Unfortunately, the seismic inversion methods give ambiguous results and must be finally calibrated with the well-log data.

In order to elaborate the model of seismic wave velocity distribution in the Mesozoic complex, both the coherency and the tomographic inversions were performed for a representative grid of seismic profiles. The anomalies were eliminated at the sites of inferior seismic data quality, and the inversion solutions at the margins of the sections were rejected. At the next processing step, the velocity values were interpolated for a defined grid of seismic profiles within the 3D structural framework based upon the interpretation of the marker seismic reflections. After the 3D interpolation, the smoothing of velocity distribution was applied. The smoothing parameters were especially selected in order to minimize the averaging degree and to eliminate the generation of fictitious seismic anomalies at the profile crossings. Additional advantage of application of the averaging filter was the generation of a field characterized by smooth lateral diversity of seismic velocities, which enabled us to avoid the distortion of seismic horizons after depth conversion resulted from excessive velocity contrast, unjustified by geological conditions.

The observed fitting errors of seismic reflections after depth conversion to stratigraphic boundaries in the wells confirm the well-known opinion that the seismic velocities determined with both the tomographic and the coherency inversion methods are overestimated in relation to well-log data. Larger differences (but not exceeding 6–7%) were obtained for velocities determined with the coherency inversion than with the tomographic one. Hence, the final velocity model was based upon the results of tomographic inversion supported by calibration procedure adjusting the obtained values to the well-log data [35]. After correction, the velocity model retained the trend of changes of inversion-based velocities but was also concordant with the well-log data at the well site. Considering the domination of clastic rocks in the Mesozoic complex, the velocities gradually increase towards the northeast with the increasing burial depth of strata. In the northeastern part of the research area, velocities decrease, which is caused by elevation of the Zechstein top surface driven by uplifting of a salt pillow.

In the Zechstein complex, the tomographic inversion solutions appeared to be too much generalized due to low vertical resolution of the method, and, thus, they did not reveal the local velocity changes referred to the zones of increased thickness of high-velocity PZ1 (Werra) anhydrites. Therefore, the construction of velocity distribution was based on the two-layer model, in which the Zechstein complex was arbitrarily divided on seismic time sections into the upper layer where Zechstein rock-salt prevails intercalated by constantly thin anhydrite beds and the lower layer dominated by anhydrites. Basing on such distribution of thickness of the Zechstein layers in time domain, the interval velocity map was calculated assuming the constant velocity values derived from well-logs: for the upper, salt-dominated layer, 4.42 m/s, and for the lower, anhydrite-dominated one, 5.81 m/s.

The time-depth conversion of seismic time sections was performed by their simple multiplication by the values of average velocities. The results of structural interpretation of seismic depth section located close to the wells are presented in Figure 5. As the one result of seismic interpretation, thickness map was created. Thickness map of J_2-T_3k depth interval in the research area is shown in Figure 6.

2. Discussion

Application of geophysical methods in hydrogeothermal practice can bring a number of benefits. The use of seismic methods is of particular importance for the good recognition of local structures and therefore limits the errors of geothermal water deposits assessment. The results of seismic interpretation allow specifying reservoir parameters such as, e.g., depth to the top surface of the reservoir, its thickness, and porosity. Furthermore, precise determination of reservoir geometry improves the results of estimating the temperature of water within reservoirs. An important element of such interpretation is also the ability to indicate deeply rooted faults, which are, in some cases, the migration ways for geothermal water. Moreover, seismic data may support the selection of areas optimal for future investments in geothermal installations.

In the central part of Poland, analysis of seismic depth sections enabled us to recognize the recharge zone of both the Lower Cretaceous and Lower Jurassic geothermal systems related to the tectonic graben and subcrops of the Upper Cretaceous, Lower Cretaceous, and Upper Jurassic rocks beneath the sub-Cenozoic surface in the southwestern part of the research area (Figure 5). The tectonic graben is framed by major listric faults and associated dislocations, which displace the Zechstein and the Triassic beds and cease in the Lower Jurassic strata. The seismic sections do not provide evidence for dislocations penetrating the Middle and Upper Jurassic and the Cretaceous deposits in the graben area and

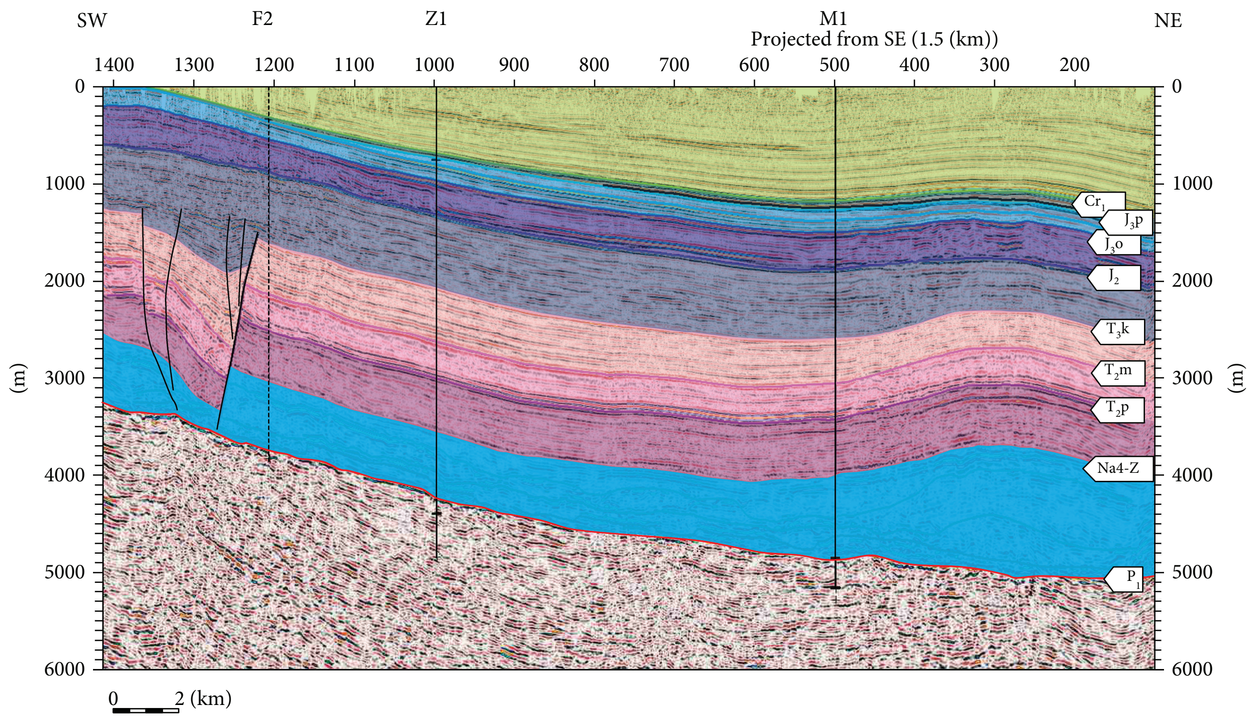

FIGURE 5: Results of structural interpretation of seismic depth section located close to the wells (red line in Figure 3). Explanations of seismic horizons: Cr_1: bottom surface of the Upper Cretaceous/top surface of the Lower Cretaceous; J_3p: bottom surface top of the Portlandian; J_3o: top surface of the Upper Jurassic (Oxfordian); J_2: top surface of the Middle Jurassic; T_3k: top surface of the Keuper; T_2m: top surface of the Muschelkalk; T_2p: top surface of the Middle Bunter Sandstone; Na4-Z: top surface of the Zechstein; P_1: bottom surface of the Zechstein/top surface of the Lower Permian.

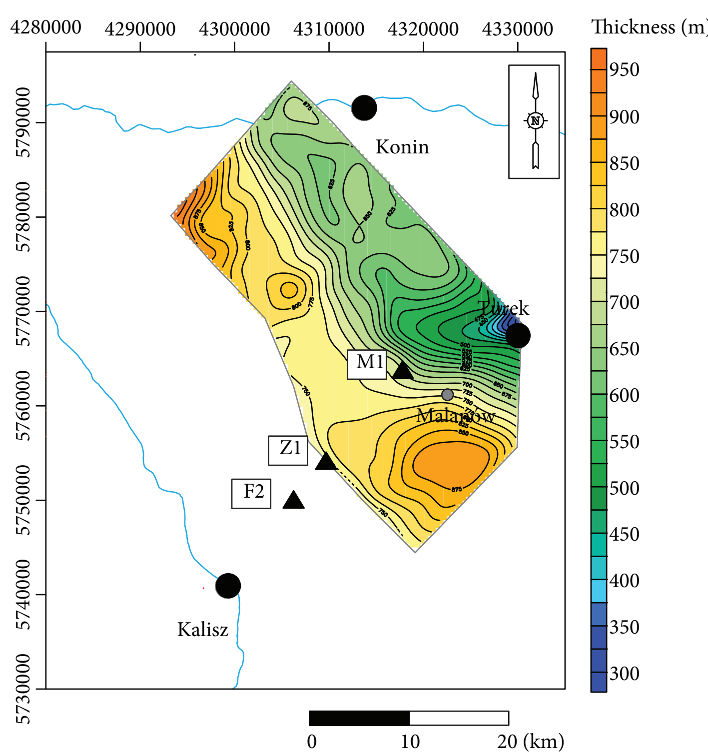

FIGURE 6: Thickness map of J_2-T_3k depth interval corresponding to cumulative thickness of Rhaetian, Lower Jurassic, and Middle Jurassic.

in its vicinity. However, it cannot be excluded that these dislocations propagate upward, even into the Cenozoic complex, as minor faults of throws below the seismic resolution. Unfortunately, deterioration of seismic data quality in the shallow part of the section precludes their recognition. The deeply rooted faults framing the graben, related to the extensional tectonic events, are presumably permeable and may provide migration pathways for brines ascending from deeper horizons and increasing the TDS in the overlying geothermal aquifers.

The seismic surveys allowed for recognition of the internal structure of the graben. The thickness of the Zechstein sequence is much reduced at the northeastern graben's margin and increases towards the southwest. Moreover, changes in thickness of the Lower Triassic are also evident, which may be the effect of tectonic reduction observed in many wells in Poland. They penetrate the main faults framing the Mesozoic tectonic grabens [36]. The increase of sediment thickness within the graben is observed for the Keuper and Lower Jurassic sequences. Outside the graben, in the area between the F2 and Z1 wells, the Portlandian sediments are absent and the Upper Kimmeridgian strata are covered by thin sequence of Lower Cretaceous sediments, in which thickness and depth increase gradually towards the northeast. Both the Kimmeridgian and the Oxfordian successions show more equal thicknesses but are useless for geothermal resource development due to poor reservoir properties.

In the northeastern part of the research area, the seismic sections disclosed a well-marked Zechstein salt pillow, so-called Turek pillow, and related suprasalt anticline, recorded in all interpreted seismic horizons (Figure 5) [37]. Outside the tectonic graben, the $T_{1+2}p$ and T_3p-T_2m complexes sandwiched between the Triassic marker reflectors do not show changes in thickness, which confirms the opinion that the salt diapirism did not begin before the end of Middle Muchelkalk deposition. In the culmination of the salt anticline, the thickness of T_3m-T_3k complex is reduced in relation to its northwestern limb. Hence, the initial salt movements must have commenced as early as in the Keuper, which means that they were coeval with the tectonic episode initiating the formation of the Mesozoic graben in the southwestern part of the research area.

The main stage of salt structure formation is recorded as diverse thickness of sedimentary successions sandwiched between the seismic horizons: T_3k (top of the Keuper) and J_2 (top of the Middle Jurassic) over the culmination of salt anticline and its southwestern limb (Figure 5). Taking into account the regional reduction of thickness of the Middle Jurassic succession to 150 m, the thickness diversity of the whole complex refers to the Rhaetian and Lower Jurassic sequences that determine the age of salt diapirism.

The map shows clear changes of thickness of the J_2-T_3k interval, which contours the range of the salt structure (Figure 6). Over the culmination near Turek town, the thickness of that interval is lower than 400 m, but it doubles towards the south to about 875 m. In that area, both the thickness and depth of the Lower Jurassic geothermal aquifer are the greatest, resulting in maximum water temperature. Considering similar depositional conditions in the whole syncline enveloping the salt structure, it is suggested that the facies development and the reservoir parameters of the Lower Jurassic sediments can be as favorable as those recognized in the M1 well.

3. Conclusions

The seismic surveys are applicable to the studies of geothermal aquifers as their results may reduce the geological risk thanks to more detailed recognition of the aquifer geometry and to reduction of estimation errors of reservoir temperature. The paper presents the results of the research project, which run in the research area located in the central part of the Polish Lowlands (Łódź Trough). This region is a subject of interest of the investors due to high geothermal potential.

The results of seismic surveys enabled us to

(1) Recognize the geological setting of the research area including the identification of faults and salt structures

(2) Determine the depths and the thicknesses of geothermal reservoirs

(3) Identify the recharge zone of the most prospective, Lower Cretaceous and Lower Jurassic geothermal aquifers

The detailed conclusions of the study are as follows:

(1) The recharge zone is related to the tectonic graben and to the subcrops of the Upper Cretaceous, Lower Cretaceous, and Upper Jurassic strata beneath the sub-Cenozoic surface

(2) The presence of faults framing the tectonic graben may influence the parameters of geothermal waters in shallower reservoirs, particularly their TDS, because of mixing of the waters from various horizons

(3) On the contrary to the Lower Cretaceous aquifer, the estimation of reservoir parameters and thickness of sandstones in the Lower Jurassic geothermal aquifer, using the seismic methods, is difficult and requires the specialized studies of reservoir seismics; however, the analyses presented above allow us to suggest that in the research area, the most favorable parameters of the Lower Jurassic geothermal aquifer can be expected along the axis of the syncline (east of Malanów village), whereas for the Lower Cretaceous aquifer, such good parameters can be expected in the northeastern part of the research area, over the salt structure and further in the northeast direction

Data Availability

"All data created during this research is openly available from the doctoral thesis under the title: Analysis of the Carboniferous-Lower Permian Petroleum System in the Context of Stratigraphic and Structural Traps Exploration in Rotliegend Deposits in the Śrem-Kalisz-Konin Zone (T. Maćkowski, 2008), http://winntbg.bg.agh.edu.pl/rozprawy2/10055/full10055.pdf."

Conflicts of Interest

The authors declare that they have no conflicts of interest.

Acknowledgments

The paper was financed by the Akademia Górniczo-Hutnicza im. Stanislawa Staszica statutory research grant no. 11.11.140.031. The project was accomplished owing to the Landmark Strategic University Grant Agreement awarded to the AGH University of Science and Technology in Krakow. The authors are grateful to Dr. B. Reicher for the kind help and support of seismic data interpretation.

References

[1] A. Sowiżdżał, "Geothermal energy resources in Poland-overview of the current state of knowledge," *Renewable and Sustainable Energy Reviews*, vol. 82, no. 3, pp. 4020–4027, 2018.

[2] W. Górecki, A. Sowiżdżał, M. Hajto, and A. Wachowicz-Pyzik, "Atlases of geothermal waters and energy resources in Poland," *Environmental Earth Sciences*, vol. 74, no. 12, pp. 7487–7495, 2015.

[3] B. Kępińska, "The State of Geothermal Energy Uses in the World and in Europe in 2013–2015," *Geological Exploration Technology, Geothermal Energy, Sustainable Development*, vol. 55, no. 1, 2016.

[4] M. Narkiewicz and R. Dadlez, "Geological regional subdivision of Poland: general guidelines and proposed schemes od sub-Cenozoic and sub-Permian units," *Polish Geological Review*, vol. 56, pp. 391–397, 2008.

[5] A. Szczepański, A. Sadurski, M. Hajto et al., *Atlas of Geothermal Resources of Mesozoic Formations in the Polish Lowlands*, W. Górecki, Ed., Ministry of Environment. ZSE AGH, 2006.

[6] A. Szczepański, A. Sadurski, M. Hajto et al., *Atlas of Geothermal Resources of Paleozoic Formations in the Polish Lowlands*, W. Górecki, Ed., Ministry of Environment. ZSE AGH, Kraków, 2006.

[7] A. Szczepański, N. Oszczypko, M. Hajto et al., *Atlas of Geothermal Waters and Energy Resources in the Western Carpathians*, W. Górecki, Ed., Ministry of Environment. Ed. ZSE AGH, Kraków, 2011.

[8] A. Sowiżdżał, J. Jasnos, B. Papiernik et al., *Geothermal Atlas of the Carpathian Foredeep*, W. Górecki, Ed., Ministry of Environment. ZSE AGH, Kraków, 2012.

[9] M. Hajto, J. Augustyńska, J. Jasnos et al., *Geothermal Atlas of the Eastern Carpathians*, W. Górecki, Ed., Ministry of Environment. ZSE AGH, Kraków, 2013.

[10] A. Barbacki, B. Bielec, A. Borsukiewicz-Gozdur et al., *Atlas of the Possible Use of Geothermal Waters for Combined Production of Electricity and Heat Using Binary System in Poland*, W. Bujakowski and B. Tomaszewska, Eds., vol. 305, MEERI PAS, Kraków, 2014.

[11] A. Sowiżdżał, B. Papiernik, G. Machowski, and M. Hajto, "Characterization of petrophysical parameters of the Lower Triassic deposits in a prospective location for enhanced geothermal system (central Poland)," *Geological Quarterly*, vol. 57, no. 4, pp. 729–743, 2013.

[12] A. Sowiżdżał, M. Hajto, B. Papiernik, K. Mitan, and E. Hałaj, "Possibilities of geothermal sector development in central Poland in reference to extended structural and parametrical analysis of Mogilno-Łódź Trough," *Geological Exploration Technology, Geothermal Energy, Sustainable Development*, vol. 56, no. 2, pp. 17–31, 2017.

[13] A. Sowiżdżał, "Prospects of use of thermal water resources of Lower Jurassic aquifer in the Szczecin Trough (NW Poland) for space heating and balneology and recreation," *Polish Geological Review*, vol. 58, no. 7, pp. 613–621, 2010.

[14] Q. Zhang, W. Ge, F. Tian et al., "Coupling empowerment based application of extension method for geothermal potential assessment," *Journal of Engineering*, vol. 2018, Article ID 4907570, 8 pages, 2018.

[15] E. Luijendijk and T. Gleeson, "How well can we predict permeability in sedimentary basins? Deriving and evaluating porosity-permeability equations for noncemented sand and clay mixtures," *Geofluids*, vol. 15, no. 1-2, pp. 67–83, 2015.

[16] B. Czerwińska, "Reinterpretation of archival seismic data for selected regions," in *Atlas of the Possible Use of Geothermal Waters for Combined Production of Electricity and Heat Using Binary System in Poland*, W. Bujakowski and B. Tomaszewska, Eds., p. 305, MEERI PAS, Kraków, 2014.

[17] W. Bujakowski, A. Barbacki, B. Czerwińska et al., "Geophysical surveys for geothermal investigation in central Poland," in *Proceedings World Geothermal Congress 2010*, Bali, Indonesia, April 2010.

[18] M. Stefaniuk, T. Maćkowski, and A. Sowiżdżał, "Geophysical methods in the recognition of geothermal resources in Poland - selected examples," in *Renewable Energy Sources: Engineering, Technology, Innovation*, K. Mudryk and S. Werle, Eds., pp. 561–570, Springer International Publishing, 2018.

[19] A. Sowiżdżał, T. Maćkowski, and A. Wachowicz-Pyzik, "Recognition of geothermal potential of central Poland with the application of geophysical methods. Sustainable water resources management," in *Min wat, international multidisciplinary conference on mineral waters: genesis, exploitation, protection and valorisation*, p. 26, Luso, Portugal, 2017.

[20] A. Sowiżdżał, "Characterization of geothermal reservoirs parameters in Polish part of Carpathian Foredeep," *Carpathian Journal of Earth and Environmental Sciences*, vol. 10, no. 2, pp. 237–246, 2015.

[21] B. Kępińska, A. P. Barbacki, B. Bielec et al., "Geothermal energy – a basis for low-emission space heating improving living conditions and sustainable development – preliminary studies for selected areas in Poland study visits," 2017, Report.

[22] J. Koziar, "Tensorial genesis of inversion in the Polish basin with reference to the tensional development of the Czech massif," in *Czech-Polish Workshop On Recent Geodynamics the Sudety Mts. and Adjacent Areas*, pp. 17–21, Kłodzko-Poland, March 2007.

[23] K. Kwolek, "The age of tectonic movements in the Poznań–Kalisz dislocation zone, Fore–Sudetic Monocline," *Geological Quarterly*, vol. 48, no. 9, pp. 804–814, 2000.

[24] E. Stupnicka, *Regional Geology of Poland*, Warsaw University Press, Warszawa, 1997.

[25] B. Wiktorowicz, *Occurrence Thermal Waters of the Basin of Łódź*, no. 1–2, 2011Geological Exploration Technology, Geothermal Energy, Sustainable Development, 2011.

[26] R. Dadlez, Z. Deczkowski, I. Gajewska et al., *Tectonic Map of the Zechstein-Mesozoic Structural Complex in the Polish Lowlands 1:500 000*, Publications of the Polish Geological Institute, 1980.

[27] R. Dadlez, A. Iwanow, K. Leszczyński, and S. Marek, "Tectonic map of the Zechstein-Mesozoic complex 1:500 000," in *Tectonic Map of the Zechstein-Mesozoic Complex in the Polish Lowlands 1:500 000*, R. Dadlez, Ed., PIG, Wyd. Kart. PAE SA, Warszawa, 1998.

[28] L. Bojarski, *Hydromatic and Hydrodynamic Atlas of the Paleozoic and Mesozoic as well as the Ascending Salinity of Groundwater in the Polish Lowlands*, PIG. Warszawa, 1996.

[29] O. Yilmaz, "Seismic data analysis," *Processing, Inversion and Interpretation of Seismic Data*, vol. 1–2, 2001.

[30] J. Pendrel, "Seismic inversion - the best tool for reservoir characterization," *CSEG Recorder*, vol. 26, pp. 16–24, 2001.

[31] D. N. Whitcombe, P. A. Connolly, R. L. Reagan, and T. C. Redshaw, "Extended elastic impedance for fluid and lithology prediction," *Geophysics*, vol. 67, no. 1, pp. 63–67, 2002.

[32] R. Simm and M. Bacon, *Seismic Amplitude*, Interpreters Handbook, Interpreters Handbook, 2014.

[33] S. Fagin, *Model-Based Depth Imaging*, Society of Exploration Geophysicists, 1998.

[34] C. H. Dix, "Seismic velocities from surface measurements," *Geophysics*, vol. 20, no. 1, pp. 68–86, 1955.

[35] E. Robein, *Velocities, Time-Imaging and Depth-Imagining in Reflection Seismic Principles and Methods*, EAGE Publication, 2003.

[36] K. Kwolek, "Analysis of the Poznań-Kalisz dislocation zone and its relation to the accumulation of natural gas," PhD thesis, the Main library of AGH University of Science and Technology, 2002.

[37] S. Marek and A. Raczyńska, "Local structural forms of central Poland," in *Geological Structure of Poland, no. 1*, W. Pożaryski, Ed., vol. 4, Geological Institute, 1974.

Hindawi
Geofluids
Volume 2019, Article ID 8492453, 21 pages
https://doi.org/10.1155/2019/8492453

Research Article

Synthetic Seismic Reflection Modelling in a Supercritical Geothermal System: An Image of the K-Horizon in the Larderello Field (Italy)

R. de Franco [1], L. Petracchini [2], D. Scrocca [2], G. Caielli [1], G. Montegrossi [3], A. Santilano [4] and A. Manzella [4]

[1] *Istituto per la Dinamica dei Processi Ambientali, CNR, Milano, Italy*
[2] *Istituto di Geologia Ambientale e Geoingegneria, CNR, Roma, Italy*
[3] *Istituto di Geoscienze e Georisorse, CNR, Firenze, Italy*
[4] *Istituto di Geoscienze e Georisorse, CNR, Pisa, Italy*

Correspondence should be addressed to L. Petracchini; lorenzo.petracchini@igag.cnr.it

Received 27 July 2018; Accepted 4 November 2018; Published 28 March 2019

Guest Editor: Matteo Lupi

We tested synthetic seismic reflection modelling along a seismic line (CROP-18A) in the geothermal field at Larderello (Italy). This seismic line is characterized by a discontinuous but locally very bright seismic marker, named K-horizon, which has been associated with various geological processes, including the presence of fluids at supercritical conditions. Geological and geophysical data were integrated in order to develop a 3D subsurface model of a portion of the Larderello field, where extremely high heat flow values have been recorded. In the study area, the K-horizon is particularly shallow and supercritical deep conditions were accessed at depth. The 2D model of the main geological units up to the K-horizon was extracted from the 3D model along the CROP-18A and used to generate the synthetic TWT stacked seismic sections which were then compared with the observed stacked CROP-18A seismic section. To build the synthetic sections, generated through the exploding reflector approach, a 2D velocity model was created assigning to each pixel of the model a constant P-wave velocity corresponding to the related geological unit. The geophysical parameters and the geological model reconstructions used in the modelling process derive from a multidisciplinary integration process including geological outcrop analogues, core samples, and geophysical and laboratory information. Two geophysical models were used to test the seismic response of the K-horizon, which is associated with (1) a lithological discontinuity or (2) a physically perturbed layer, represented by a randomized velocity distribution in a thin layer. For the latter geophysical model (i.e., the physically perturbed layer), we have tested three different scenarios changing the shape and the thickness of the modelled layer. Despite the reliable calibration implied by the use of homogeneous units, the seismic modelling clearly shows that the physically perturbed layer provides a better explanation of the reflectivity features associated with the K-horizon.

1. Introduction

Reducing uncertainties in geothermal exploration is essential in order to support the growth of this promising and sustainable energy source. This is particularly true when dealing with the exploration of supercritical geothermal systems in which the reservoir fluids are expected to be in a supercritical state (for pure water, $T > 374^\circ C$ and $P > 22$ MPa) (e.g., [1–3]). These challenging unconventional high-temperature geothermal systems, usually associated with shallow magmatic intrusion, could provide significantly higher well productivities with respect to wells drilled in classic hydrothermal systems [3].

Exploration strategies of geothermal reservoirs may significantly benefit from synthetic seismic reflection profiles that enable prospective features on acquired seismic reflection data to be detected and the geological-geophysical interpretation and model reconstructions to be calibrated ([4–6] and references therein).

We studied the Lago Boracifero sector of the Larderello geothermal field in Italy, where superheated steam is currently exploited from both a shallow reservoir in sedimentary units and a deep reservoir in crystalline rocks ([7–12] and references therein). In the Larderello geothermal field, the presence of a deep and enigmatic seismic marker, the K-horizon, has long been identified [13] in both 2D and 3D seismic surveys. Rather than being represented by a single reflection event, the K-horizon is characterized by a strip of diffused reflectivity, which is spatially and vertically localized (about 100-500 ms TWT thick), associated with lateral variations in reflectivity and sometimes by a bright spot signature [13–16]. The origin of the K-horizon has been interpreted as the manifestation of several processes including (a) the quartz α-β phase transition [17], (b) the brittle-ductile transition in extensional setting [14–18], (c) a rheological variation associated with a lithospheric thrust [19], (d) natural hydrofracturing in the proximity of lithological or petrophysical changes [20, 21], (e) the development of thermometamorphic aureola at the top of a Quaternary granitic intrusion [10], and (f) presence of warm fluids at overpressure conditions. Following the results of the San Pompeo 2 well (temperature $> 400^{\circ}$ and pressure > 24 MPa extrapolated to the depth of 2930 m, [22]), which reached the vicinity of the K-horizon, the presence of supercritical fluids confined in a relatively thin layer has also been proposed to explain its high reflectivity (e.g., [10]). This hypothesis was used to explain teleseismic converted wave behaviour [23] and was recently explored by a deep drilling project [24].

Our study had four main aims: (1) the calibration of a 2D seismic lines CROP-18A, acquired in the Italian deep crust seismic project [25], through the use of a 3D geological-geophysical model, (2) the definition of a conceptual model of the area based on a rock physics model; (3) the modelling of the seismic response of the 3D geological-geophysical model with associated implications for processing the seismic reflection data, and (4) the definition of the seismic signature of reservoir rocks possibly hosting supercritical fluids.

2. Geological Setting

The Larderello field is located in the inner part of the Northern Apennines (Figure 1), a sector of the orogenic belt of the Apennines.

Although alternative interpretations have been proposed regarding the origin of the thrust belt of the Apennines (see, for example, [19, 26–30]), the Apennines appear to have developed as the result of the westward-directed subduction of a limb of the Mediterranean Tethys along the retrobelt of the southwestward prolongation of the Alps. In this hypothesis, the westward-directed Apennines subduction gradually replaced the “east-ward” Alpine subduction [31–33]. Following the fast eastward retreat of the west-directed subduction zone, the Meso-Cenozoic sedimentary covers situated along the Apulian-Adriatic passive margin were accreted within the Apennine orogen. Contractional deformations were then followed by back-arc extensional tectonics that cross-cut the thrust pile.

However, other authors have suggested a polyphase tectonic evolution of the Northern Apennines due to an eastward-migrating compressional tectonic at the front and a subsequent eastward-migrating extensional tectonic, which has affected the inner part of the orogenic belt since at least the Early Miocene ([34, 35]; Figure 2). A complex tectonic evolution during Miocene-Pleistocene with a prevalent contribution of compressive tectonics up to the Pleistocene Epoch has also been proposed (e.g., [36]).

The geophysical data available show that southern Tuscany is characterized by a shallow Moho discontinuity (20-25 km depth), a reduced lithosphere thickness due to the uprising asthenosphere [37], and an active extensional tectonic as inferred by borehole breakout analysis [38].

The tectonic pile characterizing the study area locally crops out along ridges separated by Neogene tectonic basins filled with continental and marine sediments from the Miocene to Quaternary in age (Figure 1).

The stratigraphic scheme adopted in this work (see also [10, 39, 40]) is made up, from top to bottom, of the following main units (Figure 3):

(i) Neoautoctonous complex (Miocene-Quaternary)

(ii) Ligurian complex (Jurassic-Eocene)

(iii) Tuscan Nappe (Triassic to Miocene) and the Tectonic Wedge complex (Paleozoic-Triassic)

(iv) Crystalline Basement (Pre-Cambrian?-Paleozoic; Pliocene-Quaternary?) formed by the Metamorphic Unit (composed of the Phyllitic complex, the Mica-schist complex, and the Gneiss complex) and the Intrusive complex

The Neoautoctonous complex is composed of marine, lacustrine, and continental deposits, characterized by conglomerates, sandstone, clays, marls, and evaporites. It is mainly localized in the tectonic basins, and it lies unconformably on a deformed substratum. The Ligurian complex is composed of the Jurassic ophiolite sequence of the oceanic crust and its Jurassic-Cretaceous sedimentary cover of the Ligurian units and by the Cretaceous-Oligocene turbidites of the Sub-Ligurian units [41–43]. The Ligurian complex was thrust eastwards on the Tuscan Nappe during the Oligocene-Aquitanian. The Tuscan Nappe represents a sedimentary succession deposited from the Triassic to the Miocene on the paleomargin of the Adria Plate [43, 44]. The unit reflects the paleogeography evolution of the area passing from an evaporitic to shallow water marine environment followed by pelagic conditions. The lithostratigraphy of the Tuscan Nappe is characterized by evaporites, dolostone, and limestone (Triassic), followed by shallow water limestones (Rhaetic to early Jurassic), and by pelagic limestones, cherty limestones, and marls (Jurassic to Oligocene). During the Miocene, the marine deposits were covered by siliciclastic synorogenic deposits. In the Larderello area, the Tuscan Nappe is strongly delaminated, locally completely absent (e.g., [10–85]), while a tectonic wedge complex (TWC) is present between the Tuscan Nappe and the Metamorphic

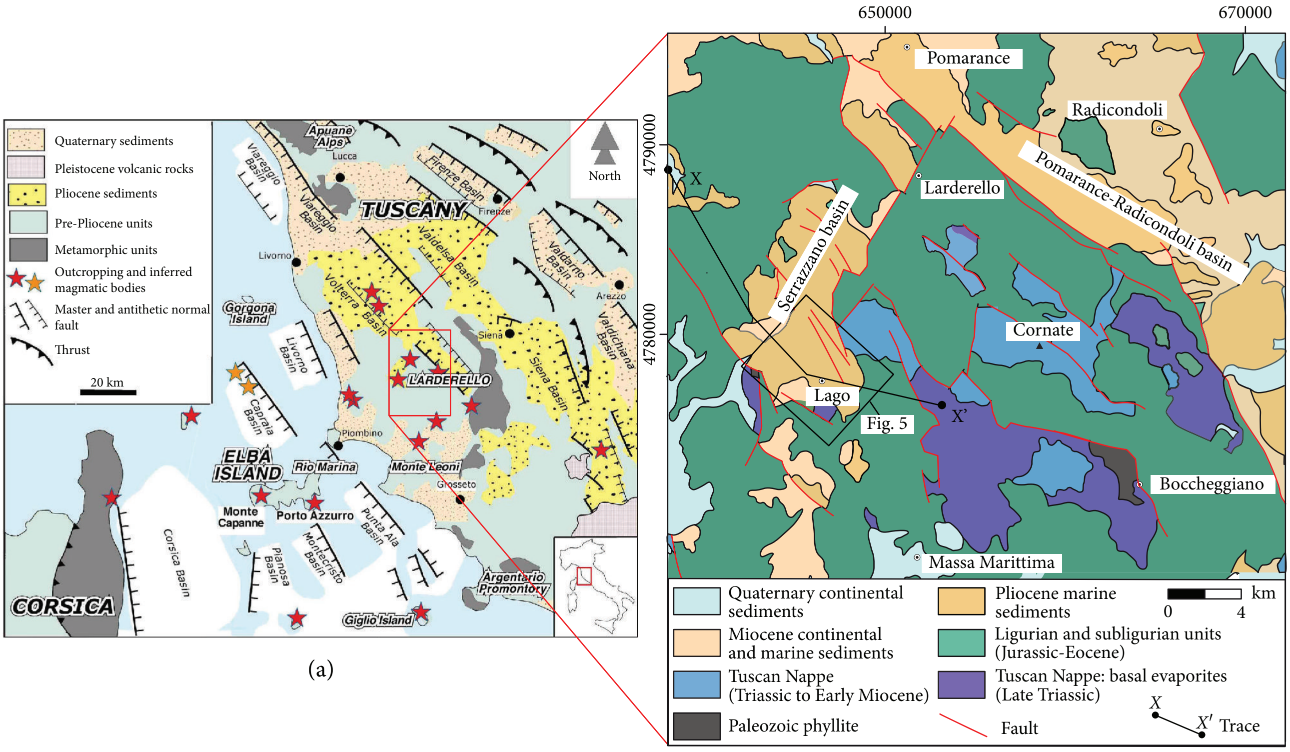

FIGURE 1: (a) Structural sketch map at a regional scale of the Northern Tyrrhenian Sea and Tuscany (modified after [77]). The main structural features and the related Pliocene-Quaternary basins are shown. The red polygon defines the study area. (b) Simplified geological map of the Larderello geothermal area (modified after [18]). The geographic coordinate system used is WGS84-UTM32N; EPSG code: 32632.

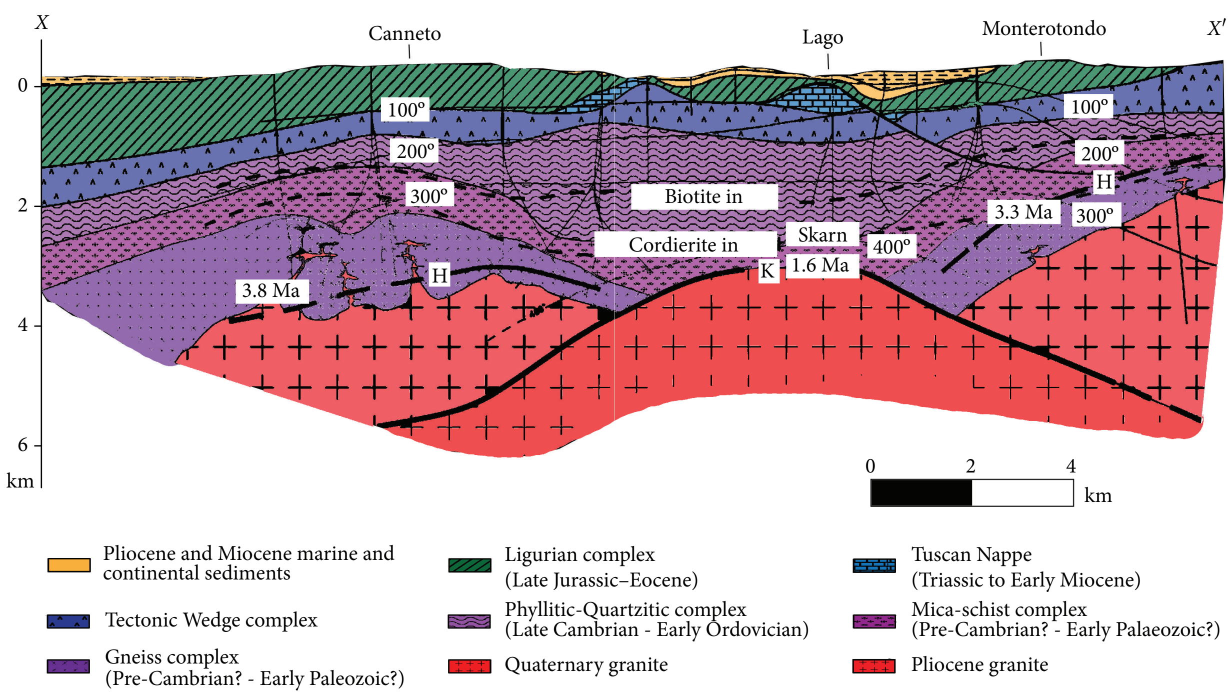

FIGURE 2: Geological cross section of the study area (see the X-X' trace in Figure 1 for the location) (modified after [10]). The contact metamorphic isograde, main seismic horizons (H and K), isotherms, and radiometric ages are reported. Note that this illustration represents one of the various geological frameworks proposed for the study area. Table 1 mentions the proposed alternative interpretations of the K-horizon.

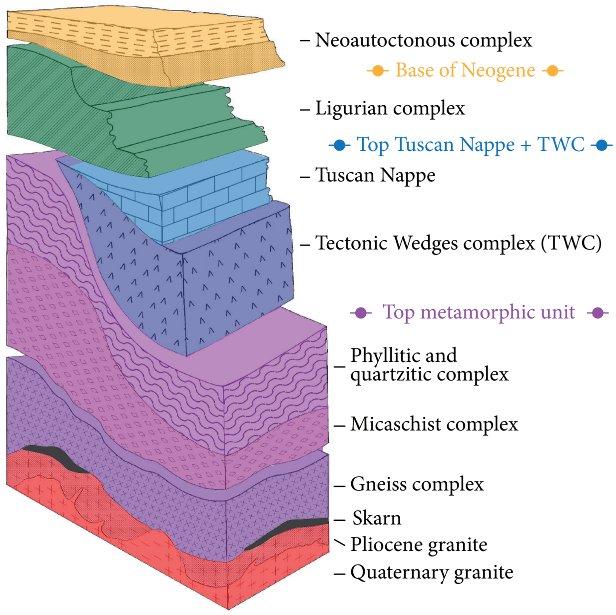

FIGURE 3: Conceptual sketch of the tectonic and stratigraphic setting of the Larderello area (modified after [10]). The surfaces modelled in the present work are the topographic surface, the Base of Neogene deposits, the top of the Tuscan Nappe plus the TWC, and the top of the Metamorphic unit. The surface representing the seismic K-horizon, not shown here, was extrapolated from the literature [11].

unit. The TWC is formed by Paleozoic metamorphic rocks, Triassic metasiliciclastics and carbonates, and Upper Triassic evaporites of the Tuscan Nappe [10, 39, 40]. The Metamorphic Unit is composed of three main complexes [10]: (i) the Phyllitic complex made up above all mainly by metagreywacke (Cambrian-Devonian in age) and locally by carbonate–siliciclastic metasediments (Silurian-Devonian in age), (ii) the Mica-schist complex (Precambrian?-Early Paleozoic? in age), and (iii) the Gneiss complex (Precambrian?-Early Paleozoic?).

With regards to the intrusive complex, granites have been cored in several deep wells and range in age from 3.8 to 1.3 Ma [45]. Accordingly, some interpretations of the deep structure of the Larderello geothermal field propose the presence of very large batholites (e.g., [10, 11, 46]), and data suggest a still active magmatic emplacement with a partial melt occurring at depth of a few kilometers (e.g., [12] and references therein).

3. Geothermal Characterization

Larderello is a small town located in Tuscany (Italy) along the metalliferous hills, which is an important mining and industrial area (Figure 1). Geothermal electricity production began in the early 1900s. Superheated steams at Larderello and surrounding areas feed an installed capacity of 795 MWe [47]. The fields of Larderello, Travale, and Radicondoli belong to a unique deep system that covers an area of about 400 km^2 [9].

Two reservoirs are used for power production. The shallow reservoir is hosted in sedimentary units and consists mostly of Mesozoic limestones and anhydrite dolostone. The deep reservoir is hosted in crystalline rocks, with temperatures exceeding 350°C [11, 48, 49] and consists of phyllite, mica-schist, gneiss, skarn, hornfelses, and granite.

Larderello is classified as a "convective intrusive geothermal play" [50], due to the presence of a plutonic heat source that feeds a wide hydrothermal system.

Geological and geophysical data and thermal numerical modelling support the hypothesis of still molten igneous intrusions ([12, 51–57] and references therein), which represent the heat source of the geothermal system.

The study area is centred on the Lago Boracifero sector in the south-easternmost part of the field (Figure 1). Recently, research has been carried out to improve, through data integration and a multidisciplinary approach, the conceptual model of the Larderello geothermal area [12–29, 31–58]. New drilling technologies have also been tested to explore deep resources at supercritical (very high temperatures and pressures) conditions, by deepening an existing dry well (Venelle 2) [24–29, 31–59].

3.1. K-Horizon. 2D and recent 3D seismic surveys have clearly detected two important seismic reflectors in the deep Larderello reservoir [13, 14, 16, 60]: (i) the H-horizon and (ii) the K-horizon (Figures 2 and 4).

The H-horizon is a discontinuous high-amplitude reflector and represents the current mining target, corresponding to highly productive intervals [10]. The K-horizon is a high-amplitude and locally bright-spot-type reflector, deeper and slightly more continuous than the H-horizon (e.g., [13, 54, 61]). In some areas, the K-horizon represents the upper boundary of a zone characterized by seismic reflectors with a lozenge-shape geometry [14, 15]. Although numerous wells have been drilled in the Larderello geothermal field (Figure 5 and Table S1 show wells used in the study area for this work), the K-horizon has never been reached and in the literature, its reconstruction derives mainly from seismic line interpretations [11, 16, 84, 86]. In 1982, the San Pompeo 2 geothermal well was drilled down to the proximity of the K-horizon, which in this area reaches its regional culmination at a depth of about 3-4 km (Figure 2). The sudden increase in temperature and unexpected blowout of the well prevented direct measurements at the bottom hole, but the temperature of >400°C and pressure of >24 MPa were extrapolated to the depth of 2930 m [22].

The origin and nature of the K-horizon are thus still highly debated in the literature and represent a key to a comprehensive understanding of the Larderello system. The models proposed in the literature to explain the nature of the K-horizon (Table 1) mostly imply the presence of fluids and a correlation with the 450°C ± 50 isotherm (from [62]).

Firstly, [14, 15, 62] interpreted the K-horizon as a brittle-ductile transition (BDT), relating the high-amplitude reflection to the fluids stored in the proximity of this interface. The authors included the activity of an extensional shear zone along the K-horizon in their interpretation, considering the reflector as a kinematically active rheological boundary. [18] also considered the role of listric shear zones as pathways for fluid migration from the K-horizon, thereby

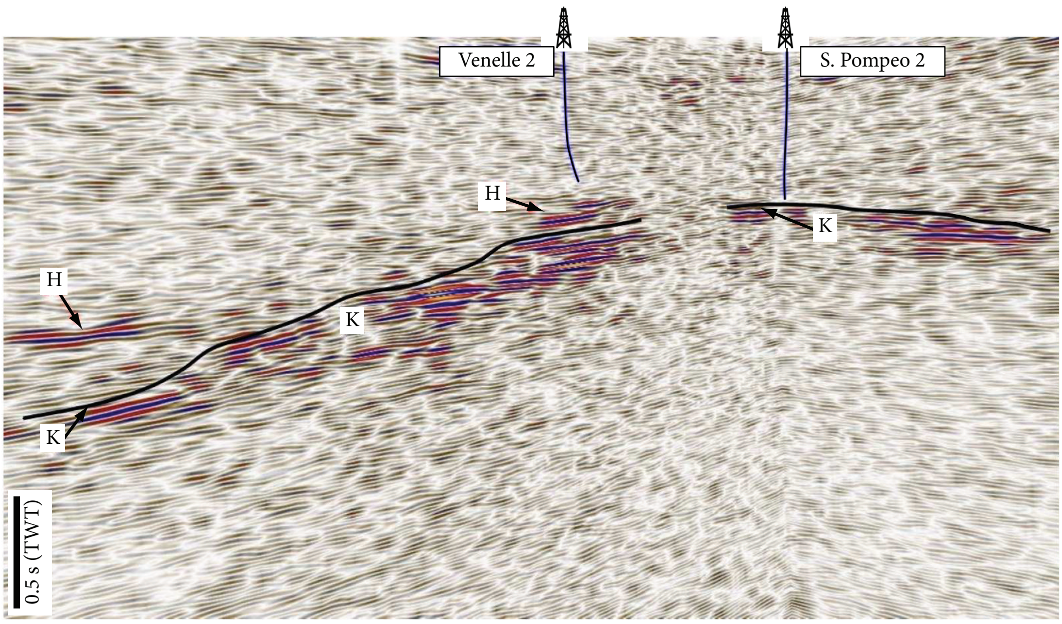

Figure 4: A reflection seismic section from the literature (modified after [16]). This figure shows the two deep seismic markers, the H-horizon and K-horizon. The K-horizon upper boundary is shown in black.

explaining the discontinuity of the reflector (local reduction of reflectivity).

Similar rheological variations with completely different tectonic implications were accounted in the interpretation of the K-horizon. For example, [19] related the horizon to a main lithospheric thrust.

A further contribution to the nature of the seismic reflector was made by [17], who also considered the volumetric thermal expansion of quartz, which is more abundant than the other minerals in the basement rock, during its α-β phase transitions. The K-horizon is presumed to be a layer of microfractured rocks roughly following the α-β quartz transition temperature which in this area is particularly shallow.

A different model was proposed by [10] who considered the K-horizon as the top of a young Quaternary granitic intrusion at the level of a thermometamorphic aureole hosting supercritical fluids.

Vanorio et al. and De Matteis et al. [20, 21] carried out a detailed analysis of various seismic parameters highlighting the occurrence of fluids at the level of the K-horizon which was attributed to natural hydrofracturing. In addition, the authors disregarded the role of BDT of the reflector and accounted for lithological or petrophysical changes immediately below the horizon.

Tinivella at al. [72] associated the high reflectivities of the K-horizon to warm fluid at overpressure conditions rising from below.

The well that has most closely approached the K-horizon is Venelle 2, which was redrilled and deepened in 2017 within the framework of the DESCRAMBLE project (see [24–29, 31–59]). This well reached a depth of 2909 m stopping in the middle of a thick pack of reflectors, and not penetrating the K horizon [16–24]. However, the new data show that the accentuated seismic reflection at a depth of 2750-2800 m corresponds to a zone of increased thermal gradient (up to 0.3°C/m and temperature of about 507-517°C at 2900 m) and of decreased pressure fracturing. Pressure decrease is also associated with an increase in both the gas content in drilling fluids and the rate of penetration during drilling activities [63]. These results suggest that the temperature just below the K-horizon depth could be as high as 600°C, corresponding to the molten phase of granite, and that the observed increase in the thermal gradient may be the manifestation of a transient thermal state induced by the recent emplacement (<50 ka) of a granitic intrusion [24–29, 31–64].

4. Data and Methods

In order to generate the 3D geological-geophysical model of the study area, an integrated approach was used to combine subsurface and superficial data. A synoptic flowchart of the methodological workflow used is shown in Figure S1.

We used well data, published geological information, subsurface geological maps, and a seismic reflection profile [9–11]. The study area (Figure 5) is characterized by numerous deep geothermal wells, and data from 69 of them are available from public databases (Table S1, [65–68, 87]). We carefully revised the original well head coordinates and converted them into our geographical system (i.e., WGS84-UTM32N; EPSG code: 32632). No information regarding their deviation surveys is available, hence all the wells were considered vertical. The stratigraphic data were revised according to the geological units described in Section 2.

The modelled geological units represent seismic units with specific seismic velocities (i.e., Neogene deposits, Ligurian complex, Tuscan Nappe, TWC, and Metamorphic Unit – Figure 3). The Tuscan Nappe and the TWC were treated as a single seismic unit as their seismic velocities are similar to the other geological units.

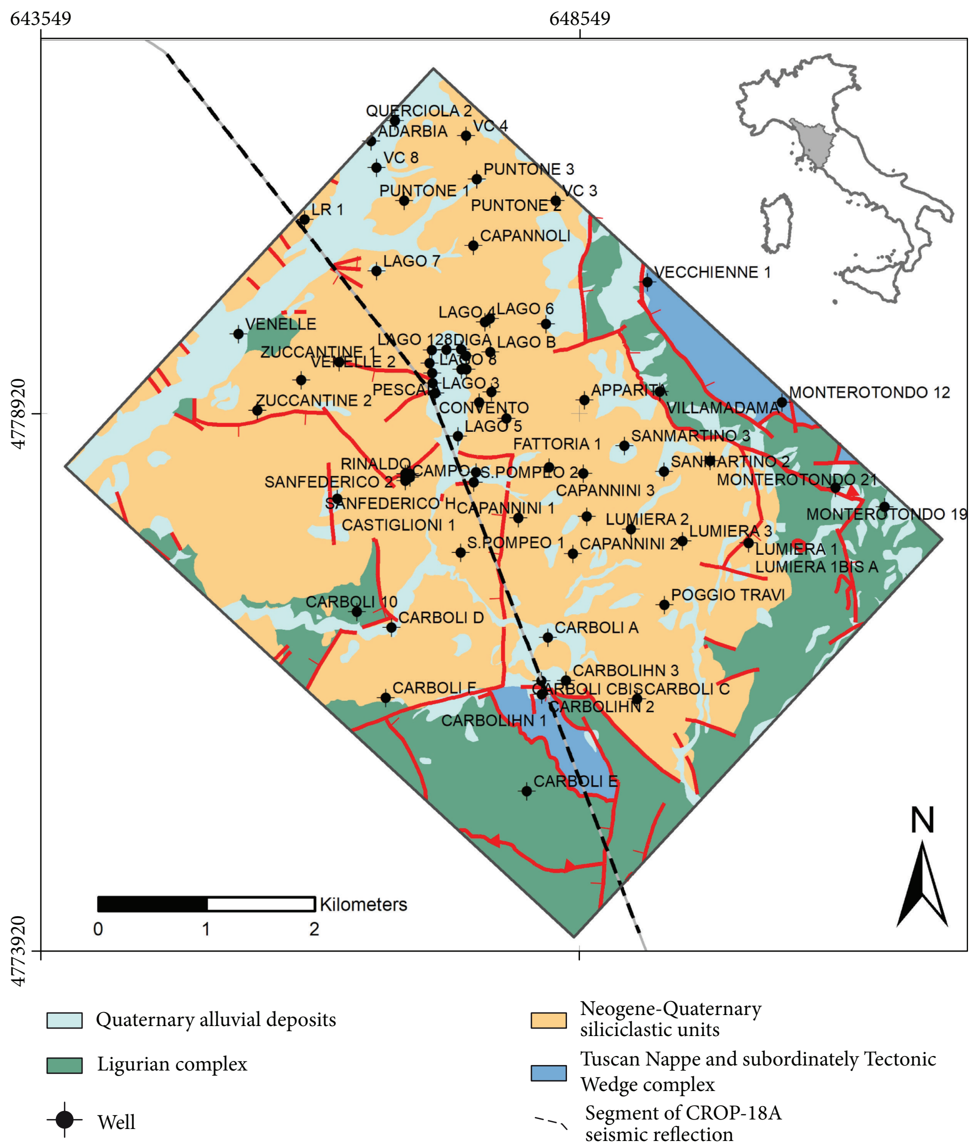

Figure 5: Simplified geological map of the study area (modified from http://www502.regione.toscana.it/geoscopio/geologia.html). The stratigraphic units have been merged to represent the geological units modelled in the present work. The wells used to constrain the geological model are shown. The dotted black line represents the segment of the CROP-18A seismic reflection line (Figure 6(b)) used in synthetic seismic reflection modelling (note in grey the continuation of the CROP-18A).

Table 1: Interpretation models proposed in the literature to explain the evidence of the K-horizon in seismic profiles in the Larderello geothermal system. The corresponding references are quoted.

Interpretation model	Source
Mineral phase transition (quartz α-β)	Marini and Manzella, 2005 [17]
Brittle-ductile transition with tectonic implication in extensional setting	Cameli et al., 1993 and 1998 [14, 15]; Liotta and Ranalli, 1999 [62]; Brogi et al., 2003 [18]
Rheological variation with tectonic implication in compressive setting	Finetti et al., 2001 [19]
Natural hydrofracturing close to lithological or petrophysical changes	Vanorio et al., 2004 [20]; De Matteis et al., 2008 [21]
Thermometamorphic aureole at the top of Quaternary granites	Bertini et al., 2006 [10]
Warm fluids at overpressure conditions	Tinivella et al., 2005 [72]

A digital elevation model (DEM) with a resolution of 20 m (http://www.sinanet.isprambiente.it/it/sia-ispra/download-mais/dem20/view) and a geological map (i.e., http://www502.regione.toscana.it/geoscopio/geologia.html) were used to better constrain the geological surfaces at a shallow level.

The geological map was projected onto the DEM surface and the geological boundary of the outcropping units. The bottom of the Neogene Unit and the top of the Tuscan Nappe plus TWC were digitized to define the emerging limits of the modelled surfaces. The area of the DEM characterized by outcrops of the Tuscan Nappe and TWC were selected and integrated into the input data as they define the emerging portion of the Tuscan Nappe plus TWC surface. In addition, geological subsurface maps [9–11] were georeferenced and digitized to constrain the Metamorphic Unit and the K-horizon at depth.

Although some faults have been interpreted in the area (e.g., [11–18]), they were not modelled in the present work since their geometry is controversial and poorly defined by the available data. Therefore, the geological model represents continuous surfaces, clearly shaped and influenced by the paleogeographic setting and subsequent tectonic processes. However, even if this simplification may have an impact on the geological interpretation of the modelled surfaces, it has exiguous effects on our analysis concerning the seismic imaging of the overburden model and of the K-horizon in their geometry and geophysical parameters (e.g., [88]).

The dataset collected (well data, portion of DEM characterized by outcrops of the modelled units, geological boundaries, and digitized isobath maps) were then imported into the Petrel software (Schlumberger). Well data were integrated with superficial geological data to better constrain the trend of the modelled surfaces at shallow depths (Figure S2). For those geological units with few or no well data (i.e., Metamorphic complex and K-horizon surface), digitized isobath maps were used to better constrain the modelling process (Figure S3). The convergent interpolation method with a grid increment of 200 m in the x- and y-directions was applied to create the surface in Petrel.

The 3D geological-geophysical model was then used to run the synthetic seismic model. Modelled geological data were extrapolated from the 3D geological-geophysical model along a segment of the seismic line CROP-18A (from CDP 629 to CDP 941). The CROP-18A seismic reflection line (hereafter CROP-18A) is a seismic line acquired within the framework of the CROP project (Italian deep crust seismic project; [25]) available both in raw and processed stacked data versions, within the seismic database of the CROP consortium (http://www.crop.cnr.it). CROP-18A was acquired using dynamite sources spaced about 180 m apart and by means of a geophone cable with group spacing of 60 m (an asymmetric split-spread geometry with offsets −3780 m and 7620 m) and a gap of 150 m obtaining 3200% coverage. The sampling time and record length were 2 ms and 25 s, respectively. The stacked data section of the line (Figure 6(a)) was obtained using standard processing.

The modelled geological surfaces were sampled along the CDPs of the CROP-18A. The collected points were subsequently interpolated with a bicubic spline, with 15 m of horizontal spacing.

To create the synthetic seismic section (Figure S1), a velocity model was imposed on the studied section by assigning to each pixel (15 × 15 m) the P velocities (constant velocity) adopted for the corresponding geological unit (Table 2) in the model calibration (see Section 5.3). A Gaussian velocity perturbation was adopted to explore an alternative hypothesis based on the physical rock-model for the K-horizon (see Section 5.4).

The synthetic seismic stack sections of CROP-18A were generated using the exploding reflector seismoacoustic approach [69] which was developed in Matlab by the CREWES consortium [85] and was partly modified by us in this application. In detail, we interfaced the "afd_explode.m" script function of CREWES [85] with a main script which allowed the construction and/or the changes of the input velocity matrix deriving from the 3D geological-geophysical model. The wave modelling parameters were then set. Matlab scripts were developed to assess the difference between the synthetic outputs and the data and to manage the model and synthetic output renderings.

The exploding reflector approach provides a rapid calculation of the zero-offset synthetic stacked sections and helped us to calibrate and validate several geological and geophysical interpretative hypotheses regarding the geothermal reservoir model of the Larderello area.

With this approach, the zero-offset synthetic stacked section is obtained by locating the sources along all reflecting interfaces of the model and the receivers on the common mid points (CMPs). The exploding reflector section is almost equivalent to the zero-offset stacked section obtainable by standard CMP seismic processing in reproducing seismic wavefields not only by travel times but also by amplitudes.

In the present study, the positions of receivers were located at the CMP positions of the line between the CMPs 629 and 941, which were spaced 30 m apart, and a time window of up to 4 s of TWT was set (Figure 6(b)). The exploding reflector approach generates the seismograms for the P-wave velocity model obtained from the section studied.

The wavefield is propagated upward in depth using a finite difference algorithm and is then convolved with the input wavelet (Ricker wavelet with 25 Hz of central frequency) to produce the seismogram at the receiver.

The central frequency was selected through a spectral analysis on the raw data of the CROP-18A stacked section (Figure 7).

Figure 7 shows the results of two mean spectra calculated along the traces corresponding to shots of the studied segment of the CROP-18A (Figure 6). The first mean spectrum (continuous line in Figure 7) was obtained considering all the traces (i.e., 8064). For the second spectrum (dotted line in Figure 7), an offset selection (i.e., between 2000 m and 7770 m) was made to evaluate the signal spectral content for offsets characterized by clear deep reflected events in the shot gathers. In the calculation of both spectra, a time window of 5 s was used for each trace.

Both spectra showed a dominant peak at about 15 Hz. The estimated central frequencies for the two mean spectra were 28 ± 3 Hz for the mean spectrum of all traces and 25 ± 3 Hz for the mean spectrum of selected traces. These were calculated using $\sum_i (f_i{}^* A_i)/\sum_i (A_i)$, where (f_i, A_i) is the $i-$th spectral point.

Although the two central frequencies and their related errors are quite similar, we chose 25 Hz as it is directly related to the signal propagated in deep structures.

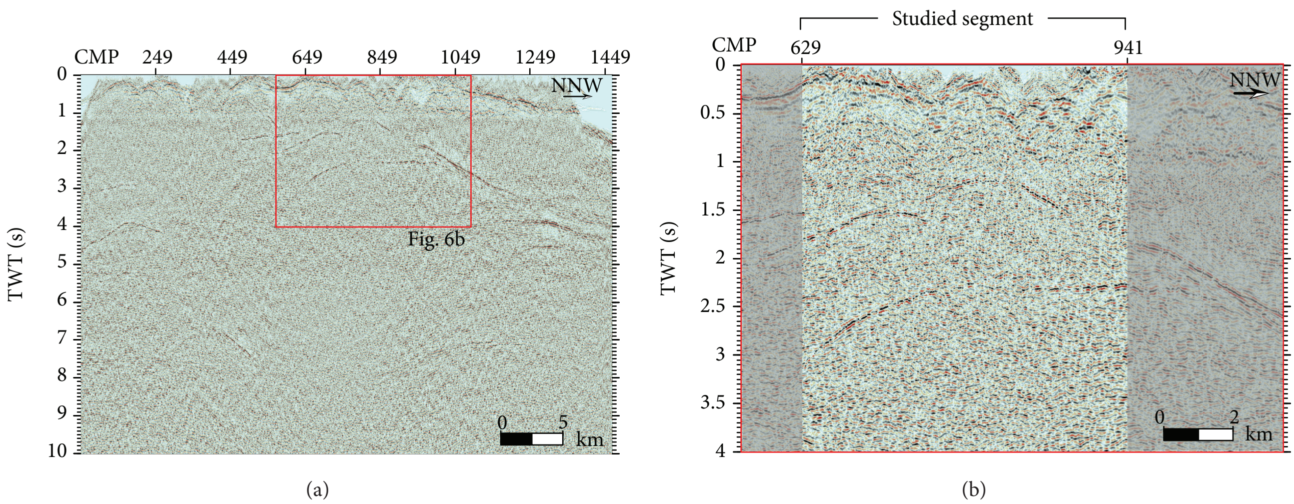

Figure 6: (a) CROP-18A stacked section. (b) Zoom of the CROP-18A stacked section of Figure 6(a). Stacked data in the CMP range from 629 to 941 were compared with the synthetic stacked sections. The trace of the studied segment of the CROP-18A section is reported in Figure 5.

Table 2: Interval velocities applied for the modelled units and their ranges from literature data. Interval velocity of the geological unit below the K-horizon represents a major issue for the seismic exploration in the Larderello area, and it depends on the geological-geophysical interpretative hypotheses assigned to the K-horizon itself (see text for details).

Layer	V. Int. (m/s)	V. Int. range (m/s)	Source
Neogene deposits	2700	2600-2800	Batini et al., 1978 [13]
Ligurian Flysch complex	3850	3000-4700	Batini et al., 1978 [13]
Tuscan units and TWC	5700	4000-6500 *3	Batini et al., 1978 and 1995 [13, 76]; Brogi et al., 2003 [18]
Metamorphic unit	5150	4400-5500	*1
Unit below the K-horizon	4400/5900	4300-6400	*2

*1 Batini et al., 1978 and 1995 [13, 76]; Bertani et al., 2005 [9]; Brogi et al., 2003 [18]; Rabbel et al., 2017 [6]. *2 Batini et al., 1995 and 2002 [70, 76]; Vanorio et al., 2004 [20]; Tinivella et al., 2005 [72]; Aleardi and Mazzotti, 2014 [73]; Rabbel et al., 2017 [6]. *3 In Brogi et al., 2003 [18], the Tuscan Nappe is divided in two subunits which are the TN 2 (Early Miocene-Rhetic sequence) and the TN 1 (Late Triassic evaporites) with 4000-4500 m/s and 5000-6500 m/s of P-wave interval velocity, respectively.

The finite difference algorithm uses a nine-point approximation of the Laplacian operator and assumes the absorbing boundaries on the three sides of the model (bottom, right, and left). Time step modelling was set to 0.1 ms, and the Courant maximum number was ~0.2. The synthetic waveforms were sampled at 2 ms, similar to CROP-18A data.

Finally, our approach is essentially a kinematic calibration (fit of the 0-offset reflected arrival times) with the support of the quali-quantitative comparison of the complete wavefields.

To perform the calibration of the reconstructed 2D model along the CROP-18A, we then compared the main seismic horizons generated in the synthetic stacked sections processed for different models with the stacked data section along the line.

5. Results and Discussion

5.1. 3D Geological-Geophysical Model. The topography, the base of the Neogene deposits, the top of the Tuscan Nappe plus TWC, the top of the Metamorphic Unit, and the K-horizon were modelled (Figure 8). Through these surfaces, it has been possible to define the major geological units of the study area characterized by specific seismic velocities and hence potentially discernible along seismic sections.

The Neogene Unit and the Ligurian complex are not always present in the model (Figure 8). In particular, the Neogene Unit is not present in the south-eastern portion of the model which is characterized by outcrops of the Ligurian complex and the Tuscan Nappe plus the TWC (Figure 8). The Tuscan Nappe plus TWC is always present in the study area, and the top of this unit is well constrained by the wells available in the area. The Metamorphic Unit is located beneath the Tuscan Nappe plus TWC and at the bottom is confined by the K-horizon. The K-horizon was modelled on the basis of a published isobath map [11]. The modelled interfaces separating the main geological units were then extracted from the 3D geological-geophysical model along the studied segment of the seismic line CROP-18A (from CDP 629 to CDP 941) and subsequently converted into a time-domain geological-geophysical model.

5.2. Velocity Model. The geological units defined for the velocity model were the Neogene deposits, the Ligurian complex, the Tuscan Nappe plus TWC, the Metamorphic Unit, and the geological unit below the K-horizon. The velocity ranges defined for the aforementioned units derive from previous literature data and are reported in Table 2. Attributing

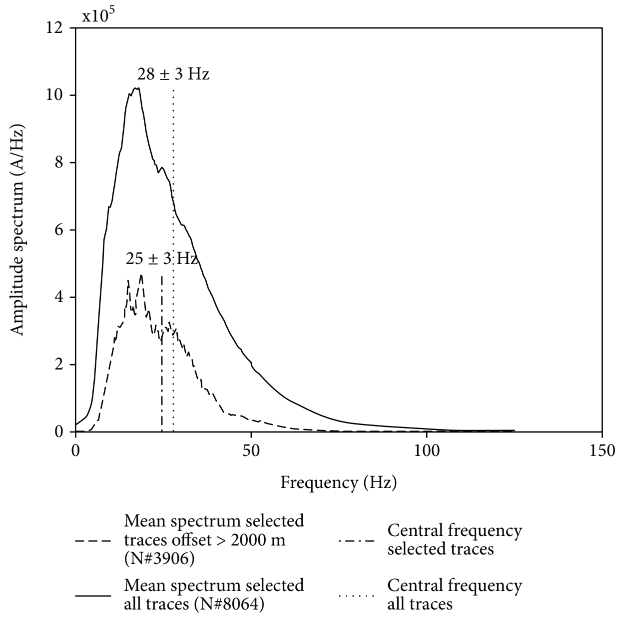

Figure 7: Raw data spectral analysis and central frequency estimate: mean spectrum on all traces (continuous line) and mean spectrum of selected trace with offsets greater than 2000 m (dashed line). Vertical lines indicate the central frequency value.

a P-wave velocity for geological units may be difficult and generally has a range of values.

In order to obtain the seismic velocity model along the studied segment of the CROP-18A (from CMP 629 to CMP 941) a constant P-wave velocity (Vp) was assigned to each unit (Table 2). For the Neogene Unit and the Ligurian complex, we chose the arithmetic average of the interval velocities (i.e., 2700 m/s and 3850 m/s, respectively) commonly adopted in the literature [13–18].

For the Tuscan Nappe plus the TWC, we adopted an interval velocity of 5700 m/s. This value, which is within the velocity ranges described in the literature (Table 2), was defined after a careful analysis of the data and taking into consideration the wide range of P-wave velocities reported in the literature (e.g., [13, 18, 76]) deriving from the considerable heterogeneity of these geological formations.

For the Metamorphic Unit, we adopted a velocity value of 5150 m/s, which is within the velocity range (i.e., 4400-5500 m/s) suggested by several authors (e.g., [6, 9, 13, 18, 76]). This velocity value was defined after analyzing the data observed in the Vp logs and in laboratory measurements of unfractured rocks from the Mica-schist complex and Gneiss complex in the depth range 1000-3500 m, as reported in the literature and summarized as follows [6, 71–75].

Seismic reflectivity modelling of the deepest reflective horizons within the metamorphic units based on VSP measurement, logs, and AVO/AVA seismic analysis highlight that reservoir rocks are made up of fractured layers, with a variable thickness from one meter to tens of meters, showing a velocity variation of up to 15-30% with respect to the average velocity value of reservoir rocks [71, 72].

Vp logs of the Larderello-Travale area, at a depth of between 2400 to 3800 m, indicate a general negative asymmetric distribution around 20-30% of the Vp velocities with respect to a reference Vp value (5000-6000 m/s [73]). Furthermore, data logs indicate that the productive levels at the log scale are characterized by more complex velocity structures at short wavelengths (few meters) not resolvable with surface seismic. This means that the fractured layers are probably about 20 m thick with a velocity variation of up to about 5-10% [73]. The Vp laboratory measurements on core samples of the metamorphic unit (i.e., Mica-schist and the Gneiss complexes) of the Larderello area in a depth range of 1000-3800 m indicate a Vp anisotropy (differences in velocity in the vertical and horizontal directions of the core axis) of about 15% for pressures >40 MPa. In particular, for the core sample of the San Pompeo 2 well (2718.1 m), the Vp velocities in the vertical and horizontal directions are 5117 m/s and 5866 m/s, respectively [6, 74, 75]. Furthermore, the laboratory measurements [75] show that the linear-asymptotic trend, corresponding to fracture closure, in the pressure-velocity diagrams generally begins in the pressure range 100-150 MPa, and that Vp value variations of 15-20% and an anisotropy percentage of up to about 30% are observed in the pressure range 15-150 MPa. In addition, [74] report that both water-steam transition in the pore and high-temperature values produce only small changes in Vp measurements. They suggest that any major decreases in velocity could be associated with phase changes in fractures and fracture zones.

Due to its geological-geophysical complexity, the assignment of a P-wave velocity value for the K-horizon and for the unit below the K-horizon is even more complex than for the other units. In fact, it depends on the geological-geophysical hypotheses of the K-horizon itself. In order to reduce this complexity, there are two feasible hypotheses: (i) a sharp discontinuity which could be related for example to a lithological change or to an abrupt rheological transition and/or (ii) a perturbed layer with probable changes in the physical status of a portion of the geological unit and, therefore, the corresponding differentiation in the mechanical hydro-geophysical properties of rocks (i.e., confining, pore and effective pressures, temperature, porosity, and permeability) and type of inclusions and their petrophysical status (i.e., composition, salinity, and phases). This perturbed layer could be related, for example, to the presence of a thermometamorphic aureole, a mineral phase transition, or a highly fractured zone.

Previous studies, which focused on the processing and interpretation of the CROP-18A data and on the seismic velocity reconstruction from local earthquake tomography, suggest a Vp for the unit below the K-horizon ranging between 4300 m/s and 6400 m/s [6, 20, 21, 23, 61, 70, 72]. In addition to the uncertainties of each interpretation (about 10%), all these studies agree that the unit below the K-horizon should be assigned a high intrinsic variability of the Vp parameter, of up to about 15-40%, with respect to the Vp mean value adopted.

5.3. Model Calibration and K-Horizon Characterization by a Sharp Velocity Discontinuity. The geological-geophysical model along the CROP-18A seismic line was calibrated by

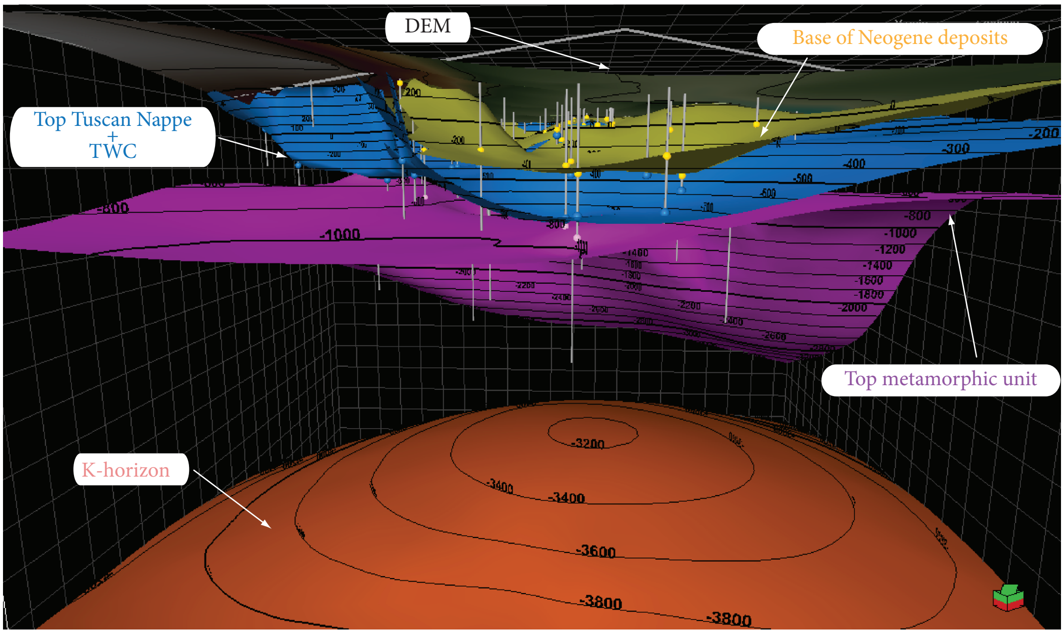

Figure 8: Stratigraphic surfaces modelled with Petrel (Schlumberger). Well data and geological maps have been used to constrain the surfaces at depth.

superimposing the synthetic stacked sections on the seismic data stack for all the reflected events.

In order to simulate the reflection event corresponding to the K-horizon, a velocity contrast should be assigned to the unit below the K-horizon with respect to the upper Metamorphic unit. On the basis of the information discussed in Section 5.2 and on the hypotheses on the nature of the K-horizon and deep unit, we assigned a Vp of 4400 m/s and 5900 m/s to the unit below the K-horizon. These Vp values are close to the end members assumed for the units below the K-horizon [6, 20, 70, 72, 73] which correspond to a contrast of ±15% with respect to the Vp of the upper metamorphic unit.

In order to evaluate which of the two values should be used, we simulated the stacked sections for both models and velocities, and then we compared the seismic features (arrivals and polarities) of the reflection K-horizon with those observed in the data stacked section (8 and 9).

Figure 9 shows the starting velocity model (named model 1) obtained from the 3D geological-geophysical reconstruction. Here, the K-horizon interface was modelled with the smooth anticlinal shape proposed by [11]. Figure 10 shows the calibrated velocity model (named model 2) where the geometry of the K-horizon was modified to produce a better fit of synthetic stacked sections with respect to the section observed.

Figures 9 and 10 report the velocity models (on top - a and b), the synthetic seismic responses (on the bottom - a$'$ and b$'$) for the two hypotheses on the P-wave velocity below the K-horizon, namely, 4400 m/s (a and a$'$ on the left) and 5900 m/s (b and b$'$, on the right). The synthetic response (in red variable area) is superimposed onto the stacked data (in grey wiggle and variable area) in order to compare the two zero-offset sections directly. This representation, in which the same plot parameters and trace normalization are used, enabled us to directly compare both data and synthetic responses in time domain and in relative normalized amplitudes.

The synthetic seismic responses indicate that model 2 is comparable with the seismic line drawing of all the main seismic reflection events detectable on the stacked CROP-18A line (Figure 10). For the K-horizon, the best seismic response of model 2 (Figure 10) was obtained by introducing a change in its original geometry as reconstructed in the 3D geological-geophysical model and reported in model 1 (Figure 9), consisting of a bulge-like structure located below the S. Pompeo 2 well area. In this area, the minimum depths of K-horizon for model 1 and model 2 are 3270 m and 2640 m, respectively.

The trace time lags obtained with trace cross-correlations between the data and synthetics signals calculated for the two velocities, in a window of 200 ms TWT including the K-event, have mean values of 5 ms and 18 ms and standard deviations of 40 ms and 73 ms, for 5900 m/s and 4400 m/s, respectively (Figure 10). The 5900 m/s simulation is characterized by the best fit with data and has a mean time lag comparable to the data sampling time of 4 ms. It reproduces the diffractions in the primary reflection between 1.2 s and 2 s TWT and the multiple events (Figure 10). Although this evidence would seem to indicate a positive contrast along the length of the K-horizon in our study area, the discontinuous pattern of the K-reflections means that there may be zones with a negative velocity contrast in other areas of Larderello.

It is interesting to note that the drilling operation for the S. Pompeo 2 well stopped at a depth of about 2767 m due to

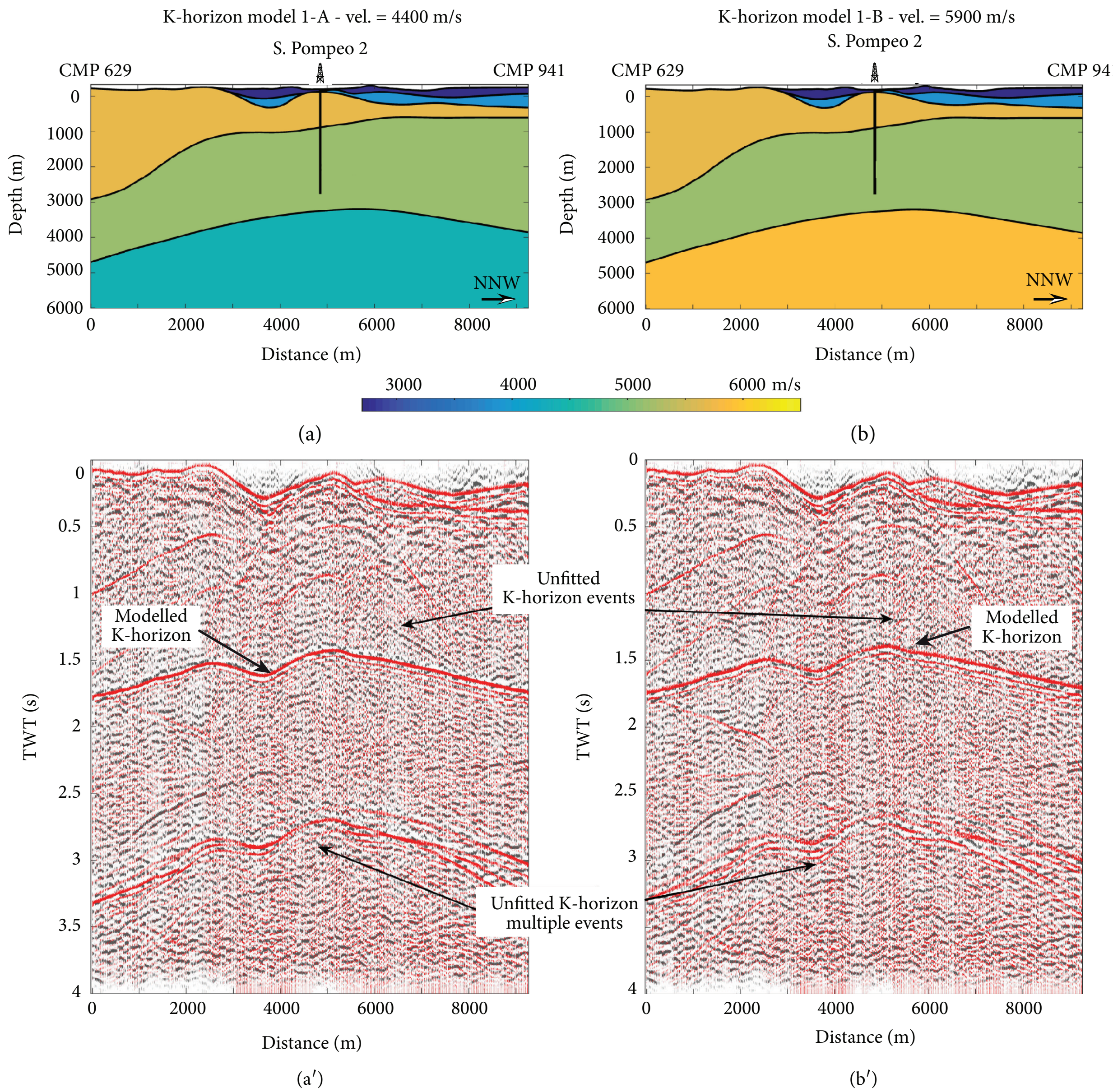

Figure 9: (a) Velocity model, named model 1-A, based on the 3D-geological reconstruction and imposing a velocity value of 4400 m/s for the geological unit below the K-horizon. (b) Velocity model, named model 1-B, based on the 3D-geological reconstruction and imposing a velocity value of 5900 m/s for the geological unit below the K-horizon. (a′) Modelled stacked sections for model 1-A (a) with P velocity of the unit below the K-horizon of 4400 m/s. (b′) Modelled stacked sections for model 1-B (b) with P velocity of the unit below the K-horizon of 5900 m/s. The modelled seismic response, plotted in positive variable area in red, is superimposed onto the processed stacked data, plotted in grey.

overpressure. This depth nearly corresponds to the top of the K-horizon, as modelled in our best fit of model 2.

In addition to the reliability of the reconstructed 3D geological-geophysical model, the results obtained by the seismic modelling indicates that

(a) The seismic response for TWTs higher than 0.5 s is mainly influenced by the geometry of shallow units. This fact should be taken into account by including the effects of the Neogene deposits and/or the Ligurian complex in the static evaluation in order to optimize the seismic processing and the K-event focusing

(b) Due to migration effects, the shape of the modelled K-horizon event in the distance range 2500-7500 m of the unmigrated seismic sections mainly depends on the geometry of the K-horizon in the model distance range of 4400-6700 m. The K-horizon in model 2 is characterized by a slightly more complex geometry than the reconstructed smoothed K-horizon of model 1 and introduces a more complex pattern of the K-related events into the time domain with unmigrated diffracted and multiple events also below the K-horizon. This pattern is in line with observations in the data stacked section. Consequently, when

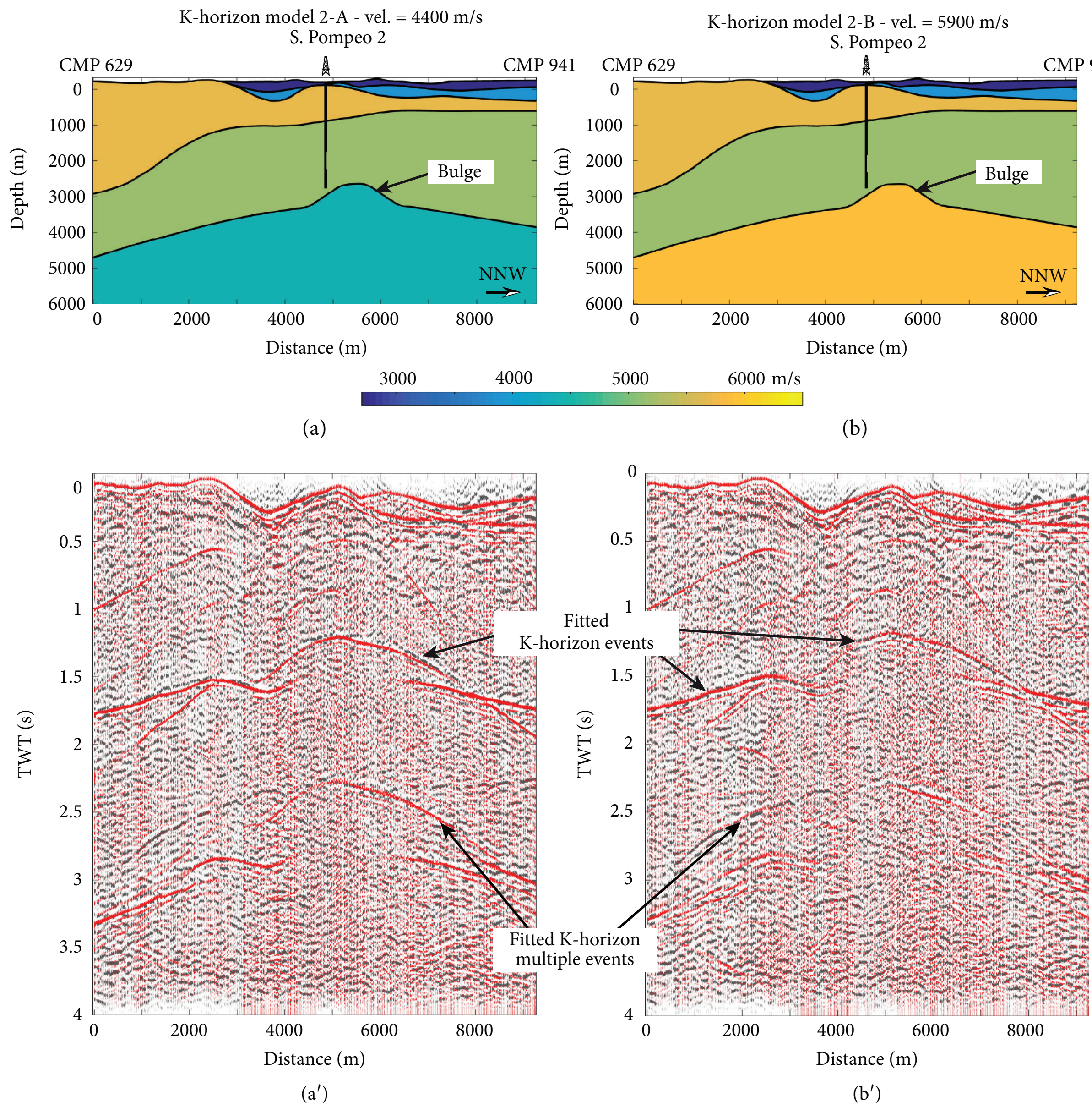

FIGURE 10: (a) Velocity model, named model 2-A, based on the 3D geological reconstruction obtained after the calibration with CROP-18A data and imposing a velocity value of 4400 m/s for the geological unit below the K-horizon. (b) Velocity model, named model 2-B, based on the 3D geological reconstruction after the calibration with CROP-18A data and imposing a velocity value of 5900 m/s for the geological unit below the K-horizon. (a′) Modelled stacked sections for model 2-A (a) with P velocity of the unit below the K-horizon of 4400 m/s. (b′) Modelled stacked sections for model 2-B (b) with P velocity of the unit below the K-horizon of 5900 m/s. The modelled seismic response, plotted in positive variable area in red, is superimposed onto the processed stacked data, plotted in grey.

interpreting unmigrated K-events in the seismic section, there is a risk of assigning structural and physical meaning to nonexistent structures.

Figure 11 shows the time-migrated section using the calibrated model 2 and a Vp value of 5900 m/s below the K-horizon. The migrated section shows a clear improvement in the event focusing and a reduction in the diffracted events demonstrating the reliability of the calibrated model. In this context, we underline the high focusing of the edge-like structure between the CMPs 749 and 849 and the two events bordering the edge structure and dipping southward and northward. In particular, the northward dipping reflectors (right side of Figure 11) seem to continue upward to the surface at about CMP 700 and border the shallow basin structure located between the CMPs 700 and 820 (2500-4700 m of distance in the model, Figure 10). The migrated section shows, at a TWT greater than 2000 ms and below the edge structure, a diffuse reflectivity, and some events have an extension variable between several hundred meters to about 3 km (e.g., the event at 2250 ms to the right end of the studied segment).

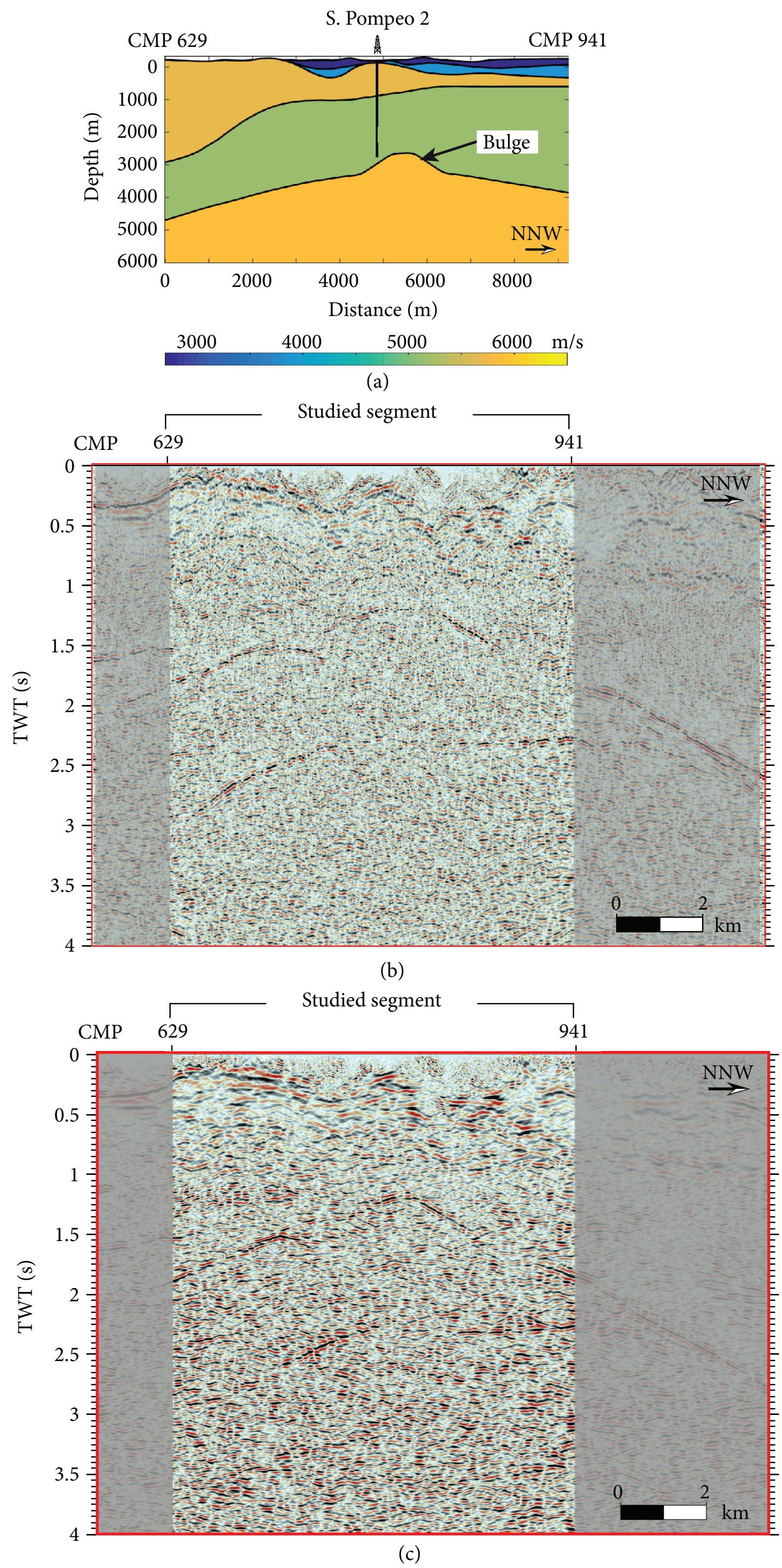

Figure 11: (a) Velocity model, named model 2-B (see Figure 10(b)). (b) Studied segment of the CROP-18A stacked section (see Figure 6(b)). (c) The figure shows the time-migrated section of the CROP-18A data, reported in Figure 11(b), obtained through the calibrated velocity model shown in Figure 11(a). The time migrated section improves event focusing and reduces diffracted events. Note the high focusing of the bulge-like structure between CMPs 749 and 849 and the two events bordering the bulge structure and dipping southward and northward.

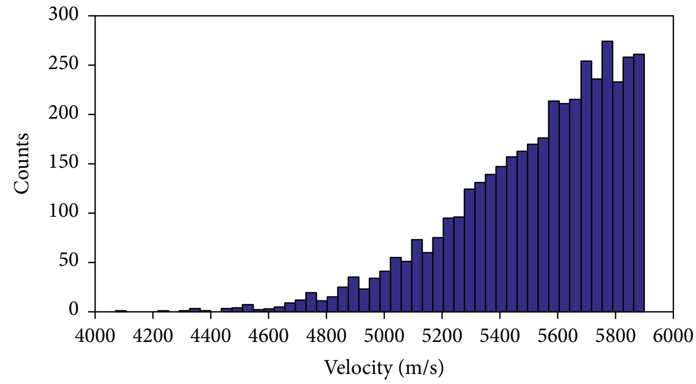

Figure 12: The velocity distribution applied considering a physical perturbed layer (PPL) 100 m in thickness.

5.4. K-Horizon Alternative Hypotheses and Modelling: Physically Perturbed Layer. The results of our model calibration and line migration, and the processing and analyses of several seismic lines in the Tuscan geothermal area reported in the literature, highlight that the geological models and the related migration velocity models (above all for the deepest reflectors like H- or K-horizon) need to be more detailed in order to correctly migrate the reflectivity features observed in the area (i.e., [4, 6, 61]). In fact, the K-horizon exhibits some very particular reflective seismic features. It shows a lateral variation of reflectivity, and it is occasionally characterized by a bright spot signature. Also, instead of single reflection events, it shows a diffuse reflectivity spatially and vertically localized (generally extended 2-5 km in space, and 100-500 ms TWT in time) sometimes with a "lozenge" pattern below the top of the diffused reflective events [14, 15].

An alternative hypothesis is that the K-horizon is associated with a physically perturbed layer, as already claimed by [4]. This hypothesis is supported by the geological evidence derived from some outcrops on Elba, which are the remnants of an ancient and exhumed geothermal system considered representative of the deepest structural level of the Tuscan geothermal system, corresponding to the current level of the seismic K-horizon [77]. The results of geological studies carried out on the Elba outcrops suggest that the K-horizon is characterized by a permeability in the range 10^{-9} and 10^{-18} m^2 and by fluid circulation. This fluid circulation has been inferred from the fluid inclusions of Elba, which reveal two main stages or groups of fluids: (a) hypersaline multiphase fluids (29-49 wt.% NaCl eq.) of lower temperature (<400°C) and (b) saline two-phase fluids (16-29 wt.% NaCl eq.) of a higher temperature (up to 600°C) [77].

Following this hypothesis, we modelled the K-horizon as a zone formed by a physically perturbed layer (PPL) characterized by a randomized P-wave velocity distribution. In our modelling hypothesis, the geological and physical properties inherent in the rock composition, density and shape of cracks, fluid characteristics, saturation conditions, and temperature and pressure conditions are reflected in the variations of velocity.

The high pore pressure in the region of a single fluid-filled pore helps to explain the resulting changes in the effective density and seismic velocities. Increased pressure within a pore tends to force the surrounding rock grains apart, thus tending to increase the pore volume. Effective density is a combination of the densities of the rock and fluid constituents of the porous medium. An increase in porosity results in a decrease in the effective density of the porous medium, as the rock is generally denser than fluid. A decrease in effective density tends to cause an increase in S-wave velocity. The effect of increased pore pressure on P-wave velocity can be seen by considering Wyllie's time-average equation for P-wave velocity in porous, isotropic, fluid-saturated rocks under high pressure [78]. Mavko et al. [79] interpreted Wyllie's equation as follows: the P-wave travel time through a fluid-saturated rock is equal to the sum of the travel time through the rock matrix and the fluid-filled pore.

In our model, we assume that the detection spatial scale of the velocity variations with seismic is comparable with the ¼ seismic wavelength (several ten of meters).

The pixel values (15 × 15 m) of the velocity perturbations inside the layer are assumed to be randomized with an asymmetric Gaussian velocity distributions according the velocity variations observed in data logs, laboratory measurements, and VSP and AVO-AVA analyses.

With an asymmetric distribution (Figure 12), the pixel velocities are set by fixing the highest Vp of the PPL equal to the one used in Section 5.3 for units beneath the K-horizon (i.e., 5900 m/s) and its negative variations are defined by the rock physical model described below.

In order to insert a velocity perturbation that is consistent with a rock physical model, we assume that the confining pressure is equal to the lithostatic charge and that the pore pressure is equal to the hydrostatic charge, and the effective pressure is the difference between them. We assume a temperature of about 400°C and an effective pressure of about 30 MPa, which is in line with those derived from the measurement in the S. Pompeo 2 well [22]. A porosity of 3% and a density of 2700 kg/m^3 were used. Density of 2700 kg/m^3 is the average value for mica-schists according to [89], and very similar values have been used to model Larderello gravity data in [90]. The porosity of 3% is an average value for mica-schist as well, and a close confirmation was found in analogue mica-schist formation at Elba [77].

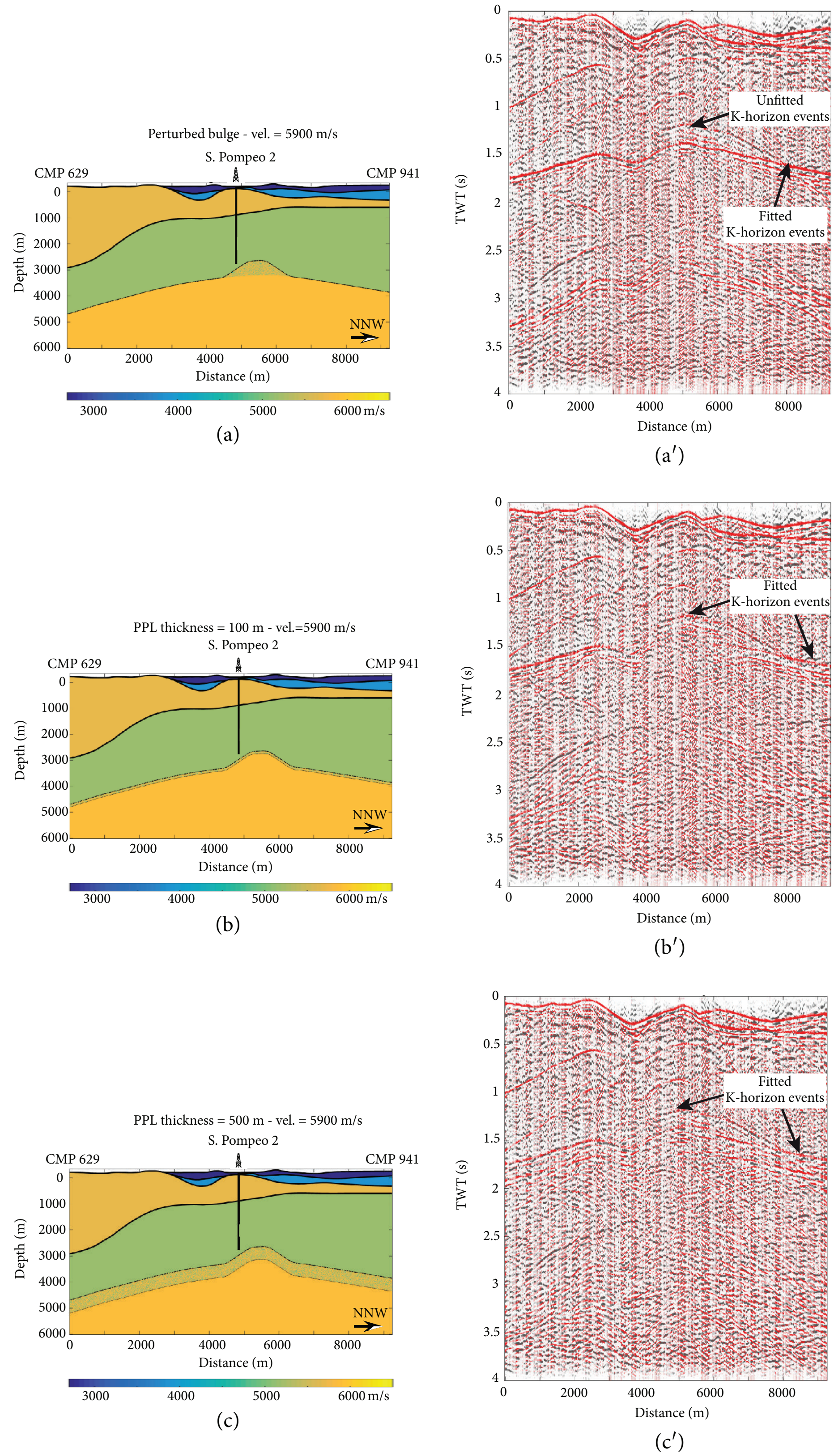

Figure 13: (a) Velocity model similar to the calibrated model in Figure 10 with a perturbed bulge. (b) Velocity model similar to the calibrated model in Figure 10 with a physical perturbed layer (PPL) of 100 m in thickness. (c) Velocity model similar to the calibrated model in Figure 10 with a physical perturbed layer (PPL) of 500 m in thickness. (a′) Modelled stacked section for the velocity model in (a). (b′) Modelled stacked section for the velocity model in (b). (c′) Modelled stacked section for the velocity model in (c). The modelled seismic response, plotted in positive variable area in red, is superimposed onto the processed stacked data, plotted in grey.

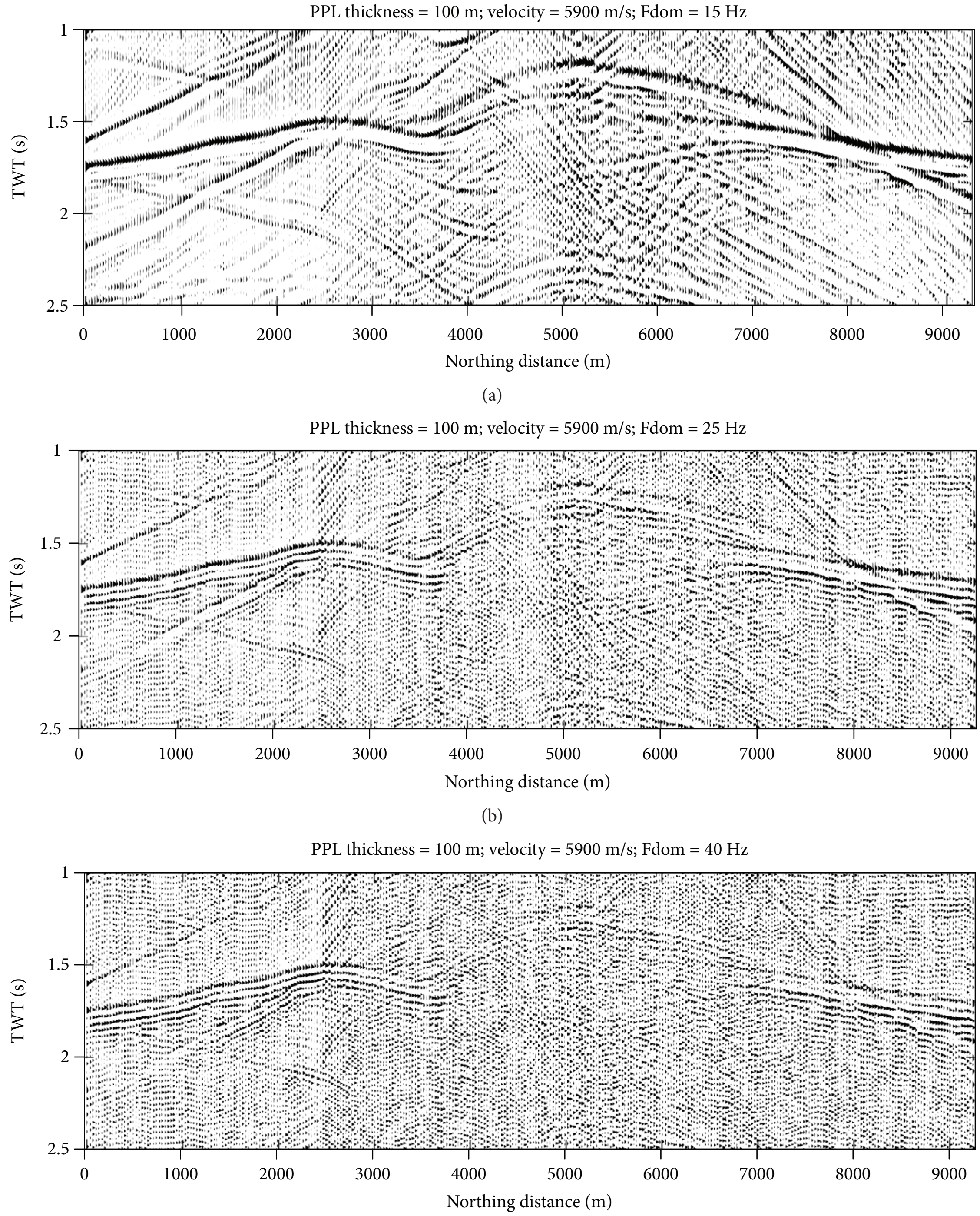

Figure 14: K-horizon synthetic response (100 m PPL model) for three different central frequencies of the source wavelet: (a) 15 Hz, (b) 25 Hz, and (c) 40 Hz.

To calculate the negative velocity variations inside the PPL, we calculated the effective velocities using the scattering theory, considering a prolate (0.02 parameter) penny crack shape that characterizes the fluid inclusions [80]. To simulate the effect of the fluid in the pore and fracture space, we used the values for the velocity and density of brine (1000 m/s and 900 kg/m^3) proposed by [81], as in other studies of the Larderello area by [21–29, 31–72]. Starting from a velocity of 5900 m/s for the unit below the K-horizon, we obtain the minimum velocity values of about 4500 m/s due to the presence of fluid-filled fractured layers, which represents the minimum value for the PPL velocity distribution (Figure 12). Furthermore, this value is about 11% less than the velocity value (5150 m/s) assigned to the overlying metamorphic rocks, causing negative velocity contrasts at the upper boundary of K-horizon. Finally, this value is in agreement with the values obtained by [72] and with laboratory velocity measurements in the same range of effective pressures (see Sections 5.2 and 5.3).

On the basis of the geological evidence observed on Elba analogue, three models were created (Figure 13): a model with the bulge structure below the San Pompeo 2 well characterized by a perturbed zone and two models with continuous perturbed layers thick 100 m and 500 m, respectively.

Figure 13 shows the synthetic stacked data obtained with the seismic responses (in red) superimposed on the stacked data (in grey).

The synthetic response for the PPL limited to the bulge structure (Figures 13(a) and (a′)) reproduces a K-horizon continuous event at the ends of the line (0-2600 m and 8000-9270), which derives from a positive velocity contrast. In this case, the K-horizon events are perturbed and lose continuity in the bulge area. On the other hand, there is a relatively continuous signal at the base of the bulge, characterized by a positive contrast. The response with a PPL of 100 m in thickness (Figures 13(b) and (b′)) is similar to the previous model although the K-horizon reflectivity at the extremities and at the base of the bulge becomes less continuous and reproduces a response that is more in agreement with the original stacked data. The response with a PPL of 500 m in thickness (Figures 13(c) and (c′)) shows a clear reflection at the base of PPL which is not clearly recognized in the stacked data. As expected, the higher the thickness of PPL, the higher the complexity of the reflection pattern below the K-horizon. The responses of model 2-B (i.e., the calibrated velocity model with a sharp discontinuity related, e.g., to a lithological change - Figure 10(b′)) and that with a PPL of 100 m in thickness (Figure 13(b′)) are quite similar, and they have the same best-fit of the primary reflection event of the K-horizon. The main difference is in slight perturbations of K-horizon event times, which are within the best-fit error limits, and in the lateral discontinuity of the signal amplitudes of the K-horizon event in the PPL model.

The amplitude lateral variation is the main reason for considering the PPL model as a more suitable physical model than model 2-B (Figure 10(b′)). The PPL may describe the amplitude features of the K-horizon reflection events observed in seismic explorations in the Tuscan geothermal region.

All the simulation results with the PPL (Figure 13) indicate a complex pattern of the multiple K-events (TWT greater than 2.3 s) with an emphasis on the lozenge feature.

We also investigated the influence of the central frequency of the Ricker source wavelet on the synthetic model response. Figure 14 reports the results considering the K-horizon considered as a PPL of 100 m in thickness (Figure 13(b)), in the TWT range 1-2.5 s, respectively, for 15 Hz, 25 Hz, and 40 Hz. These frequencies were selected on the basis of the results of the spectral analysis of raw data (Figure 7) which indicates the maximum peak at about 15 Hz, a central frequency of about 25 Hz, and its high frequency limit at about 40 Hz.

The three responses indicate a different result passing from a relatively continuous reconstruction of the K-horizon for the 15 Hz source wavelet to a highly discontinuous reflector for the 40 Hz source wavelet. Although the high-frequency response is characterized by a general lateral high resolution, in reconstructing the PLL, the response generally has a low amplitude due to its sensitivity to low-velocity contrasts and interference.

6. Conclusions

The origin of strong amplitude seismic reflectivity concentrated in an almost continuous layer, named the K-horizon, below the vapor-dominated geothermal reservoirs of Larderello, Tuscany (Italy), has been debated for decades. In our paper, we contribute to the discussion by considering two hypotheses for the K-horizon: firstly, simulating the response of a sharp change in P-wave velocity at the depth of the K-horizon, and secondly, a physically perturbed layer (PPL) of variable thickness (representing the K-horizon) characterized by P-wave velocity perturbation.

A comparison of the two model reconstructions (Figures 10 and 13) clearly shows that the best fit is obtained by a PPL with a randomized P-wave velocity distribution with a thickness of 100 m. This is able to explain the reflectivity features and pattern of the seismic marker observed on several seismic profiles in the Larderello geothermal area.

The PPL modelled could be representative of a strongly fractured horizon filled by deep fluids possibly at supercritical conditions. The presence of a PPL is in agreement with the various hypotheses proposed in the literature for the K-horizon (Table 1), which may produce a P-wave velocity perturbation due to the change in the physical properties of the modelled rocks. Furthermore, the PPL hypothesis as proposed in this work is supported by the fact that the H-horizon, the current mining target in the study area made by fractured rocks with pressurized fluids, shows similar seismic features respect to the K-horizon. In this view, even the H-horizon could be characterized by a P-wave velocity perturbation due to the change in the physical properties of the modelled rock.

DESCRAMBLE project results ruled out the presence of fluids in the Venelle 2 well, but in contrast, the blowout of the San Pompeo 2 well clearly indicates the presence of deep overpressured fluids. This topic requires further research.

In addition to the possible presence of a PPL, this paper also highlights that

(i) The deep reflection events are significantly influenced by the articulated shallow morphology of Neogene and Ligurian units. This influence should be taken into account in the seismic data processing of the line, and it poses the problem of the scale for the calculation of seismic statics. Data processing for the focusing of the deep reflecting horizons entails including the Neogene and the Ligurian units in the calculation of the statics

(ii) The seismic modelling with a Vp value of 5900 m/s for the unit below the K-horizon is characterized by the best fit with data (Figures 10 and 13). These Vp values are in line with those reported in the literature for granites ([82, 83] and references therein; [84]). This may mean that there is a granitic intrusion below the K-horizon

(iii) Different PPL thicknesses show a different seismic pattern of the reflectivity of the K-horizon. Hence, the lateral variation of reflectivity of the K-horizon, its bright spot signature, and the diffuse reflectivity could be a consequence of a lateral thickness variation in the PPL

(iv) Our study also has implications regarding the processing and interpretation of seismic reflection data in geothermal areas

(v) It confirms the difficulty in reconstructing suitable complex velocity models using only the velocity analysis from surface seismic and, as a consequence, in the migration of seismic lines. In this area, this issue is enhanced by the dual effect of static and the complexity of the K-horizon. The definition of the overburden heterogeneities (and anisotropy) using a high-resolution integrated seismic exploration approach up to 0.5 s TWT, with refraction tomography integrated with high-resolution reflection seismic, could limit the issue just to the complexity of deeper horizon response

(vi) It suggests paying particular attention to the interpretation of seismic lines. In general, the response of the randomized model, due to constructive and destructive interferences, is not directly and univocally connected to the micro- and mesoscale structures of the reservoir. As a consequence, only the macroscale pattern can be recognized (see the reconstruction of the top of the physical transitional layer – Figure 13). Only the top of K-horizon can usually be detected, even though discontinuously. On the other hand, its internal structure may not be easily discernible due to the resolution decrease related to definition of a suitable local velocity model and to the central frequency of the signal (source and propagation)

(vii) Reflectivity depends on the actual structure at the microscale, which cannot be directly reconstructed in detail from the processing of surface seismic data (vertical seismic profiling - VSP - has a better performance than surface seismic in this regard)

(viii) An optimized seismic exploration strategy entails increasing the resolution of surface seismic, by integrating it with VSP data to visualize in detail the diffuse reflectivity zone detected by surface seismic

Data Availability

All the data used are public and available through the references and the website reported within the text.

Conflicts of Interest

The authors declares that they have no conflicts of interest.

Acknowledgments

We thank two anonymous reviewers, whose comments helped to improve and clarify this manuscript. This work was supported by the EU FP7-funded Integrated Methods for Advanced Geothermal Exploration (IMAGE) Project under grant agreement (608553).

Supplementary Materials

Figure S1: synoptic flowchart of the methodological workflow used. Figure S2: figure shows some of the data used to build the geological surfaces. In particular, well data of the Tuscan Nappe plus TWC and the area of the DEM characterized by outcrops of the Tuscan Nappe plus TWC are shown. Figure S3: figure shows the digitized subsurface map of the K-horizon imported in Petrel (Schlumberger). (a) View from above of the digitized data of the K-horizon. (b) Horizontal view of the digitized data of the K-horizon. Table S1: deep geothermal wells used to calibrate geological surfaces [65–68]. The original well head coordinates have been converted into our geographical system (i.e., WGS84-UTM32N; EPSG code: 32632). No information regarding deviation survey is available. All the wells have been considered vertical. *(Supplementary Materials)*

References

[1] W. A. Elders, G. Ó. Friðleifsson, and A. Albertsson, “Drilling into magma and the implications of the Iceland Deep Drilling Project (IDDP) for high-temperature geothermal systems worldwide,” *Geothermics*, vol. 49, pp. 111–118, 2014.

[2] S. Scott, T. Driesner, and P. Weis, “Geologic controls on supercritical geothermal resources above magmatic intrusions,” *Nature Communications*, vol. 6, no. 1, article 7837, 2015.

[3] P. Dobson, H. Asanuma, E. Huenges, F. Poletto, T. Reinsch, and B. Sanjuan, *Supercritical Geothermal Systems-a Review of Past Studies and Ongoing Research Activities*, In 42nd Workshop on Geothermal Reservoir Engineering, 2017.

[4] M. Riedel, C. Dutsch, C. Alexandrakis, I. Dini, S. Ciuffi, and S. Buske, “Seismic depth imaging of a geothermal system in Southern Tuscany,” *Geophysical Prospecting*, vol. 63, no. 4, pp. 957–974, 2015.

[5] C. Schmelzbach, S. Greenhalgh, F. Reiser et al., “Advanced seismic processing/imaging techniques and their potential for geothermal exploration,” *Interpretation*, vol. 4, no. 4, pp. SR1–SR18, 2016.

[6] W. Rabbel, T. Jusri, D. Köhn et al., “Seismic velocity uncertainties and their effect on geothermal predictions: a case study,” *Energy Procedia*, vol. 125, pp. 283–290, 2017.

[7] A. Minissale, “The Larderello geothermal field: a review,” *Earth-Science Reviews*, vol. 31, no. 2, pp. 133–151, 1991.

[8] A. Barelli, G. Cappetti, and G. Stefani, “Results of deep drilling in the Larderello-Travale/Radicondoli geothermal area,” in *Proceedings World Geothermal Congress 1995*, pp. 1275–1278, IGA, Florence, Italy, 1995.

[9] R. Bertani, G. Bertini, G. Cappetti, A. Fiordelisi, and B. M. Marocco, "An update of the Larderello-Travale/Radicondoli deep geothermal system," in *Proceedings World Geothermal Congress, 2005*, Antalya, Turkey, 2005.

[10] G. Bertini, M. Casini, G. Gianelli, and E. Pandeli, "Geological structure of a long-living geothermal system, Larderello, Italy," *Terra Nova*, vol. 18, no. 3, pp. 163–169, 2006.

[11] P. Romagnoli, A. Arias, A. Barelli, M. Cei, and M. Casini, "An updated numerical model of the Larderello–Travale geothermal system, Italy," *Geothermics*, vol. 39, no. 4, pp. 292–313, 2010.

[12] G. Gola, G. Bertini, M. Bonini et al., "Data integration and conceptual modelling of the Larderello geothermal area, Italy," *Energy Procedia*, vol. 125, pp. 300–309, 2017.

[13] F. Batini, P. D. Burgassi, G. M. Cameli, R. Nicolich, and P. Squarci, "Combination to the study of the deep lithospheric profiles; "deep" reflecting horizons in Larderello-Travale geothermal field," *Memorie Società Geologica Italiana*, vol. 19, pp. 477–484, 1978.

[14] G. M. Cameli, I. Dini, and D. Liotta, "Upper crustal structure of the Larderello geothermal field as a feature of post-collisional extensional tectonics (Southern Tuscany, Italy)," *Tectonophysics*, vol. 224, no. 4, pp. 413–423, 1993.

[15] G. M. Cameli, I. Dini, and D. Liotta, "Brittle/ductile boundary from seismic reflection lines of southern Tuscany (Northern Apennines, Italy)," *Memorie Società Geologica Italiana*, vol. 52, pp. 152–162, 1998.

[16] S. Ciuffi and M. Casini, "VSP and target definition," in *DESCRAMBLE project, Final Conference*, Pisa, March 2018, http://www.descramble-h2020.eu/index.php/events/conferences.

[17] L. Marini and A. Manzella, "Possible seismic signature of the α-β quartz transition in the lithosphere of Southern Tuscany (Italy)," *Journal of Volcanology and Geothermal Research*, vol. 148, no. 1-2, pp. 81–97, 2005.

[18] A. Brogi, A. Lazzarotto, D. Liotta, and G. Ranalli, "Extensional shear zones as imaged by reflection seismic lines: the Larderello geothermal field (Central Italy)," *Tectonophysics*, vol. 363, no. 1-2, pp. 127–139, 2003.

[19] I. R. Finetti, M. Boccaletti, M. Bonini et al., "Crustal section based on CROP seismic data across the North Tyrrhenian–Northern Apennines–Adriatic Sea," *Tectonophysics*, vol. 343, no. 3-4, pp. 135–163, 2001.

[20] T. Vanorio, R. De Matteis, A. Zollo, F. Batini, A. Fiordelisi, and B. Ciulli, "The deep structure of the Larderello-Travale geothermal field from 3D microearthquake traveltime tomography," *Geophysical Research Letters*, vol. 31, no. 7, 2004.

[21] R. De Matteis, T. Vanorio, A. Zollo, S. Ciuffi, A. Fiordelisi, and E. Spinelli, "Three-dimensional tomography and rock properties of the Larderello-Travale geothermal area, Italy," *Physics of the Earth and Planetary Interiors*, vol. 168, no. 1-2, pp. 37–48, 2008.

[22] F. Batini, G. Bertini, A. Bottai et al., "San Pompeo 2 deep well: a high temperature and high pressure geothermal system," in *Proceedings of the 3rd International Seminar on European geothermal update*, vol. 3, pp. 341–353, FRG, Munich, Germany, 1983.

[23] N. Piana Agostinetti, A. Licciardi, D. Piccinini et al., "Discovering geothermal supercritical fluids: a new frontier for seismic exploration," *Scientific Reports*, vol. 7, no. 1, p. 14592, 2017.

[24] R. Bertani, H. Büsing, S. Buske et al., "The First Results of the DESCRAMBLE Project," *Proceedings of the 43rd Workshop on Geothermal Reservoir Engineering*, , pp. 12–14, Stanford University, Stanford, California, 2018.

[25] D. Scrocca, C. Doglioni, F. Innocenti, P. Manetti, A. Mazzotti, L. Bertelli, L. Burbi, and S. Doffizi, Eds., "CROP Atlas: seismic reflection profiles of the Italian crust," *Memorie Descrittive della Carta Geologica d'Italia*, vol. 62, pp. 1–194, 2003.

[26] E. Locardi and R. Nicolich, "Geodinamica del Tirreno e dell'Appennino centro-meridionale: la nuova carta della Moho. Memorie della," *Società Geologica Italiana*, vol. 41, pp. 121–140, 1992.

[27] M. Boccaletti, G. Gianelli, and F. Sani, "Tectonic regime, granite emplacement and crustal structure in the inner zone of the Northern Apennines (Tuscany, Italy): a new hypothesis," *Tectonophysics*, vol. 270, no. 1-2, pp. 127–143, 1997.

[28] C. Faccenna, F. Funiciello, D. Giardini, and P. Lucente, "Episodic back-arc extension during restricted mantle convection in the Central Mediterranean," *Earth and Planetary Science Letters*, vol. 187, no. 1-2, pp. 105–116, 2001.

[29] G. Lavecchia, P. Boncio, N. Creati, and F. Brozzetti, "Some aspects of the Italian geology not fitting with a subduction scenario," *Journal of the Virtual Explorer*, vol. 10, pp. 1–14, 2003.

[30] A. Brogi, A. Lazzarotto, D. Liotta, and G. Ranalli, "Crustal structures in the geothermal areas of southern Tuscany (Italy): insights from the CROP 18 deep seismic reflection lines," *Journal of Volcanology and Geothermal Research*, vol. 148, no. 1-2, pp. 60–80, 2005.

[31] C. Doglioni, E. Gueguen, P. Harabaglia, and F. Mongelli, "On the origin of west-directed subduction zones and applications to the western Mediterranean," *Geological Society, London, Special Publications*, vol. 156, no. 1, pp. 541–561, 1999.

[32] E. Carminati, C. Doglioni, and D. Scrocca, "Alps vs. Apennines," in *32° International Geological Congress*, pp. 141–151, Italian Geological Society, Florence, Italy, 2004.

[33] G. Molli, "Northern Apennine–Corsica orogenic system: an updated overview," *Geological Society, London, Special Publications*, vol. 298, no. 1, pp. 413–442, 2008.

[34] L. Carmignani, F. A. Decandia, P. L. Fantozzi, A. Lazzarotto, D. Liotta, and M. Meccheri, "Tertiary extensional tectonics in Tuscany (Northern Apennines, Italy)," *Tectonophysics*, vol. 238, no. 1-4, pp. 295–315, 1994.

[35] A. Brogi, "Neogene extension in the Northern Apennines (Italy): insights from the southern part of the Mt. Amiata geothermal area," *Geodinamica Acta*, vol. 19, no. 1, pp. 33–50, 2012.

[36] M. Bonini and F. Sani, "Extension and compression in the Northern Apennines (Italy) hinterland: evidence from the late Miocene-Pliocene Siena-Radicofani Basin and relations with basement structures," *Tectonics*, vol. 21, no. 3, pp. 1-1–1-32, 2002.

[37] G. Gianelli, "A comparative analysis of the geothermal fields of Larderello and Mt Amiata, Italy," in *Geothermal Energy Research Trends*, H. I. Ueckermann, Ed., pp. 59–85, Nova Science Publishers, 2008.

[38] P. Montone, M. T. Mariucci, and S. Pierdominici, "The Italian present-day stress map," *Geophysical Journal International*, vol. 189, no. 2, pp. 705–716, 2012.

[39] G. Gianelli, M. Puxeddu, and P. Squarci, "Structural setting of the Larderello-Travale geothermal region," *Memorie della Società Geoligica Italiana*, vol. 19, pp. 469–476, 1978.

[40] E. Pandeli, G. Bertini, and P. Castellucci, "The tectonic wedges complex of the Larderello area (Southern Tuscany, Italy)," *Bollettino della Societa Geologica Italiana*, vol. 110, pp. 621–629, 1991.

[41] G. Nirta, E. Pandeli, G. Principi, G. Bertini, and N. Cipriani, "The Ligurian units of southern Tuscany," *Bollettino Società Geologica Italiana*, vol. 3, pp. 29–54, 2005.

[42] M. Marroni and L. Pandolfi, "The architecture of an incipient oceanic basin: a tentative reconstruction of the Jurassic Liguria-Piemonte basin along the Northern Apennines–Alpine Corsica transect," *International Journal of Earth Sciences*, vol. 96, no. 6, pp. 1059–1078, 2007.

[43] A. Brogi, D. Liotta, G. Ruggieri, E. Capezzuoli, M. Meccheri, and A. Dini, "An overview on the characteristics of geothermal carbonate reservoirs in southern Tuscany," *Italian Journal of Geosciences*, vol. 135, no. 1, pp. 17–29, 2016.

[44] G. Bertini, F. M. Elter, and F. Talarico, "Evidenze di una fase estensionale pre-triassica nel complesso degli gneiss nell'area geotermica di Larderello (Toscana meridionale)," *Studi Geologici Camerti, Volume Speciale*, vol. 1, pp. 129–137, 1994.

[45] A. Dini, G. Gianelli, M. Puxeddu, and G. Ruggieri, "Origin and evolution of Pliocene–Pleistocene granites from the Larderello geothermal field (Tuscan Magmatic Province, Italy)," *Lithos*, vol. 81, no. 1-4, pp. 1–31, 2005.

[46] A. Arias, I. Dini, M. Casini, A. Fiordelisi, I. Perticone, and P. Dell'Aiuto, *Geoscientific Feature Update of the Larderello–Travale Geothermal System (Italy) for a Regional Numerical Modeling*, Proceedings world geothermal congress, 2010.

[47] R. Bertani, "Geothermal power generation in the world 2010–2014 update report," *Geothermics*, vol. 60, pp. 31–43, 2016.

[48] F. Batini, A. Brogi, A. Lazzarotto, D. Liotta, and E. Pandeli, "Geological features of Larderello–Travale and Mt. Amiata geothermal areas (southern Tuscany, Italy)," *Episodes*, vol. 26, no. 3, pp. 239–244, 2003.

[49] G. Bertini, G. Gianelli, and A. Battaglia, *Risultati ed interpretazione delle datazioni radiometriche (metodo 230Th/234U) dei campioni di minerali idrotermali presenti nelle rocce attraversate dai sondaggi geotermici (Larderello e Monteverdi) e negli affioramenti di rocce mineralizzate (Sassa e Canneto-Malentrata)*, ENEL-CNR-CISE internal report, Pisa, 1996.

[50] A. Santilano, A. Manzella, G. Gianelli et al., "Convective, intrusive geothermal plays: what about tectonics?," *Geothermal Energy Science*, vol. 3, no. 1, pp. 51–59, 2015.

[51] J. E. Foley, M. N. Toksoz, and F. Batini, "Inversion of teleseismic travel time residuals for velocity structure in the Larderello Geothermal Field, Italy," *Geophysical Research Letters*, vol. 19, no. 1, pp. 5–8, 1992.

[52] P. Baldi, S. Bellani, A. Ceccarelli, A. Fiordelisi, P. Squarci, and L. Taffi, "Correlazioni tra le anomalie termiche ed altri elementi geofisici e strutturali della Toscana meridionale," *Studi Geologici Camerti, Volume Speciale*, vol. 1994-1, pp. 139–149, 1994.

[53] F. Batini, A. Fiordelisi, F. Graziano, and M. N. Toksöz, "Earthquake tomography in the Larderello geothermal area," in *Proceedings of the World Geothermal Congress*, pp. 817–820, Florence, Italy, 1995.

[54] G. Gianelli, A. Manzella, and M. Puxeddu, "Crustal models of the geothermal areas of southern Tuscany (Italy)," *Tectonophysics*, vol. 281, no. 3-4, pp. 221–239, 1997.

[55] A. Manzella, G. Ruggieri, G. Gianelli, and M. Puxeddu, "Plutonic-geothermal systems of southern Tuscany: a review of the crustal models," *Memorie Società Geologica Italiana*, vol. 52, pp. 283–294, 1998.

[56] F. Mongelli, F. Palumbo, M. Puxeddu, I. M. Villa, and G. Zito, "Interpretation of the geothermal anomaly of Larderello, Italy," *Memorie Società Geologica Italiana*, vol. 52, pp. 305–318, 1998.

[57] A. Santilano, *Deep Geothermal Exploration by Means of Electromagnetic Methods: New Insights from the Larderello Geothermal Field (Italy), [PhD Thesis]*, Politecnico di Torino, Italy, 2017.

[58] IMAGE Project website, "Integrated Methods for Advanced Geothermal Exploration," http://www.image-fp7.eu/Pages/default.aspx.

[59] DESCRAMBLE Project website, "Drilling in dEep, Super-CRitical AMBient of continenta L Europe H2020 project," http://www.descramble-h2020.eu/.

[60] M. Casini, S. Ciuffi, A. Fiordelisi, A. Mazzotti, and E. Stucchi, "Results of a 3D seismic survey at the Travale (Italy) test site," *Geothermics*, vol. 39, no. 1, pp. 4–12, 2010.

[61] F. Accaino, U. Tinivella, G. Rossi, and R. Nicolich, "Imaging of CROP-18 deep seismic crustal data," *Bollettino Società Geologica Italiana*, vol. 3, pp. 195–204, 2005.

[62] D. Liotta and G. Ranalli, "Correlation between seismic reflectivity and rheology in extended lithosphere: southern Tuscany, Inner Northern Apennines, Italy," *Tectonophysics*, vol. 315, no. 1-4, pp. 109–122, 1999.

[63] M. Cei and A. Fiorentini, "Resource characterization post drilling," in *DESCRAMBLE Project, Final Conference*, Pisa, March 2018, http://www.descramble-h2020.Eu/index.Php/events/conferences.

[64] R. Bertani, "DESCRAMBLE project conclusive remarks," in *DESCRAMBLE Project, Final Conference*, Pisa, March 2018, http://www.descramble-h2020.eu/index.php/events/conferences.

[65] A. G. I. P. Mineraria, *Temperature sotterranee*, Inventario dei dati raccolti dall'AGIP durante la ricerca e la produzione di idrocarburi in Italia, San Donato Milanese (Milano), 1977.

[66] E.-A. ENEL and E. CNR, *Inventario delle Risorse Geotermiche Nazionali—Indagine D'insieme Sul Territorio Nazionale*, Ministero dell'Industria, del Commercio e dell'Artigianato (currently Ministero dello Sviluppo Economico), 1988.

[67] E. Barbier, S. Bellani, and F. Musmeci, "The Italian geothermal database," in *Proceedings World Geothermal Congress*, pp. 3991–3995, Tohoku, Japan, 2000.

[68] "Ministry of Economic Development-DGS-UNMIG," http://unmig.mise.gov.it/.

[69] D. Loewenthal, L. Lu, R. Roberson, and J. Sherwood, "The wave equation applied to migration," *Geophysical Prospecting*, vol. 24, no. 2, pp. 380–399, 1976.

[70] F. Batini, R. Bertani, B. Ciulli, A. Fiordelisi, P. Valenti, and E. G. Power, "Geophysical well logging: a contribution to the fractures characterization," in *Proceedings of the 27th Workshop on Geothermal Reservoir Engineering*, pp. 28–30, Stanford University, Stanford, USA, 2002.

[71] G. M. Cameli, A. Ceccarelli, I. Dini, and A. Mazzotti, "Contribution of the seismic reflection method to the location of deep fractured levels in the geothermal fields of southern Tuscany (Central Italy)," in *Proceedings World Geothermal Congress 2000*, Kyushu-Tohoku, Japan, 2000.

[72] U. Tinivella, F. Accaino, G. Rossi, and R. Nicolich, "Petrophysical analysis of CROP-18 crustal seismic data," *Bollettino Società Geologica Italiana*, vol. 3, pp. 205–211, 2005.

[73] M. Aleardi and A. Mazzotti, "A feasibility study on the expected seismic AVA signatures of deep fractured geothermal reservoirs in an intrusive basement," *Journal of Geophysics and Engineering*, vol. 11, no. 6, p. 65008, 2014.

[74] B. Tarquini, M. Cameli, C. Donati, and R. J. Martin, "The effect of pressure, temperature, and lithology on seismic wave velocities for rocks from the Larderello geothermal field," in *Proceedings of the 1995 World Geothermics Congress*, pp. 813–815, Florence, Italy, May 1995, https://www.geothermal-energy.org/pdf/IGAstandard/WGC/1995/2-Tarquini.pdf.

[75] G. P. Pinna, L. Burlini, D. Mainprice, and G. Gianelli, "Riflettività del basamento metamorfico di Larderello indicata da dati di petrofisica," in *18° Convegno Nazionale GNGTS*, Rome, Italy, 1999.

[76] F. Batini, S. Lisi, and E. Pinna, *Contributo dei profili sismici in pozzo per l'individuazione di potenziali serbatoi geotermici all'interno del basamento metamorfico del campo di Bruciano (area di Larderello)*, 14° Convegno annuale del gruppo di geofisica della terra solida, Roma, 1995.

[77] M. Zucchi, A. Brogi, D. Liotta et al., "Permeability and hydraulic conductivity of faulted micaschist in the eastern Elba Island exhumed geothermal system (Tyrrhenian Sea, Italy): insights from Cala Stagnone," *Geothermics*, vol. 70, pp. 125–145, 2017.

[78] M. R. J. Wyllie, A. R. Gregory, and L. W. Gardner, "Elastic wave velocities in heterogeneous and porous media," *Geophysics*, vol. 21, no. 1, pp. 41–70, 1956.

[79] G. Mavko, T. Mukerji, and J. Dvorkin, *The Rock Physics Handbook: Tools for Seismic Analysis of Porous Media*, Cambridge university press, 2009.

[80] J. G. Berryman, "Long-wavelength propagation in composite elastic media I. Spherical inclusions," *The Journal of the Acoustical Society of America*, vol. 68, no. 6, pp. 1809–1819, 1980.

[81] M. Batzle and Z. Wang, "Seismic properties of pore fluids," *Geophysics*, vol. 57, no. 11, pp. 1396–1408, 1992.

[82] F. Birch, "The velocity of compressional waves in rocks to 10 kilobars: 1," *Journal of Geophysical Research*, vol. 65, no. 4, pp. 1083–1102, 1960.

[83] F. Birch, "The velocity of compressional waves in rocks to 10 kilobars: 2," *Journal of Geophysical Research*, vol. 66, no. 7, pp. 2199–2224, 1961.

[84] Y. Aizawa, K. Ito, and Y. Tatsumi, "Compressional wave velocity of granite and amphibolite up to melting temperatures at 1 GPa," *Tectonophysics*, vol. 351, no. 3, pp. 255–261, 2002.

[85] CREWES-Consortium for Research in Elastic Wave Exploration Seismology, *CREWES MATLAB Toolbox*University of Calgaryhttps://www.crewes.org/ResearchLinks/FreeSoftware/.

[86] I. R. Finetti, "Basic regional crustal setting and superimposed local pluton-intrusion-related tectonics in the Larderello-M. Amiata geothermal province, from integrated CROP seismic data," *Bollettino Della Società Geologica Italiana*, vol. 125, no. 1, pp. 117–146, 2006.

[87] E. Trumpy and A. Manzella, "Geothopica and the interactive analysis and visualization of the updated Italian National Geothermal Database," *International Journal of Applied Earth Observation and Geoinformation*, vol. 54, pp. 28–37, 2017.

[88] C. Botter, N. Cardozo, S. Hardy, I. Lecomte, and A. Escalona, "From mechanical modeling to seismic imaging of faults: a synthetic workflow to study the impact of faults on seismic," *Marine and Petroleum Geology*, vol. 57, pp. 187–207, 2014.

[89] A. S. Zappone and R. H. Bruijn, *The Swiss Atlas of Physical Properties of Rocks (SAPHYR)*, Rapport Annuel, 2012.

[90] L. Orlando, "Interpretation of Tuscan gravity data," *Bollettino Società Geologica Italiana*, vol. 3, pp. 179–186, 2005.

Hindawi
Geofluids
Volume 2019, Article ID 7520714, 21 pages
https://doi.org/10.1155/2019/7520714

Research Article

Influence of the Main Border Faults on the 3D Hydraulic Field of the Central Upper Rhine Graben

Jessica Freymark,[1,2] **Judith Bott**,[1] **Mauro Cacace**,[1] **Moritz Ziegler**,[1,3] **and Magdalena Scheck-Wenderoth**[1,2]

[1]*GFZ German Research Centre for Geosciences, Telegrafenberg, 14473 Potsdam, Germany*
[2]*RWTH Aachen, Faculty of Georesources and Material Engineering, Lochnerstr. 4-20, 52056 Aachen, Germany*
[3]*University of Potsdam, Institute of Earth and Environmental Science, Karl-Liebknecht-Str. 24-25, 14476 Potsdam-Golm, Germany*

Correspondence should be addressed to Jessica Freymark; jessica.freymark@arcor.de

Received 17 July 2018; Revised 30 October 2018; Accepted 21 November 2018; Published 11 March 2019

Academic Editor: Domenico Montanari

The Upper Rhine Graben (URG) is an active rift with a high geothermal potential. Despite being a well-studied area, the three-dimensional interaction of the main controlling factors of the thermal and hydraulic regime is still not fully understood. Therefore, we have used a data-based 3D structural model of the lithological configuration of the central URG for some conceptual numerical experiments of 3D coupled simulations of fluid and heat transport. To assess the influence of the main faults bordering the graben on the hydraulic and the deep thermal field, we carried out a sensitivity analysis on fault width and permeability. Depending on the assigned width and permeability of the main border faults, fluid velocity and temperatures are affected only in the direct proximity of the respective border faults. Hence, the hydraulic characteristics of these major faults do not significantly influence the graben-wide groundwater flow patterns. Instead, the different scenarios tested provide a consistent image of the main characteristics of fluid and heat transport as they have in common: (1) a topography-driven basin-wide fluid flow perpendicular to the rift axis from the graben shoulders to the rift center, (2) a N/NE-directed flow parallel to the rift axis in the center of the rift and, (3) a pronounced upflow of hot fluids along the rift central axis, where the streams from both sides of the rift merge. This upflow axis is predicted to occur predominantly in the center of the URG (northern and southern model area) and shifted towards the eastern boundary fault (central model area).

1. Introduction

The Upper Rhine Graben (URG), located at the border of SW Germany and NE France (Figure 1), is an area of active geothermal exploration (e.g., [1, 2]). The graben is embedded in a low-permeable basement and filled with permeable sediments. The currently exploited geothermal resources of the URG are mostly located in the uppermost part of the fractured and faulted basement (e.g., [2]). As an active rift, the URG is bounded by two main border faults in addition to several faults of smaller extent inside the graben area. Studies investigating fault zones as naturally permeable pathways for fluid flow and related effects on the thermal field indicated a variable influence of faults on the deep thermal field (e.g., [3–7]). High-temperature anomalies in the URG like the one mapped at Soultz-sous-Forêts have been explained by fluid convection along deep-reaching fault zones (e.g., [8–11]). Several 2D numerical models have investigated the deep hydrothermal fluid flow across the URG (e.g., [9, 12–18]). In addition, smaller-scale 3D models (max. 30×30 km coverage) have been developed for some of the geothermal plants to assess the local fluid flow (e.g., [8, 19–22]).

In general, 2D numerical models for the central URG (e.g., [13, 14, 16–18]) predicted a topography-driven deep fluid flow characterized by a downflow at the borders of the URG and an upflow in the western part of the graben center. These simulations included one or more faults in the western part of the URG (mainly near to Soultz-sous-Forêts), which

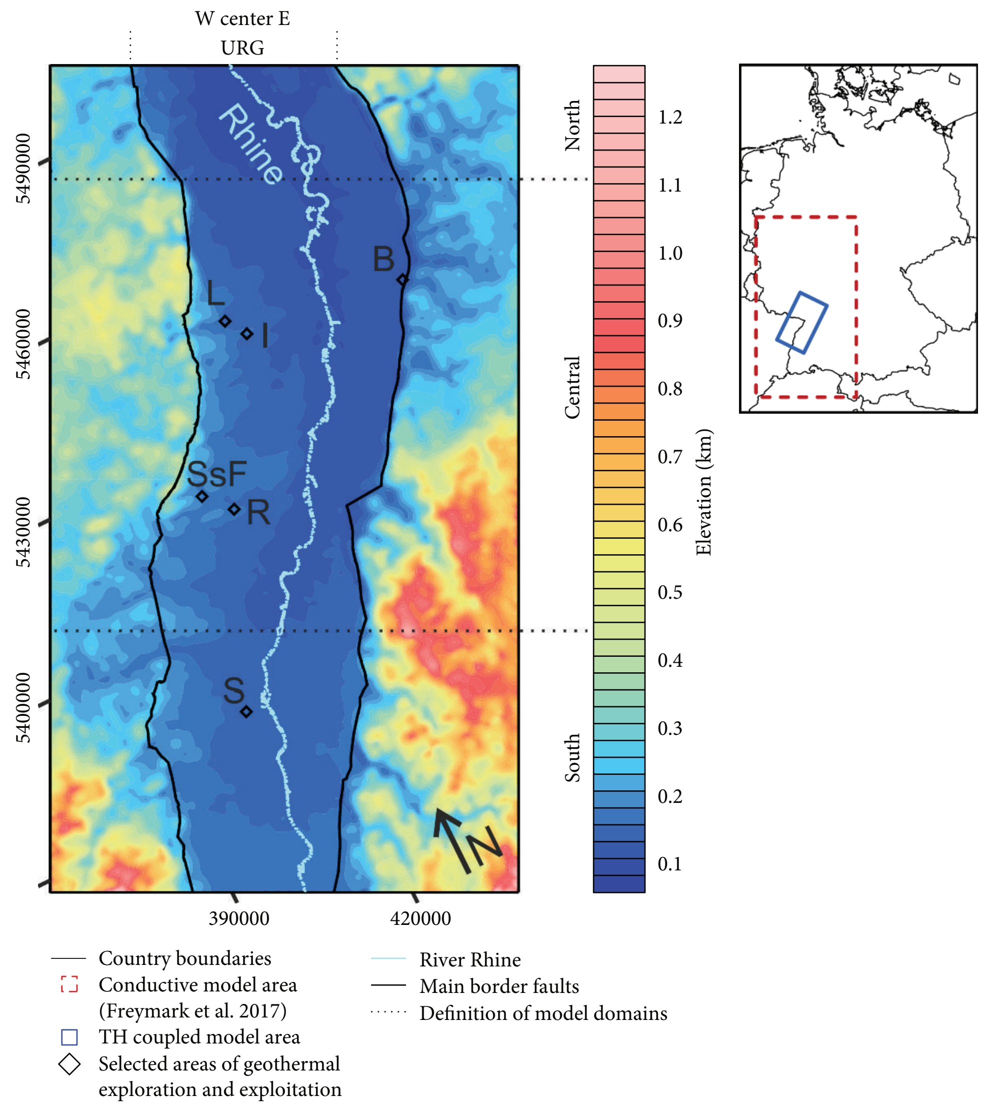

Figure 1: Topography (etopo1 [23]) of the model area in the central Upper Rhine Graben (URG) with selected areas of geothermal exploration (S: Strasbourg) and exploitation (L: Landau Pfalz; I: Insheim; B: Bruchsal; SsF: Soultz-sous-Forêts; R: Rittershoffen). The rectangular model area is elongated parallel to the main rift axis (NNE-SSW) and has a horizontal extent of 87×153 km. The red rectangle in the map on the top right indicates the area of the larger Rhine Graben model of Freymark et al. [24] based on which the geological configuration of the current model (blue rectangle) is taken. The map on the left is shown in UTM32N and rotated counter-clockwise by approximately 20°.

resulted in a preferred upflow of fluids along these faults. According to previous fluid chemistry characterization studies, it is likely that mixing of meteoric water and deep saline reservoir fluids occur at either both boundary faults (e.g., [25–29]) or at the W border fault [12, 18]. Fluid circulation is indicated by temperature profiles, for example, at Soultz-sous-Forêts and Rittershoffen (e.g., [28, 30, 31]). In summary, most studies proposed that deep convective circulation of hot fluids plays a major role in the hydraulic regime of the URG [8, 12, 14, 18, 28]. Whether the deep circulation is occurring only in the fault zones or if cross-formation flow might exert additional influence on the graben hydraulics is to the author's knowledge still to be quantified (e.g., [29]).

Although the URG is a well-studied and utilized area, an integrated three-dimensional understanding of the main controlling factors for the coupled fluid and heat transport is still lacking. Freymark et al. [24] have assessed the lithosphere-scale conductive thermal field by means of 3D simulations. Despite that their conductive simulation reproduced the general trend of observed temperatures reasonably well, local deviations between observed and predicted temperatures occurred mainly at shallower depth levels (upper 2-3 km) of the URG. This latter aspect indicates that an additional component related to heat transported by moving fluids should be considered as well.

Following on these aspects, we present a detailed numerical investigation aiming at quantifying the role of fluid circulation on the three-dimensional thermal configuration inside the main sedimentary units of the URG. In general, deep subsurface fluid flow is controlled by (i) pressure gradients imposed on the system by variable recharge through the shallow subsurface, (ii) the hydraulic properties of the subsurface geological units as differentiated by the existence of lithological variations and structural discontinuities (faults and fractures), and (iii) variations in fluid density. To implement the hydrogeological configuration of the central URG into the 3D numerical simulations of coupled heat and fluid transport, we make use of the upper part of the data-based 3D structural model of the URG [24] complemented by the well-known geometry of the main border faults of the graben. By implementing general trends in surface pressure and temperature conditions affecting the underground, these numerical experiments provide new 3-dimensional insights into the regional patterns of groundwater flow and related thermal anomalies. Of special interest in the current study is (1) to quantify, by means of a sensitivity analysis, the influence of the main border faults on the basin-wide fluid flow in the central URG and (2) to evaluate the implications for the deep temperature distribution.

2. Method

2.1. Starting Model and Model Area. The 3D structural model of Freymark et al. [24] provides the basis for the geological configuration and thus for the lithology-dependent distribution of thermal and hydraulic properties in our numerical model. The structural model covers the URG, the western Molasse Basin, and the Hessian Depression and consists of 14 lithostratigraphic units, 7 upper crustal domains, a lower crystalline crust, and 2 domains of the lithospheric mantle. The geometries of these model units were derived based on different observables (well data, reflection and refraction seismic data, geological maps, and existing 3D structural models; see references in Freymark et al. [24] for more information on the data base). In addition, 3D gravity modelling was performed to assess the internal structure of the crystalline crust while integrating all available seismic lines.

Within this study, we focus on the subsurface above a depth of 8 km of the central URG, which hosts several sites currently used for geothermal energy production like Bruchsal, Landau, Insheim, Soultz-sous-Forêts, and Rittershoffen (Figure 1). In addition, the study area comprises the area of Strasbourg, which is currently under geothermal exploration. To define the model domain for the coupled thermo-hydraulic simulations, we have combined several lithostratigraphic units with comparable properties according to Freymark et al. [24]. This results in 3 main sedimentary units within the URG that have distinct hydraulic and thermal rock properties (Table 1, Figure 2): (1) the permeable Cenozoic sands and marls; (2) the less permeable Keuper, Lias, and Dogger sediments; and (3) the permeable Muschelkalk, Buntsandstein, and Permo-Carboniferous carbonates and sandstones. Below the sedimentary units, an upper crystalline crustal layer of variable thickness has been included (at least 2 km thick). The laterally juxtaposed crystalline crustal units correspond to the upper crustal units of Freymark et al. ([24], Figure 2) and are parameterized accordingly (Table 1). In particular, the radiogenic heat production differs for the three crystalline crustal units. The base of the model is a flat surface at a depth of 8 km below sea level.

In addition to the 3D volumes representing the geological units, we have implemented the two main border faults of the URG as discrete model features, corresponding to those implemented in the model of GeORG [37]. These faults are represented as slightly undulating surfaces dipping steeply towards the graben center (Figure 2). They extend from the topography to a model depth of 6 km b.s.l. as proposed by Baillieux et al. [30].

To adequately represent these structural attributes in the numerical simulation, a fully unstructured mesh is required. However, meshing complex geological structures are still a technical challenge [52]. Each geological unit is defined as a closed 3D volume that shares the nodes with the neighboring geological units or faults. Faults are discretized as 2D elements embedded in the 3D finite element mesh such that each node of the fault is shared with the adjacent geological units. As layers and faults are defined by scattered points before meshing, their intersections have to be defined. A specific challenge is that the 3D volumes enclosed by the finite elements should not be too thin and that sharp angles should be avoided. Problems occur especially at thin, out-pinching layers. To have a good representation of the actual geometries, a large amount of elements are needed to mesh such layers, which increases the computational time for the simulations. Therefore, a balance has to be found between an adequate representation of the geology and an acceptable number of elements and thus computational time.

For our simulations, we have built a fully unstructured mesh consisting of about 1 million tetrahedral elements (Figure 2) using the software MeshIt [53]. The mesh resolves the major structural features of the graben configuration in terms of geological units of varying permeability as well as thermal properties and in terms of the 3D configuration of the major border faults of the graben.

In addition, two main structural approximations have been implemented: (1) the thin out-pinching geometry of the Keuper/Lias/Dogger unit is approximated by extending this geological domain further to the North with a finite thickness of 50 m. Thus, the unit comprising Keuper, Lias, and Dogger is 50 m thicker than in reality in the northernmost model area (Figure 3(b)). (2) The thin outcropping sediments on the graben shoulders were neglected. As a consequence, the graben shoulders are considered as upper crystalline crust without sedimentary cover.

For the numerical simulations, hydraulic and thermal properties are assigned to each model unit derived either from lab measurements or from former modelling studies (Table 1). Where lab measurements are available for subunits (e.g., Muschelkalk, Buntsandstein, and Permo-Carboniferous), we use the weighted mean considering the average thickness of each geological sublayer. Furthermore, bulk densities are calculated considering matrix densities derived by 3D gravity modelling [24] and measured porosities (Table 1).

2.2. Configuration and Physical Properties of the Geological Units. The thickness distribution of the main geological units (Figure 3) illustrates that the permeable Cenozoic sediments

Table 1: Physical properties used for the coupled thermo-hydraulic simulations (UC = upper crust).

Model unit	Prevailing lithology	Matrix porosity	Matrix permeability [m^2]	Specific heat capacity [J/(kg K)]	Matrix thermal conductivity [W/(m*K)]	Radiogenic heat production [$\mu W/m^3$]	Matrix density [kg/m^3]
Cenozoic	Marl, sand, and clay [32]	0.18 [16, 33–36]	$7E-14$ [13, 16, 29, 33, 35, 37]	860 [38]	1.3 [39]	1.0 [34]	2585 [24]
Dogger/Lias/Keuper	Clay, marlstone, limestone, and sandstone [39, 40]	0.04 [37]	$4E-16$ [35, 37]	800 [34, 41]	2.6 [39]	1.6 [34]	2667 [24]
Pre-Keuper (Muschelkalk/Buntsandstein/ Permo-Carboniferous)	Carbonates, sandstone, and rhyolites [33, 39, 40]	0.08 [16, 33, 35, 37, 39]	$2.9E-14$ [14, 29, 33, 35, 37, 39, 42]	725 [33, 34, 43]	2.9 [33, 39]	1.0 [34]	2780 [24]
UC: Mid-German Crystalline High	Granitoids [33, 44]	0.01 [34]	$3E-18$ [37]	755 [33]	2.4 [33]	1.8 [45]	2717 [24]
UC: Saxothuringian	Slate, granitoids [46, 47]	0.01 [34]	$3E-18$ [37]	900 [34]	2.5 [48]	2.5 [47]	2747 [24]
UC: Moldanubian	Gneiss, granitoids [45, 49]	0.01 [34]	$3E-18$ [37]	900 [34]	2.5 [50]	2.6 [51]	2707 [24]

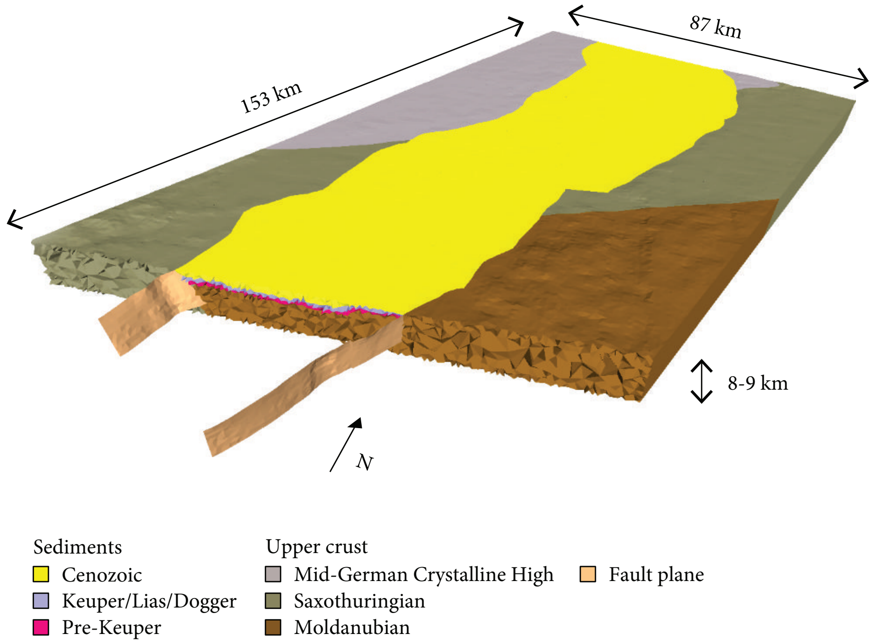

FIGURE 2: 3D finite-element mesh with differently parameterized units color-coded.

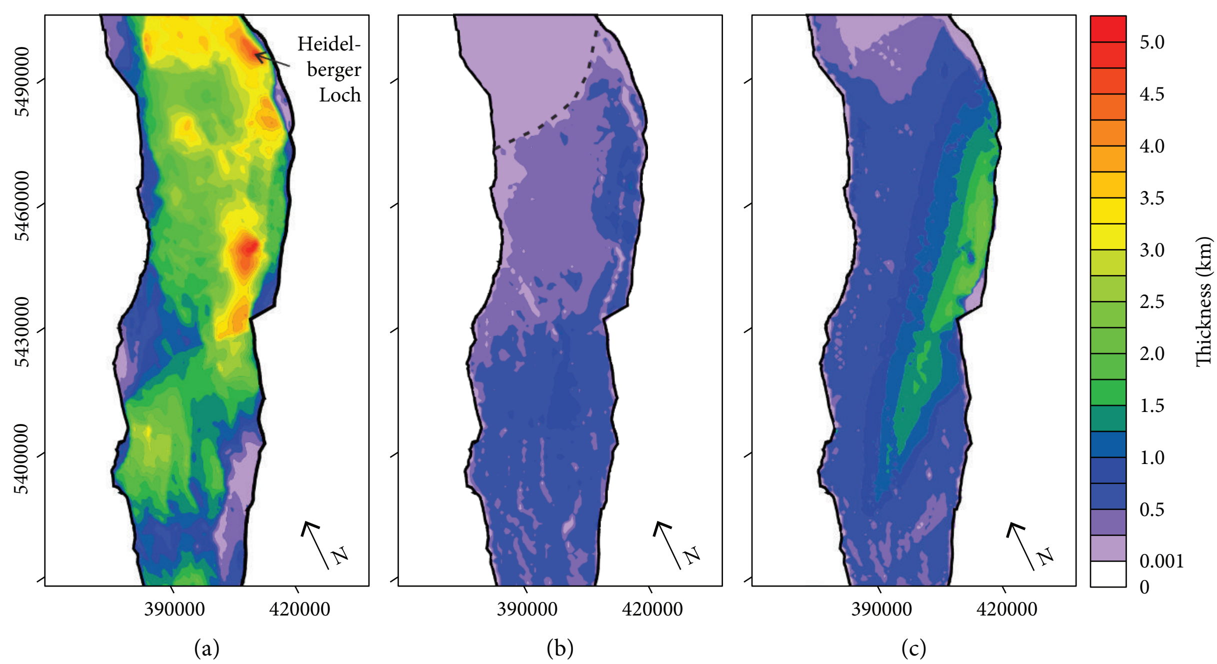

FIGURE 3: Cummulative thickness (a) of Cenozoic sediments, (b) of Keuper/Lias/Dogger, and (c) of Muschelkalk/Buntsandstein/Permo-Carboniferous (Pre-Keuper). The dashed line shows where the Keuper/Lias/Dogger sediments pinch out in reality. Maps are shown in UTM32N and rotated counter-clockwise by approximately 20°.

are thicker in the North than in the South of the model area (Figure 3(a)). Thickness maxima of 4850 m are reached locally in the "Heidelberger Loch" in the northeastern-most model area and in the E of the central model area (Figure 3(a)). The Cenozoic unit combines the Quaternary aquifer as well as Tertiary aquifers and aquitards (e.g., [16, 29]). The aquifers mainly consist of sand and gravel, while the aquitards are characterized as continental fluvial clay lenses and thin clay layers like the Rupelian "Fish shale" with a limited spatial extent (e.g., [54]). Furthermore, some Tertiary layers include rock salt. However, the predominant lithologies of the Cenozoic unit are marls and sands [32] with a relatively high average permeability ($7E-14\,\mathrm{m}^2$ [13, 16, 29, 33, 35, 37]; Table 1).

The Keuper/Lias/Dogger unit (Jurassic to Late Triassic) has an average thickness of 500 m (Figure 3(b)). It consists of shales, marls, and sandstone and is generally less permeable than the other sedimentary layers of the model ($4E-16\,\mathrm{m}^2$ [35, 37]; Table 1).

The Pre-Keuper sedimentary layer combines Triassic Muschelkalk and Buntsandstein, as well as Permo-Carboniferous sediments. This layer is predominantly characterized by a high permeability ($2.9E-14\,\mathrm{m}^2$ [14, 29, 33, 35, 37, 39, 42]; Table 1). Largest thicknesses of up to 2300 m are found in a NE-SW-striking subbasin with maximum thicknesses along the eastern border in the central model area (Figure 3(c)).

The upper crystalline crust is differentiated into the main Variscan domains (Mid-German Crystalline High, Saxothuringian, and Moldanubian; Figure 2, Table 1). In the East of the central model area, the top of the crystalline basement is deepest reflecting the asymmetric rift geometry of the URG (Figure 4). However, in the northern model portion, this asymmetry is less pronounced. In contrast, in the South the basement is deeper at the western border of the URG (Figure 4). Since previous studies have shown that the locally highly fractured basement can contain deep saline groundwater (e.g., [29, 55, 56]), the basement is characterized as not completely impermeable in this study ($3E-18\,\mathrm{m}^2$ [37]; Table 1).

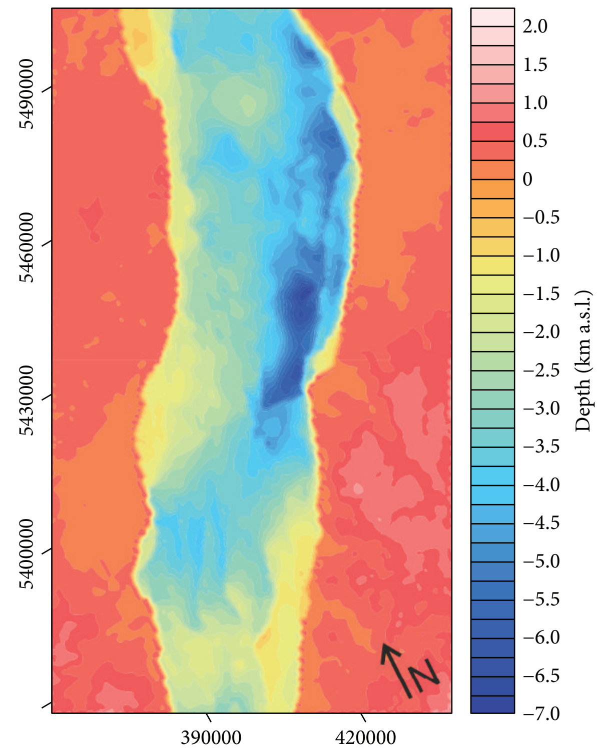

Figure 4: Depth of top basement. The map is shown in UTM32N and rotated counter-clockwise by approximately 20°.

2.3. Parameterization of the Boundary Faults. To test the influence of the main border faults on the hydraulic system, we run a suite of simulations each different in terms of the hydraulic configuration of the faults. An overview of all the model runs is given in Table 2. We have tested configurations without faults (model A), with faults of different width (models B and C) and different permeability (models B/C, D, and E). We have refrained from testing scenarios with faults acting as a barrier to fluid flow since the border faults of the central URG are generally described as hydraulically active conduits (e.g., [13]). The permeability value of $5E-14\,\mathrm{m}^2$ was chosen as a "realistic" value, as it is based on an interpretation of pumping tests on the GRT-2 well in Rittershoffen [57]. The other value of $1E-12\,\mathrm{m}^2$ was chosen to test the response of the system to a much higher permeability (model D). Hence, model A and model D represent end-member scenarios with the least and largest effects on fluid flow expected, respectively. With a much higher permeability at the eastern border fault (compared to the western fault; model E), we have tested if a one-sited increase in fluid velocities can cause a shift in fluid flow directions (and lead to an upflow of fluids in the western parts of the graben as proposed by various authors, e.g., [12, 13, 18, 29]). Since we do not have graben-wide information on the internal structural variability of the faults (e.g., on their differentiation into fault cores and damage zones with finite widths), they are modelled with a horizontally and vertically homogeneous permeability value acting across a homogeneously wide domain. To further amplify the difference in the tested scenarios, the two permeability values have been coupled with two different values for fault width (1 and 10 m, respectively). With the different scenarios tested (Table 2), we attempt to systematically quantify the sensitivity of the hydraulic and thermal regime across the entire study area to variations in the hydraulic behavior of the faults.

2.4. Boundary Conditions. The base and the lateral model boundaries are defined as no-flow boundaries in terms of fluid flow. Atmospheric pressure (0.1 MPa) is assigned to the top of the model as upper hydraulic boundary condition. Thus, the hydraulic head is fixed and it is equal to the topography (Figure 1; etopo1, [23]). The system is modelled as being fully water-saturated. Accordingly, largest pressure heads are prescribed in areas of highest elevations corresponding to up to 1070 m in the Black Forest and the Vosges Mountains in the SW and SE model area (Figure 1). Lowest pressure heads correspond to elevations of 100-200 m along the Rhine river bed (Figure 1). Despite being a simplification of the real surface hydraulic system, our choice of hydraulic boundary conditions provide a first-order approximation of the surface regional flow as believed to occur in the graben (e.g., [13]).

At the surface, the annual average surface temperature is assigned as upper thermal boundary condition (Figure 5(a)). High-resolution measurements of the annual average surface temperature in Germany [58] were complemented by a global data set for the French part of the model area [59]. Accordingly, highest average surface temperatures of 11°C are found in the URG, while coldest average surface temperatures of 5°C characterize the topographic highs in the Vosges Mountains and the Black Forest.

Table 2: Fault parameterization in the different model scenarios.

Model	Description	Fault width (m)	Permeability W-fault (m^2)	Permeability E-fault (m^2)
A	No discrete faults	/	/	/
B	Thin faults	1	$5E-14$	$5E-14$
C	Wide faults	10	$5E-14$	$5E-14$
D	High permeable faults	10	$1E-12$	$1E-12$
E	High permeable E-fault	10	$5E-14$	$1E-12$

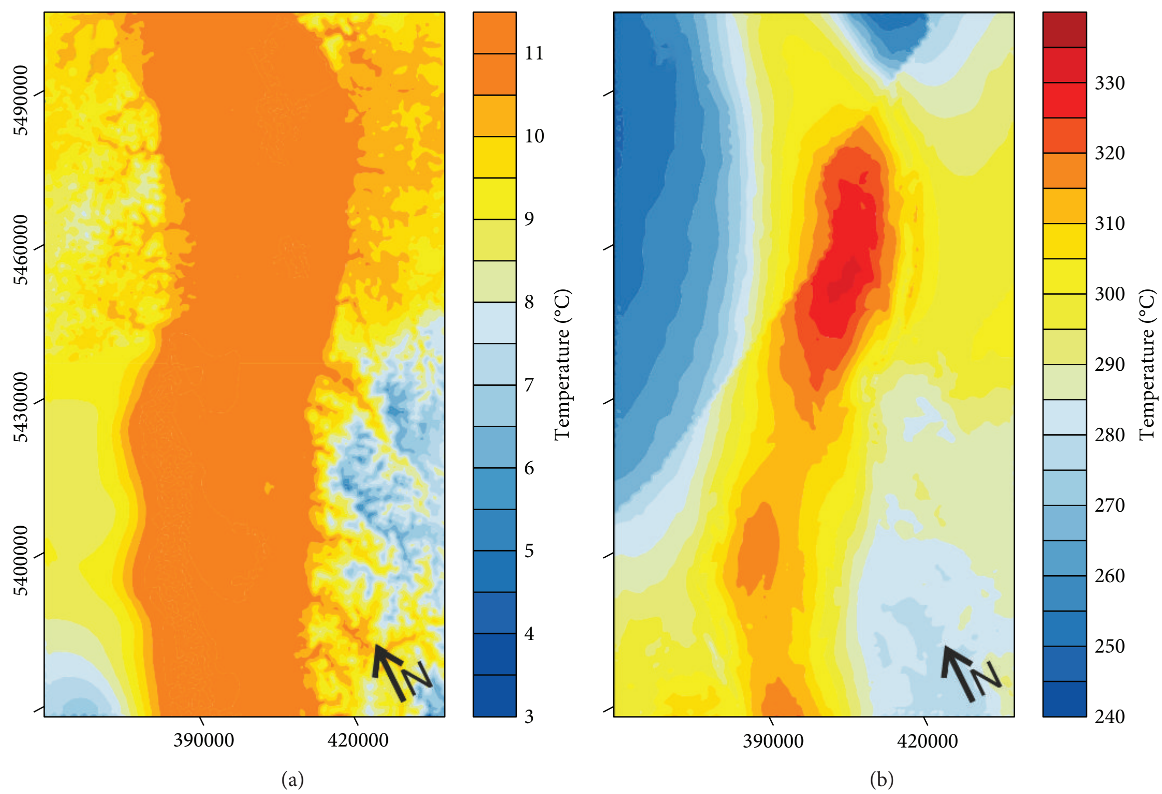

Figure 5: (a) Annual average surface temperature [58, 59] as upper thermal boundary condition and (b) temperature distribution at 8 km depth below sea level from the conductive thermal model of Freymark et al. [24] as lower thermal boundary condition. Maps are shown in UTM32N and rotated counter-clockwise by approximately 20°.

The temperature distribution of the lithosphere-scale conductive thermal model of Freymark et al. [24] at 8 km depth below sea level was extracted and assigned as lower thermal boundary condition at the base of the coupled model (Figure 5(b)). This assures that the contribution to the global heat budget from the deep crustal domain is considered. Highest basal temperatures (up to 330°C) occur below the URG in the northern central part of the model while coldest temperatures (up to 250°C) are displayed in the north-western model area. The resulting pattern of basal temperature matches the lateral distribution of radiogenic heat production of the different Variscan crustal domains, superimposed by thermal blanketing from the Cenozoic sedimentary rocks [24].

2.5. Numerical Simulation. To simulate the coupled transport of heat and fluid, we use the open-source software GOLEM [60]. Golem is a flexible, parallel scalable finite element–based simulator for thermo-hydro-mechanical process modelling in fractured porous rocks as based on the MOOSE framework [61]. In a first step, the steady-state conductive thermal field and the steady-state pore pressure distribution are calculated. The results are used as initial conditions for the thermo-hydraulically coupled simulations. As proposed by Kaiser et al. [62], we assume that forced convection is largely suppressing free convection in this setting of high gradients in hydraulic head (here equal to topography). Thus, only pressure-driven advective heat transport is considered while fluid density and viscosity are assumed constant in our simulations. The coupled fluid and heat transport is calculated by solving the equations based on conservation of (1) fluid mass, (2) fluid momentum (here implemented as a linearized Darcy's law), and (3) internal energy as

$$\frac{\phi}{k_f}\frac{\partial p_f}{\partial t} + \nabla \cdot \underline{q_D} = 0, \quad (1)$$

$$\underline{q_D} = -\frac{\underline{\underline{k}}}{\mu_f} \cdot \left(\nabla p_f - \rho_f \underline{g} \right), \quad (2)$$

$$\frac{\partial\left((\rho c)_b T\right)}{\partial t} + \nabla \cdot \left(\rho_f c_f \underline{q_D} \cdot T - \lambda_b \nabla T \right) = H, \quad (3)$$

with temperature T, time t, porosity φ, fluid modulus k_f, pore fluid pressure p_f, Darcy velocity q_D, permeability k, fluid viscosity μ_f, fluid density ρ_f, gravity acceleration g, bulk specific heat $(\rho c)_b$, bulk thermal conductivity λ_b, specific heat capacity of the fluid c_f, and radiogenic heat production H. Details of the numerical implementation are given by Cacace and Jacquey [60].

A pseudo-steady state was achieved by allowing the simulation to equilibrate for up to 2 Ma. In all runs presented in the study, we observed the reaching of pseudo-steady conditions after approximately 700 ka (Figure 6). These 700 ka represent a numerical simulation time, namely, the time after which quasi-steady-state conditions were achieved (in terms of modelled temperature). At this stage, it can be assumed that the interaction of all hydraulic and thermal controlling factors (implemented boundary conditions, physical properties, etc.) was effective throughout the complete model domain. Hence, allowing for steady-state conditions to appear is a prerequisite for fully assessing and understanding these interactions (in terms of fluid flow fields and related temperature variations).

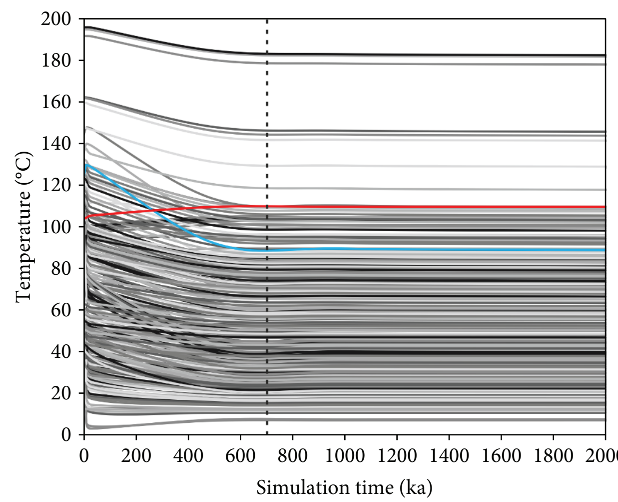

Figure 6: Temperature evolution with ongoing simulation time for model scenario B. Each line represents a point inside the model at which a temperature measurement is available. In total, 314 temperature measurements were available for this study [33, 63–68]. Exemplarily, two different trends are marked in blue and red. For more details, refer to the main text.

3. Results

3.1. Hydraulic Field of the URG. The fluid flow field calculated based on the distribution of hydraulic properties and the hydraulic boundary conditions is exemplarily described for model scenario B (Table 2; Figures 7 and 8).

In general, all model scenarios show a regional fluid flow from the surrounding basement into the sedimentary infill of the URG (Figures 7, 8, and 9(b)). Along the main border faults, fluids flow downward as, for example, west of Soultz-sous-Forêts (Figures 7(b) and 9(b)), but locally also upward (Figure 7(b)). Inside the URG, most of the basin-wide fluid flow is perpendicular to the rift axis (Figure 7(a)). In the rift center, streams from NW and SE merge, further flow towards N/NE (Figure 7(a)), and thereby form a pronounced upflow axis (Figures 7(b), 8, and 9(b)). In the central model area (compare Figure 1), this upflow axis is located near to the E border fault (Figures 7(a), 8, and 9(b)), while in the northern model area it is located close to the center of the URG (Figures 7(a) and 8).

For the entire suite of model scenarios (Table 2), predicted fluid flow velocities range from a minimum of $2.7E-8$ m/year within the basement to a maximum of 5.2 m/year in the sedimentary infill of the URG (Table 3). Even higher fluid flow velocities are predicted for the fault planes (max. 54 m/year; Table 3).

Compared to the fluid flow field of scenario B, the simulation without discrete faults (model scenario A; Table 2) shows no differences in the described basin-wide fluid flow trends, except for the fact that no fluid flow is predicted along the location of the main border faults (Figures 9 and 10(a)).

For model scenarios C, D, and E, differences in fluid flow velocity and directions are predicted locally along the main border faults (Tables 2 and 3; Figures 9 and 10). As the faults have a higher permeability than most of the surrounding geological units (models B-E), they provide preferential pathways for fluid flow. The higher the fault permeability, the higher the computed flow velocities inside the fault (Table 3). At the same time, the existence of such pathways generally enforces the downward directed flow, i.e., the infiltration rates in their direct vicinity (compare Figures 10(a) and 10(d)). This deep infiltration effect reaches even into the basement west of the fault for the scenario with an extremely conductive western fault (end-member model D). This model also shows that strong downward flow related to the fault hardly affects the basement east of the fault while it reduces the flow across the fault into the sediment fill of the graben. In general, fault-induced changes in the overall, graben-wide flow dynamics are hardly visible even when considering a very high permeability ($1E-12\,\mathrm{m}^2$) at one (Figure 9(e)) or both border faults (Figure 9(d)).

In contrast to the sensitivity of the flow fields with regard to fault permeability, variations of the fault width as chosen in the range of 1 to 10 m have no significant effect on the hydraulic field (Figures 9(b), 9(c), 10(b), and 10(c)).

The comparison of model scenarios differing in the parametrization of the main border faults allows us also to uncover characteristics of the regional fluid flow field that are common to all models and thus independent of the fault behavior. Given the chosen setup of the models

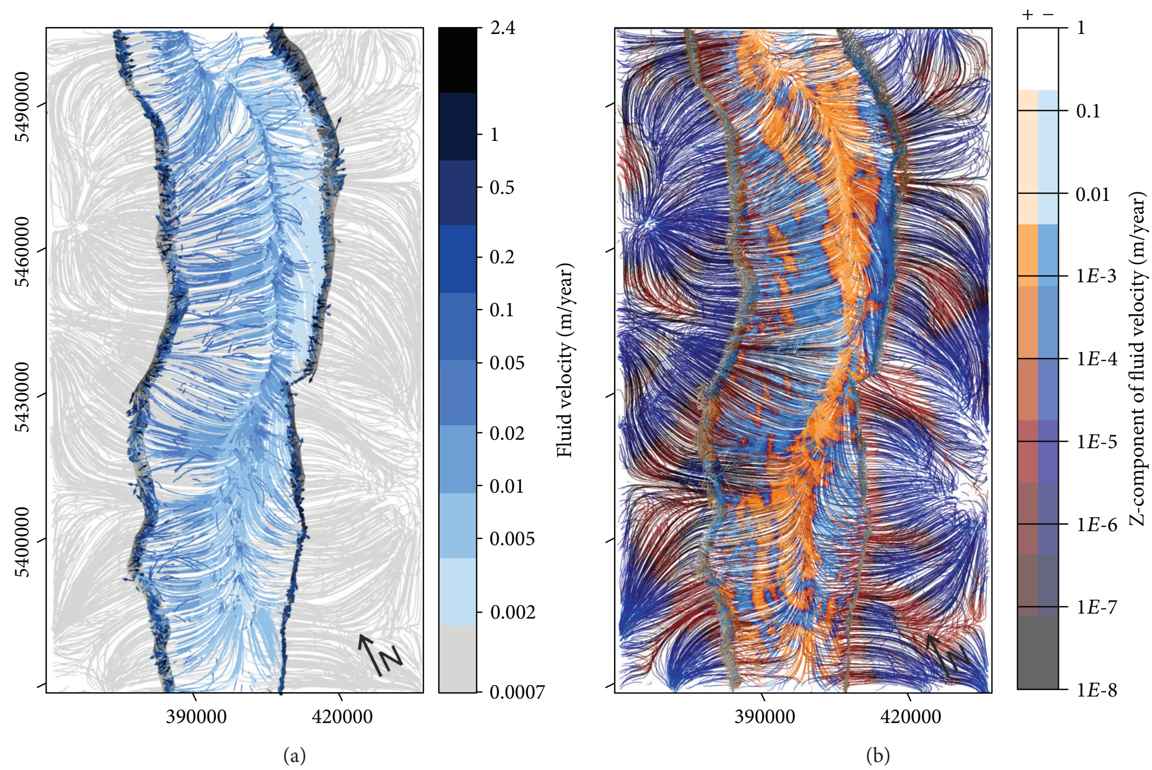

FIGURE 7: Hydraulic field (stream lines) of model scenario B, taken as exemplary for all scenarios where border faults have been implemented. (a) Fluid velocities and (b) z-component of the fluid velocity that differentiates the flow into upward (red colors) and downward (blue colors) flow. For both (a) and (b), the colored flow lines are representative for the entire depth range of the model. Maps are shown in UTM32N and rotated counter-clockwise by approximately 20°.

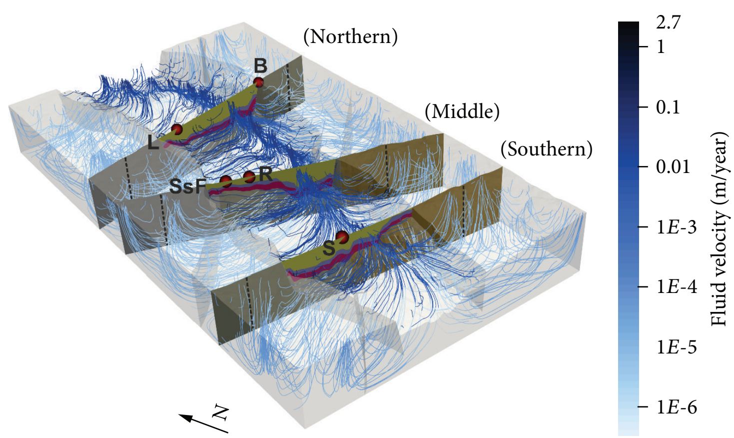

FIGURE 8: 3D fluid flow illustrated exemplarily for model scenario B. Locations of the cross sections were chosen to run through active geothermal power plants and geothermal exploration areas (L: Landau; B: Bruchsal; SsF: Soultz-sous-Forêts; R: Rittershoffen; S: Strasbourg; vertical exaggeration ×2). A zoom into the central part of the middle cross section (between vertical dashed lines) is presented in Figures 9 and 10. Details of the northern and southern cross sections are presented in the Supplementary Material 1.

in terms of hydraulic parametrization and boundary conditions, we find

(1) a basin-wide fluid flow perpendicular to the rift axis from the graben shoulders to the rift center

(2) a N/NE-directed flow in the central parts of the rift

(3) a pronounced upflow along the rift central axis, where N/NW- and E/SE-directed streams merge. In the northern and southern model area, the pronounced upflow is modelled in the center of the

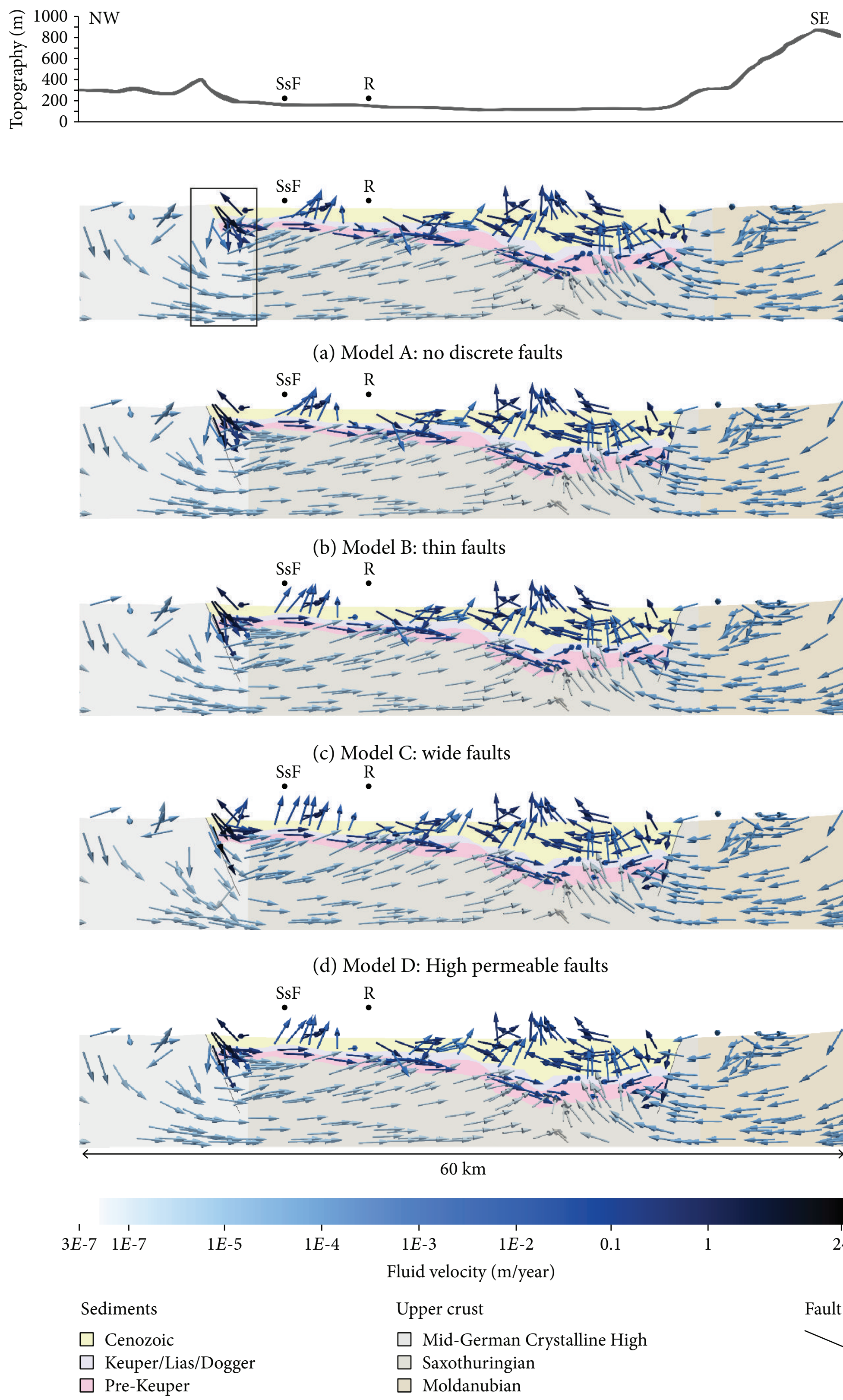

(e) Model E: High permeable E- faults

Figure 9: Fluid flow scenarios visualized for the central model area along a section crossing Soultz-sous-Forêts and Rittershoffen (for location refer to Figure 8; for model explanation, refer to Table 2). On top, the topography and thus the assigned hydraulic head are shown. Rectangle in (a) shows the area zoomed into in Figure 10.

Table 3: Simulated fluid velocity ranges for each model scenario and geological unit in m/year.

Model scenario	Cenozoic		Keuper/Lias/Dogger		Pre-Keuper		Crust		Faults	
	Min	Max	Min	Max	Min	Max	Min	Max	Min	Max
A	$4.9E-4$	5.1	$1.4E-5$	$6.1E-2$	$6.3E-5$	$8.3E-2$	$5.6E-8$	$9.3E-4$	/	/
B	$5.0E-4$	5.1	$8.9E-6$	$5.9E-2$	$7.4E-5$	$8.6E-2$	$5.7E-8$	$9.3E-4$	$1.2E-4$	4.3
C	$5.3E-4$	5.1	$2.0E-5$	$4.8E-2$	$2.9E-4$	$1.4E-1$	$5.5E-8$	$9.3E-4$	$5.5E-5$	3.6
D	$7.3E-4$	5.2	$1.2E-5$	$8.0E-2$	$2.3E-4$	$3.6E-1$	$3.8E-8$	$9.3E-4$	$4.6E-3$	54
E	$7.3E-4$	5.2	$1.3E-5$	$4.8E-2$	$1.9E-4$	$1.6E-1$	$2.7E-8$	$9.3E-4$	$4.2E-4$	42

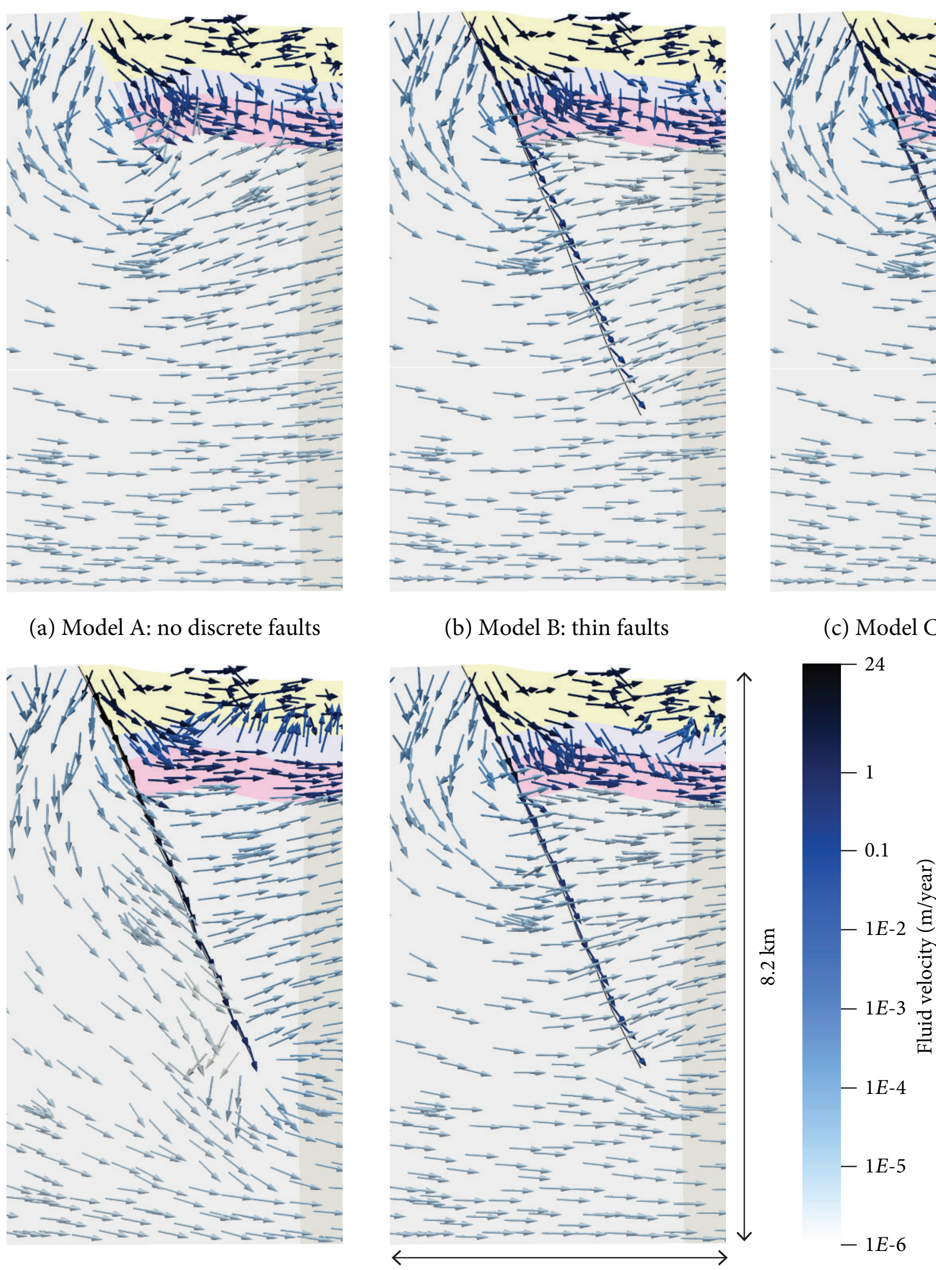

(a) Model A: no discrete faults (b) Model B: thin faults (c) Model C: wide faults

(d) Model D: High permeable faults (e) Model E: High permeable E-fault

Figure 10: Fluid flow at the W border fault in the central model area for different model scenarios (for location refer to Figure 9; for model explanation refer to Table 2, color code for geological units as in Figure 9).

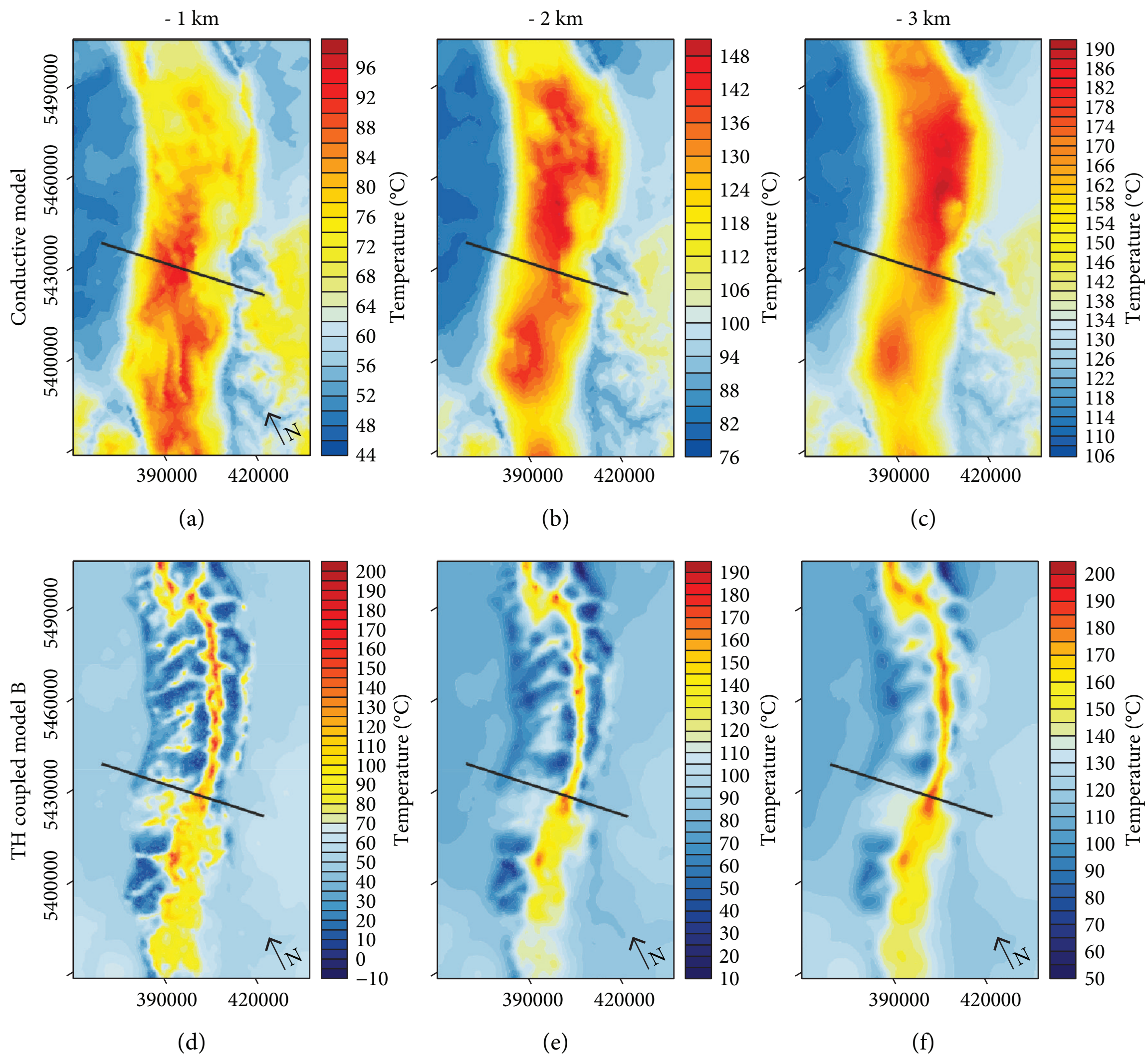

Figure 11: Temperature distribution at 1, 2, and 3 km b.s.l. depth below the URG predicted by the simulation of purely conductive heat transport (a, b, c) and by the simulation of coupled heat and fluid transport (exemplary model scenario B; d, e, f). The black line indicates location of the cross section shown in Figure 12. Maps are shown in UTM32N and rotated counter-clockwise by approximately 20°.

URG. In contrast, in the central model area the upflow is predicted near the eastern border fault

(4) a fluid flow which is partitioned between the upper Cenozoic aquifer and the deeper Permo-Mesozoic aquifer by the Mesozoic aquitard with highest flow velocities in the upper aquifer. Fluid flow is slowest in the Mesozoic aquitard and the crystalline basement (Table 3)

3.2. Thermal Field of the URG. Considering the additional heat transport by fluid flow results in clear differences in predicted temperature distribution when compared to a purely conductive model ([24], initial thermal conditions in this study). Figure 11 illustrates these differences exemplarily by comparing the temperature distributions at 1, 2, and 3 km depth below sea level predicted by the conductive simulation and by the simulation of coupled heat and fluid transport (exemplary model scenario B). It is evident that the temperature range at the same depth level is different for the two types of models and that the wavelength of temperature variations is considerably smaller in the model of coupled heat and fluid transport.

The initial thermal field as derived from a purely conductive thermal model (Figures 11(a)–11(c)) is characterized by a long-wavelength thermal anomaly in the URG, caused by (1) the higher basal heat input in response to the high radiogenic heat production of the Saxothuringian upper crust and (2) the thick thermally low conductive sediments [24]. Temperature maxima shift from the southern model area at shallow depth (Figure 11(a)) to the northern model area at greater depth (Figures 11(b) and 11(c)), which is related to the thickness distribution of the insulating Cenozoic sediments. At a depth of −3 km (Figure 11(c)), the thermal blanketing effect of the thick sediments in the North has a much stronger effect than at −1 km.

In contrast, the temperature distributions predicted by the coupled simulations of heat and fluid transport

(Figures 11(d)–11(f)) reflect the fluid flow directions. Colder temperatures are predicted along the borders of the URG, where cold water is infiltrating the system (Figure 12). Higher temperatures are predicted around the center of the rift, where flows from the E and W borders merge and circulate upward due to forced convection.

The most significant positive thermal anomaly is predicted at approximately the center of the URG caused by a pronounced upflow parallel to the graben axis (Figure 12). In addition, smaller anomalies are predicted that spatially correlate with the geothermal exploitation areas of Soultz-sous-Forêts (Figure 12(b)) and Bruchsal (Supplementary Material 1). Those thermal anomalies are caused by local forced convective upflow inside the Cenozoic sediments in addition to slightly upward-flowing fluids inside the basement (Figure 9). Such an upflow is also predicted for Rittershoffen (Figure 12(b)) and Landau (Supplementary Material 1). However, in these areas the upflow in the Cenozoic sediments is less pronounced than in the areas of Soultz-sous-Forêts and Bruchsal, causing thermal anomalies of smaller magnitudes.

Depending on the different fault configurations tested (Table 2), further differences emerge also for the temperature distribution in the respective models of coupled heat and fluid transport. We have analyzed predicted temperatures at a constant depth of 3 km below sea level, but at different distances with respect to the western border faults to compare the different models. As expected, the largest differences in modelled temperatures are observed between the end-member scenarios (models A and D) at smallest distances from the fault center (10 m): these scenarios differ by <9°C in the absolute temperatures predicted. At a distance of 5 km from the border fault, however, the end-member scenarios differ only by 1-2°C. All other scenarios tested differ by <2°C in absolute temperatures, regardless of the distance to the fault center. We take these modelling results as an indication that the graben-bordering faults can be responsible for observed thermal anomalies in their direct proximity (at distances of <5 km). Thermal anomalies occurring in the central parts of the graben (at >5 km distance), however, require additional heterogeneities in hydraulic and thermal properties (as induced by lithological variabilities or additional faults and fracture zones not yet implemented in the model). While such border-fault-related variations in hydraulic properties influence temperatures only locally, it has to be emphasized that the coupled simulations in general reveal that the component of fluid flow results in first-order variations in the resulting 3D regional thermal configuration with respect to purely conductive heat transport (Figure 12).

4. Discussion

4.1. Observational Evidence. Because of its scale and due to a scarcity of relevant information, it is difficult at this stage to validate the presented regional models with observations. The modelled fluid dynamics, however, manifest themselves in local upflow, respectively, downflow, areas which can be compared to the locations of mineral and thermal springs

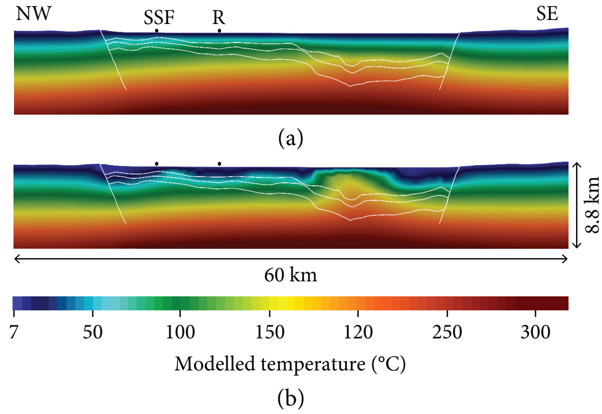

Figure 12: Cross sections through the (a) initial conductive thermal model and (b) coupled thermo-hydraulic model scenario B (location of cross section as for Figure 9; SsF: Soultz-sous-Forêts; R: Rittershoffen).

(Figure 13; [69–71]) as well as observed artesian conditions (data only available east of the river Rhine; Figure 13; [72]).

Comparing those observations with the modelled Z -component of fluid flow velocity, a spatial correlation is visible between modelled upflow areas and observed springs (e.g., model scenario B in Figures 7(b) and 13). Most of the observed springs spatially coincide with predicted upflow areas, whereby the correspondence is more evident in the northern parts of the model area than in the south.

The model, however, does not predict upflow at all locations of mineral and thermal water springs or observed artesian conditions. Most deviations of the model from these observations are located on the graben shoulders, where modelled fluid flow velocities are significantly lower (down to $5E-8$ m/year; Figure 7(a)) and boundary effects near the closed model boundaries are likely to occur. Such discrepancies between the regional model and local observations can be related to the limited structural resolution of the model that, given the large lateral extent, does not integrate details of the local lithological differentiation and fracture and fault networks. To fully explain and reproduce these local observations, further studies resolving these local conditions will be required.

Another general feature of our findings is that the modelled upflow axis spatially coincides with the location of the river Rhine (Figure 13). This shows that not only the real river path follows the gradient of lowest topography, but that this area of maximum discharge is also the domain where uprise of warm fluids is strongest in response to the 3D variation of hydraulic pressure in the subsurface.

One of our major interests initiating this study was in the assessment of the influence of groundwater flow on the thermal field. We have already shown that the difference in temperatures predicted by the coupled thermo-hydraulic models with respect to a purely conductive thermal model is significant. For a comparison with observed thermal anomalies, there is a large number of temperature measurements available at boreholes spread over much of the central URG (314 temperature measurements from 75 wells [33, 63–68];

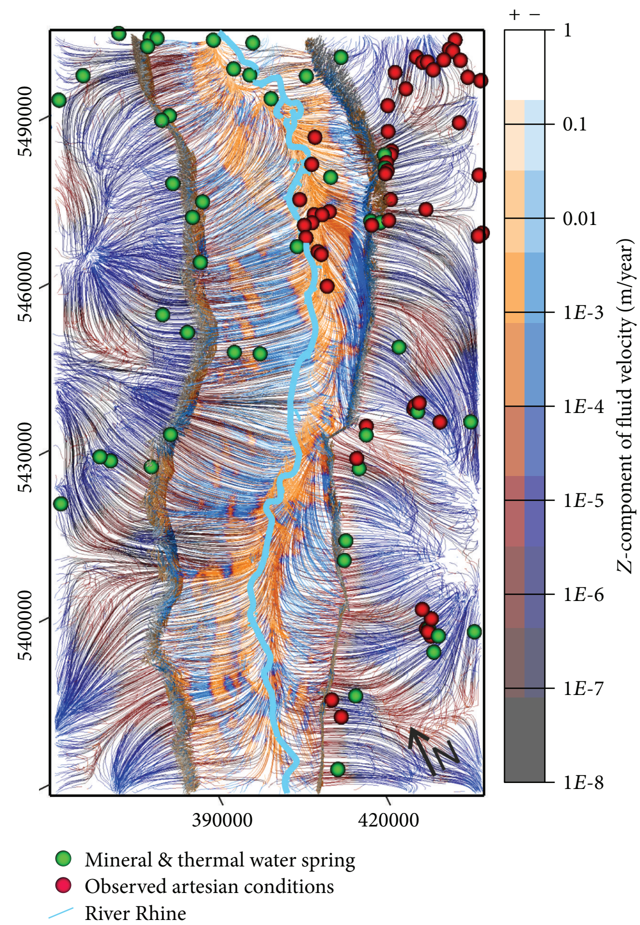

Figure 13: Observed mineral and thermal water springs (green; [69–71]), observed artesian conditions (red; only available for East of the Rhine; [72]) and the river Rhine (light blue line) on top of the Z-component of the fluid flow velocity predicting upflow areas in red/orange colors (model scenario B, compare Figure 7(b)). The map is shown in UTM32N and rotated counter-clockwise by approximately 20°.

Figure 14). Only temperature data of best and good quality according to the respective author [33, 63–68] were used, while hydraulically disturbed temperature logs were not considered. Those temperature measurements are available with different spatial coverage for different wells and regionally show a large spatial variability in absolute values. For example, south of Strasbourg measured temperatures in 2 wells, which are located 1 km apart from each other, show a difference of 32°C at the same depth level. Beside these horizontal variations, measured temperatures show large variations with depth. For example, in one of the wells south of Strasbourg, two measurements at a vertical distance of 23 m show a temperature difference of 15°C.

One trend that can be derived from the calculated temperature differences (simulated minus observed temperature; Figure 14) is that close to the western border of the graben, modelled temperatures tend to be too low. However, also too high temperatures are predicted distributed over the whole model area. Strongest misfits (positive and negative) are located at a depth range between 700 and 2000 m below sea level. Comparing different well logs, several trends are evident. For some wells in the South, calculated temperatures underestimate observed values in the upper part, while the fit to observed temperatures in the deeper parts is better. In contrast, for some wells, as for example along the eastern border fault, predicted and observed temperatures fit very well in the upper parts, but the model is too cold in the deeper parts.

As, in general, the modelled temperatures are too low at the borders of the URG, the effect of the hydraulic upper boundary condition must be discussed. By assigning the hydraulic head to the topography, large hydraulic gradients are prescribed at the borders of the graben. These high gradients likely lead to an overestimated cooling effect. However, measured hydraulic head data show the same regional trends as the topography, which means that the modelled trends in imposed fluid direction can be regarded as meaningful. It is rather the absolute temperature values that are likely too low due to overestimated fluid velocities.

Figure 15 shows exemplarily the comparison of temperatures measured in two different wells with temperatures that were predicted for the same location by the conductive and the TH coupled model scenario B. It is evident that the temperature profile of Eschau 06 (Figure 15(a)) can be reproduced only in the shallow and in the very deep parts, while the small-scale variations between −400 and −1400 m depth cannot be resolved with the regional models. In the shallow parts of this well, the prediction of the TH coupled model is even better than the purely conductive model. In contrast, the temperature log of Bruchsal 2 in the northern model area (Figure 15(b)) is well reproduced by both models (coupled and purely conductive) in the upper 1300 m, but a discrepancy between measurement and simulations is obvious in the deeper parts. Whereas the TH coupled model is colder than the measured temperatures, the conductive model is too warm in the upper Keuper/Lias/Dogger unit and too cold below −1750 m depth. Both regional models cannot fully resolve the small-scale variability in measured temperature.

Thus, our comparison of modelled and measured temperatures reveals discrepancies that cannot be correlated with certain predefined components of the model. The spatial variability of temperature misfits is much smaller in scale than the spatial extent of model units and major trends in boundary conditions. Hence, changing the parametrization of the model in its current structural form and resolution would not improve the overall fit. Neither would a more detailed analysis of misfits lead to additional conclusions with respect to regional fluid flow trends (as controlled by the border faults in particular). Improving the fit of the model would require implementing local heterogeneities in hydraulic and thermal properties as could be related to lithological variabilities and the existence of fractures and faults.

4.2. Modelling Approach and Related Insights into the Regional Fluid Flow Field. The models presented in this paper are the first 3-dimensional representations of deep regional fluid flow and related thermal anomalies for the area of the central URG. The 3D numerical models have been set up in a way to implement (i) major hydraulic and thermal rock property variations as can be derived from a data-driven geological model [24] and (ii) general trends in surface

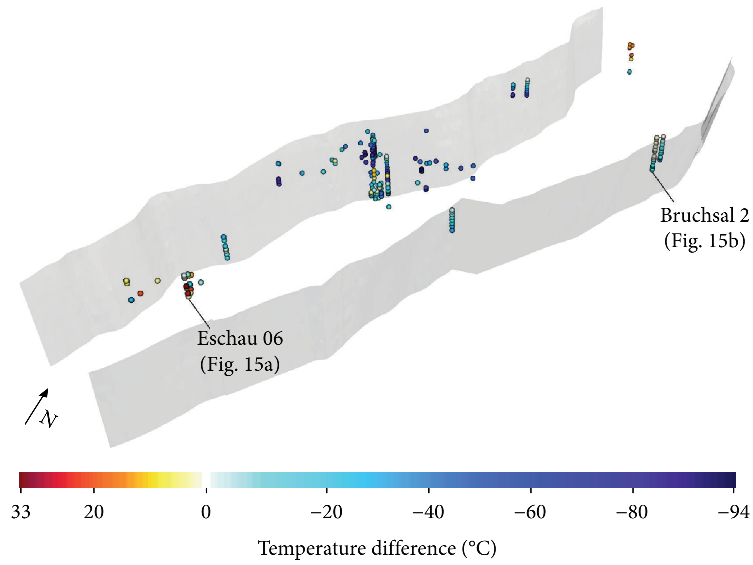

FIGURE 14: 3D perspective view on the border faults (grey shaded areas) and temperature measurement points [33, 63–68]. Points are color-coded according to the temperature differences (with model scenario B simulated minus observed temperature) (vertical exaggeration ×3; maximum depth of the faults 6 km b.s.l.).

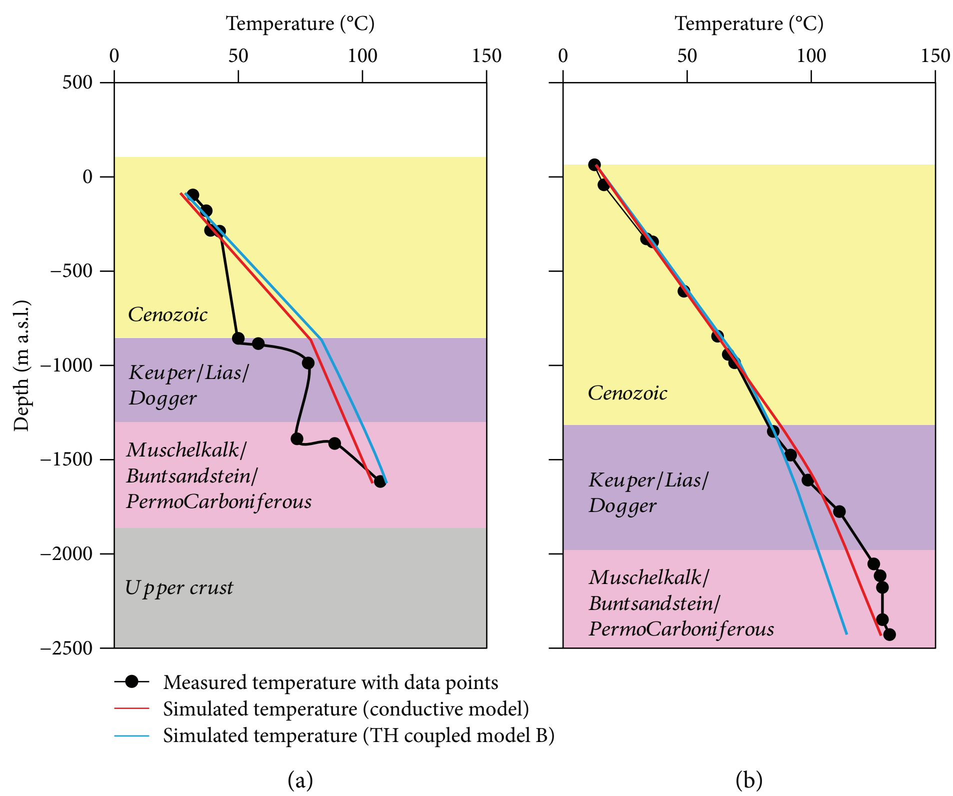

FIGURE 15: Modelled geological layers with measured and simulated temperatures (conductive and TH coupled model scenario B) at (a) Eschau 06 south of Strasbourg (measured temperature data from [68]) and (b) Bruchsal 2 (data from [67]).

temperature and pressure conditions assumed to control the subsurface thermo-hydraulic system.

The different model scenarios presented in this study have shown that major graben-bounding faults influence the fluid flow locally depending on their permeability, but do not significantly change the basin-wide hydraulic field. We are able to identify aspects that are common to all model scenarios and thus define typical characteristics of the regional fluid flow.

In agreement with former studies (e.g., [13, 18, 29, 73]), our simulations predict recharge dominating in the high-topography areas flanking the URG and discharge prevailing in the center of the graben (Figures 7–9). Due to the high hydraulic gradient and the discontinuity between high-permeable sediments and the low-permeable basement, fluid flows downward along the borders of the rift into the sedimentary infill. In addition, fluids migrate slowly through the deep basement from the areas outside the URG thereby entering the sedimentary infill in areas characterized by low hydraulic potential (Figure 9).

The most prominent difference of our 3D coupled simulations to former 2D studies is the location of the dominant upflow axis, which in our simulations locates in the (eastern) center of the URG. This result is in contrast to conclusions derived from previous studies predicting preferential upflow across the western center of the URG (e.g., [12, 13, 18, 29]). The upflow axis in the presented study results from pressure-driven forced convective processes occurring throughout the basement and the overlying porous sediments due to the lowest hydraulic potential being located in the center of the URG (compare Figure 1). Accordingly, where the lowest hydraulic potential is imposed near the eastern border fault (as in the central model domain; Figure 1), the upflow axis is shifted towards the eastern center of the URG (Figures 1 and 7).

This difference to previous 2D numerical simulations (e.g., [12–14, 16–18]) results from the consideration of the three-dimensional pressure variations in our numerical model, whereas former 2D models assumed cylindrical symmetry, and thus constant pressure conditions, perpendicular to the plane of the modelled section. With a limited 2D perspective on the topographical differences between the eastern (higher) and western (lower) graben shoulders (Figure 9), one might expect a prominent east-to-west-directed flow in the graben and upflow toward the west (cf. [13]). In contrast, due to its 3D nature, our model also captures the pressure-driven north/northeastward-directed component of the flow (Figure 7) caused by the overall south-north topographic gradient (i.e., the prevailing trend from the Alps to the Rhenish Massif). The resulting south-north potential is most significant inside the graben, where it also interacts with thickness maxima of the more permeable sedimentary units that tend to be located east of graben axis (Figure 3). Thus, we propose this interaction (of north-directed gradients and accumulation of sediments) to suppress E-W-directed flow due to the differences in hydraulic potentials as induced by the differently high graben shoulders.

Given that the setup of the presented regional models implies a number of simplifications, it is worth discussing how the main findings of this study concerning (i) the impact of border faults and (2) the main characteristics of regional fluid flow would be altered by changing the model input parameters.

4.2.1. Vertical Resolution and Parameterization. To test the influence of a vertically larger number of hydraulic units on the hydraulic field, we have performed the simulation presented in Supplementary Material 2. By vertically differentiating three additional sedimentary layers inside the central URG, however, we find the same main characteristics of the hydraulic field as in the series of the simplified models presented above. As mentioned in Section 4.1, the differentiation of hydraulic and thermal properties on the basis of regionally traceable geological units is not suitable to correctly reproduce local observations. The heat production of the Saxothuringian upper crust, for instance, is modelled as an assumed average value on a regional scale of $2.5\,\mu W/m^3$ [47], but locally increases up to $7\,\mu W/m^3$ [74, 75]. An important example for large regional variability in hydraulic parameters would be the facies variations inside the sedimentary units not accounted for in this study. Hence, addressing questions concerning the fluid dynamics of a specific site in the graben system requires setting up local models describing property variability with a critical precision. Such regional models presented here would, however, be suitable to providing the required boundary conditions for local models.

4.2.2. Fault Parameterization. Another simplification of the presented models concerns the structural and parametric representation of the main border faults. Cacace et al. [3], for example, studied the influence of the inner structure of a fault zone on the hydraulic field and demonstrated that a tight fault core inside a permeable damage zone can cause local differences compared to simulations implementing a homogenous fault. Moreover, the depths of the border faults in our sensitivity analysis represent a compromise between the proposed depths of former studies. Although some models of the area of Soultz-sous-Forêts (e.g., [30, 73]) propose a depth of −6 km for the main border faults as well, most modelling studies integrate the border faults to an average depth of around −3 km (e.g., [13, 16]). In contrast, interpretations of deep seismic lines propose a depth of −15 km and even deeper for the main border faults (e.g., [76–78]). Our choice to limit the faults to −6 km depth is motivated by the assumption that permeability generally decreases with depth so that the fault loses its role as a fluid pathway at larger depths. In general, the way we have modelled the main border faults characterizes the presented series of models as a conceptual approach towards a better understanding of the overall impact of fault properties on the graben-wide fluid flow. The models thus are not suitable for correctly reproducing local observations and predicting processes at specific locations near the fault (which would require additional local information).

4.2.3. Advective vs. Convective Heat Transport. One more simplification of the presented TH coupled simulations is that only pressure-driven advective heat transport is considered while fluid density and viscosity are assumed constant. Previous studies proposed free convection (1) in the crystalline crust below the URG (e.g., [14]), (2) at the basement/-sediment-boundary (e.g., [12, 18]), and/or (3) in the fault zones inside the URG sediments (e.g., [8, 30]). First of all, even without allowing for density-driven flow to occur in our models, there is a large number of smaller-scale convection systems predicted for the domains of the sediments and the basement as well as across the basement/sediment-boundary (Figure 9). Hence, no thermal and density-driven flow is required to explain such observations described by previous studies. In addition, it is worth mentioning that the conductive thermal field used as initial model predicts the highest deep temperatures in the eastern part of the URG (Figures 5(b) and 11(c)). In consequence, buoyancy-driven upflow, if existing, should occur in the eastern center of the URG and downflow at the borders and shoulders of the rift. Thus, the main characteristics of the flow regime would not be changed by considering temperature-dependent fluid density and viscosity.

Beside these arguments inherent in the modelled situation, the formation of density-driven convection cells in general requires very specific conditions with respect to the structure of an aquifer and the interaction with hydraulic-head imposed pressure gradients so that previous studies concluded that free convection is less likely to occur on the regional scale in nature than forced convective flow [62]. A differentiation of the URG sediments into a larger number of geological units as would be advisable according to local observations (e.g., [32]) would result in thinner aquifers divided by additional aquitards. As a result of this increased vertical heterogeneity, free convection inside the sedimentary infill of the URG would be even less likely to occur. Bjørlykke et al. [79], for instance, have shown that impermeable layers of only <1 m thickness already can split or even inhibit the formation of convection cells.

Beside temperature dependency, also variations in fluid salinity can change the density of the fluid. However, it is shown that salinity is quite heterogeneously distributed across the URG (e.g., 4-20 g/l at the western border reaches up to 120-200 g/l in Bruchsal and Bühl [12]). Thus, we assumed a constant fluid density on a pure water approach in our study, as we did not have an appropriate data base for implementing such complexity into the model.

4.2.4. Inner-Rift Faults. Whatever the physical process controlling fluid flow (free or forced convection) in specific parts of the graben system, it is the distributed occurrence of smaller-scale faults and fractures that seems to be decisive for providing the hydraulic pathways (e.g., [8, 18, 30]). For example, in Soultz-sous-Forêts most fluid flow is observed in the vicinity of deep fracture zones [80]. Accordingly, a 1-2 km thick hydrothermal alteration zone in the uppermost parts of the highly fractured basement is described [81, 82]. However, this thick hydrothermal alteration zone seems to be a local phenomenon [81]. In Rittershoffen, the hydrothermally altered granite has a thickness of approximately 200 m only, while no such zone is found in Landau and Insheim [81]. Given these large differences in the vertical extent of a strongly fractured basement domain and the lack of a regional coverage of such information, we had to refrain from implementing a corresponding additional unit into the model. Instead, we have chosen a constant permeability value for the crystalline crust down to a depth of −8 km that considers the existence of secondary permeability; i.e., representing a value still allows for fluid flow in the basement instead of regarding the crust completely impermeable.

Such inner-inner faults are observed across wide parts of the central URG, in particular within Triassic and deeper geological domains where convection is described to occur inside fracture systems connecting the basement with the main reservoirs, the latter being bounded by the impervious Muschelkalk (e.g., [81]). Based on our sensitivity analysis revealing that even the largest faults at the graben borders do affect the flow fields only in their immediate vicinity (as described in Section 3), we conclude that these inner-rift faults would also impose only localized modifications of the regional fluid flow (and heat transport). On the other hand, if pervading the geological units with a high spatial frequency, they might impose to the units a spatially continuous (and probably anisotropic) increase in hydraulic conductivities (secondary permeability). As mentioned above, in general more observations (such as from hydraulic leak tests) would be required to validate the hydraulic parametrization of the different geological units – with respect to both the consideration of structurally controlled pathways (faults and fractures) as well as the upscaling of average matrix permeabilities as derived from laboratory measurements on rock samples.

Whether fluid flow is occurring parallel to the URG inside the inner-rift faults (e.g., [8]) or if the faults are connected by convection perpendicular to the URG (e.g., [18]) is still debated. A larger impact on the basin-wide fluid field would anyway only be expected if there are large impermeable fault zones that act as hydraulic barriers. Peters [83] has performed a slip tendency analysis for a large number of faults with known geometries in the URG. This analysis has shown that there are only a few faults that are almost perpendicular to the maximum horizontal stress and thus have a low slip tendency and most likely a very low permeability. These faults strike predominantly in the ESE-WNW direction, i.e., almost parallel to fluid flow direction proposed by our simulations, and thus they would not significantly change the graben-wide fluid flow.

In general, previous studies (e.g., [13, 18, 29, 30, 73]) explain major thermal anomalies, such as the one at Soultz-sous-Forêts, as the result of a high basal heat flow and upward convection of deep and hot fluids within inner-rift faults. Our model demonstrates that the phenomenon of small-scale thermal anomalies may occur even without the existence of inner-rift faults. Thereby, our models do allow for upflow from the basement up into the Cenozoic (Figures 9 and 10), the latter being modelled with the highest permeability (according to laboratory derived measurements; Table 1) although locally being known as lower permeable and not influenced by fluid flow (e.g., as in Soultz-sous-Forêts [11]). It remains to be investigated why despite the overall high permeabilities supporting the upflow of warm fluids, the modelled temperatures along the western parts of the graben still tend to be too low (Figure 14).

4.2.5. Boundary Conditions. Finally, we have taken strong assumptions concerning the boundary conditions applied to the thermo-hydraulic simulations. Beside the hydraulic contrasts between the basement and the sedimentary graben fill, it is the hydraulic upper boundary condition that has a major effect on the calculated fluid flow fields (e.g., Figure 9). By assigning the hydraulic head to the topography, we assume the underground to be completely filled with groundwater and we likely overestimate the hydraulic gradients and thus fluid flow velocities and their effect on the modelled temperatures. This may also affect the time to reach steady-state conditions in the simulations. Extensive infiltration of cold water forced in areas of high hydraulic gradients could lead to an overestimation of deep cooling and a prolonged time of equilibration.

An alternative upper boundary condition would be interpolated hydraulic head data. Those data exist, however, only at certain measuring stations (e.g., data from the federal state office of the environment Baden-Württemberg), while using the completely known topographical variability to mimic hydraulic head gradients is possible for the entire model domain. Setting the hydraulic head equal to topography does not mean that we deny the existence of an unsaturated zone in the study area. Moreover, we are aware that the modelled fluid dynamics thus may locally not reproduce reality in terms of absolute values – which anyway is difficult to test given the scarcity of observations in terms of absolute fluid velocity and direction in the deep subsurface. With our modelling approach, we assume that the continuously available topographical trends mimic the shallow pressure conditions in terms of the locations of highs and lows. Compared to hydraulic head data that typically represent a subdued replica of topography, we present models with more extreme hydraulic gradients, in particular between the graben shoulders and the graben center. This imposes a maximum hydraulic effect to the main border faults that are located where the gradients tend to be largest. Hence, our conclusion that their effects on the regional fluid flow are minimal would be confirmed by applying hydraulic head data as upper boundary condition. Similarly, our main findings about regional flow directions seem to be confirmed when speculating about more realistic upper boundary conditions. Since the graben center hosts a major river system, the differences between topography and hydraulic heads there should be minimal while maximizing towards the graben shoulders. The related reduction of recharge rates from the graben shoulders towards the graben center would then be associated with a relative increase in the role of graben-parallel flow and low potentials related to larger thickness of more permeable sediments (Figure 3). Hence, setting up our models with observed hydraulic heads most probably will also lead to a pronounced north- and northeast-ward flow and the formation of an upflow axis in the graben center.

The northward flow predicted by our models casts some doubts also on the southern and northern lateral boundary conditions that are modelled as being closed to fluid flow. At the southern boundary, one would expect a stronger inflow into the modelled domain and thus even a reinforcement of the northward flow. It is more difficult, however, to speculate about the impacts of opening the northern boundary to fluid flow. The currently closed boundary does not seem to be associated with a significant upflow as could be expected at least (Figure 7(b)). A solution for the problem of appropriately setting lateral boundary conditions (given the lack of corresponding fluid pressure data) would be to set up hydraulic models that are even larger than the investigated central URG and derive locally predicted pressure conditions from these models.

5. Conclusion

In this conceptual study, we performed first 3-dimensional numerical simulations of coupled fluid and heat transport in the URG. With our focus on the influence of the main border faults on the 3D hydraulic field of the URG, we gained valuable new insights into the hydraulic system of the URG:

(1) A general northward flow is predicted for the subsurface of the URG by our model, which indicates the importance of 3D effects

(2) The main border faults are less important than the hydraulic head and the permeability contrast between sediments and basement

(3) Different permeabilities and widths of the main border faults in a geologically reasonable range have no significant effect on the graben-wide hydraulic and thermal field

(4) Upflow (forced convective) is predicted even without considering density-driven flow

(5) The regional deep fluid flow is directed from the margins (recharge at topographic highs) towards the center of the URG (discharge at topographic low)

(6) Previously proposed upflow in the western parts of the graben is difficult to explain by this model, but could be related to the difference between 2D and 3D

(7) Inner faults might play an important role – also for the thermal anomalies observed

(8) More realistic hydraulic boundary conditions would probably lead to more realistic results – however, the previously mentioned main conclusions stay valid

Finally, we strongly encourage further studies to test the influence of, e.g., the parameterization of the geological layers, density-driven flow, and more realistic boundary conditions on the hydraulic and thermal field of the URG.

Data Availability

The model data used to support the findings of this study are available from the corresponding author upon request.

Conflicts of Interest

The authors declare that they have no conflicts of interest.

Acknowledgments

The research leading to these results has received funding from the European Community's Seventh Framework Programme under grant agreement no. 608553 (Project IMAGE). In addition, we would like to thank the State Office of Geology, Raw Materials and Mining of the Freiburg Regional Council (LGRB) and the GeORG working group for providing us the 3D structural models of

Baden-Württemberg and the Upper Rhine Graben sedimentary infill. Furthermore, we would like to thank Rüdiger Schellschmidt from the Leibniz Institute for Applied Geophysics (LIAG) for providing us the temperature data of Bruchsal, Landau, and Baden-Baden.

Supplementary Materials

Supplementary 1. Cross sections for the northern and southern model area that show the hydraulic and thermal field in the areas of geothermal exploitation and exploration in Landau, Bruchsal, and Strasbourg.

Supplementary 2. Setup and results of a model with more geological units.

References

[1] T. Agemar, J. Weber, and R. Schulz, "Deep geothermal energy production in Germany," *Energies*, vol. 7, no. 7, pp. 4397–4416, 2014.

[2] A. Genter, C. Baujard, N. Cuenot et al., "Geology, geophysics and geochemistry in the Upper Rhine Graben: the frame for geothermal energy use," in *European Geothermal Congress 2016*, pp. 1–5, Strasbourg, France, 2016.

[3] M. Cacace, G. Blöcher, N. Watanabe et al., "Modelling of fractured carbonate reservoirs: outline of a novel technique via a case study from the Molasse Basin, southern Bavaria, Germany," *Environmental Earth Sciences*, vol. 70, no. 8, pp. 3585–3602, 2013.

[4] M. C. Cacas, J. M. Daniel, and J. Letouzey, "Nested geological modelling of naturally fractured reservoirs," *Petroleum Geoscience*, vol. 7, no. S, pp. S43–S52, 2001.

[5] Y. Cherubini, M. Cacace, M. Scheck-Wenderoth, and V. Noack, "Influence of major fault zones on 3-D coupled fluid and heat transport for the Brandenburg region (NE German Basin)," *Geothermal Energy Science*, vol. 2, no. 1, pp. 1–20, 2014.

[6] S. Hickman, M. Zoback, and R. Benoit, "Tectonic controls on reservoir permeability in the Dixie Valley, Nevada, geothermal field," in *Proceedings of the twenty-third workshop on geothermal reservoir engineering*, pp. 291–298, Stanford, CA, USA, 1998.

[7] C. Müller, S. Siegesmund, and P. Blum, "Evaluation of the representative elementary volume (REV) of a fractured geothermal sandstone reservoir," *Environmental Earth Sciences*, vol. 61, no. 8, pp. 1713–1724, 2010.

[8] D. Bächler, T. Kohl, and L. Rybach, "Impact of graben-parallel faults on hydrothermal convection––Rhine Graben case study," *Physics and Chemistry of the Earth, Parts A/B/C*, vol. 28, no. 9–11, pp. 431–441, 2003.

[9] C. Clauser, E. Griesshaber, and H. J. Neugebauer, "Decoupled thermal and mantle helium anomalies: implications for the transport regime in continental rift zones," *Journal of Geophysical Research: Solid Earth*, vol. 107, no. B11, pp. ETG 1-1–ETG 1-16, 2002.

[10] J. Henning Illies, H. Baumann, and B. Hoffers, "Stress pattern and strain release in the Alpine foreland," *Tectonophysics*, vol. 71, no. 1-4, pp. 157–172, 1981.

[11] D. Pribnow and R. Schellschmidt, "Thermal tracking of upper crustal fluid flow in the Rhine Graben," *Geophysical Research Letters*, vol. 27, no. 13, pp. 1957–1960, 2000.

[12] L. Aquilina, A. Genter, P. Elsass, and D. Pribnow, "Evolution of fluid circulation in the Rhine Graben: constraints from the chemistry of present fluids," in *Hydrogeology of Crystalline Rocks*, I. Stober and K. Bucher, Eds., pp. 177–203, Springer, Dordrecht, Netherlands, 2000.

[13] C. Clauser and H. Villinger, "Analysis of conductive and convective heat transfer in a sedimentary basin, demonstrated for the Rheingraben," *Geophysical Journal International*, vol. 100, no. 3, pp. 393–414, 1990.

[14] L. Guillou-Frottier, C. Carrė, B. Bourgine, V. Bouchot, and A. Genter, "Structure of hydrothermal convection in the Upper Rhine Graben as inferred from corrected temperature data and basin-scale numerical models," *Journal of Volcanology and Geothermal Research*, vol. 256, pp. 29–49, 2013.

[15] B. Hoffers, "A model for hydrothermal convection in the Rhine graben and its tectonic implications," *Tectonophysics*, vol. 73, no. 1–3, pp. 141–149, 1981.

[16] C. Lampe and M. Person, "Advective cooling within sedimentary rift basins—application to the Upper Rhinegraben (Germany)," *Marine and Petroleum Geology*, vol. 19, no. 3, pp. 361–375, 2002.

[17] M. Person and G. Garven, "Hydrologic constraints on petroleum generation within continental rift basins: theory and application to the Rhine Graben," *AAPG Bulletin*, vol. 76, no. 4, pp. 468–488, 1992.

[18] D. Pribnow and C. Clauser, "Heat and fluid flow at the Soultz hot dry rock system in the Rhine Graben," in *Proceedings World Geothermal Congress 2000*, pp. 3835–3840, Kyushu-Tohoku, Japan, 2000.

[19] D. Bächler, *Coupled Thermal-Hydraulic-Chemical Modelling at the Soultz-sous-Forêts HDR Reservoir (France), [Ph.D. Thesis]*, Swiss Federal Institute of Technology Zurich, 2003.

[20] P. Baillieux, E. Schill, and C. Dezayes, "3-D structural regional model of the EGS Soultz site (northern Upper Rhine Graben, France): insights and perspectives," in *36rd Workshop on Geothermal Reservoir Engineering*, pp. 1–9, Stanford, CA, USA, 2011.

[21] P. Baillieux, E. Schill, J.-B. Edel, and G. Mauri, "Localization of temperature anomalies in the Upper Rhine Graben: insights from geophysics and neotectonic activity," *International Geology Review*, vol. 55, no. 14, pp. 1744–1762, 2013.

[22] C. Kosack, *Inverse Modelling of the 2005 Tracer Circulation Test at Soultz-sous-Forêts, France*, Diplomarbeit, RWTH Aachen, 2009.

[23] C. Amante and B. W. Eakins, "ETOPO1 1 arc-minute global relief model: procedures, data sources and analysis," NOAA Technical Memorandum NESDIS NGDC-24. National Geophysical Data Center, NOAA, 2009.

[24] J. Freymark, J. Sippel, M. Scheck-Wenderoth et al., "The deep thermal field of the Upper Rhine Graben," *Tectonophysics*, vol. 694, pp. 114–129, 2017.

[25] M. Isenbeck-Schröter, W. Aeschbach, S. Al Najem, F. Freundt, and G. Schmidt, *Abschlussbericht TRACE Teil B*, 2016.

[26] M. Kraml, M. Jodocy, R. Grobe et al., *Verbundprojekt TRACE-Tiefen Reservoir-Analyse und Charakterisierung von der Erdoberfläche, Teil 1: Bestimmung chemischer und isotopischer Parameter von Fluiden und Gasen zur Fündigkeitsabschätzung und ihre Anwendbarkeit auf Tiefengeothermie-Projekte-Schlussbericht Teilvorhaben A: GeoThermal Engineering GmbH*, 2015.

[27] H. Pauwels, C. Fouillac, and A.-M. Fouillac, "Chemistry and isotopes of deep geothermal saline fluids in the Upper Rhine Graben: origin of compounds and water-rock interactions," *Geochimica et Cosmochimica Acta*, vol. 57, no. 12, pp. 2737–2749, 1993.

[28] B. Sanjuan, R. Millot, C. Innocent, C. Dezayes, J. Scheiber, and M. Brach, "Major geochemical characteristics of geothermal brines from the Upper Rhine Graben granitic basement with constraints on temperature and circulation," *Chemical Geology*, vol. 428, pp. 27–47, 2016.

[29] I. Stober and K. Bucher, "Hydraulic and hydrochemical properties of deep sedimentary reservoirs of the Upper Rhine Graben, Europe," *Geofluids*, vol. 15, no. 3, 482 pages, 2015.

[30] P. Baillieux, E. Schill, Y. Abdelfettah, and C. Dezayes, "Possible natural fluid pathways from gravity pseudo-tomography in the geothermal fields of Northern Alsace (Upper Rhine Graben)," *Geothermal Energy*, vol. 2, no. 1, 2014.

[31] J. Vidal, A. Genter, and J. Schmittbuhl, "How do permeable fractures in the Triassic sediments of Northern Alsace characterize the top of hydrothermal convective cells? Evidence from Soultz geothermal boreholes (France)," *Geothermal Energy*, vol. 3, no. 1, p. 8, 2015.

[32] K. I. Grimm, *Stratigraphie von Deutschland IX-Tertiär, Teil 1: Oberrheingraben und benachbarte Tertiärgebiete*, Schweizerbart, Stuttgart, Germany, 2011.

[33] K. Bär, *Untersuchung der tiefengeothermischen Potenziale von Hessen, [Ph.D. thesis]*, TU Darmstadt, 2012.

[34] GeORG-Projektteam, *Geopotenziale des tieferen Untergrundes im Oberrheingraben, Fachlich-Technischer Abschlussbericht des INTERREG-Projekts GeORG, Teil 3: Daten, Methodik, Darstellungsweise*, Freiburg im Breisgau, Germany, 2013.

[35] M. Jodocy and I. Stober, "Porositäten und Permeabilitäten im Oberrheingraben und Südwestdeutschen Molassebecken," *Erdöl, Erdgas, Kohle*, vol. 127, no. 1, p. 20, 2011.

[36] H. Plum, J. Ondreka, and V. Armbruster, *Hydrogeologische Einheiten in Baden-Württemberg*, LGRB-Informationen, 2008.

[37] GeORG-Projektteam, *Geopotenziale des tieferen Untergrundes im Oberrheingraben, Fachlich-Technischer Abschlussbericht des INTERREG-Projekts GeORG, Teil 1: Ziele und Ergebnisse des Projekts*, LGRB-Informationen, Freiburg im Breisgau, Germany, 2013.

[38] R. Jorand, C. Clauser, G. Marquart, and R. Pechnig, "Statistically reliable petrophysical properties of potential reservoir rocks for geothermal energy use and their relation to lithostratigraphy and rock composition: the NE Rhenish Massif and the Lower Rhine Embayment (Germany)," *Geothermics*, vol. 53, pp. 413–428, 2015.

[39] GeORG-Projektteam, *Geopotenziale des tieferen Untergrundes im Oberrheingraben, Fachlich-Technischer Abschlussbericht des INTERREG-Projekts GeORG, Teil 2: Geologische Ergebnisse und Nutzungsmöglichkeiten*, Freiburg im Breisgau, Germany, 2013.

[40] A. Koch, C. Clauser, A. Hartmann, V. Rath, D. Mottaghy, and R. Pechnig, *Erstellung statistisch abgesicherter thermischer und hydraulischer Gesteinseigenschaften für den flachen und tiefen Untergrund in Deutschland: Phase 1 – Westliche Molasse und nördlich angrenzendes Süddeutsches Schichtstufenland*, BMU-Projekt FKZ 0329985 (Final Report), 2006.

[41] I. Stober and K. Bucher, *Geothermal Energy - from Theoretical Models to Exploration and Development*, Springer, Berlin, Heidelberg, 2013.

[42] I. Stober and M. Jodocy, "Eigenschaften geothermischer Nutzhorizonte im baden-württembergischen und französischen Teil des Oberrheingrabens," *Grundwasser*, vol. 14, no. 2, pp. 127–137, 2009.

[43] C. Dezayes, A. Genter, I. Thinon, G. Courrioux, and B. Tourlière, "Geothermal potential assessment of clastic Triassic reservoirs (Upper Rhine Graben, France)," in *Proceedings, Thirty-Second Workshop on Geothermal Reservoir Engineering Stanford University*, pp. 28–30, Stanford, CA, USA, 2008.

[44] E. Stein, "The geology of the Odenwald crystalline complex," *Mineralogy and Petrology*, vol. 72, no. 1-3, pp. 7–28, 2001.

[45] R. Haenel, K. Fuchs, K. Von Gehlen, H. Mälzer, H. Murawski, and A. Semmel, "Geothermal investigations in the Rhenish Massif," in *Plateau Uplift*, pp. 228–246, Springer, Berlin, Heidelberg, 1983.

[46] R. Altherr, A. Holl, E. Hegner, C. Langer, and H. Kreuzer, "High-potassium, calc-alkaline I-type plutonism in the European Variscides: northern Vosges (France) and northern Schwarzwald (Germany)," *Lithos*, vol. 50, no. 1–3, pp. 51–73, 2000.

[47] H.-J. Berger, M. Felix, S. Görne et al., "Tiefengeothermie Sachsen," *Schriftenreihe des LfULG*, vol. 9, pp. 1–108, 2011.

[48] F. Surma and Y. Geraud, "Porosity and thermal conductivity of the Soultz-sous-Forêts granite," *Pure and Applied Geophysics*, vol. 160, no. 5, pp. 1125–1136, 2003.

[49] A. Krohe and G. H. Eisbacher, "Oblique crustal detachment in the Variscan Schwarzwald, southwestern Germany," *Geologische Rundschau*, vol. 77, no. 1, pp. 25–43, 1988.

[50] H. Wilhelm, A. Berktold, K.-P. Bonjer, K. Jäger, A. Stiefel, and K.-M. Strack, "Heat flow, electrical conductivity and seismicity in the Black Forest crust, SW Germany," in *Geophysical Monograph Series*, vol. 51 of Properties and Processes of Earth's Lower Crust, pp. 215–232, 1989.

[51] H. Landolt-Börnstein, *Zahlenwerte und Funktionen aus Naturwissenschaft und Technik*, Springer, Berlin, Germany, 1982.

[52] G. Caumon, P. Collon-Drouaillet, C. Le Carlier de Veslud, S. Viseur, and J. Sausse, "Surface-based 3D modeling of geological structures," *Mathematical Geosciences*, vol. 41, no. 8, pp. 927–945, 2009.

[53] M. Cacace and G. Blöcher, "MeshIt—a software for three dimensional volumetric meshing of complex faulted reservoirs," *Environmental Earth Sciences*, vol. 74, no. 6, pp. 5191–5209, 2015.

[54] J. Böcker and R. Littke, "Thermal maturity and petroleum kitchen areas of Liassic Black Shales (Lower Jurassic) in the central Upper Rhine Graben, Germany," *International Journal of Earth Sciences*, vol. 105, no. 2, pp. 611–636, 2016.

[55] A. Loges, T. Wagner, T. Kirnbauer et al., "Source and origin of active and fossil thermal spring systems, northern Upper Rhine Graben, Germany," *Applied Geochemistry*, vol. 27, no. 6, pp. 1153–1169, 2012.

[56] J. Vidal, A. Genter, and F. Chopin, "Permeable fracture zones in the hard rocks of the geothermal reservoir at Rittershoffen, France," *Journal of Geophysical Research: Solid Earth*, vol. 122, no. 7, pp. 4864–4887, 2017.

[57] C. Baujard, A. Genter, E. Dalmais et al., "Hydrothermal characterization of wells GRT-1 and GRT-2 in Rittershoffen, France: implications on the understanding of natural flow systems in the Rhine graben," *Geothermics*, vol. 65, pp. 255–268, 2017.

[58] DWD2013, July 2015, https://www.dwd.de.

[59] C. J. Willmott and K. Matsuura, "Terrestrial air temperature and precipitation: monthly and annual time series (1950–1999)," 2001, July 2015, http://climate.geog.udel.edu/~climate/html_pages/README.ghcn_ts2.html.

[60] M. Cacace and A. B. Jacquey, "Flexible parallel implicit modelling of coupled thermal–hydraulic–mechanical processes in fractured rocks," *Solid Earth*, vol. 8, no. 5, pp. 921–941, 2017.

[61] D. Gaston, C. Newman, G. Hansen, and D. Lebrun-Grandié, "MOOSE: a parallel computational framework for coupled systems of nonlinear equations," *Nuclear Engineering and Design*, vol. 239, no. 10, pp. 1768–1778, 2009.

[62] B. O. Kaiser, M. Cacace, and M. Scheck-Wenderoth, "3D coupled fluid and heat transport simulations of the Northeast German Basin and their sensitivity to the spatial discretization: different sensitivities for different mechanisms of heat transport," *Environmental Earth Sciences*, vol. 70, no. 8, pp. 3643–3659, 2013.

[63] D. Bonté, L. Guillou-Frottier, C. Garibaldi et al., "Subsurface temperature maps in French sedimentary basins: new data compilation and interpolation," *Bulletin de la Societe Geologique de France*, vol. 181, no. 4, pp. 377–390, 2010.

[64] C. Carré, "Cartographies thermiques du Graben du Rhin (partie française)," *Rapport de stage Master 2 Réservoirs Géologiques Montpellier*, 2011.

[65] L. Guillou-Frottier, C. Carré, and B. Bourgine, "Régimes thermiques actuels des bassins sédimentaires: traitement des données, cartographies et sources potentielles des anomalies. Exemples du graben du Rhin et du bassin de Paris," in *Rapport Final*, BRGM/RP-60355-FR. 92, 2011.

[66] D. Le Masne, M. Lambert, H. Fabriol, and A. Genter, "Aquifères profonds d'Alsace: constitution d'une base de données à usage géothermique," *Rapport BRGM/IMRG 90 NT 087 SGN/IRG*, 1991.

[67] LIAG, *Temperaturdatenbank des Leibniz-Instituts für Angewandte Geophysik in Hannover*.

[68] J. F. Vernoux and M. Lambert, "Aquifères profonds d'Alsace: constitution d'une base de données à usage géothermique," *Rapport BRGM/IMRG SGN/IRG ARG 93 T37*, 1993.

[69] BRGM, "Inventaire sur les eaux minérales et thermales," 1998, February 2018, http://infoterre.brgm.fr/.

[70] LGB-RLP, "Landesamt für Geologie und Bergbau Rheinland-Pfalz, Kartenviewer," February 2018, http://mapclient.lgb-rlp.de//?app=lgb&view_id=20.

[71] LGRB, "Regierungspräsidium Freiburg, Landesamt für Geologie, Rohstoffe und Bergbau, HÜK350: Mineral-/Thermalwässer," February 2018, http://maps.lgrb-bw.de/.

[72] ISONG, "ISONG Informationssystem Oberflächennahe Geothermie für Baden-Württemberg," 2017, December 2017, http://isong.lgrb-bw.de/.

[73] M. Cathelineau and M.-C. Boiron, "Downward penetration and mixing of sedimentary brines and dilute hot waters at 5 km depth in the granite basement at Soultz-sous-Forêts (Rhine graben, France)," *Comptes Rendus Geoscience*, vol. 342, no. 7-8, pp. 560–565, 2010.

[74] G. Grecksch, A. Ortiz, and R. Schellschmidt, "Thermophysical study of GPK2 and GPK3 granite samples," *HDR Project Soultz Report*, GGA-Bericht, Hannover, Germany, 2003.

[75] D. F. C. Pribnow, "The deep thermal regime in Soultz and implications for fluid flow," *GGA Report*, GGA Institut, Hannover, Germany, 2000.

[76] J. P. Brun, M. A. Gutscher, and DEKORP-ECORS Teams, "Deep crustal structure of the Rhine Graben from DEKORP-ECORS seismic reflection data: a summary," *Tectonophysics*, vol. 208, no. 1–3, pp. 139–147, 1992.

[77] M. Schwarz and A. Henk, "Evolution and structure of the Upper Rhine Graben: insights from three-dimensional thermomechanical modelling," *International Journal of Earth Sciences*, vol. 94, no. 4, pp. 732–750, 2005.

[78] F. Wenzel and J. P. Brun, "A deep reflection seismic line across the Northern Rhine Graben," *Earth and Planetary Science Letters*, vol. 104, no. 2–4, pp. 140–150, 1991.

[79] K. Bjørlykke, A. Mo, and E. Palm, "Modelling of thermal convection in sedimentary basins and its relevance to diagenetic reactions," *Marine and Petroleum Geology*, vol. 5, no. 4, pp. 338–351, 1988.

[80] C. Dezayes, A. Genter, and B. Valley, "Structure of the low permeable naturally fractured geothermal reservoir at Soultz," *Comptes Rendus Geoscience*, vol. 342, no. 7-8, pp. 517–530, 2010.

[81] J. Vidal and A. Genter, "Overview of naturally permeable fractured reservoirs in the central and southern Upper Rhine Graben: insights from geothermal wells," *Geothermics*, vol. 74, pp. 57–73, 2018.

[82] C. Meller and B. Ledésert, "Is there a link between mineralogy, petrophysics, and the hydraulic and seismic behaviors of the Soultz-sous-Forêts granite during stimulation? A review and reinterpretation of petro-hydromechanical data toward a better understanding of induced seismicity," *Journal of Geophysical Research: Solid Earth*, vol. 122, no. 12, pp. 9755–9774, 2017.

[83] G. Peters, *Active Tectonics in the Upper Rhine Graben-Integration of Paleoseismology, Geomorphology and Geomechanical Modeling, [Ph.D. Thesis]*, Vrije Universiteit, 2007.

Hindawi
Geofluids
Volume 2019, Article ID 4849860, 30 pages
https://doi.org/10.1155/2019/4849860

Research Article

Reconstructing Paleofluid Circulation at the Hercynian Basement/Mesozoic Sedimentary Cover Interface in the Upper Rhine Graben

Chrystel Dezayes and Catherine Lerouge

BRGM, 3, avenue Claude Guillemin, BP36009, 45060 Orléans Cedex 2, France

Correspondence should be addressed to Chrystel Dezayes; c.dezayes@brgm.fr

Received 24 April 2018; Revised 10 October 2018; Accepted 26 November 2018; Published 7 March 2019

Academic Editor: Domenico Montanari

In this paper, we focus on paleocirculation at the Hercynian basement/sedimentary cover interface in the tectonic environment of the Upper Rhine graben. The goal is to increase our understanding of the behavior of the fracture-fault network and the origin of the hydrothermal fluids. We studied orientations, mineral fillings, and fluid origins of fractures that crosscut the Hercynian granitic basement and the Permo-Triassic formations in relation to the major tectonic events. Because the Mesozoic formations and the Hercynian basement on the graben flanks and inside the graben do not have the same evolution after uplift, our study includes 20 outcrops on both graben flanks and cores of the Soultz-sous-Forêts geothermal wells located inside the graben. The Hercynian granitic basement and Permo-Triassic formations were affected by several brittle phases associated with fluid circulation pulses related to graben formation during the Tertiary. We distinguished at least four stages: (1) reactivation of Hercynian structures associated with pre-rift tectonics during the early Eocene and descending meteoric waters, characterized by shearing/cataclasis textures and precipitation of illite and microquartz; (2) initiation of convective circulation of deep hot brines mixed with descending meteoric waters at the Hercynian basement/sedimentary cover interface during this first stage of Eocene rifting, characterized by dolomite and barite fillings in reactivated Hercynian fractures; (3) N-S tension fractures associated with rift tectonics just prior to uplift of the graben shoulders during Oligocene extension and descending meteoric waters, characterized by cataclastic textures and precipitation of quartz, illite, hematite, and barite; and (4) current convective circulation of deep hot brines mixed with descending meteoric waters at the Hercynian basement/sedimentary cover interface, characterized by calcite and barite fillings within the graben. This convective circulation is today present in deep geothermal wells in the western part of the Rhine graben.

1. Introduction

In studying geothermal systems, knowledge of fluid pathways at depth is critical for improving exploration for future resources while reducing geological risk.

Fluid migration through the crust depends to a great extent on the permeability and porosity of the rocks being crosscut [1]. These two parameters represent the rock's capacity to transmit fluid. Permeability and porosity depend on the initial rock type (sediments, magmatic rocks, and metamorphic rocks) [2] and geological processes that the rock has undergone during its history. These include fluid/rock interactions (low/high fluid/rock ratios), deformation (ductile/brittle), and pressure/temperature changes (e.g., diagenesis, metamorphism, hydrothermal alteration, and weathering). In tectonically and/or thermally stable environments, permeability may reduce drastically at depth and fluid/rock interactions are likewise reduced. In more active environments, geological evidence from several studies shows that hydrological systems operate at different scales and at all depths of the continental crust [1].

Hydrogeologists and geologists want to understand the nature, origin, and role of fluids in such fundamental geological processes as hydrothermal systems [3], deep geothermal systems [4, 5], ore deposition [6, 7], hydrocarbon maturation, migration and entrapment [8], seismicity [9], and metamorphism [10–12]. In sedimentary rocks, fluid pathways include connected rock porosity and lithological changes. Burial diagenesis may significantly modify rock mineralogy and porosity. Fluid circulation in massive magmatic and metamorphic rock at depth usually occurs through fracture and fault networks at different scales [13, 14], and the porosity is predominantly fracture porosity depending on the geometry and kinematics of the fault-fracture network [15, 16]. Intense fluid/rock interactions significantly modify the mineralogy (hydrothermal alteration of the host rock, mineralization precipitated in fractures) and matrix porosity (primary) as well of fracture porosity (secondary) [17].

In active environments, rift systems such as the Rhine graben act as major conduits for both magma and hydrothermal fluids [18, 19]. The Rhine graben is part of the European Mid-Continental Rift System [20] (Figure 1(a)), which for several decades has been a target for the development of deep geothermal exploitation in the granitic basement [21]. The crust below the Rhine graben is relatively thin, and the mantle probably underlies the crust at proximal depths based on ^{3}He anomalies [22], and therefore, the heat flow is high [23]. In contrast, at the local scale a well-developed fracture network favours the development of hydrothermal cells and promotes the vertical advection of fluids and heat [16, 24]. Deep geothermal projects seek to exploit hot water at great depth (around 4 to 6 km), hosted in quasi-impermeable granite and deep sediments and where hot fluids circulate primarily within the fault-fracture network. For these reasons, deep geothermal projects are risky and require good characterization of the geometry of the fault-fracture network and its permeability and of the regional fluid flow to optimize well siting and to locate geothermal fluids at depth.

The structural, mineralogical, and petrophysical characterizations of the granitic basement within the graben remain accessible only by drilling. Some of this information can also be obtained by studying rock analogues on the graben flanks as an exhumed geothermal area affected by circulation of geothermal fluids (i.e., [25]). The uplifted flanks affect the present-day regional fluid flow [26], where the higher topography creates a hydrodynamic gradient that drives water downward into sediment-hosted aquifers [22, 27, 28]. Understanding the thermal history of the graben flanks also helps us understand the thermal regime within the graben [23, 29–31].

In this paper, we focus on the relationships between mineral filling, fluid circulation, and tectonic history in the Upper Rhine graben to characterize the hydraulic behavior of the fracture-fault network and the origin of hydrothermal fluids at the Permo-Triassic sedimentary cover/Hercynian basement interface.

The Hercynian basement and Mesozoic formations on the graben flanks have the same pre-rift history as those inside the graben but are not expected to have the same Tertiary history after the uplift subsequent to the graben collapse that has occurred since the Oligocene. Moreover, these outcropping basement and Mesozoic formations have undergone recent weathering, whereas the deep sandstones and granite have not been affected. To discriminate between the Hercynian and the graben-opening brittle tectonics, we revisited the fractures in the EPS1 well located at the Soultz-sous-Forêts EGS (enhanced geothermal system) site within the Rhine graben and compared them with fracture analysis on surface Paleozoic and Permo-Triassic outcrops and quarries at 20 different sites in the Vosges and Black Forest massifs. In the field, we described mineralized fractures, measured their orientations, and collected samples to provide details on mineralogy and microtextures (Figure 2).

2. Geological Background

2.1. Rhine Graben Setting. The Upper Rhine graben is a Cenozoic graben belonging to the west European rift system (Figure 1(a)) [20], which is well known as a result of numerous studies for petroleum and mining exploration (wells, geophysical surveys, etc.). The graben, oriented roughly N20°E (Figure 1(b)), is filled with Tertiary and Quaternary sediments with minor volcanic activity. The Tertiary cover (500 to 1000 m thick) overlies Jurassic (about 150 m thick) and Triassic (about 700 m thick) sediments and the Paleozoic crystalline basement (Figures 1(c) and 1(d)).

In this paper, we focus on the structural inheritance of the Hercynian basement and the evolution of the fracture network through the most recent Cenozoic phases. The crystalline basement is characterized by three major terranes: the Rheno-Hercynian, the Saxo-Thuringian, and the Moldanubian zones, which exhibit major lithological differences [32, 33]. These terranes were accreted during the main tectonic phases of the Carboniferous (Sudete phase) and Permian (Saalian phase) along NE-SW sutures (Figure 1(b)) [34–36]. In the Vosges [37] and along the western graben border [38], these tectonic phases caused brittle tectonics with primary fracture sets oriented N45°E, N135°E, and N-S for the Carboniferous phase and N60°E to N90°E and N120°E for the Permian phase (Figure 3).

The Hercynian terranes were intruded by Carboniferous granitoids during the Visean (-340 Ma) and Permian (-270 Ma). These granitoids exhibit a broad petrological and geochemical diversity related to a variety of deep active magmatic sources and various petrogenetic mechanisms [39, 40]. The granitoids were emplaced along a NE to NNE direction related to primary weakness zones such as collisional or shear zones (Figure 1(b)).

At the end of the Hercynian orogeny, collapse of the chain led to local extension-related basin subsidence and rhyolitic volcanic activity during the Late Carboniferous-Early Permian [41]. These fault-controlled basins are oriented in a NW direction in the Vosges and the Black Forest massifs (Figure 1(b)).

After a long period of sedimentation during the Triassic and Jurassic characterized by deposition of clastic and carbonate sediments, the area was uplifted starting in the late Jurassic and continuing until the early Eocene (Figure 3). Rifting occurred during the Tertiary, between the end of the Eocene and the beginning Miocene [42]. The inherited Hercynian NE-SW- and NNE-SSW-striking crustal weaknesses were reactivated during the formation of the Rhine

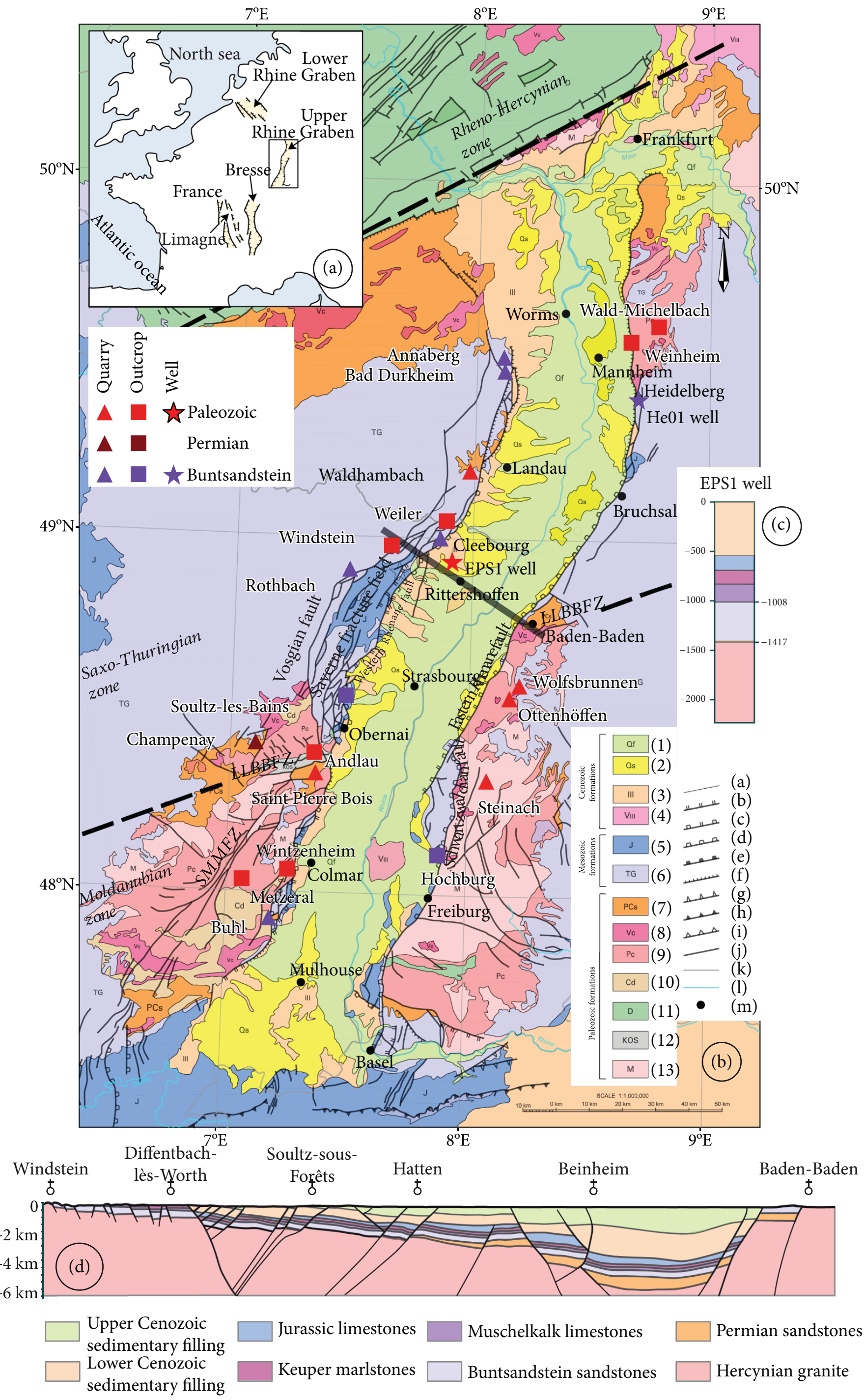

Figure 1: Geological setting. (a) Location of the Rhine graben in Western Europe. (b) Geological map from [114] showing location of sampling sites, quarries, outcrops, and wells. (1) Quaternary fluvial deposits; (2) Quaternary loess, eolian deposits; (3) Tertiary marine and lacustrine limestones, marls, evaporites; (4) Tertiary basalt; (5) Jurassic limestones; (6) Triassic sandstones, marly limestones, and anhydrite (German Triassic); (7) Permian red sandstones; (8) Carboniferous volcanism; (9) Carboniferous granites; (10) Dinantian conglomerate; (11) Ordovician-Silurian limestones and continental altered rocks; (12) Ordo-Silurian-Cambrian clay and argillaceous sandstones; (13) Siluro-Devonian paragneiss and orthogneiss. (A) Geological contact; (B) syn- to post-Quaternary fault; (C) syn- to post-Plio-Quaternary fault; (D) syn- to post-Pliocene normal fault; (E) syn- to post-Miocene normal fault; (F) undated fault; (G) syn- to post-Quaternary thrust; (H) syn- to post-Pliocene thrust; (I) undated thrust; (J) undifferentiated fault; (K) boundary; (L) main river; (M) city. (c) Geological log of the Soultz EPS1 well [59, 115]. (d) Geological W-E cross section through Soultz-sous-Forêts based on a 3D geological modem from [116]. Common legend for (c) and (d).

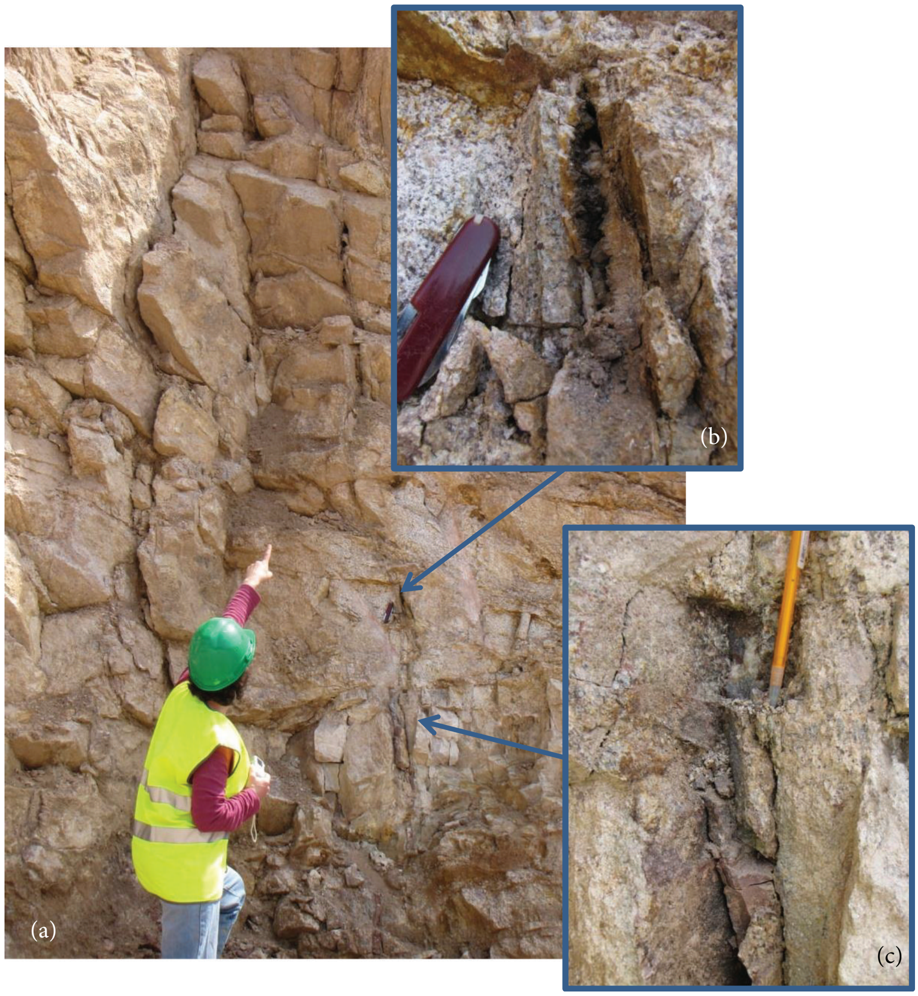

FIGURE 2: Example of fracture in granite (a) with quartz filling (b) and alteration halo (c) (Ottenhöffen quarry, Germany).

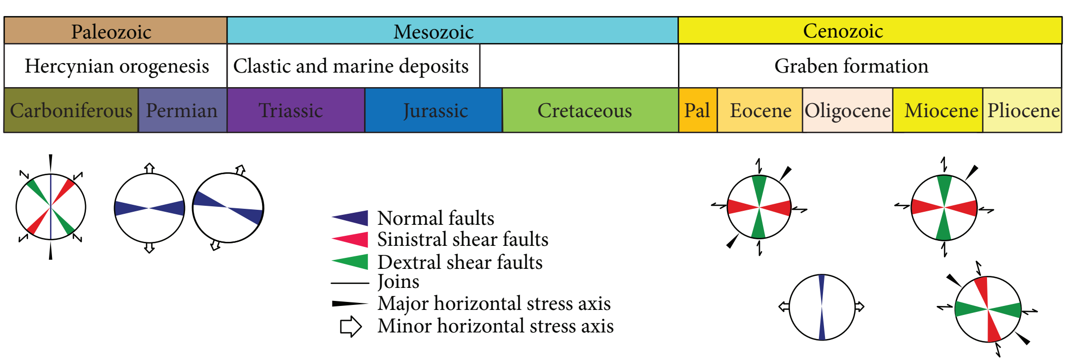

FIGURE 3: Synthesis of main brittle tectonic phases and associated fracture set directions since the Hercynian orogenesis in the Rhine graben and around the area modified after [117, 118] based on [37, 45, 48]. The circles represent the main orientation of fractures related to main stress axis (north on the top, east on the right).

graben as a result of the Africa-Europe collision [43, 44]. The first stage of this tectonic activity began during the Late Eocene with N-S compression, which affected the entire European continental platform (Figure 3) [45]. The primary phase of the opening of the Rhine graben took place during the Oligocene as a result of E-W extension (Figure 3). The direction of the stress axis did not vary, but the σ_1 and σ_2 axes reversed [45]. At this stage, normal faults appeared and blocks tilted (Figure 1(d)). The subsidence rate in the northern part of the graben differed from that of the southern part, which is bordered by the Erstein high. It constitutes the continuity between the Moldanubian and Saxo-Thuringian zones [43, 46]. A second tectonic stage occurred during the Miocene with a succession of two compressions: NE-SW compression observed everywhere in the graben and characterized by upper mantle uplift [47] and NW-SE compression that continues today and causes left-lateral shear movement in the graben (Figure 3) [48].

In the southern part of the graben, the Vosges and Black Forest massifs were uplifted during the Mio-Pliocene, probably following the Alpine phase [49]. Today, the altitude difference of the Triassic and the Paleozoic basement boundary between the summit of the Vosges massif and the deeper part of the central graben is about 3000-4000 m (Figure 1(d)). This is evidence of substantial vertical movement.

The structure of the Rhine graben is slightly sinuous in form: the northern part trends N-S, the central part trends N30°E, and the southern part N10°E (Figure 1(b)). The graben boundaries are controlled by two types of major synthetic normal faults: the internal (Rhenane) and the external (Vosgian and Schwartzwaldian) faults. These faults outline the crescent-shaped fracture fields such as the Saverne fracture field (Figure 1(b)).

Over geological history, the graben has followed a thermal evolution related to the tectonic setting [6]. The pre-rift period corresponded to an uplift of the area without any associated thermal event, and the thermal gradient is considered as normal [38]. During the Eocene, a mantle diapir formed, in association with the first important thermal flux, inducing an abnormal thermal gradient up to 80°C/km in the upper crust [6]. During the Oligocene, volcanic activity occurred and substantial fault activation caused geothermal activity associated with fluid circulation [50]. After a phase of thermal attenuation, subsidence resumed during the Miocene and Pliocene epochs; it was more active in the north, associated with a third thermal phase which remains active today. Using the geothermal gradient proposed by Robert [6], the first maximum temperature of at least 100°C was reached at the beginning of rifting (Eocene) and may be associated with a mantle diapir. A second maximum temperature >100°C was reached during the late phase of the Rhine graben formation in the Miocene and remains active today. Present-day temperatures measured at the bottom of the sediment pile are about 130°C at a depth of 1400 m [51]. The highest gradients are measured on the western flank and are more developed in the northern part of the graben due to present-day tectonic activity [52].

2.2. EPS1 as a Reference Well inside the Rhine Graben. The deep EPS1 well, drilled in 1991 as part of the European EGS project at Soultz-sous-Forêts (Alsace, France) is a geological reference well in the Rhine graben because it is the only well cored to a depth of 2222 m (all depths are measured depth below ground level). This well was fully cored from 830 m to 2222 m, including 200 m in the lower Muschelkalk, 400 m in the Buntsandstein and Permian sandstones, and 800 m in the granite basement [53]. The Buntsandstein sandstones were reached at a depth of 1008 m under the Muschelkalk limestones, Permian sandstones at a depth of 1363 m, and the crystalline basement at a depth of 1417 m (Figure 1(c)). Because the European EGS project was designed to exploit deep geothermal energy, the granite basement was studied in more detail than the overlying Cenozoic and Mesozoic formations that the well encountered.

The Buntsandstein Vosgian sandstones in the EPS1 well are classified as moderately to well-sorted rounded lithic feldspathic arenites. They consist of dominant monocrystalline and polycrystalline quartz grains and K-feldspar grains with minor lithic grains and clays. Permian sandstones are for the most part heterogranular arkoses containing numerous lithic fragments, minor plagioclase, and more abundant clay minerals. More than 300 fractures were measured on the almost 400 m of the cored sandstones, and no slickenlines were observed. The fracture network shows limited scattering around N170°E, and dips are equally balanced between west and east (Figure 4). Within the well, some intervals are grayish and more intense fracture zones associated with a quartz-barite filling are present. A first deformation zone at 1012 m separates the Muschelkalk from the Buntsandstein formations. This fracture zone is probably a normal fault oriented N130°E-80°E [54]. Within the Buntsandstein sandstones, a large fracture zone is present between 1172 m and 1210 m corresponding to the boundary between the Upper and the Lower Vosgian sandstones (Figure 5). This fracture zone contains an isolated 2 cm-thick N20°E fracture at 1173.5 m, a network of mm-to-cm-thick N-S fractures reworking a cataclasis band between 1191 m and 1195 m, and a complex 5 m-thick N160°E fault zone at 1205-1210 m. The complete fracture zone is about 30 m thick in the well (Figure 5) [54]. It is assumed that this fracture zone intersects two other nearby wells, GPK1 and 4550, where total mud losses occurred when drilling through this zone [54].

The granite in the EPS1 well is a biotite-amphibole porphyritic monzogranite [55, 56] dated at 334.0 + 3.8/−3.5 Ma (2σ) using zircon U-Pb age [57]. The granite is affected by a dense vein network and a high degree of alteration resulting from different generations of fracturation and fluid/rock interactions. Fracture fillings are heterogeneous, and polyphased, dominantly represented by major quartz, barite, pure white mica (illite), carbonates, and iron oxides [58].

More than 3000 fractures and several fracture zones have been identified in the granite between 1420 and 2222 m; they are fully described, and their orientation was measured in comparison to well images [59, 60] (Figure 6). Of them, 141 striated faults were observed and kinematic inversion showed four Cenozoic brittle tectonic phases with evidence of inherited faults [61]. These fractures are present as individual fractures and fracture zones, which are larger-scale (10-20 m) structures of highly clustered fractures [54, 58, 62]. They are grouped into two main sets roughly striking north-south (N005°E and N170°E with dips of 70°W and 70°E; Figure 6) [60]. Both sets are close to a conjugate fracture pattern of normal faults related to the Rhine graben formation [61]. Three secondary fracture sets were also identified, which are oriented E-W, NE-SW, and NW-SE (Figure 6). Moreover, the top of the granite is crosscut by numerous subhorizontal fractures that are characteristic of the top of the granite, attributed to a surface-stress relaxation effect that occurred when the batholith was unroofed during the

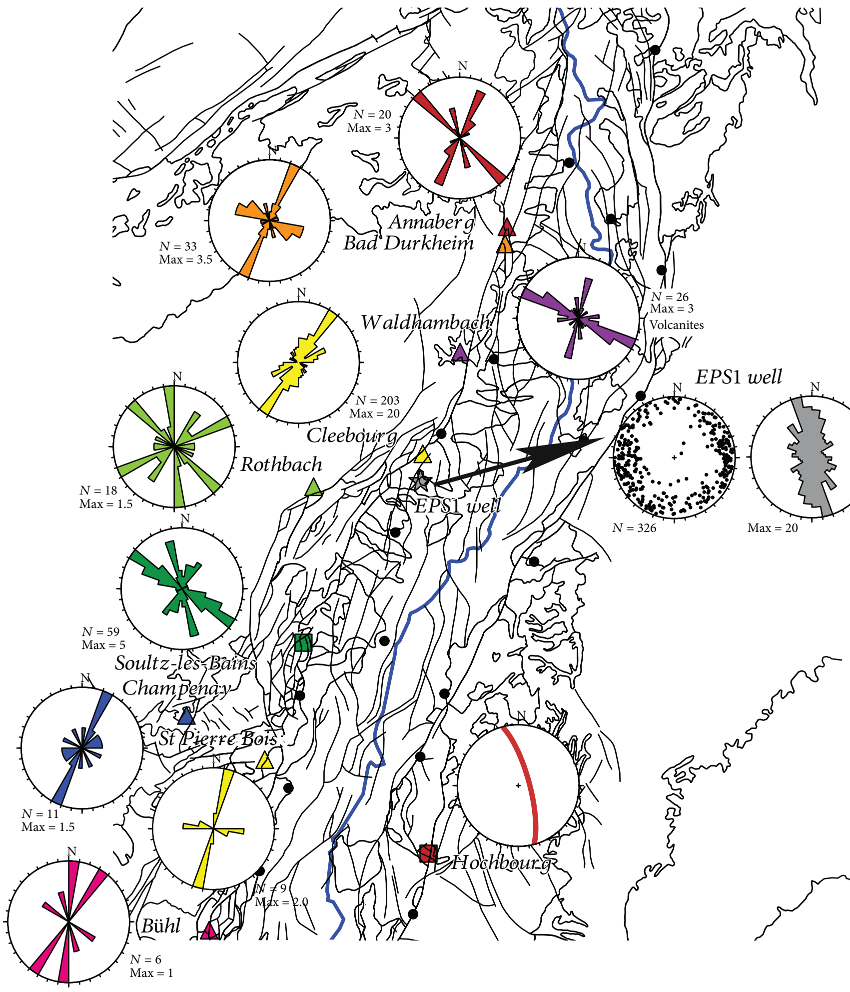

Figure 4: Fracture directions measured at the Permo-Triassic sandstone outcrops, including the measurements on cores of the EPS1 well and in Permian volcanic rocks at the Waldhambach quarry, represented on a structural map showing major structures. Bold lines represent the main faults and fine lines represent geological boundaries (same as Figure 1). For each site, the rose diagram shows the fracture directions in 10° classes. EPS1 well data, the plot diagram represents fracture pole in Schmidt's projection, lower hemisphere. The different colors correspond to each site. The location of the sites is indicated by a square for outcrops, a triangle for quarries, and a star for wells.

Permian (Figure 7) [60]. Because of the long geological history of the granitic basement, most fractures were reactivated during various tectonic phases depending on the relationship between the fracture orientation and the stress field direction [61]. Of the 3000 fractures, only five present an indication of previous fluid circulation [54].

Numerous studies have been conducted on hydrothermal alteration in the Soultz-sous-Forêts granite [60, 63–67]. This hydrothermal alteration is polyphase; early pervasive alteration affects the granite at a large scale, and later alteration is due to fluid circulation in the fracture network. Early pervasive alteration associated with rare fractures consists of a chlorite-epidote-carbonate retromorphic assemblage that affects granite even in the least fractured zones. Its role is negligible in reducing reservoir permeability [65, 68]. Fluids associated with this early alteration are moderately saline (2-7 wt% eq. NaCl) and were trapped under temperatures of 180-340°C on the basis of fluid inclusion microthermometry; they are considered to be of late Variscan age [69]. Hydrothermal alteration associated with fracture zones is dominant [70]. It results from interaction between granite and circulating fluids in the fracture network [71]. Hydrothermal minerals are quartz, clay minerals (illite, R3-type illite/smectite mixed layers, and tosudite), carbonates, barite, hematite, pyrite, and galena [54, 60, 68, 69, 72, 73]. Four primary highly fractured zones can be defined showing high content of hydrothermal minerals (Figure 7): (1) 1420-1530 m: quartz with hematite and carbonates, (2) 1620-1725 m: quartz with hematite and clay minerals, (3) 2050-2080 m: quartz with calcite and clay, and (4) 2155-2180 m: dominantly quartz [54]. Quartz-barite and quartz-ankerite veins containing a generation of lower-temperature brines (130°C–160°C) with a broad salinity range are attributed to younger, post-Oligocene up-to-the-present-day fluid-flow events [67, 69, 74]. The wall rocks of the fractures also frequently exhibit hydrothermal alteration and are marked by high porosity of up to 20% [68] due to alteration of primary minerals to clay minerals [73, 75, 76].

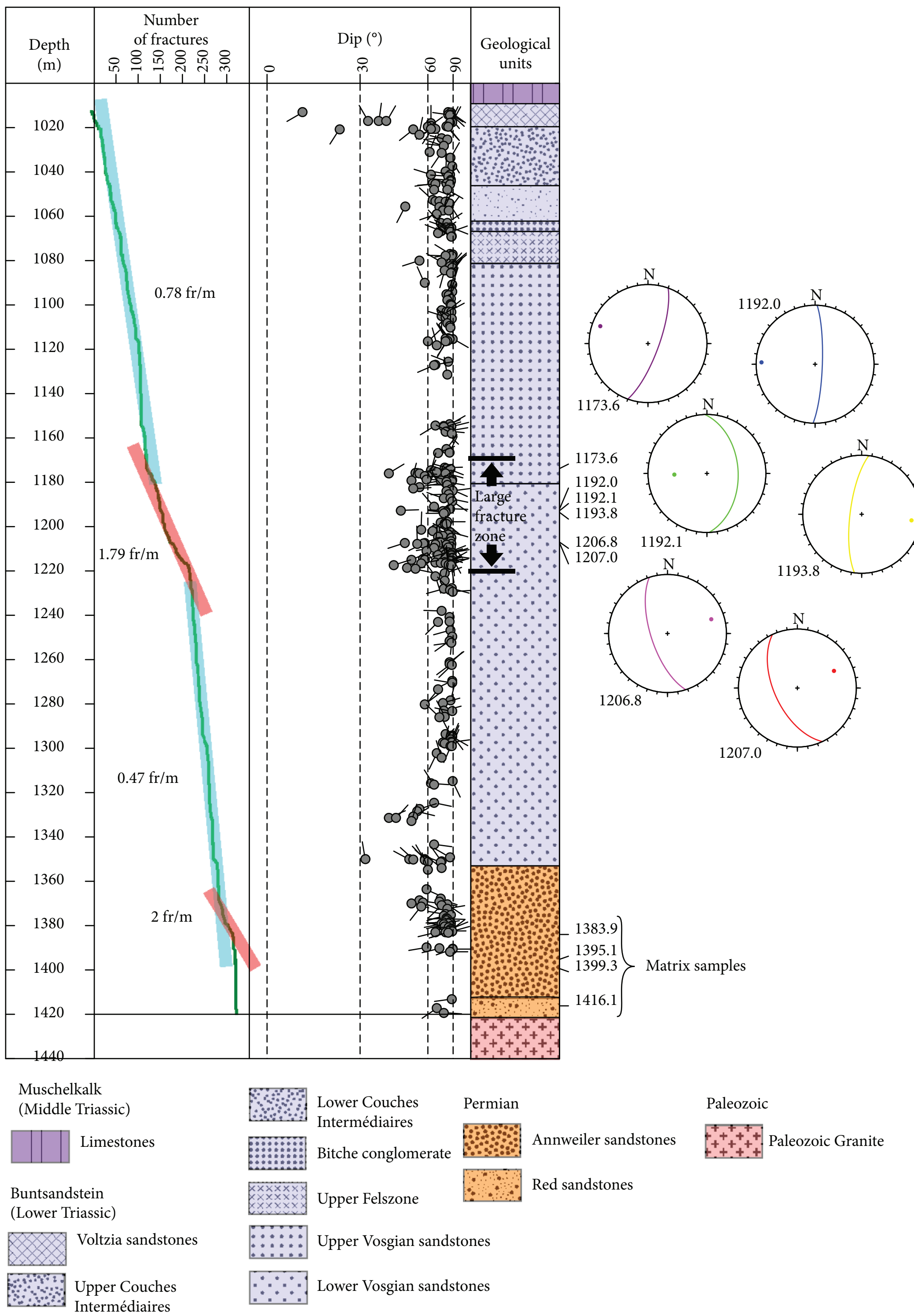

FIGURE 5: Composite log of Permo-Triassic sandstones in the EPS1 well. The first column represents the measured depth; the second, the cumulative fracture log; the third, the fracture orientation; the fourth, the geological units [115]. Sample locations are shown. The orientation (great circle and pole) of sampled fractures is represented in Schmidt's projection, lower hemisphere.

This fluid circulation within fracture and fault zones suggests that the contribution of convective heat transfer is dominant and explains the high temperature along the western margin of the graben [77, 78].

3. Rock Sample Collection

To discriminate between Hercynian and graben-opening brittle tectonics, we revisited the fractures in the EPS1 well,

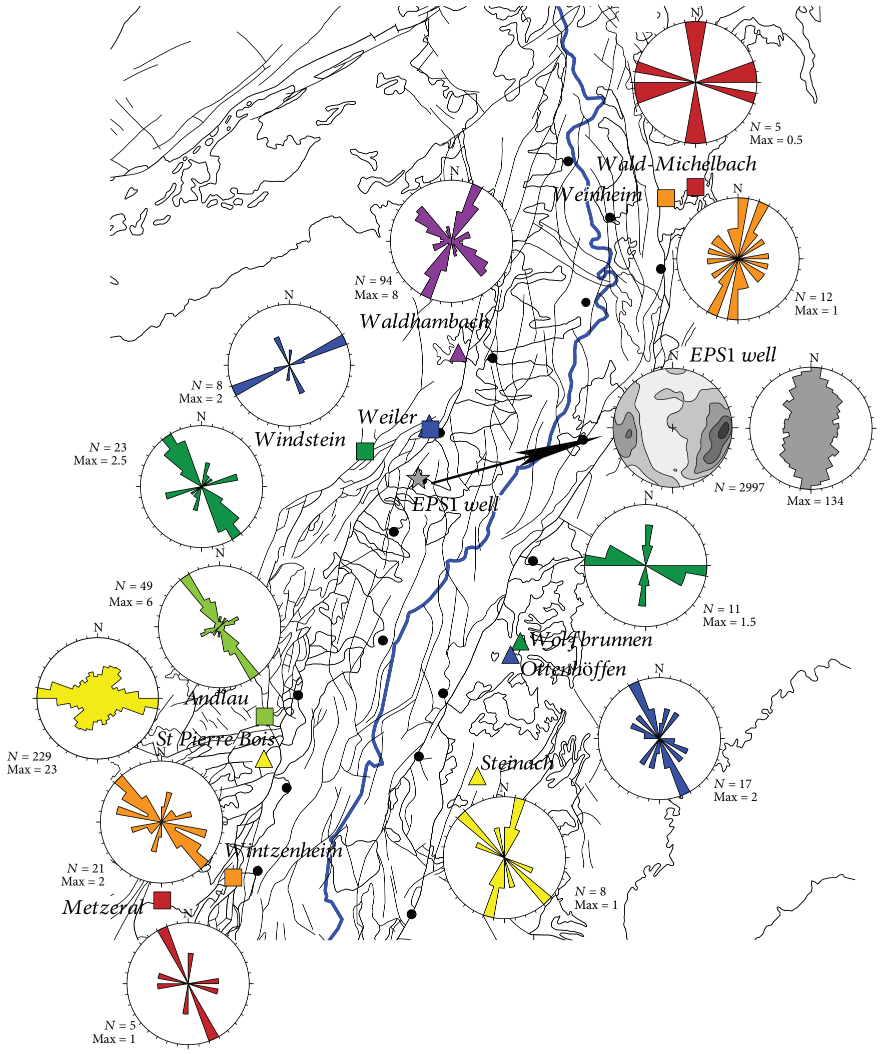

Figure 6: Fracture directions measured on Paleozoic basement outcrops including the measurements on EPS1 well cores, represented on a structural map showing major structures. Bold lines represent the main faults, and fine lines represent geological boundaries (same as Figure 1). For each site, the rose diagram shows the fracture direction with 10° classes. For EPS1 well data, contour-density diagrams in Schmidt's projection, lower hemisphere: 10%, 30%, 50%, 70%, and 90% of the fracture pole maximum frequency. The different colors correspond to each site. The location of the sites is indicated by a square for outcrops, a triangle for quarries, and a star for wells.

which is located within the Rhine graben, and compared them to fracture analysis on surface Hercynian and Permo-Triassic outcrops at 20 different sites in the Vosges and the Black Forest massifs (Figure 1(b)).

Except for the Hochburg outcrop, the eight Permo-Triassic sites are along the western border, in the Vosges massif, and in the Saint Pierre Bois and Waldhambach quarries, where both Permo-Triassic formations and Hercynian basement are present (Figure 1(b), Table 1). The 12 sites in the Hercynian basement are distributed equally on the western and eastern borders of the Rhine graben (Figure 1(b)).

Generally, these sites are quarries, either abandoned or producing, but some sites are outcrops along roads (Hochburg, Windstein, and Andlau). The quarries in the Hercynian basement exploit granite and gneiss-type rocks for rock fill, and quarries in Permian and Buntsandstein sandstones extract building stones. Except for Weiler and Andlau, which are metamorphic rocks, the other basement sites are granite (Table 1).

On the outcrops, we first measured fracture orientations to determine the statistical fault pattern and the primary sets for each site. Some sites have several outcrop directions allowing good fracture sampling (Table 1). Second, we sampled fracture infills in relation to the orientation of the fractures themselves and if possible, we oriented the samples in relation to north and to the horizontal plane.

In our study of the EPS1 Soultz well, we examined more than seventy thin sections of available cores of Triassic sandstones and Hercynian granite. Based on previous work and on these observations, we selected seventeen representative samples:

(1) six samples from the most fractured interval in the Buntsandstein sandstones, between 1170 and 1210 m, in a large shear zone (Figure 5)

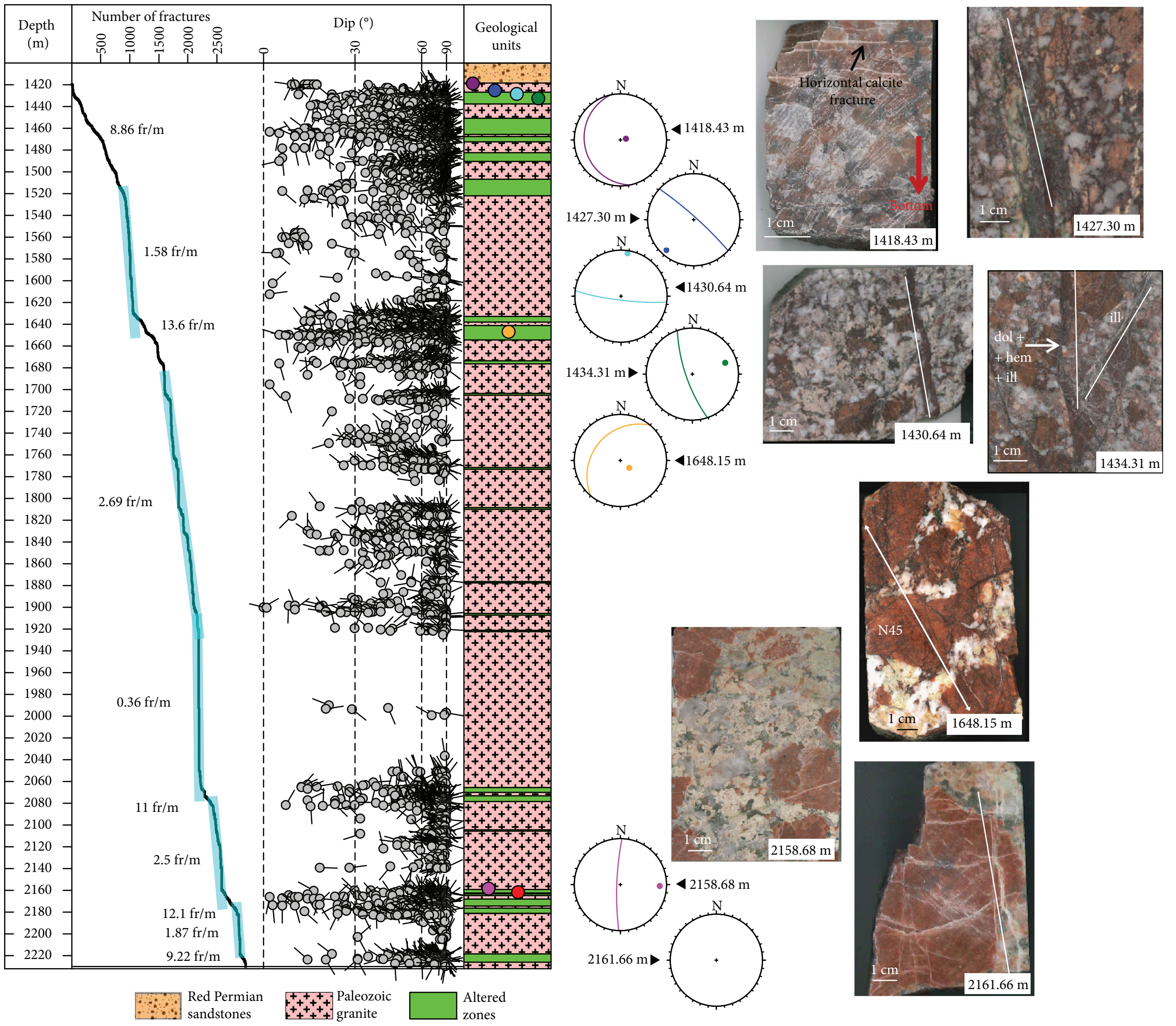

FIGURE 7: Composite log of Hercynian granite in the EPS1 well. The first column represents the measured depth; the second, the cumulative fracture log; the third, the fracture orientation; the fourth, the geological units [60]. The location and macroscopic pictures of samples are shown. The orientation (great circle and pole) of sampled fractures is represented in Schmidt's projection, lower hemisphere.

(2) four samples of the Buntsandstein/Permian sandstones near the sedimentary cover/granite interface between 1382 and 1416 m (Figure 5)

(3) four samples at the top of the pluton and specifically in the 20 meters below the sedimentary cover/granite interface, between 1417 and 1435 m (Figure 7)

(4) one sample at about 1650 m in a fracture zone (Figure 7)

(5) two samples close to the deepest fractured zone at 2158 m and 2161 m (Figure 7)

Of the six samples collected in the most fractured interval of the Buntsandstein sandstones, one sample at a depth of 1173.6 m contains an isolated fracture, three samples at depths of 1192.0 m, 1192.1 m, and 1193.8 m belong to a zone characterized by a high fracture density, and two samples at 1206.8 and 1207 m belong to the major fault zone.

In the granite, the seven large mineralized fractures have various orientations and mineral filling is studied in relation to fracture orientation (Figure 7). The upper sample is located at a depth of 1418.43 m, on the top of the granite, within the paleoweathering alteration zone (Figure 7). The fracture is oriented N170°E-14°W. This zone is characterized by a high density of subhorizontal fractures (about 9 fr/m) with a N-S average direction, attributed to a surface-stress relaxation effect during unroofing of the batholith in the Permian [60].

The three fractures at the top of the granite are located at depths of 1427.30 m, 1430.64 m, and 1434.31 m in the same

Table 1: Description of sampling sites, outcrops, and quarries, with age and type of rock, type of site, and main direction of fracture measurement scanlines.

Site name	Age	Type of rock	Description of the site	Longitude	Latitude
Annaberg	Buntsandstein	Light-colored and leached sandstones	Two small exploited quarries. Main direction of walls: NE-SW.	8.15503	49.4793
Bad Dürkheim	Buntsandstein	Beige leached sandstones	Old abandoned quarry, exploited by the Romans. Large and high wall oriented NE-SW and NW-SE.	8.15768	49.4643
Cleebourg	Buntsandstein	Pink and yellowish leached sandstones.	Small exploited quarry for ornamental stones. Large fault, enclosed in the Western Rhenane fault, intersects the quarry. Main direction of the walls: N20°E and N110°E.	7.891	49.013
Rothbach Loegel	Buntsandstein	Pink sandstones	Large quarry exploiting ornamental stones within caves. In the caves, fractures can be observed on N120°E and N30°E direction, on the roof and the footwall.	7.51753	48.9131
Soultz-les-Bains	Top of Buntsandstein (Volzia) with the transition of the shelly sandstones of Muschelkalk	Beige sandstones	Abandoned quarry, namely, “Carrière Royale”. Very tall wall with NW-SE direction and several meters long.	7.49556	48.5715
Bühl	Buntsandstein	Pink sandstones	Abandoned small quarry exploited until the 30s. Very tall wall with NW-SE direction.	7.18677	47.9344
Hochburg (Sexau)	Buntsandstein	Pink sandstones	Outcrop under the medieval castle.	7.89997	48.1167
Champenay	Permian	Coarse-grained pink sandstones	Exploited quarry for ornamental stones. Main direction wall: NW-SE and NE-SW.	7.1115	48.412
Waldhambach	Paleozoic/Triassic	Pink Buntsandstein sandstones, Permian arkose (Rotliegende) and volcanites (melaphyr), Hercynian granodiorite	Large granite quarry exploited for rock fill. The main accessible part is in granodiorite. The granodiorite is highly fractured. NW-SE lamprophyre dikes crosscut the granodiorite.	8.00256	49.1609
Saint Pierre Bois	Paleozoic/Triassic	Permian sandstones and Hercynian granite.	Exploited quarry in the granite for rock fill. Main direction of the walls: NW-SE and NE-SW.	7.3678	48.3323
Weiler	Paleozoic (Devonian)	Schistes, grauwackes, and volcanites (metamorphic volcano-sedimentary pile (Ménillet et al., 1989))	Small old quarry. Main wall oriented N-S.	7.90106	49.0436
Windstein	Paleozoic (Visean)	Altered coarse-grained biotite-amphibole-granite	Outcrops.	7.68175	48.9844
Andlau	Paleozoic (Visean)	Schists and hornfels	Several scattered outcrops.	7.36813	48.3942
Wintzenheim	Paleozoic (Visean)	Altered biotite-rich porphyritic granite	Outcrops scattered along the Western Rhenane fault.	7.27503	48.073
Metzeral	Paleozoic (Visean)	Altered coarse-grained biotite-amphibole- granite	Small outcrops in front of the quarry of coarse grain granite	7.08378	48.0213
Steinach	Paleozoic	Fine-grained granite	Large exploited quarry of granite and outcrops along the road. Main wall direction: NW-SE and NE-SW. Large fault filled by cm-sized euhedral calcite crosscut the granite.	8.06116	48.2943

Table 1: Continued.

Site name	Age	Type of rock	Description of the site	Longitude	Latitude
Ottenhöffen	Paleozoic	Highly altered granite	Small quarry exploited for sand. Main wall oriented E-W. Pieces of rocks, not in place, show vuggy quartz, cockade breccia, siliceous breccia, and finely siliceous banded veins suggesting intense low-temperature hydrothermal circulation	8.16231	48.5568
Wolfsbrünnen	Paleozoic	Slightly altered fine-grained granite	Large exploited quarry	8.62357	49.0143
Weinheim	Paleozoic		Outcrops in front of the exploited quarry. Contact between the two granites is a large mineralized fault exploited for silver during the 15th century (personal communication).	8.68631	49.5549
Wald-Michelbach	Paleozoic	Pink feldspar-rich granite-like syenite	Abandoned quarry. NW-SE main outcrops.	8.79013	49.5811

upper fractured zone (Figure 7). The fractures have various orientations: N130°E-80°NE; N100°E-80°S, and N160°E-75°SW, respectively (Figure 7). The fracture at a depth of 1648.15 m, oriented N40°E-30°NW, is contained within an open fracture zone showing geodic quartz and that has a thickness along the well of about 20-30 cm (Figure 7) [79]. The two deeper fractures are located in the 2100 m fracture zone, at depths of 2158.68 m and 2161.66 m, respectively (Figure 7). The first fracture is oriented N-S, exactly at N0°E-80°W, whereas the second is oriented NW-SE, N150°E-85°NE (Figure 7). During drilling operations, both partial mud losses and natural outflow were observed at this depth [54]. The cores show thick quartz vein deposition in these two locations, characterized by very low gamma ray values. In the peripheral area of the quartz vein, the hydrothermally altered and cataclastic granite corresponds to increased gamma ray values [58]. This increase is characteristic of clay deposition. This zone ranges in thickness from 20 to 30 m in the well.

In the eastern part of the graben, the Heidelberg well (He01; Figure 1(b)) was fully cored from the surface through the Buntsandstein sandstones to 146.70 m below ground level and through the Heidelberg granite down to a depth of 153 m. The Heidelberg granite is a beige-pink porphyritic biotite monzogranite [80]. However, because these cores were not oriented, fracture orientations could not be determined, but the fracture infills were analyzed to complete the observations.

4. Analytical Techniques

4.1. Mineralogical Characterization

4.1.1. Microscope Observations. Optical observations were carried out using an Olympus BH2 microscope under transmitted and reflected light. Complementary observations and analyses of polished thin sections of samples were performed on a scanning electron microscope (SEM) coupled with an energy-dispersive spectrometer (Kevex Quantum) tuned at 25 kV. Prior to analysis, a 10–20 nm-thick carbon layer was sputter-coated on polished thin sections (Edwards Auto 306).

Cathodoluminescence was used to discriminate carbonates precipitated from different fluids because it is a sensitive method for tracing element contents and their crystalline framework. Mn^{2+} ion and trivalent REE ions appear to be the most important activator ions of extrinsic CL, whereas Fe^{2+} is the main quencher [81, 82]. The system used was a cold cathode Cathodyne manufactured by the OPEA Society (Laboratoire Optique Electronique Appliquée). The electron beam has adjustable energies up to 26 keV and currents up to 250 μA. The cathodyne is mounted on an Olympus microscope allowing magnification up to 200. The system is equipped with a JVC KYF75U tri-CCD digital camera. The three 12 mm-sized sensors have a resolution of 1360×1024 pixels. Calcite was distinguished by its yellowish orange color; dolomite by its dark red orange to light red orange color, and ankerite by its dark color due to inhibition of extrinsic luminescence by iron.

4.1.2. Electron Microprobe. Spot analyses of carbonates and sulfates were performed on polished thin sections of samples covered with a carbon coating, using a CAMEBAX SX50 electron microprobe with an acceleration voltage of 15 kV, a current beam of 12 nA, and a 1–2 lm beam width. Peak and background counting times were 10 s for major elements. Standards used included both well-characterized natural minerals and synthetic oxides. Matrix corrections were made with a ZAF computing program.

4.2. Isotopic Analysis Techniques

4.2.1. Carbon and Oxygen Isotopes of Carbonates. The conventional method by Rosenbaum and Sheppard [83] was used to extract calcite and dolomite, successively. We analyzed the resulting CO_2 samples for their isotopic compositions using a Delta S Finnigan MAT gas-source mass spectrometer.

4.2.2. Oxygen Isotopes of Quartz. In situ oxygen isotopic compositions of quartz were measured on polished thin sections using SIMS with a Cameca IMS 1280 ion microprobe at CRPG in Nancy (France). Prior to analysis, a 10–20 nm-thick gold layer was sputter-coated on polished thin sections. Analyses were performed using a Cs primary ion beam of 10 keV, a current of 0.5 nA, and a beam size of 15 μm. Secondary ions were accelerated by applying a nominal voltage of -4.5 kV, the energy window was set to 35 eV, and no offset was applied. Quartz references were analyzed each day at the beginning and at the end of the day, to calculate the instrumental mass fractionation (IMF), as follows:

$$\mathrm{IMF} = \delta^{18}\mathrm{O}_{\mathrm{std\,ref}} - \mathrm{average}\left(\delta^{18}\mathrm{O}_{\mathrm{std\,meas}}\right)_n, \quad (1)$$

where $\delta^{18}O_{\mathrm{std\,meas}}$ is the oxygen isotopic composition of the reference by ion microprobe, $\delta^{18}O_{\mathrm{std\,ref}}$ is the oxygen isotopic composition of the standard, and n is the number of analyses. The quartz $\delta^{18}O$ measured by the ion microprobe ($\delta^{18}O_{\mathrm{Quartz\,meas}}$) was corrected from the instrumental fractionation (IMF) as follows:

$$\delta^{18}\mathrm{O}_{\mathrm{Quartz\,corr}} = \delta^{18}\mathrm{O}_{\mathrm{Quartz\,meas}} + \mathrm{IMF}_{(\mathrm{quartz})}. \quad (2)$$

All results are reported in δ units relative to international standards, defined by $d = (R_{\mathrm{Sample}}/R_{\mathrm{Standard}} - 1) \times 1000‰$, where R is the measured isotopic ratio in the sample and in the standard: standard mean ocean water (SMOW) for oxygen and Pee Dee Belemnite (PDB) for carbon. Reproducibility was ±0.2‰ for oxygen and carbon.

4.2.3. Strontium Isotopes in Dolomite and Barite. Strontium isotopic ratios were measured in dolomite and barite separated by hand picking on thin sections. Strontium was extracted by adding 10 mL of 6 N HCl solution (extra-pure-quality concentrated HCl) to crushed mineral separates in covered Teflon beakers.

The leachate was purified using an ion-exchange resin (Sr-Spec) before mass analysis according to a method adapted from Pin and Bassin [84], with blank <1 ng for the entire chemical procedure. After chemical separation, ~150 ng of Sr was loaded onto a tungsten filament with tantalum activator and analyzed using a Finnigan MAT 262 multicollector solid source mass spectrometer (Bremen, Germany). The $^{87}Sr/^{86}Sr$ ratios were normalized to a $^{86}Sr/^{88}Sr$ ratio of 0.1194. An average internal precision of 10 ppm (2 sm) was obtained, and the reproducibility of the $^{87}Sr/^{86}Sr$ ratio measurements was tested through repeated analyses of the certified NBS987 standard (0.710240).

5. Results

5.1. Permo-Triassic Formations

5.1.1. Matrix Diagenesis. Sandstones sampled in quarries on both flanks of the Rhine graben are similar to sandstones located within the Rhine graben reached by well EPS1. Buntsandstein sandstones are generally reddish, but others are white to gray, including those from the Cleebourg, Soultz-les-Bains, Bühl, and Bad Durkheim quarries and from the Hochburg outcrop, due to the absence of hematite. Some of these quarries are located inside the Western Rhenane boundary fault (Bühl, Cleebourg; Figure 1(b)) or have high fracture density (Bad Dürkheim, Soultz-les-Bains) where fluids have circulated intensely and remobilized iron from iron oxides and hydroxides.

The Buntsandstein and Permian sandstones consist essentially of monocrystalline and polycrystalline quartz grains, feldspar grains, lithic grains, and clays. K-feldspar is the major feldspar observed in these sandstones (Figure 8). The K-feldspar content of Buntsandstein sandstones in the EPS 1 well is estimated to be about 15%. Plagioclase is almost absent in Buntsandstein sandstones, whereas it is present in Permian sandstones.

Diagenesis in the Buntsandstein and Permian sandstones is marked by various degrees of alteration and dissolution of detrital minerals and by formation of authigenic minerals including dominant quartz, illite-like clays with minor alkali feldspar, barite, carbonates, and hematite (Figure 8), except in a few samples of Permian sandstones from the Waldhambach quarry where authigenic minerals are mostly absent. When authigenic minerals are present, they everywhere exhibit the same features as the samples from the EPS1 well and from the various outcrops (excluding Waldhambach).

Stability of detrital minerals is of primary importance in porosity evolution. Feldspar minerals including K-feldspar and plagioclase in Permian sandstones exhibit various degrees of alteration to microphyllites, which modifies the porosity. Detrital K-feldspar also exhibits various degrees of dissolution that give rise to secondary porosity in the Buntsandstein and Permian sandstones located both inside and outside the Rhine graben.

Authigenic illite-like clays (Ilt) are observed in small amounts in all sandstones (Figure 8). Clays essentially occur as early radial fibers growing on detrital quartz (Qz0) and K-feldspar grains (Kfs0) (Figures 8(c)–8(e)). Their presence generally inhibits the growth of quartz aureole.

Rare authigenic K-feldspar (Kfs1) is observed in all sandstones (Figure 8(h)). Authigenic K-feldspar grows as small euhedral crystals on detrital K-feldspar grains. Electron microprobe analyses show that unlike detrital K-feldspar (Kfs0), the authigenic K-feldspar (Kfs1) do not contain Ba. Authigenic and detrital K-feldspar both exhibit signs of dissolution, indicating that authigenic K-feldspar formed prior to the dissolution process.

Authigenic quartz occurs predominantly as overgrowths on detrital quartz (Qz1) (Figures 8(b), 8(e), and 8(h)) but also as microcrystalline grains associated with illite-like clays (μQz + Ilt) (Figures 8(b)–8(d), 8(g), and 8(h)) and as late fillings in dissolution cavities in K-feldspar (Qz2).

Barite (Brt) and carbonate cements grow on authigenic radial illite-like clays, quartz overgrowths, K-feldspar overgrowths, and illite-like clays, and microquartz assemblages; they also fill dissolution cavities in K-feldspar. These observations indicate that they precipitated later than all previous authigenic phases and also later than the K-feldspar dissolution process (Figures 8(g) and 8(h)). Whereas traces of barite are present everywhere in the EPS1 well sandstones, carbonates are abundantly present in the sandstones between 1382 and 1416 m near the interface with the Hercynian basement. The carbonates occur as large euhedral or poekilitic crystals that exhibit a relatively homogeneous red-orange color under cathodoluminescence (CL), with minor dark red zoning.

5.1.2. Fracture Description in Well EPS1 inside the Graben. In the well EPS1, the average fracture density in Buntsandstein and Permian sandstones is less than 1 fracture/m. Two other zones are more highly fractured; one of them is present between 1170 and 1220 m in the Vosgian sandstones, and the other is between 1370 and 1382 m in the Annweiler sandstones, with 1.79 and 2 fractures/m, respectively (Figure 5). The fracture network shows limited scattering between N20°E and N170°E, and dips are equally balanced between east and west (Figure 4).

Between the depths of 1170 and 1210 m within a large fracture zone (Figure 5), we distinguish two fracture types based on texture and fill descriptions. In the first type of fracture, which strikes N-S and dips to the west, cataclastic textures that are highly cemented with microcrystalline quartz and illite-like clays (μQz + Ilt) are observed at 1193.8 m, 1206.8 m, and 1207 m (Figure 5). Grains of partially dissolved K-feldspar are observed in the cataclasis. Considering the fragility of the partially dissolved K-feldspar, their presence strongly suggests that the dissolution process took place after the cataclasis. In wall rock of the fractures, an illite-like clay and microcrystalline quartz association was also observed at grain boundaries and in crosscutting elements.

The second fracture type, which can be observed at 1173.6 m, 1192.0 m, 1192.1 m, and 1206.8 m, is also not far from N-S but dips to the east (Figure 5) and at a depth of 1207 m exhibits mm- to cm-thick fractures filled by euhedral quartz or barite. In the fault zone at 1206.8 and 1207 m, veins of euhedral quartz and barite crosscut cohesive cataclasite, suggesting that these fillings are later than cataclasis and associated cementation. Fractures at 1173.6 m contain both

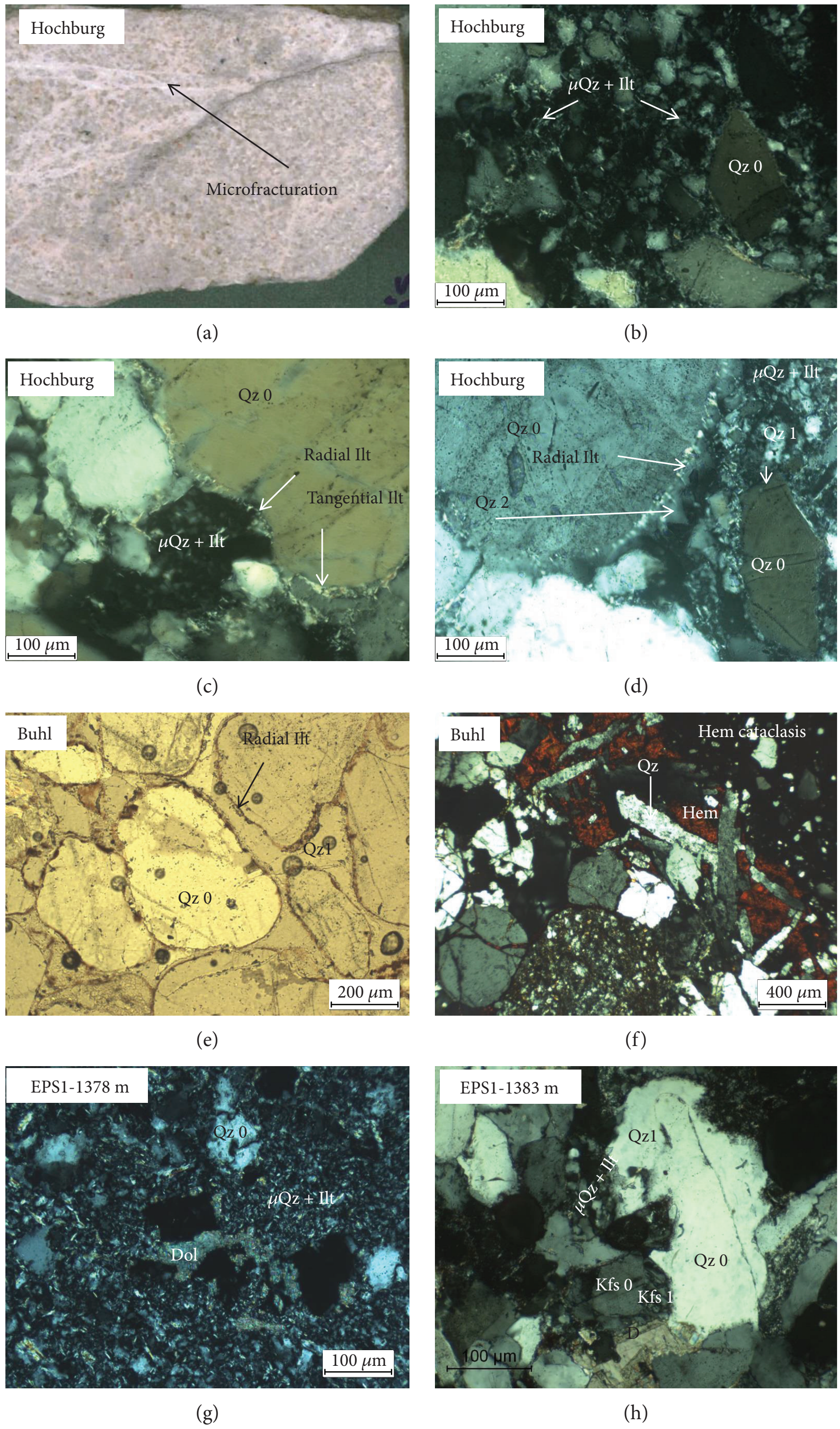

Figure 8: Fractures and matrix along fractures in sandstones. (a, b, c, d) Example from Hochburg: (a) Whitish and microfracture cutting across sandstone; (b) microscopic image of whitish microfractures that provide evidence of cohesive microcataclasite cemented by microquartz (μQz) and illite (Ilt) (polarized light); (c) detail of the matrix along the whitish microfracture, showing microquartz and illite (μQz + Ilt) and cements of radial illite and tangential illite (polarized light); (d) another detail of the matrix showing quartz overgrowth, cement of microquartz and illite, and growth of radial illite on detrital quartz cemented by diagenetic quartz (Qz1) (polarized light); (e, f) example from Buhl: (e) matrix of fractured sandstone showing massive quartz cementation (Qza) of detrital quartz surrounded by radial illite (natural light); (f) cohesive microcataclasite cemented by quartz and hematite (Hem), then crosscut by a vein of quartz and hematite (polarized light); (g, h) Examples from EPS1 well: (g) fracture at 1378 m showing cohesive cataclasite cemented by microquartz and illite, then crosscut by dolomite filling (polarized light); (h) sandstone matrix at 1383 m showing late dolomite cementing all the earlier authigenic minerals (polarized light).

quartz and barite. In this last case, barite occurs in the center of the fracture indicating that barite precipitated later than quartz. In the sandstone matrix near the quartz-filled fractures, quartz cement noted/identified as Qz2 (porosity plugging by quartz, euhedral quartz) is well developed in intergrain porosity and in K-feldspar dissolution porosity, suggesting that the K-feldspar dissolution process occurred prior to quartz filling; barite cement is rare at contacts with barite fractures. Carbonates are not present in fractures that crosscut the sandstone, but their relationships with other diagenetic minerals strongly suggest that carbonates precipitated later than the first generation of fractures associated with cataclasis and the K-feldspar dissolution process.

5.1.3. Fracture Description of Outcrops outside the Graben. Whereas numerous fractures were measured in the field, no slickenlines were observed. The Annaberg and Bad Dükheim quarries exhibit large fracture planes, almost regularly spaced out with a fracture density of approximately 1-2 fractures/m. At Cleebourg, the density is similar, approximately 1.3 fracture/m, but the density is not everywhere homogeneous and it increases closer to the Rhenane border fault, which cuts across the quarry (Figure 1(b); [85]). Although the Rothbach quarry is located close to the Vosgian fault at the border/margin of the Saverne fracture field (Figure 1(b)), fracture density is low, less than 0.5 fracture/m, making it possible to explore for ornamental rocks. Like Cleebourg, the Soultz-les-Bains quarry is highly fractured due to the presence of a large fault. Fracture density is approximately 3 fractures/m. At Bühl, in the Vosgian sandstones, large fracture planes cut across the Vosgian sandstones with a density of approximately 1 fracture/m.

In the Permian sandstones of the Saint Pierre Bois and Champenay quarries, fracture density is similar, approximately 1-2 fractures/m, even though they do not have the same spatial relationship to the Rhenane fault; Saint Pierre Bois is near the fault and Champenay is more distant (Figure 1(b)).

The fracture orientations depict an approximately N-S fracture set present in all outcrops of the Buntsandstein, corresponding to the average direction of the graben border fault (Figure 4). However, this is not always the major set, as at Annaberg and Soultz-les-Bains, where a NW-SE fracture set is dominant. The N170°E direction, very common in the EPS1 well, is less common at the surface, except at Rothbach and Soultz-les-Bains (Figure 4).

In the Waldhambach quarry, a large Permian volcanic lava flow overlies the Permian sandstone and underlies the Buntsandstein sandstones. These Permian volcanic rocks are highly hydrothermally altered and fractured. The two major fracture sets are N110°E-N130°E and N10°E-N20°E (Figure 4). Both sets are consistent with those in the Permo-Triassic sandstones, whereas the N110°E set is not present in the Permian sandstones of Champenay (Figure 4).

Sandstone cementation is minor and is characterized by growths of quartz aureoles (Qz1), K-feldspar, and radial illite-like clays. Fractures observed in sandstones collected in quarries seem poorly filled in the field: microscopic observations confirm few fillings in fractures and rare cataclastic textures. At Champenay, quartz cementation (Qz2) is observed in sandstone near a N15°E fracture. Faults and fractures striking N160°E to N170°E at Hochburg and Bühl are associated with cataclasis textures and cemented by microcrystalline quartz and illite-like clays (μQz + Ilt) (Figures 8(a) and 8(b)). This filling is also present in matrix cement near cataclastic planes. At Bühl, several N20°E quartz-hematite (Hem) veins associated with quartz cementation of the close matrix have been reworked in cataclastic planes (Figures 8(e) and 8(f)).

5.2. Paleozoic Basement

5.2.1. Fracture Description in Well EPS1 inside Graben. In the first (1418.43 m, 1427.30 m, 1430.64 m, and 1434.31 m) and second (1648.15 m) fracture zones (Figure 7), alteration of the granite matrix consists of (a) extensive sericitization of plagioclase, (b) illite-like clays + titanium oxides that replace early ferromagnesian minerals (biotite, amphibole, and muscovite), and (c) quartz + carbonate + titanium oxides that replace titanite.

At 1418.43 m, the sample contains numerous subhorizontal fractures (Figure 7) that are characteristic of the top of the granite; they are attributed to a surface-stress relaxation effect that prevailed during unroofing of the batholith in the Permian period [60]. Fracture fill consists of carbonates that have a homogeneous red-orange color under CL. Where numerous carbonate veins crosscut ancient biotite, the biotite is entirely replaced by illite-like clays + carbonate (red-orange under CL) + hematite. Where micron-sized fissures penetrate into biotite sheets, the biotite is replaced by yellowish illite with fibrous carbonate (dark red under CL) intercalated in the sheets.

The sample at 1427.30 m contains a NW-SE-oriented and centimeter-thick reddish fracture zone whose infilling is clearly polyphase (Figure 9). The first stage consists of a cohesive cataclasite cemented by illite-like clays and microquartz and rimmed by massive oriented sericite; some micron-sized monazite grains are associated with this early stage. The second stage consists of euhedral quartz and the third stage of gray carbonate (red-orange under CL) alternating with minor light-colored carbonate (dark red under CL). Minor barite (Brt) is observed in residual porosity in dolomite. The wall rock consists of altered granite marked by sericitization and iron oxide and carbonate precipitation in the secondary porosity of dissolved plagioclase. Carbonates in the wall rock have the same red-orange color under CL as dominant carbonates filling the fracture (Figure 9).

At 1430.64 m, the sample contains an E-W-oriented and 5 mm-thick dark reddish fracture within subeuhedral dark carbonate with minor euhedral quartz that crosscuts the granite (Figure 7). The color of the carbonate is largely due to an abundance of μm-sized iron oxide particles. Carbonates are red under CL. Under the microscope, the carbonate filling and the granite matrix are crosscut by an independent network of μm fissures of illite-like clays ± quartz. This texture strongly suggests that the illite/muscovite fissure network is later than the carbonate fissure network.

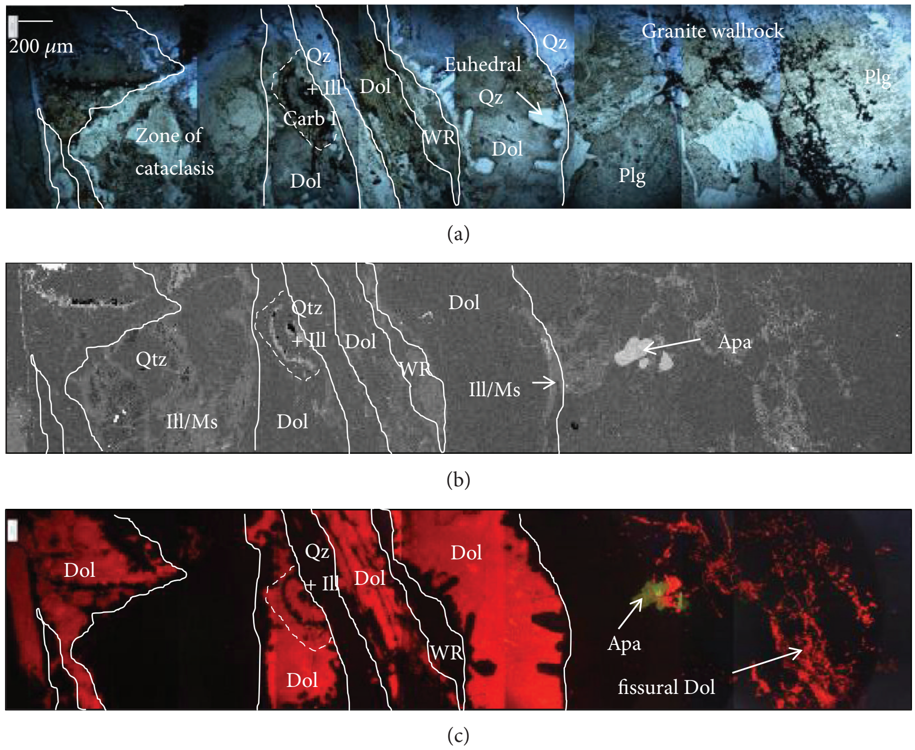

Figure 9: Image in transmitted natural light (a), backscattered electron image (b), and CL image (c) of a NW-SE mm-thick fracture and its granite wall-rock (WR) (EPS1-1427.30 m core sample) (images modified from [119]). Combined images provide evidence of polyphase filling of the fracture including a first stage of cataclasis cemented by quartz (Qz) and illite-muscovite (Ill/Ms) followed by euhedral quartz, then carbonate (dolomite) well identified by its red-orange color under CL. On the right side of the images, alteration of the wall-rock is marked by partial dissolution of plagioclase (Plg), precipitation of carbonate in secondary porosity in dissolved plagioclase and alteration of primary apatite (Apa) well identified by CL by yellowish-green color.

The sample at 1434.31 m contains two subparallel NNW-SSE <5 mm reddish fractures, the largest one being crosscut by a fine white illite-like clay fissure plane (Figure 7). The mineral infilling sequence is almost the same as that of sample at 1427.30 m. However, the microtextures are slightly different, because here the microfissures have only one filling (sericite + microquartz or carbonates that have red and dark red colors under CL). Moreover, the residual porosity is filled by carbonates (dark red under CL) and limpid quartz. Although illite fissures macroscopically seem to crosscut the reddish carbonate fracture, microscopically carbonate infills residual porosity and crosscuts an illite-like clay + quartz cataclastic zone.

At 1648.15 m, the sample is crosscut by a network of microfissures related to a NE-SW ~5 mm thick fracture (Figure 7). The fracture corresponds to a network of subparallel illite ± quartz fissures. Carbonate (dark red under CL) occurs as a discontinuous filling in this network and penetrating the granite matrix and forming a 200-300 μm-thick vein.

In the third fracture interval, the EPS1 granite has reddish silicified zones alternating with pink less-altered zones. The fracture density remains high (Figure 7). The mineralogy of the highly altered granite matrix at 2158.68 m is similar to that observed in both the first and second fracture intervals. In a less altered sample at 2161.66 m, remnant chlorite and titanite phantoms occur in the place of primary biotite. This assemblage is the early metamorphic/hydrothermal identified in the EPS1 granite. At 2158.68 m, the sample is crosscut by a network of carbonate (yellow-orange color under CL) fissures (Figure 7). A few fibrous carbonate lenses (dark red under CL) are observed in sheets of altered biotite. At 2161.43 m, the sample is crosscut by a NW-SE fracture and by a network of fissures filled predominantly by carbonate (dark red color under CL) with minor quartz (Figure 7). As we observed in the sample at 1418.43 m, dark carbonate under CL occurs as fibrous lenses intercalated in sheets of altered biotite. Yellow red carbonate under CL is present in altered plagioclase and also in a several fine veinlets crosscutting granite and also in sheets of altered biotite.

5.2.2. Fracture Description of Outcrops outside the Graben. Most granites that crop out in this study area are highly fractured, but the few striated faults that were observed were not enough to perform a significant kinematic inversion for this study. The fracture density ranges between one to more than ten fractures/m, as in the EPS1 well (Figure 7). Most sites, mainly in the Vosges and the northern Black Forest, as well as Wald-Michelbach, Weinheim, Waldhambach, Windstein, Weiler, Saint Pierre Bois, Metzeral and Wintzenheim, have rather homogeneous fracturing, with a fracture density of less than 5 fractures/m. Outcrops in the Southern Black Forest, Wolfbrunnen, Ottenhöffen, and Steinach quarries have a fracture density of more than 5 fractures/m with large

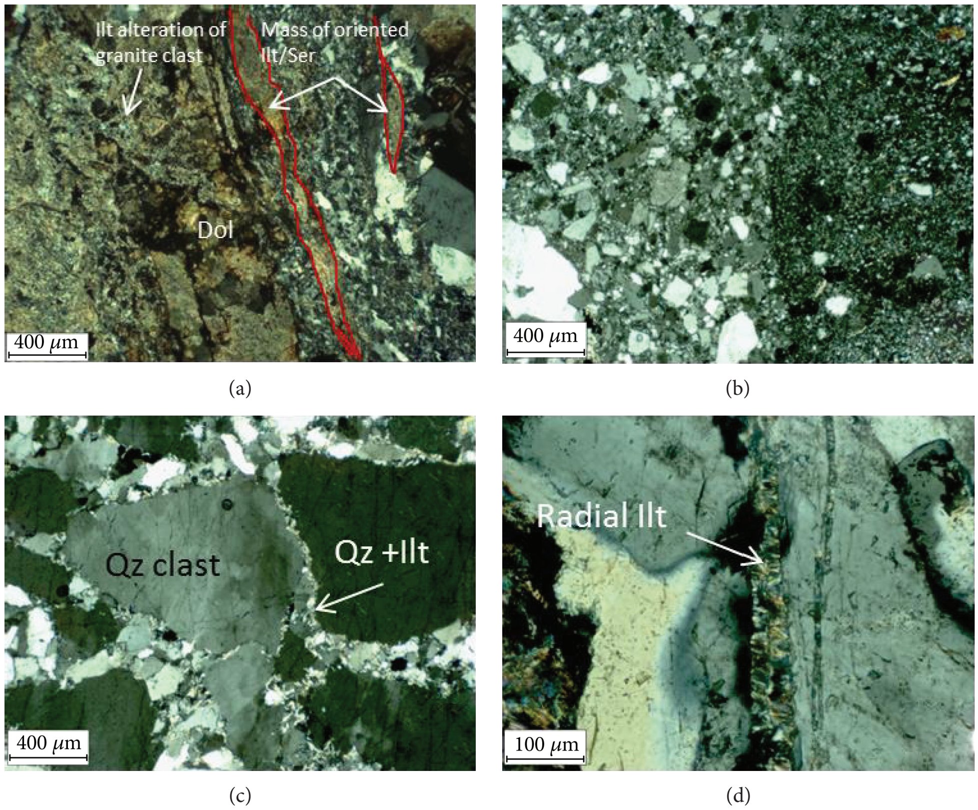

Figure 10: Microphotographs in polarized light of different types of fractures affecting granites on the flank of the Rhine Graben (images modified from [119]): (a) shear/cataclasis with sericite mass/granite clasts in a NW-SE fracture (Waldhambach); (b) cataclastic texture in a E-W fracture (Saint Pierre Bois); (c) protocataclasis of a N50°E quartz vein crosscutting Wintzenheim granite; (d) N170°E fissure filled with radial illite and crosscutting the Metzeral granite.

fracture zones that can measure several tens of meters in the vertical direction (Steinach). The most fractured outcrops are located near Andlau, where fracture density exceeds 10 fractures/m. Other authors have observed even higher fracture densities [86], most likely related to this site's location within the Lalaye-Lubine tectonic zone. This zone represents the boundary between the Saxo-Thurigian and Moldanubian domains [87], which extends under the graben and into the Black Forest near Baden-Baden (Figure 1(b)).

The predominant fracture set observed in outcrops and quarries is NW-SE. It is present at all sites except at Wolfbrünnen, where the quarry wall has almost the same orientation, and in Wald-Michelbach, where only five measurements are available (Figure 6). The conjugate set oriented NE-SW is present along with the NW-SE set at the same sites, except at Metzeral and Steinach, but in these cases not many measurements are available (5 and 8, respectively) (Figure 6). Although not a main fracture set, the N-S fracture set is present at all sites except Andlau (Figure 6).

A fourth fracture set is oriented E-W, but this set was present at only two sites, at Saint Pierre Bois and Wolfbrünnen, where it is the dominant set (Figure 6).

In granite fractures, quartz is the dominant fill mineral identified in the field. Whereas macroscopic fillings are rare, microscopic observations of thin sections provided evidence of two major types of textures and fillings: (1) cataclastic texture associated with a few quartz and illite-like clays fillings (Figures 10(b), 10(c), and 11) and (2) fractures with fillings of quartz, illite-like clays, and carbonates (Figures 10(d) and 11).

Fillings of quartz, illite-like clays, and carbonates are observed in fractures affecting granite from the Waldhambach quarry, the Heidelberg well, and the Windstein outcrop. At these three sites, the basement consists of a biotite-amphibole monzogranite. Alteration of the fracture-free granite matrix is minor, marked by partial sericitization of plagioclase and partial to complete replacement of ferromagnesian minerals by a chlorite-illite-epidote assemblage. Fractured granite samples are crosscut by NE-SW and NW-SE thin polyphase fractures.

The Weiler, Andlau, Wintzenheim, Metzeral, and Weinheim outcrops and Saint Pierre Bois, Steinach, Ottenhöffen, Wolfbrünnen quarries are predominantly biotite granite. Alteration of the granite matrix, regardless of fracture orientation, is marked by sericitization of plagioclase and muscovite and also to a certain extent by a complete breakdown of biotite/chlorite into illite-like clays and hematite. We distinguished two types of fractures: (1) fractures associated with cataclastic textures (Figures 10(a) and 10(b)) and (2) fractures without displacement and cataclasis (Figure 10(d)). Cohesive cataclasites are observed in NE-SW/NW-SE, E-W, and N-S structures (Figures 10(a)–

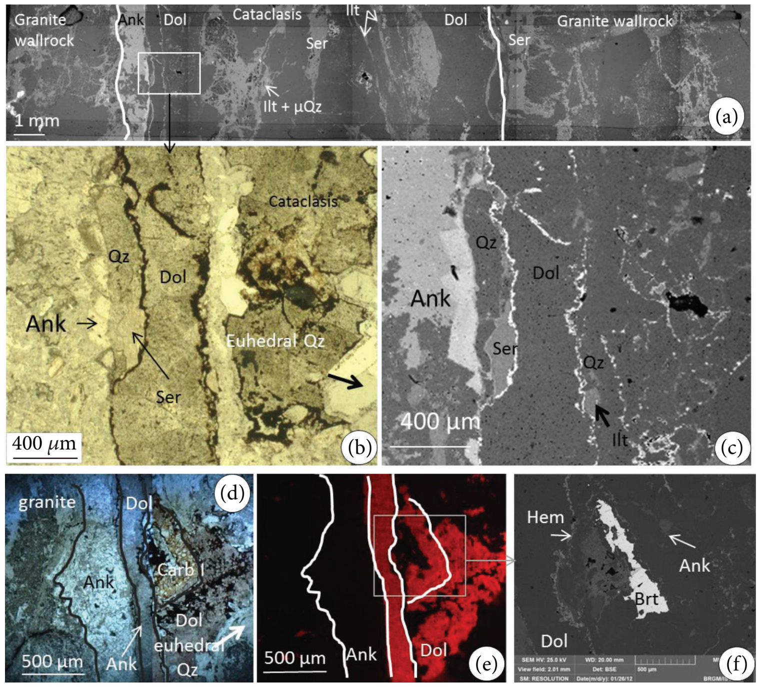

Figure 11: Polyphase filling in a microfracture that crosscuts the Waldhambach granite (images modified from [119]). (a) BSE image of the entire filling; (b) detail of textural relationships between cataclasis, euhedral quartz, and carbonates (dolomite and ankerite) (natural light); (c) the same zone in BSE; (d) detail showing the textural relationship between euhedral quartz, carbonates, and barite; (e) same image in CL: a first type of carbonates is red orange color under CL, and the second type is not luminescent (Ankerite); (f) same image in BSE.

10(d), respectively). Cohesive cataclasites are partially to totally cemented by an assemblage of microquartz and illite-like clays (Figure 10). In NE-SW and NW-SE structures at Ottenhoffen, veinlets of euhedral quartz have reworked cataclasites. Fractures without displacement that are filled with radial illite-like clays ± quartz or carbonates + quartz are everywhere observed in parts of the granite that have been preserved from direct weathering by meteoric waters (Figure 10(d)). Most of them are <200 μm fractures not visible in the outcrop; in thin sections, they are present as a network of fissures rather than as isolated fractures. For this reason, it was often difficult to measure their orientation. Only well-preserved fissures filled with radial illite-like clays are oriented at around N170°E in the Metzeral granite (Figure 10(d)).

At Waldhambach, details on a cm-thick fracture zone (Figure 11) provide evidence of polyphase filling very similar to that described in the EPS1 sample at 1427.30 m. The paragenetic sequence is defined by (1) cohesive cataclasite cemented by illite-like clays and microquartz and rimmed by massive oriented sericite (Figure 11(a)), (2) growth of euhedral quartz in the porosity of the cataclasite (Figures 11(b) and 11(c)), and (3) carbonates and finally barite (Figures 11(d)–11(f)). CL observations of carbonates show two types of carbonates: a first filling, which appears as red-orange color, and a second one that is not luminescent. Alteration of the fracture wall rocks is marked by intense sericitization of plagioclase, partial recrystallization of muscovite flakes in the sericite, and complete replacement of ferro-magnesian minerals by sericite, titanium oxides, and iron oxides (hematite).

5.3. Chemical Composition of Minerals in Cement. The electron microprobe was used to analyze feldspar in granites and in sandstones to trace the source of Ba that was precipitated from hydrothermal fluids (Supplementary Materials (available here)). Primary K-feldspar in granite and detrital K-feldspar in sandstones contain traces of Ba (1361–9538 $mg.kg^{-1}$). Rare authigenic K-feldspar does not contain Ba.

A few infrared spectra were acquired on bulk rock samples of altered granites and sandstones. Electron microprobe analyses were carried out on clay minerals observed in studied fractures that crosscut EPS1 and the Waldhambach granite and in studied EPS1 Buntsandstein sandstones and Permian arkoses of Saint Pierre Bois, to identify major clay minerals (Supplementary Materials). Infrared provides evidence of illite as a major alteration product in granites from Ottenhoffen, Wolfbrunnen, Wald-Michelbach and as a major clay mineral in the Hochburg sandstone. Most illite-like clays observed in thin sections are illite or illite-muscovite, according the triangular 4 Si-(Na + K + 2Ca)-(Mg + Fe^{2+}) diagram of Meunier and Velde [88] (Figure 12(a)).

Electron microprobe analyses were conducted on the different types of carbonates identified by CL (Supplementary Materials; Figure 12(b)). Carbonates that fill fractures in granites in the EPS1 well (EPS1-1427 m) and at

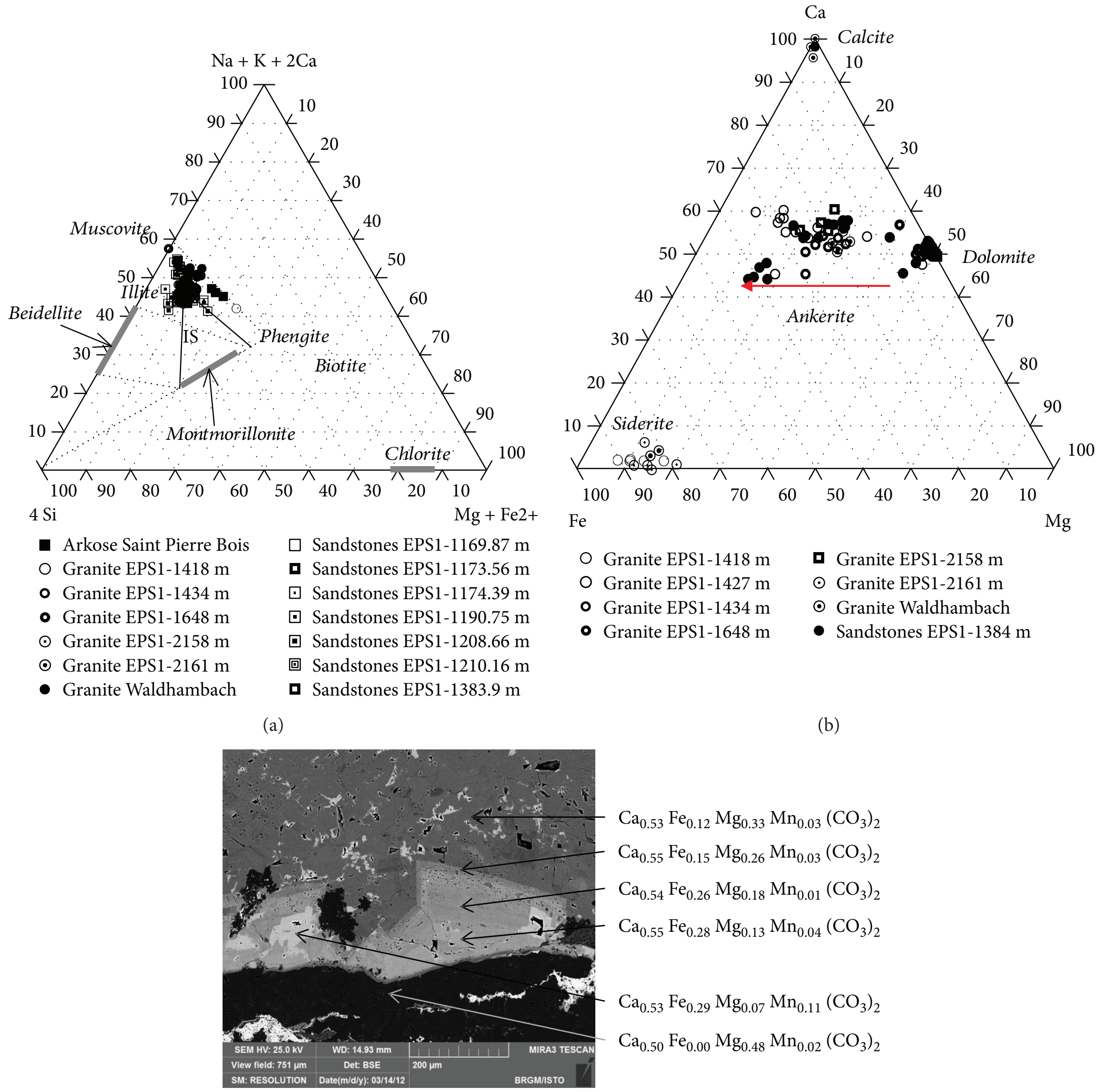

(c)

Figure 12: (a) Triangular 4 Si-(Na + K + 2Ca)-(Mg + Fe^{2+}) diagram of Meunier and Velde [94] showing the nature of the illite-like clays present in fractures of granites (EPS1 and Walhambach) and in sandstones. (b) Triangular Fe-Ca-Mg diagram showing chemical compositions of the various generations of carbonates in fractures of granites (EPS1 and Waldhambach) and in EPS1 sandstones. (c) Backscattered electron image showing chemical zoning of the dolomite-ankerite-kutnahorite solid solution (EPS1-1427 m).

Waldhambach and carbonates that cement sandstones in the EPS1 well (EPS1-1983.9 m) have an essentially homogeneous red-orange color under CL. This carbonate population is a quite pure dolomite (Dol). Dark red to nonluminescent carbonates consist of a dolomite-ankerite-kutnahorite solid solution with variable amounts of Fe (up to 24.70 wt % FeO) and Mn (up to 8.3 wt % MnO) substituting for Mg (Figure 12(c)). The luminescence of these carbonates decreases with increasing Fe and Mn in the crystal lattice. Fibrous carbonates present in biotite sheets in granite are essentially siderite that contains up to 3.5 wt % of CaO and up to 7.7 wt % of MgO. Calcite, which is yellow orange under CL, is observed in plagioclase alteration products and in some veinlets of EPS1-1648 m, EPS1-2158 m, and EPS1-2161 m.

5.4. Stable Isotopes. To determine the origins of the hydrothermal fluids, we analyzed the stable isotopes in the major minerals (carbonates, quartz, and barite) that fill both fractures and porosity in a few samples of sandstones, granites, and Permian volcanics from the EPS1 well and from quarry outcrops (Saint Pierre Bois, Waldhambach). Fractures with polyphase filling and relatively thick fractures were selected for this analytical task, but the number of selected samples

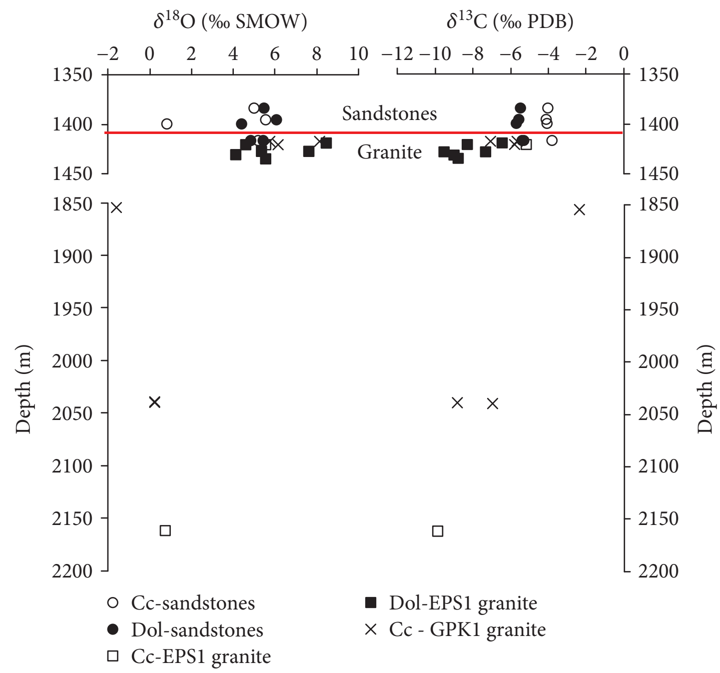

Figure 13: Profiles of $\delta^{18}O_{fluid}$ and $\delta^{13}C_{fluid}$ reported as a function of depth. The fluid data are calculated at equilibrium with calcite and dolomite in the upper part of the granite and the sandstones from the EPS1 well.

was limited due to the rarity of this type of sample. (C, O, and Sr) stable isotopes were measured on the primary carbonates (calcite and dolomite); oxygen isotopes were measured on quartz, and strontium isotopes on barite (Supplementary Materials).

The $\delta^{18}O$ values of dolomite in sandstones from the EPS1 well are almost homogeneous, ranging between +19.2 and +20.3‰$_{SMOW}$. Associated calcite, when present in the same samples, shows two populations of $\delta^{18}O$ values: (1) a value of +13.9 and (2) values of between +18.0 and +18.6‰$_{SsMOW}$. Oxygen isotopic fractionation between dolomite and calcite calculated for each sample is 5.3 between dolomite and the first population of calcite, and 2.0-2.3 between dolomite and calcite of the second population. Based on the oxygen isotopic fractionation of Sheppard and Schwarz [89], a value of 5.3 does not correspond to a consistent temperature, indicating that the first population of calcite and dolomite did not precipitate from the same fluid. On the contrary, values of 2.0-2.3 correspond to coherent temperatures of 135-160°C, indicating that dolomite and the second population of calcite precipitated from the same fluid at temperatures of 135-160°C. This temperature range is consistent with those obtained by fluid inclusion microthermometry in quartz and carbonates in veins in the EPS1 granite [67].

Fracture-fill dolomite in the first fracture interval in the upper part of the granite in the EPS1 well has homogeneous $\delta^{18}O$ values of 19.0-23.3‰$_{SMOW}$. Calcite from this interval has a similar $\delta^{18}O$ value of +18.6‰$_{SMOW}$, whereas calcite from the third fracture interval has a lower $\delta^{18}O$ value of 13.9‰$_{SMOW}$.

The $\delta^{18}O$ of euhedral quartz measured in fractures with polyphase filling that crosscuts granite in the EPS1 well at 1427.30 m and granite at Waldhambach are almost similar: +10.9 to +14.7‰ with an average value of +13.0 ± 2.1‰, and +11.6 to +14.8‰ with an average value of +13.0 ± 1.1‰, respectively.

The $\delta^{18}O$ of fluids were calculated at equilibrium with the various minerals in fractures that crosscut granite or fill porosity in the Buntsandstein, taking into account their formation temperature and fluid-mineral isotopic fractionations (for oxygen: quartz-H_2O [90]; dolomite-H_2O [91]; calcite-H_2O [92]; for carbon: dolomite-CO_2 [93]; calcite-CO_2 [94]). We used temperatures of 135-160°C obtained by calcite-dolomite oxygen thermometry for carbonate cements in sandstones from the EPS1 well. For quartz and carbonates filling fractures in granite from the EPS1 well, we used temperatures of 140-150°C according to [67] and complementary fluid inclusion microthermometry conducted on euhedral quartz in a polyphase vein of the EPS1 well, sample at -1427.3 m (Supplementary Materials). Taking into account the similarities of the polyphase fracture filling in the EPS1 granite at 1427.3 m and in the Waldhambach granite (same sequence of cementation in vein, same range $\delta^{18}O$ of quartz, and same range of $^{87}Sr/^{86}Sr$ in dolomite), we assume temperatures of 140-150°C for the quartz and carbonates filling the fracture in the Waldhambach granite.

The $\delta^{18}O$ and $\delta^{13}C$ values of the fluids (noted $\delta^{18}O_{fluid}$ and $\delta^{13}C_{fluid}$) at equilibrium with calcite and dolomite in the upper part of the granite and the sandstones from the EPS1 well are reported in Figure 13. The ranges of $\delta^{18}O_{fluid}$ at equilibrium with EPS1 dolomite in sandstones (4.4-6.1‰$_{SMOW}$) and granite (4.1 and 8.5‰$_{SMOW}$) and with a population of calcite in sandstone (5.0-5.2‰$_{SMOW}$) are almost identical; this range of $\delta^{18}O_{fluid}$ values indicates a major brine component in hydrothermal fluids. The $\delta^{18}O$ values of the fluids at equilibrium with the second population of calcite (0.8‰$_{SMOW}$) and with a euhedral quartz-filled fracture that crosscuts the upper part of the granite in the EPS1 well (-6.3 and -0.9‰$_{SMOW}$) and at Walhambach (- 5.7 to -2.5‰$_{SMOW}$) are significantly lower and provide evidence of brines with variable amounts of meteoric component.

The $\delta^{13}C_{fluid}$ at equilibrium with EPS1 calcite (-4.1 to -3.8‰$_{PDB}$) and dolomite (-5.7 to -5.3‰$_{PDB}$) in sandstones are very similar to $\delta^{13}C_{fluid}$ at equilibrium with EPS1 calcite (-5.2‰$_{PDB}$) and dolomite (-6.5‰$_{PDB}$) in granite at the interface. The $\delta^{13}C_{fluid}$ at equilibrium with EPS1 carbonates in granite decrease down to -10‰$_{PDB}$ with depth. This wide range of $\delta^{13}C_{fluid}$ suggests mixing between different carbon sources: (1) carbon derived from carbonates present in the sedimentary cover (sandstones: $\delta^{13}C_{fluid}$ ~-4‰$_{PDB}$) (2) and carbon of deep-seated origin ($\delta^{13}C_{fluid}$~-10‰$_{PDB}$).

$^{87}Sr/^{86}Sr$ ratios measured in carbonates and barite that fill fractures are representative of the fluid signature at the moment of mineral precipitation. Dolomite and barite that fill a fracture that crosscuts Permian sandstones and volcanics in the Waldhambach quarry have $^{87}Sr/^{86}Sr$ ratios of 0.709817 and 0.709753, respectively. Dolomite that fills a fracture that crosscuts granite in the Walhambach granite has a $^{87}Sr/^{86}Sr$ ratio of 0.708993. The $^{87}Sr/^{86}Sr$ ratio of dolomite that fills a crosscutting fracture in granite in the EPS1 well is 0.708685. The close similarities of $^{87}Sr/^{86}Sr$ ratios of dolomite and barite in the Permian cover, in the Waldhambach granite, and in the EPS1 well suggest that dolomite and barite precipitated from the same hydrothermal fluids circulating at the cover/granite interface. Barite in crosscutting fractures in granite at Saint Pierre Bois has a $^{87}Sr/^{86}Sr$ ratio of 0.716273, providing evidence that barite was precipitated from a different fluid circulation than at Waldhambach and in the EPS1 well.

6. Discussion

6.1. Major Fracture Sets and Their Ages. The Rhine graben has a long tectonic history beginning with the Hercynian orogeny, followed by peneplanation with Permian N-S extension and sedimentation during a lengthy period of tectonic quiescence from the Triassic to the Jurassic. The region was uplifted during the Cretaceous; the Rhine graben began to open during the Eo-Oligocene and continued with different phases throughout the Tertiary [43, 48].

Three major fracture sets were identified in the sedimentary cover and the Hercynian basement of the Rhine graben: N-S, NE-SW/NW-SE, and E-W. In spite of the long history of the Rhine graben and the reactivation of numerous fractures and faults, especially in the basement, we can associate these main fracture sets with the tectonic phases of the Rhine graben area (Figure 3).

The N-S set is associated with the main graben phases of Eocene N-S compression and Oligocene E-W extension [48]. However, in the Hercynian basement, this set was reactivated during the Carboniferous Sudete phase [44]. This fracture set predominates in the Hercynian basement inside the graben (EPS1 well), but is minor on outcrops of Hercynian basement on the flanks of the Rhine graben. Andlau is an exception, where the NE-SW Lalaye-Lubine-Baden-Baden tectonic zone has a major impact on the surrounding area and the N-S fracture set may be hidden by this tectonic structure. In the Permo-Triassic sandstones, the main fracture set orientations fall between N160°E and N40°E similar to the orientation of large mapped structures genetically related to graben opening. The direction variation depends on the proximity of observation sites to major faults. Several N-S fractures are large fault zones in the Permo-Triassic sandstones both outside the Rhine graben (Bühl sandstones) and inside the Rhine graben (fault zone between 1172 and 1210 m in the EPS1 well).

The NE-SW and NW-SE fracture sets are well represented in granite outcrops on both sides of the Rhine graben and less so in the Hercynian granite in the EPS1 well within the Rhine graben. These NW-SE and NE-SW sets in the Hercynian basement are linked to Carboniferous N-S compression that was probably reactivated in the Tertiary. The NW-SE fracture set is also present in the Permo-Triassic sandstones and is probably linked with the most recent Plio-Quaternary NW-SE compression.

The E-W fracture set is primarily observed in the Hercynian basement at Saint Pierre Bois and Wolfbrünnen (this study) and at Schauenburg near Heidelberg on the eastern flank of the Rhine graben [73] and more rarely inside the graben. Fractures belonging to this set are less frequent than fractures of other sets. The Saint Pierre Bois quarry is located in the Permian Villé Basin. This basin collapsed due to a weakness zone caused by the intersection of Lalaye-Lubine-Baden-Baden tectonic structure and the Sainte Marie aux Mines fault zone, which is oriented N30°E and crosscuts the entire southern Vosges Massif (Figure 1(b)). In this complex zone, the basement is highly fractured by N-S to E-W faults and a N130°E fault set [86, 95]. Another E-W fault also affects Permian rhyolites at Schauenburg [73]. The E-W set is linked to the most recent tectonic phases of the Hercynian stages during the Permian [46], which correspond to extension prior to the collapse of the range and peneplanation. These fractures were also reactivated by brittle deformation in the Tertiary [43].

6.2. Relation between Fracture Direction and Fracture Fillings. The combination of structural measurements and mineral sequences of fracture fillings provides evidence that some types of filling are associated preferentially with specific fracture set directions (Figure 14).

6.2.1. N-S Fracture Set. Outside the graben, N-S fractures are commonly observed in Permian-Triassic sandstones and less so in the Hercynian basement (Figures 4 and 6). Fractures generally exhibit shearing and cataclastic textures and are unfilled to poorly filled in both sandstones and Hercynian basement. Only a few fractures filled with radial illite crosscut Hercynian granite on the Metzeral outcrop. Sandstones exposed in quarries near major N-S features are highly fractured and bleached (Cleebourg, Bad Durkheim), and fillings are absent, suggesting that these N-S structures represent present-day fluid recharge zones. When fillings are present, cements are dominantly microquartz and illite

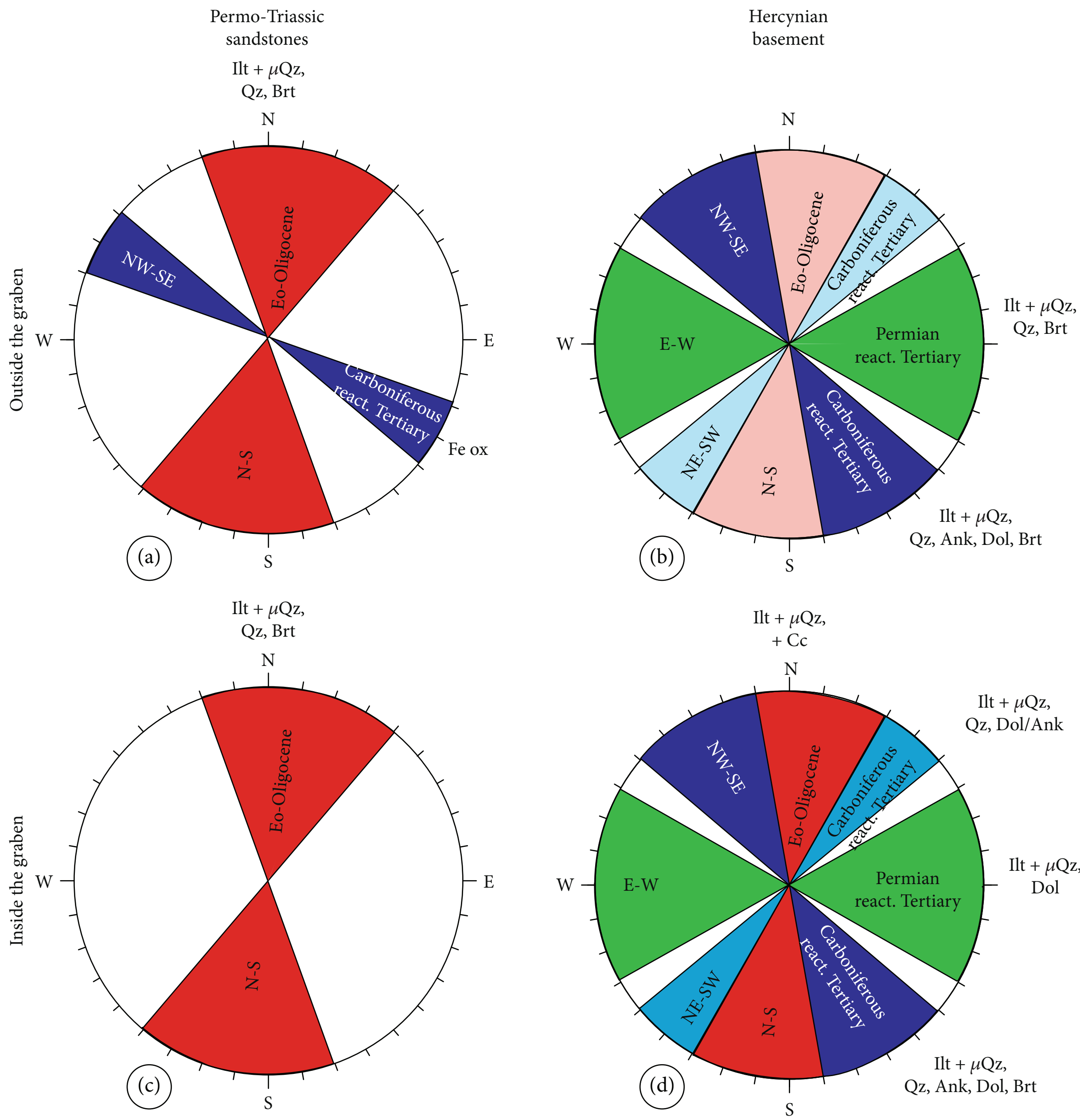

Figure 14: Synthesis of the main observed fracture directions with associated filling in the Hercynian granite and the Permo-Triassic sandstones inside and outside the graben. The Ilt + μQz combination is generally associated with cataclasis.

(Figure 14(a)). Rare quartz and/or barite veins reoccur within older cataclastic structures (Figure 14(a)). Microthermometric and oxygen isotopic data of this type of quartz in a N-S fault plane affecting Triassic sandstones at Bühl (130°C, $\delta^{18}O_{fluid}$ -1.5‰) [96] indicates that the quartz was precipitated from hot fluids composed of brines mixed with meteoric fluids. The discovery of such temperatures outside the graben indicates that these fillings formed at depth prior to graben collapse.

Inside the graben, the N-S fractures affect both the Triassic sandstones and the Hercynian basement (Figures 14(c) and 14(d)). The large fracture zone affecting Triassic sandstones at depths of 1170-1210 m is quite similar to the large fault plane at Bühl in terms of mineral fillings and formation conditions (Figures 14(a) and 14(c)). Unlike Hercynian granites outside the graben, N-S fractures in the EPS1 Hercynian granite inside the graben are filled with calcite (Figure 14(d)) precipitated from brines with a high meteoric water content ($\delta^{18}O_{fluid}$ ~0.8‰$_{SMOW}$) down to 600 m. Calcite with similar $\delta^{18}O$ was also found in the EPS1 sandstones (this study) and in granite in other wells (GPK1 at 1998.9 m; GPK2, GPK3, and GPK4 down to ~4900 m) [68, 97]. Dolomite is found only in the first and second fracture intervals of the EPS1 well corresponding to depths of 200-300 m under the cover/granite interface. Such data strongly suggest that brine that circulated at the cover/basement interface and precipitated dolomite in ancient structures prior to graben collapse continued to circulate at higher depth into the granite via tertiary N-S structures. The lower $\delta^{18}O_{fluid}$ range seems to suggest an increasing supply of meteoric waters into the fractured reservoir.

6.2.2. NE-SW and NW-SE Fracture Sets. The NE-SW and NW-SE fracture sets are primarily present in the Hercynian basement inside and outside the Rhine graben (Figures 14(b) and 14(d)).

Numerous fractures within the NE-SW and NW-SE fracture sets have polyphase fillings. This indicates that (1) various generations of fluids used these fracture sets and (2) some of this circulation occurred prior to graben collapse. The more complex polyphase filling consists of cohesive cataclasites cemented by early illite and microquartz, followed by euhedral quartz and a late stage composed of dominant dolomite, minor ankerite, and calcite (Figures 14(b) and 14(d)). The variability of the mineral fillings is representative of changes of fluid chemical composition over time. Fluid inclusion microthermometric and oxygen isotopic data available on the various mineral fillings in fractures crosscutting granite and in matrix cementing sandstones at the cover/basement transition make it possible to determine fluid origins and minimal formation temperatures:

(i) Quartz in granite in the EPS1 well precipitated from multiple generations of $NaCl-MgCl_2/CaCl_2$-rich fluids at about 140-150°C [67, 69, 74]. The highest temperatures reached values up to 200°C [67]. Quartz in granite at Waldhambach shows similar characteristics. The $\delta^{18}O_{fluid}$ (-6.3 to -0.9‰) deduced from this quartz provides evidence of brines mixed with variable amounts of meteoric waters

(ii) Dolomite in sandstones in the EPS1 well precipitated from brines at temperatures of about 135-160°C and with $\delta^{18}O_{fluid}$ of 4.4 to 6.1‰, and $\delta^{13}C_{fluid}$ of -5.7 to -5.3‰.

(iii) Dolomite in granite in the EPS1 well precipitated from brines at about 140-150°C [67, 69, 74, 98]. Dolomite in the Waldhambach granite shows similar characteristics. The $\delta^{18}O_{fluid}$ (4.4 to 8.5‰) and $\delta^{13}C_{fluid}$ (-9.0 to -6.5‰) deduced from dolomite indicate brine fluids with minor meteoric waters. The lower $\delta^{13}C_{fluid}$ values are due to the contribution of deep-seated carbon

(iv) Barite at the roof of the EPS1 granite also provide evidence of brines (with up to 23 wt% Eq NaCl) and formation temperatures of ~130°C [69, 99]

As the data demonstrates, all the fill minerals precipitated at depth within a narrow temperature range (130-150°C). The $\delta^{18}O_{fluid}$ variations provide evidence of hot brines mixed with variable amounts of meteoric waters. The origins of these brines are probably seawater-modified fluids or fluids equilibrated with Triassic evaporates as proposed by [67, 98]. Carbonates and barite precipitated from brines mixed with a minor eteoric water component. The $\delta^{13}C_{fluid}$ provides evidence of two sources: carbon derived from carbonates present in the sedimentary cover (sandstones: $\delta^{13}C_{fluid}$ ~-4‰$_{PDB}$) and carbon of deep-seated origin ($\delta^{13}C_{fluid}$ ~-9‰$_{PDB}$). These $\delta^{13}C_{CO2}$ deduced from dolomite are consistent with the $\delta^{13}C$ of CO_2 trapped in magmatic quartz in granite analyzed at different depths of the EPS1 well [100]. The range of carbonate chemistry (from pure dolomite to ankerite and siderite) and barite deposition are probably represent variable water/rock interactions between brines, Fe-Mg minerals (Fe, Mg, and Mn release), and feldspars (plagioclase: Ca release; K-feldspar: Ba release) from granite and sandstones. The distribution of dolomite/ankerite with minor barite filling in NE-SW and NW-SE fractures of the granite roof and in residual porosity in the sandstones of the EPS1 well helps define the scale of brine circulation at the cover/granite interface from the top of the sandstones down to 200-300 m into the granite. The same information is inferred from very similar low $^{87}Sr/^{86}Sr$ ratios (~0.7089-0.7098) measured in dolomite in the Waldhambach granite and overlying Permian volcanic rocks.

Unlike carbonates and barite, quartz and associated illite likely precipitated from fluids with a high meteoric water component, in agreement as described by [101]. The silica source was probably the partial dissolution of feldspars, whereas illite was an alteration product of feldspars and primary micas at 130-200°C.

6.2.3. E-W Fracture Set. Outside the graben, fractures belonging to the E-W fracture set observed in granites at Saint Pierre Bois, Wolfbrunnen (this study), and at Schauenburg [73] consist of cohesive cataclasites cemented by microquartz and illite. Euhedral quartz and barite crosscut these cataclasites in a few locations at Saint Pierre Bois (Figure 14(b)). The $^{87}Sr/^{86}Sr$ ratio of barite (~0.716) at Saint Pierre Bois is significantly higher than the $^{87}Sr/^{86}Sr$ ratio of barite that fills NW-SE fractures, indicating that they precipitated from different fluids and probably at different times. U-Th data on the Schauenburg E-W cataclastic fault provide evidence that the early cataclasis zone acts as a current recharge conduit for surficial fluids [73].

Inside the graben, only a few EW fractures are encountered in the EPS1 well. One fracture at 1430 m has a polyphase filling, including early-filling microquartz + illite followed by quartz and dolomite (Figure 14(d)).

6.3. Paleocirculation, Tectonic History, and Present-Day Circulation. The comparison of major fracture sets, their mineral fillings, and their distribution in the overlying formations and in the Hercynian basement inside and outside the graben highlights different stages of deep hot fluid circulation at the cover/basement interface that has been active since graben formation until the present. Two major types of fillings precipitated successively from fluids over the same temperature range (about 130-150°C): (a) cohesive cataclasites cemented by silicates (quartz, illite) that precipitated from brines mixed with a high meteoric water component and (b) carbonates and barite that essentially precipitated from brines. It is noteworthy that both quartz/illite and carbonates/barite cementation is present in the Hercynian NE-SW and NW-SE fracture set and in the N-S fracture set. However, they differ by the nature of the carbonate that precipitated (dolomite then calcite in Hercynian fractures inside and outside the graben, and calcite in N-S fractures in the graben), by the depth of carbonate precipitation in EPS1 granite fractures (200-300 m for dolomite and more than 600 m for calcite), and probably by their timing. From these data, at least four elements seem to determine the initiation of convection fluid cells at the graben scale: (1) introduction of meteoric waters, (2) temperature, (3) fracture directions, and (4) fluid chemistry.

Prior to graben formation, the maximum burial temperatures attained in Buntsandstein sandstones are those of Buntsandstein sandstones in the eastern part of the Paris Basin. These temperatures did not exceed 100°C, and a normal thermal gradient occurs [102, 103] thus making it impossible to reach the temperatures of approximately 130-150°C (up to 200°C) that are measured in fracture fill minerals in the Rhine graben [67]. Graben formation in the Tertiary favoured both (a) temperature conditions induced by an abnormal thermal gradient associated with volcanism [50] and (b) inflows of meteoric waters to the cover/basement interface via permeable faults that crosscut the entire thickness of the sedimentary cover down to the Hercynian basement [43, 44]. The first inflows of meteoric waters probably began during Eocene E-W compression [43, 48] first via the N-S structures (Figure 15(a)). Descending cold meteoric waters mobilized silica and increased rock permeability by alteration and dissolution of silicates such as feldspars. At the cover/basement interface, descending meteoric waters mix with upflowing hot brines through the porosity of the Permo-Triassic sandstones and via reactivated Permo-Carboniferous NE-SW and NW-SE structures, resulting in first illite/quartz cementation (stage 1; Figure 15(a)). Water influx and the high thermal gradient likely gave rise to the first convective cells of fluid circulation through the sedimentary-basement interface, favouring brine/rock interaction and leading to the earliest dolomite/barite cementation (stage 2; Figure 15(a)). During these stages, brine/rock ratios remain low, as the chemical variability of carbonates suggests.

Increasing volumes of meteoric waters penetrated into the graben during major E-W extension and the graben collapse phase of the Oligocene, via large approximately N-S faults and also reactivated older faults [48]. Descending cold meteoric waters continued to mobilize silica and increased rock permeability. Active subsidence and volcanic activity during this period, primarily occurring along the western border of the Rhine graben [50], maintained hydrothermal temperature conditions in the graben. Deposition processes involved during this period were the same as those involved in depositional stages 1 and 2 (stage 3 and 4; Figure 15(b)). With active convective circulation, fluids penetrated and altered to increasing depths into the Hercynian basement in the Rhine graben, as shown by the distribution of calcite deposits in the Soultz wells [56, 68, 97].

Today's thermal profiles to a depth of 5000 m in the Soultz-sous-Forêts wells show a convection cell in the Buntsandstein between 1000 and 3500 m in the granite [51, 104]. This convection is also present in the deep geothermal wells of Landau [105] and Rittershoffen [106], close to Soultz-sous-Forêts; it reaches the granite basement, and its basal depths are 3000 m and 2700 m, respectively. However, in the eastern part of the Rhine graben, in the geothermal wells of Bruchsal [107] and Basel [108], there appears to be no convective cell, even though the wells reach depths of 2500 m and 4680 m, respectively. At Soultz-sous-Forêts, circulation between wells has been identified primarily within the NE-SW and NW-SE fracture sets [54, 109]. Geochemical studies of geothermal brines produced in the Soultz-sous-Forêts, Rittershoffen, Landau, and Insheim (close to Landau) geothermal sites show high salinity values that indicate brines formed by heightened evaporation of seawater and low meteoric water content [110]. Moreover, the estimated geothermometers indicate an equilibrium temperature close to 225 ± 25°C at Soultz-sous-Forêts [111]. The geothermal fluids collected in the granite seem originate from Triassic sedimentary formations located at depths of more than 4 km. The formation is present at that depth in the northeastern part of the Rhine graben, where the basin is deepest. In this part, the eastern border fault of the graben is a major feature [112] and it penetrates deeper into the earth's crust [113]. Therefore, this may favour fluid penetration into the deeper part of the graben where they become mineralized at the contact with Permo-Triassic saline formations. Then, these fluids flow across the graben through the oblique NE-SW reactivated Hercynian fractures to mix with fresh meteoric waters coming from the western side of the graben (Figure 15(c)).

7. Conclusions

Examination of 20 outcrops including 16 quarries along the main border faults on both sides of the Rhine graben and analysis of cores from the EPS1 well drilled in the Rhine graben show that the Paleozoic basement and Permo-Triassic formations were affected by several phases of brittle tectonics associated with fluid circulation pulses.

The fillings of Hercynian fractures in the Paleozoic basement, oriented primarily NE-SW and NW-SE, are poly-phase. The first stage of infilling (stage 1) corresponds to a cataclastic phase associated with illite and quartz, followed by euhedral quartz infillings. The presence of this pattern in the Hercynian and Permian fracture sets, mainly observed in the EPS1 well and in the Waldhambach quarry, indicates that fluid circulation that caused these fillings occurred prior to graben opening. Stage 1 is characterized by (a) reactivation of ancient Hercynian structures at the beginning of graben opening during the early Eocene related to the N-S compression affecting the European platform and (b) the first major infiltration of meteoric fluids through the sedimentary cover into the Hercynian basement.

The second major stage (stage 2) is marked by dolomite deposition within tension fractures in the upper part of the Hercynian granite basement (first 200-300 m) and in sandstone porosity in the sedimentary cover. This stage is likely the result of convective circulation of deep hot brines mixed

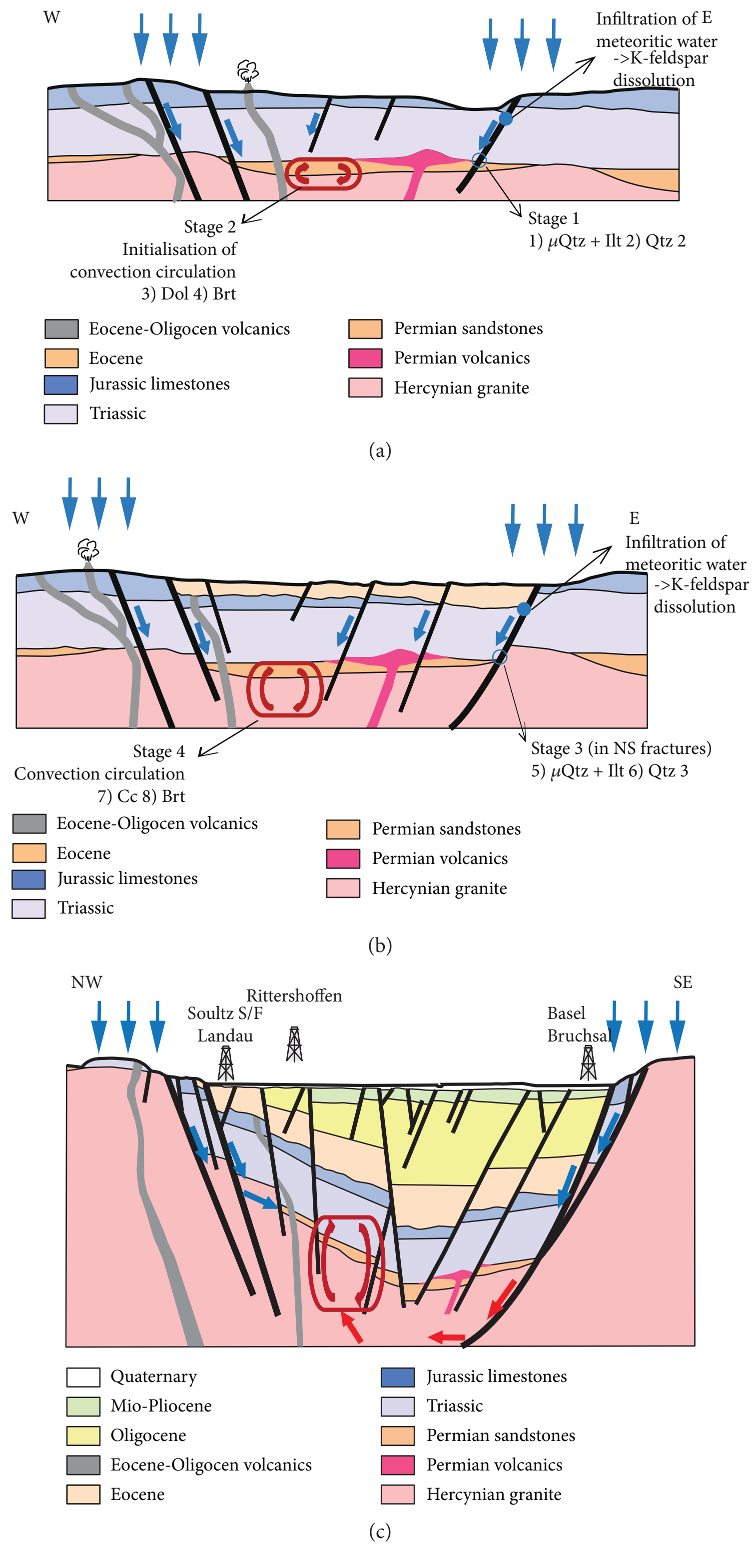

Figure 15: Schematic of fluid circulation and rock interaction during Tertiary tectonic episodes. (a) Early rifting stage during the Eocene under N-S compression associated with the paleofluid stages 1 and 2. (b) Lower Eocene and Oligocene rifting under E-W extension associated with paleofluid stages 3 and 4. (c) Present-day situation; location of geothermal sites is indicated as an approximate projection. Conceptual cross sections modified from Sittler (1992). Vertical scale is exaggerated. Blue arrows: meteoritic waters; red arrows: hot brines; curved arrows: convection cell. See explanation in the text.

with meteoric waters, probably initiated at the sedimentary cover/basement during the early stage of graben formation and associated with mantle diapirism and volcanism (Eocene-Oligocene).

A cataclasis stage is observed in the N-S fractures affecting the basement and also in Permo-Triassic sandstones, both within and outside the Rhine graben (stage 3). In outcrop, this fracture set shows few macroscopic mineralogical fillings, probably because fracture planes have been subjected to surface weathering alteration. However, at the microscopic scale, tension fissures in granite are observed to be filled with radial illite, and several large N-S shear zones affecting the Buntsandstein sandstones are filled with quartz associated with illite, hematite, and barite. Within the Rhine graben, similar quartz and barite fillings are identified in a major fracture network that affects the Buntsandstein sandstones, relatively far from the basement/cover interface. Stage 3 corresponds to the major stage of the graben opening linked with E-W extension during the Eocene-Oligocene and of a second major infiltration of meteoric fluids deeper into the Hercynian basement. Fracture fillings of this stage probably recorded fluid circulation associated with the graben opening stage just prior to and during uplift of the shoulders.

The fourth major stage (stage 4) is the continuation of convective circulation of deep hot brines mixed with meteoric-derived waters at the sedimentary cover/basement in the Rhine graben during and after the collapse. Stage 4, which is present only in the graben, is marked by barite filling N-S fractures in Buntsandstein sandstones and by calcite and barite also filling N-S fractures in the granite down to a depth of 4900 m in the Rhine graben. The Ca origin would be plagioclase dissolution and remobilization of ancient dolomite, whereas the Ba origin would be K-feldspar dissolution by descending meteoric waters. Calcite and barite continue to precipitate at depth today, and convective circulation extends deeper into the Hercynian granite basement.

To conclude, the reactivation of old Hercynian structures oriented NE-SW and NW-SE related to the earliest Eocene tectonic history of Tertiary graben formation has favoured the downflow of meteoric water and initiated fluid convection cells at the sedimentary cover-basement interface. This activity continued in the N-S structures during the Oligocene extensional phase. Today, these large N-S structures form recharge drains and promote a large-scale vertical convective circulation system in the western part of the basin, in the Buntsandstein, and in the Hercynian granitic basement.

Data Availability

The data used to support the findings of this study are available from the corresponding author upon request.

Conflicts of Interest

The authors declare that they have no conflicts of interest.

Acknowledgments

This work was funded by ADEME and BRGM within the framework of the TECITUR R&D project under agreement no. 1005C0140 and ANR under grant agreement ANR-15-CE06-0014 (Project CANTARE-Alsace). The authors thank the managers of the quarries and their associates for authorization to access the walls and site facilities. In particular, we would like to mention (i) Francine Loegel from LOEGEL for access and discussion at the Rothbach quarry; (ii) Jérémie de Bonneval and Sébastien Kuhn from LEONHART for access to the Saint Pierre Bois quarry; (iii) Willi Kuhn from GEBRUCHER KUHN for access to the Waldhambach quarry; (iv) RAUSCHER for access to the Cleebourg quarry; (v) FISHERGRANIT for access to the Wolfbrunnen quarry; and (vi) CARRIERE DE GRES DE CHAMPENAY for access to the Champenay quarry. We also thank Edgard Nitch and Wolfgang Werner from LGRB Freiburg for information about the quarries and mineralization in the Black Forest, and Albert Genter, vice general manager of ES-G, for access to the Soultz-sous-Forêts site and rock samples. For analytics, the authors thank Laurent Bailly (BRGM) for fluid inclusion microthermometry, Christine Flehoc (BRGM) for (C, O) stable isotopes, Catherine Guerrot (BRGM) for strontium isotopes, Andrey Gurenko (CRPG Nancy) for ionic probe analyses, and Guillaume Wille (BRGM) for electron microprobe and SEM images. Finally, we are also grateful to Prof. Andrea Moscariello (Universty of Geneva) for their useful comments and recommendations, which greatly improved this manuscript.

Supplementary Materials

EPS1_Cores_Sandstones: fracture orientation data on Buntsandstein EPS1 well cores. EPS1_Cores_Granite: fracture orientation data on Paleozoic granite EPS1 well cores. Outcrops-Quarries_Sandstones: fracture orientation data on Buntsandstein in outcrops and quarries. Outcrops-Quarries_Basement: fracture orientation data on Paleozoic basement in outcrops and quarries. Infrared data: on samples from Ottenhöffen, Wolfbrunnen, Wald-Michelbach, Hochburg. EPMA on feldspar: on Buntsandstein sandstone sample from the EPS1 well and Paleozoic granite sample from Waldhambach. EPMA on carbonates: on Buntsandstein sandstone and Paleozoic granite samples from EPS1 well and Paleozoic granite sample from the Waldhambach. EPMA on barite EPS1: on Buntsandstein sandstone samples from the EPS1 well. EPMA on clay minerals: on Stephanian arkose sample from Saint Pierre Bois, Paleozoic granite sample from Waldhambach, and Buntsandstein sandstone and Paleozoic granite samples from the EPS1 well. Isotopic data: on samples from Saint Pierre Bois, Steinach, Waldhambach, EPS1 well (this study), and GPK1 well [98]. *(Supplementary Materials)*

References

[1] C. E. Manning and S. E. Ingebritsen, “Permeability of the continental crust: implications of geothermal data and

metamorphic systems," *Reviews of Geophysics*, vol. 37, no. 1, pp. 127–150, 1999.

[2] C. A. J. Wibberley, G. Yielding, and G. Di Toro, "Recent advances in the understanding of fault zone internal structure: a review," *Geological Society, London, Special Publications*, vol. 299, no. 1, pp. 5–33, 2008.

[3] F. Mazzarini, I. Isola, G. Ruggieri, and C. Boschi, "Fluid circulation in the upper brittle crust: thickness distribution, hydraulic transmissivity fluid inclusion and isotopic data of veins hosted in the Oligocene sandstones of the Macigno Formation in southern Tuscany, Italy," *Tectonophysics*, vol. 493, no. 1-2, pp. 118–138, 2010.

[4] K. Bucher and I. Stober, "Fluids in the upper continental crust," *Geofluids*, vol. 10, 253 pages, 2010.

[5] D. L. Siler and B. M. Kennedy, "Regional crustal-scale structures as conduits for deep geothermal upflow," *Geothermics*, vol. 59, pp. 27–37, 2016.

[6] P. Robert, "Histoire géothermique et diagenèse organique," in *Bulletin des Centres de Recherches Exploration-Production Elf Aquitaine*, p. 345, Elf Aquitaine, 1985.

[7] F. Pirajno and M. Santosh, "Mantle plumes, supercontinents, intracontinental rifting and mineral systems," *Precambrian Research*, vol. 259, pp. 243–261, 2015.

[8] A. Aydin, "Fractures, faults, and hydrocarbon entrapment, migration and flow," *Marine and Petroleum Geology*, vol. 17, no. 7, pp. 797–814, 2000.

[9] A.-M. Boullier, K. Fujimoto, T. Ohtani et al., "Textural evidence for recent co-seismic circulation of fluids in the Nojima fault zone, Awaji island, Japan," *Tectonophysics*, vol. 378, no. 3-4, pp. 165–181, 2004.

[10] O. Dauteil and L. E. Ricou, "Une circulation de fluides de haute-température à l'origine du métamorphisme crétacé nord-pyrénéen," *Geodinamica Acta*, vol. 3, no. 3, pp. 237–249, 1989.

[11] N. H. S. Oliver, "Review and classification of structural controls on fluid flow during regional metamorphism," *Journal of Metamorphic Geology*, vol. 14, no. 4, pp. 477–492, 1996.

[12] P. Boulvais, "Fluid generation in the Boucheville Basin as a consequence of the North Pyrenean metamorphism," *Comptes Rendus Geoscience*, vol. 348, no. 3-4, pp. 301–311, 2016.

[13] D. R. Faulkner, C. A. L. Jackson, R. J. Lunn et al., "A review of recent developments concerning the structure, mechanics and fluid flow properties of fault zones," *Journal of Structural Geology*, vol. 32, no. 11, pp. 1557–1575, 2010.

[14] V. F. Bense, T. Gleeson, S. E. Loveless, O. Bour, and J. Scibek, "Fault zone hydrogeology," *Earth-Science Reviews*, vol. 127, pp. 171–192, 2013.

[15] R. H. Sibson, "Structural permeability of fluid-driven fault-fracture meshes," *Journal of Structural Geology*, vol. 18, no. 8, pp. 1031–1042, 1996.

[16] J. V. Rowland and S. F. Simmons, "Hydrologic, magmatic, and tectonic controls on hydrothermal flow, Taupo volcanic zone, New Zealand: implications for the formation of epithermal vein deposits," *Economic Geology*, vol. 107, no. 3, pp. 427–457, 2012.

[17] S. F. Cox, "The application of failure mode diagrams for exploring the roles of fluid pressure and stress states in controlling styles of fracture-controlled permeability enhancement in faults and shear zones," *Geofluids*, vol. 10, pp. 217–233, 2010.

[18] K. C. Condie, *Plate Tectonics & Crustal Evolution*, Butterworth-Heinemann, 4th edition, 1997.

[19] J. Meixner, E. Schill, J. C. Grimmer, E. Gaucher, T. Kohl, and P. Klingler, "Structural control of geothermal reservoirs in extensional tectonic settings: an example from the Upper Rhine Graben," *Journal of Structural Geology*, vol. 82, pp. 1–15, 2016.

[20] P. A. Ziegler, "European Cenozoic rift system," *Tectonophysics*, vol. 208, no. 1-3, pp. 91–111, 1992.

[21] A. Gerard and O. Kappelmeyer, "The Soultz-sous-Forets project," *Geothermics*, vol. 16, no. 4, pp. 393–399, 1987.

[22] C. Clauser, E. Griesshaber, and H. J. Neugebauer, "Decoupled thermal and mantle helium anomalies: implications for the transport regime in continental rift zones," *Journal of Geophysical Research: Solid Earth*, vol. 107, no. B11, 2002.

[23] L. Rybach, "The geothermal conditions in the Rhine Graben - a summary," *Bulletin für Angewandte Geologie*, vol. 12, pp. 29–32, 2007.

[24] E. Roulleau, F. Bravo, D. L. Pinti et al., "Structural controls on fluid circulation at the Caviahue-Copahue Volcanic Complex (CCVC) geothermal area (Chile-Argentina), revealed by soil CO_2 and temperature, self-potential, and helium isotopes," *Journal of Volcanology and Geothermal Research*, vol. 341, pp. 104–118, 2017.

[25] M. Zucchi, A. Brogi, D. Liotta et al., "Permeability and hydraulic conductivity of faulted micaschist in the eastern Elba Island exhumed geothermal system (Tyrrhenian sea, Italy): insights from Cala Stagnone," *Geothermics*, vol. 70, pp. 125–145, 2017.

[26] A. M. Schleicher, L. N. Warr, and B. A. van der Pluijm, "Fluid focusing and back-reactions in the uplifted shoulder of the Rhine rift system: a clay mineral study along the Schauenburg Fault zone (Heidelberg, Germany)," *International Journal of Earth Sciences*, vol. 95, no. 1, pp. 19–33, 2006.

[27] T. Abebe, *Geological Limitations of a Geothermal System in a Continental Rift Zone: Example the Ethiopian Rift Valley*, World Geothermal Congress, Kyushu-Tohoku, Japan, 2000.

[28] C. Lampe, M. Person, S. Nöth, and W. Ricken, "Episodic fluid flow within continental rift basins: some insights from field data and mathematical models of the Rhinegraben," *Geofluids*, vol. 1, no. 1, 52 pages, 2001.

[29] C. Lampe and M. Person, "Advective cooling within sedimentary rift basins—application to the Upper Rhinegraben (Germany)," *Marine and Petroleum Geology*, vol. 19, no. 3, pp. 361–375, 2002.

[30] H. Dresmann, N. Keulen, Z. Timar-Geng, B. Fügenschuh, A. Wetzel, and H. Stünitz, "The south-western Black Forest and the Upper Rhine Graben Main Border Fault: thermal history and hydrothermal fluid flow," *International Journal of Earth Sciences*, vol. 99, no. 2, pp. 285–297, 2010.

[31] C. Giersch, "Thermohydrodraulik des kristallinen Grundgebirges am Beispiel des östlichen Oberrheingrabens," *AGK Schriftenr*, vol. 72, pp. 1–156, 2006.

[32] J.-B. Edel and K. Schulmann, "Geophysical constraints and model of the Saxothuringian and Rhenohercynian subductions –magmatic arc system in NE France and SW Germany," *Bulletin de la Societe Geologique de France*, vol. 180, no. 6, pp. 545–558, 2009.

[33] J. B. Edel and K. Weber, "Cadomian terranes, wrench faulting and thrusting in the Central Europe Variscides: geophysical

and geological evidence," *Geologische Rundschau*, vol. 84, no. 2, pp. 412–432, 1995.

[34] P. A. Ziegler, "Geodynamic model for the paleozoic crustal consolidation of western and central europe," *Tectonophysics*, vol. 126, no. 2-4, pp. 303–328, 1986.

[35] P. Matte, "Tectonics and plate tectonics model for the Variscan belt of Europe," *Tectonophysics*, vol. 126, no. 2-4, pp. 329–374, 1986.

[36] O. Oncken, C. von Winterfeld, and U. Dittmar, "Accretion of a rifted passive margin : the Late Paleozoic Rhenohercynian fold and thrust belt (Middle European Variscides)," *Tectonics*, vol. 18, no. 1, pp. 75–91, 1999.

[37] C. Schneider, *Les granitoïdes de la partie Nors-Est des Vosges moldanubiennes: evolutions magmatique et structural. [PhD thesis of Strasbourg University]*, Strasbourg, France, 1984.

[38] T. Villemin, F. Alvarez, and J. S. Angelier, "The Rhinegraben: extension, subsidence and shoulder uplift," *Tectonophysics*, vol. 128, no. 1-2, pp. 47–59, 1986.

[39] R. Altherr, U. Henes-Klaiber, E. Hegner, M. Satir, and C. Langer, "Plutonism in the Variscan Odenwald (Germany): from subduction to collision," *International Journal of Earth Sciences*, vol. 88, no. 3, pp. 422–443, 1999.

[40] R. Altherr, A. Holl, E. Hegner, C. Langer, and H. Kreuzer, "High-potassium, calcalkaline I-type plutonism in the european variscides: northern vosges (France) and northern schwarzwald (Germany)," *Lithos*, vol. 50, no. 1-3, pp. 51–73, 2000.

[41] G. H. Eisbacher, E. Lüschen, and F. Wickert, "Crustal-scale thursting and extension in the Hercynian Schwartzwald and Vosges Central Europe," *Tectonics*, vol. 8, no. 1, pp. 1–21, 1989.

[42] S. Roussé, *Architecture et dynamique des séries marines et continentales de l'Oligocène moyen et supérieur du sud du Fossé rhénan: évolution des milieux de dépôt en contexte de rift en marge de l'avant pays alpin*, Doctoral dissertation, Strasbourg 1, 2006.

[43] M. E. Schumacher, "Upper Rhine Graben: Role of preexisting structures during rift evolution," *Tectonics*, vol. 21, no. 1, pp. 6-1–6-17, 2002.

[44] J.-B. Edel, K. Schulmann, and Y. Rotstein, "The Variscan tectonic inheritance of the Upper Rhine Graben: evidence of reactivations in the Lias, Late Eocene–Oligocene up to the recent," *International Journal of Earth Sciences*, vol. 96, pp. 305–325, 2006.

[45] F. Bergerat, *Paléo-champs de contraintes tertiaires dans la plateforme européenne au front de l'orogène alpin*, Bulletin de la Société géologique de France, 1987.

[46] T. Villemin, *Tectonique en extension, fracturation et subsidence: Le Fossé Rhénan et le bassin de Sarre-Nahe*, Doctoral dissertation, 1986.

[47] K. Fuchs, K. Bonjer, D. Gajewski et al., "Crustal evolution of the Rhinegraben area. 1. Exploring the lower crust in the Rhinegraben rift by unified geophysical experiments," *Tectonophysics*, vol. 141, no. 1-3, pp. 261–275, 1987.

[48] T. Villemin and F. Bergerat, *L'évolution structurale du fossé rhénan au cours du Cénozoïque: un bilan de la déformation et des effets thermiques de l'extension*, Bulletin de la Société géologique de France, 1987.

[49] R. Wyns, "Contraintes géologiques et géomorphologiques à l'histoire de la mobilité verticale de la lithosphère continentale en Europe de l'ouest depuis le Crétacé: relations avec la genèse des grabens et du volcanisme tertiaires," in *Colloque "Volcanismes, sédimentations et tectoniques cénozoïques périalpins"*pp. 46-47, Doc. BRGM, Aurillac.

[50] C. Sittler, "Illustration de l'histoire géologique du Fossé rhénan et de l'Alsace," *Neues Jahrbuch für Geologie und Paläontologie Abhandlungen*, vol. 186, pp. 255–282, 1992.

[51] J. Vidal, A. Genter, and J. Schmittbuhl, "How do permeable fractures in the Triassic sediments of Northern Alsace characterize the top of hydrothermal convective cells? Evidence from Soultz geothermal boreholes (France)," *Geothermal Energy*, vol. 3, no. 1, 2015.

[52] M. Tesauro, C. Hollenstein, R. Egli, A. Geiger, and H.-G. Kahle, "Continuous GPS and broad-scale deformation across the Rhine Graben and the Alps," *International Journal of Earth Sciences*, vol. 94, no. 4, pp. 525–537, 2005.

[53] A. Genter and H. Traineau, "Borehole EPS-1, Alsace, France: preliminary geological results from granite core analyses for Hot Dry Rock research," *Scientific Drilling*, vol. 2, pp. 205–214, 1992.

[54] C. Dezayes, A. Genter, and B. Valley, "Structure of the low permeable naturally fractured geothermal reservoir at Soultz," *Comptes Rendus Geoscience*, vol. 342, no. 7-8, pp. 517–530, 2010.

[55] J. Stussi, A. Cheilletz, J.-J. Royer, P. Chevremont, and G. Féraud, "The hidden monzogranite of Soultz-sous-Forêts (Rhine Graben, France)," in *Mineralogy, Petrology and Genesis*, vol. 1, pp. 45–64, Géologie de la France, 2002.

[56] G. R. Hooijkaas, A. Genter, and C. Dezayes, "Deep-seated geology of the granite intrusions at the Soultz EGS site based on data from 5km-deep boreholes," *Geothermics*, vol. 35, no. 5-6, pp. 484–506, 2006.

[57] A. Cocherie, C. Guerrot, C. M. Fanning, and A. Genter, "Datation U–Pb des deux faciès du granite de Soultz (Fossé rhénan, France)," *Comptes Rendus Geoscience*, vol. 336, no. 9, pp. 775–787, 2004.

[58] A. Genter, H. Traineau, C. Dezayes et al., "Fracture analysis and reservoir characterization of the granitic basement in the HDR Soultz project (France)," *Geothermal Science and Technique*, vol. 4, pp. 189–214, 1995.

[59] A. Genter, C. Castaing, C. Dezayes, H. Tenzer, H. Traineau, and T. Villemin, "Comparative analysis of direct (core) and indirect (borehole imaging tools) collection of fracture data in the Hot Dry Rock Soultz reservoir (France)," *Journal of Geophysical Research: Solid Earth*, vol. 102, no. B7, pp. 15419–15431, 1997.

[60] A. Genter and H. Traineau, "Analysis of macroscopic fractures in granite in the HDR geothermal well EPS-1, Soultz-sous-Forêts, France," *Journal of Volcanology and Geothermal Research*, vol. 72, no. 1-2, pp. 121–141, 1996.

[61] C. Dezayes, T. Villemin, A. Genter, H. Traineau, and J. Angelier, "Analysis of fractures in boreholes of the Hot Dry Rock project at Soulz-sous-Forêts (Rhine graben, France)," *Scientific Drilling*, vol. 5, pp. 31–41, 1995.

[62] B. Ledésert, J. Dubois, B. Velde, A. Meunier, A. Genter, and A. Badri, "Geometrical and fractal analysis of a three-dimensional hydrothermal vein network in a fractured granite," *Journal of Volcanology and Geothermal Research*, vol. 56, no. 3, pp. 267–280, 1993.

[63] H. Traineau, A. Genter, and J.-P. Cautru, "Petrography of the granite massif from drill cutting analysis and well log

interpretation in the geothermal HDR borehole GPK1 (Soultz, Alsace, France)," *Geothermal Science and Technique*, vol. 3, pp. 1–29, 1991.

[64] B. Ledésert, "Fracturation et Paléocirculations hydrothermales. Application au projet de géothermie roches chaudes sèches de Soultz-sous-Forêts (Alsace)," *Annales de la Société Géologique du Nord*, vol. T4, pp. 13–20, 1995.

[65] B. Ledésert, G. Berger, A. Meunier, A. Genter, and A. Bouchet, "Diagenetic-type reactions related to hydrothermal alteration in the Soultz-sous-Forêts granite, France," *European Journal of Mineralogy*, vol. 11, no. 4, pp. 731–742, 1999.

[66] B. Ledésert, R. Hebert, A. Genter, D. Bartier, N. Clauer, and C. Grall, "Fractures, hydrothermal alterations and permeability in the Soultz Enhanced Geothermal System," *Comptes Rendus Geoscience*, vol. 342, no. 7-8, pp. 607–615, 2010.

[67] M. Dubois, B. Ledésert, J.-L. Potdevin, and S. Vançon, "Détermination des conditions de précipitation des carbonates dans une zone d'altération du granite de Soultz (soubassement du fossé Rhénan, France) : l'enregistrement des inclusions fluides," *Comptes Rendus de l'Académie des Sciences-Series IIA-Earth and Planetary Science*, vol. 331, pp. 303–309, 2000.

[68] B. Ledésert, R. L. Hébert, C. Grall et al., "Calcimetry as a useful tool for a better knowledge of flow pathways in the Soultz-sous-Forêts Enhanced Geothermal System," *Journal of Volcanology and Geothermal Research*, vol. 181, no. 1-2, pp. 106–114, 2009.

[69] M. Dubois, M. Ayt Ougougdal, P. Meere, J.-J. Royer, M.-C. Boiron, and M. Cathelineau, "Temperature of paleo-to modern self-sealing within a continental rift basin: The fluid inclusion data (Soultz-sous-Forêts, Rhine graben, France)," *European Journal of Mineralogy*, vol. 8, no. 5, pp. 1065–1080, 1996.

[70] A. Genter, K. Evans, N. Cuenot, D. Fritsch, and B. Sanjuan, "Contribution of the exploration of deep crystalline fractured reservoir of Soultz to the knowledge of enhanced geothermal systems (EGS)," *Comptes Rendus Geoscience*, vol. 342, no. 7-8, pp. 502–516, 2010.

[71] H. Pauwels, C. Fouillac, and A.-M. Fouillac, "Chemistry and isotopes of deep geothermal saline fluids in the Upper Rhine Graben: origin of compounds and water-rock interactions," *Geochimica et Cosmochimica Acta*, vol. 57, no. 12, pp. 2737–2749, 1993.

[72] P. Durst and F.-D. Vuataz, *Fluid-Rock Interactions in Hot Dry Rock Reservoirs - a Review of the HDR Sites and Detailed Investigations of the Soultz-sous-Forêts System*, World Geothermal Congress, Beppu-Morioka, Japan, 2000.

[73] A. M. Schleicher, L. N. Warr, B. Kober, E. Laverret, and N. Clauer, "Episodic mineralization of hydrothermal illite in the Soultz-sous-Forêts granite (Upper Rhine Graben, France)," *Contributions to Mineralogy and Petrology*, vol. 152, no. 3, pp. 349–364, 2006.

[74] M. P. Smith, V. Savary, B. W. D. Yardley, J. W. Valley, J. J. Royer, and M. Dubois, "The evolution of the deep flow regime at Soultz-sous-Forfts, Rhine Graben, eastern France: Evidence from a composite quartz vein," *Journal of Geophysical Research*, vol. 103, pp. 223–237, 1998.

[75] A. Genter, H. Traineau, B. Ledésert, B. Bourgine, and S. Gentier, *Over 10 Years of Geological Investigations within the HDR Soultz Project, France*, World Geothermal Congress, Kyushu-Tohoku, Japan, 2000.

[76] D. Bartier, B. Ledésert, N. Clauer et al., "Hydrothermal alteration of the Soultz-sous-Forêts granite (hot fractured rock geothermal exchanger) into a tosudite and illite assemblage," *European Journal of Mineralogy*, vol. 20, no. 1, pp. 131–142, 2008.

[77] C. Le Carlier, J. J. Royer, and E. L. Flores, "Convective heat transfer at the Soultz-sous-Forêts Geothermal Site: implications for oil potential," *First Break*, vol. 12, pp. 553–560, 1992.

[78] L. Guillou-Frottier, C. Carrė, B. Bourgine, V. Bouchot, and A. Genter, "Structure of hydrothermal convection in the Upper Rhine Graben as inferred from corrected temperature data and basin-scale numerical models," *Journal of Volcanology and Geothermal Research*, vol. 256, pp. 29–49, 2013.

[79] C. Dezayes and A. Genter, *Large-Scale Fracture Network Based on Soultz Borehole Data*, EHDRA Scientific Conference, Soultz-sous-Forêts, 2008.

[80] S. Haffen, *Caractéristiques géothermiques du réservoir gréseux du Buntsandstein d'Alsace*, Doctoral dissertation, Université de Strasbourg, 2012.

[81] D. J. Marshall, *Cathodoluminescence of Geological Materials*, Taylor & Francis, 1998.

[82] D. K. Richter, T. Götte, J. Götze, and R. D. Neuser, "Progress in application of cathodoluminescence (CL) in sedimentary petrology," *Mineralogy and Petrology*, vol. 79, no. 3-4, pp. 127–166, 2003.

[83] J. Rosenbaum and S. M. F. Sheppard, "An isotopic study of siderites, dolomites and ankerites at high temperatures," *Geochimica et Cosmochimica Acta*, vol. 50, no. 6, pp. 1147–1150, 1986.

[84] C. Pin and C. Bassin, "Evaluation of a strontium specific extraction chromatographic method for isotopic analysis in geological materials," *Analytica Chimica Acta*, vol. 269, no. 2, pp. 249–255, 1992.

[85] J. F. Bauer, S. Meier, and S. L. Philipp, "Architecture, fracture system, mechanical properties and permeability structure of a fault zone in Lower Triassic sandstone, Upper Rhine Graben," *Tectonophysics*, vol. 647-648, pp. 132–145, 2015.

[86] L. Bertrand, J. Jusseaume, Y. Géraud et al., "Structural heritage, reactivation and distribution of fault and fracture network in a rifting context: case study of the western shoulder of the Upper Rhine Graben," *Journal of Structural Geology*, vol. 108, pp. 243–255, 2018.

[87] P. Fluck, J. B. Edel, C. Gagny et al., *Le socle vosgien, segment de la chaine varisque de l'Europe*, vol. 146, Etat des cnnaissances. Propositions d'axes de recherches, 1987.

[88] A. Meunier and B. Velde, "Solid solutions in I/S mixed layer minerals and illite," *American Mineralogist*, vol. 74, pp. 1106–1112, 1989.

[89] S. M. F. Sheppard and H. P. Schwarcz, "Fractionation of carbon and oxygen isotopes and magnesium between coexisting metamorphic calcite and dolomite," *Contributions to Mineralogy and Petrology*, vol. 26, no. 3, pp. 161–198, 1970.

[90] Y. Matsuhisa, J. R. Goldsmith, and R. N. Clayton, "Oxygen isotopic fractionation in the system quartz-albite-anorthite-water," *Geochimica et Cosmochimica Acta*, vol. 43, no. 7, pp. 1131–1140, 1979.

[91] S. I. Golyshey, N. L. Padalko, and S. A. Pechenkin, "Fractionation of stable oxygen and carbon isotopes in carbonate systems," *Geochemistry International*, vol. 18, pp. 85–99, 1981.

[92] J. R. O'Neil, R. N. Clayton, and T. K. Mayeda, "Oxygen isotope fractionation in divalent metal carbonates," *The Journal of Chemical Physics*, vol. 5, pp. 5547–5558, 1969.

[93] J. Horita, "Oxygen and carbon isotope fractionation in the system dolomite-water-CO2 to elevated temperatures," *Geochimica et Cosmochimica Acta*, vol. 129, pp. 111–124, 2014.

[94] Y. Bottinga, "Calculation of fractionation factors for carbon and oxygen isotopic exchange in the system calcite-carbon dioxide-water," *The Journal of Physical Chemistry*, vol. 72, no. 3, pp. 800–808, 1968.

[95] J. G. Blanalt, *Notice et feuille de la carte géologique de Sélestat (307)*, BRGM, Ed., Carte géologique de la France à 1/50 000, 1970.

[96] F. Surma, Y. Geraud, L. Pourcelot et al., "Porosity microstructures of a sandstone affected by a normal fault," *Bulletin de la Societe Geologique de France*, vol. 174, no. 3, pp. 295–303, 2003.

[97] C. Fouillac and A. Genter, *Etude isotopique (O, D, C) des interactions eau-roche dans le granite de Soultz-sous-Forêts, sondage GPK1, site RCS (Alsace)*, BRGM Report R30371/ANA SGN 90, 1990.

[98] M. Cathelineau and M.-C. Boiron, "Downward penetration and mixing of sedimentary brines and dilute hot waters at 5km depth in the granite basement at Soultz-sous-Forêts (Rhine graben, France)," *Comptes Rendus Geoscience*, vol. 342, no. 7-8, pp. 560–565, 2010.

[99] M. Ayt Ougougdal, M. Cathelineau, J. Pironon, M. C. Boiron, D. Banks, and B. W. D. Yardley, *Salt-Rich and Organic-Rich Fluid Migration in the Rhine Graben Triassic Sandstones (Soultz Deep Drilling)*, ECROFI XIII, Sociedad Española de Mineralogia, Sitges, España, 1995.

[100] V. Gardien, M. Rabinowicz, J.-L. Vigneresse, M. Dubois, P. Boulvais, and R. Martini, "Long-lived interaction between hydrothermal and magmatic fluids in the Soultz-sous-Forêts granitic system (Rhine Graben, France)," *Lithos*, vol. 246-247, pp. 110–127, 2016.

[101] M.-C. Boiron, M. Cathelineau, and A. Richard, "Fluid flows and metal deposition near basement/cover unconformity: lessons and analogies from Pb-Zn-F-Ba systems for the understanding of Proterozoic U deposits," *Geofluids*, vol. 10, no. 1-2, 292 pages, 2010.

[102] T. Blaise, J. Barbarand, M. Kars et al., "Reconstruction of low temperature (<100 °C) burial in sedimentary basins: a comparison of geothermometer in the intracontinental Paris Basin," *Marine and Petroleum Geology*, vol. 53, pp. 71–87, 2014.

[103] T. Blaise, N. Clauer, M. Cathelineau, M.-C. Boiron, I. Techer, and P. Boulvais, "Reconstructing fluid-flow events in Lower-Triassic sandstones of the eastern Paris Basin by elemental tracing and isotopic dating of nanometric illite crystals," *Geochimica et Cosmochimica Acta*, vol. 176, pp. 157–184, 2016.

[104] A. Genter, N. Cuenot, C. Baujard et al., "Geology, Geophysics and Geochemistry in the Upper Rhine Graben: the frame for geothermal energy use," in *Proceedings of European Geothermal Congress*, pp. 1–5, Strasbourg, France, 2016.

[105] M. Schindler, J. Baumgärtner, T. Gandy et al., "Successful hydraulic stimulation techniques for electric power production in the Upper Rhine Graben, Central Europe," in *Proceedings World geothermal congress*, pp. 1–7, Bali, Indonesia, 2010.

[106] C. Baujard, A. Genter, E. Dalmais et al., "Hydrothermal characterization of wells GRT-1 and GRT-2 in Rittershoffen, France: implications on the understanding of natural flow systems in the rhine graben," *Geothermics*, vol. 65, pp. 255–268, 2017.

[107] P. Herzberger, W. Münch, T. Kölbel et al., "The geothermal power plant Bruchsal," in *Proceedings world geothermal congress*, pp. 1–6, Bali, Indonesia, 2010.

[108] F. Ladner and M. O. Häring, *Hydraulic Characteristics of the Basel 1 Enhanced Geothermal System Hydraulic Reservoir Characterization*, GRC Transactions, 2009.

[109] S. Gentier, X. Rachez, T. D. Tran Ngoc, and C. Souque, "3D flow modelling of the medium-term circulation test performed in the deep geothermal site of Soultz-Sous-forêts (France)," in *World Geothermal Congress 2010*, pp. 25–29, Bali, Indonesia, 2010.

[110] B. Sanjuan, R. Millot, C. Innocent, C. Dezayes, J. Scheiber, and M. Brach, "Major geochemical characteristics of geothermal brines from the Upper Rhine Graben granitic basement with constraints on temperature and circulation," *Chemical Geology*, vol. 428, pp. 27–47, 2016.

[111] B. Sanjuan, R. Millot, C. Dezayes, and M. Brach, "Main characteristics of the deep geothermal brine (5km) at Soultz-sous-Forêts (France) determined using geochemical and tracer test data," *Comptes Rendus Geoscience*, vol. 342, no. 7-8, pp. 546–559, 2010.

[112] C. E. Derer, M. E. Schumacher, and A. Schäfer, "The northern Upper Rhine Graben: basin geometry and early syn-rift tectono-sedimentary evolution," *International Journal of Earth Sciences*, vol. 94, no. 4, pp. 640–656, 2005.

[113] J. P. Brun, M.-A. Gutscher, and dekorp-ecors teams, "Deep crustal structure of the Rhine Graben from dekorp-ecors seismic reflection data: a summary," *Tectonophysics*, vol. 208, no. 1-3, pp. 139–147, 1992.

[114] A. Genter, L. Guillou-Frottier, J. P. Breton et al., *Typologie des systèmes géothermiques HDR/HFR en Europe*, Rapport final BRGM/RP-53452-FR, 2004.

[115] J. F. Vernoux, A. Genter, P. Razin, and C. Vinchon, *Geological and Petrophysical Parameters of a Deep Fractured Sandstone Formation as Applied to Geothermal Exploitation, EPS-1 Borehole*, Rapport BRGM R38622, Soultz-sous-Forêts, France, 1995.

[116] GeORG Team, *Potentiel géologique profound du Fossé Rhénan Supérieur*, Partie 1- Rapport Final BRGM/RP-61945-FR, 2013.

[117] A. Genter, "Géothermie roches chaudes sèches: le granite de Soultz-sous-Forêts (Bas-Rhin, France)," in *Fracturation naturelle, altérations hydrothermales et interactions eau-roche*, p. 201, Thèse Université d'Orléans, 1989.

[118] B. Valley, *The Relation between Natural Fracturing and Stress Heterogeneities in Deep-Seated Crystalline Rocks at Soultz-sous-Forêts (France)*, Doctoral dissertation, ETH Zurich, 2007.

[119] C. Dezayes, C. Lerouge, C. Ramboz, and G. Wille, *Relative Chronology of Deep Circulations within the Fractured Basement of the Upper Rhine Graben*, European Geothermal Congress, Pisa, Italy, 2013.

Hindawi
Geofluids
Volume 2019, Article ID 4503943, 28 pages
https://doi.org/10.1155/2019/4503943

Research Article

A Methodology for Assessing the Favourability of Geopressured-Geothermal Systems in Sedimentary Basin Plays: A Case Study in Abruzzo (Italy)

Alessandro Santilano ,[1] Eugenio Trumpy,[1] Gianluca Gola,[1] Assunta Donato,[1] Davide Scrocca,[2] Federica Ferrarini,[3] Francesco Brozzetti,[3] Rita de Nardis,[4] Giusy Lavecchia,[3] and Adele Manzella[1]

[1]*CNR, Institute of Geosciences and Earth Resources (IGG), Via Moruzzi 1, 56124 Pisa, Italy*
[2]*CNR, Institute of Environmental Geology and Geoengineering (IGAG), P.le Aldo Moro 5, 00185 Roma, Italy*
[3]*CRUST, DiSPUTer, Università "G. d'Annunzio", Via dei Vestini 31, 66013 Chieti Scalo, Italy*
[4]*DPC, Dipartimento della Protezione Civile, Via Vitorchiano, 4, 00189 Rome, Italy*

Correspondence should be addressed to Alessandro Santilano; alessandro.santilano@igg.cnr.it

Received 24 April 2018; Revised 29 September 2018; Accepted 8 October 2018; Published 4 March 2019

Guest Editor: Matteo Lupi

We exploit the concept of the geothermal favourability, widely used for hydrothermal and EGS systems, to present an innovative methodology for assessing geopressured-geothermal resources occurring in terrigenous units in sedimentary basin plays. Geopressured-geothermal systems are an unconventional resource for power trigeneration exploiting three forms of energy from hydrocarbons, hydrothermal fluids, and well-head overpressure. This paper is intended to be a practical analytical framework for the systematic integration of the relevant data required to assess geopressured-geothermal resources. For this purpose, innovative parameters were also implemented in the methodology. The final result is the favourability map for identifying prospective areas to be further investigated for the appraisal of the geopressured-geothermal potential. We applied our methodology to the foredeep-foreland domains of the Apennines thrust belt in the Abruzzo region (central Italy). We analysed hundreds of deep hydrocarbon wells in order to create 3D geological and thermo-fluid dynamic models at a regional scale as well as to obtain information on the pressure regimes and on the chemistry of the system. The final favourability map for the Abruzzo case study is a first attempt at ranking these kinds of unconventional geothermal resources in a region that has been historically explored and exploited mostly for hydrocarbons.

1. Introduction

Geothermal exploration is a complex, time-consuming, and expensive activity. Integrating geological, geochemical, and geophysical data can speed up exploration stages. Very few reference studies are available regarding the assessment at regional scale of geopressured-geothermal resources, which industrial interest is recently increasing worldwide.

We present a new methodology to assess the favourability of geopressured-geothermal systems occurring in terrigenous units in sedimentary basin plays. The aim is to drive effective exploration to the most promising areas throughout a systematic data integration. The research was developed within the framework of the Geothermal Atlas of Southern Italy Project [1].

Geopressured-geothermal systems (hereafter also referred to as "geopressured") are an unconventional resource for power trigeneration. They exploit three forms of energy [2]: (i) chemical energy from the combustion of hydrocarbons, (ii) thermal energy from hydrothermal fluids, and (iii) kinetic energy from well-head overpressure due to abnormal geopressured regimes. This resource is of particular interest due to the possibility of improving the economic feasibility of an industrial geothermal project or of uneconomic/depleted hydrocarbon wells.

The USA focused on geopressured systems from the 1970s to the 1990s above all for industry and produced extensive knowledge of the geopressured system of the Gulf of Mexico (e.g., [3, 4]). Such industrial interest has recently been renewed with projects aimed at demonstrating their commercial feasibility, as in Louisiana [5]. With regard to Europe, Hungary has been developing geopressured projects [6] while cogeneration plants for the direct use of geothermal heat and dissolved methane are in operation. Previous works have described the prospective factors for the assessment of geopressured systems (e.g., [7]), mainly aimed at the Gulf of Mexico. Italy has also been involved in some works, for example Alimonti and Gnoni [8] presented a study on the heat recovery from depleted wells in a well-known geopressured field in the Po Plain (Northern Italy).

In the recent scientific literature, the geothermal favourability concept has been widely proposed in order to study geothermal systems, focusing on hydrothermal and enhanced geothermal systems (EGS). Various approaches have been exploited in order to quantitatively integrate different sources of data, usually organized in information layers in a GIS environment [9–18]. The favourability consists in a semiquantitative data integration for identifying prospective areas to be further investigated for the appraisal of the geothermal potential.

Our methodology is based on the integration of layers of evidence by Index Overlay. Data analysis by the Index Overlay method has been widely proposed in literature (e.g., [9, 16]) for the assessment of other types of geothermal systems. We provide a novel tool for assessing geopressured resources that considers specific prospective factors. We applied our methodology to the foredeep-foreland domains of the Apennines thrust belt in the Abruzzo region (central Italy). This is one of the first attempts to assess geopressured systems at the regional scale in Italy. Favourability maps were computed in order to assess the geopressured resources that would be suitable for power production.

The Abruzzo case study is also important due to the possibility of developing geothermal projects in a region belonging to the Adriatic petroleum province [19–21] and in a gas (methane)-prone area, characterized by low geothermal gradients.

We analysed hundreds of deep hydrocarbon wells, and we carried out geological modelling and coupled thermo-fluid dynamic numerical simulations. Information on the pressure regimes and on the chemistry of the system was also obtained. The final favourability map for the Abruzzo region was computed which provides a ranking of the most prospective areas.

Once having described the general approach, the article focuses on the application to the test site in Abruzzo in order to better explicate the various steps of the methodology. Finally, the obtained maps are analysed and discussed.

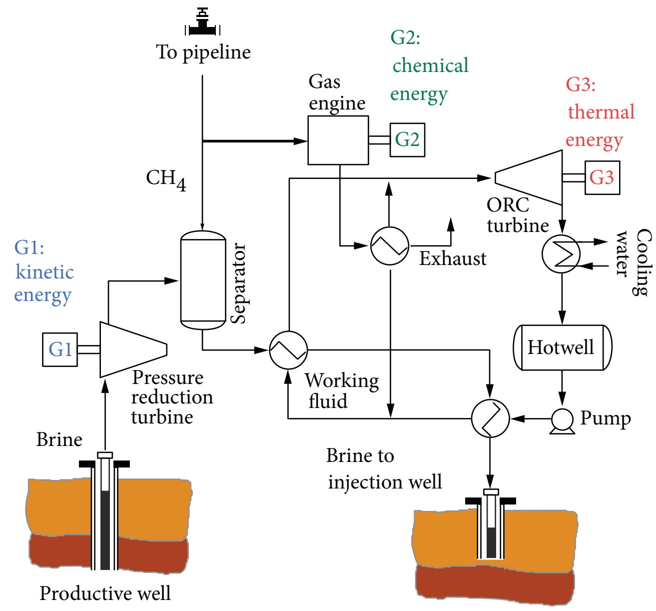

Figure 1: Flow diagram of the hybrid power system for the trigeneration from geopressured-geothermal resources (modified from [23, 91]).

2. Geopressured-Geothermal Systems: State of the Art and Prospective Factors

A geopressured-geothermal system is constituted by a hydrothermal reservoir with a higher pore pressure than the hydrostatic reference and contains dissolved gaseous hydrocarbons. The first patent for exploiting this resource was filed in 1966 [22]. The trigeneration of energy derives from the abnormal formation pressure, the occurrence of dissolved methane, and the heat transferred by the fluid. Due to various technical problems (e.g., the sustainability of the exploitation), geopressured systems are still considered unconventional, i.e., requiring technological development. Figure 1 shows the classic flow diagram for trigeneration as proposed by Hughes [23].

The literature contains a few studies regarding the exploration of this resource worldwide (e.g., [24]) and several works from related congresses, held in the USA, and technical reports (e.g., [7, 25–28]). The most studied geopressured systems are located onshore of the Gulf of Mexico, particularly in Texas and Louisiana. In the USA, following the oil crisis in the 1970s, the DOE (Department of Energy) funded two important research programs [27]. Numerous abandoned hydrocarbon wells were tested, and new wells were drilled in prospective areas. The most important productive well was the "Pleasant Bayou 2" located in Texas, a test site in which the technical feasibility of power production was demonstrated [29].

The concomitant occurrence of hydrothermal resources and hydrocarbons, in abnormal pressure regimes, makes the genesis of geopressured systems particular to specific geological environments. The play concept [30–32] is of primary importance in the favourability assessment.

Table 1: Main prospective factors for the characterization of geopressured-geothermal systems in terrigenous sedimentary basin plays, at regional or local scale.

	Information at regional scale	Information at local or well scale
Prospective factors to be investigated		
Depositional environment	x	
Deposition rate	x	
Temperature	x	x
Pressure	x	x
Salinity of fluid		x
Gas/water ratio		x
Percentage of methane in free gases		x
Methane solubility		x
Occurrence of dissolved gaseous hydrocarbons	x	x
Depth of geopressured reservoir	x	x
Size of reservoir	x	
Flow rate		x
Permeability		x
Faults and fractures	x	x
Lithology	x	x

The most suitable plays are mainly related, but not limited, to clastic depositional environments. Although sedimentary basin plays are not usually suitable for high-temperature hydrothermal resources, their geological features favour the occurrence of strata overpressure and hydrocarbon accumulations.

Table 1 summarizes the main prospective factors for the characterization of geopressured systems in such plays.

In a sedimentary basin environment, compaction disequilibrium is the predominant process that leads to pore (or formation) overpressure, and this is related to subsidence, burial, and compaction of sediments. The overpressure gradient is directly proportional to the deposition rate and inversely proportional to the permeability [33]. These basin sectors that experience the fast deposition of interbedded clays and sands are favoured. Other processes that influence the formation of pressure are the thermal expansion of brine, the occurrence of hydrocarbons, and tectonics [33, 34].

Loucks et al. [3] classified the Gulf of Mexico geopressured system into three main pressure regimes: (i) hydrostatic, (ii) "soft" geopressured, and (iii) "hard" geopressured. The latter, with gradients higher than 0.7 psi/ft (15.83 bar/100 m) and marked by a change in electrical resistivity, is also characterized by an increase in the thermal gradient at its top. The authors related this observation to the decrease in thermal conductivity as a consequence of higher porosity, following the theory proposed by Lewis and Rose [35], given a constant heat flow.

The sedimentary processes underlying such geopressured sedimentary basins also promote gaseous hydrocarbons, mainly methane, which occur in the formation as dissolved gas in brines or also as "free" exsolved gas in saturated conditions. The continuous burial of an enormous amount of organic matter is key to the formation of hydrocarbons. In geopressured systems, the methane exploited is mainly in solution in the hydrothermal fluid, and the gas/water ratio and the methane solubility are fundamental. The P/T and salinity conditions of the fluid strongly influence the solubility of methane; i.e., the amount of exploitable gas for a certain flow rate of the fluid. The methane solubility is directly proportional to the pressure and temperature and inversely proportional to the salinity of the fluid [36].

Geothermal exploration, in particular for power production, searches for the hottest hydrothermal resource and highest geothermal gradients. In the case of geopressured systems, the geological conditions that usually facilitate their development are unfavourable to high-geothermal gradients, such as those in volcanic or intrusive geothermal plays. For example, fast sedimentation environments are related to a decrease in the thermal gradient. The thermal regime is, however, a fundamental factor in deriving the economic value of the geopressured resource, since thermal energy plays a major role in trigeneration.

Permeability is another key factor. In geopressured systems, the lithology and the primary permeability play important roles, characterizing (i) the clayey seals, with a low permeability that favours the development of overpressure regimes, and (ii) the productive intervals, usually in sandy formations. The structural setting is a key factor in the evolution of such systems, for example, the possibility of characterizing permeable and nonpermeable faults as well as growth faults.

3. Methodology

GIS spatial analysis for mapping the geothermal potential or favourable areas has been extensively used following different approaches in order to speed up the exploration stages [9–18, 37, 38].

In cases of abundant data availability, the spatial layers in a GIS environment can be treated on the basis of statistical estimations. Otherwise, the processing of layers can rely on the knowledge of experts. The first case is known as the data-driven method, while the second is referred to as the knowledge-driven method [39].

In many cases, the information available makes it impossible to carry out a probabilistic analysis. We therefore applied a knowledge-driven method using the Index Overlay (IO) technique to combine geological, geophysical, and geochemical information. The IO is a simple and flexible way to linearly integrate different spatial information ensuring a common scale of value. The resulting map is obtained from (1), where F is the favourability for each pixel, W_i is the weight for the ith map, and S_{ij} is the score for the jth class of the ith map [39]:

$$F = \frac{\sum_{i=1}^{n} S_{ij} W_i}{\sum_{i=1}^{n} W_i}. \quad (1)$$

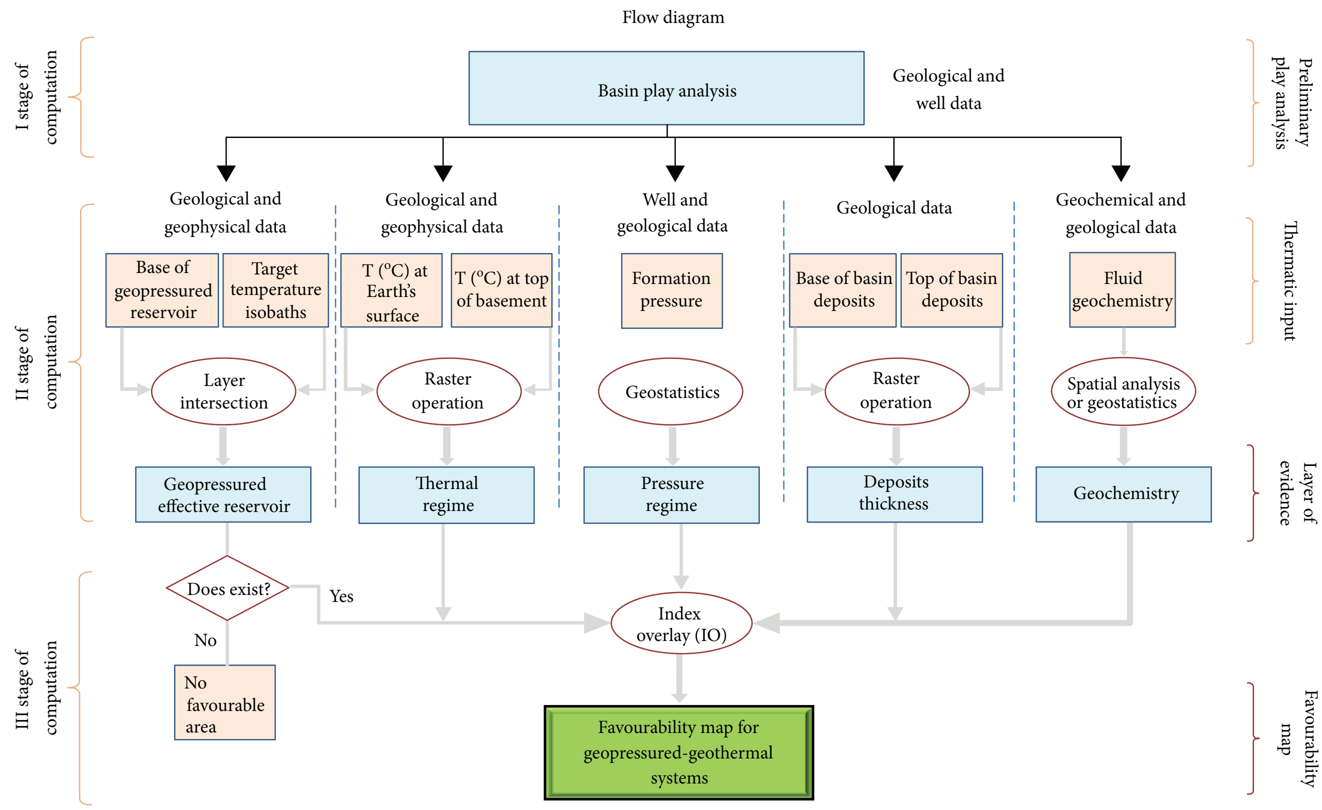

Figure 2: Flow diagram for computing the geothermal-geopressured favourability in basin plays.

The workflow setup for the computation of the favourability map is organized into three stages, as shown in Figure 2. It starts with a preliminary geological analysis of the play. Indeed, the methodology focuses on the sedimentary terrigenous basin plays and the study area should be selected accordingly.

The second stage of computation requires the collection and processing of geological, well logs, geochemical, and geophysical datasets. The following thematic inputs are properly set up: (i–ii) depth of the top and base of the geopressured-geothermal reservoir, (iii) depth of the top and base of basin deposits, (iv) isobaths of the target temperature, (v–vi) temperature at the Earth's surface and at the top of the basement underlying the reservoir, (vii) digital elevation model. (viii) formation pressure, and (ix) fluid and gas geochemistry.

The thematic inputs are combined by means of GIS spatial analysis tools to obtain the layers of evidence.

The layers of evidence are the spatial representation of the main prospective parameters described in Section 2. The methodology includes the following layers: (i) the effective geopressured reservoir, (ii) the thermal regime, (iii) the pressure regime, (iv) the deposit thickness, and (v) the geochemistry.

The five layers of evidence are combined to produce the final favourability map for geopressured systems as a result of the last stage of the workflow. The layers are in turn scored and weighted following the Index Overlay method ((1)). The classification for each layer of evidence consists of identifying five ranges of score values (classes). The classes are scored from 1 to 5, "very low" (less favourable area) to "very high" (most promising area), respectively. In order to combine the layers of evidence, each was weighted with values whose sum is equal to 1 (Table 2). The weights, classes, and scores were set based on generic features of terrigenous sedimentary basins.

In this work, all the computations were performed in the Open Source Quantum GIS environment exploiting SAGA and GRASS GIS tools [40]. The resolution of the combined maps is the same, with the grid nodes of each layer overlapping.

3.1. Effective Geopressured-Geothermal Reservoir. The effective reservoir concept was initially proposed in Trumpy et al. [9] for hydrothermal conventional systems in carbonates. Here, we adapted the idea of "effective" reservoir in order to develop a new concept for geopressured systems in sedimentary basin plays: the geopressured-geothermal effective reservoir. This layer of evidence is intended to assess only that part of a geopressured reservoir with a temperature suitable for geothermal exploitation. In this paper, a threshold value of 90°C was set as target, considering the technology of a conventional power production plant. The threshold temperature is chosen accordingly to the aim of exploration (e.g., power production, and direct use of heat). Basically, the idea is to disregard those sectors of reservoir that are colder than the threshold temperature. The layer is computed by means of a layer intersection between the depth of the

Table 2: Scores (S) of classes and weights (W) for layers of evidence, used in the favourability analysis.

Layer of evidence	Weight (W)	Unit	Score (S) favourability				
			5 (very high)	4 (high)	3 (medium)	2 (low)	1 (very low)
Geopressured effective reservoir	0.4	m b.g.l. (depth of the top)	0–1500	1500–2500	2500–3500	3500–4500	>4500
Geochemistry	0.1		Clear indications of CH_4-saturated waters				No indications of CH_4-saturated waters
Pressure regime	0.3	Bar/100 m (pressure gradient)	>18.82	15.82–18.82	12.52–15.82	10.52–12.52	0–10.52
Thermal regime	0.1	°C/1000 m (geothermal gradient)	>50	40–50	30–40	15–30	0–15
Deposits thickness	0.1	m	>8000	6000–8000	4000–6000	2000–4000	0–2000

90°C isotherm and the base of the reservoir. Where the isotherm is deeper than the base of the reservoir, i.e., no effective reservoir occurs, the corresponding areas are neglected from the computation and considered as not favourable. Conversely, if the 90°C isotherm rests above the base, an effective reservoir is identified and the depth of the top is recorded in this layer of evidence. The result is a grid layer of a ranked depth of the top of the effective geopressured-geothermal reservoir.

The ranking classes (score, S) are related to the depth to be drilled in order to reach the top of the effective reservoir: the shallower the top, the higher the favourability. The choice of limit values (Table 2) was driven by economic considerations regarding geothermal drilling, based on worldwide studies [41, 42]. For example, the lowest class is for a drilling depth of higher than 4500 meters. The effective geopressured reservoir is the layer with the highest weight in the Index Overlay calculus for the final map with a value of 0.4 by 1.

The concept is properly illustrated in Subsection 6.1, using the 3D geological model of the study area.

3.2. Thermal Regime. The layer of evidence named the thermal regime includes information related to the variation in the thermal state of the underground. In our study, the thermal regime is parameterized by the thermal gradient (see Table 2). Thus, higher thermal gradients imply shallower high temperatures.

The method to compute the thermal gradient is dependent upon the kind of available datasets. The thermal gradient is ranked following the range presented in Table 2, whereas the weight assigned for this layer of evidence is 0.1 by 1.

3.3. Pressure Regime. We propose to produce a map of the pressure gradient through geostatistical analyses of pressure data (e.g., drill steam tests) along wells. The construction of this layer of evidence requires a careful data analysis due to the variability of pressure conditions both vertically and horizontally. For this reason, we rank the gradient computed in the targeted geopressured interval: the larger the overpressure, the higher the favourability.

The limits of the classes (see Table 2) are in part based on the hydrostatic (1st class), soft (3rd), and hard (4th) geopressured regimes as proposed by Loucks et al. [3]. We also used a "light" class (2nd) and the most favourable class (5th) for values larger than 18.82 bar/100 m, i.e., the "near-lithostatic" class. The pressure regime, which plays a very important role in the favourability computation, has a weight of 0.3 by 1.

3.4. Deposit Thickness. The deposit thickness takes into account the role of the compaction disequilibrium for the genesis of overpressure regimes. The importance of a larger thickness of the (effective) reservoir can influence the quality of the resource in terms not only of pressure but also of temperature. In fact, assuming that the thermal gradient is not driven by pure convection, higher temperatures can be reached at larger depths.

This layer of evidence is obtained by simply classifying the thickness of the deposits of the studied basin. The classes (Table 2) were set based on knowledge-driven considerations related to the thicknesses of basin deposits worldwide. The weight is 0.1 by 1.

3.5. Geochemistry. The decision to focus on terrigenous sedimentary basin plays is driven by the possible assumption that their formation waters are saturated in methane. This layer of evidence is aimed at ranking the study area according to the evidences of the occurrence of CH_4 in reservoir. Due to the vertical and horizontal variability of the CH_4 content, the spatial mapping of this layer is extremely difficult.

The score is simply classified according to the occurrence or not of clear indications of CH_4-saturated and oversaturated water, 5th and 1st classes, respectively (see Table 2). The weight of the layer of evidence is 0.1.

4. Geological-Structural Setting of Eastern Abruzzo (Italy)

The study area is located in the central-eastern sector of the Italian Apennines (inset in Figure 3(a)), which experienced several deformation events in response to the late Neogene tectonic convergence between the European and African plates. The outcropping tectonic units (Figure 3(a)) derived from the deformation of both shallow-water limestones (carbonate platform domains) and deeper-water carbonate (slope and pelagic basin domains) successions deposited on the southern Neotethyan passive margin ([43] and references therein). Since the very late Messinian, these successions were affected by eastward-directed fold and thrusting which led, initially, to the growth of the main Apenninic ridges (Gran Sasso and Majella) and later (Late Pliocene–Early Pleistocene) of the Apennines and peri-Adriatic foothills [43–52].

The contractional deformation [53–55] piled the Apennine thrust units onto the Adriatic foreland (Triassic–Early Miocene) consistently with an overall in-sequence regional propagating model [44, 56, 57] (Figure 3(b)). From the Late Pliocene-Early Pleistocene, the western Abruzzo chain area was affected by an extensional tectonic regime which was responsible for the formation of an articulated system of normal faults [58, 59] and associated Quaternary continental basins (Figure 3(a)).

The study area (Figure 3) also includes the Neogene-Quaternary Abruzzo foredeep and the adjacent Adriatic foreland [60–62]. From a structural point of view, the foredeep can be subdivided into two sectors. The western sector is characterized by outcrops of syn-orogenic turbiditic successions of the upper Laga (Late Messinian) and Cellino (Zanclean) Formations. The eastern sector is dominated, at the surface, by late-orogenic shelf clays, evolving upward to coastal sands of the Late Pliocene-Pleistocene age (Mutignano Fm [63, 64]).

Active deformation characterizes the eastern foredeep sector, which since early Pleistocene times has been undergoing eastward overthrusting above the Adriatic foreland [65, 66]. Instrumental seismicity and borehole breakouts (Figure 3(a)) show a near horizontal WSW-ENE

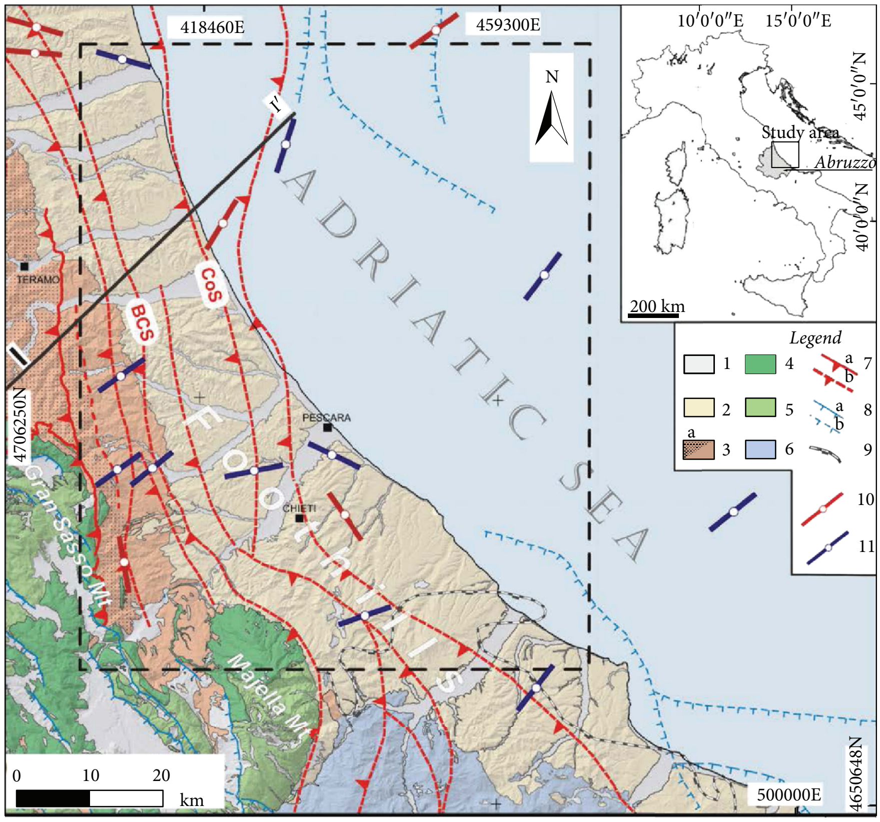

(a)

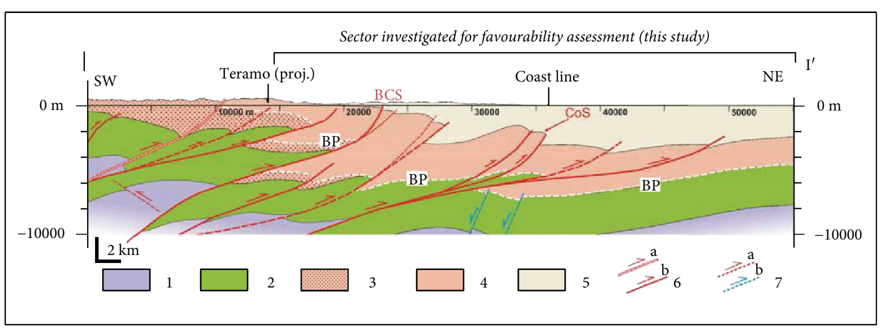

(b)

Figure 3: (a) Simplified geological-structural map of the study area with the main lithological units and tectonic structures. All information was derived from geological maps on a 1:100.000 [92] and 1:50.000 [93] scale and from [68]. Tectonic structures were mainly derived from CNR [76]. Key: (1) continental deposits (Quaternary), (2) marly and clayey deposits of the Mutignano Fm and equivalent units (Late Pliocene-Early Pleistocene), (3) arenaceous and pelitic deposits of the Laga (A) and Cellino Fms and equivalent deposits (Late Messinian–Early Pliocene), (4) slope-to-basin and basinal carbonatic deposits (Late Triassic–Miocene), (5) platform carbonatic deposits (Late Triassic–Miocene), (6) undifferentiated deposits pertaining to the allochthonous Molise Nappe (Upper Cretaceous–Upper Miocene), (7) main thrusts ((a) outcropping, (b) inferred or buried), (8) normal faults ((a) outcropping, (b) inferred or buried), (9) boundary of the allochthonous Molise Nappe, CoS = coastal anticline, (10) direction of the minimum horizontal stress (SHmin) referring to a selection of A and B quality borehole breakout data as reported in [94], and (11) P-axes from a compilation of focal mechanisms taken from the RCMT and TDMT catalogues [95] plus other focal solutions deduced from specific papers (e.g., [96]) for the Italian earthquakes with Mw > 4.0 occurring between 1968 and May 2016. BCS = Bellante-Cellino structure. The black dotted box includes the sector investigated for favourability assessment. (b) Interpretative geological section (trace in (a)) showing the main thrusts deforming the carbonatic and foredeep deposits of the outer Abruzzo region. The outcropping successions and their thickness were constrained with information from geological cartography [92, 93]. The thicknesses of the Mezo-Cenozoic carbonatic deposits in the Adriatic foreland were extracted from [78], while most of the data concerning the depth of the base of Pliocene deposits come from the present study (see Subsection 5.1). Key: (1) Late Triassic dolostone and evaporites, (2) Jurassic-Cretaceous to Middle Miocene undifferentiated carbonates, (3) Late Miocene (upper Messinian) foredeep deposits (Laga Fm), (4) Lower-Pliocene foredeep deposits, (5) Upper Pliocene foredeep and Quaternary marine deposits, (6) thrusts ((a) outcropping, (b) buried), (7) hypothesized faults ((a) reverse, (b) normal). BP = base of the Pliocene foredeep deposits (see Subsection 5.1).

compressional deformation, on average characterized by a low seismic budget (~ 0.3 mm/year) [67].

The lower Pliocene succession (Cellino Fm and equivalent units) is particularly important for our study, since it is the possible overpressured target. Its stratigraphic range spans from the Sphaeroidinellopsis sp. to the *G. puncticulata* biozones [64, 68]. Its succession is up to 2 km thick and consists of several alternations of poorly cemented arenaceous bodies and thick pelitic units. On the whole, this succession is sandwiched in between the post-evaporitic pelites of the topmost Laga Fm and the thick package of clays of the lower Mutignano Fm.

Thrust and folds, affecting the Laga and Cellino deposits, are well documented in the subsurface of the Abruzzo periadriatic area. Two main buried structural trends are defined in the literature, referred to as the "Bellante-Cellino structure" (BCS) and the "Coastal anticline" (CoS), from west to east (Figure 3(a); [46, 60–62, 69]). Between the BCS and the CoS, the upper Pliocene sedimentary wedge reaches a maximum thickness of 2000 m and is slightly folded. The Pleistocene succession is only slightly deformed in an E-dipping, low-angle monocline. East of the leading edge of the Apennine outer thrust, the Adriatic foreland is characterized by a west-dipping low-angle regional monocline, affected by minor normal faulting, due to flexural retreat, on which the Plio-Pleistocene siliciclastic succession lies conformably above the Mezo-Cenozoic carbonates [70].

The foredeep-foreland system of the Abruzzo region belongs to the Adriatic petroleum province [19–21], where many exploration plays and productive oil and gas fields have been in operation. Different kinds of plays occur both in siliciclastic basinal and carbonate platform systems. Gas fields are present in the Plio-Pleistocene turbiditic sequences in channelized or deep-sea fan deposits [19, 69].

With regards to the geothermal resources, the geological conditions of the study area do not favour the development of high temperature systems. Mezo-Cenozoic carbonates represent the regional-scale reservoir for hydrothermal resources. The heat flow map of Italy by Della Vedova et al. [71] shows values mainly in the range of 40–50 mW/m^2 in the study area, with a positive anomaly in the south-eastern offshore part (up to 80 mW/m^2). This pattern is expected in areas experiencing a very high sedimentation rate. The geothermal gradient values are in the range of 30–40°C/km regarding the onshore areas, as shown in the Italian geothermal ranking by Cataldi et al. [72].

5. Source of Data from the Abruzzo Case Study

The favourability computation of the geopressured-geothermal system of Abruzzo was based on a critical review of a large dataset. The main focus was the analysis of about 200 deep hydrocarbon wells, extracted from the Italian National Geothermal Database (BDNG) [73]. For each well, we gathered, from the BDNG, detailed information sheets related to headings (e.g., well name, coordinates), fluid geochemistry, temperature, formation tests, lithology, stratigraphy and ages, drilling (e.g., deviation), and occurrence of formation fluids (water, hydrocarbons).

We have also checked the original master logs, provided by the Italian Ministry of Economic Development [74], in order to support the additional analysis of selected wells, e.g., homogenization of stratigraphic information, and assessment of the validity of the pressure measurements from formation tests (as described in the next subsections).

Beside the well logs and data from the scientific literature, we carried out a geological modelling and coupled thermo-fluid dynamic numerical simulations in order to provide a reliable temperature distribution at depth. Indeed, we used as input for building the layers of evidence both measured data and modelled data.

5.1. Geological Data and Modelling. We reconstructed the base of the Pliocene foredeep deposits (hereafter BP) in the study area by exploiting and integrating datasets from the literature (Figure 4) and the abovementioned BDNG. This involved identifying the lowermost position of the base of Pliocene foredeep deposits, disregarding the local interposition of tectonic slices which could have piled up and thickened the foredeep succession. These particular settings were especially investigated in the northern Abruzzo (offshore) and in the southern Abruzzo (onshore) sectors. In the former, the compressive deformation also affected the foredeep deposits (see cross section in Figure 3(b)) from the uppermost Early Pliocene to the Early Pleistocene (moving from west to east). In the latter, minor slices of the Molise Allochthonous units have been sandwiched between lower-middle Pliocene deposits [75]. In both cases, the lowermost contacts (both stratigraphic or tectonic) were considered.

We first extracted information on the depth of BP from the stratigraphy reported in the wells drilled for petroleum exploration [74] and organized in the BDNG (Figure 4(a)). More than 180 wells were found to clearly intercept this level. Most (about 170) reported the stratigraphic contact of the lower Pliocene successions (conformable or unconformable) above terms belonging to the different basinal (northern sector) or slope-to-basin and platform (southern sector) depositional areas.

In our reconstruction, we also considered isobaths of the BP already reported in the literature. Different studies were considered in the north-western and south-eastern offshore areas. In the north-western area, since no well clearly reached the BP in the foredeep depocentral areas, we exclusively adopted the isobaths reported by CNR [76] and shown in Figure 4(b). In the south-eastern offshore areas, we integrated the isobaths with those reported in Argnani et al. [77] (Figure 4(c)) converting the available isochrones into isobaths using published average velocities for the Pliocene and Pleistocene units (e.g., [44]). A recent interpretation of the M13–14 CROP seismic line [78], which crosses the Adriatic offshore, was also considered (section trace in Figure 4(a)).

We achieved our final target by converting all data into feature datasets (point and lines) in order to process them into a common georeferenced framework in a GIS environment. Finally, we integrated all the collected data and converted them into point features which were interpolated

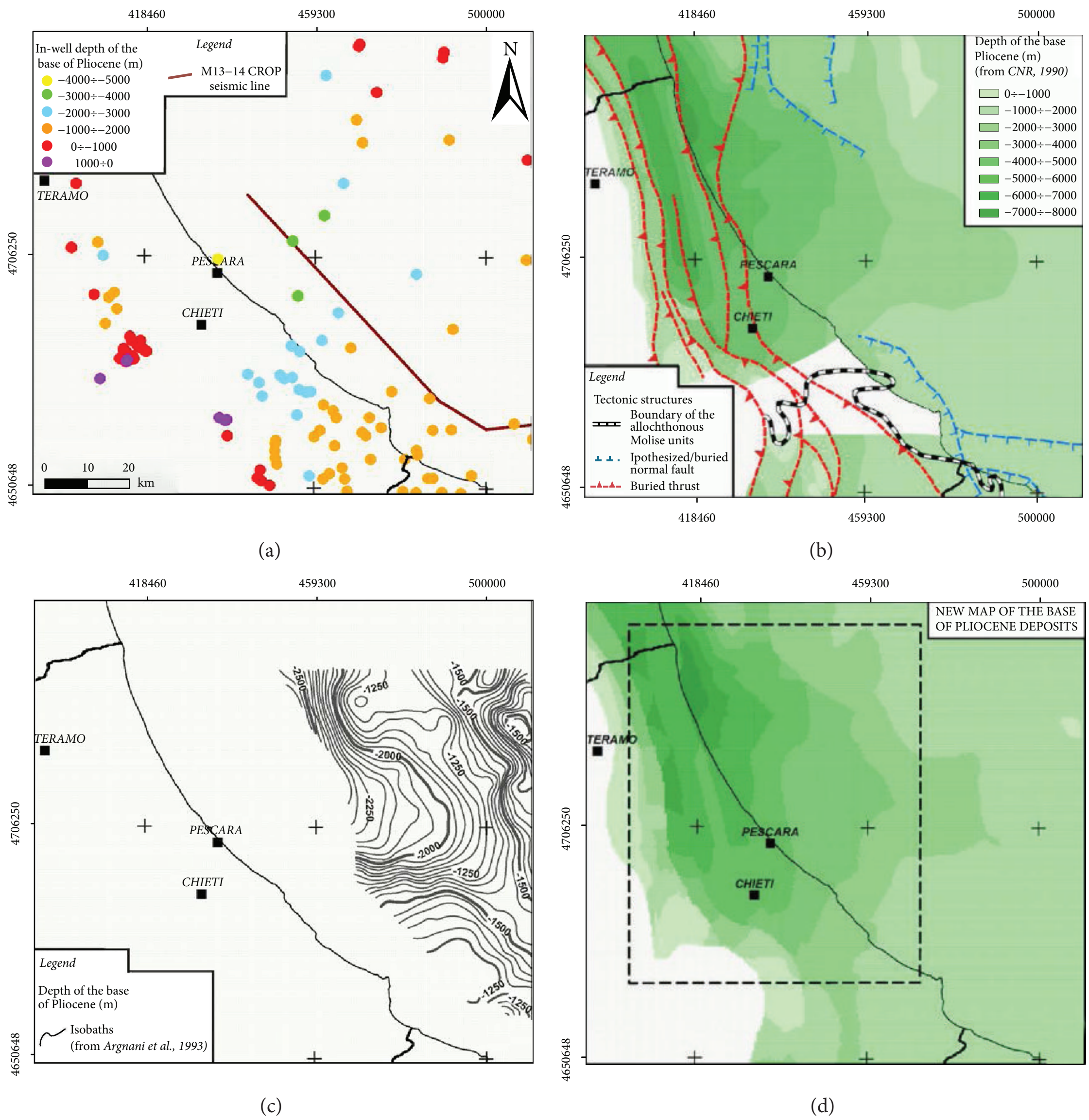

Figure 4: Three main databases (a, b, c) used for the reconstruction of the new map of the base of Pliocene deposits (d) in the outer sector of the Abruzzo region. (a) In-well BP depth as reported in the wells drilled for petroleum exploration [73, 74]; the trace of the seismic line M13–14 CROP is reported in brown from [78]. (b) Isobaths of the BP with main tectonic structures. (c) Map of the isobaths of the BP redrawn from [77]. (d) New map of the BP deposits as reconstructed for the study area. The tectonic structures and the colour-scale legend of isobaths are the same as in (b). The dotted black box includes the sector investigated for the favourability assessment.

through an inverse distance weighting (IDW) method, using local barriers represented by the main tectonic structures reported for the study area and/or hypothesized from lateral discontinuities observed in the in-well stratigraphy.

A 3D surface with 1000 m pixel resolution was obtained and is shown in the new map of the base of Pliocene in the Abruzzo outer sector (Figure 4(d)).

5.2. Pressure Data. The pressure conditions in the periadriatic FTB-foredeep-foreland system are well known, above all in the northern sector. Carlin and Dainelli [79] reviewed pressure well data in order to define the various pressure systems in the Adriatic foredeep. Abnormal pressure regimes occur mainly in the Pliocene basin deposits, whereas the underlying carbonates are mainly in hydrostatic conditions. The authors defined three pressure regions in the Plio-Pleistocene succession, from the innermost: (i) inner thrust, (ii) deformation front, and (iii) undeformed foredeep. The compaction disequilibrium is the major cause for overpressures, coupled with a minor contribution of tectonics. The top of the geopressured zone corresponds to the base of the Pleistocene, which led us to target the Pliocene basin deposits as also highlighted by the temperature analysis. Our study area was only partially covered by Carlin and Dainelli [79] in their analysis. Thus, a careful analysis of the pressure well data was performed here in order to estimate the pressure gradients along available wells and to obtain first-order information on the pressure conditions.

The dataset is composed of hundreds of drill stem tests (DSTs) and some repeat formation tests (RFTs). Each test

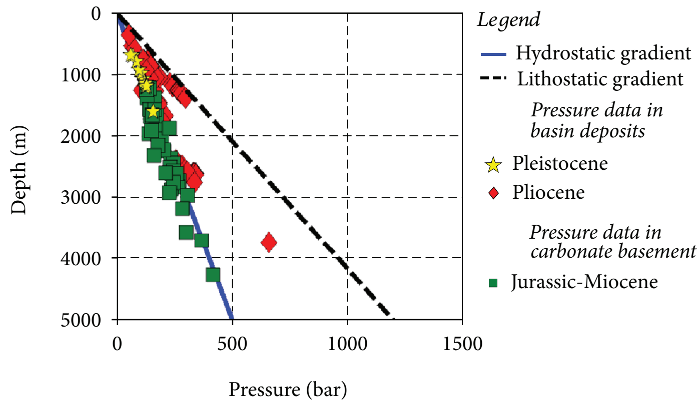

Figure 5: Depth vs pressure plot for the well dataset from the BDNG [73, 74] in the studied area.

is described with additional information such as the measured (MD) and true vertical (TVD) depths, lithology, stratigraphy, type of fluid, measured pressure, and above all the duration of all the phases of the tests. In fact, we considered the stabilized pressures measured after a greater shut-in time than the flowing periods. The tests were grouped according to the geological unit tested belonging to Mezo-Cenozoic carbonates or Plio-Pleistocene basin deposits.

In Figure 5, the complete dataset is summarized in a depth vs pressure plot. The pressure data are plotted and classified on the basis of the geological unit. The analysis highlights mainly hydrostatic pressure conditions for the carbonate basement as well as for the Pleistocene sediments, whereas abnormal pressure regimes occur in the Pliocene deposits, in some cases approaching lithostatic conditions (the epochs refer to the GSA scale v4.0 from [80]).

A pressure gradient was estimated for each well in the targeted Pliocene interval. We firstly selected those wells with more than one pressure value in the Pliocene succession in order to compute the pressure gradient by linear regression. In some sectors, where only one pressure value was available in the Pliocene succession along a well, we extrapolated the pressure at the top of Pliocene from the surface assuming a hydrostatic regime in the overlying Pleistocene deposits. We also considered six pressure profiles from Carlin and Dainelli [79] for a total amount of 24 deep hydrocarbon wells suitable for the study of the pressure regimes in the Pliocene succession.

Table 3 summarizes the main information on the pressure data indicating the location of the wells (see the ID) and the pressure regimes in Figure 6.

5.3. Thermal Data and Modelling. In order to evaluate the regional thermal structure of the study area, we solved the mathematical model for geothermal heat and mass transfer.

The bottom-hole temperatures (BHTs), measured in the deep hydrocarbon exploratory wells, were used as control points in order to compare the numerical results with the borehole data (Figure 7(b)). The thermal effects due to the drilling had been previously evaluated in order to correct the BHT data [81, 82]. Although the corrected BHTs had a mean error of the order of ±10%, they were suitable for highlighting the main regional thermal structure.

The sets of partial differential equations which describe the principles of conservation of mass, momentum, and energy are approximated through the finite element method in the COMSOL Multiphysics environment [83, 84]. The steady-state solution was evaluated within a numerical domain of $130 \times 100 \times 20\,\mathrm{km}^3$ accounting for the whole regional thermal structure of the Abruzzo-Molise outer sector. The tetrahedral mesh-grid counts $>3.6{\cdot}10^6$ nodes and the length of tetrahedron edges vary from a minimum of 100 m to a maximum of 1000 m, allowing the numerical mesh to fit the spatial variations of the boundary surfaces. The regional fluid circulation occurs within the permeable Mezo-Cenozoic carbonate units, and in the eastern Abruzzo geological framework, the Plio-Pleistocene foredeep deposits act as the cap-rock of the deep-seated low-temperature hydrothermal system, almost throughout the entire investigated area. The carbonate units outcropping in the Apennine chain represent the main recharge areas of the regional reservoir.

The geometrical model considers three main lithothermal units, from the top to the bottom: (i) the impervious sedimentary cover unit acting as a cap-rock, (ii) the tectonically thickened carbonate units hosting the main regional reservoir, and (iii) the basement unit. Each lithothermal unit is composed of different rocks with similar thermal and hydraulic properties. The rocks were treated as a homogeneous and downward anisotropic porous material. Mixing laws were applied to estimate the effective thermal and hydraulic properties of the rock-fluid system accounting for the in situ conditions [85]. In the cover and basement domains, a purely conductive heat transport takes place, while in the carbonate reservoir, the regional hydraulic gradient and the thermal convection affect the temperature distribution by mass and energy transport. The buried upper and basal boundaries of the reservoir are set impermeable to fluid flow, allowing only conductive heat transfer.

Accounting for the recharge zones, we applied a stress boundary condition where the reservoir units crop out (Figure 7(a)). As the reservoir is assumed to be fully saturated, the pressure on those boundaries is set as equal to

Table 3: Pressure measurements in wells. The ID refers to the location in Figure 6. The type of pressure test is reported plus information on measured depth (MD) lithology, age, and the geological unit.

ID	X WGS84 UTM33N	Y WGS84 UTM33N	Name	Test	*MD (m)	Pressure (bar)	Lithology**	Age**	Geological unit**
1	467486	4683474	Aguglia 1D	RFT	1069	112	Sandy stratum in clay	Pleistocene (uncertain)	Basin deposits
1	467486	4683474	Aguglia 1D	RFT	1072	111	Sandy stratum in clay	Pleistocene (uncertain)	Basin deposits
1	467486	4683474	Aguglia 1D	RFT	1074	116	Sandy stratum in clay	Pleistocene (uncertain)	Basin deposits
1	467486	4683474	Aguglia 1D	RFT	1134	124	Interbedded silty-clay and marly-clay	Pleistocene (uncertain)	Basin deposits
1	467486	4683474	Aguglia 1D	RFT	1148	124	Interbedded silty-clay and marly-clay	Pleistocene (uncertain)	Basin deposits
1	467486	4683474	Aguglia 1D	RFT	1203	124	Conglomerate	Pleistocene (uncertain)	Basin deposits
2	426176	4697027	Caprara 1	DST	1664	211	Clay and silty clay	Pliocene	Basin deposits
3	424550	4691862	Città S. Angelo 1	DST	525	63	Clay with thin sandy strata	Pliocene	Basin deposits
4	406998	4712354	Fino 2	DST	1305	135	Marly clay with interbedded sand	Pliocene	Basin deposits
4	406998	4712354	Fino 2	DST	1426	157	Marly clay with interbedded sand	Pliocene	Basin deposits
5	411053	4744028	Fonte Armata 1 DIR	RFT	2602	330	Interbedded clay, silt, and sand	Pliocene	Basin deposits
5	411053	4744028	Fonte Armata 1 DIR	RFT	2608	331	Interbedded clay, silt, and sand	Pliocene	Basin deposits
5	411053	4744028	Fonte Armata 1 DIR	RFT	2612	341	Interbedded clay, silt, and sand	Pliocene	Basin deposits
5	411053	4744028	Fonte Armata 1 DIR	RFT	2612	338	Interbedded clay, silt, and sand	Pliocene	Basin deposits
5	411053	4744028	Fonte Armata 1 DIR	RFT	2613	335	Interbedded clay, silt, and sand	Pliocene	Basin deposits
5	411053	4744028	Fonte Armata 1 DIR	RFT	2620	334	Interbedded clay, silt, and sand	Pliocene	Basin deposits
5	411053	4744028	Fonte Armata 1 DIR	RFT	2629	341	Interbedded clay, silt, and sand	Pliocene	Basin deposits
6	419361	4723269	Fonte Dell'Olmo 1 DIR	DST	758	133	Clay with interbedded sandy strata	Pliocene	Basin deposits
6	419361	4723269	Fonte Dell'Olmo 1 DIR	DST	758	117	Clay with interbedded sandy strata	Pliocene	Basin deposits
6	419361	4723269	Fonte Dell'Olmo 1 DIR	DST	758	114	Clay with interbedded sandy strata	Pliocene	Basin deposits
6	419361	4723269	Fonte Dell'Olmo 1 DIR	DST	849	149	Clay with interbedded sandy strata	Pliocene	Basin deposits
6	419361	4723269	Fonte Dell'Olmo 1 DIR	DST	849	146	Clay with interbedded sandy strata	Pliocene	Basin deposits
6	419361	4723269	Fonte Dell'Olmo 1 DIR	DST	849	146	Clay with interbedded sandy strata	Pliocene	Basin deposits
6	419361	4723269	Fonte Dell'Olmo 1 DIR	DST	1044	186	Clay with interbedded sandy strata	Pliocene	Basin deposits
6	419361	4723269	Fonte Dell'Olmo 1 DIR	DST	1044	172	Clay with interbedded sandy strata	Pliocene	Basin deposits
7	435683	4708320	Greta 1	DST	2485	284	Silty clay with interbedded sand	Pliocene	Basin deposits
8	453858	4755065	Milli 1	DST	927	97	Clay with interbedded sandy strata	Pleistocene ***	Basin deposits
8	453858	4755065	Milli 1	DST	1184	130	Clay with interbedded sandy strata	Pleistocene ***	Basin deposits
8	453858	4755065	Milli 1	DST	1670	210	Clay with interbedded sandy strata	Pliocene	Basin deposits

TABLE 3: Continued.

ID	X WGS84 UTM33N	Y WGS84 UTM33N	Name	Test	*MD (m)	Pressure (bar)	Lithology**	Age**	Geological unit**
9	409409	4695990	Montebello di Bertona 1	DST	1248	104	Clay with interbedded sandy strata	Pliocene	Basin deposits
9	409409	4695990	Montebello di Bertona 1	DST	1720	145	Interbedded clay and sand	Pliocene	Basin deposits
10	412573	4725288	Morro D'oro 1	DST	2664	259	Clay with interbedded sandy strata	Pliocene	Basin deposits
10	412573	4725288	Morro D'oro 1	DST	3737	660	Clay with interbedded sandy strata	Pliocene	Basin deposits
11	432011	4687606	*S. Barbara* 1 DIR	RFT	1603	157	Interbedded clay, silt, and sand	Pleistocene ***	Basin deposits
11	432011	4687606	S. Barbara 1 DIR	RFT	1607	158	Interbedded clay, silt, and sand	Pleistocene ***	Basin deposits
11	432011	4687606	S. Barbara 1 DIR	RFT	1608	158	Clay with interbedded sand	Pleistocene ***	Basin deposits
12	476663	4654451	S. Salvo 18	DST	792	85	Sand with interbedded clayey strata	Pleistocene ***	Basin deposits
13	460849	4652300	S.Buono 1	DST	1110	140	Mainly marls	n.a.	Allochthonous
13	460849	4652300	S.Buono 1	DST	1265	170	Mainly marls	n.a.	Allochthonous
14	401564	4737592	S.Omero W1	DST	928	127	Sand with interbedded clayey strata	Pliocene	Basin deposits
14	401564	4737592	S.Omero W1	DST	1066	147	Sand with interbedded clayey strata	Pliocene	Basin deposits
15	425177	4695464	S.Salvatore 1	DST	1745	193	Clay and sand	Pliocene	Basin deposits
16	455226	4682931	S.Vito Chietino 1	DST	688	61	Sandy lens in clay	Pleistocene ***	Basin deposits
17	402492	4729249	San Silvestro 1	DST	2388	255	Marls with interbedded sand	Pliocene	Basin deposits
17	402492	4729249	San Silvestro 1	DST	2575	305	Marls with interbedded sand	Pliocene	Basin deposits
18	418324	4726514	Savini 1	RFT	1140	229	Clay with interbedded sand	Pliocene	Basin deposits
18	418324	4726514	Savini 1	RFT	1192	240	Clay with interbedded sand	Pliocene	Basin deposits
18	418324	4726514	Savini 1	RFT	1253	264	Clay with interbedded sand	Pliocene	Basin deposits
18	418324	4726514	Savini 1	RFT	1254	265	Clay with interbedded sand	Pliocene	Basin deposits
18	418324	4726514	Savini 1	RFT	1274	271	Clay with interbedded sand	Pliocene	Basin deposits
18	418324	4726514	Savini 1	RFT	1298	277	Clay with interbedded sand	Pliocene	Basin deposits
18	418324	4726514	Savini 1	RFT	1374	296	Clay with interbedded sand	Pliocene	Basin deposits
19	470602	4670874	Sinello 1	RFT	980	107	Conglomerate with sand and clay	Pleistocene ***	Basin deposits
19	470602	4670874	Sinello 1	RFT	1423	143	Clay with interbedded sand	Pliocene	Basin deposits
19	470602	4670874	Sinello 1	RFT	1424	146	Clay with interbedded sand	Pliocene	Basin deposits
19	470602	4670874	Sinello 1	RFT	1439	143	Clay with interbedded sand	Pliocene	Basin deposits
19	470602	4670874	Sinello 1	RFT	1439	143	Clay with interbedded sand	Pliocene	Basin deposits
19	470602	4670874	Sinello 1	RFT	1439	143	Clay with interbedded sand	Pliocene	Basin deposits
19	470602	4670874	Sinello 1	RFT	1443	143	Clay with interbedded sand	Pliocene	Basin deposits
19	470602	4670874	Sinello 1	RFT	1459	158	Clay with interbedded sand	Pliocene	Basin deposits
19	470602	4670874	Sinello 1	RFT	1586	174	Clay with interbedded sand	Pliocene	Basin deposits

Table 3: Continued.

ID	X WGS84 UTM33N	Y WGS84 UTM33N	Name	Test	*MD (m)	Pressure (bar)	Lithology**	Age**	Geological unit**
20	469004	4756862	Stefania 1	DST	700	69	Clay and sandy clay	Pleistocene	Basin deposits
21	406048	4727393	Villa Torre 1	DST	1452	184	Sand with interbedded clayey strata	Pliocene	Basin deposits
21	406048	4727393	Villa Torre 1	DST	1482	184	Sand with interbedded clayey strata	Pliocene	Basin deposits
21	406048	4727393	Villa Torre 1	DST	2758	335	Sand	Pliocene	Basin deposits
22	461034	4669078	Villalfonsina 3	DST	1436	160	Clay with interbedded sand	Pliocene	Basin deposits

*The depth is referred to the recording device or to the top of the tested interval. **The geological model, age, and lithology refer to the tested interval whose depth can be different with the depth of the recording device. ***The Pleistocene can be reported in the logs as Upper Pliocene.

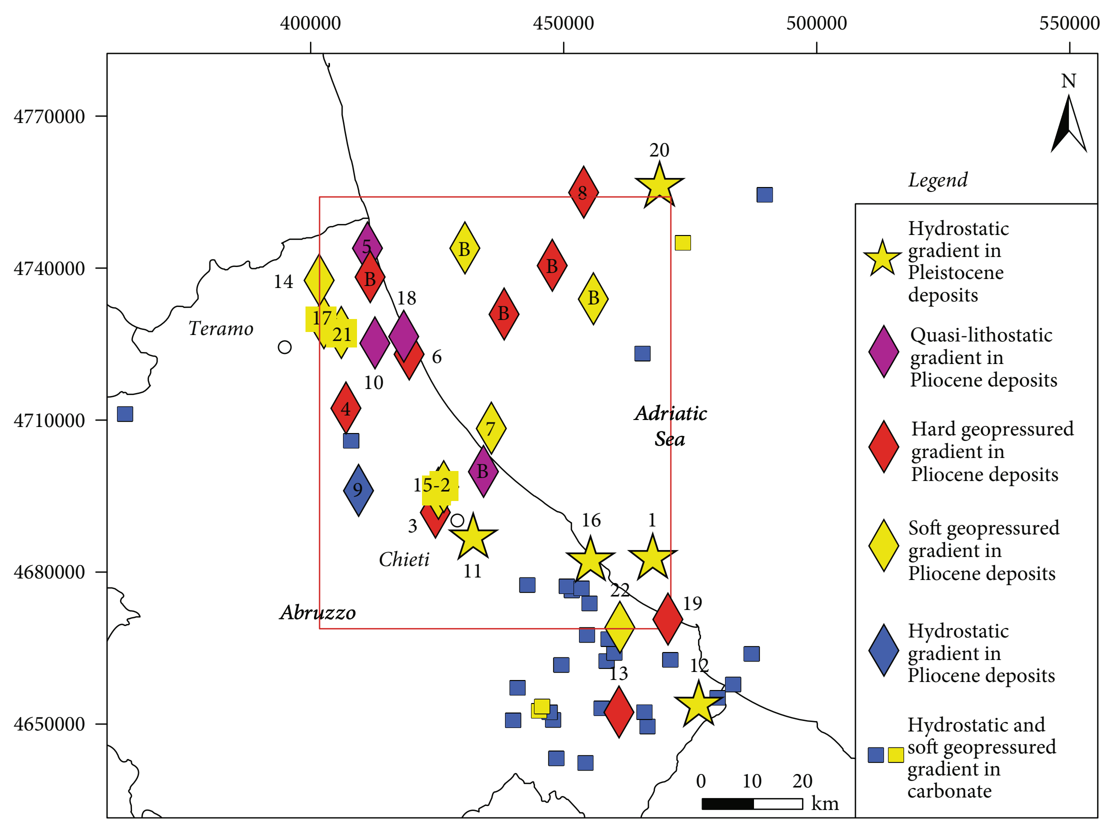

Figure 6: Location of wells with available pressure measurements. The wells were grouped according to the calculated pressure regime. The ID (1–22) of each well corresponds to the ID in Table 3, which reports the main information (from [73, 74]), whereas the wells marked with B are from Carlin and Dainelli [79]. The area in red is the study area for the favourability assessment.

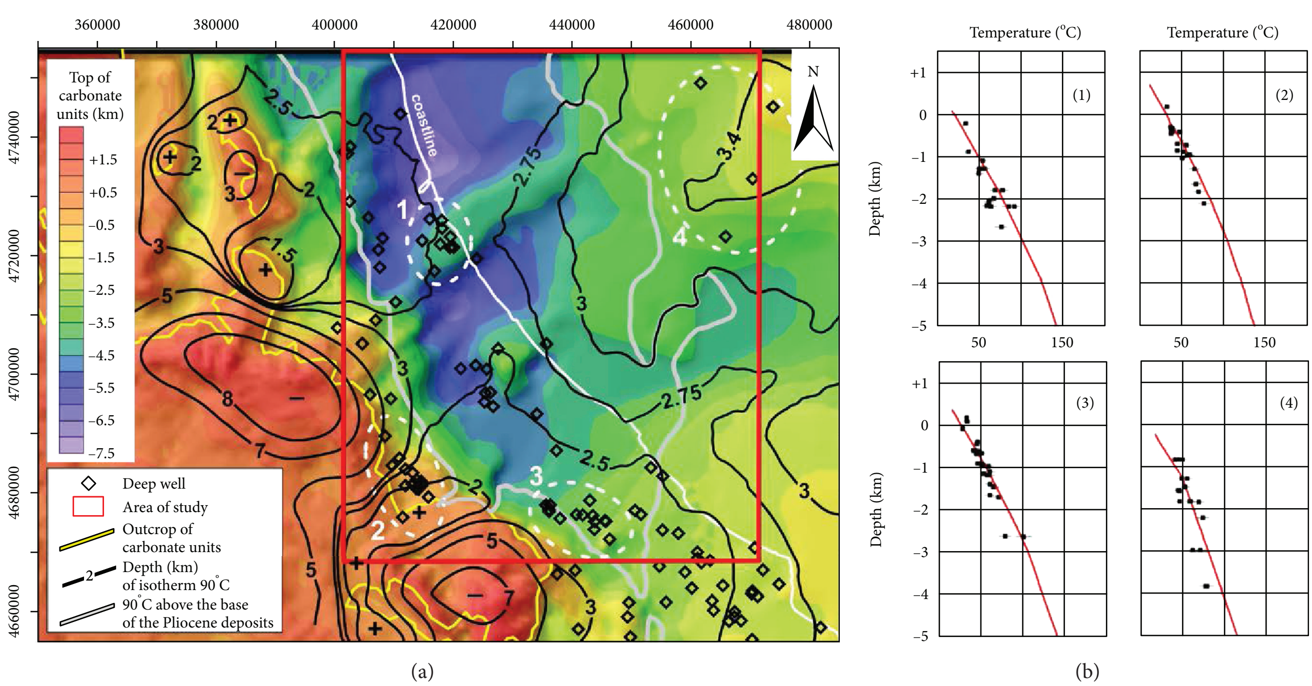

Figure 7: Thermal model. (a) Elevation map of the top of carbonate units hosting the regional reservoir together with the depth (referring to the sea level) of the 90°C isotherm. The gray lines encompass the sector in which the threshold temperature of 90°C is above the base of the Pliocene deposits. The main recharge areas (outcrops of carbonate units) and the deep exploratory wells are also reported. (b) Comparison between the corrected bottom hole temperatures (black square) and the modelled thermal profiles from selected clusters of wells ((a), dashed white lines). The error bar of ±10% is also reported.

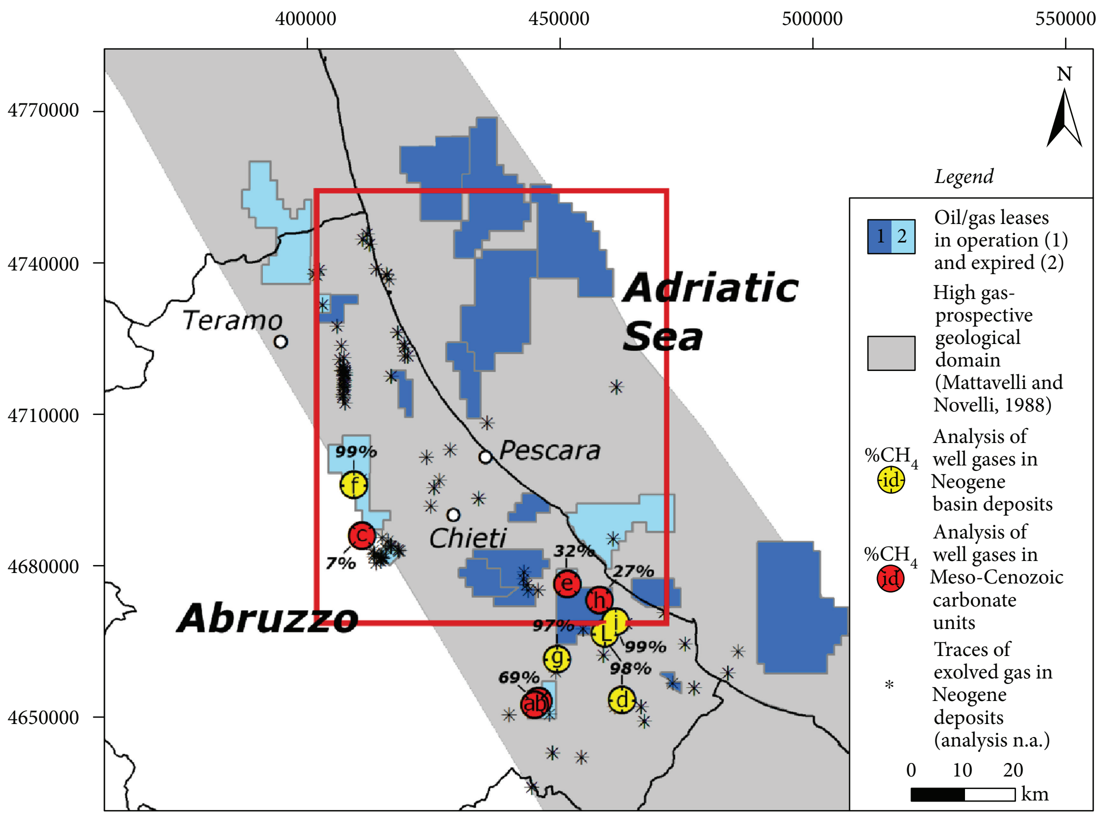

Figure 8: Location of wells with chemical analyses available on gas and with traces of exsolved gas (data from [74]). The oil and gas leases are from [74, 97], whereas the area with a high occurrence of hydrocarbons is from Mattavelli and Novelli [88]. The data shown are only for Abruzzo. The area in red is the study area for the favourability assessment.

the freshwater head calculated with a reference water density of 1000 kg/m^3 and the sea level as datum. Regarding the upper and lower thermal boundaries, we defined the mean annual soil temperature and a specific isotherm at a 20 km depth, respectively. The vertical boundaries of the numerical domain do not allow a horizontal flow of fluid and heat.

A good fit between the measured and simulated temperatures was achieved for a basal temperature of 350°C and an average permeability of the regional carbonate reservoir of $1.6\cdot10^{-16}$ m^2.

The observed geothermal gradients spanned from 20 to 50°C/km, and the mean value was 28°C/km. The highest and lowest values were observed in the mountainous zones in which the heat advection, controlled by the regional groundwater flow, modifies the conductive thermal structure. Regarding the thermal structure of the study area, we computed the depth (a.s.l.) of the 90°C isotherm (also referred to as z90). The isobaths show two minima (z90 > 5 km) in the south-western corner separated by an upwelling zone (z90 ≈ 2 km). In the mainland, far from the carbonate outcrops, z90 settles around 2.5–2.7 km and deepens toward the offshore sector to 3–3.4 km.

On the basis of the thermal and geological models, the sectors in which z90 is above the base of the Pliocene deposits represent the target areas (Figure 7(a)).

5.4. Geochemistry. In our case study, the geochemical analyses on fluids sampled in wells were used to analyse known methane-prospective areas (corresponding to tectonic elements), whereas a geostatistical analysis was not possible.

Minissale et al. [86, 87] clearly defined multiple sources of gas discharge manifestations in central Italy. Along a transect crossing the Northern Apennine, the inner part of the chain is mostly characterized by CO_2-rich emissions, whereas CH_4-rich emissions are predominant in the outer part of the Apennines along the Adriatic coast, where the study area is located. The source of CH_4 in the Adriatic sector is related to the sedimentary process in the Periadriatic foredeep. In fact, Italy is considered a gas (methane)-prone area, the formation and accumulation of which are strictly related to the tectono-sedimentary evolution and specific areas.

Mattavelli and Novelli [88] identified a narrow area, corresponding to the foredeep of the Apennine belt, where 77% of Italian natural gases were discovered (Figure 8). Here, the synsedimentary tectonics, the highly efficient turbidite systems coupled with subsidence, favoured the generation (and also trapping) of natural gases. Eighty-two per cent of natural gas in this area is biogenic, characterized by almost pure and isotopically light CH_4 with C_2 (ethane) and other components (<0.5%). The authors found strong evidence for in situ generation of gas, through bacterial or diagenetic processes. The gaseous hydrocarbons are mainly stored in Plio-Pleistocene sediments.

We focused on the gas chemistry of sampled fluids in wells. Several chemical analyses of major ions were available for the water samples with complementary notes on the

Table 4: Well gas chemical analyses, in relation to the CH_4 and CO_2 percentage. The ID refers to the location in Figure 8.

ID	X WGS84 UTM33N	Y WGS84 UTM33N	Name	MD (m)	Test	Gas analysis CH_4 (%)	$C0_2$ (%)	Lithology	Age	Geological unit
a	445825	4653324	Bomba 1	1222	DST	68,91	0,73	Wackestone and packstone	Miocene	Carbonate basement
b	445031	4652621	Bomba 2	1378	DST	69,14	0,7	Wackestone and packstone	Miocene	Carbonate basement
c	410927	4685976	Bonanno 1	1680	DST	7,5	36	Limestone	Miocene	Carbonate basement
d	464912	4656839	Gissi 2	1021	DST	98,37	0,32	Packstone and marls	Miocene (allochthonous)	Basin deposits
e	451540	4676478	Lanciano 2	2721	DST	31,84	13	Wackestone and packstone	Cretaceous	Carbonate basement
f	409409	4695990	Montebello di Bertona 1	1248	DST	99,19	0,04	Intercalated shale and sandstone	Pliocene	Basin deposits
f	409409	4695990	Montebello di Bertona 1	2925	DST	16,03	53,3	Wackestone and packstone	Cretaceous	Carbonate basement
g	449486	4661657	Perano 1	979	DST	97,4	0,06	Shale	Pliocene (uncertain)	Basin deposits
h	457847	4673292	S. Maria 2	2194	DST	26,67	1,83	Limestone	Cretaceous	Carbonate basement
i	461034	4669078	Villalfonsina 3	1436	DST	99,33	n.a	Sandy shale	Pliocene	Basin deposits
L	458910	4666716	Paglieta 3	700	DST	98,5	n.a.	Limestone and marls	Miocene (allochthonous)	Basin deposits

occurrence of gas (generic) or smell of hydrocarbons. A few were coupled with chemical analyses of well gases.

The analyses of well gases sampled in Plio-Pleistocene deposits show an amount of CH_4 that is always higher than 97% and CO_2 lower than 1%. In addition, tens of wells record exsolved gas traces in the Plio-Pleistocene interval. The same analyses in the underlying carbonates show lower and highly variable amounts of CH_4. These gases were sampled in relation to supposed hydrocarbon targets in the carbonates. Figure 8 shows the wells with measured CH_4, as well as those with traces of exsolved gas.

An example is given by the well "Montebello di Bertona 1" in which well gases were analysed both in terrigenous sediments and in carbonate successions. The gas sampled in the interbedded shale and sand, Pliocene in age, is composed of 99% of CH_4, whereas in the underlying carbonates, CH_4 abruptly decreases and CO_2 increases to over 50%.

The analyses led us to assume formation water saturated and oversaturated in methane, with a clear indication of the diffuse presence of CH_4 in the Plio-Pleistocene deposits, which is locally accumulated. Table 4 summarizes the well gas analyses. We also computed the methane solubility in water by using the empirical method by Price et al. [36] and taking as an example the conditions at depth along the well "Morro D'oro 1" from a test in water with dissolved gas. Considering a formation pressure of 660 bar at 3733 m, a temperature of 90°C, and water salinity of 28.6 g/l, the solubility of methane is 28.75 SCF/Bbl. The solubility we computed is close to the values reported for the geopressured system of the Gulf of Mexico [27, 36].

6. Layers of Evidence

With regard to the Abruzzo case study, in the first stage, a preliminary analysis was carried out in order to identify the areas to be assessed, those strictly related to the concept of sedimentary basin plays. The study area corresponds to the foredeep-foreland domains of the Apennines thrust belt in Abruzzo. The targets are the geopressured resources hosted in the Plio-Pleistocene siliciclastic succession. Basically, the sectors in which the depth of the 90°C isotherm is above the base of the Pliocene deposits represent the target areas.

We then created the layers of evidence by combining different thematic inputs throughout the spatial analyses. These layers of evidence were related to the favourable factors and referred to (see details in Section 3): (i) the effective geopressured-geothermal reservoir, (ii) the thermal regime, (iii) the pressure regime, (iv) the deposit thickness, and the (v) geochemistry.

The five layers of evidence were combined by Index Overlay to produce the final favourability map as a result of the last stage of the workflow. The layers of evidence have been computed with the same spatial resolution, 1×1 km, and with the grid nodes of each layer overlapping.

6.1. Effective Geopressured-Geothermal Reservoir. The concept of the effective geopressured-geothermal reservoir is illustrated in Figure 9, using an example from the 3D model of the study area. In this paper, a threshold value of 90°C was set considering the geothermal power production purposes. The layer was built by applying a layer intersection between the depth of the 90°C isotherm and the bottom surface of

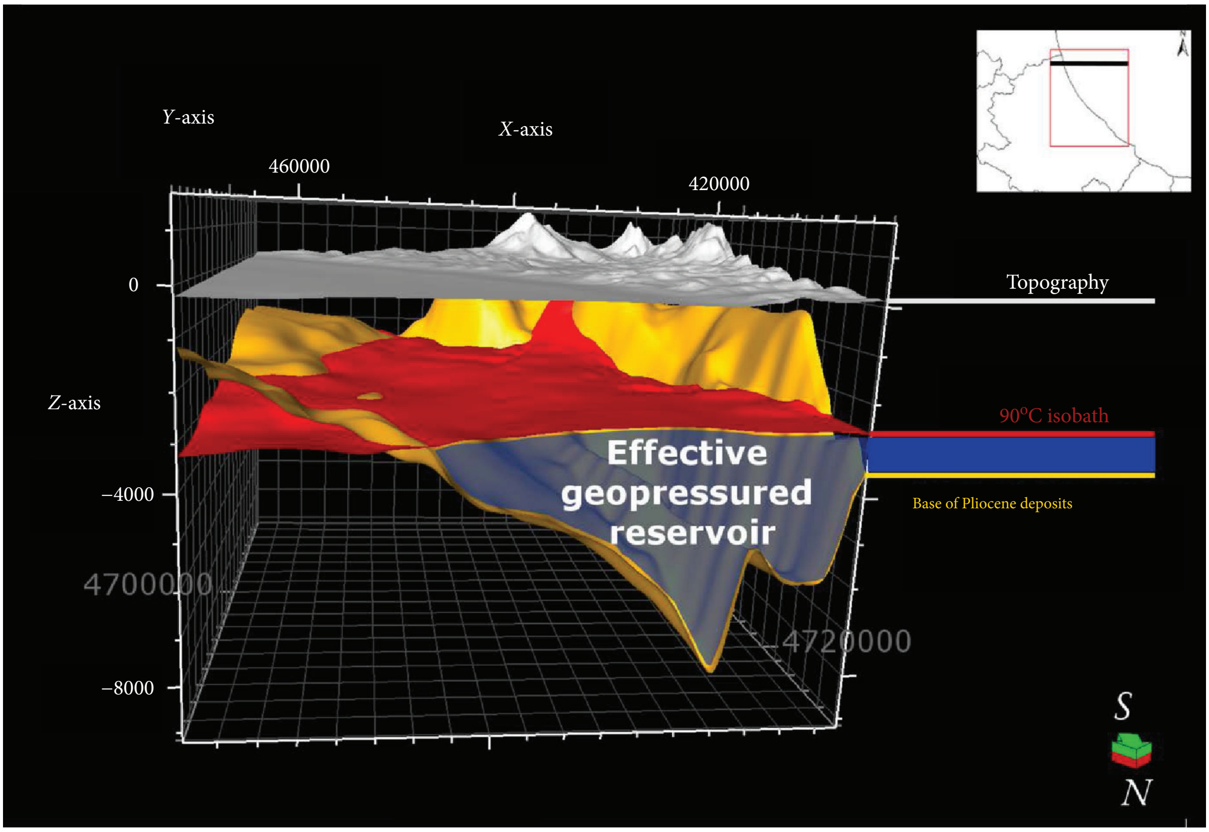

Figure 9: View of the 3D geological model of the study area explaining the concept of an effective geopressured-geothermal reservoir. The trace of the intersection plane is reported in black (upper right corner). The axes are in meters.

the Pliocene deposits. The result is a grid layer of a ranked depth of the top of the effective geopressured-geothermal reservoir (Figure 10).

Where the isotherm is deeper than the base of the Pliocene deposits, i.e., no effective reservoir occurs, the corresponding areas are neglected from the computation.

The ranking classes and the weight are listed in Table 2.

6.2. Thermal Regime. In our study, the thermal regime is parameterized by the thermal gradient.

The thermal gradient was computed starting from the average air temperature, which varies on the basis of the topography elevation, and using the layer of the temperature at the top of the carbonate formations. By a raster computation, we obtained an average air temperature for each cell from the digital elevation model (DEM) layer applying a lapse rate of 0.0065 (°C/m) and 0.0045 (°C/m) for positive (i.e., above sea level) and negative (i.e., below sea level) elevations, respectively [89, 90]. A further raster computation then enabled us to define the thermal gradient map (Figure 11). The thermal regime was ranked and weighted as shown in Table 2.

6.3. Pressure Regime. We obtained information of the pressure regions through geostatistical analyses on the pressure gradients computed in the wells reaching the Pliocene succession. A statistical analysis showed only a partial trend along the X and Y coordinates. After various attempts, we have chosen the resulting interpolation obtained with the Universal Kriging algorithm, which guaranteed the least root-mean-square error. The resulting grid layer is shown in Figure 12.

The rank is related to the amount of overpressure that occurs in the Pliocene sedimentary succession.

6.4. Deposit Thickness. This layer of evidence was obtained by simply classifying the thickness of the basin deposits (i.e., the Pliocene bottom depth from the ground level) using the raster recode function (Figure 13). The classes and weights are listed in Table 2.

6.5. Geochemistry. This layer of evidence, for the Abruzzo case study, is essentially based on the ranking of the methane-prospective area, corresponding to the foredeep domain, proposed by Mattavelli and Novelli [88] (Figure 14). We assigned the highest class (5th) to this area, assuming the occurrence of CH_4-saturated and oversaturated waters in reservoir. The available geochemical dataset on fluids sampled in wells supports this assumption (see Section 5.4). The dataset was not complete enough to compute geostatistical analysis. The remaining part of the area, not included in this CH_4-prospective domain, was ranked with the less favourable class (1st).

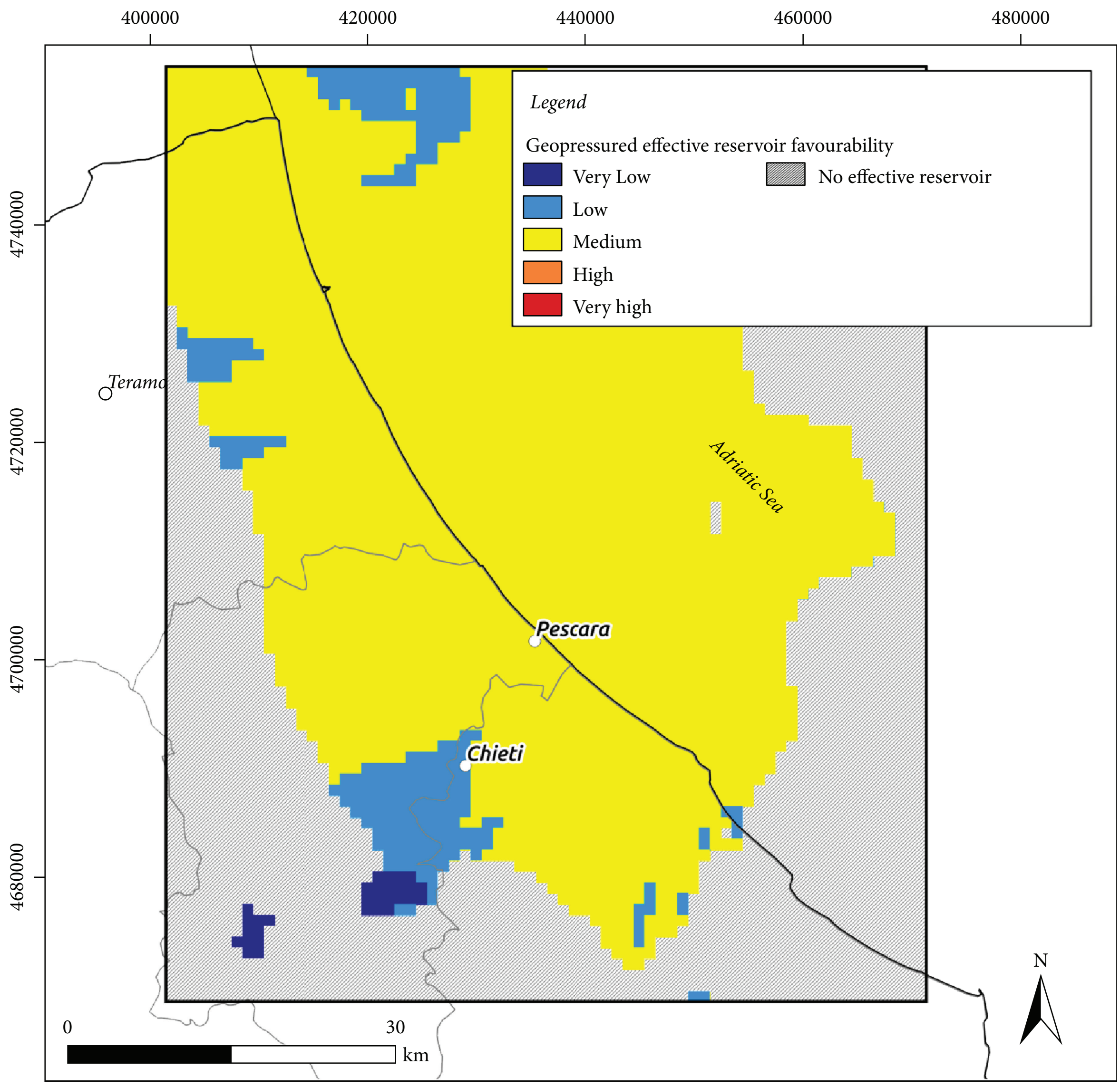

Figure 10: Geopressured effective reservoir layer of evidence.

7. The Favourability Map of Abruzzo: Results and Discussion

The quantitative integration of data using the Index Overlay method (see Section 6) resulted in the favourability map of a geopressured-geothermal system for the foredeep-foreland basin play of Abruzzo, shown in Figure 15.

The role of the prospective factors at regional scale (Table 1) has been addressed in the five layers of evidence. The geopressured effective reservoir takes into account the depositional environment, the temperature, the depth of the reservoir, and intrinsically the lithology. Pressure and temperature have been considered in the pressure and thermal regime layers of evidence, respectively. The deposit thickness takes into account the depositional environment, the deposition rate, the size of the reservoir, and the lithology. The geochemistry layer provides information on the occurrence of dissolved gaseous hydrocarbons.

A point that deserves a clarification is the use or not of the faults as permeability indicator. The main limit of its use in the favourability computation is the possible hydraulic behaviour of the faulted volume of rocks. A fault can act as a permeability barrier or can enhance the permeability. At regional scale, it is not accurate and reliable to assign a favourable value around a fault trace. At local (i.e., exploration licence) or well scale, the detailed geophysical and geological studies allow the understanding of the hydraulic feature of a fault. We decided to disregard this contribution in our computation at regional scale, but we consider the structural setting a key information to be addressed during a local exploration project.

The study area was mostly ranked from not to low/-medium favourable, with one exception corresponding to a wide continuous prospective sector in the centre. The most favourable sector, with a rank up to the 4th class, extends for less than 1000 km^2 and runs parallel to the shoreline along a

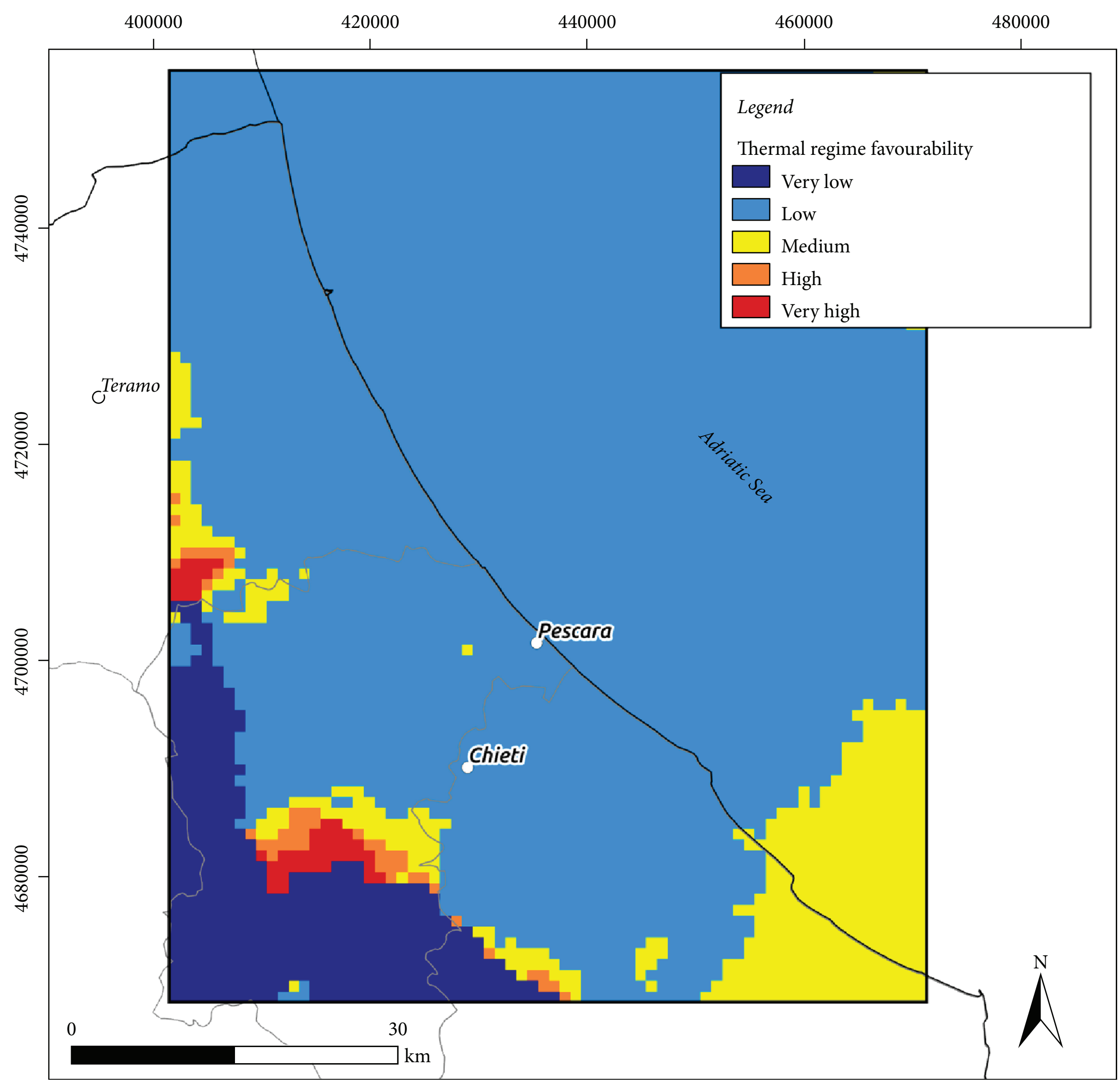

Figure 11: Thermal regime layer of evidence.

NW-SE direction, both offshore and onshore. The 5th class (very favourable) was not retrieved. The cells of the grid that have been ranked (from 1st to 5th class) are those where the effective reservoir was detected; otherwise, the cells were not considered favourable.

We assigned the highest weight in the Index Overlay computation to the effective reservoir layer of evidence (0.4; see Table 2) because it takes into account (i) the minimum temperature requirement for the exploitation, (ii) the financial factors related to the depth of the drilling target, and (iii) the occurrence of a potential reservoir. Since the subsurface temperature is usually close or lower than the average continental reference in the study area, the depth of the top of the effective reservoir belongs mostly to the medium and low favourable classes with scores of 3 and 2, respectively. This means that in the best scenario, wells should reach a 2.5–3 km depth to exploit 90°C.

The second most weighted layer of evidence (0.3; see Table 2) is the pressure regime. Our study area is mostly characterized by high to very high favourable classes (4 and 5 scores) with hard geopressured gradients in the Pliocene succession, locally approaching the lithostatic reference. We consider this layer of evidence as a useful first-order approximation of pressure regions. However, due to the low number of pressure data, the spatial analysis cannot be used to evaluate a precise value at depth of the formation pressure. As expected, the most abnormal pressure regime occurs along the deformation front subparallel to the coast. The inner sector (westwards) shows hydrostatic to soft geopressured regimes, whereas the undeformed foredeep (eastwards) shows soft to hard geopressured regimes. The results of our analysis are in good agreement with the pressure regions identified by Carlin and Dainelli [79] for the northern sectors of the Adriatic Sea.

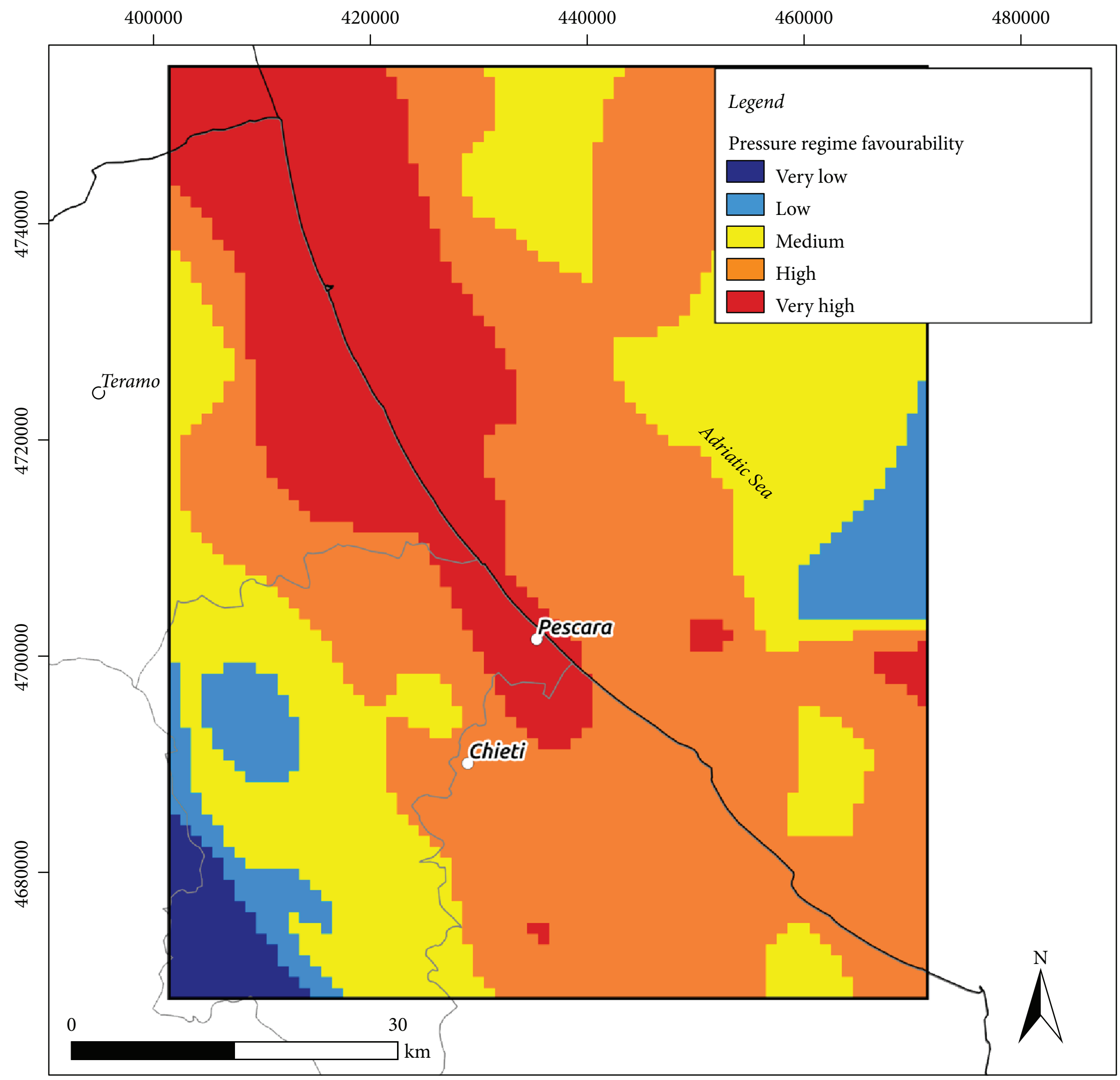

Figure 12: Pressure regime layer of evidence.

Although temperature is embedded in the concept of the effective reservoir, which considers the 90°C isotherm, we included a layer of evidence exclusively related to the thermal regime, with a weight of 0.1 by 1. We thus included information on the occurrence of positive thermal anomalies. As expected, most of the study area shows low values of geothermal gradient except for the southern part, where higher values belonging to the 3rd class were found. Here, the deep water rising toward the groundwater base level can affect the conductive thermal gradient within the impermeable cover.

The layer of evidence related to the deposit thickness shows higher values, up to the 4th class, only in a small sector located in the deformation front along the northern coastal zone. The weight assigned is the same as the thermal regime, i.e., 0.1 by 1. We chose a weight value lower than the effective reservoir and pressure regime because this layer is mainly related to geological conditions that can indirectly favour the presence of geopressured resources and less direct information is provided, such as the possible extent at depth of reservoirs. We stress that the deposit thickness is correlated with the deposition rate, but it is also controlled by tectonics in the study area.

The aim of this study was to assess the geopressured resources occurring in terrigenous sedimentary basin plays, as they favour the generation of overpressure and above all widespread dissolved gaseous hydrocarbons. The importance of methane is already embedded in this focus. Furthermore, we assumed that there are methane-saturated waters in the CH_4-prospective area [88] corresponding to the foredeep domain, after a duly analysis, assigning the highest class (5th). In our case study, the geochemical dataset was too poor to rank the area accordingly and the assigned weight is 0.1 by 1.

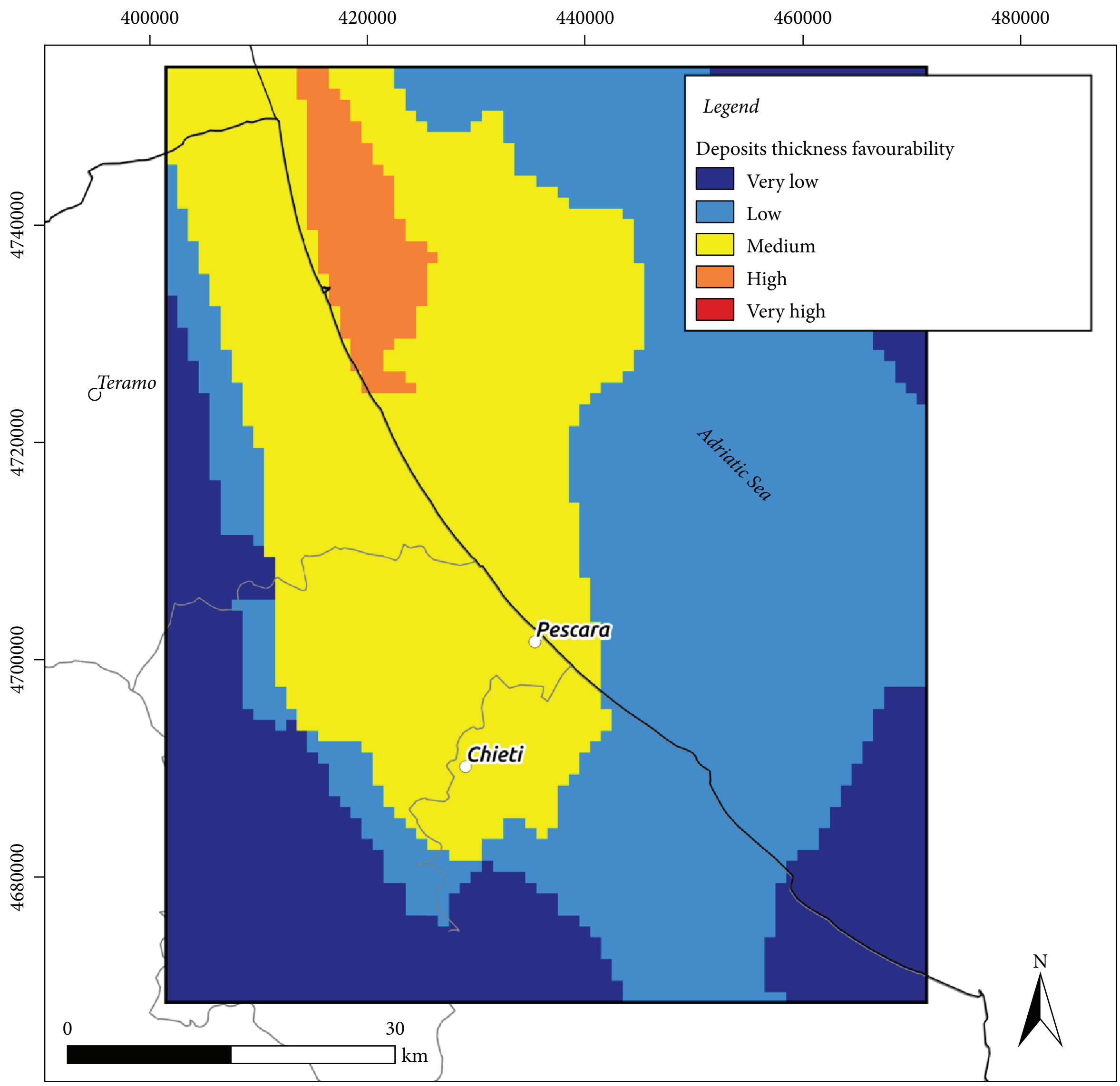

Figure 13: Deposit thickness layer of evidence.

The procedure can be improved with a quantitative ranking of the layer of evidence regarding the geochemistry (e.g., percentage of methane in free gases, methane solubility) by using geostatistical tools.

From a practical point of view, the map can be considered constrained where direct data along deep wells are available. For this reason, we provide the final favourability map coupled with the well locations. Moreover, to further assess and exploit the geopressured resources in the study area, it should be considered that the favourable part located in the offshore is limited by technical (even if the sea floor of the Adriatic Sea is really shallow) and nontechnical (e.g., legal regulations) barriers.

7.1. Sensitivity Analysis. In order to verify the stability of the resulting favourability map and the reliability of our knowledge-driven choices, we have computed a sensitivity analysis in which the influence of input variations is evaluated on the outcomes.

A deterministic sensitivity analysis was computed as follows:

(i) The favourability map of the Abruzzo (Figure 15) is set as reference outcome (out_{ref}) as well as the weights ($W_{i-\text{ref}}$) of each layer of evidence

(ii) The weight of the first layer of evidence ($W_{i=1}$) was perturbed in the range 0.1–0.9 while homogenously distributing the remaining weight to the other layers (being the sum of the weights equal to 1). The procedure is repeated for each layer of evidence. For each scenario, a favourability map (out_{n}) was computed by IO (see (1)). We stress that the classes of each layer of evidence are kept equal to the reference scenario

(iii) The percentage change in the output (Δout) of each scenario is computed for each pixel with respect to the reference map

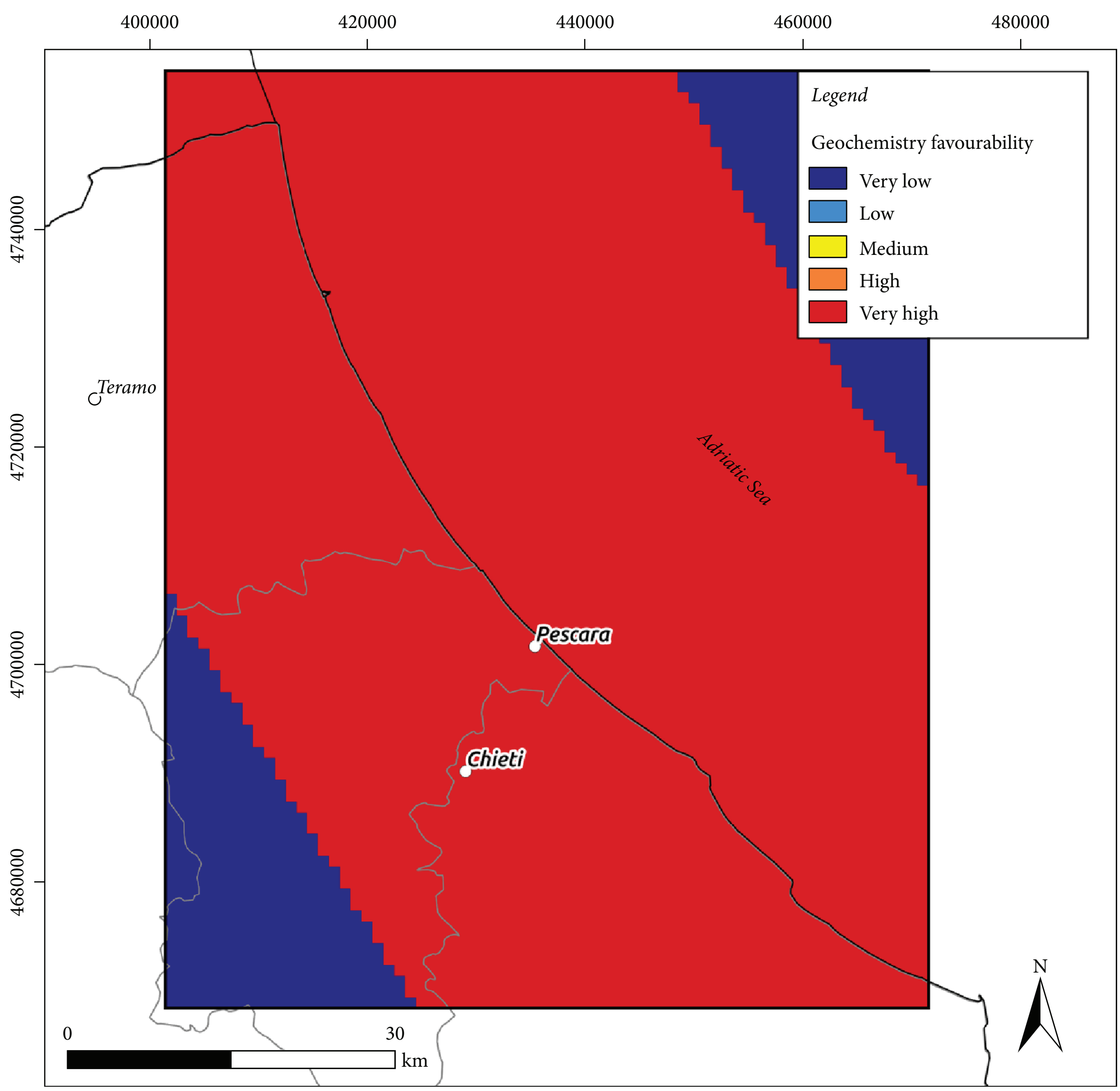

FIGURE 14: Geochemistry layer of evidence.

(iv) The percentage change in the weight (ΔW_i) of each scenario is computed with respect to the reference weights ($W_{i-\text{ref}}$)

(v) The sensitivity s for each scenario is computed pixel by pixel as the ratio between percentage changes in the output and weights, as follows:

$$s = \frac{\Delta \text{out}}{\Delta W_i} \tag{2}$$

The results are summarized in Figure 16. We show the sensitivity maps evaluated for each layer of evidence with weights varying from 0.1 to 0.9 with a step of 0.2.

The comparison among the various sensitivity maps highlights a larger sensitivity to the geopressured effective reservoir and the pressure regime layers of evidence. The main variations of the sensitivity index mimic the spatial distribution of the pressure regime, highlighting a very important role of this layer. This behaviour is expected because among the most weighted layers, the pressure regime shows the largest spatial variability; on the contrary, the effective reservoir is almost homogenous.

Conversely, our reference map is slightly sensitive to the perturbation on the thermal regime, geochemistry, and the deposits thickness layers, except for a few restricted areas. Particularly, the sector in the southwestern corner of the map shows larger sensitivity. This response corresponds to an area at the contact of outcropping carbonates where very high thermal gradients are modelled. This computation appears to be a local artefact, due to the fact that the thickness of the impermeable cover is really short and the resulting thermal gradients were extremely high.

8. Conclusions

This paper is intended to be a practical analytical framework for the systematic integration of the relevant data required to

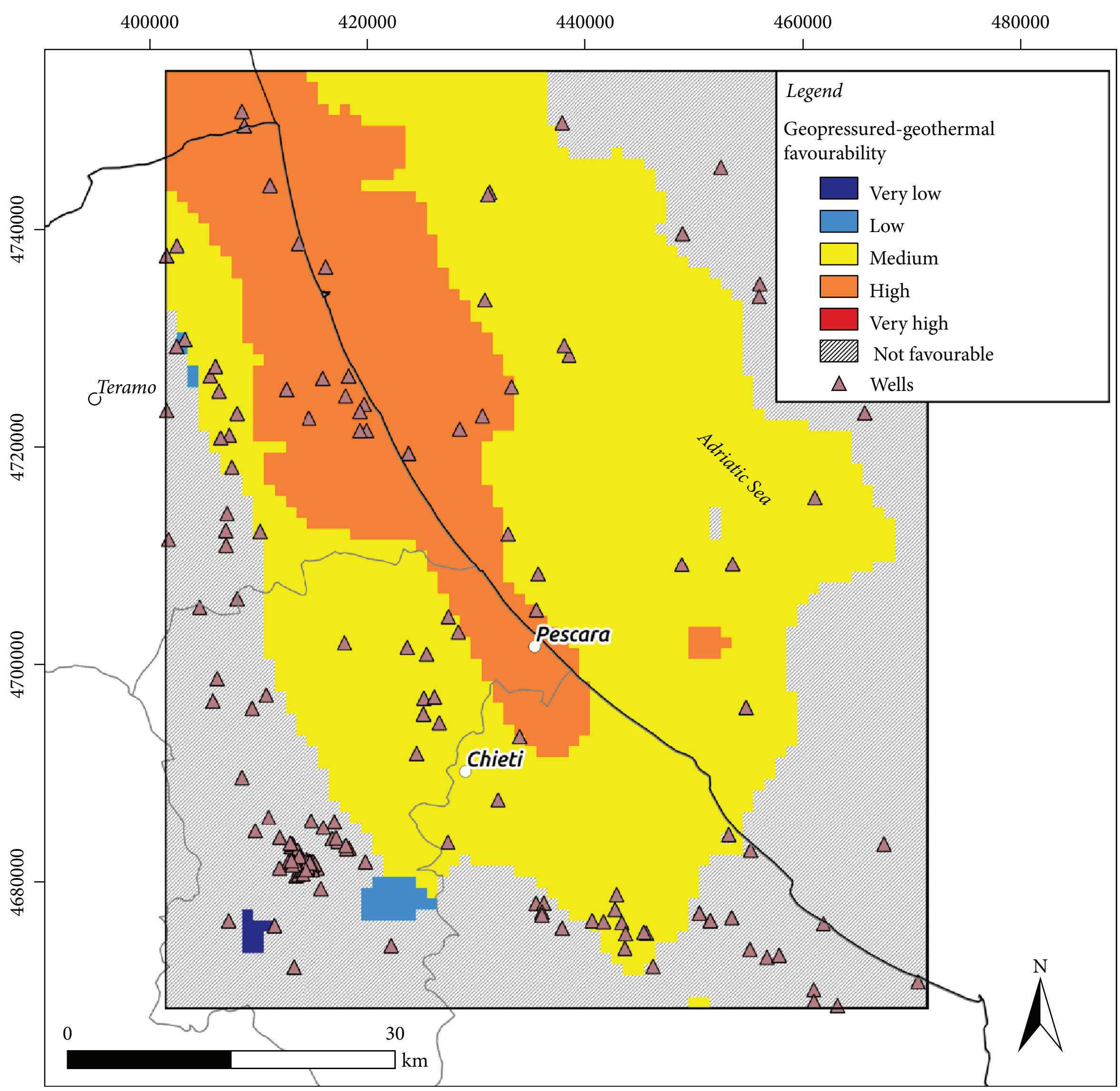

Figure 15: Favourability map of the geopressured-geothermal system for Abruzzo.

assess the geopressured-geothermal resources. The approach described can be considered valid and applicable at a global scale as the whole procedure is based on generic features of terrigenous sedimentary basins and was further tested on the Abruzzo case study.

The main results of this study can be summarized as follows:

(i) We propose a novel integrated methodology aimed at assessing and mapping the favourability of geopressured resources in sedimentary basin plays worldwide. We used a consolidated system of weighting and scoring in a GIS environment, the Index Overlay, to analyse various prospective parameters.

(ii) We identified five layers of evidence that describe the prospective factors needed for assessing such unconventional resources: (i) the effective geopressured-geothermal reservoir, (ii) the thermal regime, (iii) the pressure regime, (iv) the deposit thickness, and (v) the geochemistry. The effective geopressured-geothermal reservoir is a concept that can be of help for the industrial exploration. The depth of its top is a key parameter, easy to map.

(iii) Regarding the Abruzzo case study, an updated dataset of subsurface data was organized and important outcomes are now available such as the 3D geological model, including an up-to-date base of Pliocene deposits, and the study on the pressure and thermal regimes.

(iv) The final favourability map for the Abruzzo case study is a first attempt at ranking these kinds of unconventional geothermal resources in a region that has been historically explored and exploited

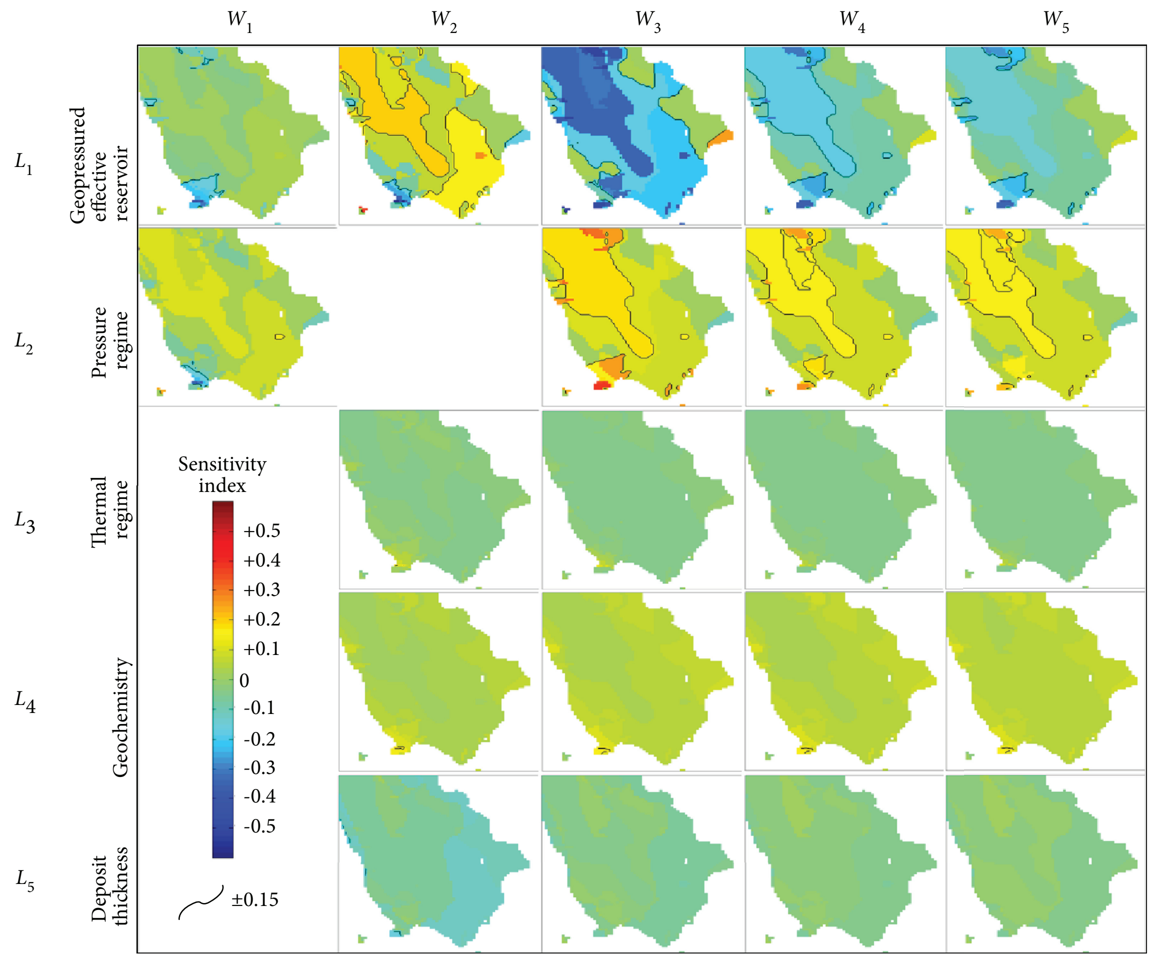

FIGURE 16: Sensitivity analysis for the favourability map of the Abruzzo region. The outcomes refer to the computation of the sensitivity by perturbing weights of a selected layer of evidence while distributing homogeneously the remaining part of the weight to the other layers (by sum equal to 1). $W_1 = 0.1$, $W_2 = 0.3$, $W_3 = 0.5$, $W_4 = 0.7$, and $W_5 = 0.9$. The contour of the value ±0.15 is shown. The missing outcomes are those with the perturbed weight of the selected layer of evidence equal to the reference weight.

only for hydrocarbons. In order to provide a quantitative estimation of the resources required for industrial projects, detailed exploration activities at the local scale (research permits) are required.

Data Availability

(1) The official geological maps for the study area are available at the following links: (i) ISPRA, 2017a. Geological maps of Italy, scale 1 : 100.000 (sheets 133, 134, 140, 141, 146, 147,148, 152, 153, 154), Istituto Superiore per la Protezione e la Ricerca Ambientale. http://193.206.192.231/carta_geologica_italia/default.htm; (ii) ISPRA, 2017b. Geological maps of Italy, scale 1 : 50.000, sheet 339. Istituto Superiore per la Protezione e la Ricerca Ambientale. http://www.isprambiente.gov.it/Media/carg/339_TERAMO/Foglio.html. (2) The master logs of the deep hydrocarbon wells analysed in this work are available at ViDEPI project website. Visibilità dei dati afferenti all'attività di esplorazione petrolifera in Italia (Visibility of data related to the hydrocarbon exploration in Italy). http://unmig.sviluppoeconomico.gov.it/videpi/pozzi/pozzi.asp. (3) The deep hydrocarbon well data are organized in the following database: Trumpy, E., Manzella, A., 2017. Geothopica and the interactive analysis and visualization of the updated Italian National Geothermal Database, International Journal of Applied Earth Observation and Geoinformation, 54, 28–37. 10.1016/j.jag.2016.09.004. Available at: http://geothopica.igg.cnr.it/. (4) Information on the pressure regimes in the Northern Adriatic Foredeep was obtained from Carlin, S., Dainelli, J., 1998. Pressure regimes and pressure systems in the Adriatic foredeep (Italy). In: Law, B.E., Ulmishek, G.F., Slavin, V.I. eds. Abnormal pressures in hydrocarbons environments. AAPG Memoir, 70, 145–160. (5) This work was carried out within the framework of the Geothermal Atlas of Southern Italy Project. Thematic maps produced in the frame of the Project are available at http://atlante.igg.cnr.it/index.php/prodotti/mappe.

Conflicts of Interest

The authors declare that there are no conflicts of interest regarding the publication of this paper.

Acknowledgments

This work was carried out within the framework of the Geothermal Atlas of Southern Italy Project, funded by the Italian National Research Council. The Project is aimed at verifying, locating, and generating an updated atlas of geothermal resources usable for the production of geothermal energy in the southern regions of Italy.

References

[1] Geothermal Atlas for Southern Italy Project website, "Progetto Atlante Geotermico del Mezzogiorno. CNR per il mezzogiorno," January 2018 http://atlante.igg.cnr.it/.

[2] R. H. Wallace Jr., T. F. Kraemer, R. E. Taylor, and J. B. Wesselman, "Assessment of geopressured-geothermal resources in the Northern Gulf of Mexico basin," in *Assessment of Geothermal Resources of the United States –1978*, United States Geological Survey Circular, L. J. P. Muffler, Ed., pp. 132–155, U.S. Geological Survey, 1979No. 790.

[3] R. G. Loucks, D. L. Richmann, and K. L. Millken, *Factors Controlling Reservoir Quality in Tertiary Sandstones and Their Significance to Geopressured Geothermal Production. Report of Investigation No. 111*, Bureau of Economic Geology, University of Texas, 1981.

[4] J. S. Griggs, "A re-evaluation of geopressured-geothermal aquifers as an energy resource," *Proceedings Thirtieth Workshop on Geothermal Reservoir Engineering, Stanford University*, 2005, Stanford, California, January–February 2005, 2005SGP-TR-176.

[5] DOE (United States Department of Energy), *Geothermal Energy Production with Co-produced and Geopressured Resources*, DOE/GO-102010-3004, 2010.

[6] M. Árpási, Á. Lorberer, and S. Pap, "High pressure and temperature (geopressured) geothermal reservoirs in Hungary," in *Proceedings of World Geothermal Congress 2000*, Kyushu - Tohoku (Japan), 2000.

[7] D. G. Bebout, B. R. Weise, A. R. Gregory, and M. B. Edwards, *Wilcox Sandstone Reservoirs in the Deep Subsurface along the Texas Gulf Coast: Their Potential for Production of Geopressured Geothermal Energy. Report of Investigation, No. 117*, Bureau of Economic Geology, 1982.

[8] C. Alimonti and A. A. Gnoni, "Harnessing the fluids heat to improve mature oil field: the Villafortuna–Trecate case study," *Journal of Petroleum Science and Engineering*, vol. 125, pp. 256–262, 2015.

[9] E. Trumpy, A. Donato, G. Gianelli et al., "Data integration and favourability maps for exploring geothermal systems in Sicily, Southern Italy," *Geothermics*, vol. 56, pp. 1–16, 2015.

[10] R. M. Prol-Ledesma, "Evaluation of the reconnaissance results in geothermal exploration using GIS," *Geothermics*, vol. 29, no. 1, pp. 83–103, 2000.

[11] M. F. Coolbaugh, J. V. Taranik, G. L. Raines et al., "A geothermal GIS for Nevada: defining regional controls and favorable exploration terrains for extensional geothermal systems," *Transactions-Geothermal Resources Council*, vol. 26, pp. 485–490, 2002.

[12] M. Coolbaugh, R. Zehner, C. Kreemer et al., *Geothermal Potential Map of the Great Basin, Western United States*, Nevada Bureau of Mines and Geology, 2005.

[13] Y. Noorollahi, R. Itoi, H. Fujii, and T. Tanaka, "GIS model for geothermal resource exploration in Akita and Iwate prefectures northern Japan," *Computational Geosciences*, vol. 33, no. 8, pp. 1008–1021, 2007.

[14] Y. Noorollahi, R. Itoi, H. Fujii, and T. Tanaka, "GIS integration model for geothermal exploration and well siting," *Geothermics*, vol. 37, no. 2, pp. 107–131, 2008.

[15] H. Yousefi, Y. Noorollahi, S. Ehara et al., "Developing the geothermal resources map of Iran," *Geothermics*, vol. 39, no. 2, pp. 140–151, 2010.

[16] N. Tufekci, M. Lutfi Suzen, and N. Gulec, "GIS based geothermal potential assessment: a case study from Western Anatolia, Turkey," *Energy*, vol. 35, no. 1, pp. 246–261, 2010.

[17] M. K. Moghaddam, Y. Noorollahi, F. Samadzadegan, M. A. Sharifi, and R. Itoi, "Spatial data analysis for exploration of regional scale geothermal resources," *Journal of Volcanology and Geothermal Research*, vol. 266, pp. 69–83, 2013.

[18] M. K. Moghaddam, F. Samadzadegan, Y. Noorollahi, M. A. Sharifi, and R. Itoi, "Spatial analysis and multi-criteria decision making for regional-scale geothermal favorability map," *Geothermics*, vol. 50, pp. 189–201, 2014.

[19] L. Mattavelli, L. Novelli, and L. Anelli, "Occurrence of hydrocarbons in the Adriatic basin," *Spec. Publ. EAPG (European Association of Petroleum Geoscientists)*, vol. 1, pp. 369–380, 1991.

[20] P. Casero and S. Bigi, "Structural setting of the Adriatic basin and the main related petroleum exploration plays," *Marine and Petroleum Geology*, vol. 42, pp. 135–147, 2013.

[21] F. Cazzini, O. D. Zotto, R. Fantoni, M. Ghielmi, P. Ronchi, and P. Scotti, "Oil and gas in the Adriatic foreland, Italy," *Journal of Petroleum Geology*, vol. 38, no. 3, pp. 255–279, 2015.

[22] C. E. Hottman, "Method for producing a source of energy from an overpressured formation," 1966, United States Patent Office 3258069.

[23] E. E. Hughes, "Gas/geothermal hybrid experiment," in *DOE/-GRI Industry Meeting March 4-5, 1986, Review of Geopressured-Geothermal and Co-production Research*, H. F. Coffer and R. W. Howell, Eds., Idaho National Engineering Laboratory (INEL), 1987.

[24] S. K. Garg, T. D. Riney, and R. H. Wallace Jr, "Brine and gas recovery from geopressured systems," *Geothermics*, vol. 15, no. 1, pp. 23–48, 1986.

[25] W. J. Bernard, "Reservoir mechanics of geopressured aquifers," in *Proceeding of the First Geopressured Geothermal Energy Conference*, Austin, Texas, 1975.

[26] S. D. S. R. Karamchetty, H. M. Liebowitz, and J. M. Oliver, "Geopressured-geothermal: a multi-energy resource," in *Proceedings of Fifth Conference Geopressured–Geothermal Energy*, U.S. Gulf Coast, October 1981.

[27] C. J. John, G. Maciasz, and B. J. Harder, *Gulf Coast Geopressured-Geothermal Program Summary Report Compilation, Volumes I-III. Work Performed under U.S*, Department of Energy, 1998, Contract No. DE-FG07-95ID13366.

[28] J. Negus de Wys and M. Dorfman, "The geopressured-geothermal resource: transition to commercialization," *Geothermal Resources Council Transactions*, vol. 14, no. 1, pp. 537–545, 1990.

[29] T. D. Riney, *Pleasant Bayou Geopressured-Geothermal Reservoir Analysis-January 1991. Topical Report, Performed for the Center for Energy Studies (University of Texas at Austin) Under U.S*, Department of Energy Cooperative, 1991, Agreement No.DE-FC07-85NV10412.

[30] P. A. Allen and J. R. Allen, *The Petroleum Play, in: Basin Analysis-Principles and Applications*, Blackwell Science Ltd., Oxford, UK, 2005.

[31] I. S. Moeck, "Catalog of geothermal play types based on geologic controls," *Renewable and Sustainable Energy Reviews*, vol. 37, pp. 867–882, 2014.

[32] A. Santilano, A. Manzella, G. Gianelli et al., "Convective, intrusive geothermal plays: what about tectonics?," *Geothermal Energy Science*, vol. 3, no. 1, pp. 51–59, 2015.

[33] D. M. Mann and A. S. Mackenzie, "Prediction of pore fluid pressures in sedimentary basins," *Marine and Petroleum Geology*, vol. 7, no. 1, pp. 55–65, 1990.

[34] N. Yassir, "Overpressuring in compressional stress regimes-causes and detection," *Overpressures in Petroleum Exploration: Workshop Proceedings: Elf Exploration Production Memoir*, vol. 22, 1999, pp. 13–18, Pau, France, April 1998.

[35] C. R. Lewis and S. C. Rose, "A theory relating high temperatures and overpressures," *Journal of Petroleum Technology*, vol. 22, no. 1, pp. 11–16, 1970.

[36] L. C. Price, C. W. Blount, D. Mac Gowan, and L. Wenger, "Methane Solubility in Brines with Application to the Geopressured Resource," in *Proceedings Fifth Conference Geopressured-Geothermal energy*, April 1981Baton Rouge, Louisiana.

[37] A. Santilano, A. Donato, A. Galgaro et al., "An integrated 3D approach to assess the geothermal heat-exchange potential: the case study of western Sicily (southern Italy)," *Renewable Energy*, vol. 97, pp. 611–624, 2016.

[38] M. Kiavarz and M. Jelokhani-Niaraki, "Geothermal prospectivity mapping using GIS-based Ordered Weighted Averaging approach: a case study in Japan's Akita and Iwate provinces," *Geothermics*, vol. 70, pp. 295–304, 2017.

[39] G. F. Bonham-Carter, *Geographical Information Systems for Geoscientists: Modelling with GIS. Computer Methods in the Geosciences*, vol. 13, Pergamon, Pergamon, New York, 1994.

[40] Quantum GIS Website, "Quantum GIS geographic information system. Open Source Geospatial Foundation Project," December 2017 http://qgis.osgeo.org.

[41] C. Augustine, J. W. Tester, B. Anderson, S. Petty, and B. Livesay, "A comparison of geothermal with Oil and Gas well drilling costs," *7th Proceedings, Thirty-First Workshop on Geothermal Reservoir Engineering, Stanford University*, 2006, Stanford, California, January–February 2006, 2006SGP-TR-179.

[42] IFC, *Success of Geothermal Wells: a Global Study. Report by International Finance Corporation*, International Finance Corporation (World Bank Group), Washington (USA), 2013.

[43] D. Cosentino, P. Cipollari, P. Marsili, and D. Scrocca, "Geology of the central Apennines: a regional review," *Journal of the Virtual Explorer*, vol. 36, 2010.

[44] A. W. Bally, L. Burbi, C. Cooper, and R. Ghelardoni, "Balanced sections and seismic reflection profiles across the Central Apennines," *Memorie della Societa Geologica Italiana*, vol. 35, pp. 237–310, 1986.

[45] E. Patacca, P. Scandone, M. Bellatalla, N. Perilli, and U. Santini, "La zona di giunzione tra l'arco appenninico settentrionale e l'arco appenninico meridionale nell'Abruzzo e nel Molise," *Studi Geologici Camerti*, vol. Spec. 1991-2, pp. 417–441, 1991.

[46] V. Scisciani and R. Montefalcone, "Evoluzione neogenico-quaternaria del fronte della catena centro-appenninica: vincoli dal bilanciamento sequenziale di una sezione geologica regionale," *Bollettino della Società Geologica Italiana*, vol. 124, pp. 579–599, 2005.

[47] D. Scrocca, "Thrust front segmentation induced by differential slab retreat in the Apennines (Italy)," *Terra Nova*, vol. 18, no. 2, pp. 154–161, 2006.

[48] E. Patacca and P. Scandone, "Geology of the southern Apennines," *Bollettino della Società Geologica Italiana*, vol. 7, Spec. Issue, pp. 75–119, 2007.

[49] R. Fantoni and R. Franciosi, "Tectono-sedimentary setting of the Po Plain and Adriatic foreland," *Rendiconti Lincei*, vol. 21, Supplement 1, pp. 197–209, 2010.

[50] L. Vezzani, A. Festa, and F. Ghisetti, "Geology and tectonic evolution of the Central-Southern Apennines, Italy," p. 469, 2010, GSA Special Papers.

[51] A. Artoni, "The Pliocene-Pleistocene stratigraphic and tectonic evolution of the central sector of the Western Periadriatic Basin of Italy," *Marine and Petroleum Geology*, vol. 42, pp. 82–106, 2013.

[52] S. Bigi, A. Conti, P. Casero, L. Ruggiero, R. Recanati, and L. Lipparini, "Geological model of the central Periadriatic basin (Apennines, Italy)," *Marine and Petroleum Geology*, vol. 42, pp. 107–121, 2013.

[53] G. Lavecchia, F. Brozzetti, M. Barchi, M. Menichetti, and J. V. A. Keller, "Seismotectonic zoning in east-central Italy deduced from an analysis of the Neogene to present deformations and related stress fields," *GSA Bulletin*, vol. 106, no. 9, pp. 1107–1120, 1994.

[54] R. W. H. Butler, S. Mazzoli, S. Corrado et al., "Applying thick-skinned tectonic models to the Apennine thrust belt of Italy–limitations and implications," *Thrust Tectonics and Hydrocarbon Systems*, K. R. McClay, Ed., vol. 82, pp. 647–667, AAPG Memoir, 2004.

[55] E. Patacca, P. Scandone, E. di Luzio, G. P. Cavinato, and M. Parotto, "Structural architecture of the central Apennines: interpretation of the CROP 11 seismic profile from the Adriatic coast to the orographic divide," *Tectonics*, vol. 27, no. 3, 2008.

[56] G. Lavecchia, G. Minelli, and G. Pialli, "The Umbria-Marche arcuate fold belt (Italy)," *Tectonophysics*, vol. 146, no. 1–4, pp. 125–137, 1988.

[57] E. Patacca and P. Scandone, "The Plio-Pleistocene thrust belt-foredeep system in the southern Apennines and Sicily (Italy)," in *Special volume of the Italian geological society for the 32 th IGC*, Florence, 2004.

[58] M. A. Romano, R. De Nardis, M. Garbin et al., "Temporary seismic monitoring of the sulmona area (Abruzzo, Italy): a quality study of microearthquake locations," *Natural Hazards and Earth System Sciences*, vol. 13, no. 11, pp. 2727–2744, 2013.

[59] G. Lavecchia, G. M. Adinolfi, R. de Nardis et al., "Multidisciplinary inferences on a newly recognized active east-dipping extensional system in Central Italy," *Terra Nova*, vol. 29, no. 1, pp. 77–89, 2017.

[60] U. Crescenti, C. D'amato, A. Balduzzi, and M. Tonna, "Il Plio-Pleistocene del sottosuolo abruzzese-marchigiano tra Ascoli Piceno e Pescara," *Geologica Romana*, vol. 19, pp. 63–84, 1980.

[61] R. Casnedi, "L'avanfossa abruzzese fra i fiumi Vomano e Pescara nel Pliocene inferiore: rapporti tra sedimentazione e tettonica," *Studi Geologici Camerti*, vol. Spec. 2, pp. 375–379, 1991.

[62] G. G. Ori, G. Serafini, C. Visentin et al., "The Pliocene-Pleistocene Adriatic Foredeep (Marche and Abruzzo,

Italy): an integrated approach to surface and subsurface geology," *3rd EAPG Conference, Adriatic Foredeep Field Trip Guide Book*, pp. 26–30, EAPG and AGIP, Florence, Italy, 1991.

[63] U. Crescenti, M. L. Milia, and G. Rusciadelli, "Stratigraphic and tectonic evolution of the Pliocene Abruzzi basin (Central Apennines, Italy)," *Bollettino della Società Geologica Italiana*, vol. 123, no. 2, pp. 163–173, 2004.

[64] F. Brozzetti, "Tectono-Stratigraphic review of the outer sector of the north Abruzzi Apennines: new data from the 339-Teramo sheet of the Carta Geologica d'Italia (CARG Project)," *Rendiconti Online Societa Geologica Italiana*, vol. 12, Supplement, pp. 9–12, 2011.

[65] G. Lavecchia, P. Boncio, and N. Creati, "A lithospheric-scale seismogenic thrust in central Italy," *Journal of Geodynamics*, vol. 36, no. 1-2, pp. 79–94, 2003.

[66] G. Lavecchia, R. De Nardis, F. Visini, F. Ferrarini, and M. S. Barbano, "Seismogenic evidence of ongoing compression in eastern-central Italy and mainland Sicily: a comparison," *Bollettino della Società Geologica Italiana*, vol. 126, no. 2, pp. 209–222, 2007.

[67] F. Visini, R. de Nardis, and G. Lavecchia, "Rates of active compressional deformation in central Italy and Sicily: evaluation of the seismic budget," *International Journal of Earth Sciences*, vol. 99, Supplement 1, pp. 243–264, 2010.

[68] ISPRA, *Note illustrative della Carta Geologica d'Italia alla scala 1:50.000, foglio 339 Teramo*, Istituto Superiore per la Protezione e la Ricerca Ambientale, 2017, http://www.isprambiente.gov.it/Media/carg/note_illustrative/339_Teramo.pdf.

[69] R. Casnedi, "Hydrocarbon-bearing submarine fan system of Cellino Formation, Central Italy," *AAPG Bulletin*, vol. 67, no. 3, pp. 359–370, 1983.

[70] C. Nicolai and R. Gambini, "Structural architecture of the Adria platform-and-basin system," *Bollettino della Società Geologica Italiana*, vol. 7, pp. 21–37, 2007.

[71] B. Della Vedova, S. Bellani, G. Pellis, and P. Squarci, "Deep temperatures and surface heat flow distribution," in *Anatomy of an Orogen*, G. B. Vai and I. P. Martini, Eds., pp. 65–76, The Apennines and Adjacent Mediterranean Basins. Kluwer Ac. Publ, Great Britain, 2000.

[72] R. Cataldi, F. Mongelli, P. Squarci, L. Taffi, G. Zito, and C. Calore, "Geothermal ranking of Italian territory," *Geothermics*, vol. 24, no. 1, pp. 115–129, 1995.

[73] E. Trumpy and A. Manzella, "Geothopica and the interactive analysis and visualization of the updated Italian National Geothermal Database," *International Journal of Applied Earth Observation and Geoinformation*, vol. 54, pp. 28–37, 2017.

[74] ViDEPI project website, "Visibilità dei dati afferenti all'attività di esplorazione petrolifera in Italia (Visibility of data related to the hydrocarbon exploration in Italy)," May 2017 http://unmig.sviluppoeconomico.gov.it/videpi/pozzi/pozzi.asp.

[75] L. Vezzani and F. Ghisetti, *Carta Geologica dell'Abruzzo, 1:100000*, SELCA, Firenze, 1998.

[76] CNR, "Progetto Finanziato Geodinamica: structural model of Italy 1:500.000 and gravity map, sheet n. 1–6," in *Quad. Ric. Sci.*, vol. 114, S.EL.CA., Firenze, Italy, 1990.

[77] A. Argnani, P. Favali, F. Frugoni et al., "Foreland deformational pattern in the Southern Adriatic Sea," *Annals of Geophysics*, vol. 36, no. 2, pp. 229–247, 1993.

[78] M. Santantonio, D. Scrocca, and L. Lipparini, "The Ombrina-Rospo Plateau (Apulian Platform): evolution of a carbonate platform and its margins during the Jurassic and Cretaceous," *Marine and Petroleum Geology*, vol. 42, pp. 4–29, 2013.

[79] S. Carlin and J. Dainelli, "Pressure regimes and pressure systems in the Adriatic foredeep (Italy)," in *Abnormal Pressures in Hydrocarbons Environments*, B. E. Law, G. F. Ulmishek, and V. I. Slavin, Eds., vol. 70 of AAPG Memoir, , pp. 145–160, AAPG, 1998.

[80] J. D. Walker, J. W. Geissman, S. A. Bowring, and L. E. Babcock, "Geologic time scale v. 4.0," Geological Society of America, 2012.

[81] V. Pasquale, P. Chiozzi, G. Gola, and M. Verdoya, "Depth--time correction of petroleum bottom-hole temperatures in the Po Plain, Italy," *Geophysics*, vol. 73, no. 6, pp. E187–E196, 2008.

[82] G. Gola, A. Manzella, E. Trumpy, D. Montanari, and J. D. Van Wees, "Deep-seated geothermal resource assessment of the VIGOR project regions, Italy," in *Proceedings of the European geothermal congress 2013*, Pisa, Italy, June 2013.

[83] R. Castaldo, G. Gola, A. Santilano et al., "The role of thermo-rheological properties of the crust beneath Ischia Island (Southern Italy) in the modulation of the ground deformation pattern," *Journal of Volcanology and Geothermal Research*, vol. 344, pp. 154–173, 2017.

[84] D. Montanari, A. Minissale, M. Doveri et al., "Geothermal resources within carbonate reservoirs in western Sicily (Italy): a review," *Earth-Science Reviews*, vol. 169, pp. 180–201, 2017.

[85] V. Pasquale, G. Gola, P. Chiozzi, and M. Verdoya, "Thermophysical properties of the Po Basin rocks," *Geophysical Journal International*, vol. 186, no. 1, pp. 69–81, 2011.

[86] A. Minissale, W. C. Evans, G. Magro, and O. Vaselli, "Multiple source components in gas manifestations from north-central Italy," *Chemical Geology*, vol. 142, no. 3-4, pp. 175–192, 1997.

[87] A. Minissale, G. Magro, G. Martinelli, O. Vaselli, and G. F. Tassi, "Fluid geochemical transect in the Northern Apennines (central-northern Italy): fluid genesis and migration and tectonic implications," *Tectonophysics*, vol. 319, no. 3, pp. 199–222, 2000.

[88] L. Mattavelli and L. Novelli, "Geochemistry and habitat of natural gases in Italy," *Advances in Organic Geochemistry*, vol. 13, no. 1-3, pp. 1–13, 1988.

[89] A. Giorgetti, "Climatological analysis of the Adriatic Sea thermohaline characteristic," *Bollettino Di Geofisica Teorica Ed Applicata*, vol. 40, pp. 53–73, 1999.

[90] I. I. Mokhov and M. G. Akperov, "Tropospheric lapse rate and its relation to surface temperature from reanalysis data," *Izvestiya, Atmospheric and Oceanic Physics*, vol. 42, no. 4, pp. 430–438, 2006.

[91] R. Fortuna and A. Jelacic, "The geopressured-geothermal research program: an overview," in *Proceeding of the natural gas R & D contractors review meeting*, Morgantown WV, April 1989.

[92] ISPRA, *Geological Maps of Italy, Scale 1:100.000 (Sheets 133, 134, 140, 141, 146, 147,148, 152, 153, 154)*, Istituto Superiore per la Protezione e la Ricerca Ambientale, 2017, http://193.206.192.231/carta_geologica_italia/default.htm.

[93] ISPRA, *Geological Maps of Italy, Scale 1:50.000, Sheet 339*, Istituto Superiore per la Protezione e la Ricerca Ambientale, 2017, http://www.isprambiente.gov.it/Media/carg/339_TERAMO/Foglio.html.

[94] P. Montone and M. T. Mariucci, "The new release of the Italian contemporary stress map," *Geophysical Journal International*, vol. 205, no. 3, pp. 1525–1531, 2016.

[95] INGV Catalogs and databases website, February 2018 http://istituto.ingv.it/it/archivi-e-banche-dati.

[96] A. Frepoli and A. Amato, "Contemporaneous extension and compression in the Northern Apennines from earthquake faultplane solutions," *Geophysical Journal International*, vol. 129, no. 2, pp. 368–388, 1997.

[97] UNMIG Website, *Ufficio nazionale minerario per gli idrocarburi e le georisorse (National Mining Office for hydrocarbons and Georesources)*, Italian Ministry of Economic Development, May 2017 http://unmig.mise.gov.it/.

Hindawi
Geofluids
Volume 2019, Article ID 8161469, 20 pages
https://doi.org/10.1155/2019/8161469

Research Article

Fluid Circulations at Structural Intersections through the Toro-Bunyoro Fault System (Albertine Rift, Uganda): A Multidisciplinary Study of a Composite Hydrogeological System

Bastien Walter,[1] **Yves Géraud**,[1] **Yann Hautevelle**,[1] **Marc Diraison**,[1] **and François Raisson**[2]

[1]*GeoRessources, UMR 7359, Université de Lorraine, CNRS, CREGU, ENSG Campus Brabois, 2 Rue du Doyen Roubault, BP10162, F-54505 Vandoeuvre les Nancy, France*
[2]*Total CSTJF, Avenue Larribau, F-64016 Pau Cedex, France*

Correspondence should be addressed to Bastien Walter; bastien.walter@univ-lorraine.fr

Received 8 May 2018; Revised 22 September 2018; Accepted 28 October 2018; Published 27 February 2019

Academic Editor: Domenico Montanari

Regional fault structures along rift basins play a crucial role in focusing fluid circulation in the upper crust. The major Toro-Bunyoro fault system, bounding to the east of the Albertine Rift in western Uganda, hosts local fluid outflow zones within the faulted basement rocks, one of which is the Kibiro geothermal prospect. This major fault system represents a reliable example to investigate the hydrogeological properties of such regional faults, including the local structural setting of the fluid outflow zones. This study investigated five sites, where current (i.e., geothermal springs, hydrocarbon seeps) and fossil (i.e., carbonate veins) fluid circulation is recognized. This work used a multidisciplinary approach (structural interpretation of remote sensing images, field work, and geochemistry) to determine the role of the different macroscale structural features that may control each studied fluid outflow zones, as well as the nature and the source of the different fluids. The local macroscale structural setting of each of these sites systematically corresponds to the intersection between the main Toro-Bunyoro fault system and subsidiary oblique structures. Inputs from three types of fluid reservoirs are recognized within this fault-hosted hydrogeological system, with "external basin fluids" (i.e., meteoric waters), "internal basin fluids" (i.e., hydrocarbons and sediment formation waters), and deep-seated crustal fluids. This study therefore documents the complexity of a composite hydrogeological system hosted by a major rift-bounding fault system. Structural intersections act as local relative permeable areas, in which significant economic amounts of fluids preferentially converge and show surface manifestations. The rift-bounding Toro-Bunyoro fault system represents a discontinuous barrier for fluids where intersections with subsidiary oblique structures control preferential outflow zones and channel fluid transfers from the rift shoulder to the basin, and vice versa. Finally, this work contributes to the recognition of structural intersections as prime targets for exploration of fault-controlled geothermal systems.

1. Introduction

Large varieties of potentially geothermal systems are nowadays recognized, depending on their geological, hydrogeological, and heat source and transfer characteristics (e.g. [1–7]). Current technology development thus broadens the geothermal play types that can be operated, especially in intracratonic area [8]. In order to catalog the geological controls on geothermal resources, Moeck [9] proposed a new geologically based classification, involving both magmatic vs. nonmagmatic and convective vs. conductive dominated geothermal systems. Classification of the different geothermal play types can therefore significantly help in the choice of exploration methods and heat and power production techniques subsequently.

Among the different geothermal play types defined by Moeck [9], geothermal systems are broadly prospected especially in "extensional domain play type (CV3)." This geothermal play type consists in nonmagmatic convection-dominated domains, where active faulting represents pathways for fluid flow and is responsible for regional high heat flow associated to crustal tectonic thinning (e.g., [10, 11]). This geothermal play type represents a significant part of the worldwide geothermal potential, with many prime examples (e.g., Eastern African Rift System (EARS), European Cenozoic Rift System, and Great Basin Region in USA) (e.g., [12–14]). These fault-controlled plays necessitate a particularly good understanding of the hydrogeological behavior of the structural features and the identification of favorable structural settings. Such identification is critical for extensional basins where geothermal resources may have little or no surface manifestations [15–17]. On the basis of surface geothermal emission locations relative to recurring fault patterns, several authors proposed a general catalog and a ranking of the most favorable structural settings for geothermal activity (e.g., [18–21]). This cataloging approach aims at defining exploration guides for potential evaluation of known resources and discovery of unknown subsurface systems. Despite this, development of geothermal systems needs determination where fluid migration specifically occurs in fault-controlled plays. Unfortunately, examples of field geothermal exploration of fault-controlled systems are poorly represented.

The western branch of the EARS (western Uganda), along which several significant geothermal surface manifestations are now investigated (e.g., Kibiro, Buranga, and Katwe) [22] is an ideal place to study a fault-controlled geothermal play and to develop a play-type-specific field reconnaissance as part of the early stage exploration. This study was carried out along the Lake Albert eastern shore near the Kibiro main hydrothermal site (Figure 1). Several current and fossil fluid circulation zones were identified within the faulted basement rocks of the rift. This work used a multidisciplinary approach (structural geology, geochemistry, and petrology) to investigate (1) the local structural setting of each studied fluid outflow zones and (2) the nature and the source of these fluids. Field work and detailed analyses of fluid circulation features sampled within fractures and breccias of fault rocks, including hydrocarbon materials and carbonate veins, were performed. As the Kibiro geothermal prospect has been already studied, literature data from this site was also synthetized and integrated here. This study contributes to the recognition of generic favorable structural settings of fault-controlled geothermal prospects. Finally, this work also provides new datasets from a scarcely documented area, where fault-controlled fluid recharge and discharge are poorly understood, and provides insights on the hydrogeological behavior of this regional-scale fault system.

2. Geological Setting

In western Uganda, the Albertine Rift System (ARS) forms the northernmost segment of the western branch of the EARS. It extends from the Virunga volcanic province and the Lake Edward in the south to the northern end of Lake Albert within Precambrian magmatic and metamorphic basement rocks. The ARS development was controlled by the regional Precambrian NE-trending structural inheritance and rock fabric [12, 23, 24]. This complex graben system is made up of a series of intracontinental normal fault-bounded basins, each of about ~60–100 km in length and several km in depth, and segmented by transfer faults [25]. The ARS is one of the major hydrocarbon and hydrothermal prospective regions of Eastern Africa, representing an exploration area over 400 km in length and of about 60 km in average width (e.g., [22, 26, 27]).

The Lake Albert basin shows the unique configuration in the western branch of the EARS of a full-graben, bounded by two major antithetic NE-trending fault systems [28]. The eastern flank of this basin is bounded by the Toro-Bunyoro fault system (TBFS) (Figure 1). This fault system was developed through Precambrian basement rocks mainly consisting in different granitoid rock units [29, 30]. Different high-grade banded metamorphic gneisses to granulitic gneisses with variable compositions (granite, tonalite-trondhjemite-granodiorite suite) are recognized in this area. The felsic granulite of the Karuma Complex was dated around 2991 ± 9 Ma [30], while similar TTG gneiss found further south in the foothills of the Rwenzori Mountains were dated by U-Pb age determinations of zircon cores at 2584 ± 18 Ma, 2637 ± 16 Ma, and 2611 ± 14 Ma [31]. The major TBFS is mainly composed of two ~100 km long steeply NW-dipping NE-trending faults connected by the ENE-trending Kaiso transfer structure (Figure 1). The surface expression of this fault system corresponds to subcontinuous 300–400 m high escarpment bordering the lake. Along the fault scarp, only the footwall can be reached and studied thanks to several sedimentary platforms emerging from the lake, notably along the main Kaiso-Tonya (KT) platform, whereas the hanging wall is systematically hidden in the basin.

3. Analytical Methods

Detailed structural and microstructural analysis was carried out for each of the selected working sites. Interpretation of satellite images was correlated with field observations to determine the main structural features of each investigated site. Representative deformed basement rock samples, as well as mineralized veins and hydrocarbon fracture fillings, were collected at the different outcrops in order to describe the deformation state and the fluid migration along the TBFS.

Optical and cathodoluminescence (CL) microscopy observations were used to describe the carbonate grains within the mineralized veins. The CL observations were conducted with vacuum of 50 mTorr, a voltage of 12 kV, and current of 0.2 μA. Fluid inclusion (FI) analyses were conducted on doubly polished sections (200–300 μm thick). Microthermometry was explored using a Linkam MSD600 heating-freezing stage, adapted to an Olympus microscope. Analyses were calibrated with melting-point standards at $T > 25^{\circ}$C and natural and synthetic fluid inclusion standards at $T < 0^{\circ}$C. Heating rate was software-monitored to obtain a $\pm 1^{\circ}$C accuracy. Homogenization temperature (T_{h}) of the FI was measured during heating stages. However, due to their small size, results of the low-temperature microthermometry analyses (freezing stage) were not clearly interpretable. Additionally, in situ SIMS oxygen and carbon isotopic

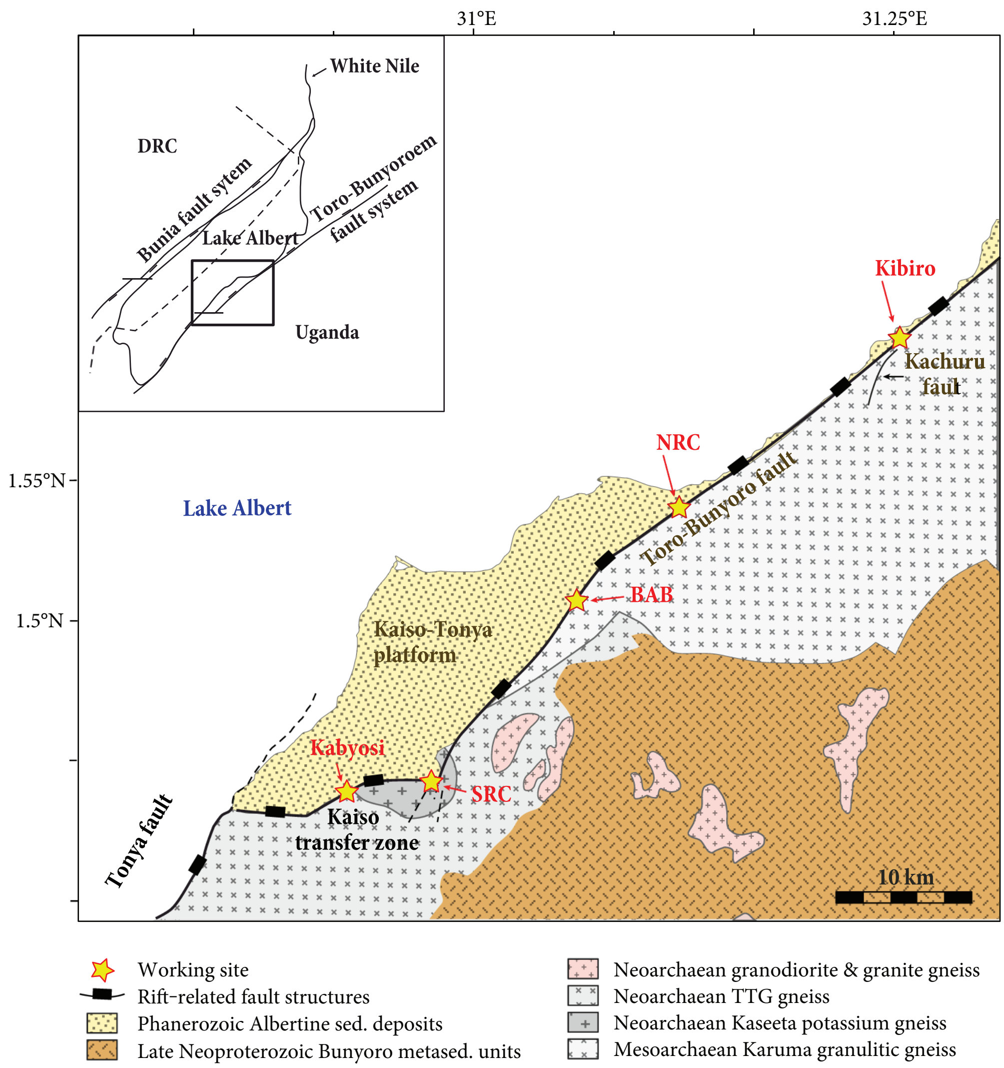

Figure 1: Geological map of the study area and location of the working sites (modified from [29]).

analyses were carried out on carbonate grains from different mineralized veins using a CAMECA IMS 1270 (Cs^+ source) at the CRPG-CNRS laboratory (Nancy, France) following the analytical methods described by Rollion-Bard et al. [32]. Results are expressed using the usual δ notation (‰), with $\delta^{13}C$ and $\delta^{18}O$ values, respectively, relative to the Pee Dee Belemnite (PDB) marine carbonate and Standard Mean Ocean Water (SMOW) reference materials.

Organic geochemistry analyses were performed at the GeoRessources Laboratory (University of Lorraine, France). Asphalt samples were dissolved in dichloromethane in order to recover its soluble fraction. An aliquot of each organic extracts was then diluted into 100 ml of pentane under heating (55°C) and stirring in order to precipitate asphaltene compounds. Asphaltenes were then removed by filtration. The nonasphaltenic fractions (maltenes) were recovered and then fractionated in order to get 3 separate fractions, namely, aliphatic (nonaromatic hydrocarbons), aromatic (aromatic hydrocarbons), and the polar (compounds bearing heteroatoms) fractions. Fractionations were carried out using a Gilson ASPEC instrument and Strata SPE CN cartridges filled up with 1 g of silica gel. The solvents used to recover each fraction were hexane, dichloromethane, and finally a dichloromethane/methanol mixture. These three fractions were analyzed by gas chromatography coupled to mass spectrometry (GC-MS) in order to determine their molecular composition. The GC-MS was a Shimadzu GCMS-QP2010 Plus with a 60 m J&W DB-5 capillary column. The MS operated in the electron impact mode (EI) at 70 eV ionization energy, and mass spectra were scanned from 50 to 500 Da using a quadrupole detector.

4. Geological Characterization of the Studied Sites

This work investigated 5 sites located along the TBFS, where current and fossil fluid migrations were recognized within the faulted basement footwall (Figure 1, Table 1). In order to investigate the role of the different macroscale structural features that may control these fluid circulation zones, a large-scale high-resolution remote sensing digital elevation model (DEM) of the area was used to describe the nearby

Table 1: Working site location and associated fluid circulation marker type.

Site	GPS coordinates	Fluid circulation markers
Kibiro	N1.6737; E31.2557	Current hydrothermal and hydrocarbon seepages
NRC	N1.5650; E31.1175	Fossil hydrothermal veins
Babouns	N1.5095; E31.0572	Fossil hydrothermal veins
SRC	N1.4020; E30.9694	Fossil hydrothermal veins
Kabyosi	N1.3971; E30.9240	Current hydrocarbon seepages

structural lineaments and is presented below. In the field, all these sites were found at the foot of the 300–400 m high fault escarpment where heavily fractured or cataclastic basement rocks were observed. For each of these sites, local aerial images and field observations of the various structural and fluid circulation features are also described thereafter. In comparison to the other working sites of this study, the Kibiro area is the only one where previous geophysical and geochemical studies were published. These data are synthetized and used to build conceptual geological model.

4.1. DEM Structural Analysis of the TBFS Footwall. A large-scale structural study of the TBFS footwall along the KT platform based on manual picking of lineaments from DEM interpretation in geographic information system (GIS) was carried out (Figure 2). Lineament picking and statistical analysis of fracturing of the TBFS footwall was limited landward to a ~5 km wide band from the main fault scarp. High-resolution picking of structural lineaments was performed on a LIDAR 1 m composite DEM image at a sampling scale of 1/50000. In this study, a lineament was considered to be a linear element with a unique length and direction. In order to focus this analysis on the structural features of the TBFS footwall, the main trace of the TBFS (in orange in Figure 2) was not taken into account into the following statistical analysis. 255 lineaments were picked on the analyzed surface. Lineament orientations are represented in a length-weighted rose diagram in Figure 2.

The DEM structural analysis reveals two main NNW- and NNE-striking lineament sets, many of which intersect the main TBFS especially nearby the 5 working sites (Figure 2). A secondary ENE-striking set is also observed, corresponding to lineaments mostly developed along the ENE-trending Kaiso transfer structure. A minor ESE-striking lineament set is additionally recognized in this area. A dense network of oblique structural features therefore affects the TBFS footwall, with a large number of lineaments intersecting the main fault scarp.

4.2. The Kibiro Site. The Kibiro site is located ~20 km northeast of the KT platform, situated on a fan delta of about 0.5×1.5 km along the NE-trending TBFS scarp (Figure 1). With several active hot springs, Kibiro is the main area where thermal fluid discharges occur along Lake Albert. Over the few past decades, several studies were undertaken on this potential geothermal field and various geological, geophysical, and geochemical results were published [22, 33]. The Kibiro active hydrothermal manifestations consist in a main hot spring area called Mukabiga with a few meter large hot water pool directly located at the base of the fault scarp and the two Mwibanda and Muntere salt gardens associated with hot springs located over ~100 m from the scarp through the sedimentary platform (Figure 3(a)). On the lower slopes of the scarp, at about 500 m SW from the Mukabiga springs, several heavily fractured and brecciated basement outcrops show sulfur-related minerals precipitated in cracks. No rising steam was observed but strong smell and fresh sulfur deposits suggested active H_2S (hydrogen sulphide) leakage. Fillings of biodegraded organic material (asphalt) were also observed and sampled from some of these fractures in order to be analyzed for this study.

The main Mukabiga hot springs are located in the axis of a fault-controlled NNW-trending river incision, which intersects the major NE-trending TBFS scarp (Figure 3(a)). Mawejje et al. [34] presented a mapping study of the active and fossil fluid surface manifestations (e.g., hot springs, gas fumaroles, calcite veins and travertines, and silica veins) within an area of ~10 km around the main Kibiro hot springs. According to this study, fluid flow manifestations along the scarp are more pronounced at intersections with other secondary faults, especially where the fault density is higher. Electric, gravity, and magnetic geophysical surveys undertaken in this area showed that the subsurface geothermal resource can be identified landward along the traces of oblique fault lineaments recognized in the rift shoulder [35].

Several geochemical studies of the hot springs and the surrounding area of the Kibiro geothermal prospect presented different results, consisting in geochemical analyses of rock and water samples, stable isotope ratios, spring flow and gas content measurements, and geothermometry modeling. Water samples from all the hot springs of the three main areas (Mukabiga, Mwibanda, and Muntere, Figure 3(a)) have similar geochemical features. These waters are characterized by neutral pH, Na-Cl-dominated salinity up to 4–5 $g{\cdot}kg^{-1}$ total dissolved solids, and a gas content dominated by methane [33, 36]. At the main Mukabiga area directly located at the base of the main fault scarp, the flow rate is about $4\,l{\cdot}s^{-1}$ and the temperature ranges between 57 and 86°C. At Mwibanda and Muntere, located over ca. 100 m from the scarp, flow rates and temperature are about $2.5\,l{\cdot}s^{-1}$ and undocumented and are from 33 to 72°C and up to 45°C, respectively [33, 37]. Stable isotope compositions of water samples indicate that meteoric water contributes as a major component of the Kibiro hot spring recharge. δ^2H data suggest that this meteoric water is originating from a higher elevation point, which can be represented by the high ground of the Mukhihani-Waisembe Ridge located 20 km southeast of Kibiro. On the other hand, the quite different lake and hot spring water d^2H signatures indicate low interaction between both reservoirs during hydrothermal activities [22]. The isotope composition of sulfur and oxygen in sulfates ($\delta^{34}S_{(SO4)}$, $\delta^{18}O_{(SO4)}$) suggest an interaction with crustal materials related to the water-rock interaction highlighted by the strontium isotopes ($^{87/86}Sr_{H2O}$, $^{87/86}Sr_{Rock}$) of the groundwater and the granitic gneiss basement of this area [22]. Using different isotope- or chemical-based geothermometers and

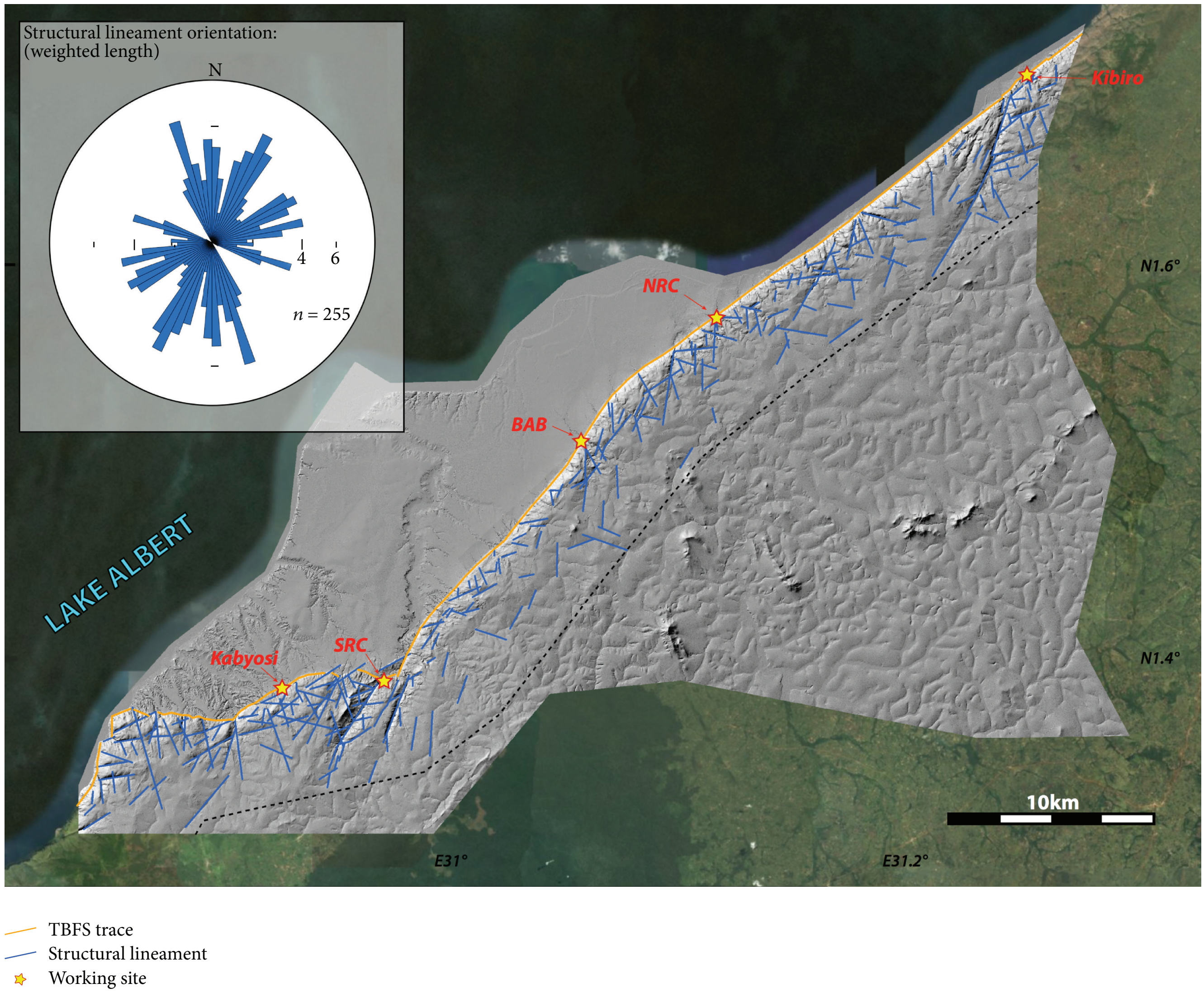

FIGURE 2: Structural analysis of the TBFS basement footwall on a LIDAR 1 m composite DEM image of the Kaiso-Tonya area.

chemical mixing models (e.g., SiO_2-CO_2), several authors suggest that the Kibiro reservoir has a first subsurface equilibrium temperature of about 200°C. The geothermal fluids have mixed with cold groundwater, producing a second subsurface equilibrium at about 150°C [22, 38, 39]. In conjunction to the geological information, these geochemistry analyses finally suggest that the Kibiro hot springs are most likely associated with an active ~150°C fault-hosted upflow with no direct magmatic heating [33].

4.3. The "North Roadcut" Site. The site called the "North Roadcut" (NRC) is located at the northern end of the KT platform (Figure 1). This winding road cuts the basement footwall of the NE-trending TBFS scarp and exposes the various fractured basement rocks along outcrops up to ~10 m high over a lateral distance of about 200 m (Figure 3(b), Figures 4(a) and 4(b)). Nearby the NRC, N-trending structural lineaments can be recognized with satellite images intersecting the TBFS (Figures 2 and 3(b)). On the field, massive unlithified fault gouge is identified along the northwesternmost part of the NRC, where the major fault structure can be traced, whereas basement with varying densities of fracturing (~10–50 frac·m^{-1}) can be observed further from the base of the scarp. Significant petrographic variations are also observed along this roadcut with ortho- and paraderived gneiss, mica schist, and mafic dykes (Figure 4(b)). Rock samples taken at this site generally contain a complex set of cross-cutting mineralized fractures filled with calcite. The aspect of some of the thicker veins (up to 1–1.5 mm thick) with host-rock microbreccia suggests hydraulic fracturing without kinematic markers. Undeformed millimeter-thick K-feldspar veins are also identified in the various basement rocks of this site (Figures 4(c) and 5(a)). These veins clearly predate the calcite veins observed here.

4.4. The "Baboons" Site. The "Baboons" (BAB) site is located near the central part of the KT platform, where a major incision river cuts the NE-trending TBFS scarp (Figure 1). The

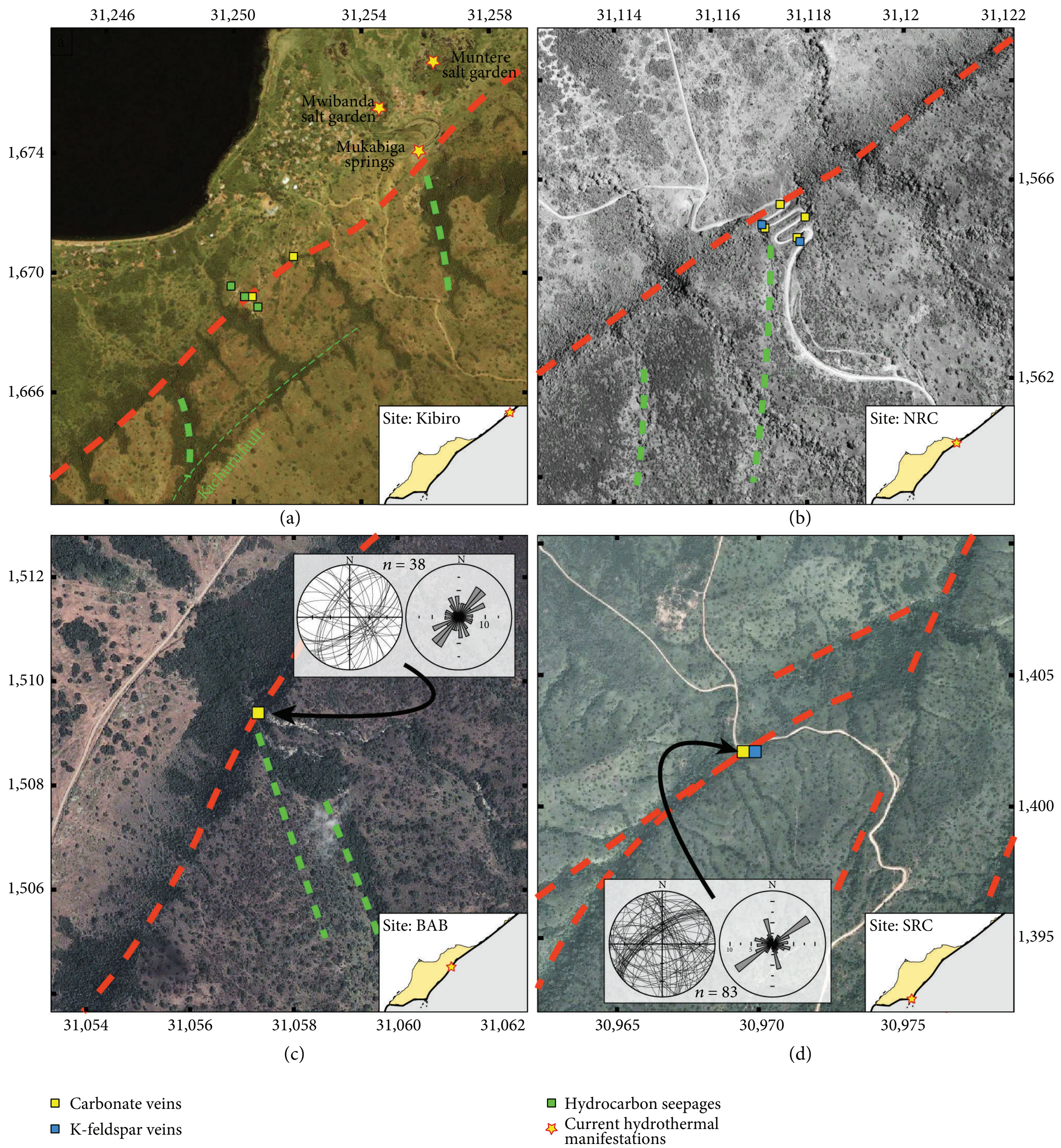

Figure 3: Location maps of the different fluid circulation manifestations identified at the sites (a) Kibirio, (b) NRC, (c) BAB, and (d) SRC. Red dotted lines represent the trace of the TBFS. Stereographic projections (lower hemisphere) and rose diagrams represent carbonate vein orientation measured at sites BAB and SRC, respectively.

last part of this river before flowing down the scarp is controlled by a significant NNW-trending structural lineament intersecting the major rift-bounding normal fault (Figures 3(c) and 4(d)). At the base of the steep fault scarp, the faulted basement appears as rather homogeneous dark grey rocks, with no apparent rock fabric, and consists in cohesive cataclastic rocks (Figure 4(e)). Microstructural observations show that these rocks are composed of a dark micrometric-sized matrix and isolated subangular 10–500 μm fragments of quartz, plagioclase, K-feldspar, and other accessory minerals (Figures 6(a) and 6(b)). Many opaque ultracataclastic bands a few tens of μm thick are also observed. A complex network of fractures and carbonate veins crosscuts these cataclastic rocks (Figure 4(e)). Calcite

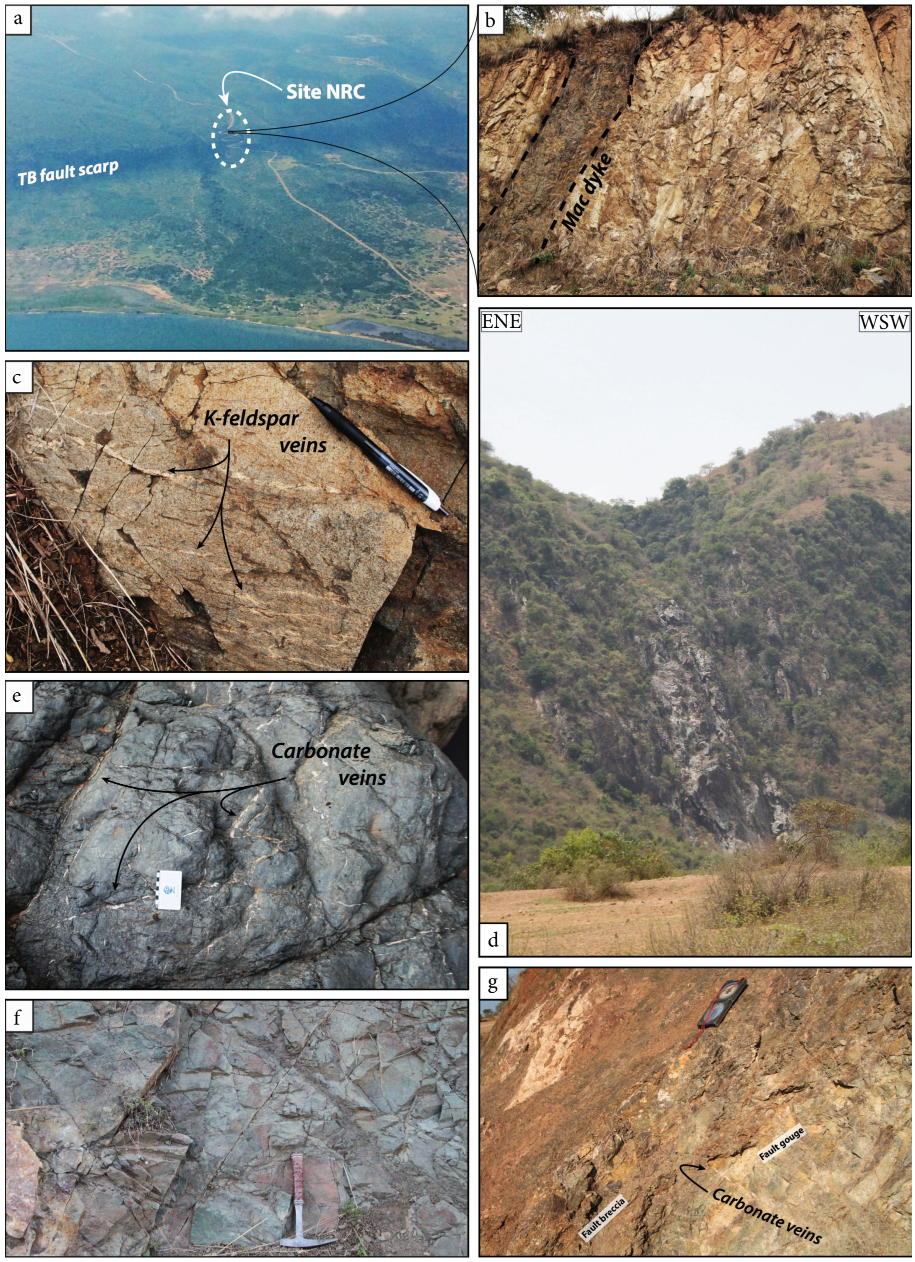

FIGURE 4: (a) Aerial photograph of site NRC; (b) fractured orthogneiss with mafic dyke intrusion observed at site NRC; (c) multiple K-feldspar veins through gneissic basement at site NRC; (d) long-distance photograph of the fault scarp river incision where site BAB is located; (e) complex network of carbonate veins through the dark cataclastic basement rocks at site BAB; (f) greenish mafic-derived cataclastic rocks overprinted by a dense fracture network observed at site SRC; (g) fault gouge and breccia at site SRC, crosscut by carbonate veins.

veins, up to 1 mm thick, are clearly undeformed and postdate the development of the cataclastic material. Orientation measurements on the field focused on these veins show that the dominant set of these filled fractures follows the NE direction with a high (~70°) NW or SE dip, reflecting the orientation of the TBFS producing the scarp (Figure 3(c)). A secondary set of NNW- to N-striking subvertical veins is also observed, whose orientation is similar to that of NNE-trending structural lineaments intersecting the major rift-bounding fault at this location. E-W oriented calcite veins form also a minor set. Rare K-feldspar veins crosscutting the cataclastic rocks are also observed (Figure 6(b)).

4.5. The "South Roadcut" Site. The "South Roadcut" (SRC) site is located in the relay area between the ENE-trending Kaiso transtensive fault and the NE-trending normal Toro-Bunyoro fault (Figure 1). In this area, this major rift-bounding fault subcontinuous over 100 km long terminates while slightly rotating to NNE trend and splitting into two relatively short subparallel faults about 5 km long (Figure 3(d)). This complex structural accommodation zone consists in a relay ramp about 1 km wide, where the fractured basement is sporadically exposed along the SRC slightly descending to the north-west. The main outcrop is found near the base of the scarp, at the contact between the

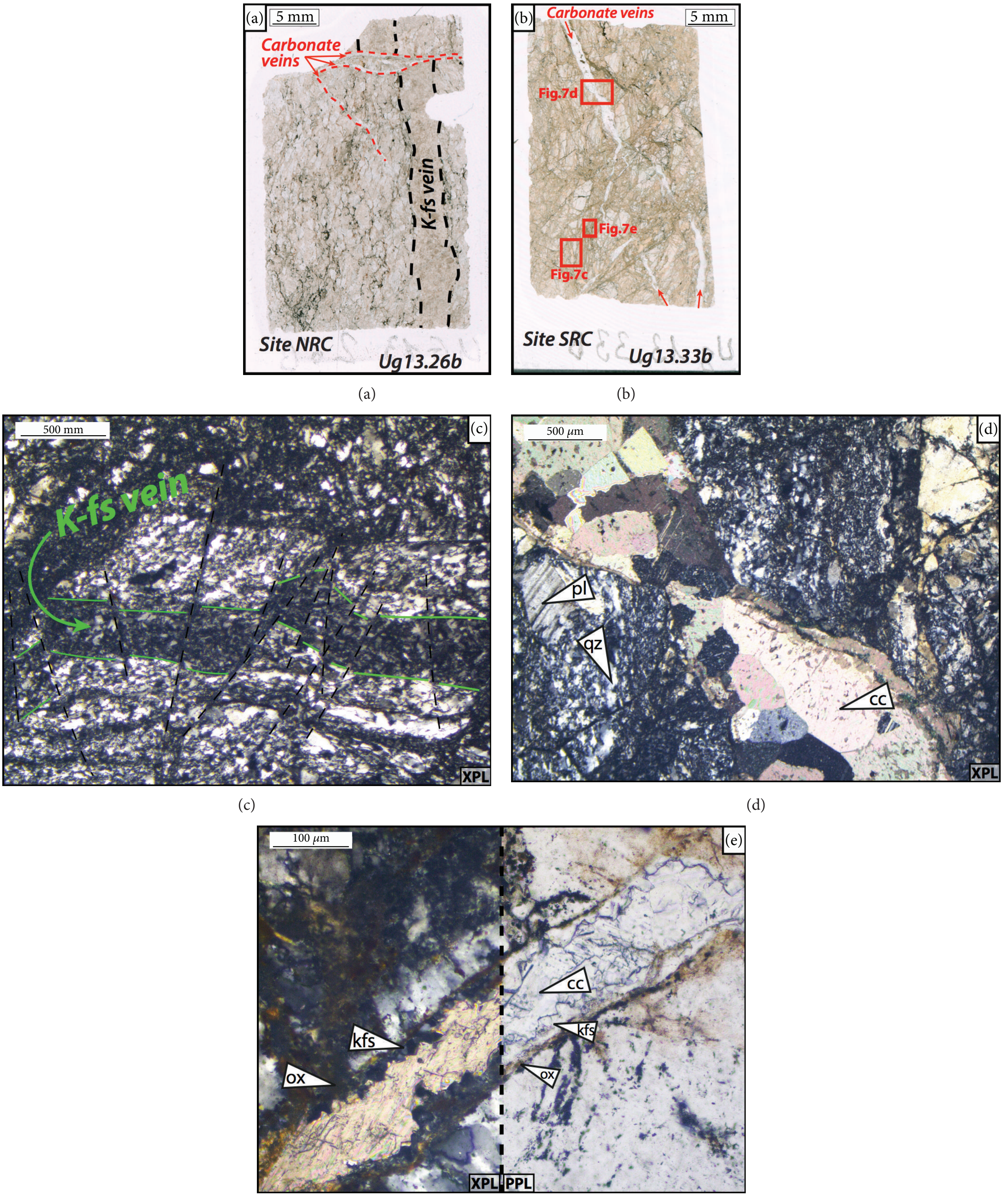

Figure 5: (a) Thin-section scan of a gneissic sample from site NRC crosscut successively by K-feldspar and carbonate veins; (b) thin-section scan of a brecciated rock sample from site SRC crosscut by various veins and microphotograph location; (c) highly fractured K-feldspar vein; (d) slightly fractured carbonate vein through the cataclastic rock matrix; (e) undeformed vein with successive K-feldspar (and oxides) and carbonate mineralization. (pl: plagioclase; qz: quartz; cc: carbonate; ox: oxide; kfs: K-feldspar; XPL: cross-polarized light; PPL: plane-polarized light).

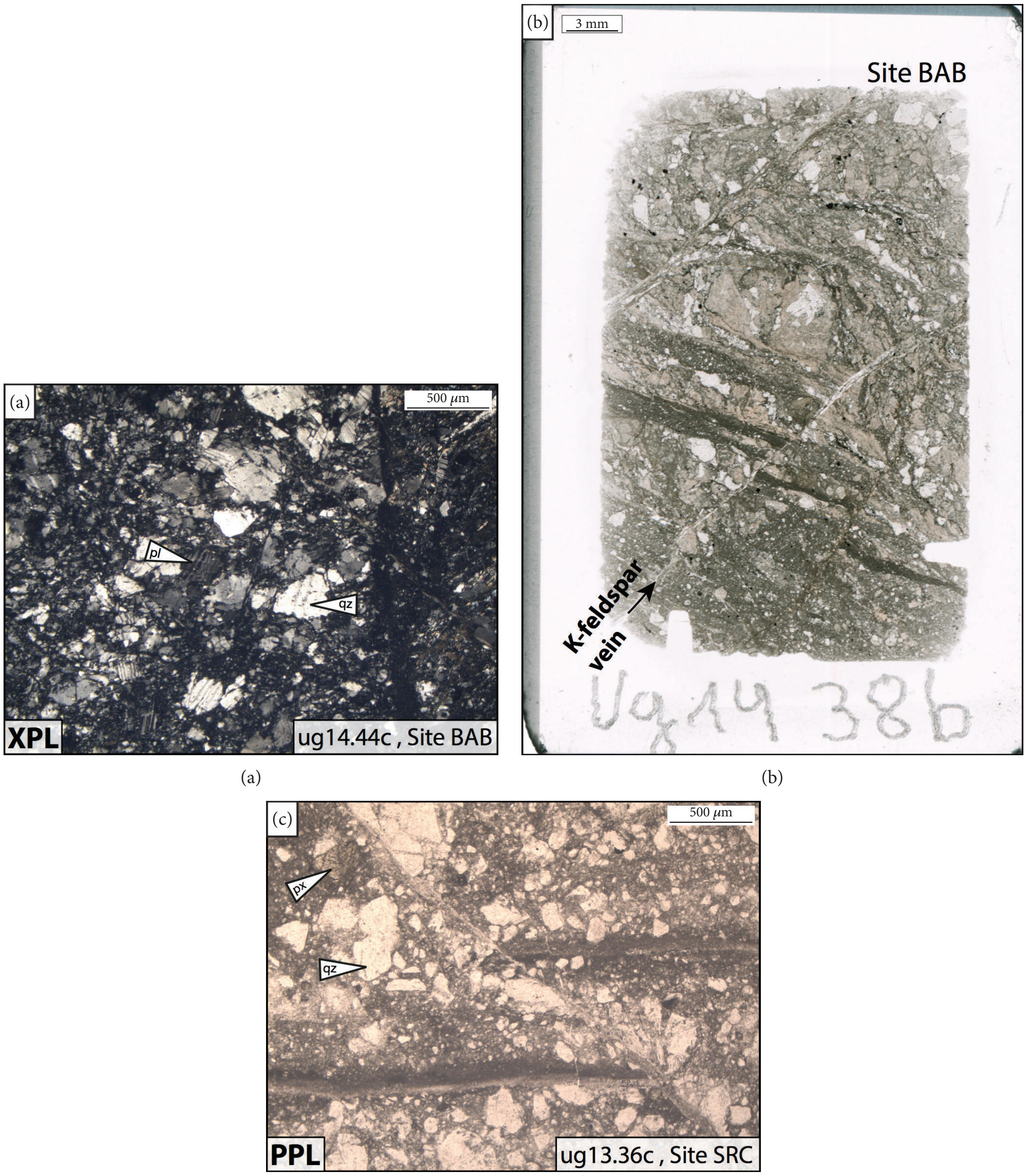

(a)

(b)

(c)

Figure 6: Microphotographs (a, c) and scan of thin section (b) illustrating the cataclastic deformation observed at sites BAB and SRC (pl: plagioclase; qz: quartz; px: pyroxene; XPL: cross-polarized light; PPL: plane-polarized light).

sedimentary units of the KT platform and the faulted basement of the relay ramp. This large outcrop of ~100 m long and several meters high corresponds to the footwall of the fault. The highly deformed basement of this outcrop is composed of greenish mafic rocks and granitoids with diffuse and unclear contacts (Figures 4(f) and 4(g)). Thin-section observations of the mafic rocks show that cataclasis occurred with the development of dark fine-grained matrix and isolated subangular 10–300 μm fragments of plagioclase, pyroxene, and quartz (Figure 6(c)). Granitoid rocks are generally highly brecciated but do not show such cataclasite texture. A number of K-feldspar veins are heavily deformed by the brecciation process (Figures 5(b) and 5(c)). However, later K-feldspar mineralization appears also to develop after rock breccia, associated with a complex and dense set of crosscutting calcite veins (Figure 4(g), 6(b), and 7(a)). Microstructural observations show that some minor K-feldspar precipitation predates the carbonate deposits, using the same undeformed veins through the cataclastic rocks (Figures 5(d) and 5(e)). Consequently, all the carbonate veins appear to postdate the high deformation developed by the fault zone, whereas fluid circulation associated to the K-feldspar precipitates seems more diachronous regarding the relative fault zone activity. Some of the thicker calcite veins (up to 2 mm thick) show elongated grains and host-rock microbreccia, suggesting hydraulic fracturing process during development (Figures 7(b) and 7(c)). Along the western part of the outcrop through both mafic and granitoid rocks, the dominant calcite veins follow mainly the NE direction with a high (~70°) NW dip (Figure 3(d)). Other minor subvertical vein sets are also observed with NNW and E-W strikes.

4.6. The Kabyosi Site. The Kabyosi site is located along the ENE-trending Kaiso transfer fault (Figure 1). Several hydrocarbon seepages are located at the base of the scarp and along a fault-controlled river incision (Figure 8(a)). Two main structural lineament sets are observed in the footwall of this complex area, respectively, characterized by ENE trend, parallel to the fault scarp, and by variable NNW to NNE trend. Five oil seeps were identified, systematically located at the intersection between these two lineament sets. Most of the hydrocarbons soak highly fractured and brecciated crystalline basement material (Figures 8(b)–8(d)), and it is still wet and viscous, confirming these fluid circulations to be subcurrent. Except for the northernmost seepage located at the base of the major fault scarp, these faults are ~10–15 m thick with a minimum fracture density of ~30 frac·m^{-1}. These structures are generally characterized by a fault core up to few meters thick, where breccia and fracture densities over 100 frac·m^{-1} are observed, associated with the highest hydrocarbon volumes. Dominant fractures follow mainly the ENE direction with a high (~60–70°) WNW dip, reflecting the Kaiso transfer fault orientation. Minor subvertical fracture sets are also identified with variable NW-SE to NNE-SSW strike (Figure 8(a)).

5. Geochemistry

Different features of current and fossil fluid circulations from the five working sites presented above were investigated to obtain information on their composition and source. Results of hydrocarbon analyses gathered from both Kibiro and Kabyosi sites and petrological and geochemical data of carbonate veins sampled at sites NRC, BAB, and SRC are then presented.

5.1. Molecular Composition of Asphalt Filling from Kibiro and Kabyosi Sites. At the Kibiro and Kabyosi sites, asphalt was found as fracture fillings or part of breccia matrix in basement fault zones. Their molecular composition can provide information on these organic fluids as their origin, in terms of source rocks, and their evolution during their migration throughout the fault zone. Two samples from the Kibiro site and four from the Kabyosi site were analyzed to assess their molecular signature.

These asphalt fillings were mostly soluble in dichloromethane and most of its soluble fraction was mainly composed of asphaltenes, which cannot be precisely characterized. The maltene fraction of these asphalts showed a rather unusual molecular composition with a total absence of characteristic standard components of crude oil like *n*-alkanes and acyclic isoprenoids. Most of the maltene compounds were present in the aliphatic fractions.

Chromatograms of the aliphatic fractions of the Kibiro samples shows the presence of an unresolved complex mixture (UCM) and sulfur as well as hopanoid compounds (Figure 9(a)). Hopanoids are pentacyclic triterpenoids initially present in the cell walls of bacteria and are widely distributed in sedimentary organic matter due to the abundance of bacteria in all environments. Consequently, precise identification of hopanoids can carry many valuable postdepositional information. For instance, in bacteria, hopanoids are present in the biological configuration (17β(H),21β(H)) and are then gradually transformed into a geological configuration (17α(H),21β(H)) via thermal maturation. Identification of these hopanoids is indicated in Figure 9(a) for the Kibiro samples. These hopanoids were composed of C_{27}, C_{29}, and C_{30} hopanes as well as hopenes (unsaturated hopanes). Two of the hopanes presented a biological configuration and no hopane with a geological configuration was detected. Chromatograms of the aliphatic fractions of the Kabyosi samples do not present an unresolved complex mixture as in the Kibiro samples and are also characterized by the presence of hopanoids even if they are different from those of the Kibiro site (Figure 9(b)). These hopanes consist of C_{27}, C_{28}, and C_{29} hopanes while C_{30} hopanes were only present at low contents. For samples of both sites, homohopanes (>C_{30} hopanes) are absent. The large predominance of hopanoids, which are widely synthetized by bacteria together with the lack of acyclic alkanes, which are the first compounds assimilated by microorganisms, suggests that the oil was intensively affected by biodegradation processes after its migration in the faulted basement. This intense biodegradation is moreover attested by the presence of 17α(H),21β(H)-25-norhopane in the Kabyosi samples since this molecular biomarker is typically produced by hydrocarbon-degrading bacteria. Furthermore, hopenes and hopanes presenting the biological configuration (17β(H),21β(H)) disappear during maturation of organic matter. This is why they are systematically present in immature source rocks but never recovered in conventional oils. Therefore, their occurrence should be unlikely in the asphalt fillings at Kibiro and can only be explained by a late bacterial origin. The presence of such hopanoids, which are much more abundant than the other compounds, also supports an intense biodegradation of the initial crude oil. Unfortunately, the original molecular signatures were deeply affected and most of the molecular biomarkers that bear information on the source of the oil were totally consumed by hydrocarbon-degrading bacteria.

In an attempt to recover the initial molecular signatures of these deeply biodegraded asphalt samples, artificial maturations were carried out on the asphaltene fractions of the Kabyosi samples (Figure 9(c)). Despite clear information about the origin of these fluids, regarding the sampling location and the proven oil resources of the Lake Albert, the HC seepages observed in the faulted basement footwall of the

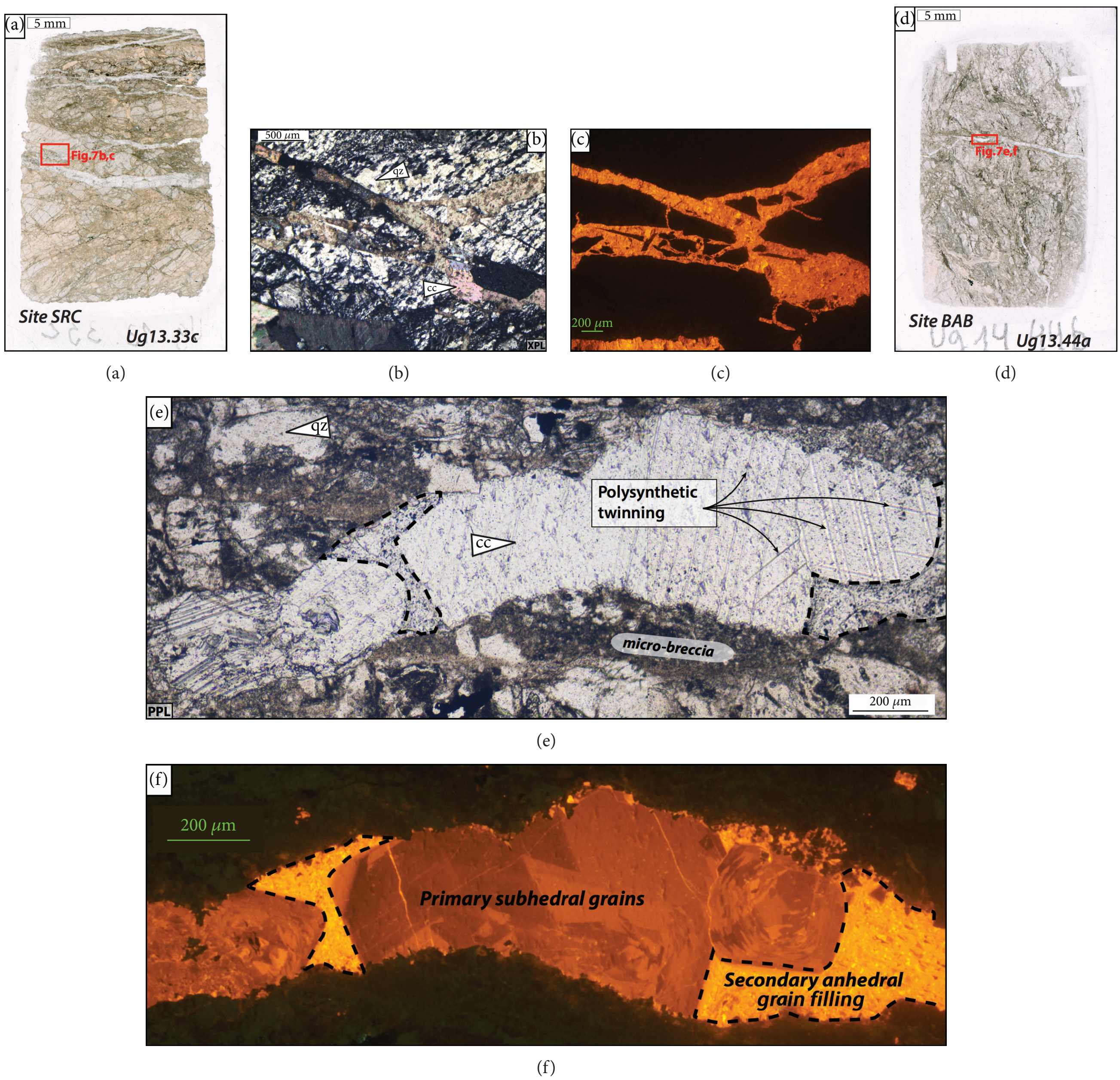

Figure 7: (a) Thin section scan of a brecciated rock sample from site SRC crosscut by undeformed veins and microphotograph location; (b) cross-polarized light and (c) cathodoluminescence microphotographs of a complex carbonate vein network with host-rock microbreccias; (d) thin-section scan of a cataclastic rock sample from site BAB crosscut by undeformed carbonate veins and microphotograph location; (e) plane-polarized light and (f) cathodoluminescence microphotographs of a polyphased carbonate vein with primary twinned subhedral grains and secondary nontwinned anhedral grains. (qz: quartz; cc: carbonate; XPL: cross-polarized light; PPL: plane-polarized light).

TBFS can be assumed to be related to a sedimentary source rock from the ARS basin. Oils are transformed during their transfer by bacterial activity.

5.2. Calcite Vein Analysis. Complex sets of carbonate veins cross-cutting the massive cataclastic rocks of the faulted basement footwall were recognized in the study areas along the major fault scarp (Figures 5, 7). Assuming these cataclasites were formed by the TBFS activation during the ARS evolution since Upper Miocene, the cross-cutting mineralized fractures filled with carbonate are locally postdating the major deformation episodes. Similar carbonate veins were identified in the fractured basement of the Kibiro site near the main active hot springs [34]. These carbonate veins can therefore represent relatively recent fossil fluid circulation zones.

At NRC, BAB, and SRC, the mineralized fractures are generally organized according to several subvertical orientation sets. These orientation sets appear to reflect the local orientations of the fault scarp and macroscale structural lineaments (cf. BAB, SRC sites, Figures 3(c) and 3(d)). No apparent criteria could be observed to identify any relative

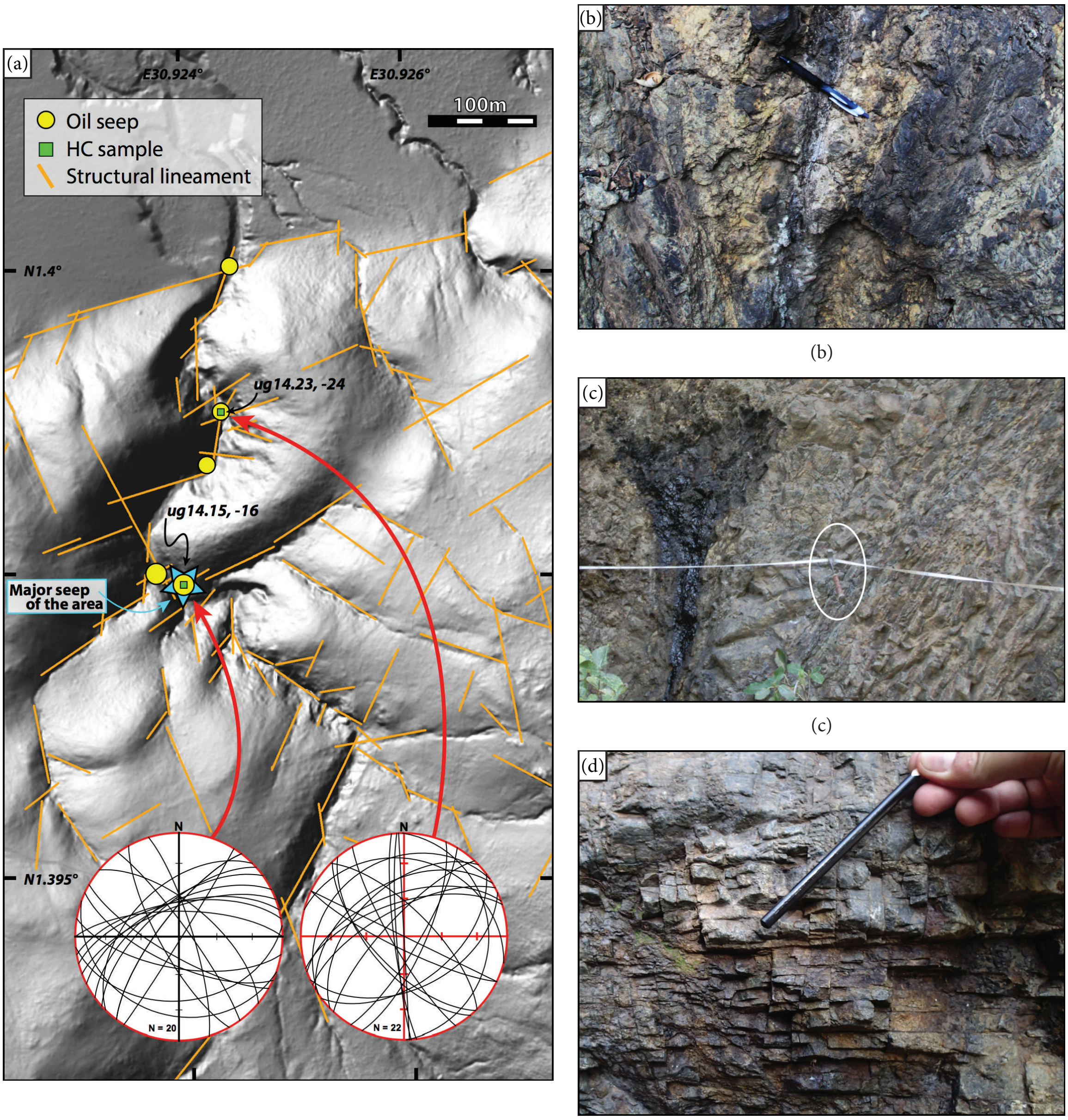

(b)

(c)

(a)

(d)

Figure 8: (a) Hydrocarbon (HC) seeps and sample location map and structural lineament interpretation based on a 1-meter DEM image of the Kabyosi area. Stereographic projections (lower hemisphere) represent fracture orientation measured close by two seeps; photographs illustrating the high brittle deformation associated to the Kabyosi HC seeps; (b) fault gouge and adjacent fractured rocks soaked with HC and sulfur deposits; (c) photograph of the major leakage of the area, occurring in the middle of a ~10 m thick fault zone; (d) dense fracture network near the major seep with isotropic HC flow.

chronology relationship between the different sets. Veins are 0.1 to 1–2 mm thick and show no relationship with orientation. Host-rock hydraulic microbreccias are commonly observed. Under cathodoluminescence (CL), all the carbonate veins are characterized by brown-orange shades, with slight color variations highlighting grain geochemical zonation and growth orientation (Figures 7(c) and 7(f)). Regarding the borders of the veins, no clear grain preferential orientation or elongation can be observed, which could have suggested tensional or shear fractures. Veins with aperture > 200 μm generally show relatively large subhedral carbonate grains and anhedral secondary filling grains (Figures 7(d)–7(f)). Thinner veins are generally composed of subhedral grains and do not show clear polyphasing relationships. In the wider veins, deformation polysynthetic twinning with variable orientations of the subhedral grains is often observed (Figure 7(e)), whereas no twinning is observed in the secondary anhedral filling grains.

Fluid inclusions (FI) were recognized in most of the carbonate veins, with size ranging from ~1 up to 10 μm. Vapor bubbles visible in the largest FI were observed generally moving rapidly at room temperature. No fluorescence of the

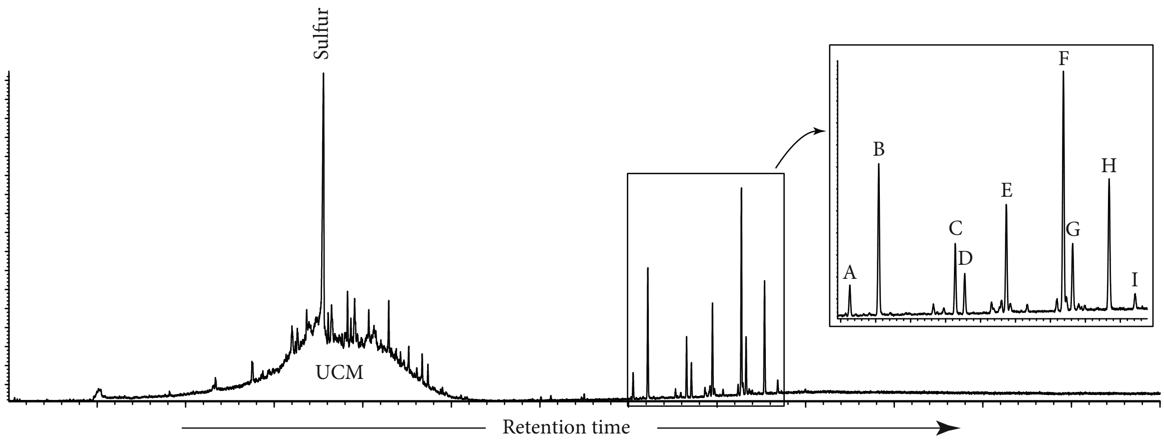

A : 22,29,30-trisnorhop17(21)-ene
B : 17β(H)22,29,30-trisnorhopane
C : hop-17(21)-ene
D : 17β(H),21α(H)-normoretane
E : 17β(H),21β(H)-norhopane
F : C31-homohopene
G : Unidentified compound
H : C31-homohopene

(a) Kibiro site

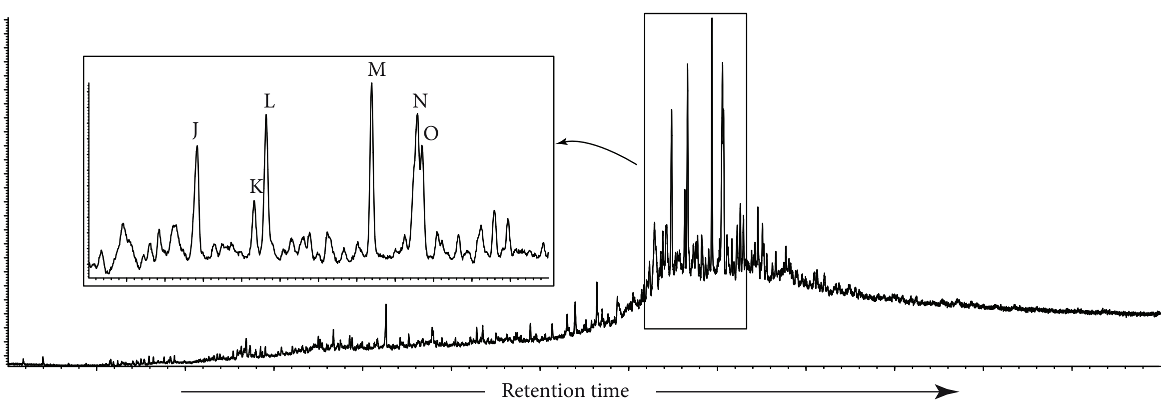

J : 17α(H)-22,29,30-trisnorhopane
K : Trisnorhopane
L : Bisnorhopane
M : 17α(H),21β(H)-25-norhopane
N : 30-norhopane
O : 30-norhopane

(b) Kabyosi site

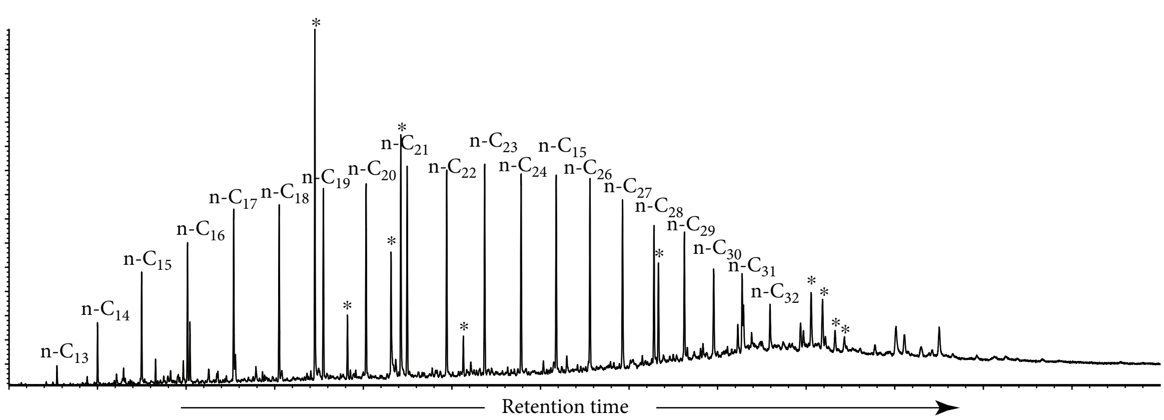

n C_{xx} :*n* - alcanes (xx indicates the number of carbon atoms)
* Contaminants

(c) Artificial maturation products of asphaltenes from the Kabyosi site

Figure 9: (a, b) Gas chromatograms of the aliphatic fractions of the asphalt fillings from the Kibiro and Kabyosi sites, respectively; (c) gas chromatogram of the artificial maturation products of asphaltenes recovered from the Kabyosi asphalt fillings.

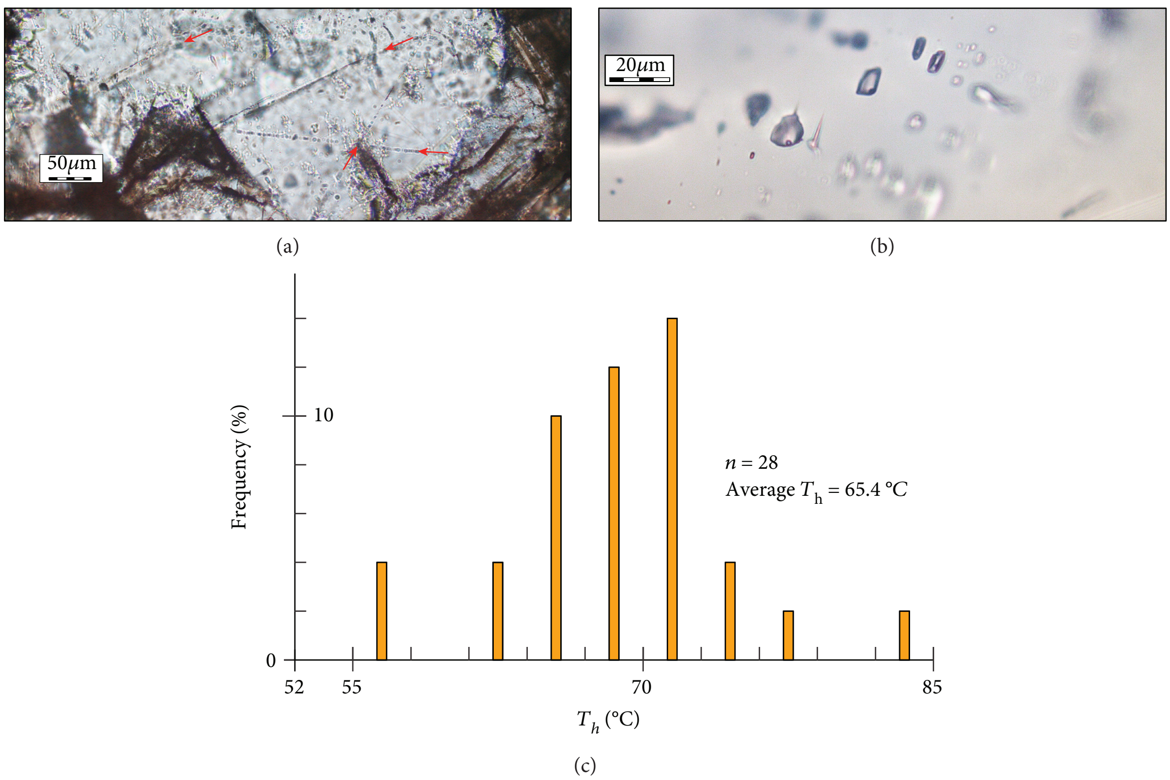

Figure 10: Plane-polarized light microphotographs of sample ug13.33 (site SRC) of (a) fluid inclusion secondary trails in large subhedral twinned carbonate grains (indicated with red arrows); (b) irregular-shaped fluid inclusions in a secondary anhedral nontwinned carbonate grain; (c) frequency plot of homogenization temperatures (T_h) of fluid inclusions measured in a sample ug13.33 (site SRC).

liquid phase was observed under ultraviolet (UV) light. FI were found in both twinned and nontwinned carbonate grains. In large subhedral twinned grains, FI are generally observed as secondary trails, where inclusions are elongated according to the trail axes (Figure 10(a)). In secondary anhedral nontwinned grains, FI are generally slightly bigger with irregular morphologies and form assemblages of 2–10 inclusions (Figure 10(b)). Only the thickest carbonate veins from sample ug13.33 (site SRC) were sufficiently large to prepare fragments for FI microthermometry analysis. 28 FI were heated to measure homogenization temperatures (T_h) in both trails within subhedral grains and subisolated assemblages within anhedral secondary grains. T_h values range from 54 to 80°C, with a majority of data lying between 64 and 70°C (Figure 10(c)). Phase transitions during low-temperature microthermometry analysis (freezing stage) were not clearly interpretable.

Oxygen and carbon stable isotope analyses were carried out on carbonate grains in different mineralized fractures from NRC, BAB, and SRC. Results are reported in Figure 11 and Table 2. CL imaging allowed to separate the measurement points between the different grains, in order to average the isotopic ratio data per grain. Both twinned subhedral and nontwinned anhedral grain types were easily recognized on the analyzed veins of sample ug14.44 from BAB (Figures 7(e), 7(f)) and their isotope analysis results are therefore distinct. The isotopic values measured in carbonate veins from sample ug13.16 (NRC) range between 13.7 and 20.7‰ for δ^{18}O (SMOW) and between 2.6 and 14.8‰ for δ^{13}C (PDB). Those from sample ug13.33 (SRC) have δ^{18}O and δ^{13}C values ranging from 22.9 to 30.2‰ SMOW and from −5.2 to 6.9‰ PDB, respectively. In sample ug14.44 (BAB), large subhedral twinned grains show δ^{18}O and δ^{13}C values, respectively, ranging from 16.1 to 19.6‰ SMOW and from 1.0 to 8.1‰ PDB. Values from secondary anhedral filling grains measured in the same veins are different, with δ^{18}O and δ^{13}C ranging from 20.1 to 24.3‰ SMOW and from −0.5 to 2.7‰ PDB, respectively.

Oxygen isotopic compositions of the fluids from which the different carbonate veins precipitated were determined using the fractionation curve formula between calcite and water following this expression:

$$10^3 \ln\left(\frac{\delta^{18}O_{cc} + 1000}{\delta^{18}O_{H2O} + 1000}\right) = 4.01\left(\frac{10^6}{T^2}\right) - 4.66\left(\frac{10^3}{T}\right) + 1.71, \quad (1)$$

where $\delta^{18}O_{cc}$ and $\delta^{18}O_{H2O}$ are the oxygen isotopic ratio of the carbonate and the forming fluid, respectively, and T is the precipitation temperature (in Kelvin). Temperature value used in this formula corresponds to the average T_h of 65.4°C measured in sample ug13.33 by FI microthermometry. As no T_h could not be measured because of the small-size FI in the other samples, this average temperature value was also applied to samples ug13.16 and ug14.44 calculation. Using the $\delta^{18}O_{cc}$ values obtained for the analyzed grains in the different veins, oxygen isotopic composition of the fluids obtained for samples ug13.33 and ug13.16 ranges from −0.27 to 6.88‰ SMOW and −9.50 to −2.46‰ SMOW, respectively (Table 2). Polyphased carbonate veins in sample ug14.44 show different $\delta^{18}O_{H2O}$ values between primary subhedral and secondary anhedral filling grains, varying from −6.97 to −3.52‰ SMOW and −3.05 to 1.12‰ SMOW, respectively.

6. Discussion

The hydrogeological behavior of regional-scale fault zones in rift basins is critical for many practical fluid flow applications. Regarding the Lake Albert basin economic potential for both geothermal and hydrocarbon energies, especially as a prospective fault-controlled "extensional domain play-type (CV3)" geothermal system [9], insights into the hydrogeological system of the eastern rift-bounding TBFS need to be enhanced. From the data of the five different working sites presented in this study, we will discuss hereafter the control of the structural features on this hydrogeological system, as well as the fluid sources that supply it.

6.1. The Transfer Plumbing System. Transfers are constrained by several objects or structures: the NE-trending normal TBFS and associated structures, the fault network, and the relay ramp of Kaiso. All together, they contribute to define the plumbing usable to fluid transfer.

6.1.1. The TBFS. Major faults with thick fault core of clayey-rich gouge or lithified cataclastic material may act as impermeable barrier for fluid flow [40, 41]. Regarding the thick fault core materials observed on the basement footwall of the scarp at each working site and the systematic fault intersection setting identified at the investigated fluid circulation zones, most parts of the TBFS without such passing through structural pattern appear impermeable to fluid flow. In classic models of fault zone architecture, the localized high-strain impermeable fault core is surrounded by a distributed zone of highly connected and dense fractures and faults, corresponding to the relatively permeable damage zone [41, 42]. The transfer properties of the fault core produce a compartmentalization between potential basin fluids and meteoric fluids on the shoulders.

6.1.2. Fracture and Fault Network. Large-scale DEM analysis of the area shows a dense network of oblique lineaments intersecting the TBFS, with a dominant NNW to NNE direction (Figure 2). Locally, the setting of the three northernmost investigated fluid circulation sites consists in the intersection between the NE-trending normal TBFS and N- (cf. site NRC) or NNW-trending (cf. Kibiro, site BAB) structural lineaments identified through the basement footwall (Figures 2 and 3(a)–3(c)).

Considering that the fault core rocks observed along the scarp developed during paroxysmal deformation events during the long-term tectonic evolution since Upper Miocene [12, 28], the fracture networks crosscutting the cataclastic material were active at least once after the fault core cataclasis development and postdate these events. These fracture networks developed at structural intersections through the fault core of the TBFS represent then connected pathways for fluid flow between the damage zones on both sides of the fault structure as developed at Kibiro. They contributed subsequently to produce "x-crossing" fracture networks through the fault core rocks of the TBFS.

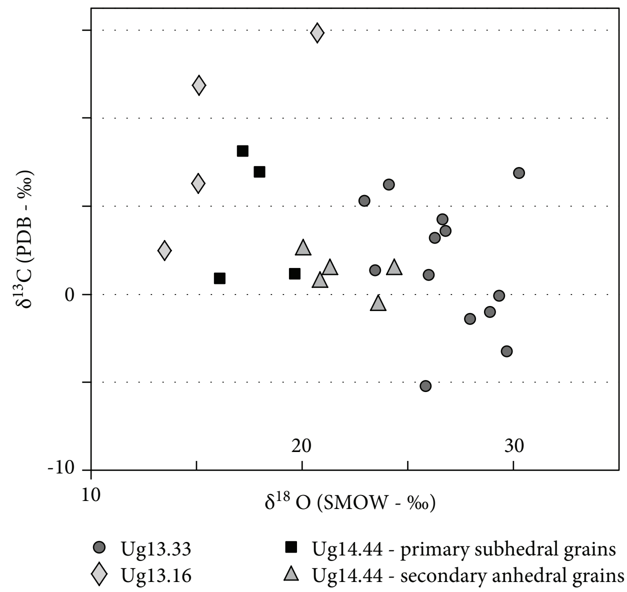

Figure 11: Average isotopic compositions ($\delta^{18}O$ and $\delta^{13}C$, ‰) of different grains measured in carbonate veins from the three working sites SRC (sample ug13.33), NRC (sample ug13.16), and BAB (sample ug14.44, see text for more information).

At the outcrop scale, the different orientations of the soaked hydrocarbon or carbonate-filled fracture sets measured at the three working sites Kabyosi, SRC, and BAB form "x-crossing" structural pattern, reflecting the local macro-scale fault intersections.

Intersection lines of "x-shaped" fault and fracture sets produce dilatational zones under various tectonic stress regimes and provide lateral and vertical optimal channels for fluid flow (e.g., [11, 43–45]). Such structural intersections represent thus "pipe-like" structures that can act as fluid preferential pathways and may be kept open even in compressional stress field [46]. Therefore, the current and fossil fluid outflows at the different working sites highlight that this local "x-crossing" structural pattern produces sufficient relative vertical fracture permeability to drive significant amount of fluids, in regard to other locations along the TBFS without structural intersection.

6.1.3. The Relay Zone of Kabyosi. The Kabyosi hydrocarbon seeps are located at the intersection of ENE-trending faults, parallel to that of the main Kaiso transfer structure, and of secondary NNW- to NNE-trending structural lineaments (Figure 8(a)). Lastly, the SRC site is located at the southern termination of the NE-trending Toro-Bunyoro fault, where it splits into shorter subparallel segments and intersects the ENE-trending Kaiso transfer zone (Figure 3(d)). This geometry could be related to a relay ramp structure with the NE-trending faults, the main faults, and the ENE-trending faults that breach between both the main faults. Fractures, in this relay structure, increase in intensity, and the great

Table 2: Oxygen and carbon isotopic data ($\delta^{18}O_{cc}$ and $\delta^{13}C_{cc}$, ‰) of the analyzed carbonate veins. Oxygen isotopic ratio $\delta^{18}O_{H2O}$ of the carbonate vein source fluids is calculated using Zheng (1999) formula (see text for more information).

Sample	Number of grains analyzed	# of grain	Measurements	$\delta^{13}C_{cc}$ (‰ PDB) average per grain	$\delta^{18}O_{cc}$ (‰SMOW) average per grain	$\delta^{18}O_{H2O}$ (‰ SMOW) average per grain
ug13.33b	13	1	1	6.12	24.08	0.86
		2	1	5.26	22.92	−0.27
		3	1	6.88	30.24	6.88
		4	1	4.15	26.63	3.35
		5	1	3.57	26.81	3.53
		6	1	−0.15	29.33	6.00
		7	1	−3.25	29.69	6.35
		8	1	−5.17	25.88	2.62
		9	2	1.13	25.97	2.71
		10	2	3.18	26.30	3.03
		11	3	−1.01	28.87	5.54
		12	3	1.36	23.46	0.26
		13	3	−1.37	27.97	4.67
ug13.16c	4	1	2	2.57	13.48	−9.50
		2	4	6.35	15.07	−7.94
		3	2	14.78	20.68	−2.46
		4	4	11.84	15.12	−7.89
ug13.44a primary subhedral grains	4	1	6	1.00	16.07	−6.97
		2	3	1.16	19.59	−3.52
		3	8	6.97	17.94	−5.14
		4	1	8.12	17.15	−5.91
ug13.44a secondary anhedral grains	5	1	2	0.75	20.88	−2.26
		2	2	−0.45	23.57	0.36
		3	2	2.68	20.08	−3.05
		4	3	1.64	24.34	1.12
		5	2	1.53	21.30	−1.85

range of orientation leads to a high permeability zone. Following the model proposed by Fossen and Rotevatn [47], this relay ramp locates a fluid flow pattern oriented vertically and parallel to the main fault structure composed by the dense fracture network and reinforced by the impermeable sail formed by the TBFS fault core. It is able to focus fluids coming from the basin.

Consequently, this rift-bounding fault system corresponds to a discontinuous barrier for fluids, with local pathways for transfers from the rift shoulder toward the basin, and vice versa. Relative to barrier parts where fluid pressure may accumulate, local structural intersections and associated "x-crossing" fracture networks therefore represent hydraulically active shear fractures in relatively low compressive stress areas along-strike the normal faults and low fluid pressure areas. Consequently, such areas can either act in the hydrogeological system as discharging zones for connected overpressured fluids (cf. Kabyosi) or as favorable down- and upflow zones that may favor subsurface convection cell development (cf. Kibiro).

Outflows occurring predominantly at the interaction zone and intersection of multiple faults have been described for different fault-controlled geothermal systems in the world (e.g., [18, 48, 49]). A number of studies performed in the Great Basin region (USA) highlighted by an inventory over 400 geothermal active sites that more than half of the sites are hosted by fault interaction features, as step-overs or relay ramps, and fault intersections [19, 20, 50, 51]. Further, the exclusive location of these fluid circulation zones at fault intersections between the TBFS and subsidiary oblique structures suggests that outflow does not significantly occur along the major fault scarp without such a structural interaction. This agrees with the rare occurrence in the Great Basin of geothermal systems along planar midsegments of major faults where displacement generally peaks [19, 20]. Fault intersections and the relay ramp therefore appear as reliable prime targets for exploration, especially as geothermal resources may have little or no surface manifestation (e.g., [15–17]). As part of a petroleum system, the identification of such structural intersections is also critical, as they can represent either reservoir charging or leakage pathways (e.g., [52]).

6.2. A Complex Fluid Mixing Zone. This study and previous investigations allowed to identify three main fluid reservoirs for the current and fossil fluids recognized along the TBFS.

The different fluid inputs and their mixing are schematically represented in Figure 12 and discussed below.

6.2.1. The Meteoric Reservoirs. A number of geochemical and geophysical studies of the Kibiro geothermal prospect area showed that the main recharging fluid of this current system corresponds to meteoric water infiltrated along faults in the eastern rift basement shoulder, along which it percolated underground up to the intersection with the TBFS [22]. Similar results were obtained with this study from oxygen isotopic composition analysis of carbonate veins at sites NRC and BAB (cf. ug13.16 and ug14.44 samples). With both sites located also at the intersection between the TBFS and subsidiary oblique faults, source fluid of these veins also appears to have been infiltrated underground through the faulted basement rift shoulder (Figure 12). The standard fresh surface water values is assumed at $-8 \pm 7‰$ SMOW [53]. This meteoric fluid contribution therefore represents the "external basin fluids" input of the fluid circulations within the TBFS.

6.2.2. The Basin Reservoirs. Hydrocarbon material was sampled from the soaked fractures of the faulted basement footwall in both Kibiro and Kabyosi sites. Due to severe biodegradation of the organic material, their source could not be determined. However, regarding the sampling location along Lake Albert and the proven oil resources in this basin (e.g., [27]), these seepages are assumed to be driven from the petroleum system of the lake. The contribution of basin water is also supported by some relatively high $\delta^{13}C$ values (>6‰ PDB) of carbonate veins measured at sites NRC, BAB, and SRC, where no organic material has been recognized nearby. These unusual values suggest that carbonate source has been partly affected by bacterial methanogenic processes [54–56]. Such isotopic signature could be derived from fluids affected by organic-related processes of the basin sedimentary deposits. Furthermore, Lake Albert water samples show average $\delta^{18}O$ composition of 5.23‰ SMOW ([22]) clearly resulting from an interaction between lake's sediments and meteoric and connate waters [57, 58]. Thus, these lake-related fluids reflect the "internal basin fluid" input of the fluid circulations within the TBFS (Figure 12).

6.2.3. The Deep Reservoirs. Fluid source of the K-feldspar veins identified at NRC, BAB, and SRC, as well as that of the carbonate veins from SRC (cf. ug13.36 sample), is less clear. Adularia is a rather common K-feldspar polymorph, whose mineralization is generally associated to low-temperature hydrothermalism and host-rock alteration in active rifts [59, 60]. The K-feldspar veins observed in this study are therefore considered here as adularia veins. Except being emplaced prior to the carbonate veins, no clear relative timing relationship of these adularia veins during rift evolution could be determined. A number of highly deformed adularia veins are recognized in fault core cataclasis samples from the SRC site, while those from the NRC site look undeformed. Assuming these fault core rocks to be developed during rift-related paroxysmal deformation events, the different adularia veins would have crystallized during rather early stages of the rifting.

6.2.4. Mixing of the Fluids and Transfer. Later carbonate veins observed at site SRC appear different from those characterized at both NRC and BAB sites and those described in the Kibiro geothermal prospect area. Calculated oxygen isotope ratios of fluid source from these veins generally show positive values up to 6.88‰ SMOW (average 3.5‰ SMOW), significantly different from standard fresh surface water values ($-8 \pm 7‰$ SMOW) [53] and Kibiro hot spring water samples (−2.05‰ SMOW) [22]. Such data suggest that meteoric water is clearly not the fluid source for the SRC site carbonate veins. Lake Albert water samples show average $\delta^{18}O$ composition of (5.23‰ SMOW [22]). With similar positive values, the fluid source $\delta^{18}O$ composition of the SRC site carbonate veins is then compatible either with a lake-water origin or with a formation water origin [57, 58], which could both support the "internal basin fluid" input in the hydrogeological TBFS.

The positive $\delta^{18}O$ values from sample ug13.33 are however also compatible with oxygen isotopic composition of deep-seated metamorphic or magmatic fluids [61]. Despite such fluids were not clearly recognized in this study, several arguments support the hypothesis that deep-seated fluids flow up to the TBFS scarp. The strontium isotope analyses of sulfates precipitated at Kibiro indicate an interaction with crustal materials [22]. Evidences of deep circulation of fluids are recognized southwestward along major faults of the ARS basin. The Buranga hydrothermal system, located along the Rwenzori Mountains at about 150 km southwest from Kibiro, is one other major geothermal prospect of the ARS. Meteoric water from the adjacent Rwenzori high ground is recognized as the main recharging fluid of the system but a magmatic gas input, associated to an underlying magmatic heat source, is also strongly suggested by geochemical analyses [22, 62, 63]. Furthermore, a microseismic monitoring campaign of the Rwenzori area showed several earthquake (EQ) clusters between 5 to 16 km deep, localized in the prolongation of the TBFS at about 100–150 km from our study area [64]. From EQ parameters and cluster shape, these authors suggest that these EQ swarms are triggered by deep crustal fluid and gas migration, rising from a postulated magmatic body in the upper mantle. From these arguments, a deep-seated source fluid contribution is therefore considered in the hydrogeological TBFS (Figure 12). Fluid flow along the deeply rooted crustal-scale ARS-bounding faults may contribute to the circulations that formed some of the identified adularia and carbonate veins, as well as other potential mineral phases unseen during this study.

Information from the fluid circulation investigations along the TBFS indicates therefore that this rift-bounding structure is connected to three sorts of fluid reservoirs providing "external basin fluids" (i.e., meteoric waters), "internal basin fluids" (i.e., HC and sediment formation waters), and deep-seated crustal fluids (i.e., magmatic or deep down flowing meteoric fluids) (Figure 12). The fault core of the TBFS contributes to a compartmentalization of the hydrogeological system, but the other elements of the

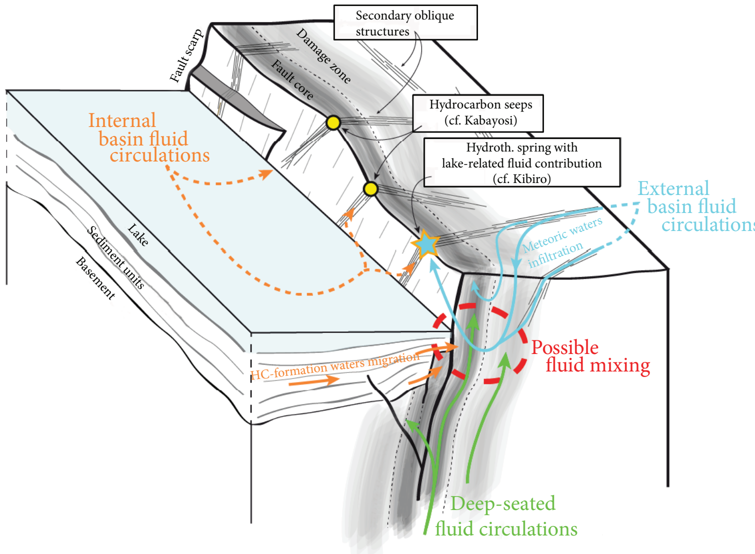

Figure 12: Schematic 3D bloc model of a rift-bounding fault system illustrating the three fluid inputs that flow and mix into the damage zone and fault core compartments (see text for more information). Oblique preexisting reactivated faults or new rift-related conjugated faults can drive fluids in the hydrogeological system. Structural intersections with the main fault system represent preferential discharging zone for subsurface fluids.

hydrogeological system contribute to interrupt and pass through the barrier. The damage zones of the TBFS, the deeply rooted major structure, are able to flow up deep fluids. The relay zone and the oblique structures are the main pathway to transport basin fluids, including hydrocarbons, toward the rift shoulders and through the TBFS fault core. The dense fracture network developed in the rift shoulder is the preferential pathway to flow down the meteoric fluids toward the deep part of the rift especially through the "x-crossing" fracture.

All these features form a composite hydrogeological system, where fluids circulate within the highly fractured fault compartments and converge preferentially up to the surface along relatively low-stress zones formed by structural intersections between the TBFS and subsidiary oblique structures. Through the "x-crossing" fracture networks associated to these intersections, fluid inputs can flow and mix across the fracture porosity of the fault system damage zones.

7. Conclusion

This study documents the complexity of a hydrogeological system hosted by a major rift-bounding fault system and suggests that a number of internal- and external-rift basin fluids can supply it over time. Structural and petrological data gathered along the TBFS emphasize the role of local structural intersections with subsidiary oblique structures for fluid flow. It therefore contributes to the recognition of generic favorable structural settings of fault-controlled geothermal systems or hydrocarbon storage. With fault intersections providing local relatively permeable and low-stress areas, the rift-bounding fault system represents a discontinuous barrier for fluids where structural intersections control preferential outflow zones and channel fluid transfers from the rift shoulder to the basin, and vice versa. Inputs from 3 types of fluid reservoirs are recognized within this fault-hosted hydrogeological system, with "external basin fluids" (i.e., meteoric waters), "internal basin fluids" (i.e., hydrocarbons and sediment formation waters), and deep-seated crustal fluids (i.e., magmatic fluids) (Figure 12). Such a major rift-bounding fault system finally represents a composite hydrogeological system in which significant economic amounts of fluids preferentially converge and show surface manifestations locally at structural intersections. Fault intersections therefore appear as reliable prime targets for exploration of fault-controlled geothermal systems.

Data Availability

Samples and datasets used and produced during this study are all available at the GeoRessources Lab (University of Lorraine, France).

Conflicts of Interest

The authors declare that they have no conflicts of interest.

Acknowledgments

This work was supported by a PhD grant from Total and GeoRessources Lab.

References

[1] R. Bertani, "Geothermal power generation in the world 2010–2014 update report," *Geothermics*, vol. 60, pp. 31–43, 2016.

[2] K. C. Lee, "Classification of geothermal resources by exergy," *Geothermics*, vol. 30, no. 4, pp. 431–442, 2001.

[3] J. W. Lund and T. L. Boyd, "Direct utilization of geothermal energy 2015 worldwide review," *Geothermics*, vol. 60, pp. 66–93, 2016.

[4] P. Muffler and R. Cataldi, "Methods for regional assessment of geothermal resources," *Geothermics*, vol. 7, no. 2-4, pp. 53–89, 1978.

[5] S. K. Sanyal, "Classification of geothermal systems–a possible scheme," in *Thirtieth Workshop on Geothermal Reservoir Engineering*, pp. 85–88, Stanford University, Stanford, CA, USA, 2005.

[6] C. F. Williams, M. J. Reed, and A. F. Anderson, "Updating the classification of geothermal resources," in *Proceedings, Thirty-Sixth Workshop on Geothermal Reservoir Engineering*, Stanford, CA, USA, 2011.

[7] M. Wilmarth and J. Stimac, "Power density in geothermal fields," in *Proceedings World Geothermal Congress 2015*, p. 7, Melbourne, Australia, 2015.

[8] J. Limberger, P. Calcagno, A. Manzella et al., "Assessing the prospective resource base for enhanced geothermal systems in Europe," *Geothermal Energy Science*, vol. 2, no. 1, pp. 55–71, 2014.

[9] I. S. Moeck, "Catalog of geothermal play types based on geologic controls," *Renewable and Sustainable Energy Reviews*, vol. 37, pp. 867–882, 2014.

[10] D. Mckenzie, "Some remarks on the development of sedimentary basins," *Earth and Planetary Science Letters*, vol. 40, no. 1, pp. 25–32, 1978.

[11] R. H. Sibson, "Fluid involvement in normal faulting," *Journal of Geodynamics*, vol. 29, no. 3-5, pp. 469–499, 2000.

[12] C. J. Ebinger, "Tectonic development of the western branch of the East African rift system," *Geological Society of America Bulletin*, vol. 101, no. 7, pp. 885–903, 1989.

[13] J. E. Faulds, N. Hinz, C. Kreemer, and M. Coolbaugh, "Regional patterns of geothermal activity in the Great Basin region, Western USA: correlation with strain rates," *Geothermal Resources Council Transactions*, vol. 36, pp. 897–902, 2012.

[14] A. Genter, L. Guillou-Frottier, J.-L. Feybesse, N. Nicol, C. Dezayes, and S. Schwartz, "Typology of potential hot fractured rock resources in Europe," *Geothermics*, vol. 32, no. 4-6, pp. 701–710, 2003.

[15] M. F. Coolbaugh, G. L. Raines, R. E. Zehner, L. Shevenell, and C. F. Williams, "Prediction and discovery of new geothermal resources in the Great Basin: multiple evidence of a large undiscovered resource base," *Geothermal Resources Council Transactions*, vol. 30, pp. 867–873, 2006.

[16] M. C. Hanson, C. Oze, and T. W. Horton, "Identifying blind geothermal systems with soil CO_2 surveys," *Applied Geochemistry*, vol. 50, pp. 106–114, 2014.

[17] M. Person, S. Kelley, R. Kelley et al., "Hydrogeologic windows: detection of blind and traditional geothermal play fairways in southwestern New Mexico using conservative element concentrations and advective-diffusive solute transport," *Geothermal Resources Council Transactions*, vol. 39, pp. 751–759, 2015.

[18] D. Curewitz and J. A. Karson, "Structural settings of hydrothermal outflow: fracture permeability maintained by fault propagation and interaction," *Journal of Volcanology and Geothermal Research*, vol. 79, no. 3-4, pp. 149–168, 1997.

[19] J. E. Faulds and N. H. Hinz, "Favorable tectonic and structural settings of geothermal systems in the Great Basin region, Western USA: proxies for discovering blind geothermal systems," in *Proceedings World Geothermal Congress 2015*, p. 6, Melbourne, Australia, 2015.

[20] J. E. Faulds, N. H. Hinz, M. F. Coolbaugh et al., "Assessment of favorable structural settings of geothermal systems in the Great Basin, Western USA," *GRC Transactions*, vol. 35, pp. 777–783, 2011.

[21] N. H. Hinz, M. Coolbaugh, L. Shevenell, P. Stelling, G. Melosh, and W. Cumming, "Favorable structural – tectonic settings and characteristics of globally productive arcs," in *41st Workshop on Geothermal Reservoir Engineering*, Stanford University, Stanford, CA, USA, 2016.

[22] G. Bahati, Z. Pang, H. Ármannsson, E. M. Isabirye, and V. Kato, "Hydrology and reservoir characteristics of three geothermal systems in western Uganda," *Geothermics*, vol. 34, no. 5, pp. 568–591, 2005.

[23] K. Aanyu and D. Koehn, "Influence of pre-existing fabrics on fault kinematics and rift geometry of interacting segments: analogue models based on the Albertine Rift (Uganda), western branch-East African Rift system," *Journal of African Earth Sciences*, vol. 59, no. 2-3, pp. 168–184, 2011.

[24] A. B. Katumwehe, M. G. Abdelsalam, and E. A. Atekwana, "The role of pre-existing Precambrian structures in rift evolution: the Albertine and Rhino grabens, Uganda," *Tectonophysics*, vol. 646, pp. 117–129, 2015.

[25] C. K. Morley, *Geoscience of Rift Systems: Evolution of East Africa*, AAPG studies in geology. American Association of Petroleum Geologists, Tulsa, Okla, 1999.

[26] D. Abeinomugisha and R. Kasande, "Tectonic control on hydrocarbon accumulation in the intracontinental Albertine Graben of the East African Rift system," *Tectonics and Sedimentation*, vol. 100, pp. 209–228, 2013.

[27] D. Lirong, W. Jianjun, C. Dingsheng et al., "Geological conditions and petroleum exploration potential of the Albertine Graben of Uganda," *Acta Geologica Sinica - English Edition*, vol. 78, no. 4, pp. 1002–1010, 2004.

[28] T. Karp, C. A. Scholz, and M. M. McGlue, "Structure and stratigraphy of the Lake Albert Rift, East Africa; observations from seismic reflection and gravity data," *AAPG Memoir*, vol. 95, pp. 299–318, 2012.

[29] P. Virransalo, P. Härmä, J. Pokki, T. Manninen, M. Lehtonen, and T. Koistinen, *Geological Map of Uganda, Hoima, Sheet N° NA-36-9., Scale 1/250000*, GTK Consortium, 2012.

[30] A. B. P. Westerhof, P. Härmä, E. M. Isabirye et al., *Geology and Geodynamic Development of Uganda with Explanation of the 1:1,000,000-Scale Geological Map, Special Paper /Geological Survey of Finland*, Geological Survey of Finland, Espoo, Finland, 2014.

[31] K. Link, D. Koehn, M. G. Barth et al., "Continuous cratonic crust between the Congo and Tanzania blocks in western Uganda," *International Journal of Earth Sciences*, vol. 99, no. 7, pp. 1559–1573, 2010.

[32] C. Rollion-Bard, D. Mangin, and M. Champenois, "Development and application of oxygen and carbon isotopic measurements of biogenic carbonates by ion microprobe," *Geostandards and Geoanalytical Research*, vol. 31, no. 1, pp. 39–50, 2007.

[33] K. B. Alexander, W. Cumming, and L. Marini, "Technical review of geothermal potential of Kibiro geothermal prospect, Uganda," in *Proceedings of the 6th African Rift Geothermal Conference*, Addis Ababa, Ethiopia, 2016.

[34] P. Mawejje, V. Kato, J. Nnakirijja et al., "The geology and potential of Kibiro geothermal field in Albertine Graben, western Uganda," *Proceedings of the World Geothermal Congress*, 2015, pp. 1–11, Melbourne, Australia, 2015.

[35] I. Tumwikirize, "Thoughts about techniques applicable in exploration of geothermal resources in Uganda," in *Proceedings of the Third East African Rift Geothermal Conference*, pp. 121–138, Djibouti, Djibouti, 2010.

[36] G. Bahati, K. Vincent, and N. Catherine, "Geochemistry of Katwe-Kikorongo, Buranga and Kibiro geothermal areas, Uganda," in *Proceedings of the Third East African Rift Geothermal Conference*, pp. 223–230, Djibouti, Djibouti, 2010.

[37] J. F. Natukunda, "Geology of Kibiro, Katwe and Buranga geothermal prospects of Uganda," in *Proceedings of the World Geothermal Congress*, pp. 1–13, Bali, Indonesia, 2010.

[38] H. Ármannsson, *Geochemical Studies on Three Geothermal Areas in West and Southwest, Uganda. Final Report*, Geothermal Exploration UGA/92/003, UNDESD, GSMD, Uganda, 1994.

[39] D. K. Muhwezi, "The potential relationship of some geothermal field in Uganda," in *Proceedings of the Third East African Rift Geothermal Conference*, pp. 365–382, Djibouti, Djibouti, 2010.

[40] V. F. Bense, T. Gleeson, S. E. Loveless, O. Bour, and J. Scibek, "Fault zone hydrogeology," *Earth-Science Reviews*, vol. 127, pp. 171–192, 2013.

[41] J. S. Caine, J. P. Evans, and C. B. Forster, "Fault zone architecture and permeability structure," *Geology*, vol. 24, no. 11, pp. 1025–1028, 1996.

[42] D. R. Faulkner, C. A. L. Jackson, R. J. Lunn et al., "A review of recent developments concerning the structure, mechanics and fluid flow properties of fault zones," *Journal of Structural Geology*, vol. 32, no. 11, pp. 1557–1575, 2010.

[43] D. A. Ferrill, A. P. Morris, and R. N. McGinnis, "Crossing conjugate normal faults in field exposures and seismic data," *AAPG Bulletin*, vol. 93, no. 11, pp. 1471–1488, 2009.

[44] M. Person, A. Hofstra, D. Sweetkind et al., "Analytical and numerical models of hydrothermal fluid flow at fault intersections," *Geofluids*, vol. 12, no. 4, pp. 312–326, 2012.

[45] R. H. Sibson, "Structural permeability of fluid-driven fault-fracture meshes," *Journal of Structural Geology*, vol. 18, no. 8, pp. 1031–1042, 1996.

[46] I. S. Moeck, S. Uhlig, B. Loske, A. Jentsch, R. F. Mählmann, and S. Hild, "Fossil multiphase normal faults - prime targets for geothermal drilling in the Bavarian Molasse Basin?," in *Proceedings World Geothermal Congress 2015*, p. 7, Melbourne, Australia, 2015.

[47] H. Fossen and A. Rotevatn, "Fault linkage and relay structures in extensional settings-a review," *Earth-Science Reviews*, vol. 154, pp. 14–28, 2016.

[48] J. V. Rowland and R. H. Sibson, "Structural controls on hydrothermal flow in a segmented rift system, Taupo Volcanic Zone, New Zealand," *Geofluids*, vol. 4, no. 4, pp. 259–283, 2004.

[49] A. Taillefer, R. Soliva, L. Guillou-Frottier, E. Le Goff, G. Martin, and M. Seranne, "Fault-related controls on upward hydrothermal flow: an integrated geological study of the Têt Fault System, Eastern Pyrénées (France)," *Geofluids*, vol. 2017, pp. 1–19, 2017.

[50] N. H. Hinz, M. F. Coolbaugh, J. E. Faulds, D. L. Siler, and G. Dering, "Building the next generation of regional geothermal potential maps: examples from the Great Basin region, Western USA," in *Proceedings World Geothermal Congress 2015*, p. 12, Melbourne, Australia, 2015.

[51] D. L. Siler, J. E. Faulds, B. Mayhew, and D. D. McNamara, "Analysis of the favorability for geothermal fluid flow in 3D: Astor Pass geothermal prospect, Great Basin, northwestern Nevada, USA," *Geothermics*, vol. 60, pp. 1–12, 2016.

[52] A. Gartrell, Y. Zhang, M. Lisk, and D. Dewhurst, "Fault intersections as critical hydrocarbon leakage zones: integrated field study and numerical modelling of an example from the Timor Sea, Australia," *Marine and Petroleum Geology*, vol. 21, no. 9, pp. 1165–1179, 2004.

[53] R. E. Criss, *Principles of Stable Isotope Distribution*, Oxford University Press, New York, NY, USA, 1999.

[54] J. M. Budai, A. M. Martini, L. M. Walter, and T. C. W. Ku, "Fracture-fill calcite as a record of microbial methanogenesis and fluid migration: a case study from the Devonian Antrim Shale, Michigan Basin," *Geofluids*, vol. 2, no. 3, pp. 162–183, 2002.

[55] C. D. Curtis, M. L. Coleman, and L. G. Love, "Pore water evolution during sediment burial from isotopic and mineral chemistry of calcite, dolomite and siderite concretions," *Geochimica et Cosmochimica Acta*, vol. 50, no. 10, pp. 2321–2334, 1986.

[56] J. Hoefs, *Stable Isotope Geochemistry*, Springer Berlin Heidelberg, Berlin, Heidelberg, 2009.

[57] F. J. Longstaffe, "Stable isotope studies of diagenetic processes," in *Stable Isotope Geochemistry of Low Temperature Processes, Short Course Handbook*, T. K. Kyser and R. Kerrich, Eds., p. 452, Mineralogical Association of Canada, Saskatoon, Saskatchewan, 1987.

[58] Z. Sharp, *Principles of Stable Isotope Geochemistry*, Pearson/-Prentice Hall, Upper Saddle River, NJ, USA, 1st edition, 2007.

[59] P. Černy and R. Chapman, "Adularia from hydrothermal vein deposits; extremes in structural state," *Canadian Mineralogist*, vol. 24, pp. 717–728, 1986.

[60] G. Dong and G. W. Morrison, "Adularia in epithermal veins, Queensland: morphology, structural state and origin," *Mineralium Deposita*, vol. 30, no. 1, pp. 11–19, 1995.

[61] H. L. Barnes, Ed., *Geochemistry of Hydrothermal Ore Deposits*, Wiley, New York, NY, USA, 3rd edition, 1997.

[62] V. Kato and M. Kraml, "Geochemistry of Rwenzori hot spring waters," in *Proceedings of the 3rd East African Rift Geothermal Conference*, p. 12, Djibouti, Djibouti, 2010.

[63] J. F. Natukunda and G. Bahati, "Status of geothermal energy exploration at Buranga prospect western Uganda," in *Proceedings of the 6th African Rift Geothermal Conference*, p. 13, Addis Ababa, Ethiopia, 2016.

[64] M. Lindenfeld, G. Rümpker, K. Link, D. Koehn, and A. Batte, "Fluid-triggered earthquake swarms in the Rwenzori region, East African Rift—evidence for rift initiation," *Tectonophysics*, vol. 566-567, pp. 95–104, 2012.

Hindawi
Geofluids
Volume 2019, Article ID 1379093, 24 pages
https://doi.org/10.1155/2019/1379093

Review Article

Assessment of Chaves Low-Temperature CO_2-Rich Geothermal System (N-Portugal) Using an Interdisciplinary Geosciences Approach

J. M. Marques,[1] **P. M. Carreira**,[2] **L. A. Aires-Barros**,[1] **F. A. Monteiro Santos**,[3] **M. Antunes da Silva**,[4] **and P. Represas**[5]

[1]*Instituto Superior Tecnico (CERENA/IST), Universidade de Lisboa, Av. Rovisco Pais 1049-001 Lisboa, Portugal*
[2]*Centro de Ciências e Tecnologias Nucleares, Instituto Superior Técnico (C²TN/IST), Universidade de Lisboa, Estrada Nacional 10, ao km 139, 7 2695-066 Bobadela LRS, Portugal*
[3]*Universidade de Lisboa-DEGGE-IDL, Campo Grande Ed. C8, 1749-016 Lisboa, Portugal*
[4]*Super Bock Group, Apartado 1044, 4466-955 S. Mamede de Infesta, Portugal*
[5]*Laboratório Nacional de Energia e Geologia, Estrada da Portela, Bairro do Zambujal, Apartado 7586-Alfragide 2610-999 Amadora, Portugal*

Correspondence should be addressed to J. M. Marques; jose.marques@tecnico.ulisboa.pt

Received 2 July 2018; Revised 31 October 2018; Accepted 26 November 2018; Published 25 February 2019

Guest Editor: Matteo Lupi

This paper reviews the results of a multi- and interdisciplinary approach, including geological, geomorphological, tectonic, geochemical, isotopic, and geophysical studies, on the assessment of a Chaves low-temperature (77°C) CO_2-rich geothermal system, occurring in the northern part of the Portuguese mainland. This low-temperature geothermal system is ascribed to an important NNE-trending fault, and the geomorphology is dominated by the "Chaves Depression," a graben whose axis is oriented NNE-SSW. The study region is situated in the tectonic unit of the Middle Galicia/Trás-os-Montes subzone of the Central Iberian Zone of the Hesperic Massif comprising mainly Variscan granites and Paleozoic metasediments. Chaves low-temperature CO_2-rich geothermal waters belong to the Na-HCO_3-CO_2-rich-type waters, with pH ≈ 7. Total dissolved solids range between 1600 and 1850 mg/L. Free CO_2 is of about 500 mg/L. The results of SiO_2 and K^2/Mg geothermometers give estimations of reservoir temperature around 120°C. $\delta^{18}O$ and δ^2H values of Chaves low-temperature CO_2-rich geothermal waters indicate a meteoric origin for these waters. No significant ^{18}O-shift was observed, consistent with the results from the chemical geothermometry. $\delta^{13}C_{CO2}$ values vary between −7.2 and −5.1‰ vs. V-PDB, and $CO_2/^3He$ ratios range from 1×10^8 to 1×10^9, indicating a deep (upper mantle) source for the CO_2. $^3He/^4He$ ratios are of about 0.9 (R/Ra). The Chaves low-temperature CO_2-rich geothermal waters present similar $^{87}Sr/^{86}Sr$ ratios (between 0.728035 and 0.716713) to those of the plagioclases from granitic rocks (between 0.72087 and 0.71261) suggesting that water mineralization is strongly ascribed to Na-plagioclase hydrolysis. Geophysical methods (e.g., resistivity and AMT soundings) detected conductive zones concentrated in the central part of the Chaves graben as a result of temperature combined with the salinity of the Chaves low-temperature CO_2-rich geothermal waters in fractured and permeable rock formations. This paper demonstrates the added value of an integrated and multi- and interdisciplinary approach for a given geothermal site characterization, which could be useful for other case studies linking the assessment of low-temperature CO_2-rich geothermal waters and cold CO_2-rich mineral waters emerging in a same region.

1. Introduction

The aim of this paper is to present an overview of the results achieved on the assessment of the Chaves low-temperature CO_2-rich geothermal system, occurring in the northern part of the Portuguese mainland. Low-temperature geothermal systems are those where the reservoir temperature is below 150°C and often characterized by hot or boiling springs (see [1, 2]). A multi- and interdisciplinary approach, including geological, tectonic, geochemical, isotopic, and geophysical studies, has been established in order to update the conceptual circulation model of a Chaves low-temperature CO_2-rich geothermal system. The Chaves low-temperature CO_2-rich geothermal waters flow from natural springs (66°C) and boreholes (77°C) and are mainly used, in a cascade system, for space heating (municipal swimming pool and a hotel) and balneotherapy (at the local spa). At Chaves, the depth reached by the exploitation boreholes is around 150 m depth.

In both high- and low-temperature geothermal systems, surface manifestations of geothermal fluids circulation are usually a subject of large scientific importance. Hot mineral waters discharging in a given area, hydrothermal alteration features identified in drill cores from boreholes, and deposition materials around springs can be detected and carefully studied providing a lot of data with rather low costs (e.g., [3, 4]). Usually, travertine depositions around springs are indicators of geothermal reservoir temperatures that may be too low to generate electricity but may have direct-use applications such as for greenhouses or hot-water heating for nearby communities. As described by [5], potential problems with well-scaling may also be present. Such type of information should be used in geothermal resource assessment of a possible area for development. Exploration-data (e.g., geological, geotectonical, hydrogeological, geochemical, isotopic, and geophysical) should be used to develop a "clear picture" of a given low-temperature geothermal system and, when used in parallel, can provide key information on the origin and "age" of the geothermal waters, underground flow paths, and water-rock interaction occurring at depth and could assist in selecting future drilling sites (e.g., [2]).

In the map of Figure 1, we can observe the distribution of the geothermal heat flow density ($mW.m^{-2}$) in Europe [6]. According to [7], the thermal models for the study region indicate a mean heat flow value of 95 $mW.m^{-2}$, derived from borehole measurements. Heat flow measurements and the estimation of geothermal gradients are essential aspects of geothermal resource research, providing a good approximation of the temperature at the top of the reservoir (e.g., [2]).

Carbon dioxide (CO_2-rich) geothermal waters have been of interest to people, historically since the Roman times and possibly beyond, and surface manifestations in the form of springs are an important resource, exploited for health, consumption, and industrial use as well as having religious and political importance to certain regions of the world [8, 9]. The global prevalence of these waters is widespread, with CO_2-rich spring waters discharging in a variety of geological and tectonic settings, a source of specific geochemical characteristics (e.g., [10, 11]).

Several studies propose that areas of high heat flow in Western, Central, and Eastern Europe correspond to areas of CO_2 discharge originating from the metamorphism of marine carbonates, as well as a mantle origin (e.g., [12]). The extent of CO_2 production in Europe and central Asia is much larger than that of the Pacific ring, which is proposed to be at least partly due to the extensive orogenic belts of Europe and Asia Minor and the related regional metamorphism (e.g., [13]).

Some important European case studies of reference are here synthetically reviewed, in consideration of the multidisciplinary studies involved and due to the fact that in such hydrogeological systems (as in the Chaves region) both geothermal and cold CO_2-rich springs are present, with the cold CO_2-rich springs those presenting the highest mineralization.

Western Germany is home to geological terrains of important volcanic and tectonic activity, with numerous occurrences of naturally emerging CO_2-rich springs in the Rhenish Massif. The CO_2-rich waters which emerge in the Rhenish Massif contain gas of mantle origin and discharge in a geological setting of Cenozoic alkali basaltic volcanism, with the CO_2 discharges concentrated in volcanic fields (e.g., [14, 15]). The Massif Central (France), an extensive area of recent volcanism and tectonic activity, is host to many CO_2-rich geothermal springs. These CO_2-rich waters also have gas of mantle origin and emerge from Quaternary volcanic rocks or Paleozoic granites at temperatures up to 80°C (e.g., [16–19]). In central Italy, the topographically low-lying hydrogeological setting is composed of several Quaternary volcanic systems, with many geothermal springs. The CO_2-rich springs have a mixture of mantle and biogenic CO_2 and emerge in volcanic and carbonate terrains (e.g., [20]). Galicia, northwest Spain, is home to CO_2-rich geothermal and mineral waters. These geothermal and mineral waters range in temperature, from 15°C to 57.2°C with a pH ranging from 5.96 to 9.83. In Ourense, Galicia, high-temperature springs emerge within granitic rocks which form part of the Hesperian Massif. These Spanish springs are located on the same NNE-SSW fault lineament of the Chaves spring's emergence. The Ourense springs have a temperature ranging from 46 to 69°C, with the origin of CO_2 likely from an upper mantle source (e.g., [21]). The Reykjanes Peninsula, located in southwest Iceland, exhibits a high-temperature basaltic geothermal system with high-temperature (>220°C) CO_2-rich geothermal fluids at a depth of up to 1200 m. The mantle-based origin of CO_2 is due to mid-ocean ridge spreading, and the presence of water at this depth is due to an influx of seawater (e.g., [22]). Karlovy Vary, Czech Republic, located in the Sokolov Basin, has CO_2-rich geothermal springs with temperatures of up to 73°C. The recharge of these waters originates in granitic blocks on the sides of the valley, with water deeply circulating (2,000-2,500 m) along faults (e.g., [23]). The CO_2 origin is from a deep source, likely the mantle (e.g., [24]). Hot CO_2-rich geothermal springs emerge in Kuzuluk/Adapari, northwestern Turkey, an extensional tectonic setting within the seismically active North Anatolian Fault Zone. CO_2 originates from decomposition of marine carbonates and mantle outgassing (e.g., [25]).

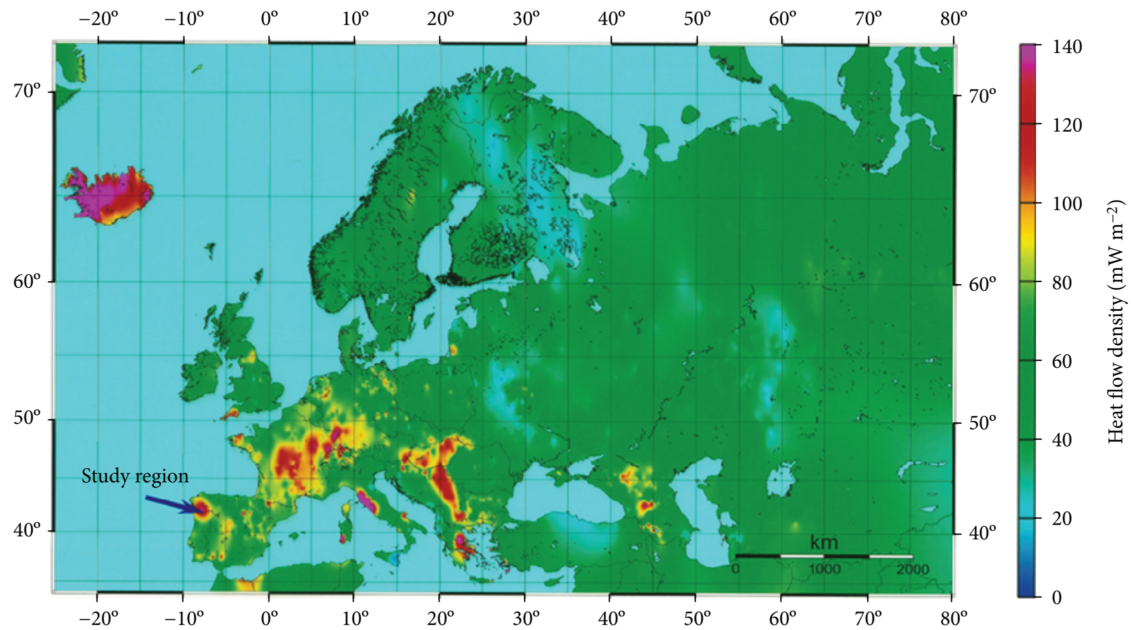

Figure 1: Distribution of the geothermal heat flow density (mW.m^{-2}) in Europe (courtesy Hurter, 1999, taken from [27]).

As already mentioned, in most of the case studies referred above, geothermal and cold CO_2-rich mineral waters discharge in the same region, as in the case of the Chaves geothermal area. As discussed by [25, 26], in CO_2-rich mineral water systems, water-rock interaction is enhanced at low temperature, since the resulting increased solubility of CO_2 in water reduces the pH of the waters and increases the water aggressiveness to the rock. This explains the higher total dissolved solids (TDS) in the cold CO_2-rich mineral waters of a given hydrogeological system.

Several studies carried out on the northern part of the Portuguese mainland (e.g., [27–38]) have provided a comprehensive characterization of the Chaves low-temperature CO_2-rich geothermal system. Several hypotheses have been formulated to assess the origin of the low-temperature geothermal waters and the mechanisms of their being upward from the reservoir towards the surface. In this paper, a review of the results obtained so far will be presented and discussed, with a special emphasis on the multi- and interdisciplinary approaches which enabled the development of the hydrogeological conceptual circulation model of the Chaves low-temperature CO_2-rich geothermal system. Geochemical and isotopic signatures of local/regional cold (≈17°C) CO_2-rich mineral waters from Vilarelho da Raia (N of Chaves) and Vidago/Pedras Salgadas (S of Chaves) are also presented and discussed, for comparison with the Chaves low-temperature CO_2-rich geothermal waters.

2. Geomorphologic, Geological, and Tectonic Settings

From the hydrogeological point of view, fractures and discontinuities are amongst the most important of geological structures. Most rocks (like granitic rocks) possess fractures and other discontinuities which facilitate storage and movement of ascendant fluids through them [39]. The Chaves geothermal area (Figure 2) is located in the tectonic unit of the Middle Galicia/Trás-os-Montes subzone of the Central Central-Iberian Zone of the Hesperic Massif [40, 41].

From the hydrogeologic point of view, such terrains are comprehensive archives of the continental crust, including outstanding information on its magmatic, tectonic, and metamorphic evolution. These issues are extremely important to understand where the hottest low-temperature geothermal waters are found in Portuguese mainland (discharge temperature at Chaves – 77°C).

The geomorphology is controlled by the so-called Chaves Depression, a graben whose axis is NNE-SSW-trending. The eastern block of Chaves graben is formed by the edge of the Padrela Mountain escarpment (with a 400 m throw). At the west, several grabens, coming in a staired tectonic configuration from the Heights of Barroso towards the "Chaves Depression," can be found [42].

The regional geology (Figure 2) has been described by [42–44]. According to those authors, the main geological formations are (i) Hercynian granites (syn-tectonic: 310 Ma and post-tectonic: 290 Ma) and (ii) Silurian metasediments (quartzites, phyllites, and carbonaceous slates). On the W block of Chaves graben, the syn-tectonic granites present a medium- to coarse-grained texture, with abundant biotite and muscovite (approximately 10 to 15% of the modal composition). Quartz appears strongly tectonized. Na-plagioclase (An7–An8) is occasionally intensely sericitized while K-feldspar remains unaltered. Biotite is locally chloritized. On the E block of Chaves graben, the post-tectonic granites have a coarse-grained to porphyritic texture, with biotite and muscovite (with biotite being predominant). Microcline-perthite and Na-plagioclase (near the limit albite/oligoclase) can also be observed. Biotite is

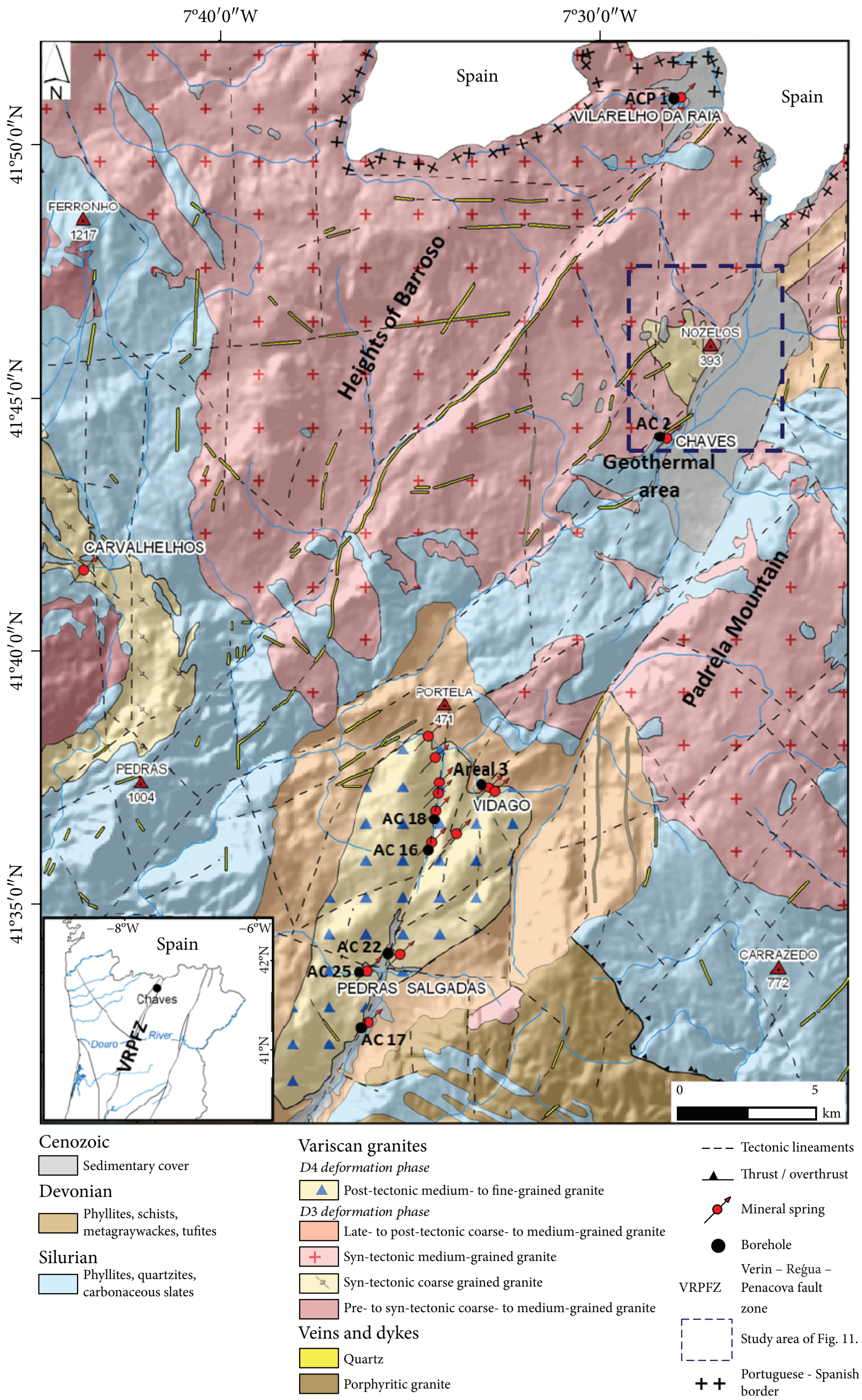

Figure 2: Regional geological map of the Chaves region (NW Portugal), showing the location of Vilarelho da Raia, Chaves, Vidago, and Pedras Salgadas CO_2-rich mineral waters. Adapted from [27].

very chloritized. At Vidago–Pedras Salgadas areas (S of the Chaves geothermal area – Figure 2), the post-tectonic granites present a medium- to fine-grained texture (sometimes porphyritic). K-feldspar (orthoclase and microcline) quartz, Na-plagioclase, and biotite occur as major minerals. Quartzites comprise a mosaic of fine-grained quartz intergrown with an intensely indented granoblastic texture, with discrete thin beds of white mica spread in the quartz grains. Sometimes, micaceous films (mainly muscovite) are present, giving a schistose texture enhancing strong tectonization. The phyllites (andalusitic) have a granoblastic texture, showing a silky sheen on schistosity surfaces. The carbonaceous slates present a lepido-granoblastic texture and a well-marked foliation. Graphite (very abundant) alternates with beds of white mica and occurs in continuous beds, sometimes forming small lenticules. The most recent geological formations are Miocene-Pleistocene graben-filling sediments with their maximum development along the central axis of Chaves graben [42–44] (Figure 2).

Concerning fracture and structural main features, [45] considered three main Late-Variscan strike-slip fault systems in the northern sector of Iberia: the dominant NE-NNE (always sinistral), the subordinate and conjugate NW-NNW (dextral), and the E-ENE (mainly sinistral). From this geometry and kinematics, [45] concluded that the N-S maximum compressive stress field was responsible for the development of the whole of the fracture/faulting network in Iberia.

In the Chaves region, the ascending low-temperature CO_2-rich geothermal waters are structurally controlled by the so-called Verin-Régua-Penacova fault zone (VRPFZ – Figure 2) [40, 41, 46], related to Alpine Orogeny, which trends 70°-80°E and is hydrothermally active along a belt extending 150 km through mainland Portugal (Figure 3). Along this tectonic megalineament lie not only the Chaves low-temperature CO_2-rich geothermal waters (the only geothermal waters in the study region) but also numerous emanations of cold (17°C) CO_2-rich mineral waters (e.g., Vilarelho da Raia, Vidago, and Pedras Salgadas), with no signs of a geothermal origin as discussed in detail by [27–38], which are used in local spas (see Figures 2 and 3).

As stated by [44], the Chaves low-temperature CO_2-rich geothermal waters and the cold CO_2-rich mineral waters discharge preferentially in places where some of the following subvertical fracture systems intersect: (1) N-S to NNE-SSW, (2) ENE-WSW, (3) NNW-SSE to NW-SE, and (4) WNW-ESE to W-E. It is also important to emphasise that, since the NNE-SSW megalineament reaches great depths (≈ 30 km) in the study region, as referred by [43], it should play an important role, not only on geothermal and mineral waters ascent but also in CO_2 extraction and migration from a deep (upper mantle) source to the surface. In the study region, geothermal waters issue (with discharge temperature of 77°C) only at the Chaves area ascribed to the fact that they emerge within a wide morphotectonic structure (the Chaves Graben - 3 km width by 7 km length – see Figures 2 and 3) with a thickness of graben filling sediments greater than 250 m, as stated by [43, 44]. On the other hand, in the case of Vidago and Pedras Salgadas cold (17°C) CO_2-rich mineral waters, they issue in locations where local structures (small grabens) do not show such huge structural signatures (see Figures 2 and 3).

In fact, the model proposed by [43] for the Vidago and Pedras Salgadas regions, based on tectonic and geomorphological features, points out the existence of a narrow graben (1 to 2 km wide) related with an also shallow reservoir. Therefore, as stated by [43, 44], deeper low-temperature geothermal water circulation occurs only in the Chaves area because of (i) high relief, (ii) deep fracturing, and (iii) thickness of graben-filling sediments (see [38]).

As can be observed in Figure 3, the crossed graben-horst system, comprising of the fracture families NNE-SSW and ENE-WSW, is associated to a tectonic lineament originated by the Hercynian fracturing of the Hesperic Massif [43, 44]. This system, which is currently active, was reactivated in the Cenozoic due to the compressional tectonics of the Alpine orogeny, with the local formation of pull-apart basins [43, 44]. The location of the CO_2-rich springs is mainly determined by the tectonic structures of the region, being situated in the areas of the longitudinal grabens (NNE-SSW) where subsidence is significant and at the intersection of these grabens with the transverse graben-horst systems.

3. Geochemistry of the Waters

Water samples for chemical and isotopic analyses were collected from (i) the Chaves low-temperature CO_2-rich geothermal system (from geothermal springs and boreholes); (ii) the Vilarelho da Raia, Vidago, and Pedras Salgadas cold (≈ 17°C) CO_2-rich mineral waters (from boreholes), and (iii) the local/regional shallow cold dilute normal groundwater systems (from springs). Temperature (°C), pH, and electrical conductivity (μS/cm) were measured in situ. Chemical analyses were performed at the Laboratório de Mineralogia and Petrologia do Instituto Superior Técnico, Universidade Técnica de Lisboa (LAMPIST), Portugal, using the methodology described in [27]. Chaves low-temperature CO_2-rich geothermal waters (discharged from springs and exploited from boreholes – AC1 and AC2) are Na-HCO_3-CO_2-rich-type waters, which display temperatures between 66 and 77°C, dry residuum (DR) ranging from 1600 to 1850 mg/L, and free CO_2 from 350 to 1100 mg/L (see [29, 33, 36, 38]). The associated gas phase issued from the CO_2-rich springs at Chaves is practically pure at $CO_2 \approx 99.5\%$ volume ($O_2 = 0.05\%$, $Ar = 0.02\%$, $N_2 = 0.28\%$, $CH_4 = 0.009\%$, $C_2H_6 = 0.005\%$, $H_2 = 0.005\%$, and $He = 0.01\%$ in [47]).

In many parts of the world, and Portugal is not an exception, it is not uncommon to find natural springs of CO_2-rich waters discharging at surface with various temperatures at a distance of few km (e.g., [21, 25, 48]). In fact, in the Chaves region, the tectonic/geomorphological structures (Chaves, Vidago, and Pedras Salgadas grabens – see Figure 3) and the different kinds of granitic and schistose rocks results in the occurrence of the Chaves low-temperature CO_2-rich geothermal waters and the cold CO_2-rich mineral waters of Vilarelho da Raia, Vidago, and Pedras Salgadas, discharging along the same NNE-trending fault. According to [29, 33, 36, 38], the Vilarelho da Raia cold (≈ 17°C) spring and borehole CO_2-rich mineral waters show similar chemical composition comparatively to Chaves low-temperature CO_2-rich geothermal waters. DR values are between 1790 and 2260 mg/L, and free CO_2 is of about 790 mg/L. Vidago and Pedras Salgadas cold (≈ 17°C) spring and borehole CO_2-rich mineral waters present higher Ca^{2+}, Mg^{2+}, and free CO_2 content (up to 2500 mg/L). In the Piper diagram

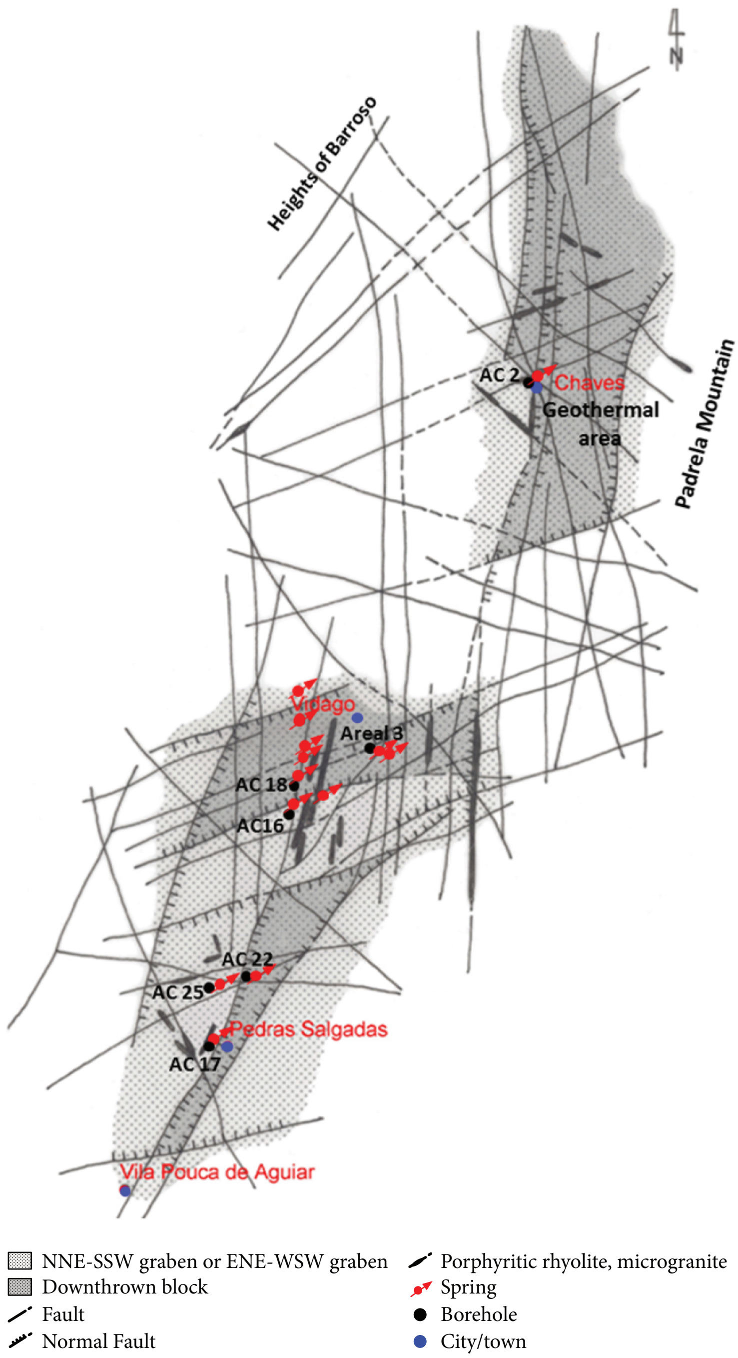

Figure 3: Structural lineation map showing the subsidence zones in the Chaves, Vidago, and Pedras Salgadas basins. Adapted from [106].

of Figure 4, one can observe that the cold CO_2-rich mineral waters of Vidago and Pedras Salgadas, although strongly dominated by HCO_3^- and Na^+, present relatively high-alkaline earth metal (Ca^{2+} and Mg^{2+}) concentrations indicative of the increasing solubility of these divalent ions with decreasing temperature, as described by [25, 34]. From the observation of the ternary Cl-HCO_3-SO_4 diagram of Figure 4, it is possible to conclude that there is no mixing trend between the CO_2-rich mineral waters and the local shallow cold dilute normal groundwaters of the region (which commonly belong to the Na-HCO_3-type waters).

Like in other parts of the world (e.g., [21, 25, 48]), the studied cold CO_2-rich mineral waters show much higher mineralization. In some cases, as in Vidago AC18 borehole waters, DR ($\approx$ 4300 mg/L) is more than twice the TDS of the Chaves low-temperature CO_2-rich geothermal waters (e.g., [29]). Representative analyses of the studied low-temperature CO_2-rich geothermal waters and of the cold CO_2-rich mineral waters, as well as of the local shallow cold dilute normal groundwaters, are presented in Table 1.

As described by [25, 48], in CO_2-rich hydromineral systems, carbon dioxide is one of the most important

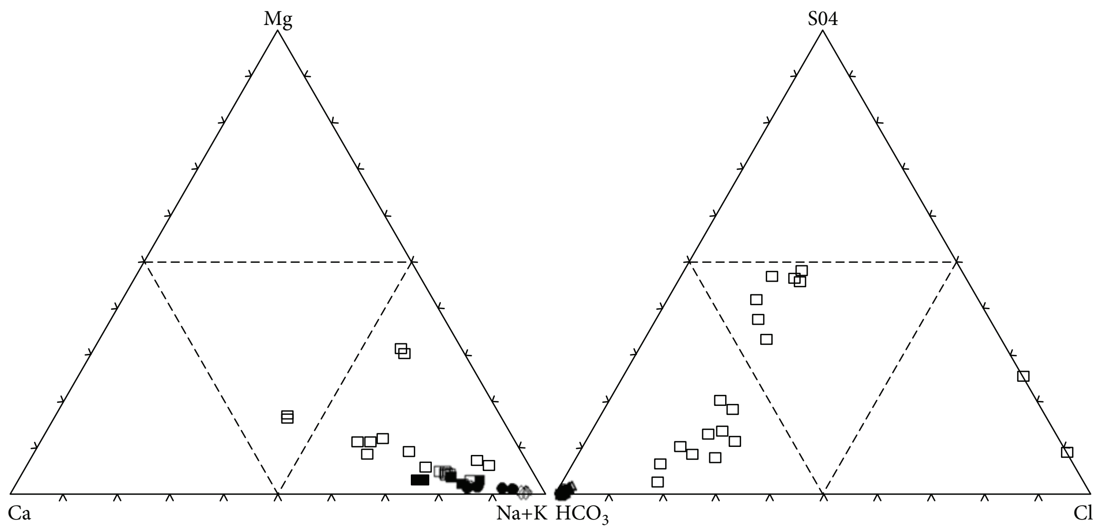

FIGURE 4: Piper diagram for the (△) Chaves low-temperature CO_2-rich geothermal waters and the (⋄) Vilarelho da Raia, (•) Vidago, and (■) Pedras Salgadas cold CO_2-rich mineral waters. For comparison, the (□) local shallow cold dilute normal groundwaters of the region were also plotted. Taken from [30].

TABLE 1: Representative physicochemical data of the Chaves low-temperature CO_2-rich geothermal system and the cold CO_2-rich mineral waters of the region. Typical physicochemical signatures of the local shallow cold dilute normal groundwaters were also included. Concentrations in mg/L. Table 1 is reproduced from Marques et al. (2006) [under the Creative Commons Attribution License/public domain].

Reference	Local	Type	T (°C)	pH	Cond.	Na	K	Ca	Mg	Li	HCO_3	SO_4	Cl	NO_3	F	SiO_2	DR
ACP1 (⋄)	Vilarelho da Raia	(bw)	17.2	6.6	2350	600	22.8	26.3	5.25	1.20	1579	13.0	21.5	0.3	5.40	54.9	1523
AC2 (△)	Chaves	(bw)	77.0	6.9	2550	668	62.5	22.1	5.25	2.68	1707	18.3	35.3	n.d.	7.20	86.1	1702
Nas. (△)	Chaves	(sp)	66.0	6.8	2430	633	63.0	23.4	5.75	2.56	1604	23.8	38.1	0.3	6.90	82.9	1634
Castelões (□)	Chaves	(sp)	11.6	5.8	36	5	0.5	1.3	0.40	0.04	12	0.4	2.7	1.8	0.15	21.6	31
AC16 (●)	Vidago	(bw)	17.6	6.1	1910	423	37.3	73.5	11.50	1.94	1286	7.9	17.3	n.d.	3.50	58.4	1217
AC18 (●)	Vidago	(bw)	17.0	6.7	6230	1525	106.5	223.0	37.00	6.40	4689	1.9	66.0	1.6	3.40	59.8	4346
Areal 3 (●)	Vidago	(bw)	12.3	6.9	6250	1585	96.5	132.0	28.00	9.44	5418	n.d.	54.0	n.d.	2.70	68.1	4205
Baldio (□)	Vidago	(sp)	11.9	6.4	74	9	0.2	2.8	1.25	0.01	11	10.3	5.3	3.8	n.d.	26.5	76
AC17 (■)	Pedras Salgadas	(bw)	16.1	6.3	2880	580	28.3	183.5	26.00	2.00	2010	10.3	32.0	n.d.	2.50	79.9	1886
AC25 (■)	Pedras Salgadas	(bw)	17.9	6.4	4120	957	48.5	193.0	50.00	3.10	3057	2.3	32.6	n.d.	1.50	73.9	2781
AC22 (■)	Pedras Salgadas	(bw)	14.8	6.5	5340	1285	37.0	227.0	41.00	1.00	4546	n.d.	51.0	n.d.	1.00	61.2	3663

Notes: T: water temperature; Cond. : electrical conductivity in μS/cm; DR: dry residuum; n.d.: not detected (below detection limits). (△) Chaves low-temperature CO_2-rich geothermal waters; cold CO_2-rich mineral waters from (⋄) Vilarelho da Raia, (●) Vidago, and (■) Pedras Salgadas. (□) stands for local shallow cold dilute normal groundwaters. sp: stands for spring waters; bw: stands for borehole waters.

"components/parameters" that influences the physical and chemical signatures of the fluids. Low temperatures enhance water-rock interaction since the solubility of CO_2 in water increases with decreasing temperature. Therefore, the pH of the cold groundwaters will decrease as the result of the CO_2 incorporation in a shallow low-temperature environment and the aggressiveness, of the waters will increase leading to a more active water-rock interaction and metal dissolution. This trend could explain the higher mineralization of most of the cold CO_2-rich mineral waters found in the region (e.g., Vidago AC18, Areal 3, and Pedras Salgadas AC22 borehole waters).

The mineralization of the Chaves low-temperature CO_2-rich geothermal waters and of the cold CO_2-rich mineral waters is strongly controlled by HCO_3^- and Na^+ (see Table 1), pointing to the hydrolysis of the Na-plagioclases of the granitic rocks as the main water-rock interaction process responsible for the water chemistry (see [26] and Figure 5). Also, as stated by [49], acid hydrolysis of plagioclase and biotite could be the main source of salinity in groundwaters percolating through granitic rocks.

Besides, as stated by [29], the constant ratios of major ionic species (e.g., HCO_3 and Na) plotted against a conservative element such as Cl indicate that the chemistry of these waters would be related with a similar geological environment. By observing Figure 5, we can formulate the hypothesis that Cl^- present in the Chaves low-temperature CO_2-rich geothermal waters and in the cold CO_2-rich mineral waters

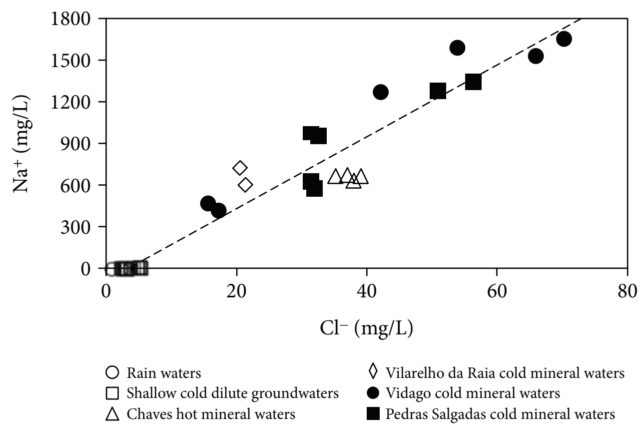

Figure 5: Cl^- vs. Na^+ for the studied waters. The dashed line stands for a concentration trend from the regional dilute groundwaters towards the high mineralized waters. Figure 5 is reproduced from Marques et al. (2006) [under the Creative Commons Attribution License/public domain].

is also the result of water-rock interaction, since the increase in Na^+ concentration in these waters is accompanied by an increase of Cl^-.

Chloride is found in small amounts in some silicate and phosphate minerals, usually found in different minerals from granitic rocks, including biotite, amphibole, and apatite (e.g., [50]). In the diagram of Figure 5, the data from Chaves low-temperature CO_2-rich geothermal waters (from borehole AC2 and a spring) form a cluster, which is a good indication of the existence of a common reservoir for these waters.

On the other hand, the Vilarelho da Raia, Vidago, and Pedras Salgadas cold CO_2-rich mineral waters have different chemical tracer contents, indicating different underground flow paths and/or water-rock interaction with different types of granitic rocks. Higher salinities (e.g., Vidago AC18 CO_2-rich borehole waters) should correspond to larger residence times associated to shallow underground flow paths, since Vidago AC18 are cold waters.

In the case of Chaves low-temperature CO_2-rich geothermal waters, the reservoir fluid may become mixed with cold groundwaters at shallow levels, resulting in the change of the deep fluid chemistry by leaching and reaction with wall rocks during the upflow. Therefore, the results of chemical geothermometers were interpreted with caution and correlated with the results achieved by other disciplines such as isotope hydrology and geophysics.

Many chemical geothermometers have been proposed, both qualitative and quantitative. The most usually used include the quartz and chalcedony geothermometers [51–54], the feldspar (Na-K) geothermometers [55, 56], the Na-K-Ca and Na-K-Ca-Mg geothermometers [57, 58], and the Na-Li geothermometer [59].

As mentioned by [60], in the case of Chaves low-temperature CO_2-rich geothermal waters and Vilarelho da Raia, Vidago, and Pedras Salgadas cold CO_2-rich mineral waters, the results of SiO_2 and K^2/Mg geothermometers are in fair agreement (see Table 2). However, the Na/K and Na-K-Ca geothermometers give higher temperatures, and the Na/Li geothermometer, indicated by [61] as a good thermometric index for CO_2-rich waters of the French Massif Central, seems to give rise to an overestimation of the deep temperatures.

As stated by [26, 62], the lower SiO_2 contents observed in Vilarelho da Raia, Vidago, and Pedras Salgadas cold CO_2-rich mineral waters should be faced as a clear indication for rather low water-rock interaction temperatures (see [26]), in a shallow environment, and should not be attributed to silica deposition during ascent of the waters, because precipitation of chalcedony or quartz is very rare at low temperatures.

In order to solve the discrepancies related to silica and some of the cation geothermometers, [60] have adopted a methodology described by [21]. According to that approach, in a log (H_4SiO_4) vs. log (Na/K) diagram, where the equilibrium quartz/chalcedony–adularia–albite was assessed, the whole studied CO_2-rich waters lie in the domain of not equilibrated waters. Using the methodology developed by [63, 64], the same authors [60] concluded that, in the classical $Na/400–Mg^{1/2}–K/10$ diagram, the Chaves, Vidago, and Pedras Salgadas CO_2-rich waters are immature waters, while the Vilarelho da Raia CO_2-rich waters are located in the area of partial equilibrium with the host rocks at much higher temperatures (between 160°C and 180°C) than those presented in Table 2.

These results seem to indicate that chemical geothermometers should be applied with great caution to the Chaves low-temperature CO_2-rich geothermal waters and that in the case of the cold CO_2-rich mineral waters the circulation depth should be assessed using the results from other disciplines such as hydrogeochemistry and isotope hydrology, namely bearing in mind the presence of tritium in the cold CO_2-rich mineral waters (as discussed later in Section 4).

Even considering all restrictions on the applicability of chemical geothermometers to CO_2-rich waters, it makes sense to consider acceptable the estimations of deep temperature around 120°C, for the Chaves low-temperature CO_2-rich geothermal waters, which are in agreement with the discharge temperature (77°C) of these waters. Considering the mean geothermal gradient of 30°C/km [7], a maximum depth of about 3.5 km reached by the Chaves water system was estimated [29]. This value was obtained considering that

$$\text{Depth} = (T_r - T_a)/\text{gg}, \tag{1}$$

where T_r is the reservoir temperature (120°C), T_a is the mean annual air temperature (15°C), and gg is the geothermal gradient (30°C/km).

Accepting that water mineralization is more controlled by the availability of CO_2 rather than by the temperature (see [26]), the cold (≈ 17°C) CO_2-rich mineral waters from Vilarelho da Raia, Vidago, and Pedras Salgadas should be faced as different stages of water-rock interaction processes involving local circulation of cold shallow groundwaters. As stated by [65], carbon dioxide waters, if they are not thermal,

Table 2: Reservoir temperatures (°C) of Chaves low-temperature CO_2-rich geothermal waters and of Vilarelho da Raia, Vidago, and Pedras Salgadas cold CO_2-rich mineral waters, estimated from chemical geothermometers. Adapted from [29, 60].

Local	Ref.	Chalc. (1)	Quartz (2)	Na-K-Ca (3)	Na-K-Ca (Mg) (4)	Na/K (5)	Na/Li (6)	K^2/Mg (7)
V. da Raia	Facha **	70	100	146•	124	101	116	103
Chaves	AC1*	90	120	203+	118	188	178	120
	AC2 *	91	121	210+	132	204	193	125
	Spr. 3 **	92	121	206+	121	191	178	123
Vidago	AC16*	72	102	126•	96	176	211	93
	AC18*	74	104	177•	89	171	188	111
P. Salgadas	AC17*	92	121	106•	92	127	177	80

Notes: (1) Fournier and Truesdell (1974) - in [54]; (2) [56] - cooling by conduction; (3) [57]; (4) [58]; (5) White and Ellis (1970) - in [56]; (6) [59]; and (7) [63]. *Borehole water; **spring waters; $^{+}\beta = 1/3$; $\bullet\beta = 4/3$.

are not indicative of hydrothermal systems in the subsurface. According to the convention adopted in the "Atlas of Geothermal Resources in Europe" [66], a given groundwater is considered to be thermal if the discharge temperature exceeds 20°C.

4. Isotopic Composition of the Waters and Gas Phase

Isotope geochemistry has greatly contributed to (i) the present understanding of the Chaves low-temperature CO_2-rich geothermal system and (ii) the increase in knowledge on the relations with the regional cold CO_2-rich mineral waters from Vilarelho da Raia, Vidago, and Pedras Salgadas, discharging along the same NNE-trending fault. In this paper, we review the use of isotope geochemistry to address key questions to update the conceptual model of the Chaves low-temperature CO_2-rich geothermal system, in particular to recharge and underground flow paths, emphasising the use of stable isotope data integrated with chemical and other relevant data, such as lithology, geomorphology, and geophysics, in order to achieve important results.

δ^2H and δ^{18}O were determined three times for each water sample in order to increase the analytical precision. All isotopic determinations were performed in the former Instituto Tecnológico e Nuclear (ITN) – Chemistry Department, Sacavém, Portugal – presently Centro de Ciências e Tecnologias Nucleares, Instituto Superior Técnico (C^2TN/IST), Universidade de Lisboa, Portugal. The measurements were conducted on a mass spectrometer SIRA 10-VG ISOGAS using the methods described in [67, 68] for ^{2}H and ^{18}O, respectively. The tritium content was determined using the electrolytic enrichment and liquid scintillation counting method described by [69] and by [70], using a Packard Tri-Carb 2000 CA/LL (see [31, 32]). The error associated to the ^{3}H measurements (usually around 0.7 TU) varies with the ^{3}H concentration in the sample.

With exception of Vilarelho da Raia, all sampled boreholes are CO_2-exsolving wells. So, in these cases the gases were collected by using a homemade gas-water separator. Separated gas was flown through a glass flask with two-way stopcocks having a volume of about 30 mL. At Vilarelho da Raia, water samples for dissolved gas analyses were collected in glass bottles hermetically sealed in the field with gas-tight teflon-rubber septa taking care to not include air bubbles. Gases were extracted and analysed at the laboratories of the Istituto Nazionale di Geofísica e Vulcanologia (Palermo, Italy) using the methods described by [32] and references therein.

The δ^{18}O and δ^2H values of Chaves low-temperature CO_2-rich geothermal waters (see Table 3) lie on or close to the GMWL ($\delta^2\text{H} = 8\delta^{18}\text{O} + 10$) defined by [71] and later improved by [72–74]. According to [29, 35, 36, 75], this trend indicates (i) that they are meteoric waters which have been recharged without evaporation, and (ii) that there is no water-rock interaction at very high temperatures, consistent with the results of chemical geothermometers (Figure 6).

As in the diagram of Figure 5, the δ^{18}O and δ^2H data from Chaves low-temperature CO_2-rich geothermal waters form a cluster, supporting the existence of a common system for these waters (see Figure 6). On the other hand, the δ^{18}O and δ^2H data of Vilarelho da Raia, Vidago, and Pedras Salgadas cold CO_2-rich mineral waters, although following the GMWL (also indicating a meteoric origin for these waters), have different stable isotopic (δ^{18}O and δ^2H) composition, indicating different aquifer systems with diverse recharge altitudes and different underground flow paths.

Based on δ^{18}O and δ^2H values of the shallow cold dilute normal spring water samples collected at different altitudes in the Chaves region, the local meteoric water line (LMWL: $\delta^2\text{H} = 7.01 \pm 0.74\delta^{18}\text{O} + 4.95 \pm 3.9$) was calculated ([30] - see Figure 6). The stable isotopic composition of the shallow cold dilute normal groundwaters indicates that the more depleted waters are those related to sampling sites located at higher altitudes (see Table 3), as previously referred by [28–30]. The isotopic gradients obtained for ^{18}O (−0.23‰ and −0.22‰ per 100 m of altitude, respectively) are in good agreement with the values found in Mediterranean regions [76]. The altitude dependence of the isotopic composition of the Chaves low-temperature CO_2-rich geothermal waters has been reported by [28, 30, 76]. As referred by those authors, the depleted δ^{18}O values of the Chaves low-temperature CO_2-rich geothermal waters require that these waters were derived from meteoric waters at more

Table 3: Representative stable ($\delta^{18}O$ and $\delta^{2}H$) and radioactive (^{3}H) isotopic data of groundwaters from the Chaves region. Table 3 is reproduced from Marques et al. (2006) [under the Creative Commons Attribution License/public domain].

Ref.	Local	Altitude	$\delta^{18}O$	$\delta^{2}H$	^{3}H
ACP1 (⋄)	Vilarelho da Raia	370	−7.71	−53.2	1.7 ± 1.0
Assureiras (□)	Chaves	690	−7.52	−50.7	6.4 ± 1.1
Castelões (□)	Chaves	980	−7.72	−50.1	8.2 ± 1.0
Campo de futebol (□)	Chaves	360	−5.76	−38.5	7.0 ± 1.0
AC2 (△)	Chaves	350	−8.03	−55.9	0.0 ± 1.0
Nasc. (△)	Chaves	350	−7.96	−54.9	0.5 ± 0.9
Baldio (□)	Vidago	510	−6.73	−42.9	4.3 ± 1.0
N3 (□)	Vidago	480	−6.20	−40.8	3.6 ± 1.4
N6 (□)	Vidago	420	−6.42	−41.6	4.7 ± 1.0
N7 (□)	Vidago	580	−6.73	−42.5	7.2 ± 1.3
AC16 (●)	Vidago	355	−6.63	−48.0	4.1 ± 1.0
AC18 (●)	Vidago	325	−6.81	−44.5	−0.3 ± 0.9
Areal 3 (●)	Vidago	350	−7.12	−52.2	−1.6 ± 1.0
N1 (□)	Pedras Salgadas	660	−6.53	−40.1	4.2 ± 1.0
N2 (□)	Pedras Salgadas	1080	−6.79	−40.0	5.3 ± 1.1
N5 (□)	Pedras Salgadas	885	−7.20	−45.8	6.9 ± 1.0
AC17 (■)	Pedras Salgadas	580	−7.26	−47.3	2.2 ± 1.0
AC25 (■)	Pedras Salgadas	560	−7.70	−53.1	0.0 ± 1.0
AC22 (■)	Pedras Salgadas	570	−8.27	−53.5	−0.3 ± 1.0

Notes: (□) shallow cold dilute normal groundwaters; (△) Chaves low-temperature CO_2-rich geothermal waters; cold CO_2-rich mineral waters from (⋄) Vilarelho da Raia, (●) Vidago, and (■) Pedras Salgadas. Altitude in m a.s.l.. $\delta^{18}O$ and $\delta^{2}H$ in ‰ vs. V-SMOW. ^{3}H in TU.

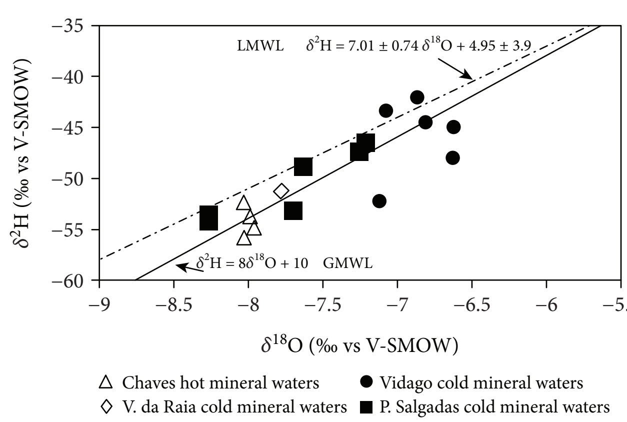

Figure 6: δ^2H vs. $\delta^{18}O$ relationship of Chaves low-temperature CO_2-rich geothermal waters. The $\delta^{18}O$ and δ^2H values of the cold CO_2-rich mineral waters from Vilarelho da Raia, Vidago, and Pedras Salgadas areas are also plotted. Figure 6 is reproduced from Marques et al. (2006) [under the Creative Commons Attribution License/public domain].

than 1150 m a.s.l. These elevations are attained in the Padrela Mountain (NE-Chaves), probably the main recharge area for the Chaves low-temperature CO_2-rich geothermal system.

As stated by [28–30, 33, 35, 36], the systematic presence of tritium (2 to 4.5 TU) measured in some of the Vidago (AC16 borehole) and Pedras Salgadas (AC17 borehole) cold CO_2-rich mineral waters should not be attributed to mixing with shallow cold dilute normal groundwaters (sampling campaign carried out during 2000). Also, as referred by [33, 35, 36], the lower Cl^- concentration of Vidago cold CO_2-rich mineral waters (AC16 borehole - see Table 1) could be faced as a signature of mixing, which is not consistent with the calculated PCO_2 values (around 1.20 atm, see [29]). Furthermore, Pedras Salgadas cold CO_2-rich mineral waters (AC25 borehole) present similar Cl^- contents to the Pedras Salgadas (AC17 borehole) cold CO_2-rich mineral waters (see Table 1), but no ^3H content (see Table 3). So, the systematic presence of ^3H in Vidago AC16 and Pedras Salgadas AC17 cold CO_2-rich mineral waters should be ascribed to shallow (and short) underground flow paths, with the water mineralization being strongly controlled by the CO_2 content [33, 35, 36, 77].

The income of carbon-14 free CO_2 (mantle derived) to the studied CO_2-rich geothermal and cold mineral water systems must produce erroneous groundwater age estimations [31]. In fact, the radiocarbon content (^{14}C activity from 4.3 up to 9.9 pmC) determined in some of the cold CO_2-rich mineral waters from Vidago and Pedras Salgadas [31] mismatched the systematic presence of ^3H (from 1.7 to 7.9 TU), demonstrating the importance of a good knowledge

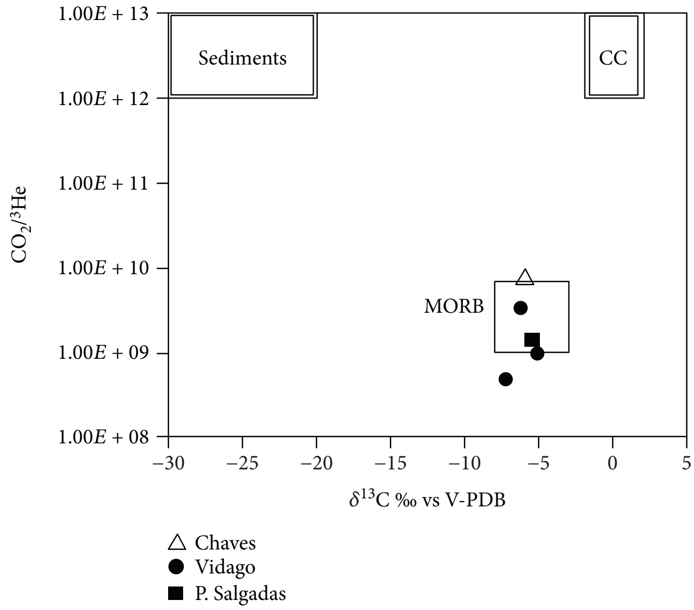

Figure 7: $CO_2/^3He$ ratio *vs.* $\delta^{13}C$ of the gas phase within the typical MORB formations, the fields were defined based on [104, 107, 108]. The $CO_2/^3He$ ratios for crustal and MORB fluids are from [107, 109]. The symbols stand for (△) Chaves, (•) Vidago, and (■) Pedras Salgadas. Adapted from [81].

on these cold CO_2-rich mineral water systems for the development of the hydrogeological conceptual model of the Chaves low-temperature CO_2-rich geothermal system, in which it is very difficult to make sound conclusions on the use of carbon-14 isotopic data for groundwater dating.

In low-temperature geothermal systems, carbon dioxide can be derived from many sources, such as organic matter oxidation, interaction with sedimentary carbonates, metamorphic devolatilisation, and magmatic degassing (e.g., [78, 79]).

According to [77], the $\delta^{13}C$ determinations carried out on total dissolved inorganic carbon (TDIC) of the Chaves low-temperature CO_2-rich geothermal waters are in the range of −6‰ to −1‰, corroborating the previous $\delta^{13}C$ values ($\delta^{13}C_{CO2} = -5.72$‰ vs. PDB) presented by [47] of CO_2 gas samples of Chaves low-temperature CO_2-rich geothermal waters.

Later on, [32] reported $\delta^{13}C_{CO2}$ varying between −7.2 and −5.1‰ vs. V-PDB. Given the range of the $\delta^{13}C$ values, the deep-seated (upper mantle) origin for the CO_2 should be considered a likely hypothesis, given the tectonic/fracture scenario of the study region. According to [80], concerning the discussion on the $^3He/^4He$ and $^4He/^{20}Ne$ ratios from terrestrial fluids in the Iberian Peninsula, the helium isotopic signatures in a fluid sample from Cabreiroá cold CO_2-rich mineral waters, located in Spain at the same NNE-trending fault of the Chaves low-temperature CO_2-rich geothermal waters, are significantly higher than those of typical crustal helium ($^3He/^4He$ value of 0.69). Those authors estimated that in Cabreiroá fluid sample the helium's fractions from atmospheric, crustal and mantle reservoirs were 0.02%, 91.62% and 8.35%, respectively. The relatively high $^3He/^4He$ found in the Cabreiroá sample corroborates a significant mantle-degassing component. The isotopic ratios of carbon and helium ($\delta^{13}C$, $^3He/^4He$) and the geochemical signatures of the gas phase ascribed to the Chaves low-temperature CO_2-rich geothermal waters and the cold CO_2-rich mineral waters of Vidago and Pedras Salgadas were used by [31, 32, 81], to identify contributions of deep crustal and mantle volatile components associated to the NNE-trending fault (see Figure 7). The $^3He/^4He$ ratios found in the gas phase of the CO_2-rich waters ranged between 0.89 and 2.68 times the atmospheric ratio (Ra) at Chaves (AC1 borehole) and Pedras Salgadas (AC25 borehole), respectively, being higher than those expected for a pure crustal origin (≈ 0.02 Ra). Also, the $CO_2/^3He$ values, from 5.1×10^8 to 7.5×10^9, are typical of MORB fluids [32, 81].

In a region where recent volcanic activity is absent, the mantle-derived component of the released deep-seated fluids indicates that extensive neo-tectonic structures (i.e., the NNE-trending fault) are still active [31, 32].

5. Water-Rock Interaction and Water/Rock Ratios

Increasing intensity of low-temperature geothermal water use all over the world and possible groundwater-related conflicts between stakeholders (e.g., society, governments, industry, and nature) puts increasing pressure on the natural groundwater environment. At present, 82 countries utilize the low-temperature geothermal water for direct applications with an installed thermal power capacity of 70,885 MW and a thermal energy use of 164,635 GWh/year [82]. For decision-making purposes (e.g., exploitation rates, avoiding overexploitation), indicators such as those presented in this chapter should be accepted as driving forces to simplify complex information (such as the interrelationship between several hydrogeological systems).

The $^{87}Sr/^{86}Sr$ ratios are powerful hydrogeochemical tracers as strontium atomic weight avoids easy isotopic fractionation by any natural process. Commonly, the measured differences in the $^{87}Sr/^{86}Sr$ ratios in waters can be ascribed to Sr derived from different rock sources with different isotopic signatures [83], where the $^{87}Sr/^{86}Sr$ ratios in waters depend on the Rb/Sr ratios and the age of the percolated rocks [83].

Several studies have used Sr isotope ratios to update knowledge on the chemical evolution of geothermal and mineral waters (e.g., [84–92]). In this paper, we review the use of Sr geochemical and isotopic signatures to improve knowledge on the relation between the Chaves low-temperature CO_2-rich geothermal waters and the cold CO_2-rich mineral waters from Vilarelho da Raia, Vidago, and Pedras Salgadas, discharging along one of the major NNE-SSW-trending faults in northern Portugal, with special emphasis on (i) identifying the reservoir rocks, (ii) recognizing the existence (or not) of mixing processes, and (iii) improving knowledge on water-rock interaction processes at depth.

Sampling procedures in order to collect representative water and rock samples of the region for Sr concentrations and $^{87}Sr/^{86}Sr$ ratios are described in detail by [38]. Sr concentrations and $^{87}Sr/^{86}Sr$ ratios in waters and rocks were determined by Geochron Laboratories (a division of Krueger Enterprises Inc./Cambridge, Massachusetts, USA), following the methods described in [38]. Sample preparation for isotopic analysis on silicate minerals was performed at Centro de Petrologia e Geoquímica, Instituto Superior Técnico - CEPGIST - Lisbon, Portugal (see [38]).

Strontium concentrations and isotope ratios from waters and rocks (including mineral separates) from the Vilarelho da Raia/Pedras Salgadas region, northern Portugal, are reported in Tables 4 and 5, respectively.

Figure 8 shows a plot of 1/Sr vs. $^{87}Sr/^{86}Sr$ for the studied low-temperature CO_2-rich geothermal waters and cold CO_2-rich mineral waters [38]. The $^{87}Sr/^{86}Sr$ of the studied low-temperature CO_2-rich geothermal waters and cold CO_2-rich mineral waters increase from south to north (Pedras Salgadas $^{87}Sr/^{86}Sr = 0.716713$ to 0.717572; Vidago: $^{87}Sr/^{86}Sr = 0.720622$ to 0.72428; and Vilarelho da Raia/-Chaves: $^{87}Sr/^{86}Sr = 0.727154$ to 0.728035) along the NNE mega-lineament of the Verin-Régua-Penacova fault zone (VRPFZ – see Figure 2). This trend could suggest the possible existence of groundwater flow from south to north. However, this assumption is not realistic since according to [28, 36, 93] the studied low-temperature CO_2-rich geothermal waters and cold CO_2-rich mineral waters have different $\delta^{18}O$ and $\delta^{2}H$ signatures (see Figure 6).

These Sr isotopic signatures corroborate the idea that the Chaves low-temperature CO_2-rich geothermal system is distinct, recharged at high-altitude sites ($\delta^{18}O$ and $\delta^{2}H$ values), and ascribed to water-rock interaction within a granitic environment with specific Sr isotopic composition. The fact that there is no hydraulically connection from Pedras Salgadas towards Vilarelho da Raia, along the Verin-Régua-Penacova fault zone, has strong implications for the sustainable management of the Chaves low-temperature CO_2-rich geothermal system. In fact, if such hydraulically connected flow path occurred, it would produce a general increase in the water mineralization from south to north, which also is not the case (see [28, 36, 93]).

Table 4: Sr concentrations and isotope ratios from waters in the Vilarelho da Raia/Pedras Salgadas region, northern Portugal. Table 4 is reproduced from Marques et al. (2006) [under the Creative Commons Attribution License/public domain].

Ref.	Local	Sr (ppm)	$^{87}Sr/^{86}Sr$
ACP1 (◇)	Vilarelho da Raia	0.5827	0.728033
CH1Ch. (*)	Chaves	0.0010	0.710599
Assureiras (□)	Chaves	0.0242	0.729536
Castelões (□)	Chaves	0.0059	0.722967
Campo de futebol (□)	Chaves	0.2942	0.723488
AC2 (△)	Chaves	0.4349	0.727191
Nasc. (△)	Chaves	0.4181	0.727154
CH1 V. (*)	Vidago	0.0015	0.710804
Baldio (□)	Vidago	0.0254	0.717003
N3 (□)	Vidago	0.0060	0.722858
N6 (□)	Vidago	0.0089	0.719087
N7 (□)	Vidago	0.0104	0.714352
AC16 (●)	Vidago	0.3424	0.723194
AC18 (●)	Vidago	1.3977	0.724280
Areal 3 (●)	Vidago	1.2130	0.720622
CH1 P.S. (*)	Pedras Salgadas	0.0013	0.711326
N1 (□)	Pedras Salgadas	0.0075	0.715094
N2 (□)	Pedras Salgadas	0.0018	0.730712
N5 (□)	Pedras Salgadas	0.0098	0.731135
AC17 (■)	Pedras Salgadas	0.7001	0.716969
AC25 (■)	Pedras Salgadas	0.8195	0.717572
AC22 (■)	Pedras Salgadas	1.3250	0.716754

Notes: (*) rain waters; (□) shallow cold dilute normal groundwaters; (△) Chaves low-temperature CO_2-rich geothermal waters; cold CO_2-rich mineral waters from (◇) Vilarelho da Raia, (●) Vidago, and (■) Pedras Salgadas.

As referred by [34–36], the spreading of the Sr data can be understood through the presence of three end-members ((a) Vilarelho da Raia/Chaves, (b) Vidago, and (c) Pedras Salgadas) of a concentration tendency, from rain waters towards the low-temperature CO_2-rich geothermal waters and cold CO_2-rich mineral waters (1/Sr vs. $^{87}Sr/^{86}Sr$ ratios, see Figure 8).

Since the radioactive decay of ^{87}Rb promotes an emplacement by ^{87}Sr, which enters more rapidly into solution [83], the $^{87}Sr/^{86}Sr$ ratios of groundwaters interacting with older granitic rocks (e.g., Chaves low-temperature CO_2-rich geothermal waters and Vilarelho da Raia cold CO_2-rich mineral waters) are naturally larger than the $^{87}Sr/^{86}Sr$ ratios of Vidago and Pedras Salgadas cold CO_2-rich mineral waters, ascribed to water-rock interaction with younger (post-tectonic) granitic rocks (see Figure 2 and [83–85]).

The presence of low-temperature CO_2-rich geothermal waters and diverse groups of cold CO_2-rich mineral waters is also corroborated by the structural tectonic environment of the region, namely, by the existence of important structural lineation enhancing the subsidence zones in the Chaves,

Table 5: Sr concentrations and isotope ratios of rocks and mineral separates from Vilarelho da Raia/Pedras Salgadas region, northern Portugal. Table 5 is reproduced from Marques et al. (2006) [under the Creative Commons Attribution License/public domain].

Samples from outcrops				
Reference	Local	Lithology	Sr (ppm)	$^{87}Sr/^{86}Sr$
AM1*	Vilarelho da Raia	Granite	74.0	0.777260
AM60	Chaves	Andaluzitic slate	63.5	0.777421
AM1164	Chaves	Graphitic slate	14.4	0.737563
AM1163	Chaves	Quartzite	16.8	0.726642
AM1149	Chaves	Chaves granite	87.6	0.753397
AM1150	Chaves	Outeiro Seco granite	99.5	0.757173
AM1160	Chaves	Faiões granite	93.1	0.743689
AM1161	Chaves	Faiões granite	97.5	0.735697
AM2*	Vidago	Vila Pouca de Aguiar granite	98.0	0.735900
Pflum7	Vila Real	Carbonates	2348	0.709485
Samples from drill cores				
Ref. (depth)	Local	Lithology	Sr (ppm)	$^{87}Sr/^{86}Sr$
VR13 (53.0 m)	Vilarelho da Raia	Granite	20.1	0.942148
VR18 (70.5 m)	Vilarelho da Raia	Granite	58.8	0.789683
VR70 (195.30 m)	Vilarelho da Raia	Granite	58.7	0.765128
AC21a (14.8 m)	Pedras Salgadas	Vila Pouca de Aguiar granite	59.91	0.763068
AC21e (106.35 m)	Pedras Salgadas	Vila Pouca de Aguiar granite	35.99	0.784371
AC26a (25.15 m)	Vidago	Vila Pouca de Aguiar granite	54.67	0.762890
AC26b (34 m)	Vidago	Vila Pouca de Aguiar granite	57.63	0.761298
Minerals				
Reference	Local	Mineral	Sr (ppm)	$^{87}Sr/^{86}Sr$
AM1*	Vilarelho da Raia	Microcline	152.0	0.76359
AM1*	Vilarelho da Raia	Plagioclase	108.0	0.72087
AM1*	Vilarelho da Raia	Muscovite	26.0	0.84459
AM1*	Vilarelho da Raia	Biotite	11.0	4.18370
AM2*	Vidago	Microcline	101.0	0.75644
AM2*	Vidago	Plagioclase	75.0	0.71261
AM2*	Vidago	Muscovite	12.0	2.43938
AM2*	Vidago	Biotite	108.0	0.70948

Note: *Data from [29].

Vidago, and Pedras Salgadas basins (see [38, 43, 44]). Such features explain the existence of similar but distinct hydrogeological systems rather than a single system (see Figure 3).

Plagioclases and biotite usually supply most of dissolved ions to the water, when compared to K-feldspars and quartz which are slightly attacked [85]. Studies performed in the study region [34, 35, 38] gave emphasis to the fact that although the low-temperature CO_2-rich geothermal waters and cold CO_2-rich mineral waters sampled at Chaves/Vilarelho da Raia areas, respectively, present the highest $^{87}Sr/^{86}Sr$ ratios, Sr isotope ratios of granitic rock samples from the study region (see Table 5) are far higher than the Sr isotope ratios from the water samples (e.g., Vilarelho da Raia granite: $^{87}Sr/^{86}Sr = 0.789683$; Vidago granite: $^{87}Sr/^{86}Sr = 0.762890$). From these observations, [34, 35, 38] concluded that (i) no equilibrium was attained between the waters and the whole-rocks and (ii) that the Sr isotope values were achieved from equilibrium between the waters and specific minerals from the granitic rocks. As referred by [38], the mean Sr isotopic ratio of the low-temperature CO_2-rich geothermal waters and cold CO_2-rich mineral waters ($^{87}Sr/^{86}Sr_{mean} = 0.722419$) is comparable to the Sr isotopic ratios of the plagioclases of the granitic rocks presented by [29]: Vilarelho da Raia$_{plagioclase}$ $^{87}Sr/^{86}Sr = 0.72087$ and Vidago$_{plagioclase}$ $^{87}Sr/^{86}Sr = 0.71261$. These results are in good agreement with the chemistry of the studied low-temperature CO_2-rich geothermal waters and cold CO_2-rich mineral waters which is strongly dominated by the HCO_3^- and Na^+ ions (see Section 3) as the result of the hydrolysis of the Na-plagioclases of the granitic rocks (see [38]).

Concerning water-rock interaction studies, thin sections of drill cores from Vilarelho da Raia AC2 borehole were studied in detail, at LAMPIST, to characterize their

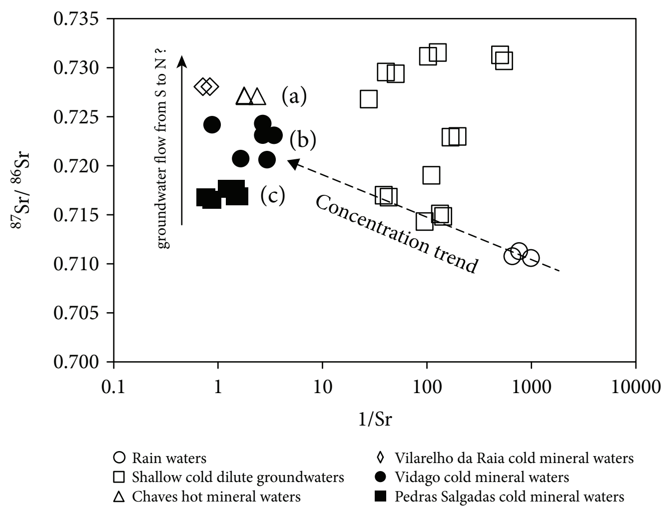

Figure 8: Plot of 1/Sr vs. $^{87}Sr/^{86}Sr$ for the studied low-temperature CO_2-rich geothermal waters and cold CO_2-rich mineral waters. Figure 8 is reproduced from Marques et al. (2006) [under the Creative Commons Attribution License/public domain].

mineralogical composition and textural relations (see [37]). Sample preparation for isotopic analysis on granitic rocks and silicate minerals is referred in detail in [37]. Stable isotope analyses of granitic whole-rock samples and selected mineral separates were performed at Delta Isotopes Laboratory (The Netherlands), at XRAL Laboratories (Canada), and at Geochron Laboratories/USA, respectively, following the methodology described in [37] and references therein.

Joined geochemical and isotopic data to characterize and identify the nature of the water-rock interaction between the low-temperature CO_2-rich geothermal waters and Hercynian granitic rocks (and host rock minerals) in the northern part of the Portuguese mainland was used by [37]. The origin of the fluids responsible for the hydrothermal alteration and the water-rock (W/R) ratios recorded in the vein alteration zones were assessed using stable ($^{18}O/^{16}O$ and $^{2}H/^{1}H$) isotope analysis of whole rocks and mineral separates from the granitic rocks.

This approach was developed considering that

(i) the geothermal boreholes at Chaves were not cored

(ii) Chaves low-temperature CO_2-rich geothermal waters and Vilarelho da Raia cold CO_2-rich mineral waters show similar geochemical and isotopic signatures

(iii) Vilarelho da Raia exploration boreholes also penetrate Hercynian granitic rocks

(iv) the alteration features observed in the Vilarelho da Raia drill cores could be interpreted as manifestations of a "fossil" geothermal system

(v) they can be used as an analogue for the Chaves geothermal field

According to [37, 93] in the vein alteration zones of the granitic rock samples (along rock fractures), all minerals are replaced by secondary quartz and white mica, mainly muscovite $2M_1$. Illite, halloysite, chlorite, and vermiculite were also found in the same samples.

In order to characterize the meteoric origin of fluids responsible for the vein alteration observed in the drill cores from the Vilarelho da Raia AC2 borehole (see [37]), these authors estimated the $\delta^{18}O$ and $\delta^{2}H$ values of the water in equilibrium with mineral separates such as muscovite and chlorite (Table 6). Whole-rock samples displaying vein alteration signatures were also analysed for $\delta^{18}O$ and $\delta^{2}H$ to estimate the water/rock (W/R) ratios along vein alteration zones (Table 7).

As proposed by [94], in water-rock exchange processes, the water/rock (W/R) ratios can be estimated by using the equation

$$\frac{W}{R_{\text{closed}}} = \frac{\left(\delta^{18}O_{\text{final-rock}} - \delta^{18}O_{\text{initial-rock}}\right)}{\left(\delta^{18}O_{\text{initial-fluid}} - \delta^{18}O_{\text{final-fluid}}\right)}, \quad (2)$$

where W and R are the atom percentages in the fluid (W) and in the rock (R). As mentioned by [37], in an open system, the most reliable situation in this case study, the heated water is lost from the system by escape to the surface, making only a single pass through the system from recharge to discharge areas; we have [94]

$$\frac{W}{R_{\text{open}}} = \ln\left(\frac{W}{R_{\text{closed}}} + 1\right). \quad (3)$$

According to [37], the main problems regarding the application of the abovementioned equations are related to the initial isotopic composition of the rock ($\delta^{18}O_{\text{initial-rock}}$) and fluid ($\delta^{18}O_{\text{initial-fluid}}$). In the studies presented by [37], the initial oxygen isotope composition of the country rocks is represented by the $\delta^{18}O$ values of the least ^{18}O-depleted rock samples (AM3 and AM80) from Vilarelho da Raia granitic outcrops outside the spring area (Table 6). These

Table 6: Isotopic composition of whole rocks and mineral separates from Vilarelho da Raia AC2 drill cores. After [37].

Sample	Type of alteration	Depth (m)	Whole-rock		Muscovite		Chlorite	
			$\delta^{18}O$	$\delta^{2}H$	$\delta^{18}O$	$\delta^{2}H$	$\delta^{18}O$	$\delta^{2}H$
AM3	Pervasive (low)	(Surface)	+11.41	−75.0				
AM80	Pervasive (low)	(Surface)	+11.47	−66.1	+9.7	−70		
VR23	Pervasive	81.15			+8.5	−44		
VR27a	Vein	89.70	+10.10	−42.0	+9.1			
VR27b	Pervasive	89.70	+10.18	−69.0	+11.6		+6.3	−53.0
VR32a	Pervasive	100.55	+11.25	−66.4	+8.6			
VR32b	Vein	100.55	+10.91	−44.5	+9.1	−42		
VR39	Vein	129.70	+10.80	−65.0	+10.2	−70	+5.2	−75.0
VR41	Pervasive	140.50			+9.8	−64		
VR70a	Vein	195.30	+10.82	−56.0	+9.4	−45		
VR70b	Pervasive	195.30	+10.91	−44.5	+9.3			

Note: The term "low" means a rock sample displaying low pervasive alteration characteristics (almost an unaltered rock sample).

Table 7: Water/rock (W/R) ratios related to vein alteration zones, Vilarelho da Raia AC2 drill cores. After [37].

Sample depth	$\delta^{18}O_{\text{initial}}$ rock	$\delta^{18}O_{\text{final}}$ rock	$\delta^{18}O_{\text{initial}}$ water	$\delta^{18}O_{\text{final}}$ water	(W/R) (*)	(W/R) (**)
VR32b	+11.47	+10.91	−5.76	−0.55	0.10 (a)	0.09 (a)
(100.55 m)	+11.47	+10.91	−6.68	+3.84	0.05 (b)	0.05 (b)
VR39	+11.47	+10.80	−9.26	−0.65	0.08 (a)	0.07 (a)
(129.70 m)	+11.47	+10.80	−10.18	+3.73	0.04 (b)	0.05 (b)
VR70a	+11.47	+10.82	−6.13	−0.64	0.11 (a)	0.08 (a)
(195.30 m)	+11.47	+10.82	−7.06	+3.75	0.06 (b)	0.05 (b)

Notes: * W/R ratios calculated using the δ^2H values of muscovites along open-space filling zones of the granite, the muscovite-water fractionation equation proposed by [96], and the Global Meteoric Water Line. ** W/R ratios calculated assuming that the final δ^2H of the altered rock samples, along open-space filling zones of the granite, has approached the δ^2H of the circulating meteoric waters, and the Global Meteoric Water Line (a) W/R ratios calculated at 150°C; (b) W/R ratios calculated at 230°C.

values ($\delta^{18}O = +11.41$‰ and +11.47‰) fall within the "high-^{18}O granites" group [37, 94].

A meteoric origin for the water responsible for the vein alteration process was assumed by [37], and therefore, the initial water composition was calculated from the $^2H/^1H$ ratio of the alteration assemblage (along veins) and the Global Meteoric Water Line (GMWL: $\delta^2H = 8\,\delta^{18}O + 10$), defined by [71], assuming that the $^2H/^1H$ ratios of the vein fluids had not been affected by water-rock interaction [37]. According to [94], the final δ^2H of the rocks is dependent upon exactly how the meteoric water enters in the system and, consequently, for small amounts of water the final δ^2H of the rock could approach the δ^2H values of the meteoric waters due to the fact that there is not much H in the rocks (see [37]).

Thus, according to [37], the initial $\delta^{18}O$ values of the water were estimated by means of

(i) the δ^2H values of the muscovites located along veins (see [95] - pages 289 and 290)

(ii) the muscovite-water fractionation equation proposed by [96]

(iii) the Global Meteoric Water Line ($\delta^2H = 8\,\delta^{18}O + 10$) defined by [71].

According to [37], the values obtained (from −10‰ to −6‰) are reliable. Those authors stated that considering vein alteration features observed in the Vilarelho da Raia granitic drill cores as manifestations of a "fossil" geothermal system, the methodology used to estimate the water/rock ratios along veins [94, 95] predicted initial $\delta^{18}O$ values of the water that are rather similar to the present-day meteoric waters (see Figure 6).

The final $\delta^{18}O$ values for the rock used in the calculations (from +10.80‰ to +10.91‰) were the values measured on core samples from vein alteration bands [37]. The final water composition was estimated by the [97] plagioclase-water isotope fractionation equation [37], assuming that $\delta^{18}O_{\text{plagioclase}} \approx \delta^{18}O_{\text{whole-rock}}$ (final composition), as plagioclase is the main mineral in the rock and exhibits the greatest rate of ^{18}O exchange with an external fluid phase (corroborated by the Sr isotopic data).

As noted above in discussing the vein alteration zones, vein water-rock interaction temperatures (150°C < T < 230°C) proposed by [37] were estimated through the stability fields of the alteration minerals (e.g., muscovite, illite, halloysite, chlorite, and vermiculite), as suggested by [98–100]. Given these temperatures, the W/R ratios obtained by [37] for the open system are between 0.08 and 0.11 and between 0.04 and 0.06 (Table 7), for 150 and 230°C, respectively, suggesting a rock-dominated system (as indicated by the Sr chemical and isotopic data) where a relatively small volume of meteoric water was involved in vein formation [37].

Based on these results, it was suggested that isotopic data on hydrothermal minerals (e.g., muscovite and chlorite) should be used as a natural analogue for assessing the present-day hydrochemical and isotopic evolution of the Chaves low-temperature CO_2-rich geothermal system [37].

In granitic environments chosen for Enhanced Geothermal Systems (EGS) development, one of the most important questions is determining the relevance of hydrothermal events and their relationships to the history of the granite. Here, the results of the mineralogical, chemical, and isotopic investigations of the silicates from granitic rocks were used to derive a better understanding of past water-rock reactions in the area and information on conditions leading to hydrothermal alteration and fracture fillings. What was learned could be useful in deciding where to develop an EGS exchanger in the subsurface, as it would help estimate the type and intensity of mineral deposition that is likely to occur during its operation.

6. Geophysical Approach

Since 1990, various geophysical methods, mainly gravity, resistivity, scalar audio-magnetotellurics (AMT), and magnetotellurics (MT), have been used to study the shallow and deep structures of the Chaves graben (e.g., [101–103]), mostly associated to the geometry of the shallow groundwater circulation zones related with the deep fracture system (see [27]). In this publication, only results from resistivity and AMT will be presented, since they are the ones that better fit our objectives.

According to [102], the resistivity survey comprised 29 Schlumberger vertical electrical soundings (VES), dipole-dipole lines, pole-dipole-lines, and rectangle surveys. The VES were carried out with current electrodes expanding approximately in the NNE-SSW direction and with a maximum spacing ranging from 1200 to 2000 m (Figure 9).

The VES apparent resistivity curves can be grouped into two main groups, representing the geological and geoelectrical diversity [27, 102, 104]. The first group of soundings, comprising curves showing a decrease in the resistivity up to large AB/2 values, were obtained in the eastern and central part of the graben, where the sedimentary sequences are thick (VES 11, 15, and 29 in Figure 9). The second group of VES comprises curves obtained in areas where the bedrock is shallow, i.e., mainly in the western part of the graben (VES 24 in Figure 9).

The 1D inversion results of the VES data [27, 75] were combined to obtain a map of the low-resistivity layer associated with the geothermal reservoir (Figure 9). Additionally, two resistivity cross sections along N-S and E-W directions were obtained combining the 1D inversion results (Figure 10). These figures show that low-resistivity zones (resistivity values between 10 and 60 ohm-m) are concentrated in the central part of the graben because of high temperatures combined with the high salinity of the geothermal waters in fractured and permeable rock formations.

There are several shallow groundwater boreholes drilled along the N-S axis of the basin (Figures 9 and 10). None of the boreholes reaches the basement of the basin, and neither touches the high temperature reservoir. The most part of the well drill in the Quaternary overburden is represented by the first layer in the VES models. This layer shows resistivity values varying between 70 and 800 ohm-m (Figure 10).

The deepest part of the basin (basement) is represented by the last layer of the VES models and shows high-resistivity values (greater than 500 ohm-m), except in the central part of the graben where the NNE-SSW and NNW-SSE fault systems cross the area.

An audio-magnetotellurics (AMT) survey including more than 100 soundings, in the frequency range from 2300 to 4.1 Hz, was carried out in the graben area [101]. The 1D models calculated from AMT soundings revealed an excellent agreement with those obtained from the Schlumberger apparent resistivity curves [27, 75]. As derived from the 1D inversion of the AMT data [27, 101, 104], the contour map of the conductance values (the ratio thickness/resistivity at each sounding) in the conductive layer is shown in Figure 11.

The high values roughly match the zones of great depth of the bedrock as determined from 1D interpretation of the VES. The conductance anomalies show a preferential (approximately) N-S direction that seems to be perturbed by WNW-ESE structures. The high conductance zones were interpreted as related to the geothermal aquifer in the Chaves graben and may expose the preferential zones for the hot waters' ascent.

In fact, as stated by [105], in a magnetotellurics survey of the Milos Island (Greece) geothermal prospect, the maximum conductance values approximately agree with the maximum temperature gradient. It should be emphasised that the temperature measurements in boreholes from the Chaves graben [7] point towards a similar behaviour.

As already mentioned in Section 2 (Figure 3), geological and tectonic studies evidence the existence of deep fractures trending approximately NW-SE, ENE-WSW, and N-S either in the Chaves graben or in the surroundings. The geophysical results also confirm the presence of such directions (differences in the directions are due to the scarcity of geophysical data), reflecting the pattern of geothermal fluids circulation along the fault system (Figures 9 and 11). As referred by [27, 101, 104], such faults, and mainly their intersection, would provide an efficient conduit system for geothermal fluids ascending from the reservoir, in the deep part of the Chaves graben.

7. Chaves Low-Temperature CO_2-Rich Geothermal System vs. Cold CO_2-Rich Hydromineral Systems: Conceptual Models

Low-temperature CO_2-rich geothermal resources represent somewhat complex systems which are not easy to understand

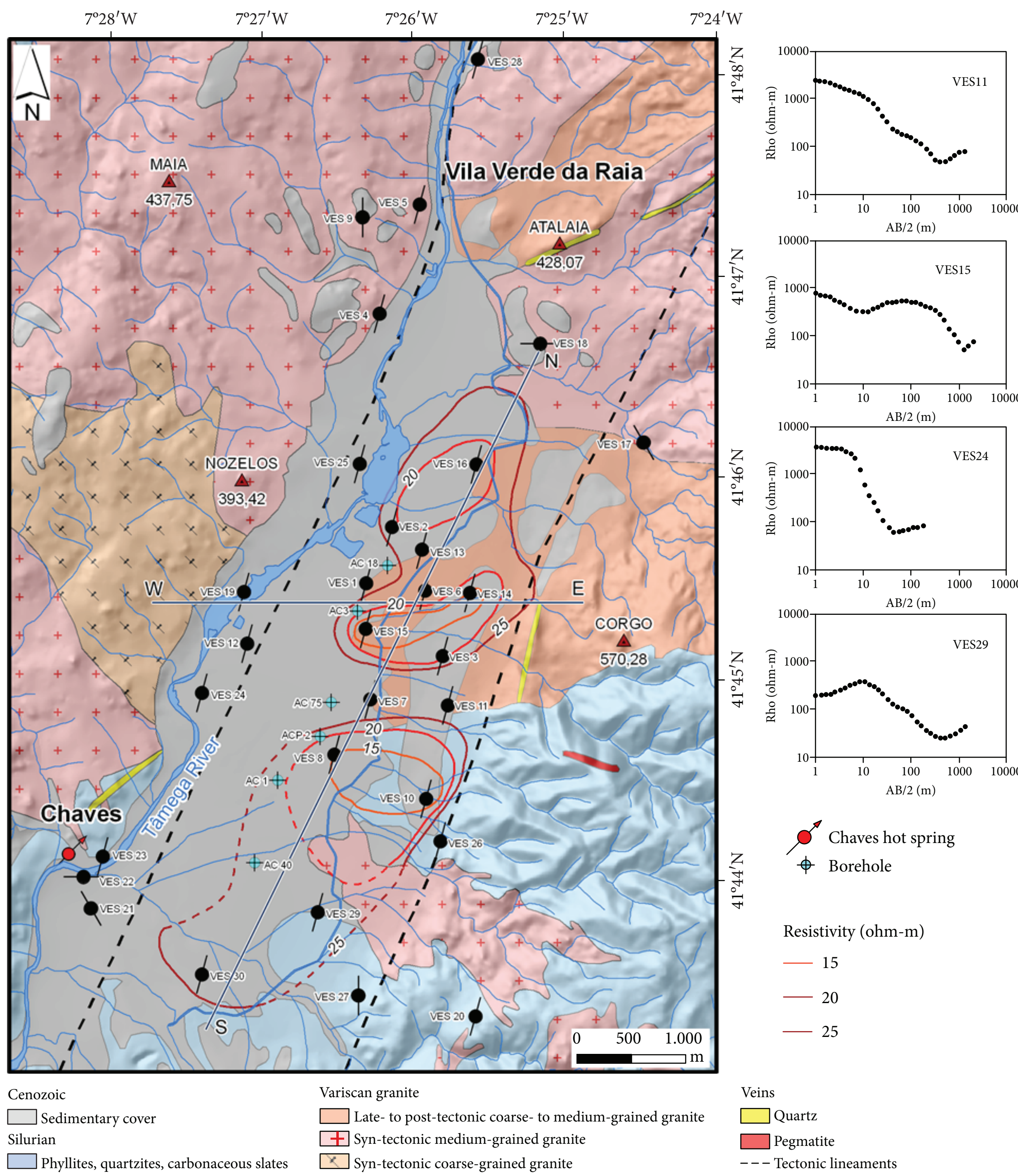

Figure 9: Location of the VES carried out in Chaves graben and example of apparent resistivity curves acquired. Geological background adapted from [110, 111]. Lines in the filled circles represent the VES direction. Also shown are the contours of the low resistivity zones in the central part of the graben (approximate depth of 350 m) as determined from 1D interpretation of VES. Adapted from [27].

under multifaceted hydrogeological conditions, particularly in areas where low-temperature CO_2-rich geothermal waters and cold CO_2-rich mineral waters discharge a few kilometres apart. According to [9], the conventional description of a groundwater conceptual model is a usually qualitative and often graphic explanation of the groundwater system, including a delineation of the hydrogeologic units, the system boundaries, inputs/outputs, and a description of soils and rocks. Hydrogeological conceptual models are simplified representations of a given hydrological and hydrochemical cycle within a geological environment ascribed to an aquifer system. These are developed by hydrogeologists normally based on important data sets collected in the scope of regional investigations.

In this paper, a special emphasis was put on the review of the contribution of a multidisciplinary approach

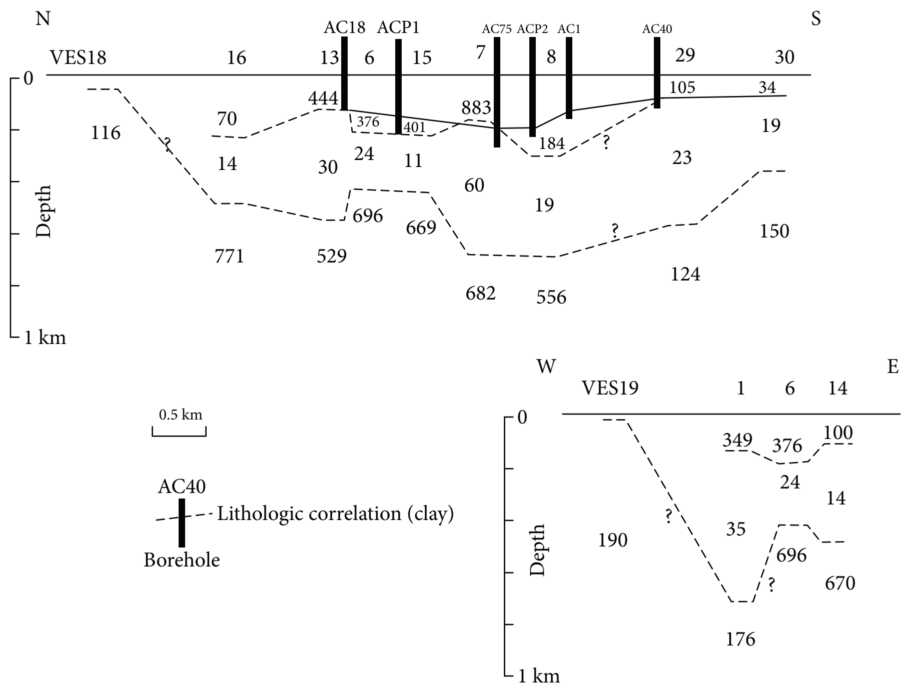

Figure 10: Resistivity 1D sections along N-S and E-W directions. Values are in ohm-m. Taken from [27]. AC and ACP stand for diverse boreholes from the Chaves graben.

(geology, geomorphology, tectonics, hydrogeology, geochemistry, isotope hydrology, and geophysics) to the development of the hydrogeological conceptual model of Chaves low-temperature CO_2-rich geothermal waters, linking to the case of the Vilarelho da Raia, Vidago, and Pedras Salgadas cold CO_2-rich mineral waters.

As stated by [31–33], chemical and isotopic data reveal that the studied CO_2-rich waters are part of an open system to the influx of CO_2 gas from a deep-seated source ($\delta^{13}C_{CO2}$ values and $CO_2/^3He$ ratios) and that water-rock reactions are mainly controlled by the amount of dissolved CO_2 (g) rather than by the water temperature. The most probable explanation by which carbon dioxide could be transported from its deep source to the surface involves migration as a separate gas phase being incorporated in the infiltrated meteoric waters (i) at considerable depth in the case of the Chaves low-temperature CO_2-rich geothermal waters and (ii) at shallow levels in the case of cold CO_2-rich mineral waters from Vilarelho da Raia, Vidago, and Pedras Salgadas (see [32] and Figure 12). Solutes such as Na and HCO_3 are originated from the local granitic rocks, with their concentration in the waters favoured by the CO_2 dissolution at low temperatures, ascribed to shallow circulation paths (Figure 12), lowering the pH and increasing water-rock interaction, as revealed by the higher mineralization of most of the studied cold CO_2-rich mineral waters.

The Sr isotopes and Sr concentrations in the waters and rocks provided a clear picture on the influence of varying rock types on the CO_2-rich water signatures [34, 38]. The Sr-isotope data presented in this study strongly suggest that Chaves low-temperature CO_2-rich geothermal waters and Vilarelho da Raia, Vidago, and Pedras Salgadas CO_2-rich mineral waters should be faced as surface manifestations of different hydrogeological systems and underground flow paths.

Particularly, and ascribed to the updating of the hydrogeologic conceptual model of the Chaves low-temperature CO_2-rich geothermal system (Figure 13), geological studies evidenced the existence of deep NW-SE- (dextral-) and ENE-WSW- (sinistral-) trending faults, either in the Chaves graben or in the surrounding area, reflecting the pattern of geothermal fluid circulation, which discharge mainly in places where those trending faults intersect at the Chaves graben (see Figure 3).

The ENE-WSW-trending faults provide effective conduits for the meteoric waters ($\delta^{18}O$ and δ^2H values) infiltration and deep circulation (chemical geothermometers), while the NW-SE lineaments promote the geothermal fluids ascending from the reservoir to the surface. The meteoric water infiltrates on the highest topography (the altitude effect), where rainfall is important (Padrela Mountain, NE-Chaves), percolates at great depth through granitic rocks (geology, geochemistry of the waters - Na-HCO_3-type waters, and Sr isotopic data) along the open fault/fracture systems (vein alteration signatures), and then emerges in a discharge area at lower altitude on the Chaves plain (tectonics/geophysics). Solutes such as Na^+ and HCO_3^- are originated from the hydrolysis of the plagioclases of local granitic rocks (Sr isotopic data), being favoured by the incorporation of the deep-seated CO_2 in the circulating waters.

In this case, the distance between recharge and discharge areas is relatively large and groundwater flow paths should also be long (i.e., on the order of decades to centuries). However, the determination of the geothermal waters' "age"

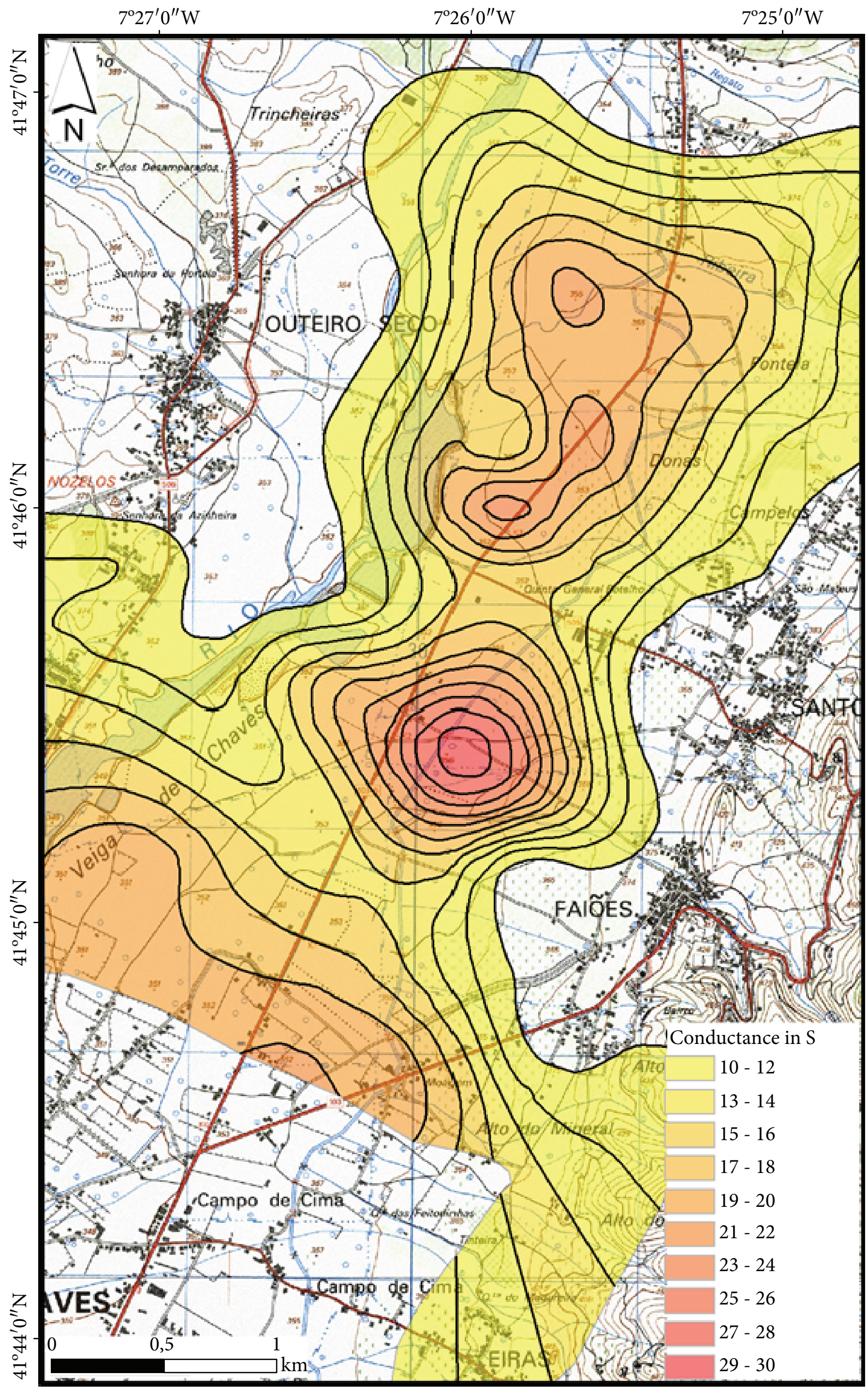

Figure 11: Contour map of conductance in the low resistivity layer associated with the geothermal reservoir as derived from AMT data. Taken from [27].

is difficult due to the presence of mantle-derived CO_2 (^{14}C free), as described by [31]. Nevertheless, the results from chemical geothermometers seem to indicate a considerable depth reached by the thermal water system, ascribed to long underground flow paths.

The release of deep-seated fluids having a mantle-derived component in a region without recent volcanic activity suggests that active neo-tectonic structures originating during the Alpine Orogeny (i.e., Chaves Depression) tap mantle carbon and helium [32].

8. Main Conclusions

This paper review the usefulness of geologic, tectonic, geochemical, isotopic, and geophysical studies on the assessment of Chaves low-temperature (77°C) CO_2-rich geothermal

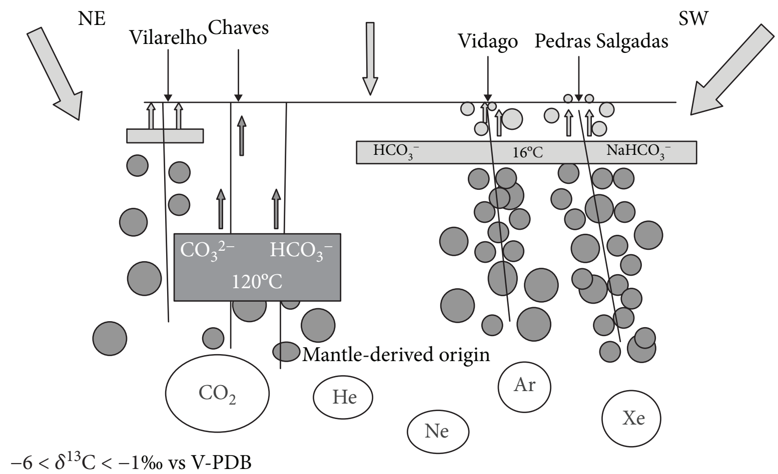

FIGURE 12: Regional conceptual model of the studied CO_2-rich mineral waters, along the Penacova-Verin fracture zone, between Vilarelho da Raia and Pedras Salgadas (N of Portugal). The filled circles stand for the amount of dissolved deep CO_2 gas; the lines stand for fault systems; down arrows stand for meteoric waters (recharge); up arrows stand for deep/shallow groundwater ascent, boxes stand for a schematic representation of the CO_2-rich aquifer systems. Adapted from [81].

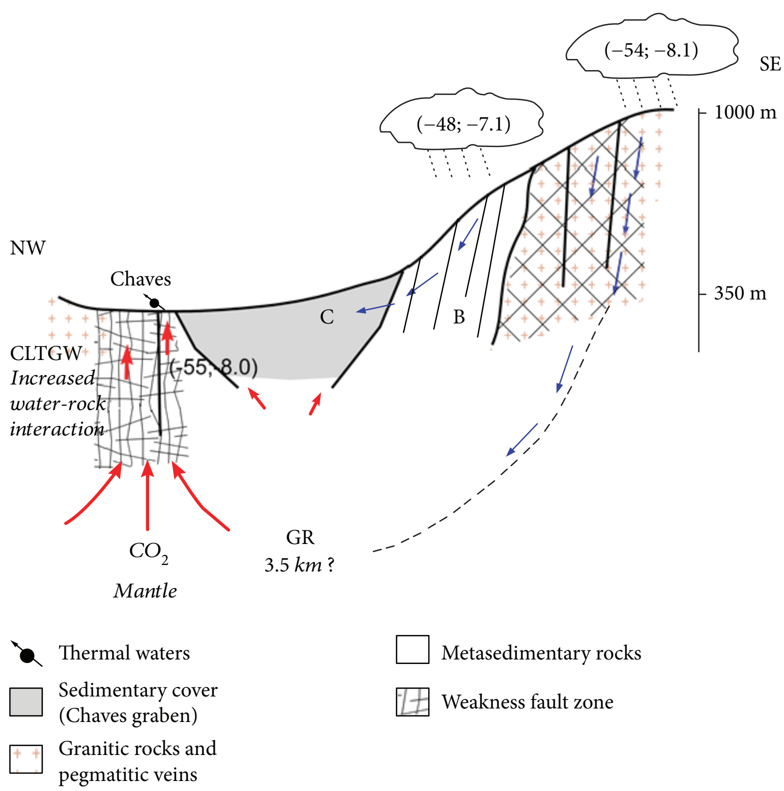

FIGURE 13: Hydrogeological conceptual circulation model of Chaves low-temperature CO_2-rich geothermal system. B stands for granitic and metasedimentary rocks; C stands for cover deposits; CLTGW stands for Chaves low-temperature CO_2-rich geothermal waters; GR stands for geothermal reservoir; (−54; −8.1) stands for the isotopic composition (δ^2H; $\delta^{18}O$) of the waters. Taken from [27].

system issuing in the northern part of the Portuguese mainland. In this region, a suite of cold (17°C) CO_2-rich mineral waters (Vilarelho da Raia, Vidago, and Pedras Salgadas) also occur along the same NNE-trending fault. The data reviewed highlight the complexity in studying and linking low-temperature CO_2-rich geothermal waters and cold CO_2-rich mineral waters discharging in the same region. Knowledge of groundwater circulation and possible interactions between the low-temperature geothermal and the cold mineral waters is an important factor to ensure economic use of (i) deep hot waters as a geothermal resource and (ii) shallow cold mineral waters as drinkable mineral waters, as well as in terms of potential future overexploitation. The integration of the results of studies from different geosciences approaches strongly suggests that the Chaves low-temperature CO_2-rich geothermal waters and Vilarelho da Raia, Vidago, and Pedras Salgadas cold CO_2-rich mineral waters should be faced as surface manifestations of different hydrogeological systems ascribed to diverse underground flow paths. This paper is aimed at reviewing the value of an integrated and multi- and interdisciplinary approach for a given geothermal site characterization. The existing integrated model could be useful for other case studies linking the assessment of low-temperature CO_2-rich geothermal waters and cold CO_2-rich mineral waters emerging in a same area. The data acquired so far could be extremely useful for future numerical simulation of Chaves low-temperature CO_2-rich geothermal reservoirs, a very useful instrument for making decisions about the upcoming strategies of field exploitation and for analysing the behaviour of the whole rock-geofluid system. In fact, numerical model construction must be supported by a detailed knowledge of the spatial distribution of reservoir properties in the form of a robust conceptual model. Furthermore, the spas of northern Portugal are of special commercial value and should not be impacted by future water resource development.

Conflicts of Interest

The authors declare that they have no conflicts of interest.

Acknowledgments

The CERENA/IST author acknowledges the FCT (the Portuguese Foundation for Science and Technology) support through the UID/ECI/04028/2019 Project, the C^2TN/IST author gratefully acknowledges the FCT support through the UID/Multi/04349/2013 Project, and the DEGGE-IDL author thankfully acknowledges the FCT Project UID/-GEO/50019/2013. An early draft of this manuscript was critically read by two anonymous reviewers, and we gratefully acknowledge their contribution. The authors also would like to thank José Teixeira and Helder Chaminé for redrawing Figures 2, 9, 10, 11, and 13.

References

[1] K. Nicholson, *Geothermal fluids*, Springer Berlin Heidelberg, Berlin, 1993.

[2] M. H. Dickson and M. Fanelli, “Geothermal background,” in *Geothermal Energy, Utilization and Technology*, M. H. Dickson and M. Fanelli, Eds., pp. 1–25, UNESCO, Paris, 2003.

[3] R. W. Henley and A. J. Ellis, “Geothermal systems ancient and modern: a geochemical review,” *Earth-Science Reviews*, vol. 19, no. 1, pp. 1–50, 1983.

[4] F. Goff and L. Shevenell, “Travertine deposits of Soda Dam, New Mexico, and their implications for the age and evolution of the Valles caldera hydrothermal system,” *Geological Society of America Bulletin*, vol. 99, no. 2, p. 292, 1987.

[5] A. J. Ellis and W. A. J. Mahon, *Chemistry and Geothermal Systems*, Academic Press, New York, 1977.

[6] R. Haenel and S. Hurter, *Atlas of Geothermal Resources in Europe*, Commission of the European Communities, Brussels, Luxemburg, 2002.

[7] M. R. A. Duque, F. M. Santos, and L. A. Mendes Victor, “Heat flow and deep temperatures in the Chaves geothermal system, northern Portugal,” *Geothermics*, vol. 27, no. 1, pp. 75–87, 1998.

[8] C. W. Fetter, *Applied Hydrogeology*, Prentice Hall, New Jersey, 2001.

[9] J. E. Moore, *Field Hydrogeology: A Guide for Site Investigations and Report Preparation*, Lewis Publishers, a CRC Press Company, New York, 2nd edition, 2003.

[10] I. Barnes, P. Irwin, and D. E. White, *Global Distribution of Carbon Dioxide Discharges, and Major Zones of Seismicity*, U.S. Geological Survey Water-Resources, 1978.

[11] S. Schofield and J. Jankowski, “Hydrochemistry and isotopic composition of Na–HCO_3-rich groundwaters from the Ballimore region, central New South Wales, Australia,” *Chemical Geology*, vol. 211, no. 1-2, pp. 111–134, 2004.

[12] I. Cartwright, T. Weaver, S. Tweed et al., “Stable isotope geochemistry of cold CO_2-bearing mineral spring waters, Daylesford, Victoria, Australia: sources of gas and water and links with waning volcanism,” *Chemical Geology*, vol. 185, no. 1-2, pp. 71–91, 2002.

[13] P. Bissig, N. Goldscheider, J. Mayoraz, H. Surbeck, and F.-D. Vuataz, “Carbogaseous spring waters, coldwater geysers and dry CO_2 exhalations in the tectonic window of the Lower Engadine Valley, Switzerland,” *Eclogae Geologicae Helvetiae*, vol. 99, no. 2, pp. 143–155, 2006.

[14] E. Griesshaber, R. K. O'Nions, and E. R. Oxburgh, “Helium and carbon isotope systematics in crustal fluids from the Eifel, the Rhine Graben and Black Forest, F. R. G,” *Chemical Geology*, vol. 99, no. 4, pp. 213–235, 1992.

[15] F. May, “Alteration of wall rocks by CO_2-rich water ascending in fault zones: natural analogues for reactions induced by CO_2 migrating along faults in siliciclastic reservoir and cap rocks,” *Oil & Gas Science and Technology*, vol. 60, no. 1, pp. 19–32, 2005.

[16] F. Batard, J. C. Baubron, B. Bosch, A. Marcé, and J. J. Risler, “Isotopic identification of gases of a deep origin in French thermomineral waters,” *Journal of Hydrology*, vol. 56, no. 1-2, pp. 1–21, 1982.

[17] H. Pauwels, C. Fouillac, F. Goff, and F.-D. Vuataz, “The isotopic and chemical composition of CO_2-rich thermal waters in the Mont-Dore region (Massif-Central, France),” *Applied Geochemistry*, vol. 12, no. 4, pp. 411–427, 1997.

[18] F. H. Weinlich, “Isotopically light carbon dioxide in nitrogen rich gases: the gas distribution pattern in the French Massif Central, the Eifel and the western Eger Rift,” *Annals of Geophysics*, vol. 48, no. 1, pp. 19–31, 2005.

[19] G. Vasseur, G. Michard, and C. Fouillac, “Contraintes sur la structure et le fonctionnement du système hydrothermal de Chaudes-Aigues (France),” *Hydrogéologie*, vol. 4, pp. 3–17, 1997.

[20] A. Minissale, “Origin, transport and discharge of CO_2 in central Italy,” *Earth-Science Reviews*, vol. 66, no. 1-2, pp. 89–141, 2004.

[21] G. Michard and C. Beaucaire, “Les eaux thermales des granites de Galice (Espagne): des eaux carbogazeuses aux eaux alcalines (thermal waters from granites of Galicia (Spain):

from CO_2-rich to high-pH waters)," *Chemical Geology*, vol. 110, no. 4, pp. 345–360, 1993.

[22] A. J. E. Freedman, D. K. Bird, S. Arnórsson, T. Fridriksson, W. A. Elders, and G. Ó. Fridleifsson, "Hydrothermal minerals record CO_2 partial pressures in the Reykjanes geothermal system, Iceland," *American Journal of Science*, vol. 309, no. 9, pp. 788–833, 2010.

[23] Z. Krejbichová, "Radioactivity of mineral waters in Bohemia," *Czechoslovak Journal of Physics*, vol. 49, no. S1, pp. 127–132, 1999.

[24] F. H. Weinlich, J. Tesar, S. M. Weise, K. Brauer, and H. Kampf, "Gas flux distribution in mineral springs and tectonic structure in the western Eger Rift," *Journal of the Czech Geological Society*, vol. 43, pp. 1-2, 1998.

[25] E. Greber, "Deep circulation of CO_2-rich palaeowaters in a seismically active zone (Kuzuluk/ Adapazari, Northwestern Turkey)," *Geothermics*, vol. 23, no. 2, pp. 151–174, 1994.

[26] W. Stumm and J. Morgan, *Aquatic Chemistry – an Introduction Emphasizing Chemical Equilibria in Natural Waters*, Wiley-Interscience, New-York, 2nd edition, 1981.

[27] J. M. Marques, P. M. Carreira, J. E. Marques et al., "The role of geosciences in the assessment of low-temperature geothermal resources (N-Portugal): a review," *Geosciences Journal*, vol. 14, no. 4, pp. 423–442, 2010.

[28] L. Aires-Barros, J. M. Marques, and R. C. Graça, "Elemental and isotopic geochemistry in the hydrothermal area of Chaves / Vila Pouca de Aguiar (Northern Portugal)," *Environmental Geology*, vol. 25, no. 4, pp. 232–238, 1995.

[29] L. Aires-Barros, J. M. Marques, R. C. Graça et al., "Hot and cold CO_2-rich mineral waters in Chaves geothermal area (Northern Portugal)," *Geothermics*, vol. 27, no. 1, pp. 89–107, 1998.

[30] M. P. L. Andrade, "Isotopic geochemistry and thermomineral waters. Contribution of Sr ($^{87}Sr/^{86}Sr$) and Cl ($^{37}Cl/^{35}Cl$) isotopes to the elaboration of circulation models," *The case of some CO_2-rich waters from N Portugal. Dissertation, [M.S. thesis]*, Technical University of Lisbon - IST, 2003.

[31] P. M. Carreira, J. M. Marques, R. C. Graça, and L. Aires-Barros, "Radiocarbon application in dating "complex" hot and cold CO_2-rich mineral water systems: a review of case studies ascribed to the northern Portugal," *Applied Geochemistry*, vol. 23, no. 10, pp. 2817–2828, 2008.

[32] P. M. Carreira, J. M. Marques, M. R. Carvalho, G. Capasso, and F. Grassa, "Mantle-derived carbon in Hercynian granites. Stable isotopes signatures and C/He associations in the thermomineral waters, N-Portugal," *Journal of Volcanology and Geothermal Research*, vol. 189, no. 1-2, pp. 49–56, 2010.

[33] J. M. Marques, P. M. M. Carreira, L. Aires-Barros, and R. C. Graça, "Nature and role of CO_2 in some hot and cold $HCO_3/Na/CO_2$-rich Portuguese mineral waters: a review and reinterpretation," *Environmental Geology*, vol. 40, no. 1-2, pp. 53–63, 2000.

[34] J. M. Marques, M. Andrade, L. Aires-Barros, R. C. Graça, and H. G. M. Eggenkamp, "Antunes da Silva M (2001) $^{87}Sr/^{86}Sr$ and $^{37}Cl/^{35}Cl$ signatures of CO_2-rich mineral waters (N-Portugal): preliminary results," in *New Approaches Characterizing Groundwater Flow*pp. 1025–1029, A.A. Balkema.

[35] J. M. Marques, M. Andrade, P. M. Carreira, R. C. Graça, and L. Aires-Barros, *Evolution of CO_2-Rich Mineral Waters from Hercynian Granitic Rocks (N-Portugal): Questions and Answers*, Proceedings of the International Conference on Groundwater in Fractured Rocks, J. Krásny, Z. Hrkal, and J. Bruthans, Eds., UNESCO, Paris, France, 2003.

[36] J. M. Marques, M. Andrade, P. M. Carreira et al., "Chemical and isotopic signatures of $Na/HCO_3/CO_2$-rich geofluids, North Portugal," *Geofluids*, vol. 6, no. 4, 287 pages, 2006.

[37] J. M. Marques, M. J. Matias, M. J. Basto, P. M. Carreira, L. A. Aires-Barros, and F. E. Goff, "Hydrothermal alteration of Hercynian granites, its significance to the evolution of geothermal systems in granitic rocks," *Geothermics*, vol. 39, no. 2, pp. 152–160, 2010.

[38] J. M. Marques, P. M. Carreira, F. Goff, H. G. M. Eggenkamp, and M. Antunes da Silva, "Input of $^{87}Sr/^{86}Sr$ ratios and Sr geochemical signatures to update knowledge on thermal and mineral waters flow paths in fractured rocks (N-Portugal)," *Applied Geochemistry*, vol. 27, no. 8, pp. 1471–1481, 2012.

[39] B. B. S. Singhal and R. P. Gupta, *Applied Hydrogeology of Fractured Rocks*, Springer, New York, 1999.

[40] A. Ribeiro, M. C. Kullberg, J. C. Kullberg, G. Manuppella, and S. Phipps, "A review of Alpine Tectonics in Portugal: foreland detachment in basement and cover rocks," *Tectonophysics*, vol. 184, no. 3-4, pp. 357–366, 1990.

[41] A. Ribeiro, J. Munhá, R. Dias et al., "Geodynamic evolution of the SW Europe Variscides," *Tectonics*, vol. 26, no. 6, 2007.

[42] M. Portugal Ferreira, A. Sousa Oliveira, and A. N. Trota, "Chaves geothermal pole," in *Geological Survey, I and II. Joule I Program, DGXII, CEE. UTAD (University of Trás-os-Montes and Alto Douro, Portugal)*, p. 44, Internal Report, 1992.

[43] J. Baptista, C. Coke, R. Dias, and A. Ribeiro, "Tectonics and geomorfology of Pedras Salgadas region and associated mineral springs," in *Comunicações da XII Reunião de Geologia do Oeste Peninsular*, A. Chambel, Ed., vol. 1, Évora University, 1993.

[44] A. Sousa Oliveira and M. P. Portugal Ferreira, "Structural control of the hydromineral springs from Pedras Salgadas region (Vila Pouca de Aguiar - Northern Portugal)," in *Porto University, Faculty of Sciences, Museum and Mineralogical and Geological Laboratory*, vol. 4, pp. 485–489, Memória, 1995.

[45] F. Arthaud and P. Matte, "Les decrochements tardi-hercyniens du sud-ouest de l'europe. Geometrie et essai de reconstitution des conditions de la deformation," *Tectonophysics*, vol. 25, no. 1-2, pp. 139–171, 1975.

[46] J. Cabral, "An example of intraplate neotectonic activity Vilariça Basin, Northeast Portugal," *Tectonics*, vol. 8, no. 2, pp. 285–303, 1989.

[47] F. M. Almeida, "Novos dados geotermométricos sobre águas de Chaves e de S. Pedro do Sul," *Comunicações Serviços Geológicos Portugal*, vol. 68, no. 2, pp. 179–190, 1982.

[48] A. Criaud and C. Fouillac, "Etude des eaux thermominérales carbogazeuses du Massif Central Français. II. Comportement de quelques métaux en trace, de l'arsenic, de l'antimoine et du germanium," *Geochimica et Cosmochimica Acta*, vol. 50, no. 8, pp. 1573–1582, 1986.

[49] W. M. Edmunds, R. L. F. Kay, and R. A. McCartney, "Origin of saline groundwaters in the Carnmenellis granite (Cornwall, England): natural processes and reaction during hot dry rock reservoir circulation," *Chemical Geology*, vol. 49, no. 1-3, pp. 287–301, 1985.

[50] D. C. Kamineni, P. Fritz, and S. K. Frape, "Halogen-bearing minerals in plutonic rocks: a possible source of chlorine in

saline groundwater in the Canadian Shield," in *Saline Water and Gases in Crystalline Rocks*, vol. 33, pp. 69–80, Geological Association of Canada Special Paper, 1987.

[51] R. O. Fournier and J. J. Rowe, "Estimation of underground temperatures from the silica content of water from hot springs and wet-steam wells," *American Journal of Science*, vol. 264, no. 9, pp. 685–697, 1966.

[52] W. A. J. Mahon, "Silica in hot water discharged from drillholes at Wairakei, New Zealand," *New Zealand Journal of Science*, vol. 9, pp. 135–144, 1966.

[53] S. Arnórsson, "Application of the silica geothermometer in low temperature hydrothermal areas in Iceland," *American Journal of Science*, vol. 275, no. 7, pp. 763–784, 1975.

[54] R. O. Fournier, "Chemical geothermometers and mixing models for geothermal systems," *Geothermics*, vol. 5, no. 1-4, pp. 41–50, 1977.

[55] A. J. Ellis, "Quantitative interpretation of chemical characteristics of hydrothermal systems," *Geothermics*, vol. 2, pp. 516–528, 1970.

[56] A. H. Truesdell, "Geochemical techniques in exploration," in *Proceedings of the 2nd United Nations Symposium on the Development and Use of Geothermal Resources*, vol. 1, pp. 53–79, San Francisco, 1975.

[57] R. O. Fournier and A. H. Truesdell, "An empirical Na-K-Ca geothermometer for natural waters," *Geochimica et Cosmochimica Acta*, vol. 37, no. 5, pp. 1255–1275, 1973.

[58] R. O. Fournier and R. W. Potter II, "Magnesium correction to the Na-K-Ca chemical geothermometer," *Geochimica et Cosmochimica Acta*, vol. 43, no. 9, pp. 1543–1550, 1979.

[59] C. Fouillac and G. Michard, "Sodium/lithium ratio in water applied to geothermometry of geothermal reservoirs," *Geothermics*, vol. 10, no. 1, pp. 55–70, 1981.

[60] J. M. Marques, L. Aires-Barros, and R. C. Graça, "Geochemical and isotopic features of hot and cold CO_2-rich mineral waters of northern Portugal: a review and reinterpretation," *Bulletin d'Hydrogéologie*, vol. 17, pp. 175–183, 1999.

[61] C. Fouillac, "Chemical geothermometry in CO_2-rich thermal waters. Example of the French Massif Central," *Geothermics*, vol. 12, no. 2/3, pp. 146–160, 1983.

[62] R. O. Fournier, "Application of water geochemistry to geothermal exploration and reservoir engineering," in *Geothermal Systems: Principles and Case Histories*, L. Rybach and L. J. P. Muffler, Eds., pp. 109–143, Wiley, Chichester, 1981.

[63] W. F. Giggenbach, "Geothermal solute equilibria. Derivation of Na-K-Mg-Ca geoindicators," *Geochimica et Cosmochimica Acta*, vol. 52, no. 12, pp. 2749–2765, 1988.

[64] W. F. Giggenbach, "Graphical techniques for the evaluation of water/rock equilibration conditions by use of Na, K, Mg and Ca contents of discharge waters," in *Geothermal Institute, University of Auckland*, Proc. 8th. New Zealand Geothermal Workshop, pp. 37–44, Auckland, New Zealand, 1986.

[65] S. Arnórsson, "Carbon dioxide waters and chemical geothermometer interpretation," *Proceedings 5th African Rift geothermal Conference*, 2014, p. 9, 2014.

[66] R. Haenel and E. Staroste, *Atlas of Geothermal Resources in the European Community*, Commission of the European Communities, Brussels-Luxembourg, 1988.

[67] I. Friedman, "Deuterium content of natural waters and other substances," *Geochimica et Cosmochimica Acta*, vol. 4, no. 1-2, pp. 89–103, 1953.

[68] S. Epstein and T. Mayeda, "Variation of ^{18}O content of waters from natural sources," *Geochimica et Cosmochimica Acta*, vol. 4, no. 5, pp. 213–224, 1953.

[69] IAEA, "Procedure and technique critique for tritium enrichment by electrolysis at IAEA laboratory," in *Technical Procedure n°19*, International Atomic Energy Agency, Vienna, 1976.

[70] L. L. Lucas and M. P. Unterweger, "Comprehensive review and critical evaluation of the half-life of tritium," *Journal of Research of the National Institute of Standards and Technology*, vol. 105, no. 4, pp. 541–549, 2000.

[71] H. Craig, "Standard for reporting concentrations of deuterium and oxygen-18 in natural waters," *Science*, vol. 133, no. 3467, pp. 1833-1834, 1961.

[72] K. Rozanski, L. Araguás-Araguás, and R. Gonfiantini, *Isotopic Patterns in Modern Global Precipitation*, vol. 78, Climate change in continental isotopic records, 1993.

[73] G. J. Bowen and B. Wilkinson, "Spatial distribution of $\delta^{18}O$ in meteoric precipitation," *Geology*, vol. 30, no. 4, pp. 315–318, 2002.

[74] S. Terzer, L. I. Wassenaar, L. J. Araguás-Araguás, and P. K. Aggarwal, "Global isoscapes for $\delta^{18}O$ and $\delta^{2}H$ in precipitation: improved prediction using regionalized climatic regression models," *Hydrology and Earth System Sciences*, vol. 17, no. 11, pp. 4713–4728, 2013.

[75] J. M. Marques, F. A. Monteiro Santos, M. Andrade et al., "Conceptual modelling of the nature of complex thermomineral systems / CO_2-rich waters (N-Portugal): a review on the geochemical and geophysical approaches," *Geothermal Resources Council Transactions*, vol. 29, pp. 277–281, 2005.

[76] IAEA, "Stable isotope hydrology. Deuterium and oxygen-18 in the water cycle. IAEA, Vienna," in *Technical Reports Series 210*, International Atomic Energy Agency, Vienna, 1981.

[77] J. M. Marques, P. M. Carreira, L. Aires-Barros, and R. C. Graça, "About the origin of CO_2 in some HCO_3/Na/CO_2-rich Portuguese mineral waters," *Geothermal Resources Council Transactions*, vol. 22, pp. 113–117, 1998.

[78] A. H. Truesdell and J. R. Hulston, "Isotopic evidence on environments of geothermal systems," in *Handbook of Environmental Isotope Geochemistry*, P. Fritz and F. J. Ch, Eds., vol. 1, pp. 179–226, The Terrestrial Environment, 1980.

[79] I. D. Clarke and P. Fritz, *Environmental Isotopes in Hydrogeology*, Lewis Publishers, New York, 1997.

[80] N. M. Pérez, S. Nakai, H. Wakita, J. F. Albert-Bertrán, and R. Redondo, "Preliminary results on $^{3}He/^{4}He$ isotopic ratios in terrestrial fluids from Iberian Peninsula: seismoctectonic and neotectonic implications," *Geogaceta*, vol. 20, no. 4, pp. 830–833, 1996.

[81] M. R. Carvalho, P. M. Carreira, J. M. Marques et al., "The origin of gases and their influence in the mineralization of gasocarbonic waters associated to the Régua-Verin structure (Portugal)," in *Associação Portuguesa dos Recursos Hídricos - APRH*, Proceedings of the Seminário sobre Águas Subterrâneas, CD-ROM, Lisboa, Portugal, 2007.

[82] J. W. Lund and T. L. Boyd, "Direct utilization of geothermal energy 2015 worldwide review," *Geothermics*, vol. 60, pp. 66–93, 2016.

[83] G. Faure, *Principles of Isotope Geology*, John Wiley & Sons, New York, 2nd edition, 1986.

[84] A. Stettler, "^{87}Rb-^{87}Sr systematics of a geothermal water-rock association in the Massif Central, France," *Earth and Planetary Science Letters*, vol. 34, no. 3, pp. 432–438, 1977.

[85] A. Stettler and C. J. Allègre, "^{87}Rb-^{87}Sr studies of waters in a geothermal area, the Cantal, France," *Earth and Planetary Science Letters*, vol. 38, no. 2, pp. 364–372, 1978.

[86] F. Goff, H. A. Wollenberg, D. C. Brookins, and R. W. Kistler, "A Sr-isotopic comparison between thermal waters, rocks, and hydrothermal calcites, Long Valley caldera, California," *Journal of Volcanology and Geothermal Research*, vol. 48, no. 3-4, pp. 265–281, 1991.

[87] P. Négrel, C. Fouillac, and M. Brach, "A strontium isotopic study of mineral and surface waters from the Cézallier (Massif Central, France): implications for mixing processes in areas of disseminated emergences of mineral waters," *Chemical Geology*, vol. 135, no. 1-2, pp. 89–101, 1997.

[88] F.-D. Vuataz, F. Goff, C. Fouillac, and J.-Y. Calvez, "A strontium isotope study of the VC-1 core hole and associated hydrothermal fluids and rocks from Valles Caldera, Jemez Mountains, New Mexico," *Journal of Geophysical Research*, vol. 93, no. B6, p. 6059, 1988.

[89] P. Négrel, "Geochemical study in a granitic area, the Margeride, France: chemical element behavior and $^{87}Sr/^{86}Sr$ constraints," *Aquatic Geochemistry*, vol. 5, no. 2, pp. 125–165, 1999.

[90] P. Négrel, J. Casanova, and J. F. Aranyossy, "Strontium isotope systematics used to decipher the origin of groundwaters sampled from granitoids: the Vienne case (France)," *Chemical Geology*, vol. 177, no. 3-4, pp. 287–308, 2001.

[91] R. Millot, P. Négrel, and E. Petelet-Giraud, "Multi-isotopic (Li, B, Sr, Nd) approach for geothermal reservoir characterization in the Limagne Basin (Massif Central, France)," *Applied Geochemistry*, vol. 22, no. 11, pp. 2307–2325, 2007.

[92] R. Millot, C. Guerrot, C. Innocent, P. Négrel, and B. Sanjuan, "Chemical, multi-isotopic (Li-B-Sr-U-H-O) and thermal characterization of Triassic formation waters from the Paris Basin," *Chemical Geology*, vol. 283, no. 3-4, pp. 226–241, 2011.

[93] J. M. Marques, L. Aires-Barros, R. C. Graça, M. J. Matias, and M. J. Basto, *Fluid Chemistry and Water-Rock Interaction in a CO_2-Rich Geothermal Area, Northern Portugal*, Proceedings of the 9th International Symposium on Water-Rock Interaction - WRI-9 / Taupo, G. B. Arehart and J. R. Hulstron, Eds., A.A. Balkema, New Zealand, 1998.

[94] H. P. Taylor Jr, "Oxygen and hydrogen isotope studies of plutonic granitic rocks," *Earth and Planetary Science Letters*, vol. 38, no. 1, pp. 177–210, 1978.

[95] H. Rollinson, "Using geochemical data: evaluation, presentation, interpretation," in *Longman Scientific & Technical*, John Wiley & Sons, Inc., New York, 1997.

[96] S. J. Lambert and S. Epstein, "Stable isotope investigations of an active geothermal system in Valles Caldera, Jemez Mountains, New Mexico," *Journal of Volcanology and Geothermal Research*, vol. 8, no. 1, pp. 111–129, 1980.

[97] J. R. O'Neil and H. P. Taylor Jr, "The oxygen and cation exchange chemistry of feldspars," *American Mineralogist*, vol. 52, pp. 1415–1437, 1967.

[98] A. Genter, "Géothermie roches chaudes sèches: le granite de Soultz-sous-Forêts (Bas-Rhin, France)," in *Fracturation naturelle, altérations hydrothermales et interaction eau-roche*, vol. 88, pp. 1–193, Document du BRGM, 1990.

[99] E. Petrucci, S. M. F. Sheppard, and B. Turi, "Water/rock interaction in the Larderello Geothermal Field (Southern Tuscany, Italy): an and isotope study," *Journal of Volcanology and Geothermal Research*, vol. 59, no. 1-2, pp. 145–160, 1993.

[100] S. J. Lutz, J. N. Moore, and D. Benoit, "Alteration mineralogy of the Dixie Valley geothermal system, Nevada," in *Transactions - Geothermal Resources Council*, vol. 20, pp. 353–362, Geothermal Resources Council, 1996.

[101] F. A. M. Santos, A. Dupis, A. R. A. Afonso, and L. A. Mendes-Victor, "An audiomagnetotelluric survey over the Chaves geothermal field (NE Portugal)," *Geothermics*, vol. 25, no. 3, pp. 389–406, 1996.

[102] F. A. M. Santos, A. R. A. Afonso, and L. A. M. Victor, "Study of the Chaves geothermal field using 3D resistivity modeling," *Journal of Applied Geophysics*, vol. 37, no. 2, pp. 85–102, 1997.

[103] F. A. Monteiro Santos, A. Dupis, A. R. Andrade Afonso, and L. A. Mendes-Victor, "Magnetotelluric observations over the Chaves geothermal field (NE Portugal) - preliminary results," *Physics of the Earth and Planetary Interiors*, vol. 91, no. 4, pp. 203–211, 1995.

[104] H. Ármannsson, J. Benjaminsson, and A. W. A. Jeffrey, "Gas changes in the Krafla geothermal system, Iceland," *Chemical Geology*, vol. 76, no. 3-4, pp. 175–196, 1989.

[105] V. Hutton, D. Galanopoulos, G. Dawes, and G. Pickup, "A high resolution magnetotelluric survey of the Milos geothermal prospect," *Geothermics*, vol. 18, no. 4, pp. 521–532, 1989.

[106] A. Sousa Oliveira, *Hidrogeologia dos sistemas gasocarbónicos da província hidromineral transmontana: Ribeirinha (Mirandela), Sandim (Vinhais), Segirei e Salgadela (Chaves). Unpublished [Ph.D. thesis]*, Trás-os-Montes and Alto Douro University, Department of Geology (in Portuguese), 2001.

[107] Y. Sano and H. Wakita, "Precise measurement of helium isotopes in terrestrial gases," *Bulletin of the Chemical Society of Japan*, vol. 61, no. 4, pp. 1153–1157, 1988.

[108] P. Allard, "The origin of hydrogen, carbon, sulfur, nitrogen and rare gases in volcanic exhalations: evidence from isotope geochemistry," in *Forecasting Volcanic Events*, H. Tazieff and J. C. Sabroux, Eds., pp. 337–386, Elsevier, Amsterdam, 1983.

[109] B. Marty and A. Jambon, "$C/^3He$ in volatile fluxes from the solid Earth: implications for carbon geodynamics," *Earth and Planetary Science Letters*, vol. 83, no. 1-4, pp. 16–26, 1987.

[110] C. Teixeira and A. Cândido de Medeiros, *Geological Report on the Chaves Sheet No. 6-B (1:50,000)*, Portuguese Geological Survey, Lisbon, 1974.

[111] E. Pereira, A. Ribeiro, F. Marques et al., *Geological Map of Portugal (1:/200,000), sheet 2*, Portuguese Geological Survey, Lisbon, 1st edition, 2000.

Hindawi
Geofluids
Volume 2019, Article ID 8573182, 18 pages
https://doi.org/10.1155/2019/8573182

Research Article

Assessment of Energy Production in the Deep Carbonate Geothermal Reservoir by Wellbore-Reservoir Integrated Fluid and Heat Transport Modeling

Fengyu Li ,[1] Tianfu Xu ,[1] Shengtao Li,[1,2] Bo Feng ,[1] Xiaofeng Jia,[2] Guanhong Feng,[1] Huixing Zhu,[1] and Zhenjiao Jiang [1]

[1]*Key Laboratory of Groundwater Resources and Environment, Ministry of Education, College of New Energy and Environment, Jilin University, Changchun 130021, China*
[2]*Center for Hydrogeology and Environmental Geology Survey, China Geological Survey, Baoding 071051, China*

Correspondence should be addressed to Bo Feng; fengbo234@126.com

Received 25 May 2018; Revised 6 October 2018; Accepted 31 October 2018; Published 7 February 2019

Guest Editor: Philippe Calcagno

Geothermal energy is clean and independent to the weather and seasonal changes. In China, the huge demanding of clean energy requires the geothermal energy exploitation in the reservoir with depth larger than 1000 m. Before the exploitation, it is necessary to estimate the potential geothermal energy production from deep reservoirs by numerical modeling, which provides an efficient tool for testing alternative scenarios of exploitation. We here numerically assess the energy production in a liquid-dominated middle-temperature geothermal reservoir in the city of Tianjin, China, where the heat and fluid transport in the heterogeneous reservoir and deep wellbores are calculated. It is concluded that the optimal injection/production rate of the typical geothermal doublet well system is 450 m^3/h, with the distance between geothermal doublet wells of 850 m. The outflow temperature and heat extraction rate can reach 112°C and 43.5 MW, respectively. Through decreasing injection/production rate lower than 450 m^3/h and optimizing layout of the injection well and production well (avoiding the high permeability zone at the interwell sector), the risk of heat breakthrough can be reduced. If the low permeability zone in the reservoir is around injection well, it usually leads to abnormal high wellhead pressure, which may be solved by stimulation technique to realize stable operation. The methodology employed in this paper can be a reference for a double-well exploitation project with similar conditions.

1. Introduction

In China, coal burning contributes 70% of CO_2 emissions, 80% of SO_2 emissions, and 70% of soot emissions [1], which caused serious environmental pollution. It is estimated that in northern China, there are 42.3 days on average every year suffering from smog from 1999 to 2013 [2] with mean PM2.5 concentration reaching 93 $\mu g/m^3$ [3]. It is of critical importance to increase the use of clean energy and reduce the proportion of fossil fuels in total energy consumption. As one of the most important renewable and clean energy, geothermal energy is expected to occupy 3% of total energy utilization in China by 2030, which will be mainly used for heat supply in winter and electrical power generation as well [4].

Most of the geothermal resources in China are of middle and low temperature. Among 2700 geothermal wells and thermal springs, only 700 spots have the temperature higher than 80°C [4]. To obtain the high-temperature geothermal resource, it is desirable to explore and exploit the geothermal energy in the reservoir with the depth more than 1000 m. In Tianjin, located in Northern China Plain, the target geothermal reservoir in the next five years moves to Wumishan

Formation, which is buried in a depth of 1600–2000 m with the temperature of 96–108°C. Sixteen wells have been drilled into this geothermal reservoir. Due to the large-scale serious problem of groundwater level drop in this region, it is required that the geothermal exploitation should be operated together with the water injection, to maintain the water-mass balance [5]. Before the geothermal energy exploitation and continuing with further drilling, it is necessary to evaluate the energy production in this deep geothermal reservoir by fully understanding the coupled processes of fluid and heat transport (HT).

The HT processes relating to the cold water injection into the geothermal reservoir environment have been evaluated by analytical and numerical methods. Gringarten and Sauty [6] developed an analytical model to describe the non-steady-state temperature behavior of production wells during the reinjection of cold water into aquifer by neglecting the horizontal thermal conduction in the aquifer and the confining rocks. The model was then employed to evaluate thermal breakthrough in the geothermal doublet system [7] and to describe horizontal conduction and convection in the reservoir and vertical conduction in the confining rock (caprock and bedrock) [8–10]. Nonisothermal heat exchange between fluid in the fractures and matrix [11] and coupled heat-fluid transport processes in both wellbore and reservoirs were considered as well [12–14]. The analytical solutions offered fast and sound tools to understand the principles of HT processes in the subsurface. However, most were established based on certain simplifications when compared to the real geothermal system, which often has a low accuracy in predicting the heat production from a specific reservoir.

In contrast, the numerical models can address the complex conditions in the field, such as irregular boundary conditions and heterogeneous distribution of hydraulic and thermal parameters. These numerical models include TOGUH2 and FEFLOW, which can simulate two-dimensional [15] and three-dimensional [16] fluid and heat transport in both porous and fractured media. A numerical model developed by Ghassemi and Kumar [17] can simulate HT processes in fractured media, based on a dual media model, and the finite element method developed by Aliyu and Chen [18] can simulate HT processes in the discrete fracture network. For the deep reservoirs, the heat and fluid transport processes in the long wellbore significantly affect the prediction of heat production, which was coupled with the HT processes in the reservoir. Typically, COMSOL can simulate 1D–3D wellbore-reservoir flow modelling [19], where the fluid flow in the wellbore is described by non-Darcy flow. Furthermore, T2WELL was established based on TOUGH2, which can simulate the HT processes in both reservoir and wellbores and considers the heat and fluid exchange between wellbore and surrounding rocks [20].

We here employed T2WELL to simulate the HT processes in a typical geothermal reservoir in Tianjin, where the fluid processes in the wellbore are described by 1D non-Darcy flow, while in the reservoir 3D fluid and heat transport processes are calculated. We compared the energy production under 5 scenarios of geothermal exploitation in the heterogeneous geothermal reservoir. As a result, the potential production rate in this geothermal field is determined.

2. Study Area

2.1. Geological Background. The Shanlingzi Geothermal Field in the eastern Tianjin, China, is located in the Panzhuang Uplift, surrounded by the Cangdong Fault, Tianjin Fault, Hangu Fault, and Haihe Fault (Figure 1(a)). There exists, from top to bottom, the Quaternary, Neogene, Qingbaikou, and Jixian Formations (Figure 1(b)). The Cangdong Fault is a compressional torsional and normal fault dipping in South-East direction with an angle of 3° to 48°, which allows the heat transport upward into different aquifers by advection, forming a series of geothermal reservoirs. The Wumishan Formation, in the depth between 1665 m and 1820 m, is the target geothermal reservoir in this study. The average outflow temperature in the well penetrating into this formation can reach 96 to 108°C. The chemical analysis for groundwater collected in six wells suggests that the groundwater is the type of $Cl{\cdot}HCO_3$-Na [21].

This geothermal reservoir is composed of carbonate rocks. The downhole logs in well DL-4 and aquifer tests in 9 wells yield that the porosity in the reservoir ranges from 1.9% to 9.4% and permeability from 1.0×10^{-16} m^2 to 1.25×10^{-12} m^2 (Table 1). Groundwater flows towards southwest with an average gradient less than 1.9‰.

2.2. Model Domain. Following the geological conditions in the Shanlingzi Geothermal field, we selected an area of 48 km^2 to investigate the penitential heat production potential based on a double well heat extraction method: one well for injection and another for extraction. The maximum depth of the model reaches 4000 m, corresponding to the bottom of the Wumishan geothermal reservoir. Within this depth, there are seven layers of formations and lithology logs in seven deep boreholes (Figures 1(c) and 2) determine the shape of each formation. Each layer is discretized into 43456 elements (in the study area of 6418×9671 m^2), and the area of each element on the X-Y plane is less than 100×100 m^2.

3. Governing Equations

TOUGH2-WELL [20] integrated the flow and heat processes in both wellbore and reservoir, which is capable to simulate the nonisothermal, multiphase, multicomponent flows in the deep wellbore-reservoir system. In the reservoir, the heat and fluid transport processes are described by a uniform governing equation:

$$\frac{d}{dt}\int M^{\kappa} dV_{\mathrm{n}} = \int \mathbf{F}^{\kappa} \cdot \mathbf{n} d\Gamma_{\mathrm{n}} + \int q^{\kappa} dV_{\mathrm{n}}, \tag{1}$$

where V_{n} is the element volume bounded by the closed surface Γ_{n}, M^{κ} is the mass accumulation term, $\mathbf{F}$ denotes mass or heat flux, and q denotes sinks and sources.

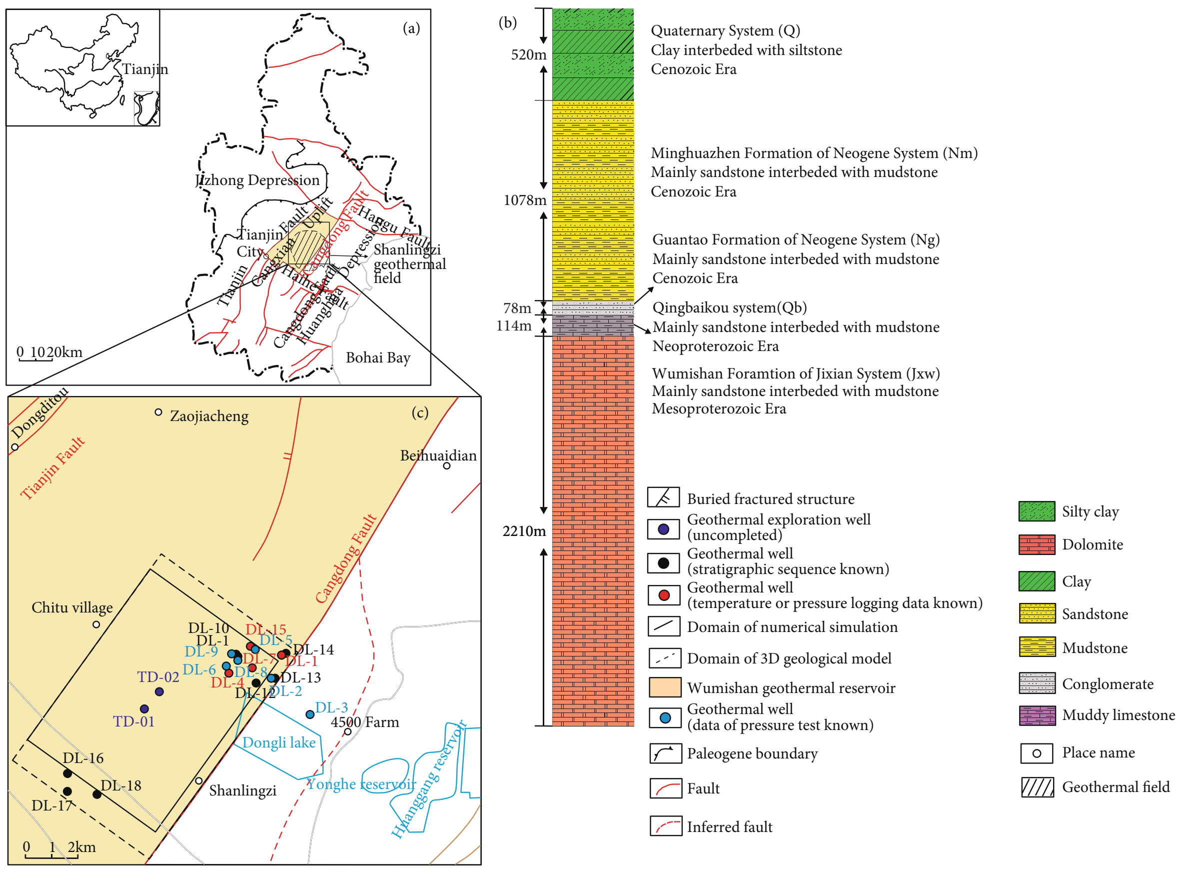

Figure 1: (a) Location of the Wumishan geothermal reservoir, Tianjin, China, (b) stratigraphy in the research area, and (c) the position of existing boreholes in the model domain.

Table 1: Permeability and porosity measured in 9 wells.

Well number	Start buried depth	End buried depth	Thickness of exposed Wumishan Formation	Permeability (m^2)	Porosity (%)
DL-1	1800	2328	528	3.65×10^{-13}	
DL-2	1798	2100	302	1.0×10^{-12}	
DL-3	3481	3634	153	2.09×10^{-13}	
DL-4	—	2122	—	1.25×10^{-12}	
DL-5	1846	2384	538	4.89×10^{-13}	5%–6%
DL-6	—	2533	—	4.88×10^{-13}	
DL-7	1655	2327	672	3.07×10^{-13}	
DL-8	—	2373	—	2.77×10^{-13}	
DL-9	—	2495	—	2.63×10^{-13}	
DL-4 (well logging data)	1938.7	2314.9	—	1.0×10^{-16}-4.7×10^{-15}	1.9%–9.4%

For the fluid flow,

$$M^{\kappa} = \varphi \sum_{\beta} \rho_{\beta} S_{\beta} X_{\beta}^{\kappa}, \tag{2}$$

$$\mathbf{F}^{\kappa} = \sum_{\beta} \rho_{\beta} \boldsymbol{u}_{\beta} X_{\beta}^{\kappa}, \tag{3}$$

where $\boldsymbol{u}_{\beta}$ in the energy conservation is the Darcy velocity in phase β.

For the heat transport,

$$M^{\kappa} = (1-\varphi)\rho_R C_R T + \varphi \sum_{\beta} \rho_{\beta} S_{\beta} \boldsymbol{u}_{\beta}, \tag{4}$$

$$\mathbf{F}^{\kappa} = -\lambda \nabla T + \sum_{\beta} h_{\beta} \rho_{\beta} \boldsymbol{u}_{\beta}. \tag{5}$$

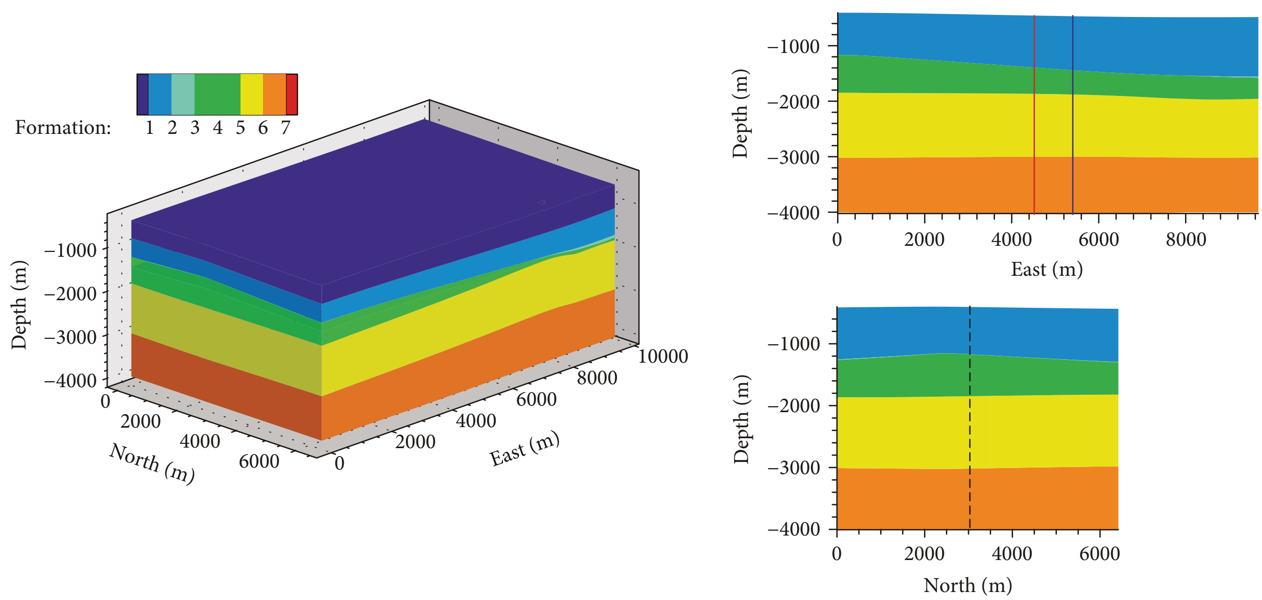

Figure 2: Lithology structure of the study area (rectangular area of the dotted line in Figure 1(c)) (formation 1: the Quaternary Formation, formation 2: the Mesozoic Formation, formation 3: the Neogene Formation, formation 4: the Ordovician formation, formation 5: the Cambrian Formation, formation 6: Neoproterozoic Formation, and formation 7: Wumishan Formation).

In the wellbore, the fluid flow is described by

$$\frac{\partial}{\partial t}\left(\sum_{\beta}\rho_\beta S_\beta u_\beta\right)+\frac{\partial}{\partial t}\left(\sum_{\beta}\rho_\beta S_\beta u_\beta^2\right)=-\frac{\partial P}{\partial z}-\frac{\Gamma\tau_w}{A}-\sum_{\beta}\rho_\beta S_\beta g\cos\theta, \tag{6}$$

where U_β and $1/2\,(u_\beta)^2$ are the internal energy of phase β and the kinetic energy per unit mass, respectively, while u_β is the velocity of phase β in the wellbore, and

$$\tau_{\mathrm{w}}=\frac{1}{2}f\rho_m|u_m|u_m, \tag{7}$$

when using equation (1) to describe the heat transport processes,

$$M^\kappa=\sum_{\beta}\rho_\beta S_\beta\left(U_\beta+\frac{u_\beta^2}{2}+gz\cos\theta\right),$$

$$F^\kappa=-\lambda\frac{dT}{dz}-\frac{1}{A}\sum_{\beta}\frac{\partial}{\partial z}\left[A\rho_\beta S_\beta u_\beta\left(h_\beta+\frac{u_\beta^2}{2}+gz\cos\theta\right)\right]-q'. \tag{8}$$

It is noted that the q' means the wellbore heat loss/gain per unit length of wellbore. In a leaking/feeding zone of the wellbore, the mass or energy inflow/outflow terms are calculated as in standard TOUGH2 (i.e., the flow through the porous media).

The heat exchange between wellbore and reservoir is determined by

$$Q_i^3=-A_{wi}(K_{wi})\left[\frac{T_i-T_\infty(z)}{rf(t)}\right]+\sum_{\beta}\left(\rho_\beta u_\beta g\cos\theta\right)_i, \tag{9}$$

$$f(t)=\frac{1}{-\ln\left[r/2\sqrt{\alpha t}\right]-0.29}, \tag{10}$$

where $f(t)$ is Ramey's well heat loss function [22]. The interpretation of every term involved in the equations can be seen in Nomenclature.

4. Numerical Modeling

4.1. Geothermal Background. Due to the heavy cost of drilling, limited data are available regarding the temperature and pressure measurement at the depth from 3300 m to 4000 m. In this study area, temperature and pressure are measured in four boreholes, within the maximum depth of 2750 m (Figures 3(a)–3(c)). The quality and reliability of the data, thermophysical parameters, and hydrogeological parameters are obtained from the published data in the studying area of the same lithology [23–26], as shown in Table 2. In the area of Tianjin, the Quaternary is mainly composed of clay, silt clay, and silt and the heat conductivity of which is between 1.2 W/m °C and 1.6 W/m °C. The main lithology of the Neogene and Qingbaikou system is sandstone, and the heat conductivity of which is between 2.0 W/m °C and 3.5 W/m °C. The Wumishan Formation is mainly composed of dolomite with the heat conductivity between 2.5 W/m °C and 3.8 W/m °C. The reference range

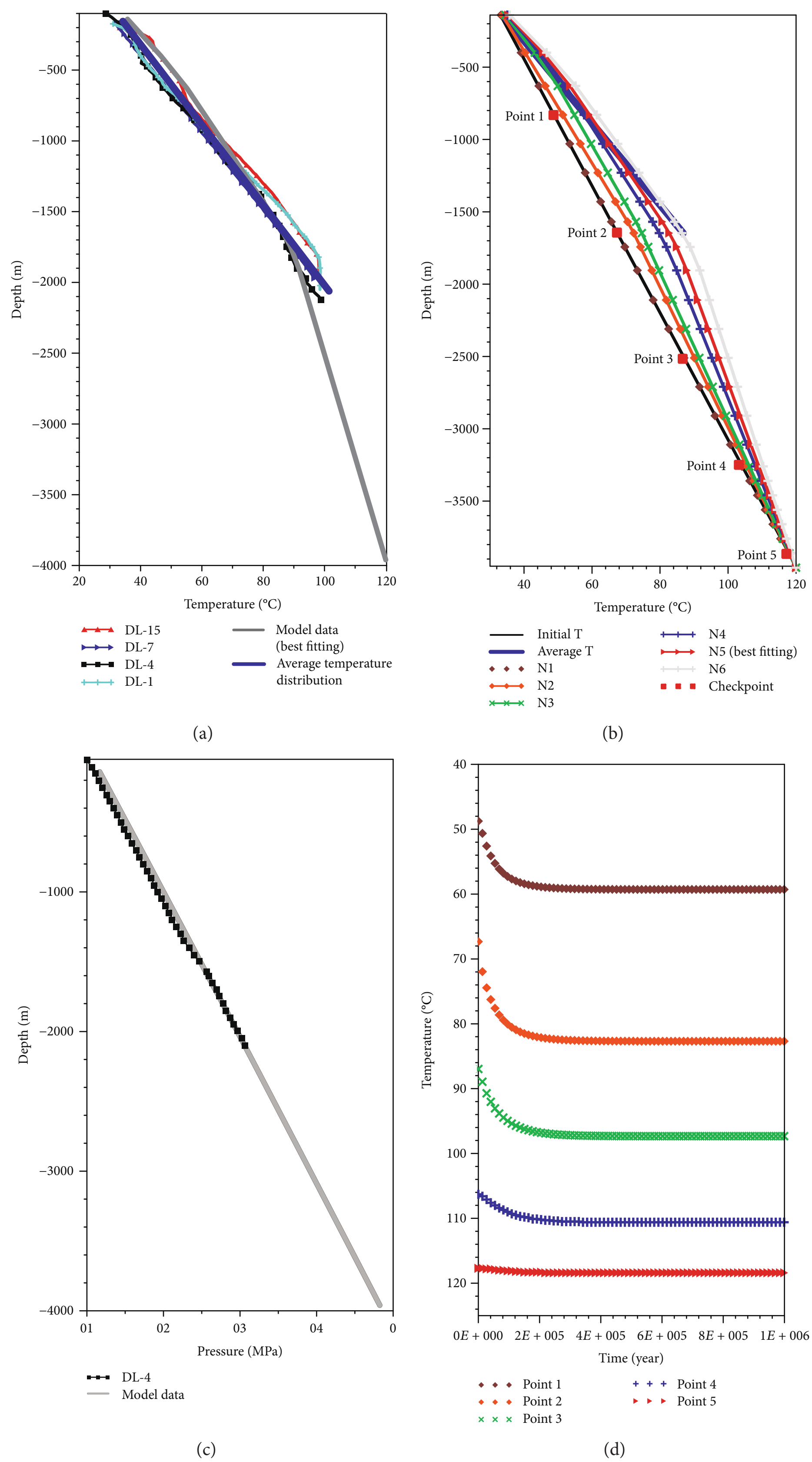

FIGURE 3: The temperature (a) and pressure (c) measured in the shallow aquifers extended to the deep geothermal reservoir by a 1D natural state model. The steady temperature distribution (b) of cases (N1–N6) with calibrated heat conductivity. Temperature variation with time (d) of 5 points in (b).

Table 2: Key thermal properties of the western thermal reservoir of Cangdong Fault (the solid rectangular zone as shown in Figure 1(c)) (Q: Quaternary caprock; N_m: Minghuazhen group of Neogene; N_g: Guantao group of Neogene; Q_n: Qingbaikou system; J_{xw}: Wumishan group of Jixian).

Properties	Thickness (m)	Porosity	Permeability (m^2)	Rock gain density (kg/m^3)	Specific heat (J/kg °C)
Q	520	0.25	2.37×10^{-17}	2232	920
N_m	1078	0.29	4.65×10^{-13}	1930	958
N_g	78	0.32	6.6×10^{-13}	2012	909
Q_n	114	0.05	2.09×10^{-13}	2600	909
J_{xw}	2110	0.05	3.65×10^{-13}	2677	838
Bottom boundary	100	0.05	3.65×10^{-13}	2677	2000

Table 3: Heat conductivity setting of each case (N1–N6) (Q: Quaternary caprock; N_m: Minghuazhen group of Neogene; N_g: Guantao group of Neogene; Q_n: Qingbaikou system; J_{xw}: Wumishan group of Jixian).

Cases		N1	N2	N3	N4	N5	N6
Heat conductivity W/m °C	Q	2.5	2.0	1.48	1.48	1.48	1.48
	N_m	2.5	2.0	2.0	2.00	2.00	2.00
	N_g	2.5	2.5	2.5	2.50	2.50	2.50
	Q_n	2.5	2.5	2.5	2.50	2.50	2.50
	J_{xw}	2.5	2.5	2.5	2.85	3.20	3.80
	Bottom boundary	2.5	2.5	2.5	2.85	3.20	3.80

of the above heat conductivity provides the basis for the model solution.

The rational of using a 1D model to describe the heat transport processes in the natural status is that the geothermal energy and groundwater in the deep thermal reservoir have not yet been extensively exploited and the groundwater flow velocity in the aquifer is extremely low (1–10 m/yr) [27]. Thus, it can be assumed that no groundwater flow to drive lateral heat advection in Shanlingzi geothermal field. In addition, according to the downhole temperature logs in four wells (Figure 3(a)), at the same depth, the temperature in different wells is almost the same, which suggest that the temperature in the lateral direction reaches a balance, and there is no heat conduction in the horizontal direction as well. Therefore, only the heat conduction in the vertical direction is simulated here.

The temperature and pressure logging data are collected about 1–1.5 months before the exploitation season. The equilibration time can be at least 6 months, for the heating period in Tianjin is from November 15th to March 15th of the following year. The test data can represent the temperature and pressure distribution of the reservoir after the thermal-hydraulic conduction process between water and rock matrix is fully balanced under the hydrostatic condition.

4.2. Natural State Model. In order to obtain thermal-physical parameters of geological layers, a 1D model based on real geological conditions is established. The cases from N1 to N6 is set up with different heat conductivity, and other properties are the same (summarized in Table 2). The same heat conductivity of 2.5 W/m °C is used in all the layers in the model of case N1, because it is basically the mean value of heat conductivity in sandstone and dolomite. In cases N2 and N3, the heat conductivity of the Minghuazhen group and the Quaternary is lowered. The heat conductivity of Wumishan Formation is increased in cases N4, N5, and N6 on the basis of case N3. Specific setting of heat conductivity of each case can be seen in Table 3.

The thickness of each layer is given as the average values according to the downhole logs in seven boreholes (Figure 1(c), Table 2). The temperature at the model top (at the depth of 140 m) is given a measured mean temperature of 34.4°C in Tianjin, while the pressure in the model is obtained by the relationship between hydrostatic pressure and depth. The initial temperature distribution follows the average temperature gradient of 2.24°C, as shown in Figure 3(b). At the model bottom, a constant heat flux boundary of 80 mW/m^2 [28] is used. The calculation results of the model indicate that the temperature of the bottom boundary is basically stable at 120°C. The running time of the natural steady-state model must be long enough to make sure that the thermal-physical parameters are stable. In this paper, the final running time of the natural model is set to 10^6 years.

In the sedimentary basin, the heat transfer speed of the caprock with low heat conductivity (caprock) is low, which leads to the high gradient of geothermal temperature. With the same heat flux, the bedrock usually has high heat conductivity and high heat transfer speed, which leads to the low temperature gradient. When all the layers in the model have the same heat conductivity, the temperature in the steady state has changed a little, compared with the initial temperature (Figure 3(b)). When the heat conductivity of the Minghuazhen group and the Quaternary decreases, the temperature gradient of caprock (above 1800 m depth) increases and the temperature gradient of bedrock reduces (cases N2 and N3). When the heat conductivity of the Wumishan Formation increases (cases N4, N5, and N6),

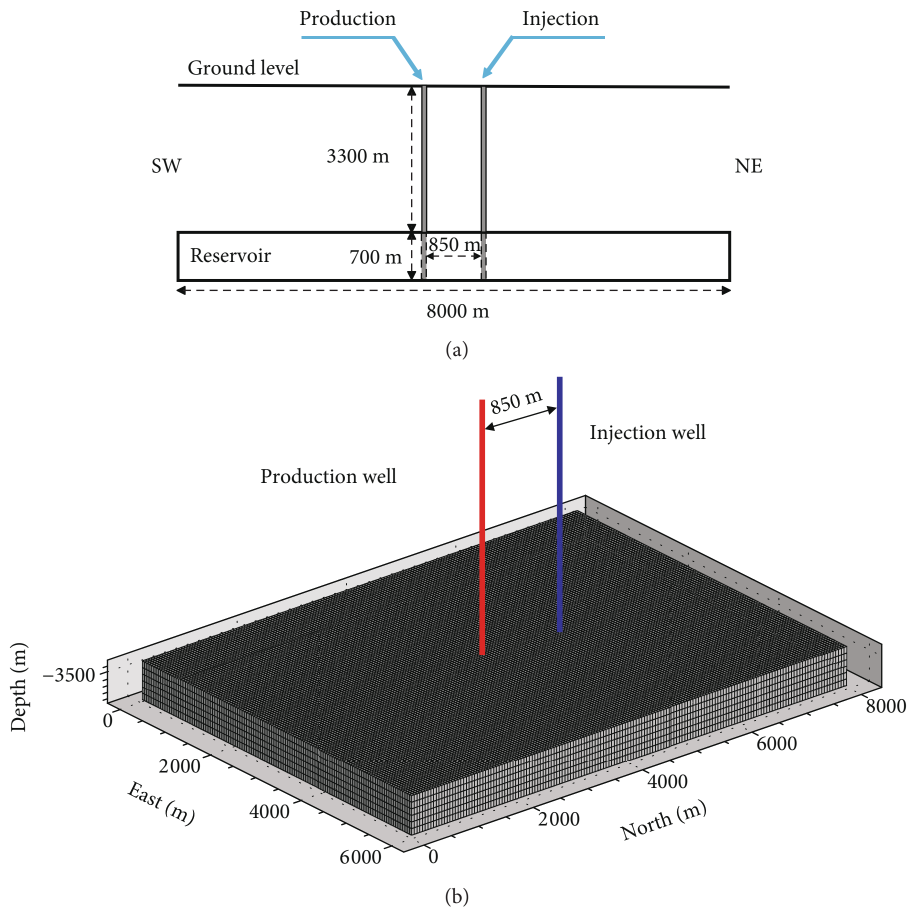

Figure 4: (a) Lateral 2D cross section of the model and (b) well placement in the model domain and discretization.

the temperature gradient of caprock increases obviously in the temperature distribution of the steady state (Figure 3(b)) and is closer to measured data than that of case N3. By the contrastive analysis between the measured average temperature and the calculation results in cases N4, N5, and N6, the temperature distribution of case N5 fits to the measured data best.

Based on the heat conductivity and hydrogeological parameters in case N5 (best fitting), the different specific heat of the Wumishan Formation (808 J/kg °C, 838 J/kg °C (N5), 868 J/kg °C, 898 J/kg °C) is set up to determine the influence on temperature distribution in the steady state. When the natural state model reaches the steady state, temperature distribution almost does not change with different specific heat of bed rock. At present, the measured data of the specific heat capacity of the rock is still limited. In the future, the influence of specific heat of caprock and bedrock on the heat transfer mechanism of the steady-state model will be explored.

The 5 spots with different depths (Figure 3(b), points 1–5 with red blocks) in the model of case N5 are monitored to verify the stability of the natural state model. As shown in Figure 3(d), the natural state model with the running time of 1000000 years can reach stable states. As a consequence, the temperature distribution in the geothermal reservoir is obtained, which increases from 33.4°C to 88.8°C in the depth of 1800 m with a gradient of 3.3°C/100 m (caprock) and increases from 88.8°C to 120°C with a gradient of 1.41°C/100 m in the depth from 1800 m to 4000 m in the bedrock. The variation of thermal gradient in the vertical direction is mainly induced by the differences of the heat conductivity between caprock and bedrock and specific boundary conditions. The calibrated 1D natural state model agrees reasonably well with history log data of temperature and pressure (Figures 3(a) and 3(c)).

Table 4: Geological and thermophysical parameters of wellbore.

Wellbore parameter	
Roughness (mm)	0.046
Diameter (m)	0.15
The distance between wells (m)	850
Range of buried depth (m)	3300–4000
Reinjection temperature	30
Temperature (°C)	111–120°C
Pressure (MPa)	32.6–38.3

4.3. Exploitation Method. The double well geothermal system is established in the Wumishan reservoir. One well is used for heat extraction and another well for fluid injection, to maintain the water balance. A 3D conceptual model with the

Table 5: Parameter setting of the modeling cases.

Cases	Injection/production rate (m^3/h)	Porosity	Permeability (m^2)	Homogenization or heterogeneity
Reference case simulation (RCS)	450	0.05	3.65×10^{-13}	Homogenization
H1	150	0.05	3.65×10^{-13}	Homogenization
H2	300	0.05	3.65×10^{-13}	Homogenization
H3	600	0.05	3.65×10^{-13}	Homogenization
H4	750	0.05	3.65×10^{-13}	Homogenization
H5	900	0.05	3.65×10^{-13}	Homogenization
C1–C5	450	0.01–0.09	3.65×10^{-15}–3.65×10^{-11}	Heterogeneity

Table 6: The logging interpretation of the geothermal reservoir at DL-6 well.

Sequence number	Start depth (m)	End depth (m)	Thickness (m)	Porosity (%)	Permeability (m^2)
1	1938.7	1944.9	6.2	9.36	4.71×10^{-15}
2	1959.4	1965.5	6.1	3.69	5.00×10^{-16}
3	1972.7	1977.6	4.9	4.64	4.10×10^{-16}
4	1982.5	1989.5	7.0	2.70	1.10×10^{-16}
5	1998.6	2004.8	6.2	7.25	2.63×10^{-15}
6	2011.7	2030.4	18.7	6.36	1.66×10^{-15}
7	2048.0	2055.7	7.7	4.01	4.70×10^{-16}
8	2090.5	2105.4	14.9	4.49	4.50×10^{-16}
9	2119.1	2132.0	12.9	7.74	2.76×10^{-15}
10	2132.0	2138.5	6.5	3.63	1.40×10^{-16}
11	2147.0	2150.1	3.1	7.35	1.67×10^{-15}
12	2153.2	2157.7	4.5	6.55	9.70×10^{-16}
13	2159.5	2161.7	2.2	3.02	1.2×10^{-16}
14	2166.9	2182.1	15.2	1.85	1.00×10^{-16}
15	2192.7	2199.4	6.7	6.90	1.72×10^{-15}
16	2212.2	2216.7	4.5	3.57	1.50×10^{-15}
17	2221.5	2224.8	3.3	3.54	1.30×10^{-16}
18	2255.4	2267.9	12.5	5.19	6.80×10^{-16}
19	2274.9	2278.4	3.5	4.48	4.60×10^{-16}
20	2292.4	2297.0	4.6	4.34	6.00×10^{-16}
21	2314.9	2317.3	2.4	4.21	4.80×10^{-16}

domain size of 6000 m × 8000 m × 700 m is established (Figure 4), including 2 wellbores and a reservoir. According to the data of geological design of TD-01 and TD-02, the distance between 2 wellbores is 850 m and the average thickness of the reservoir is 700 m. The model is divided into seven layers with 134448 elements. An equivalent porous medium (EPM) [29] is performed in the model. The thermophysical parameters in the Wumishan Formation and wellbores are summarized in Tables 2 and 4, respectively.

In the model domain, the injection and extraction via two wells interrupt the fluid and heat transport near the wells, but does not affect the lateral boundaries that are far enough from the wells, where constant pressure and temperature boundary conditions are employed. The heat transfer between wellbore and surrounding rock is calculated by Q_i^3 (equation (9)). At the bottom of the exploitation model, a constant heat flux of 80 mW/m^2 is assigned [28], while on the top of the exploitation model, a semianalytical method is used for modeling heat exchange with confining beds. Following the requirement of heat supply [30, 31], the extraction rate and reinjection are given in the range of 80–380 m^3/h. After heat extraction, cool fluid is reinjected into the reservoir under a constant rate equal to the extraction rate. The injection temperature is given at 30°C, following the average reinjection temperature of geothermal tail water in Tianjin [26]. The sensitivity of heat production to the extraction rate and the permeability in the reservoir are analyzed based on the scenario in Table 5, where the case with a flow rate of 450 m^3/h and permeability of 3.65×10^{-13} m^2 is used as a reference case simulation (RCS). The heat production and temperature distribution in the reservoir are calculated in a period of 50 years.

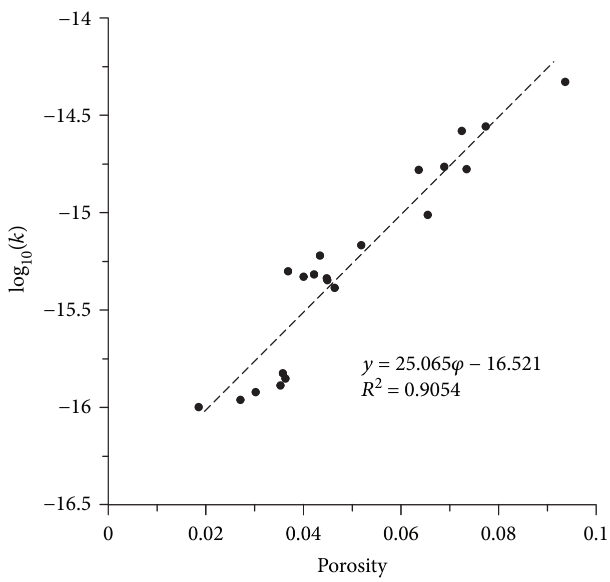

FIGURE 5: The relationship between permeability and porosity of dolomite in Wumishan Formation of typical geological conditions.

4.4. Heterogeneity Implementation. There is no such a deep geothermal well with completion depth more than 4000 m finished in Dongli District, which brings a difficulty in sample gathering, including groundwater samples and rock samples. In real strata, density, porosity, permeability, heat conductivity, and specific heat can vary a lot from different rock types. When the fluids flow through the aquifer, it may give priority to the high porosity and permeability zone. As for the above thermophysical parameters of the reservoir, the permeability and porosity have the largest effect on flow field and heat extraction [32]. Therefore, permeability and porosity are considered as the main variables to study the heterogeneity effects.

In this paper, 5 scenarios were designed for comparison in which the permeability and porosity of the subdomain are heterogeneous. There will be a great difference in the distribution of porosity and permeability in the actual reservoir, but the correlation of porosity and permeability has facilitated the study of the heterogeneity of the reservoir.

Bryant et al. [33], Brant [34], and Neuzil [35] observed a log-linear relationship between permeability and porosity for argillaceous sediments. The log-linear equation can be expressed by

$$\log(k) = (a \cdot \varphi) + \mathrm{b}, \tag{11}$$

where k is the permeability in m^2, φ is porosity, and a and b are fitting parameters. Tian et al. [36] used the empirical relationship between porosity and permeability obtained by field data in the Jianghan Basin [37] to explore impacts of hydrological heterogeneities on caprock mineral alteration.

$$\log(k) = (21.581 \cdot \phi) - 18.272, \tag{12}$$

where the coefficient of determination (R^2) is equal to 0.93.

Compared with clastic rock, different kinds of the relationship between porosity and permeability of carbonate reservoirs are much more complex [38–40]. In this study, we obtained a log-linear equation for porosity-permeability by regression analysis of logging interpretation results of DL-4 (Table 6, Figure 5).

$$\log(k) = (25.065 \cdot \phi) - 16.521, \tag{13}$$

where R^2 is 0.9054.

The permeability is generated randomly following the log-normal distribution [41, 42] in a subzone defined by following range of coordinates: $X = 1000{\sim}2000$ m, $Y = 2575{\sim}4375$ m, and $Z = 3300{\sim}4000$ m. The porosity limited by equation (13) obeys a normal distribution. In order to describe the spatial distribution of reservoir permeability and porosity more realistically, we introduced the variation function, a geostatistics concept, to determine and limit the spatial distribution of permeability and porosity by assigning variance and correlation length which strongly depends on the variation function type and the model scale [43]. Here, a variance of 0.8 and correlation length of 300 m are used in our model [36]. TOUGH2 family codes provide a feature that applies permeability modification coefficients for individual grid blocks according to

$$k_n{}' = k_n \cdot \xi_n, \tag{14}$$

where k_n is specified in data block ROCKS for the initial permeability of grid block, while ξ_n is the permeability modification coefficient. More details about the generation process of permeability modification coefficients and the achievement of heterogeneity can be found in the previous study [36].

Five representative distributions of permeability and porosity are selected and discussed (Figure 6): (a) high permeability between the two wells with low permeability at the bottom of production well (case 1) and injection well (case 2), respectively, (b) the production well is in the low permeability zone and the injection well is in the high permeability zone (case 3), (c) the injection well is in the low permeability zone and the production well is in the high permeability zone (case 4), and (d) low permeability between the two wells (case 5).

5. Results and Discussion

5.1. Production Rate. The heat production is under a constant rate of 450 m^3/h for 50 years, the bottom pressure in injection well increases to 38.64 MPa (increased by 1.10% when compared to the initial pressure), and the bottom pressure in production well decreases to 38.11 MPa (reduced by 0.28%) (Figure 7(c)). The injected cold water migrates towards the production well, with the minimum influence distance (the isothermal surface of 50 °C) of 268 m at depth of 3300 m and the maximum influence distance of 441 m at depth of 4000 m. As a consequence, the outflow temperature

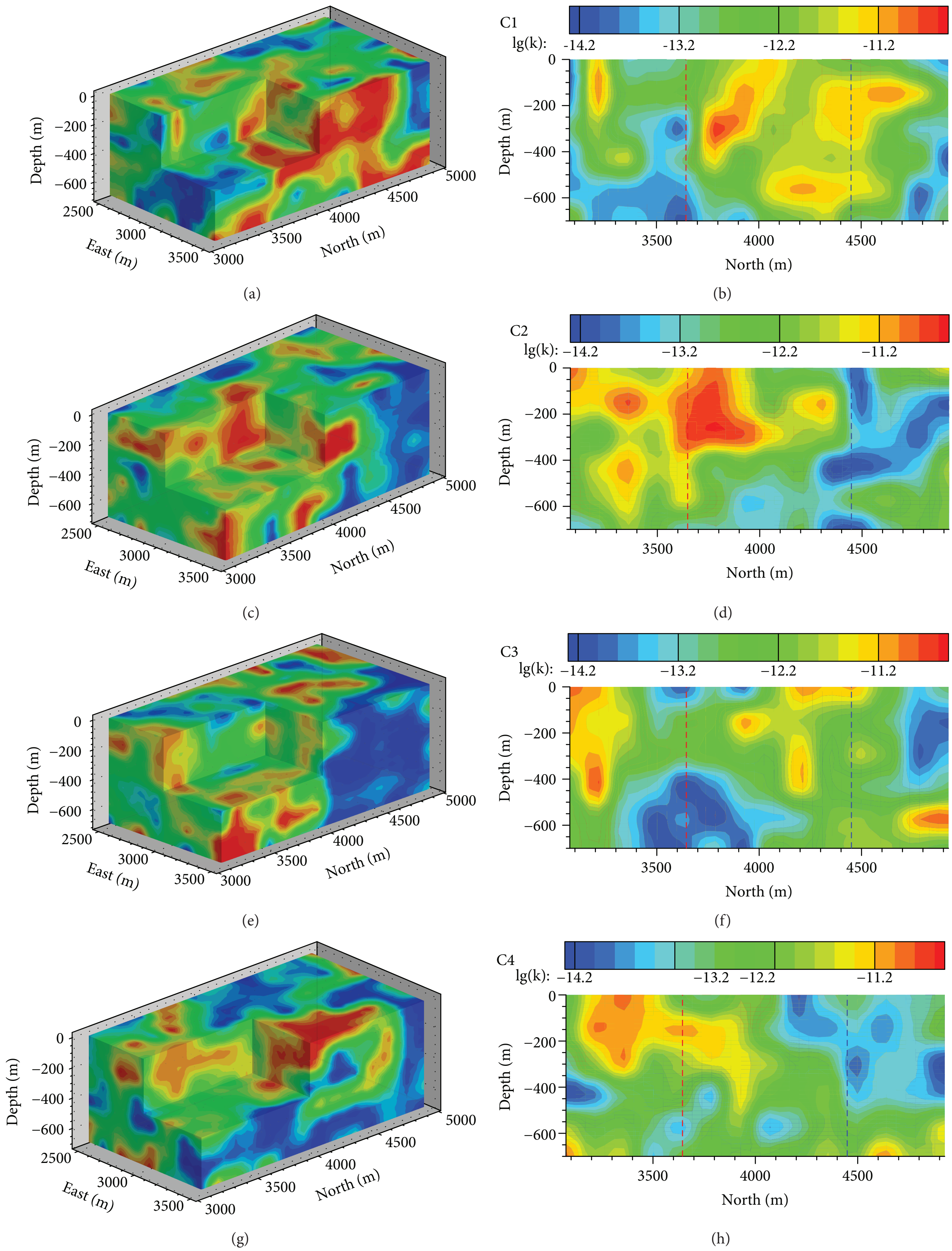

Figure 6: Continued.

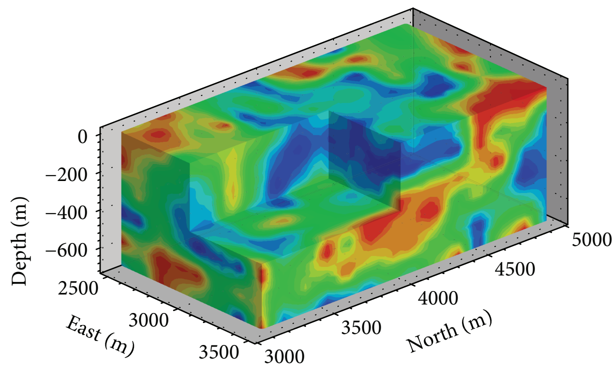

(i)

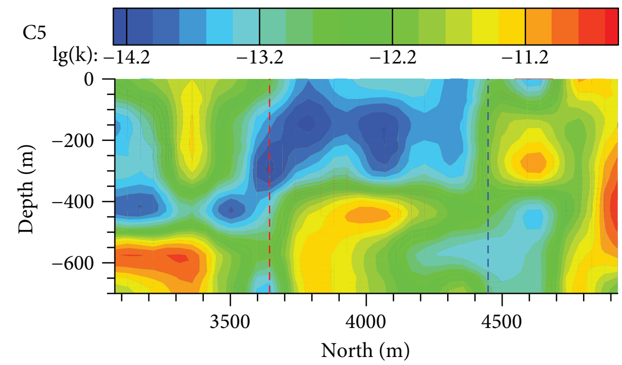

(j)

FIGURE 6: Five hypothetical heterogeneous permeability distributions ((a) C1, (c) C2, (e) C3, (g) C4, and (i) C5) and the corresponding two-dimensional cross sections (b, d, f, h, j) at east 3000 m. Red dashed lines and blue dashed lines indicate the location of production well and injection well, respectively.

decreased by 0.49°C in 50 years (Figure 8(a)). As illustrated in Figure 7(c), the injection/production rate of 450 m^3/h does not induce significant pressure changes in the reservoir. Whereas the cold plume between the injection well and production well may cause heat breakthrough, i.e., the cold water reaches the production well without sufficient heat transfer. In order to figure out the TH coupling process of geothermal doublets and the exploitable volume within the lifespan over 50 years, another five cases with different constant production/injection rates are added.

The wellhead temperature, under the constant rate of 150 m^3/h and 300 m^3/h, increases to about 1.65°C and 0.65°C after 50 years, compared with the base case of 450 m^3/h (Figure 8(a)). Because the minor exploitation rate is not enough to cause heat breakthrough and the cold water is still dominated by downward movement, more geothermal water from deep sectors of the reservoir is driven by the cold plume towards the production well. With the further increase of the production and injection rate (from 600m^3/h to 900 m^3/h), the breakthrough occurs and leads to the rapid reduction of the outflow temperature and heat extraction rate after 50 years (Figures 8(a) and 8(b)). The influence range of the injected cold water increases with the production/injection rate, which leads the decreases of outflow temperature. It is tested that when the injection rate increases to 900 m^3/h, the influence range of cold water reaches to extraction well extensively (Figure 7(b)), over a volume having an approximate diameter of 1.5 km, which leads the temperature in the production well to reduce 8.08°C in 50 years.

Fluid temperature, pressure, enthalpy, and operating cost should be considered when evaluating the productivity of geothermal extraction engineering. Due to negligible effect of the pressure on energy balance, the heat extraction rate (G) is calculated with the following equation:

$$G = \mathrm{MF}_{(\mathrm{pro})} \times h_{(\mathrm{pro})} - \mathrm{MF}_{(\mathrm{inj})} \times h_{(\mathrm{inj})}, \tag{15}$$

where MF is the mass flow rate (kg/s) and h is the specific enthalpy (kJ/kg). The subscripts (inj) and (pro) stand for the injection well and production well, respectively.

It is illustrated in Figure 8 that under the production rate of 450 m^3/h, the maximum outflow temperature can basically remain stable of 112°C, with a limited drop of 0.49°C in 50 years, and heat extraction rate can reach average of 43.5 MW with a decrease of 0.73%. When the injection/production rate is higher than 450 m^3/h, heat breakthrough occurs, which cause significant decreases of outflow temperature over a lifespan of 50 years. To increase the heat extraction rate and maintain a high outflow temperature, a production rate of 450 m^3/h can be achieved if the reservoir formation is hydrologically homogeneous.

5.2. Heterogeneity. As shown in Figure 9, the flow paths and temperature distribution in the reservoir are largely affected by the permeability distribution. High permeability zone between the injection well and production well in cases C1 and C2 (Figures 6(a)–6(d)) accelerates the heat breakthrough, where the injected cold water flows towards extraction well rapidly in the depth of 3300 m to 3600 m (Figure 10(b)), which causes the outflow temperature to decrease by 3.1°C and 6.93°C in the 50th year, respectively (Figure 10(d)). In contrast, in cases C3 and C4, where low permeability zone is between injection well and production well (Figures 6(e)–6(h)), the injected cold water is impeded at the bottom of production well with a low flow rate at the depth from 3700 m to 4000 m (Figure 10(b)). This causes the cold water to move in the opposite direction of production well with no heat breakthrough. The outflow temperature in cases C3 and C4 is stable and is reduced by 0.85°C and 0.6°C in the 50th year, respectively (Figure 10(d)). In case C5, with the low permeability at the upper part of the reservoir and high permeability at the lower part (Figures 6(i) and 6(j)), the cold plume tends to move towards the bottom of the reservoir (Figure 9(f)), which drives hot water to flow from the deep sector towards the production well. From the flow rate along production well (Figure 10(b)), the outlet water is mainly consisted of geothermal water at the depth from 3700 m to 4000 m in the reservoir. In the first 20 years, the output temperature is almost constant, but keeps a decreasing trend from the 20th year to the 50th year, with the temperature reduction by 8.5°C (Figure 10(d)). It is

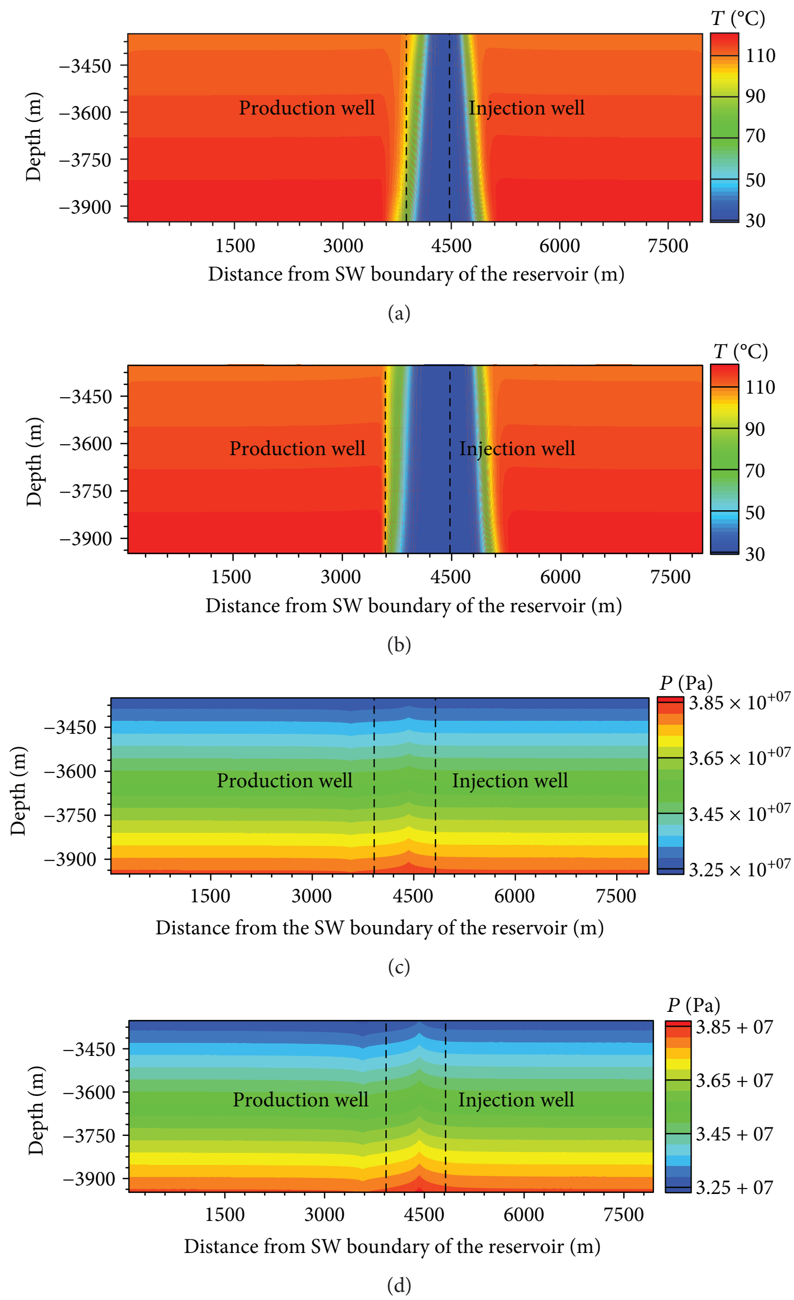

Figure 7: Temperature (a) and pressure (c) field distributions at the injection/production rate of 450 m^3/h, and temperature (b) and pressure (d) field distributions at the injection/production rate of 900 m^3/h along a 2D SW-NE trending cross section of the reservoir (50 years). Black dotted lines represents the location of injection well and production well.

because the primary hot water at bottom of production well has been used up and the cold water from injection well becomes the main part of output water.

5.3. Wellhead Pressure. In the actual application, the injection and production rate is controlled by wellhead pressure of both wells. The different geological conditions and flow rates lead to the variation of wellhead pressure (Figure 11). Accordingly, the wellhead pressure variation with time based on different cases with heterogeneity of permeability needs to be predicted to offer a reference for the application and safety of geothermal water exploitation. When the low permeability sector is around injection well, the injected water needs to be driven by high pressure difference between wellhead and the reservoir, which leads to the increase of wellhead pressure of injection well. While the high permeability sector is around injection well, the lower wellhead pressure is needed to realize the reinjection process. The production of geothermal water needs depressurization of wellhead. In the same way, if the low permeability exists around production well, the wellhead pressure of production well may decrease. Hence, the reservoir with low permeability sectors around the injection well and production well can bring difficulties to stable

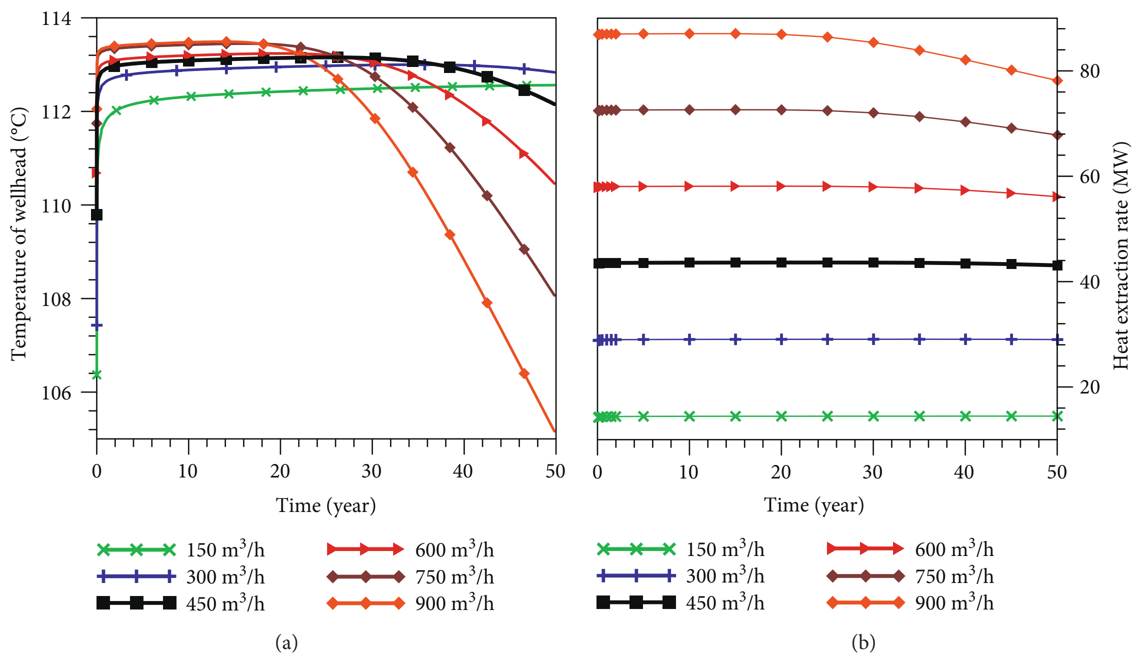

FIGURE 8: Temperature of outlet water (a) and heat extraction rate (b) variation for different constant production rates.

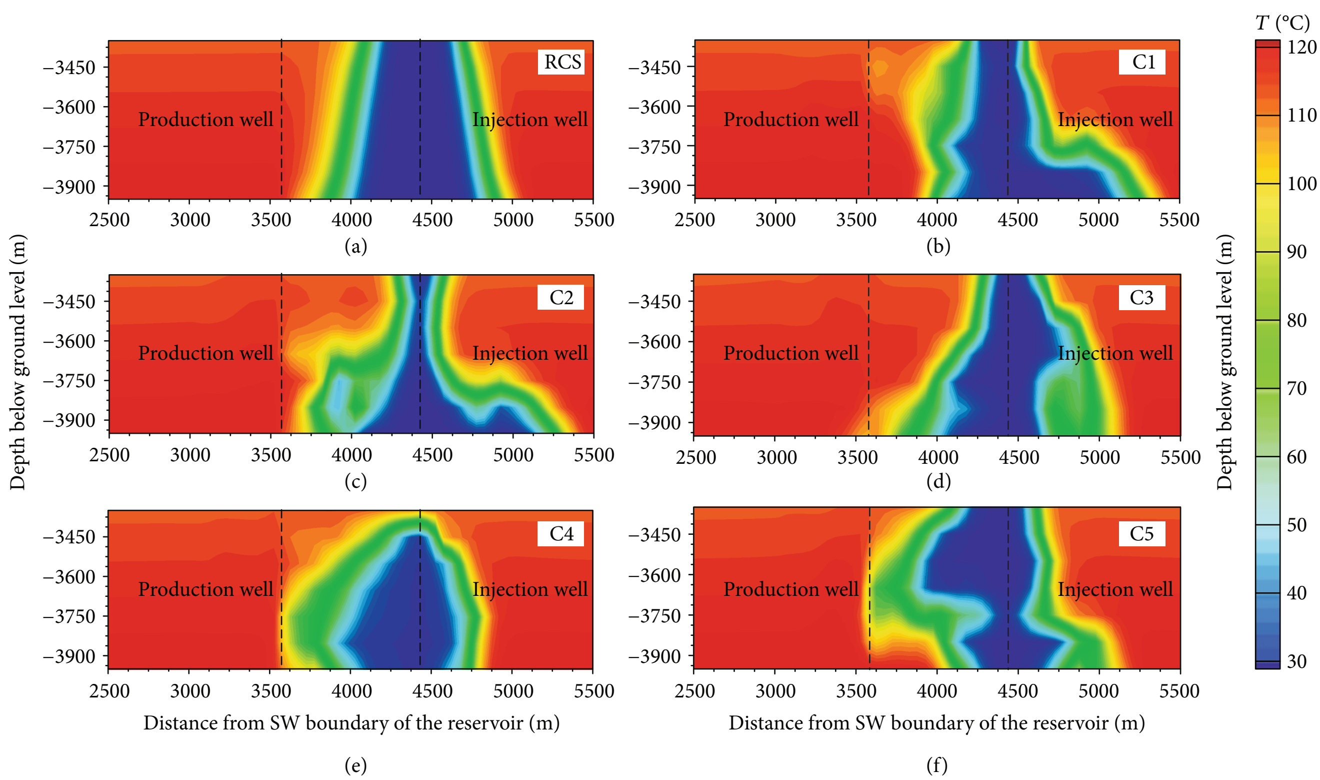

FIGURE 9: The temperature distribution along a 2D SW-NE trending cross section of the reservoir after 50 years in the reference case simulation ((a) RCS) and five cases in the heterogeneity of permeability ((b) C1, (c) C2, (d) C3, (e) C4, and (f) C5). Black dotted lines represents the location of injection well and production well.

operation of the doublet well, as a result of increasing injection pressure or lowering production pressure, which will increase operating costs and risk.

In summary, when the high permeability zone exists between the wells, heat breakthrough may occur and the lifetime is approximately lower than 20 years. However, the

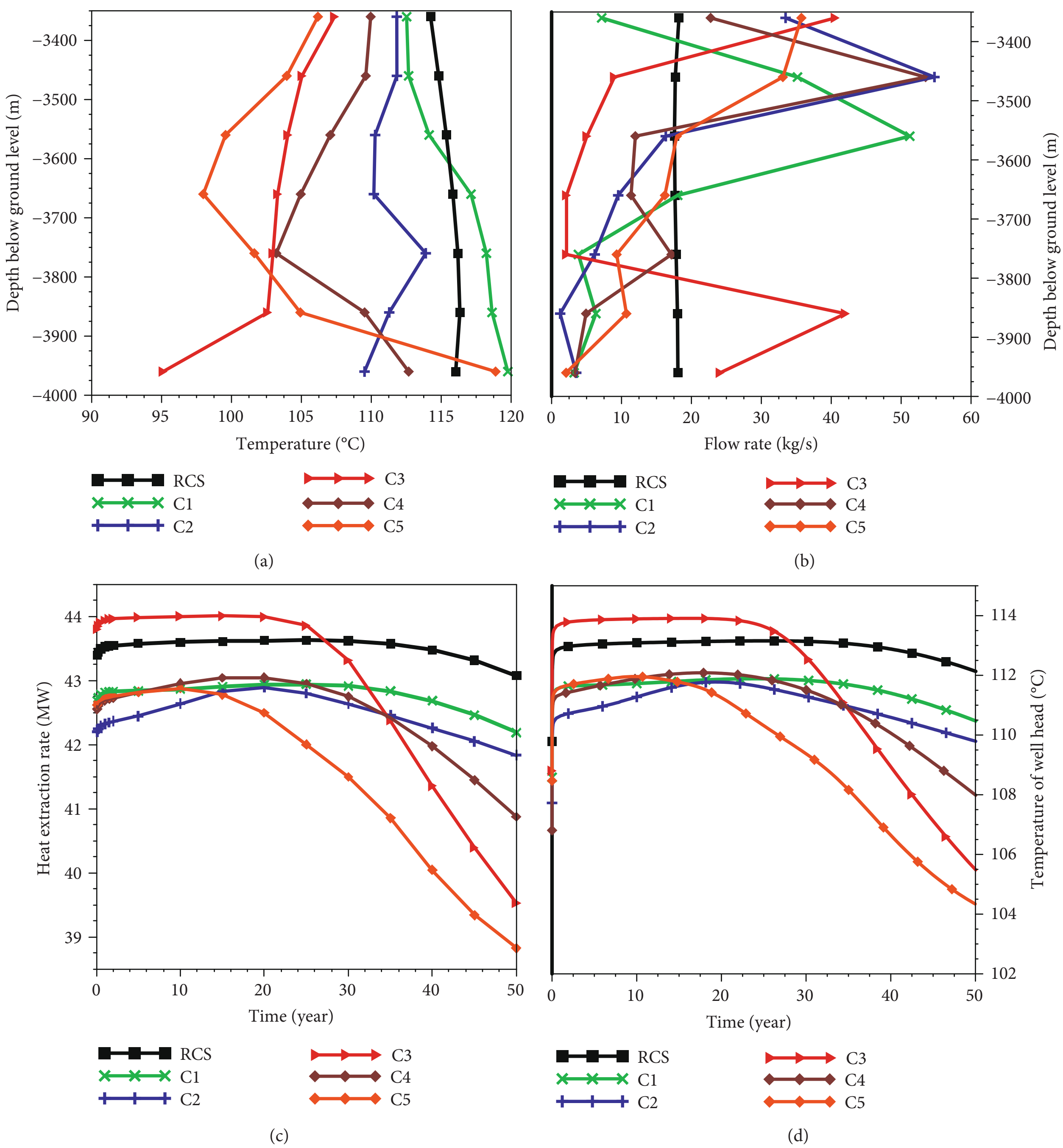

Figure 10: The temperature profile (a) and flow rate variation (b) along open-hole section of production well after 50 years. Heat extraction rate variation (c) and output temperature variation (d) over time. Different cases including the RCS and five cases (C1, C2, C3, C4, and C5) in the heterogeneity of permeability are analyzed.

existence of the high permeability zone also reduces the reinjection costs of the doublet well at some extent. Low permeability zone at the interwell sector may prolong the lifetime of the heat extraction system and promote stability, and it can also retard injection of tail water when the low permeability zone is at the vicinity of injection well. Thus, it is necessary to determine subsurface heterogeneity in a high resolution based on such as a tracer test and geophysical prospecting before sitting the extraction and injection segment in a deep geothermal reservoir. When the optimized layout of doublet well system is considered, the high permeability zone at the interwell sector should be avoided.

Thermal hydraulic coupling process, as the basis, should be first taken into the research of the doublet well geothermal system, especially for a planar fracture in the hot dry rock reservoir [44]. In the fracture network involved in geothermal exploitation, the thermal stress caused by the injection of cold water changes the fracture aperture width [45] and

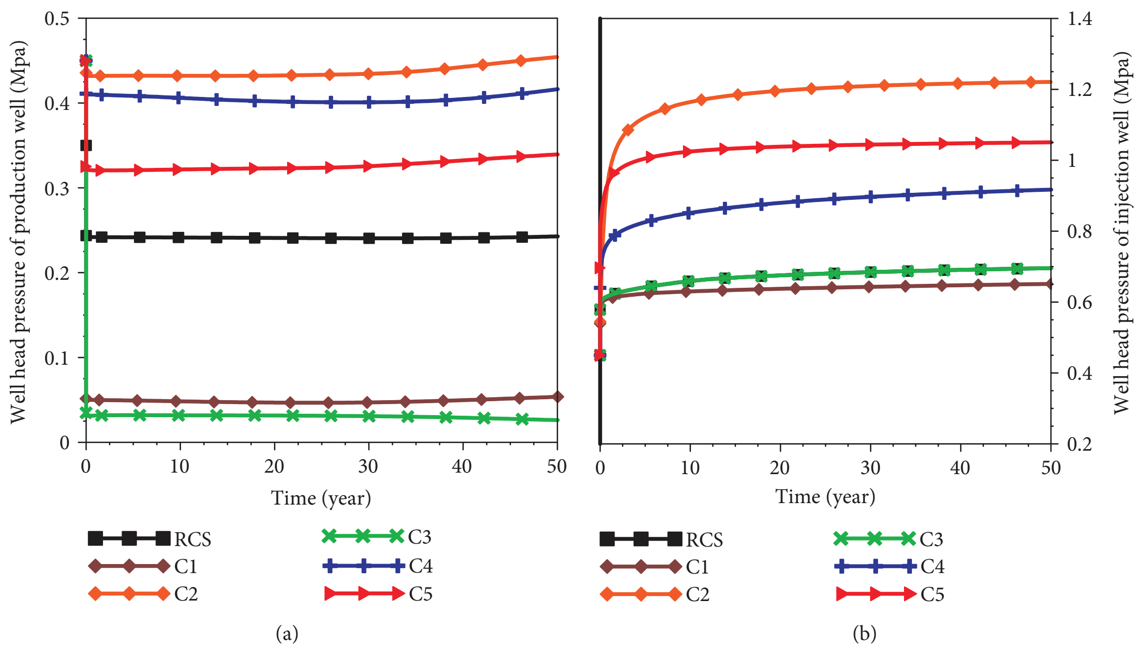

Figure 11: Wellhead pressure of production well (a) and injection well (b) over time by contrasting the RCS and five heterogeneous cases (C1, C2, C3, C4, and C5).

has a serious impact on the percolation path, which may have an important impact on geothermal production safety such as microseism [46] and well stability [47]. The distribution and properties of the fracture network and related microseismic data of the reservoir have not been obtained, so the procedure of thermal mechanics in the wellbore-reservoir coupled model will be developed further.

Almost all the ways of geothermal exploitation encounter scaling problems of wellbores. The process of mineral dissolution and precipitation [48] can also affect the porosity and permeability in the reservoir after the injection of cold water [49]. When the fluid is produced from the wellbore, a sharp decline of temperature and pressure may lead to fluid supersaturation and the occurrence of reaction of mineral precipitation. The hydrochemistry components of injection water, the characteristic of initial water in the reservoir, and mineral composition have not been obtained, so the process of reactive transport in the wellbore and reservoir [50] deserves further research.

6. Conclusions

This study optimized the injection/production rate and evaluated the energy productions in the deep geothermal reservoir in Tianjin, China, in a lifespan of 50 years. The temperature and pressure distribution under unexploited conditions is evaluated by a 1D heat conduction model. Furthermore, an integrated 1D–3D wellbore-reservoir model is established by the T2WELL simulator.

It is concluded that the optimal (maximum) injection/production rate for typical geothermal doublet well system studied here with a reservoir thickness of 700 m and a well distance of 850 m is 450 m^3/h. Under the production rate of 450 m^3/h, the maximum outflow temperature can basically remain stable of 112°C and thermal energy extraction rate can reach average of 43.5 MW.

The high-permeability channels at the interwell sector should be avoided, when the optimization layout of the doublet well system is considered. The heterogeneous distribution of porosity and permeability causes significant changes in the outflow temperature. In the case that a high permeability zone exists between injection and production wells, the outflow temperature can decrease by 4–8°C when compared to the homogeneous case. When a low permeability zone occurs between two wells, the outflow temperature can basically keep stable and lifetime of the heat extraction system can reach 50 years at least.

The wellhead pressures of injection well and production well can be intensely influenced by the distribution of a low permeability zone. If the low permeability zone in the reservoir is around injection well, it usually leads to higher wellhead pressure than that in the homogeneous strata. When the low permeability zone is around production well, the wellhead pressure needs to be depressurized to maintain the profitable output of geothermal water. The existence of low permeability zone around the wellbores does not benefit the stable operation and cost saving and may be solved by the technique of formation acidizing to increase production or lower operation costs.

Further, the detailed geochemistry of water, geology of reservoir, and geophysical parameters are needed to run the T- (thermal-) H- (hydraulic-) C- (chemical-) M (mechanics) model to evaluate the influence of thermal stress and wellbore scaling on the heat breakthrough. The effect of economic parameters (electricity price, heat price, and discount rate) should be considered to optimize the cost of reservoir exploitation in combination with numerical results in further study. More accurate main parameters, related coupling processes, and cost analysis should be updated and added into the model to get accurate results to achieve optimum performance.

Nomenclature

M^{κ}: Mass accumulation term, kg m^{-3}
F: Mass or heat flux, W m^{-1}
V_n: An arbitrary subdomain of the flow system
S_β: The saturation of phase β
$\boldsymbol{u}_\beta$: Darcy velocity in phase β, m s^{-1}
X_β: Mass fraction of component κ present in phase β
k: Absolute permeability to phase β, m^2
k_r: Relative permeability, m^2
P: The pressure of a reference phase and usually taken to be the gas phase, Pa
q: Sinks and sources, kg m^{-3} s^{-1}
U_β: The internal energy of phase β, J kg^{-1}
u_β: The velocity of phase β in the wellbore, m s^{-1}
$1/2\,(u_\beta)^2$: The kinetic energy per unit mass
A: Well cross-sectional area, m^2
z: Distance along-wellbore coordinate (can be inclined), m
C_R: Specific heat of rock, J kg^{-1}°C^{-1}
h_β: Specific enthalpy of fluid phase β, J kg^{-1}
g: Gravitational acceleration, m s^{-2}
q': The wellbore heat loss/gain per unit length of wellbore, kg m^{-3} s^{-1}
A_{wi}: The lateral area between wellbore and surrounding formation, for grid cell i (wellbore), m^2
K_{wi}: The overall heat transfer coefficient of wellbore and formation, W^{-1} K^{-1} m^{-1}
T_i: The temperature of ith wellbore node, °C
$T_\infty(z)$: Ambient temperature, °C
r: Radium of the wellbore, m
$f(t)$: Ramey's well heat loss function
u_m: The velocity of mixture (liquid water in our model), m s^{-1}
k: Permeability
a: Fitting parameter
b: Fitting parameter.

Greek Letters

φ: Porosity
ρ_β: The density of phase β, kg m^{-3}
λ: Heat conductivity, W^{-1} K^{-1} m^{-1}
ρ_R: Grain density, kg m^{-3}
μ_β: Viscosity, kg m^{-1} s^{-1}
λ: The area-averaged heat conductivity of the wellbore (contains the fluids and possible solid portion), W^{-1} K^{-1} m^{-1}
θ: Incline angle of wellbore, °
Γ_n: Area of closed surface, m^2
α: The thermal dispersivity of the surrounding formation, m^2 s^{-1}
Γ: Perimeter of wellbore, m
τ_w: The wall shear tress, MPa
ρ_m: The mixture density (liquid water), kg m^{-3}.

Subscripts and Superscripts

β: Refers to liquid water in this paper
κ: The index for the components, 1 for H_2O, 4 for energy.

Data Availability

We can directly link the dataset in this manuscript by providing the relevant information. The data in this manuscript is available and can be found in the database linking page.

Conflicts of Interest

The authors declare that they have no conflicts of interest.

Acknowledgments

This study is supported by the National Key Research and Development Program of China (no. 2016YFB0600804), National Natural Science Foundation of China (no. 41572215, 41402205, and 41502222), Center for Hydrogeology and Environmental Geology Survey, China Geological Survey (DD20179621 and DD20189113), Special Project for New Energy, Jilin Province (SXGJSF2017-5), Graduate Innovation Found of Jilin University (no. 101832018C052), and the Major Project of China National Science and Technology (no. 2016ZX05016-005).

References

[1] M. Shen, "Environmental pollution and prevention of coal burning," *Northwest Coal*, vol. 6, no. 1, pp. 46–48, 2008.

[2] X. Li, "Empirical analysis of the smog factors in Beijing-Tianjin-Hebei region," *Ecological Economy*, vol. 32, no. 3, pp. 144–150, 2016.

[3] Ministry of Ecology and Environment of the People' s Republic of China (original Ministry of Environment Protection of the People' s Republic of China), *Air Quality Analysis of Key Regions and 74 Cities in China Reported by Ministry of Environment Protection of the People's Republic of China*, 2015.

[4] J. Hou, M. Cao, and P. Liu, "Development and utilization of geothermal energy in China: current practices and future strategies," *Renewable Energy*, vol. 125, pp. 401–412, 2018.

[5] L. Zhu, H. Gong, X. Li et al., "Land subsidence due to groundwater withdrawal in the northern Beijing plain, China," *Engineering Geology*, vol. 193, pp. 243–255, 2015.

[6] A. C. Gringarten and J. P. Sauty, "A theoretical study of heat extraction from aquifers with uniform regional flow," *Journal of Geophysical Research*, vol. 80, no. 35, pp. 4956–4962, 1975.

[7] A. C. Gringarten, "Reservoir lifetime and heat recovery factor in geothermal aquifers used for urban heating," *Pure and Applied Geophysics*, vol. 117, no. 1-2, pp. 297–308, 1978.

[8] S. K. Sanyal, M. Sengul, and H. T. Meidav, "A semi-analytical approach to geothermal reservoir performance prediction," in *Proceedings Second Workshop Geothermal Reservoir Engineering*, Stanford, CA, USA, December 1976.

[9] C. S. Chen and D. L. Reddell, "Temperature distribution around a well during thermal injection and a graphical technique for evaluating aquifer thermal properties," *Water Resources Research*, vol. 19, no. 2, pp. 351–363, 1983.

[10] S. Ganguly and M. S. Mohan Kumar, "Analytical solutions for transient temperature distribution in a geothermal reservoir due to cold water injection," *Hydrogeology Journal*, vol. 22, no. 2, pp. 351–369, 2014.

[11] F. Ascencio, F. Samaniego, and J. Rivera, "A heat loss analytical model for the thermal front displacement in naturally fractured reservoirs," *Geothermics*, vol. 50, no. 3, pp. 112–121, 2014.

[12] Y.-S. Wu and K. Pruess, "An analytical solution for wellbore heat transmission in layered formations (includes associated papers 23410 and 23411)," *SPE Reservoir Engineering*, vol. 5, no. 4, pp. 531–538, 1990.

[13] J. Wu, Y. Liu, and H. Yang, "Analytical solution of the productivity equation for a vertical fractured well in 3D anisotropic oil reservoirs," *Liquid Fuels Technology*, vol. 34, no. 4, pp. 433–441, 2014.

[14] B. Izgec, C. S. Kabir, D. Zhu, and A. R. Hasan, "Transient fluid and heat flow modeling in coupled wellbore/reservoir systems," *SPE Reservoir Evaluation & Engineering*, vol. 10, no. 3, pp. 294–301, 2007.

[15] S. Ganguly, M. S. M. Kumar, A. Date, and A. Akbarzadeh, *Numerical Modeling and Analytical Validation for Transient Temperature Distribution in a Heterogeneous Geothermal Reservoir Due to Cold-Water Reinjection*, World Geothermal Congress, 2015.

[16] V. Hamm and S. Lopez, "Impact of fluvial sedimentary heterogeneities on heat transfer at a geothermal doublet scale," *Proceedings, Thirty - Seventh Workshop on Geothermal Reservoir Engineering*, Stanford University, Stanford, CA, USA, 2012.

[17] A. Ghassemi and G. Suresh Kumar, "Changes in fracture aperture and fluid pressure due to thermal stress and silica dissolution/precipitation induced by heat extraction from subsurface rocks," *Geothermics*, vol. 36, no. 2, pp. 115–140, 2007.

[18] M. D. Aliyu and H. P. Chen, "Optimum control parameters and long-term productivity of geothermal reservoirs using coupled thermo-hydraulic process modelling," *Renewable Energy*, vol. 112, pp. 151–165, 2017.

[19] V. Hamm, M. Bouzit, and S. Lopez, "Assessment of complex well architecture performance for geothermal exploitation of the Paris basin: a modeling and economic analysis," *Geothermics*, vol. 64, pp. 300–313, 2016.

[20] L. Pan and C. M. Oldenburg, "T2Well-an integrated wellbore-reservoir simulator," *Computers & Geosciences*, vol. 65, no. 65, pp. 46–55, 2014.

[21] Y. Hu, B. Gao, B. Jin, and J. Wang, "Chemical distribution and forming mechanism of the geothermal water in Tianjin," *Geological Survey and Research*, vol. 30, no. 3, pp. 213–218, 2007.

[22] H. J. Ramey Jr, "Wellbore heat transmission," *Journal of Petroleum Technology*, vol. 14, no. 4, pp. 427–435, 1962.

[23] Z. Peng, *Geothermal Reinjection Numerical Simulation and Resource Evaluation of the Wumishan Group in Dongli District of Tianjin*, China University of Geosciences, Beijing, 2016.

[24] G. Tian, *Sustainable Development and Utilization of Geothermal Resources in the Donglihu Hot Spring Resort of Tianjin*, China University of Geosciences, Beijing, 2014.

[25] A. Franco and M. Vaccaro, "Numerical simulation of geothermal reservoirs for the sustainable design of energy plants: a review," *Renewable & Sustainable Energy Reviews*, vol. 30, no. 2, pp. 987–1002, 2014.

[26] L. Lin, *Sustainable Development and Utilization of Thermal Groundwater Resources in the Geothermal Reservoir of the Wumishan Group in Tianjin*, China University of Geosciences, Beijing, 2006.

[27] G. Garven, "Continental-scale groundwater flow and geologic processes," *Annual Review of Earth and Planetary Sciences*, vol. 23, no. 1, pp. 89–117, 1995.

[28] S.-B. Hu, L.-J. He, and J.-Y. Wang, "Compilation of heat flow data in the China continental area (3rd edition)," *Chinese Journal of Geophysics*, vol. 44, no. 5, pp. 604–618, 2001.

[29] H. A. Loaiciga, D. R. Maidment, and J. B. Valdes, "Climate--change impacts in a regional karst aquifer, Texas, USA," *Journal of Hydrology*, vol. 227, no. 1-4, pp. 173–194, 2000.

[30] N. Zhao, "Geochemical simulation of lake water injection into the geothermal reservoir in Tianjin, China," in *Geothermal Training Programme*, United Nations University, 2010.

[31] C. Ruan, "Numerical modeling of water level changes in Tianjin low-temperature geothermal system, China," in *Geothermal Training Programme*, United Nations University, 2011.

[32] T. Xu, H. Zhu, G. Feng, Y. Yuan, and H. Tian, "On fluid and thermal dynamics in a heterogeneous CO_2 plume geothermal reservoir," *Geofluids*, vol. 2017, Article ID 9692517, 12 pages, 2017.

[33] W. R. Bryant, W. Hottman, and P. Trabant, "Permeability of unconsolidated and consolidated marine sediments, Gulf of Mexico," *Marine Geotechnology*, vol. 1, no. 1, pp. 1–14, 1975.

[34] W. R. Bryant, "Permeability of clays, silty-clays and clayey-silts," *Gulf Coast Association of Geological Societies Transactions*, vol. 52, pp. 1069–1077, 2002.

[35] C. E. Neuzil, "How permeable are clays and shales?," *Water Resources Research*, vol. 30, no. 2, pp. 145–150, 1994.

[36] H. Tian, F. Pan, T. Xu, B. J. McPherson, G. Yue, and P. Mandalaparty, "Impacts of hydrological heterogeneities on caprock mineral alteration and containment of CO_2 in geological storage sites," *International Journal of Greenhouse Gas Control*, vol. 24, pp. 30–42, 2014.

[37] Z. Guo, X. Hu, and C. Cheng, "Affecting factors of Cretaceous-Paleogence shalecap in Jianghan Plain," *Journal of Jianghan Petroleum University of Staff and Workers*, vol. 17, no. 2, pp. 10–13, 2004.

[38] L. He, L. Zhao, J. Li et al., "Complex relationship between porosity and permeability of carbonate reservoirs and its controlling factors: a case study of platform facies in Pre-Caspian Basin," *Petroleum Exploration and Development*, vol. 41, no. 2, pp. 225–234, 2014.

[39] B. Esrafili-Dizaji and H. Rahimpour-Bonab, "Effects of depositional and diagenetic characteristics on carbonate reservoir quality: a case study from the South Pars gas field in the Persian Gulf," *Petroleum Geoscience*, vol. 15, no. 4, pp. 325–344, 2009.

[40] H. C. Moore, "Carbonate reservoirs: porosity evolution and diagenesis in a sequence stratigraphic framework," *Developments in Sedimentology*, vol. 55, pp. 80–122, 2001.

[41] S. Haldar and G. L. S. Babu, "Effect of soil spatial variability on the response of laterally loaded pile in undrained clay," *Computers and Geotechnics*, vol. 35, no. 4, pp. 537–547, 2008.

[42] G. B. Baecher and J. T. Christian, *Reliability and Statistics in Geotechnical Engineering*, Wiley, 2003.

[43] G. Feng, T. Xu, F. Gherardi, Z. Jiang, and S. Bellani, "Geothermal assessment of the Pisa plain, Italy: coupled thermal and hydraulic modeling," *Renewable Energy*, vol. 111, pp. 416–427, 2017.

[44] A. Ghassemi, S. Tarasovs, and A. H.-D. Cheng, "An integral equation solution for three-dimensional heat extraction from planar fracture in hot dry rock," *International Journal for Numerical and Analytical Methods in Geomechanics*, vol. 27, no. 12, pp. 989–1004, 2003.

[45] A. Ghassemi, S. Tarasovs, and A. H. D. Cheng, "Integral equation solution of heat extraction-induced thermal stress in enhanced geothermal reservoirs," *International Journal for Numerical and Analytical Methods in Geomechanics*, vol. 29, no. 8, pp. 829–844, 2005.

[46] K. F. Evans, A. Zappone, T. Kraft, N. Deichmann, and F. Moia, "A survey of the induced seismic responses to fluid injection in geothermal and CO_2 reservoirs in Europe," *Geothermics*, vol. 41, pp. 30–54, 2012.

[47] P. Yang, M. Chen, Y. Jin et al., "Mechanical-thermal-chemical coupled research of wellbore stability in Jabung Oil Field, Indonesia," *Advanced Materials Research*, vol. 402, pp. 709–714, 2012.

[48] T. Xu, Y. Ontoy, P. Molling, N. Spycher, M. Parini, and K. Pruess, "Reactive transport modeling of injection well scaling and acidizing at Tiwi Field, Philippines," *Geothermics*, vol. 33, no. 4, pp. 477–491, 2004.

[49] C. Rawal and A. Ghassemi, "A reactive thermo-poroelastic analysis of water injection into an enhanced geothermal reservoir," *Geothermics*, vol. 50, pp. 10–23, 2014.

[50] F. Nitschke, S. Held, T. Himmelsbach, and T. Kohl, "THC simulation of halite scaling in deep geothermal single well production," *Geothermics*, vol. 65, pp. 234–243, 2017.

Hindawi
Geofluids
Volume 2019, Article ID 3031586, 14 pages
https://doi.org/10.1155/2019/3031586

Research Article

Evaluation of Caldera Hosted Geothermal Potential during Volcanism and Magmatism in Subduction System, NE Japan

Fajar F. Amanda,[1] Ryoichi Yamada,[2] Masaoki Uno,[1] Satoshi Okumura,[3] and Noriyoshi Tsuchiya[1]

[1]*Graduate School of Environmental Studies, Tohoku University, Sendai 980-8579, Japan*
[2]*Graduate School of Science, Tohoku University, Sendai 980-8578, Japan*
[3]*Department of Earth Science, Tohoku University, Sendai 980-0845, Japan*

Correspondence should be addressed to Fajar F. Amanda; fajar@geo.kankyo.tohoku.ac.jp

Received 25 May 2018; Revised 20 September 2018; Accepted 26 October 2018; Published 21 January 2019

Guest Editor: Matteo Lupi

Deep-seated geothermal reservoirs beneath calderas have high potential as sources of renewable energy. In this study, we used an analysis of melt inclusions to estimate the amount of water input to the upper crust and quantify the properties of a deep-seated geothermal reservoir within a fossil caldera, the late Miocene Fukano Caldera (formation age 8–6 Ma), Sendai, NE Japan. Our research shows that Fukano Caldera consists of the southern part and northern part deposits which differ in the age and composition. The northern deposits are older and have higher potassium and silica contents than the southern deposits. Both the northern and southern deposits record plagioclase and plagioclase–quartz differentiation and are classified as dacite–rhyolite. The fossil magma chamber underlying the caldera is estimated to have a depth of ~2–10 km and a water content of 3.3–7.0 wt.%, and when the chamber was active it had an estimated temperature of 750°C–795°C. The water input into the fossil magma chamber is estimated at 2.3–7.6 t/yr/m arc length based on the magma chamber size the water content in the magma chamber and the length of volcanism periods of Fukano Caldera, NE Japan arc. The total amount of water that is stored in the chamber is ~10^{14} kg. The chamber is saturated in water and has potential as a deep-seated geothermal reservoir. Based on the shape of the chamber, the reservoir measures ~10 km × 5 km in the horizontal dimension and is 7–9 km in vertical extent. The 0th estimate shows that the reservoir can hold the electric energy equivalent of 33–45 GW over 30 years of power generation. Although the Fukano reservoir has great potential, commercial exploitation remains challenging owing to the corrosive nature of the magmatic fluids and the uncertain permeability network of the reservoir.

1. Introduction

The supercritical geothermal potential that is located near or below the brittle–ductile transition zone has attracted much research interest in recent years [1] because such a supercritical geothermal system could yield high well productivity owing to a higher fluid enthalpy of >150–225°C [2–4]. Increasing the enthalpy of fluid could improve the energy productivity of a power plant; e.g., in Iceland, it has been numerically estimated that a supercritical reservoir could produce about tenfold the amount of energy of currently producing wells [1, 5]. In Japan, an attempt to drill to supercritical conditions was made in the Kakkonda Geothermal Field in 1994–1995 [6]. Well WD-1a was drilled to a depth of 3729 m with a bottom-hole temperature of 500°C [1, 7]. The brittle–ductile transition in this well was indicated by an inflection in the temperature profile at ~380°C [8]. This attempt has opened up the possibility of drilling into crust with supercritical conditions.

However, the extraction of energy from supercritical geothermal systems remains challenging on account of the permeability of the host materials and the characteristics of the fluids. Initial studies suggested that permeability shows a marked decrease at the brittle–ductile transition (BDT) [9–11]. However, later investigations showed that sufficient permeability is maintained at the BDT, with evidence being found from outcrops [12, 13], laboratory experiments [14, 15], and geophysical studies [16]. The primary limiting factor is the properties of the fluids produced in supercritical geothermal systems, which are dominated by magmatic fluids. Such fluids are corrosive, meaning that fluid extraction using current technologies is challenging. Therefore, more in-depth research needs to be performed to overcome this problem. Although commercial utilization is not yet possible, an understanding of the properties of supercritical geothermal systems, including the evaluation and estimation of the energy potential, should provide us with a better picture of this prospective energy source.

At a large scale, water supply and budget are essential aspects of a subduction system as they affect the productivity of the arc magma, the cycling of volatiles in the mantle, and the rheology of the mantle [17]. The transportation and distribution of a large volume of water beneath an arc affect the seismicity, rheology, ore deposits, and geothermal energy of the overlying arc crust [18]. Knowledge of magmatic processes is essential to understanding deep-seated geothermal reservoirs and to estimate water inputs to the upper crust. Melt inclusions (MIs) in caldera-fill sediments provide petrological evidence of magmatic processes in the crust. As these inclusions formed at high pressure and are contained within a relatively uncompressible mineral host, MIs preserve the pre-eruption volatile composition of the magma [19].

Extensive studies of silicate MIs have been conducted to understand petrogenetic processes such as assimilation [20] and fractional crystallization [21]. The characteristics of silicate MIs and the methods used for their analysis have been summarized in reviews [19, 22]. Silicate MIs contain information on the dissolved volatile concentrations of igneous rocks. A variety of analytical and thermobarometric methods can be used to study MIs, leading to a better understanding of magma volatile concentrations, the compositions of exsolved magmatic fluids, and the pressure–temperature conditions under which magmas crystallize [19]. Silicate MIs from a single phenocryst (when analyzed for volatile content) might represent the composition of the melt at the time of crystallization and help determine whether variations in volatile concentrations are consistent with a specific physical–chemical magmatic process [22]. A recent study [23] of silicate MIs in deposits of the Shirasawa caldera, NE Japan, showed that MIs could be useful for the assessment of geothermal resources.

NE Japan (Tohoku District) contains ca. 45% of the geothermal potential of the entire country [24, 25]. The ductile zone is relatively shallow around active volcanic fronts (<3 km) [10], and at least 80 caldera collapse structures are recognized in NE Japan, with these structures having a close genetic relationship with the occurrence of granitic plutons [26]. The mass balance analysis of crust–melt reaction zones [13] indicates that the original >5.0–5.6 wt.% of H_2O within the arc magma is partitioned into ≤3.7 wt.% H_2O consumed by the hydration of local crustal material and ≥1.3–1.9 wt.% H_2O expelled to the overlying upper crust. The ascent of magmatic water may increase pore fluid pressure, thereby reducing the strength of the crust, or it may generate hydrothermal fluids that could produce ore deposits [27] and/or deep geothermal resources within the crust [13].

In this study, MIs were used to evaluate the properties of a potential geothermal reservoir (magma chamber) in Fukano Caldera, NE Japan, including (1) the magmatic processes that occurred within the magma chamber, (2) the distribution of the geothermal reservoir, and (3) estimations of the water input to the upper crust and of the geothermal energy.

2. Geological Setting

Fukano Caldera is located ~10 km east of the present volcanic front, near Sendai City, NE Japan (Figure 1). The most recent period of volcanic activity in NE Japan is an island-arc stage (13–0 Ma), which can be divided into submarine volcanism, late Miocene caldera formation, Pliocene caldera formation, and a compressional volcanic arc phase (the present active volcanic front). These changes in the mode of igneous activity are correlated with the stress regime, which is controlled mainly by Eurasia and Pacific plate motion, and with the evolutionary path typical of arc magmatism. Fukano Caldera is classified within the late Miocene Caldera Group, which has a close genetic relationship with granitic plutons [26]. This caldera was chosen because of the proximity to the city compared with the present/recent volcanic front and the availability of geophysical data.

Fukano Caldera contains two calderas: Fukano Caldera itself (the northern part) and Tenjin Caldera (the southern part). In plain view, Fukano and Tenjin calderas have elliptical shapes, elongate N–S (Figure 1). The major and minor axes of these elliptical shapes are 10 and 5 km long, respectively. Fukano Caldera has been active since ~8–7 Ma, with activity in Tenjin Caldera commencing later at ~7–6 Ma. The timing of these events is based on the local stratigraphy and fossil data [28–30]. The Akiu Group (including the Fukano and Tenjin formations) unconformably overlies the Natori Group (Tsunaki Formation; 10.0–8.3 Ma) and is overlain unconformably by the Sendai Group (~6.4 Ma), as determined by fission track dating, planktonic foraminifera, and diatom analyses [29].

In this study, Fukano and Tenjin calderas are termed the northern and southern parts of Fukano Caldera, respectively, based on the regions in which sampling was conducted (Figure 1). The Sakunami Fault bounds the western margin of the two-caldera structure. This fault comprises two parallel fault systems. One trends N–S and dips 40°–80° to the west, and it forms the boundary between the Aone Formation (to the west) and the Sakunami Formation (to the east). A second fault, which dips 60°–80° to the east, marks the boundary between the Sakunami Formation and the caldera volcanic rocks (the Fukano Formation and the Tenjin Tuff Member). Pumice tuffs in a fine-grained matrix and laminated sandy tuffs are distributed near the Sakunami Fault. In contrast, the eastern margin of the caldera structure is overlain by cross-laminated sandy tuffs that dip gently to the west [31].

3. Materials and Methods

3.1. Analyzed Samples. Caldera-fill samples from the southern and northern parts of Fukano Caldera were obtained

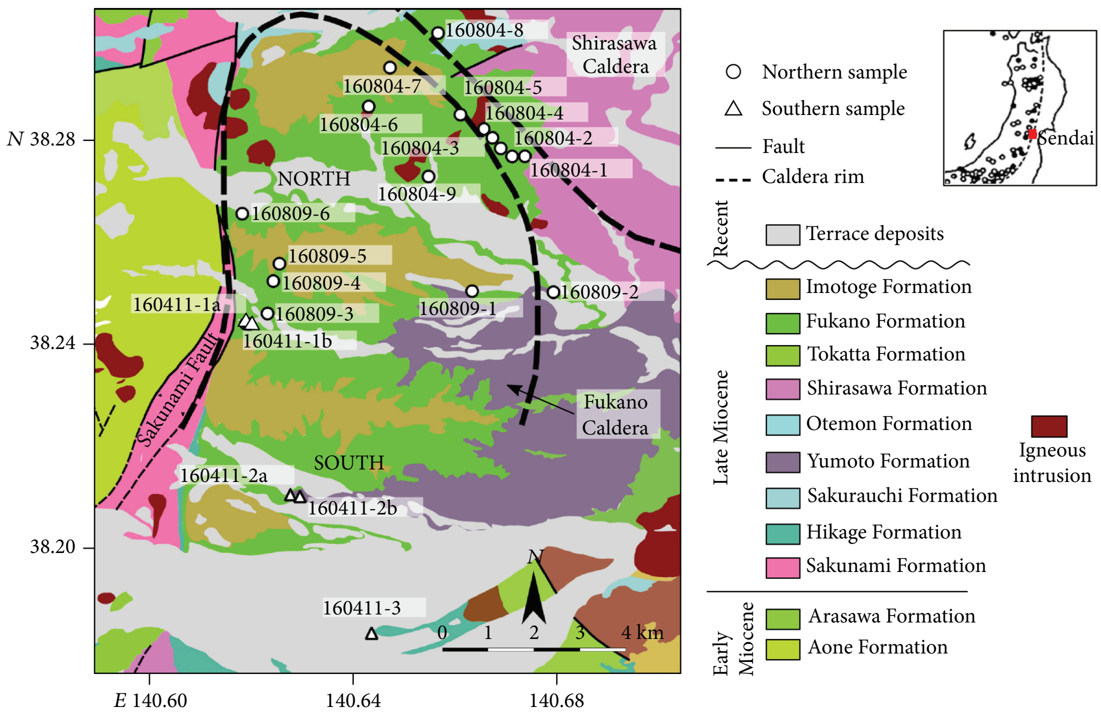

Figure 1: Geological map of Fukano Caldera (modified from Kitamura et al. [32]) showing the distribution of formations and sampling points. The red square in then inset at the top right shows the location of Fukano Caldera. The open circles and triangles show the locations of northern and southern samples, respectively. The thick dashed lines indicate the distribution of the caldera rims.

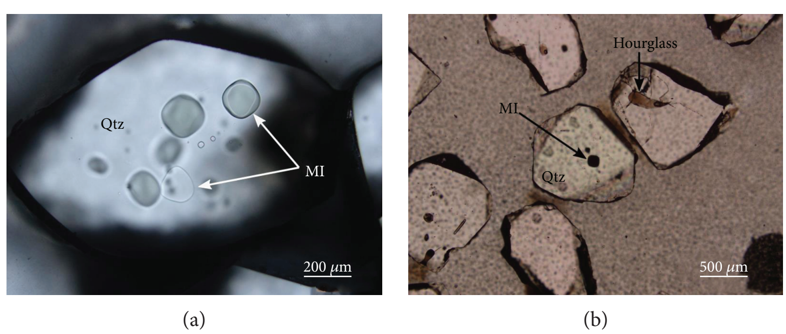

Figure 2: Melt inclusions (MIs) from Fukano Caldera. (a) Quartz crystal from the northern part of the caldera showing large, round colorless glassy inclusions in sample 160804-5 (Table 1 and Table 2). (b) Quartz crystals from the southern part showing rounded, dark crystalline inclusions in sample 160411-1a (Table 1 Table 2). The hourglass-type inclusions observed in the samples were not analyzed (see text for details).

from 20 locations on the caldera from the margin to the center (Figure 1). The five samples taken from the southern part of the caldera (Tenjin Tuff Member of the Fukano Formation and the Motoisago Formation) consist of fine tuff and pumice tuff, with mineral assemblages of quartz, plagioclase, biotite, and magnetite. Apatite occurs as inclusions in quartz. Zircon crystals have been identified in the deposits of the Fukano and Tenjin formations through heavy liquid separation (R. Takashima, Tohoku University; pers. comm.).

The 15 samples taken from the northern part of the caldera (the Fukano, Shirasawa, and Imotoge formations) consist of pumice tuff, welded tuff, fine tuff, muddy fine tuff, volcanic breccia, and pyroclastic breccia, with mineral assemblages of quartz, plagioclase, alkali feldspar, biotite, hornblende, and magnetite. Apatite occurs as inclusions in quartz.

The MIs examined in this study were all hosted in quartz crystals. MI diameters range from <1 to 200 μm, and they commonly occur as homogeneous glassy inclusions. However, bubbles and daughter minerals are also present in some samples and are termed "crystalline inclusions" (Figure 2; Table 1). The crystalline inclusions were not suitable for electron probe and water content analyses owing to the inhomogeneous nature of the inclusions. The crystalline inclusions therefore underwent homogenization treatment using a Linkam TS1500 heating stage with a maximum temperature of 1500°C and maximum quenching rates of 100°C/min. So-called "hourglass" inclusions also appear in some samples (Figure 2(b)). An hourglass inclusion is a melt inclusion that consists of glass or crystallized melt connected to the exterior of the host crystal by a canal or capillary [33],

Table 1: Morphology of melt inclusions from Fukano Caldera.

Sample	Group[1]	ID	Rock classification, formation	Sample condition	Melt inclusion morphology[2] Glassy Rounded	Glassy Elongated	Glassy Angular	Crystalline Rounded	Crystalline Angular	Bubble[2]	Daughter mineral[2]	Hourglass[2]
160411-1a	SP	111a	Fine tuff, Fukano F. (Tenjin)	Fresh	X	X	X	O	Δ	Δ	O	Δ
160411-1b	SP	111b	Pumice tuff, Fukano F. (Tenjin)	Fresh	X	X	X	O	Δ	Δ	O	Δ
160411-2a	SP	112a	Pumice tuff, Motosaigo F.	Fresh	O	Δ	X	X	X	Δ	X	Δ
160411-3a	SP	113a	Pumice tuff, Motosaigo F.	Fresh	O	X	Δ	X	X	Δ	Δ	Δ
160411-3b	SP	113b	Pumice tuff, Motosaigo F.	Fresh	O	Δ	Δ	X	X	Δ	X	Δ
160804-1	NP	041	Pumice tuff, Fukano–Shirasawa F.	Fresh	O	Δ	X	X	X	Δ	X	Δ
160804-2	NP	042	Pumice tuff, Fukano F.	Fresh	O	X	Δ	Δ	X	Δ	Δ	Δ
160804-3s	NP	043s	Stream sediment	Fresh	O	Δ	Δ	Δ	X	Δ	Δ	Δ
160804-3	NP	043	Pyroclastic breccia, Fukano F.	Fresh	O	Δ	Δ	Δ	X	Δ	Δ	Δ
160804-4	NP	044	Volcanic breccia, Fukano F.	Fresh	O	Δ	Δ	Δ	X	Δ	Δ	O
160804-5	NP	045	Fine tuff, Fukano F.	Fresh	O	X	Δ	X	X	Δ	X	Δ
160804-6	NP	046	Muddy fine tuff, Fukano F.	Fresh	Δ	X	X	X	X	Δ	Δ	Δ
160804-7	NP	047	Welded tuff, Imotoge F.	Fresh	O	X	X	Δ	X	Δ	X	O
160804-8	NP	048	Muddy fine tuff, Fukano F.	Altered	X	X	X	O	X	O	X	Δ
160804-9	NP	049	Pumice tuff, Fukano F.	Fresh	O	Δ	X	X	X	Δ	X	Δ
160809-1	NP	091	Pumice tuff, Fukano F.	Fresh	Δ	X	Δ	Δ	X	Δ	Δ	Δ
160809-3	NP	093	Muddy fine tuff, Fukano F.	Fresh	Δ	X	X	O	X	O	O	O
160809-4	NP	094	Argillized pumice tuff/Fukano F.	Altered	O	Δ	Δ	Δ	Δ	Δ	Δ	Δ
160809-5	NP	095	Strongly hydrothermally altered rocks, Fukano F.	Altered	O	Δ	Δ	Δ	Δ	Δ	Δ	Δ
160809-6	NP	096	Volcanic breccia, Fukano F.	Altered	Δ	X	Δ	Δ	X	Δ	Δ	Δ

[1]NP = northern part of the caldera; SP = southern part of the caldera. [2]X = absent; Δ = exists; and O = abundant.

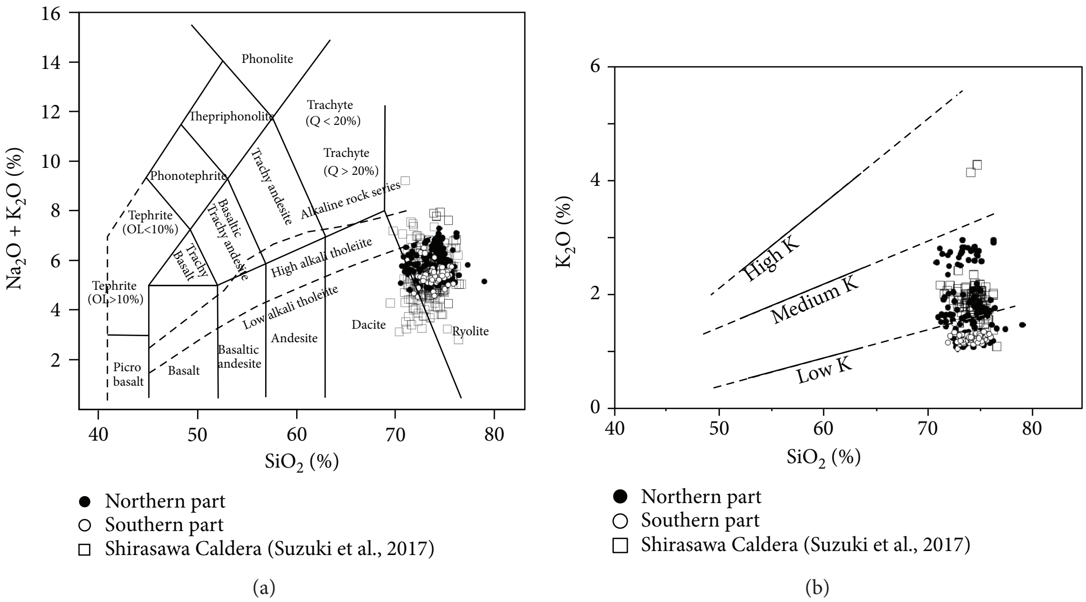

Figure 3: (a) Total alkalis vs. silica (TAS) diagram [35] and (b) SiO_2 vs. K_2O classification diagram [36] showing the compositions of MIs from the northern and southern parts of Fukano Caldera, compared with data for Shirasawa Caldera [23]. Ol: olivine; Q: quartz.

allowing volatiles and other elements to diffuse at the time of crystallization. Therefore, this type of inclusion was not analyzed in the present study.

3.2. Analytical Procedures. Quartz phenocrysts were hand-picked, washed ultrasonically in water, and dried overnight at room temperature. The quartz was then mounted in resin and polished until the MIs were exposed at the surface. The samples were analyzed in the following order to avoid damage and element loss during measurement: Fourier transform–infrared (FT–IR) spectroscopy, secondary electron microscopy–energy-dispersive spectroscopy (SEM–EDS), and laser ablation–inductively coupled plasma–mass spectrometry (LA–ICP–MS).

Major element compositions (SiO_2, TiO_2, Al_2O_3, MnO, MgO, CaO, Na_2O, K_2O, and P_2O_5) for MIs were determined using a JEOL JSM-7001F SEM–EDS at the Department of Earth Science, Tohoku University, Japan. The analytical conditions were an accelerating voltage of 15 kV, a probe current of 1.4 nA, a magnification of 5000x, and a working distance of 10.00 mm. Sodium loss associated with alkali migration during electron bombardment was prevented by using a low probe current and low magnification.

Trace element concentrations were measured for 10 MIs in two samples from the southern part of the caldera and for 3 MIs in one sample from the northern part. Trace element (Cs, Rb, Ba, Th, U, Nb, Ta, La, Ce, Pb, Pr, Sr, Nd, Sm, Zr, Hf, Eu, Gd, Tb, Dy, Y, Ho, Er, Tm, Yb, and Lu) concentrations were determined using an Analyte Excite excimer laser and a PerkinElmer ELAN 9000 Quadrupole ICP–MS at the Graduate School of Environmental Studies, Tohoku University, Japan. These analyses used a laser wavelength of 193 nm, a laser spot diameter of 50 μm, 80% power, a repetition rate of 20 Hz, and an ablation time of 15 s. Standard samples (NIST 611, 612, and 614) were used to determine the detection limits of the instrumental measurements. MIs with diameters of >100 μm were chosen for analysis to accommodate the laser spot diameter and to prevent ablation of the surrounding quartz.

Water and CO_2 contents were determined using a Thermo Scientific Nicolet iN10 transmission FT–IR at the Department of Earth Science, Tohoku University, Japan. These analyses used an aperture of 30 μm × 30 μm and wave numbers of 675–6000 cm^{-1}. Infrared absorption bands were assigned as 1630 cm^{-1} for the bending mode of H_2O, 3600 cm^{-1} for the stretching mode of H_2O and OH, and 5230 and 4500 cm^{-1} for the combination of the stretching and bending modes of H_2O and OH [34], respectively. Given that the 3600 cm^{-1} peak was oversaturated in this study, the 5230 and 4500 cm^{-1} absorption bands were used.

4. Results and Discussion

4.1. Major Elements. Major elements were measured for 232 MIs in samples from the northern part of Fukano Caldera and 81 MIs in samples from the southern part. Melt from the northern region is classified as low–high-alkali tholeiitic dacite–rhyolite of low–medium-K composition (SiO_2: 70.53–77.02 wt.%; K_2O: 0.98–3.07 wt.%), whereas magma from the southern region is classified as low-alkali tholeiitic dacite–rhyolite of low-K composition (SiO_2: 71.59–75.69 wt.%; K_2O: 1.03–2.29 wt.%) (for details, see Figure 3, Table 2, and Supplementary Table St-1).

The major element compositions of MIs were also used to calculate the crystallization pressures of the host quartz. The pressure was estimated using the DERP (determining rhyolite pressure) [37] geobarometer. This geobarometer is based on the pressure dependence of the cotectic curve separating the quartz and feldspar stability fields in the rhyolite system Qtz–Ab–Or(–An–H_2O). DERP is calibrated for pressures in

Table 2: Major element contents of melt inclusions from Fukano Caldera.

Group	Sample	Id	Points	Major elements (wt.%)										
				SiO_2	TiO_2	Al2O_3	FeO	MnO	MgO	CaO	Na_2O	K_2O	P_2O_5	Total
Southern part	160411-1a	111a	1604111a-g5-1b	73.84	0.00	10.75	1.54	0.00	0.25	1.28	4.39	1.69	0.40	94.13
	160411-1b	111b	1604111b-4-1	74.60	0.27	10.18	1.07	0.05	0.00	1.43	4.42	1.26	0.08	93.37
	160411-2a	112a	2aG1	74.59	0.01	11.03	1.45	0.04	0.26	1.74	4.24	1.26	n.d	94.55
			2aG1b	75.03	0.12	11.05	1.33	0.07	0.20	1.80	4.37	1.18	n.d	95.05
			2aG2	74.36	0.15	11.18	1.57	0.10	0.10	1.81	4.12	1.24	0.02	94.64
			2aG3	75.33	0.04	11.22	1.31	0.15	0.17	1.72	4.21	1.18	n.d	95.23
			2aG4bb	73.74	0.17	10.89	1.64	0.05	0.19	1.63	3.52	1.22	n.d	93.00
			2aG4a	75.17	0.32	11.11	1.58	0.02	0.16	1.77	3.72	1.28	n.d	95.03
	160411-3a	113a	3aG2a2	74.61	0.02	10.94	1.78	0.05	0.17	1.48	4.45	1.23	n.d	94.73
			3aG3a1	73.66	0.26	10.98	1.56	0.08	0.18	1.73	4.40	1.24	n.d	94.09
			3aG4	73.72	0.22	11.04	1.39	0.19	0.22	1.74	4.28	1.13	n.d	93.74
			3aG5a	74.21	0.13	10.87	1.44	n.d	0.21	1.74	3.97	1.18	n.d	93.57
			3aG5b2	72.09	0.22	11.10	1.44	0.04	0.23	1.76	3.77	1.40	n.d	91.99
			3aG5c	72.65	0.26	10.79	1.44	0.06	0.24	1.65	4.03	1.22	n.d	92.28
	160411-3b	113b	3b#3G3	74.05	0.31	10.73	1.25	0.14	0.24	1.84	3.89	1.20	n.d	93.60
			3b#3G4	72.29	0.11	11.14	1.62	n.d	0.20	1.85	3.59	1.28	n.d	91.82
			3b#3G5	72.78	0.28	11.27	1.53	0.06	0.32	1.97	4.02	1.11	n.d	93.25
			3b#3G6	72.86	0.21	11.03	1.36	0.08	0.23	1.64	4.19	1.22	n.d	92.79
			3b#3G7a	72.24	0.16	10.73	1.62	n.d	0.19	1.69	4.01	1.32	n.d	91.83
			3b#3G7b	73.69	0.13	11.07	1.53	0.06	0.18	1.58	3.92	1.24	n.d	93.26
Northern part	160804-1	041	041G1a-1	72.93	0.15	11.07	1.52	0.12	0.17	1.64	4.00	1.14	n.d	92.62
			041G1b	73.13	0.22	10.90	1.36	0.19	0.20	1.63	3.85	1.18	0.07	92.74
	160804-2	042	042G1	73.31	0.12	10.87	1.22	0.14	0.19	1.80	3.99	1.15	0.02	92.82
			042G2a	73.32	0.08	10.90	1.38	n.d	0.22	1.76	3.94	1.14	n.d	92.58
			042G2b	73.91	0.31	11.10	1.60	0.07	0.14	1.72	4.01	1.14	n.d	93.89
	160804-3	043	043G1a1	74.03	0.10	11.15	0.92	0.03	0.11	1.00	3.97	2.76	n.d	94.05
			043G10a	73.14	0.18	11.53	1.08	0.13	0.18	1.07	3.98	2.79	n.d	94.06
			043G11a	74.37	0.22	11.09	0.73	0	0.13	0.92	3.91	2.72	n.d	93.99
	160804-3s	043s	043sG1	73.92	0.20	11.30	1.62	0.01	0.24	1.92	3.84	1.52	n.d	94.47
			043sG2b	74.89	0.06	11.01	1.37	0.12	0.14	1.30	4.01	1.60	0.02	94.54
			043sG3a	76.07	0.03	10.84	1.48	0.03	0.22	0.84	4.28	1.74	n.d	95.50
	160804-4	044	044G1	73.33	0.41	10.82	1.72	0.10	0.23	1.74	3.96	1.28	0.01	93.60
			044G2a	73.73	0.07	10.83	1.00	0.01	0.12	0.95	4.02	2.61	n.d	93.32
			044G3	73.97	0.25	10.64	1.66	0.12	0.28	1.91	3.90	1.29	0.01	94.03
	160804-5	045	045G1a	74.68	0.11	11.31	1.41	0.15	0.21	2.06	4.26	1.18	n.d	95.23
			045G1a	74.68	0.11	11.31	1.41	0.15	0.21	2.06	4.26	1.18	n.d	95.23
			045G1b	74.77	0.21	11.18	1.65	n.d	0.16	1.80	4.19	1.18	n.d	95.03
	160804-6	046	046G1	72.96	0.05	11.00	1.51	0.03	0.25	1.43	4.17	1.21	n.d	92.55
	160804-7	047	47G1a2	73.08	0.15	10.80	1.75	0.17	0.33	1.72	4.17	1.17	n.d	93.25
			47G1b	73.05	0.22	10.57	1.75	0.10	0.15	1.77	3.90	1.16	n.d	92.59
			47G2a1	73.91	0.11	10.77	1.24	0.14	0.08	0.77	4.76	2.04	n.d	93.72
	160804-8	048	048HSG1	75.09	0.23	10.70	1.43	0.02	0.13	1.37	5.05	1.49	n.d	95.39
	160804-9	049	049G1a	75.03	0.23	10.83	1.42	0.09	0.12	1.49	4.37	1.19	0.07	94.83
			049G1b	75.12	0.16	11.18	1.26	n.d	0.19	1.50	4.42	1.27	n.d	94.84
			049G5	73.69	0.11	11.14	1.39	0.04	0.25	1.70	4.13	1.25	0.01	93.72
	160809-1	091	091G2a	73.51	0.23	10.73	1.55	0.05	0.13	1.38	4.17	1.62	0.07	93.43
			091G2b	73.62	0.23	10.59	1.34	0.12	0.16	1.51	3.89	1.83	0.02	93.32

Table 2: Continued.

Group	Sample	Id	Points	Major elements (wt.%) SiO$_2$	TiO$_2$	Al2O$_3$	FeO	MnO	MgO	CaO	Na$_2$O	K$_2$O	P$_2$O$_5$	Total
	160809-3	093	093HSG1b	74.09	0.23	11.70	1.51	0.02	0.15	1.40	5.05	1.49	n.d	95.53
			093HSG1c	75.77	0.23	10.35	1.44	0.19	0.15	1.04	4.26	1.45	n.d	94.84
	160809-4	094	Q16b-1	71.66	0.31	10.35	1.21	n.d	0.23	1.46	4.34	1.99	0.08	91.60
			Q16a-1	73.01	0.33	10.70	1.80	0.11	0.33	1.68	4.14	1.97	0.08	94.16
	160809-5	095	095G1a	74.61	0.21	11.06	1.64	0.11	0.25	1.93	3.93	1.25	0.02	94.99
			095G1b	74.16	0.19	10.71	1.51	0.01	0.26	1.77	4.11	1.4	0.03	94.16
	160809-6	096	096G6b	73.89	0.22	10.98	1.58	n.d	0.21	1.69	4.13	1.16	n.d	93.69
			096G8b	72.50	0.25	10.69	1.49	0.05	0.12	1.65	2.84	2.49	n.d	91.93

the range 50–500 MPa and takes into account the effect of normative An content as well as of water content in melt [37]. As the geobarometer was applied to MIs that were in direct contact with one mineral only (i.e., quartz), we cross-checked the congruence of the resulting pressure determination with the water saturation pressure (discussed in Magma Chamber Depth).

DERP was used to calculate pressures from the data of 313 melt inclusions. As the pressure estimation is dependent on the water content in the melt, we varied the water content from the lowest measured water content (3 wt.%) to the highest (7 wt.%) to estimate the uncertainty, which was determined to be ±25 MPa. The pressure calculated using this method varied from 0.7 to 450 MPa for the northern samples and from 0.7 to 511 MPa for the southern samples. Assuming that pressure follows the lithostatic gradient with a crustal density of 2.7 g/cm^3, the crystallization depth ranged from 0.02 to 17 km and from 0.02 to 19 km for the northern and southern samples, respectively.

Histograms of quartz crystallization pressure were constructed for the northern and southern parts of the caldera (Figure 4(a)) to reveal the vertical distribution of pressure calculated using the MI data. The magma chamber model (Figure 4(b)) was based on the vertical distribution of the MIs (Figure 4(a)), with higher frequencies of crystallization pressure corresponding to wider sections of the magma chamber for each part of the caldera. The inferred depth of the magma chamber for the southern part of the caldera (~7 km) is slightly greater than that for the northern part (~5 km). However, given the uncertainty of the data (±25 MPa; ~1 km), both chambers are placed at a similar depth and might have formed a single magma chamber. The deposits of the northern part of the caldera (Fukano Formation, 8–7 Ma) are older and have a higher potassium content than the deposits of the southern part (Tenjin Tuff Member, 7–6 Ma) [28]. This may indicate the input of less-evolved magma into the chamber during the formation of the southern part deposits.

4.2. Trace Elements. The trace element concentrations of 10 MIs in two samples from the southern part of the caldera and for 3 MIs in one sample from the northern part were measured to determine the differentiation of the magma beneath Fukano Caldera and to estimate the magma chamber temperature. The concentrations were normalized to a basaltic andesite sample (ZA1011) from Zao Volcano [38] (see Supplementary Table St-2). This sample is expected to be compositionally similar to the parental magma of Fukano Caldera samples on account of its relatively close spatial proximity. To determine the differentiation patterns of the samples, the normalized concentrations were plotted on a spider diagram (Figure 5).

Except for two samples from the northern part of the caldera, which show higher concentrations of trace elements compared with the other samples, samples from both the northern and southern parts of the caldera have a close correlation to those of the Zao basaltic andesite with marked depletions and enrichment. Strontium and europium are depleted relative to the Zao basaltic andesite. Apart from europium and strontium, the trace elements in the Fukano Caldera samples are enriched relative to the Zao basaltic andesite (Figure 5).

The partition coefficients of strontium and europium are higher in plagioclase compared with other elements. As such, strontium and europium concentrations in magma decrease with plagioclase crystallization. Those elements with concentrations higher than the Zao basaltic andesite are presumed to have been affected by the crystallization of minerals such as quartz. Such elements are not compatible in quartz, meaning that their concentrations in the melt increase during quartz crystallization as SiO_2 decreases.

Zircon saturation temperatures were calculated using a solubility model [39]. The calculations were conducted on six MIs from the northern and southern parts of the caldera (Supplementary Table St-4). The existence of zircon was confirmed to ensure that the samples were saturated in this phase. Because the zircon saturation thermometer [39] is calibrated only for subaluminous and peraluminous melt compositions, only the samples that fell within this compositional range were selected for the calculations. The results show no systematic difference in the zircon saturation temperature between the northern and southern part samples. The calculated temperatures vary from 750°C to 795°C, with an average magma temperature of ~774°C ± 18°C.

4.3. Water Contents. Water content was measured for 5 MIs from the northern part of the caldera and for 3 MIs from the southern part. MIs that were heated using the heating stage

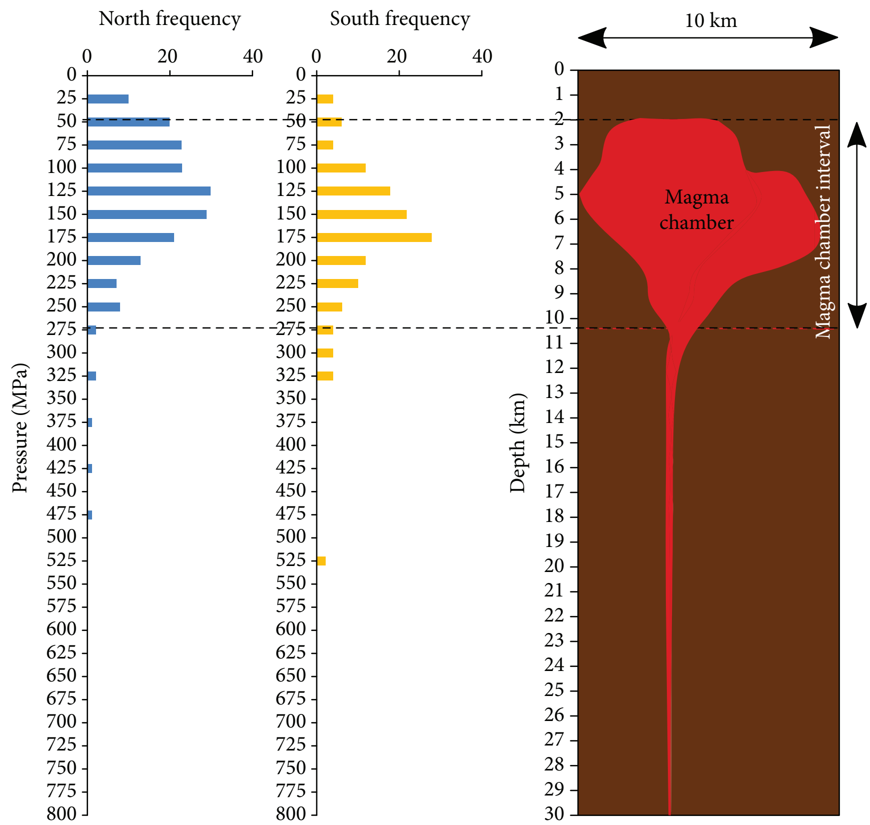

Figure 4: (a) Histograms showing quartz crystallization pressures (calculated from MI data) with depth in the northern (blue bars) and southern (yellow bars) parts of Fukano Caldera. The pressures were calculated based on an average water content in the samples (~5 wt.%). The vertical axis is the crystallization pressure, and the horizontal axis is the frequency of pressures in a specific class. (b) Model of the magma chambers based on the distribution of pressures in the histogram. The vertical axis indicates the depth corresponding to the crystallization pressures of the histogram vertical axis.

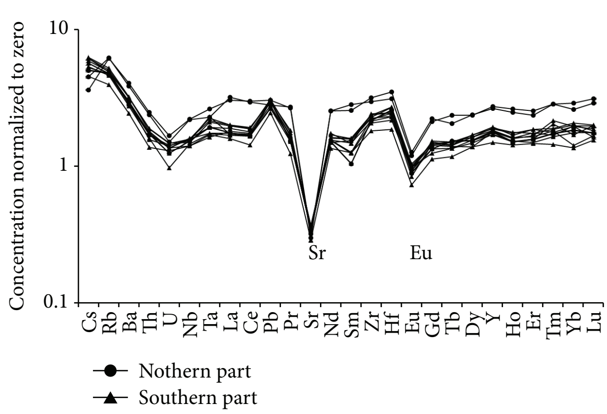

Figure 5: Trace element patterns of Fukano Caldera MIs normalized to Za1011 (Zao basaltic andesite) from Tatsumi et al. [38], showing the similar elemental concentrations of the samples. Depletions of strontium and europium resulting from plagioclase crystallization are evident.

were avoided because of the potential loss of volatiles. The total water contents of MIs in the northern part vary from 4.2 to 7.0 wt.%, and those in the southern part from 3.3 to 7.0 wt.% (Figure 6(a), Supplementary Table St-3). CO_2 absorbance could not be determined from either set of samples and was therefore presumed to be 0 ppm (Figure 6(b)).

The CO_2–H_2O saturation pressure is determined by the pressure of water saturation based on the measured water content in MIs using the formula provided by Liu et al. [40]. The formula expresses the temperature- and pressure-dependent H_2O and CO_2 solubility of rhyolite based on synthetic haplogranitic and natural rhyolitic melt experiments. In general, the water-saturated pressures range from 60 to 250 MPa (see Supplementary Table St-3), and the pressures calculated from major element data vary from 0.7 to 511 MPa but are clustered in the range 25–275 MPa. These data indicate that the samples from Fukano Caldera are mostly water-saturated.

4.4. Magma Chamber Depth. The depth of the magma chamber in this study, as described above, was estimated using the DERP geobarometer. Based on this method, magma chamber pressure estimates ranged from 0.7 to 511 MPa with an uncertainty of ±25 MPa. However, this method has a limited calibration that is restricted to the range 50–500 MPa (~2–18 km), so the pressures below and above this range were discarded. Although the samples fell within a wide range of pressure, the histogram (Figure 4) shows a cluster

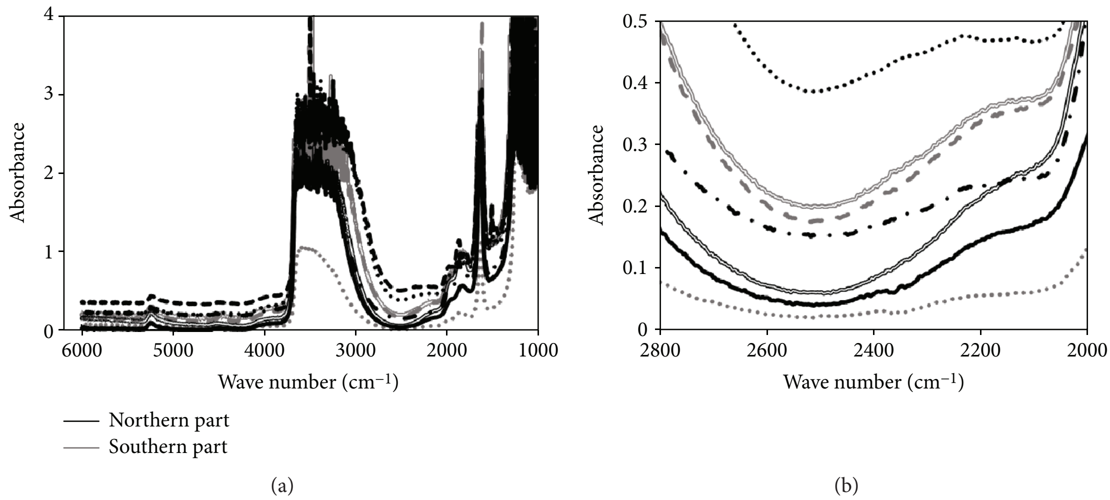

Figure 6: Water content and CO_2 absorbance for the studied MIs. (a) Transmission FT–IR measurement results showing the spectrum of each measurement for the MIs. The 5230 and 4500 cm^{-1} peaks were used to determine the water content of the MIs. (b) CO_2 absorbance spectra show no evidence for CO_2 in the samples.

at pressures between 50 and 275 MPa (Figure 4), with ~2–10 km being the inferred depth range of the magma chamber.

The water saturation pressure ranges from 60 to 250 MPa (~2–9 km). These data agree with the quartz crystallization pressure of 50–275 MPa (~2–10 km) within the ±25 MPa error. The fact that most of the samples fall within the water saturation pressure indicates that the magma was saturated with water and may have been able to form a supercritical geothermal reservoir.

The ascent of water-saturated magma may promote the expulsion of supercritical water from the magma body into the overlying crust. The formation of a supercritical geothermal reservoir above the intrusion is controlled by the brittle–ductile transition temperature (T_{BDT}), host rock permeability, and magma emplacement depth [41]. Increasing the T_{BDT} (i.e., from 450°C to 550°C) creates a larger supercritical zone without dramatically changing the thermo-hydraulic conditions [41]. The host rock permeability strongly affects the extent of supercritical temperature. Supercritical-temperature resources have smaller extents in highly permeable (10^{-14} m^2) host rock compared within moderately permeable (10^{-15} m^2) host rocks because the rate of convective water circulation surpasses the ability of the intrusion to heat most of the circulating water to supercritical temperatures [41]. The location of magma emplacement influences whether the system above the intrusion exceeds the critical pressure. In Fukano Caldera, the emplacement of the magma chamber is estimated to be ~2–10 km (~50–275 MPa), above the critical pressure of water (~22 MPa). The brittle–ductile transition zone is observed at a temperature of ~380°C [8], above the critical temperature of water (374°C), and fluid migration at a depth of 4–6 km suggests the existence of an intermediate-permeability zone (10^{-15} m^2) [14, 16] in the NE Japan region. Therefore, it is possible that a supercritical geothermal reservoir has formed beneath Fukano Caldera.

The above-mentioned petrological data are also in agreement with the seismic tomography map of Nakajima et al. [42] (Figure 7). A region of low seismic velocity is observed at depths of 5 to 10 km [42] (Figures 7(a) and 7(b)) and is consistent with the depth range of the magma chamber identified in the present study (~2–10 km). The existence of melt-filled pores can reduce seismic velocity and increase Poisson's ratio independent of the shape of pores, whereas H_2O-filled pores have a different effect on seismic velocity, especially on Poisson's ratio, which is affected by the shape of the pores, specifically the aspect ratio, which is defined as the ratio of the minor radius to the major radius of fluid-filled oblate spheroidal pores [42]. H_2O-filled pores with an aspect ratio of less than ~0.1 increase Poisson's ratio and decrease the seismic velocity, giving the same effect as melt-filled pores, whereas H_2O-filled pores with an aspect ratio of greater than ~0.1 will reduce Poisson's ratio and decrease seismic velocity [43]. The observed region of low seismic velocity with slightly higher Poisson's ratio at depths of ~5–10 km suggests the existence of melt- or H_2O-filled pores [42].

4.5. Water Budget. Water plays an essential role in a subduction system, as it is a critical factor in the formation of magma and the storage of energy. Two studies that have investigated the amount of water subducted beneath the NE Japan arc [17, 44] estimated the water budget by using a slab-water-dehydration model to determine the amount and rate of water released from the slab during dehydration. The rate of water release from the slab in the NE Japan arc during subduction is estimated to be ~34 t/yr/m arc length [44]. Kimura and Nakajima [17] used the geochemical and petrological model Arc Basalt Simulator version 4 (ABS4) to calculate that about 38% of the ~34 t/yr/m (~13 t/y/m) migrates into the crust. In the present study, we estimated the amount of water input to the upper crust using MI data from the caldera system (Figure 8).

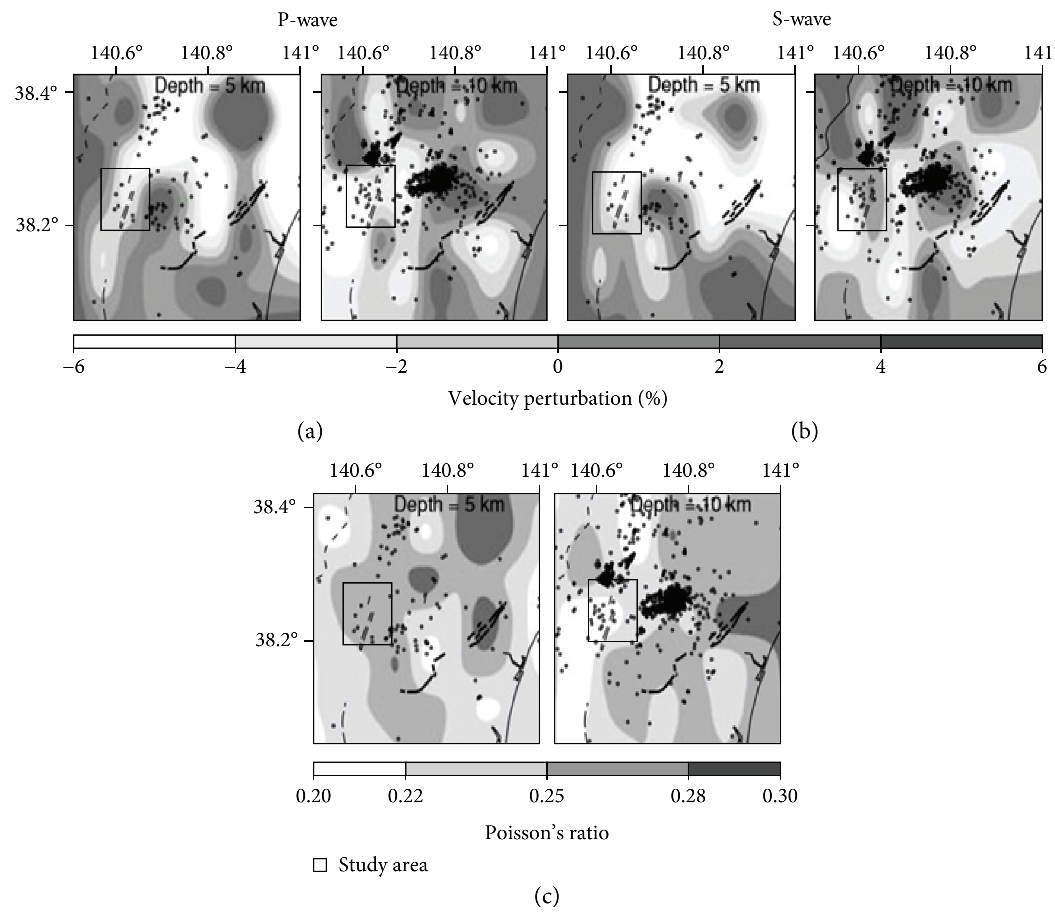

Figure 7: Seismic tomography maps showing (a) primary wave (P-wave) velocity perturbation (%), (b) secondary wave (S-wave) velocity perturbation (%), and (c) Poisson's ratio, modified from Nakajima et al. [42]. A zone of low seismic velocity at depths of 5 and 10 km is observed in the study area (open square), indicated by a lighter shade. This zone is suggested to indicate the vertical extent of the magma chamber, in agreement with our study. The slightly higher Poisson's ratio observed at a depth of 5 km indicates the existence of melt- or H_2O-filled pores. Black dots show earthquake swarms within ±2.5 km of the corresponding depth.

The northern and southern magma chambers of Fukano Caldera are estimated to occupy a depth range of 2–10 ± 1 km; that is, they have vertical extents of 7–9 km (Figure 4). To simplify the calculation, the northern and southern magma chambers were treated as a single large magma chamber. The extent of this magma chamber was estimated from the caldera rim structure, which extends for ~10 km N–S and ~5 km E–W. For a caldera with a roof aspect ratio of ≤1 (the ratio of the caldera diameter to the distance between the ground surface and the top of the magma chamber), the gravity-driven normal faults form as a border to the caldera and propagate from the surface to the magma chamber margin [46–49] with vertical or subvertical dips of ~60°–90° [47, 50, 51]. Therefore, the lateral extent of the magma chamber can be estimated at ~9.7–10.0 km for the major axis and ~4.7–5.0 km for the minor axis.

The NE Japan arc extends N–S, and therefore, the length of the arc supplying water to the crust can be assumed as the width of the magma chamber in the N–S direction, which is 9.7–10 km. We assumed the water content of the magma chamber to be the same as those in the studied MIs (3.3–7.0 wt.%). We also assumed that the magma density is similar to the MI density, which was calculated using the formula of Okumura and Nakashima [34]. The density of magma varied from 2254 to 2306 kg/m^3 (Supplementary Table St-3). To predict a yearly supply of water, we assumed that the accumulation period of the caldera was 3 Myr, based on the stratigraphic interval of the volcanic products [29] of the Akiu Group.

Using the above data and assumptions, the amount of water contained in the magma chamber is calculated to be 6.8×10^{13} to 2.3×10^{14} kg, which accumulated during a 3 Myr period along the 9.7–10 km arc length. Therefore, the yearly water input into the magma chamber is 2.3–7.6 t/yr/m arc length (Supplementary Calculation Sc-1). In the study of Kimura and Nakajima [17], it was assumed that hydration and water input along the arc are uniform. In our study, the estimation is based on only one caldera (Fukano Caldera); however, multiple calderas are present along the NE Japan arc, which have varying sizes and water contents as well as patterns of spatial distribution [26]. Throughout the NE Japan arc, calderas are dispersed in groups called "hot fingers" correlated to local hot regions within the mantle wedge [52], suggesting that conditions along the arc are heterogeneous. However, our estimate of the amount of water that

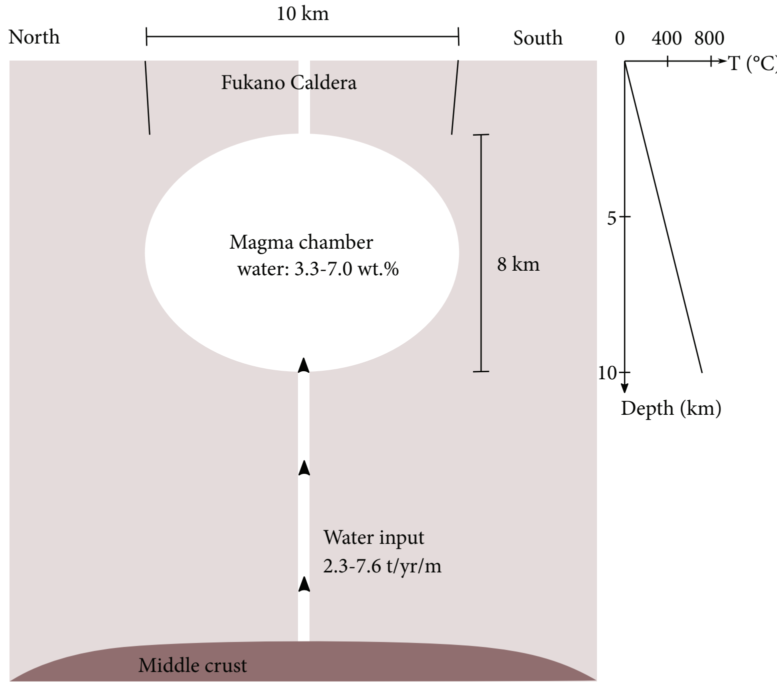

Figure 8: Depiction of the estimated amount of water input to the magma chamber based on MI data from this study. The percentage of water in the magma chamber is 3.3–7.0 wt.% (6.8×10^{13} to 2.3×10^{14} kg), which accumulated during a 3 Myr period along the ~10 km arc length of the chamber. The right-hand part of the diagram shows the geothermal gradient of Shirasawa Caldera (located immediately to the NE of Fukano Caldera), and its surrounds (70°C/km) [45].

is input into the upper-crustal magma chamber is of the same order as the subarc water input reported by Kimura and Nakajima [17] (13 t/yr/m).

Using the volume and temperature of the magma chamber, the probable geothermal energy can be estimated. The energy stored in the Fukano chamber reservoir was evaluated using the volumetric method [53, 54]. The calculation is based on the thermal energy in the rock and in the fluid that could be extracted based on the specified reservoir volume, reservoir temperature, and reference temperature (see Supplementary Calculation Sc-1 for details). The temperature of the magma chamber during crystallization was estimated above using the Zr saturation temperature (~774°C). However, this is not the actual present-day temperature because the magma chamber may have cooled down over the millions of years that have elapsed since crystallization. Therefore, the geothermal gradient (70°C/km) [45] of Shirasawa Caldera and its surrounding which represents the geothermal gradient beneath the ancient caldera were adopted to predict the present-day temperature of the reservoir (Figure 8).

As the Fukano chamber is a high-enthalpy reservoir, the reference depth (Zr) was set to a depth corresponding to a temperature of 150°C [2–4] using a geothermal gradient of 70°C/km. The average annual temperature of Sendai was taken as 12°C and set as the reference temperature (T_{ref}). The depth of the reservoir corresponding to a temperature of ~150°C in Fukano Caldera is therefore 2 km (152°C). This depth represents the high enthalpy reservoir. The maximum depth of the reservoir was set at 10 km (712°C), corresponding to the bottom of the magma chamber. The volumetric density of rocks + water was set at 2.7 J/cm^{3}°C. The total reservoir energy (Qr) is calculated as 1.6×10^{18} kJ, which, with a 25% rate of recovery of energy, gives a result of 4×10^{17} kJ. To determine the energy that can be obtained from the reservoir, we first assumed that the depth of the borehole used for extracting the hot fluid is 3 km (220°C). The hot fluid that rises from this depth does so against gravity, meaning that some energy loss may occur during extraction. Therefore, we calculate the available work (W_a) based on the enthalpy at the well source and the reference. Also, energy loss will occur because of conversion efficiency of the power plant. For water-dominated systems, it is set to be ~0.4. Using this method, the amount of electric energy can be calculated, including the upper and lower bounds on reservoir energy. We calculate that the electrical energy that could be obtained from Fukano Caldera is $3.16–4.25 \times 10^{16}$ kJ, and the electric energy obtained over 30 years of power generation is 33–45 GW (Supplementary Calculation Sc-1).

The estimation of geothermal energy is approximate because of the many simplifying assumptions that are made, such as the continuity of the magma chamber and the treatment of the reservoir as a water-dominated system regarding energy recovery rate and efficiency. The geothermal gradient may not be valid in such a deep system, and the reservoir is assumed to have sufficient permeability. Although commercial exploitation is not yet possible, the deep-seated geothermal reservoir beneath Fukano Caldera has a huge potential as an energy source in the future.

5. Conclusions

The Fukano Caldera fossil magma chamber in NE Japan lies at depths of 2–10 ± 1 km and has a water content of 3.3–7.0 wt.%. The rate at which water is supplied to the overlying crust during subduction in the NE Japan arc was used to estimate the amount of water accumulating in the fossil magma chamber, which is calculated to be 2.3–7.6 t/yr/m arc length. The magma chamber is saturated in water, and a 0-order estimation suggests that the energy potential is 33–45 GW over 30 years of power generation.

Our study shows that melt inclusion analysis is a useful tool in determining the magmatic processes and properties of a magma chamber as well as estimating the water budget within the crust. It is also reflecting the significance of deep-seated geothermal reservoir in the matter of energy potential. The energy potential of the deep-seated geothermal reservoir at Fukano Caldera is very high. However, the practical exploitation of this reservoir is not yet possible with current technology, given the challenges presented by the corrosive nature of the fluids and the uncertain permeability network of the reservoir. Further assessments of the Fukano reservoir and improvements in extraction technology will need to be made before its energy can be exploited.

Data Availability

The experimental data used to support the findings of this study are included in the supplementary data file.

Conflicts of Interest

The authors declare that there is no conflict of interest regarding the publication of this paper.

Acknowledgments

This research was supported by JST/JICA SATREPS and by JSPS KAKENHI Grant Number JP25000009. Our sincere thanks go to Nobuo Hirano (Graduate School of Environmental Studies, Tohoku University) for providing access to laboratories and research facilities. Without his support, this research would not have been possible.

Supplementary Materials

The supplementary material consists of one excel file. Included in this file are four supplementary tables and one supplementary calculation. Supplementary Table includes all of the measurement results (major element, trace element, and water content) and calculation results (zircon saturation temperature, water saturation pressure, melt inclusion density and the crystallization pressure per water contents) labeled with St-x (1–4): Supplementary Table-1 (St-1): major element composition and the crystallization pressure per water content of melt inclusion in Fukano Caldera. Supplementary Table-2 (St-2): trace element composition of melt inclusion in Fukano Caldera. Supplementary Table-3 (St-3): water content, water saturation pressure, and density of melt inclusion in Fukano Caldera. Supplementary Table-4 (St-4): zircon saturation temperature calculated after Watson and Harrison [35] shows the magma chamber temperature at the crystallization of the host quartz. Supplementary calculation labeled as Sc-1 consists of the water budget, the geothermal energy potential, and the illustration of magma chamber dimension. *(Supplementary Materials)*

References

[1] T. Reinsch, P. Dobson, H. Asanuma, E. Huenges, F. Poletto, and B. Sanjuan, "Utilizing supercritical geothermal systems : a review of past ventures and ongoing research activities," *Geotherm. Energy*, vol. 5, no. 1, 2017.

[2] M. P. Hochstein, "Classification and assessment of geothermal resources," in *Small Geothermal resources - A guide to Development and Utilization*, M. H. Dickson and M. Fanelli, Eds., pp. 31–59, UNITAR/UNDP Centre on small Energy Sources, 1990.

[3] K. Nicholson, "Geothermal systems," in *Geothermal Fluids*, pp. 1–18, Springer, Berlin Heidelberg, 1993.

[4] E. Kaya, S. J. Zarrouk, and M. J. O'Sullivan, "Reinjection in geothermal fields: a review of worldwide experience," *Renewable and Sustainable Energy Reviews*, vol. 15, no. 1, pp. 47–68, 2011.

[5] G. O. Fridleifsson and W. A. Elders, "The Iceland Deep Drilling Project: a search for deep unconventional geothermal resources," *Geothermics*, vol. 34, no. 3, pp. 269–285, 2005.

[6] H. Muraoka, T. Uchida, M. Sasada et al., "Deep geothermal resources survey program: igneous, metamorphic and hydrothermal processes in a well encountering 500°C at 3729 m depth, Kakkonda, Japan," *Geothermics*, vol. 27, no. 5-6, pp. 507–534, 1998.

[7] K. Ikeuchi, N. Doi, Y. Sakagawa, H. Kamenosono, and T. Uchida, "High-temperature measurements in well WD-1A and the thermal structure of the kakkonda geothermal system, Japan," *Geothermics*, vol. 27, no. 5-6, pp. 591–607, 1998.

[8] O. Kato, N. Doi, Y. Sakagawa, and T. Uchida, "Fracture systematics in and around well WD-1, kakkonda geothermal field, Japan," *Geothermics*, vol. 27, no. 5-6, pp. 609–629, 1998.

[9] R. O. Foumier, "The transition from hydrostatic to greater than hydrostatic fluid pressure in presently active continental hydrothermal systems in crystalline rock," *Geophysical Research Letters*, vol. 18, no. 5, pp. 955–958, 1991.

[10] N. Tsuchiya, H. Asanuma, A. Okamoto et al., "Fundamental study for beyond brittle geothermal reservoirs," in *Proceedings World Geothermal Congress 2015*, Melbourne, Australia, April 2015.

[11] H. Saishu, A. Okamoto, and N. Tsuchiya, "The significance of silica precipitation on the formation of the permeable-impermeable boundary within Earth's crust," *Terra Nova*, vol. 26, no. 4, pp. 253–259, 2014.

[12] F. Higashino, T. Kawakami, M. Satish-Kumar et al., "Chlorine-rich fluid or melt activity during granulite facies metamorphism in the Late Proterozoic to Cambrian continental collision zone—an example from the Sør Rondane Mountains, East Antarctica," *Precambrian Research*, vol. 234, pp. 229–246, 2013.

[13] M. Uno, A. Okamoto, and N. Tsuchiya, "Excess water generation during reaction-inducing intrusion of granitic melts into ultramafic rocks at crustal P–T conditions in the Sør Rondane

Mountains of East Antarctica," *Lithos*, vol. 284-285, pp. 625–641, 2017.

[14] N. Watanabe, T. Numakura, K. Sakaguchi et al., "Potentially exploitable supercritical geothermal resources in the ductile crust," *Nature Geoscience*, vol. 10, no. 2, pp. 140–144, 2017.

[15] C. E. Manning and S. E. Ingebritsen, "Permeability of the continental crust: implications of geothermal data and metamorphic systems," *Reviews of Geophysics*, vol. 37, no. 1, pp. 127–150, 1999.

[16] T. Okada, T. Matsuzawa, N. Umino et al., "Hypocenter migration and crustal seismic velocity distribution observed for the inland earthquake swarms induced by the 2011 Tohoku-Oki earthquake in NE Japan: implications for crustal fluid distribution and crustal permeability," *Geofluids*, vol. 15, pp. 293–309, 2015.

[17] J. I. Kimura and J. Nakajima, "Behaviour of subducted water and its role in magma genesis in the NE Japan arc: a combined geophysical and geochemical approach," *Geochimica et Cosmochimica Acta*, vol. 143, pp. 165–188, 2014.

[18] P. Weis, T. Driesner, and C. A. Heinrich, "Porphyry-copper ore shells form at stable pressure-temperature fronts within dynamic fluid plumes," *Science*, vol. 338, no. 6114, pp. 1613–1616, 2012.

[19] J. B. Lowenstern, "Application of silicate-melt inclusions to the study of magmatic volatiles," *Magmas, Fluids and Ore Deposits. Mineralogical Association of Canada Short Course*, vol. 23, pp. 71–99, 1995.

[20] O. Reubi and J. Blundy, "Assimilation of plutonic roots, formation of high-K 'exotic' melt inclusions and genesis of andesitic magmas at volcán De Colima, Mexico," *Journal of Petrology*, vol. 49, no. 12, pp. 2221–2243, 2008.

[21] D. W. Peate, I. U. Peate, M. C. Rowe, J. M. Thompson, and A. C. Kerr, "Petrogenesis of high-MgO lavas of the lower mull plateau group, Scotland: insights from melt inclusions," *Journal of Petrology*, vol. 53, no. 9, pp. 1867–1886, 2012.

[22] C. Cannatelli, A. L. Doherty, R. Esposito, A. Lima, and B. De Vivo, "Understanding a volcano through a droplet: a melt inclusion approach," *Journal of Geochemical Exploration*, vol. 171, pp. 4–19, 2016.

[23] T. Suzuki, M. Uno, S. Okumura, R. Yamada, and N. Tsuchiya, "Differentiation of eruptive magma in the late Miocene Shirasawa Caldera and present geothermal reservoir," *Journal of the Geothermal Research Society of Japan*, vol. 39, pp. 25–37, 2017.

[24] N. Tsuchiya, R. Yamada, and M. Uno, "Supercritical geothermal reservoir revealed by a granite–porphyry system," *Geothermics*, vol. 63, pp. 182–194, 2016.

[25] N. Tsuchiya, R. Takeda, and N. Hirano, "Novel geothermal exploration techniques by thermoluminescence of minerals," in *Proceedings World Geothermal Congress 2015*, pp. 3–6, Melbourne, Austrialia, April 2015.

[26] T. Yoshida, "The evolution of arc magmatism in the NE Honshu arc, Japan," *Tohoku Geophysical Journal*, vol. 36, pp. 131–149, 2001.

[27] R. W. Henley and A. J. Ellis, "Geothermal systems ancient and modern: a geochemical review," *Earth-Science Reviews*, vol. 19, no. 1, pp. 1–50, 1983.

[28] K. Otsuki, J. Nemoto, S. Hasegawa, and T. Yoshida, *Geology of the Valley of Hirosegawa River*, Sendai City Environment Bureau, Environmental Planning Division, 1994.

[29] O. Fujiwara, Y. Yanagisawa, T. Irizuki, and M. Shimamoto, *Chronological Data for the Middle Miocene to Pliocene Sequence around the Southwestern Sendai Plain, with Special Reference to the Uplift History of the Ou Backbone Range Hiroki Hayashi*, Tohru Danhara, Keisuke Fuse and Hideki Iwano, 2008.

[30] H. Okutsu, "On the stratigraphy and paleobotany of the Cenozoic plant beds of the Sendai area," *The science reports of the Tohoku University. Second series, Geology*, vol. 26, pp. 1–35, 1955.

[31] T. Takahashi, Y. Nagashashi, T. Yoshida, and Y. Yanagisawa, "P-192 Geology of Pliocene Fukano and Tenjin calderas at western part of Sendai city," in *Annual Meeting of the Geological Society of Japan*, Chiba Prefecture, Japan, September 2004.

[32] M. Kitamura, T. Ishi, A. Sagawa, and H. Nakagawa, *1:50000 Geological Map 'Sendai,'*, Miyagi Perfecture, 1986.

[33] A. T. Anderson, "Hourglass inclusions: theory and application to the bishop rhyolitic tuff," *American Mineralogist*, vol. 76, p. 530, 1991.

[34] S. Okumura and S. Nakashima, "Molar absorptivities of OH and H2O in rhyolitic glass at room temperature and at 400–600°C," *American Mineralogist*, vol. 90, no. 2-3, pp. 441–447, 2005.

[35] R. W. Le Maitre, B. Zanettin, B. Bonin, A. Streckeisen, M. J. Le Bas, and P. Bateman, *Igneous Rocks: A Classification and Glossary of Terms. A 547 Classification of Rocks and Glossary of Terms*, vol. 140, no. 3, 1989Blackwell, 1989.

[36] M. Best and E. Christiansen, *Igneous Petrology*, Blackwell Science, 2001.

[37] S. Wilke, F. Holtz, D. A. Neave, and R. Almeev, "The effect of anorthite content and water on quartz-feldspar cotectic compositions in the rhyolitic system and implications for geobarometry," *Journal of Petrology*, vol. 58, no. 4, pp. 789–818, 2017.

[38] Y. Tatsumi, T. Takahashi, Y. Hirahara et al., "New insights into andesite genesis: the role of mantle-derived calc-alkalic and crust-derived tholeiitic melts in magma differentiation beneath Zao Volcano, NE Japan," *Journal of Petrology*, vol. 49, no. 11, pp. 1971–2008, 2008.

[39] E. B. Watson and T. M. Harrison, "Zircon saturation revisited: temperature and composition effects in a variety of crustal magma types," *Earth and Planetary Science Letters*, vol. 64, no. 2, pp. 295–304, 1983.

[40] Y. Liu, Y. Zhang, and H. Behrens, "Solubility of H_2O in rhyolitic melts at low pressures and a new empirical model for mixed H_2O–CO_2 solubility in rhyolitic melts," *Journal of Volcanology and Geothermal Research*, vol. 143, no. 1-3, pp. 219–235, 2005.

[41] S. Scott, T. Driesner, and P. Weis, "Geologic controls on supercritical geothermal resources above magmatic intrusions," *Nature Communications*, vol. 6, no. 1, pp. 1–6, 2015.

[42] J. Nakajima, A. Hasegawa, S. Horiuchi, K. Yoshimoto, T. Yoshida, and N. Umino, "Crustal heterogeneity around the Nagamachi-Rifu fault, northeastern Japan, as inferred from travel-time tomography," *Earth, Planets and Space*, vol. 58, no. 7, pp. 843–853, 2006.

[43] Y. Takei, "Effect of pore geometry on VP/VS: from equilibrium geometry to crack," *Journal of Geophysical Research*, vol. 107, no. B2, 2002.

[44] P. E. Van Keken, B. R. Hacker, E. M. Syracuse, and G. A. Abers, "Subduction factory: 4. Depth-dependent flux of H2O

from subducting slabs worldwide," *Journal of Geophysical Research - Solid Earth*, vol. 116, no. B1, 2011.

[45] Y. Yano, A. Tanaka, M. Takahashi, Y. Okubo, M. Sasada, and K. Umeda, *Japan Geothermal Gradient Map 1: 3000000*, Geological Survey of Japan, 1999.

[46] R. Scandone and V. Acocella, "Control of the aspect ratio of the chamber roof on caldera formation during silicic eruptions," *Geophysical Research Letters*, vol. 34, no. 22, 2007.

[47] O. Roche, T. H. Druitt, and O. Merle, "Experimental study of caldera formation," *Journal of Geophysical Research*, vol. 105, no. B1, pp. 395–416, 2000.

[48] S. Kusumoto and K. Takemura, "Caldera geometry determined by the depth of the magma chamber," *Earth, Planets and Space*, vol. 57, no. 11, pp. e17–e20, 2005.

[49] J. W. Cole, D. M. Milner, and K. D. Spinks, "Calderas and caldera structures: a review," *Earth-Science Reviews*, vol. 69, no. 1-2, pp. 1–26, 2005.

[50] V. Acocella, "Understanding caldera structure and development: an overview of analogue models compared to natural calderas," *Earth-Science Reviews*, vol. 85, no. 3-4, pp. 125–160, 2007.

[51] A. Geyer, A. Folch, and J. Martí, "Relationship between caldera collapse and magma chamber withdrawal: an experimental approach," *Journal of Volcanology and Geothermal Research*, vol. 157, no. 4, pp. 375–386, 2006.

[52] Y. Tamura, Y. Tatsumi, D. Zhao, Y. Kido, and H. Shukuno, "Hot fingers in the mantle wedge: new insights into magma genesis in subduction zones," *Earth and Planetary Science Letters*, vol. 197, no. 1-2, pp. 105–116, 2002.

[53] A. Franco and F. Donatini, "Methods for the estimation of the energy stored in geothermal reservoirs," *Journal of Physics Conference Series*, vol. 796, article 012025, 2017.

[54] Y. Miyazaki, H. Tsu, Urai M., S. Takakura, Y. Okubo, and K. Ogawa, "Assessment of geothermal resources of Japan-1990," in *National Geothermal Resource Evaluation Study*, pp. 17–43, Geological Survey of Japan, 1991.

Hindawi
Geofluids
Volume 2018, Article ID 6509420, 24 pages
https://doi.org/10.1155/2018/6509420

Research Article

Laboratory Leaching Tests to Investigate Mobilisation and Recovery of Metals from Geothermal Reservoirs

Máté Osvald,[1] **Andrew D. Kilpatrick**,[2] **Christopher A. Rochelle**,[2] **János Szanyi**,[1] **Tamás Medgyes**,[1] **and Balázs Kóbor**[1]

[1]*University of Szeged, Department of Mineralogy, Geochemistry and Petrology, Egyetem u. 2, Szeged H-6722, Hungary*
[2]*British Geological Survey, Nicker Hill, Keyworth, Nottingham NG12 5GG, UK*

Correspondence should be addressed to Máté Osvald; osimate@geo.u-szeged.hu

Received 27 July 2018; Accepted 24 September 2018; Published 13 December 2018

Guest Editor: Domenico Montanari

The H2020 project "Combined Heat, Power and Metal extraction" (CHPM2030) aims at developing a novel technology which combines geothermal energy utilisation with the extraction of metals in a single interlinked process. In order to improve the economics of geothermal-based energy production, the project investigates possible technologies for the exploitation of metal-bearing geological formations with geothermal potential at depths of 3–4 km or deeper. In this way, the coproduction of energy and metals would be possible and could be optimized according to market demands in the future. This technology could allow the mining of deep ore bodies, particularly for critical metals, alongside power production, while minimizing environmental impact and costs. In this paper, we describe laboratory leaching experiments aimed at quantifying the relative rates and magnitudes of metal release and seeing how these vary with different fluids. Specific size fractions (250–500 μm) of ground mineralised rock samples were investigated under various pressures and temperatures up to 250 bar and 250°C. Initial experiments involved testing a variety of potential leaching fluids with various mineralised samples for a relatively long time (up to 720 h) in batch reactors in order to assess leaching effectiveness. Selected fluids were used in a flow-through reactor with shorter contact time (0.6 h). To ensure possible application in a real geothermal reservoir, a range of fluids were considered, from dilute mineral acid to relatively environmentally benign fluids, such as deionised water and acetic acid. The main findings of the study include fast reaction time, meaning that steady-state fluid compositions were reached in the first few hours of reaction and enhanced mobilisation of Ca, Cd, Mn, Pb, S, Si, and Zn. Some critical elements, such as Co, Sr, and W, were also found in notable concentrations during fluid-rock interactions. However, the amount of these useful elements released is much less compared to the common elements found, which include Al, Ca, Fe, K, Mg, Mn, Na, Pb, S, Si, and Zn. Even though concentrations of dissolved metals increased during the tests, some remained low, and this may present technical challenges for metal extraction. Future efforts will work toward attaining actual fluids from depth to more tightly constrain the effect of parameters such as salinity, which will also influence metal solubility.

1. Introduction

The strategic objective of the CHPM2030 project is to develop a novel technological solution (combined heat, power, and metal extraction from ultradeep ore-bearing rocks), to make geothermal energy more attractive, and to reduce Europe's dependence on the import of metals and fossil fuels [1].

The idea of using geothermal brines for mineral extraction has existed for decades. One key element of interest is lithium [2–4], but a wide spectrum of elements that may be suitable for extraction is present in geothermal reservoirs and fluids [5, 6].

Current demand for metals is driving an expansion in mining operations aided by scientific and technical advances in, for example, the use of robotics, nano-mining, laser

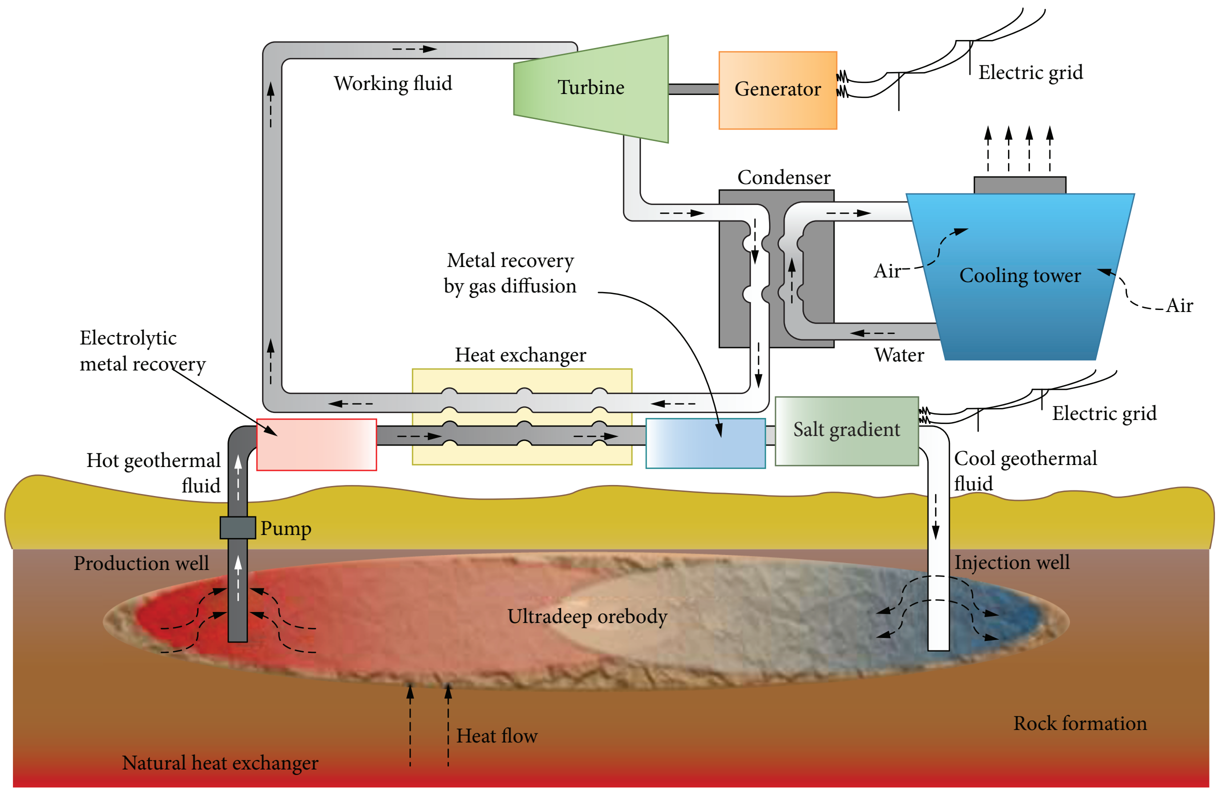

Figure 1: Schematic representation of the CHPM concept. The information presented in this report relates to the release of metals from the "ultradeep orebody" and into the recirculating geothermal fluid.

mining [7, 8], etc. These developing technologies reduce the exposure of miners to hazardous underground environments and make possible the selective transport of valuable metals to the surface rather than moving large amounts of material which will eventually go to waste.

In the envisioned CHPM technology, an enhanced or engineered geothermal system (EGS) is established within a metal-bearing geological formation at depths of 3–4 km or more (Figure 1). Based on geological and hydrogeological settings, EGS could be hydrothermal or petrothermal (a hot dry rock (HDR) system) [9]. The concept involves the manipulation of a theoretical petrothermal system such that the coproduction of energy and metals will be possible [10]. Through experiments at the laboratory scale, we have investigated the leaching potential of various fluids and whether such enhancement of geothermal systems can make them more attractive economically, i.e., whether metals can be leached from orebodies in economic concentrations over prolonged periods, and if leaching might increase the system's performance over time (through, for example, silicate dissolution and permeability enhancement), negating or reducing the use of more common methods of reservoir stimulation.

A key aspect of the CHPM2030 concept is that metals can be transported in solution from mineralised structures at depth to surface infrastructure where they can be extracted (Figure 1). Based on current technology, which often relies on exchange or adsorption processes, the extraction process will be more effective with higher dissolved concentrations of metals [11] and hence with faster rates of dissolution of metal-bearing minerals. However, too large a dissolved load may lead to problems of precipitation within production boreholes or surface infrastructure, and hence, it increases maintenance needs and costs. Thus, there is a need to balance the potential for increased revenue generation from recovering more metals against potential increased costs resulting from increased maintenance operations. There is also a need to consider the wider physical environment in which the systems will need to operate as well as issues of public acceptance [12]. This includes being mindful of environmental considerations and the carefully controlled use of additives that are relatively environmentally benign.

Factors underpinning the above aspects are the rates and magnitudes of metal release, and laboratory experiments simulating in situ conditions are a useful way to provide well-constrained data to help understand these. Such experiments also allow us to test different fluid compositions in order to ascertain if there are specific additives that may improve the metal recovery process [13].

Our approach has been to work initially at lower temperatures with a focus on a few mineralised samples (mainly on material from Cornwall, southwest England) in order to investigate the leaching potential of various fluids. Here, we present results from experiments using samples of mineralisation from Cornwall reacted with deionised water, acetic acid, and a mixture of hydrochloric and nitric acid. Samples from the Banatitic Magmatic and Metallogenetic Belt in Romania (BMMB Masca-Cacova Ierii) and Hungary (Rudabánya and Recsk) were also tested with deionised water and acetic acid. These fluids have been chosen to represent the scale from very benign (deionised water) to more aggressive

Table 1: Major geological and mineral properties of the samples.

Sample ID	Sample locality	Geological setting	Summary of bulk mineralogy (as determined by XRD)
HTLMix	Herodsfoot, SW England	Baked sediments with partial quartz vein	87% quartz, 5% muscovite, 2% dolomite, 5% galena, minor albite, chlorite, pyrite, and sphalerite
HTL315	South Caradon, SW England	Mainstage mineralisation associated with granite bodies	70% quartz, 7% schorl, 5% chlorite, 2% calcite, 10% pyrite, 5% arseonpyrite, and minor greigite and biotite
HTL319	Cligga Head, SW England	Tin-tungsten mineralisation associated with granite bodies	88% quartz, 2% muscovite, 3% cassiterite, 3% columbite, and 4% ferberite
HTL321	Masca-Cocovaleni, Romania	Mineralised skarn country rock	22% dolomite, 49% pyrite, 27% magnetite, minor quartz, calcite, and barite
HTL322	Rudabánya, NE Hungary	Carbonate hosted lead-zinc mineralisation	8% quartz, 2% calcite, 68% magnesite, 6% cerussite, 1% sphalerite, 1% columbite, 11% barite, 2% magnetite, and minor dolomite
HTL324	Recsk, NE Hungary	Porphyry sulphide polymetallic ore	74% quartz, 5% calcite, 9% pyrite, 11% magnetite, minor albite, dolomite, and sphalerite

but still reasonably acceptable (0.1 M acetic acid or 'vinegar') and to very aggressive and environmentally unacceptable mineral acid.

Experiments were run using both batch equipment, where materials are reacted in a closed system, and from which samples are withdrawn regularly, and also flow-through equipment, where fluid is passed once through the system.

2. Materials

The solids used in the experimental work are detailed in Table 1. Samples generally consist of either massive mineralisation or mineralised material together with some surrounding country rock.

All samples were repeatedly crushed in a tempered steel jaw crusher to obtain a powdered fraction of <500 μm. This fraction was then sieved to produce a 500–250 μm fraction, which was used for the experimental and analytical work. This fraction was cleaned to remove fines and surface impurities, by repeated rinsing in acetone, until the supernatant ran clear. These "washed" samples were then oven dried at 30°C.

Solid samples will be referred to by their unique three-digit identifier throughout this report. Samples collected by British Geological Survey were from sites in South West England and labelled HTL315, HTL319, and HTLMix which is a mixed sample from materials representative of a mineralised quartz vein (containing galena, sphalerite, and some chalcopyrite) found at Herodsfoot, southwest England. The mixture was used to provide more representative "bulk" mineralogy for use in experiments. HTL321 originates from a skarn deposit in the BMMB Masca-Cacova Ierii in Romania which is a magnetite deposit also enriched in sulphides with visible chalcopyrite. HTL322 is from Rudabánya, Hungary, from a Mississippi Valley Type (MVT) deposit. The sample is characterised by banded baritic lead ore from a metasomatic deposit hosted by limestone; galena grains in dark bands can be recognized with coarse-grained white barite lenses and fine-grained limonitic matrix. HTL324 from Recsk, Hungary, represents porphyry mineralisation sampled from an intrusion related to porphyry copper deposits and includes a breccia with sulphide matrix and veins [14]. Starting materials were characterised using X-ray diffraction for bulk mineralogy and BET (Brunauer–Emmett–Teller) analysis for surface area.

Details of the solid samples, including their sampling location, geological setting, and a summary of their bulk composition, as determined by XRD, can be found in Table 1. All samples were collected from the surface, generally from mine dumps or rockfalls adjacent to exposures. Efforts were made to ensure that the material used for the experiments was as pristine as possible, i.e., materials at or near (within ~10 cm) weathered surfaces were avoided. A variety of solutions were used in the experiments in order to test their relative potential for liberation of metals from ore-bearing deposits. Most of these were created using one or two reagents dissolved or diluted to the desired concentration. The fluids used in the experiments reported here as well as the temperature/pressure conditions of the experiments using various solids are summarised in Table 2.

3. Method

3.1. Batch Experiments. Two different methods were used for the batch experiments, which are chosen according to the experimental conditions (i.e., pressure and temperature) required. Initial experiments were carried out at atmospheric pressure, using high-density polyethylene (HDPE) bottles fixed into a rotating mixing assembly. Solid samples were carefully weighed and added to the appropriate fluid in a 40 : 1 fluid : rock ratio. The relatively high fluid to rock ratio was chosen to meet fluid sampling requirements while minimising changes in reaction rate due to relative changes in fluid : rock ratio due to sampling. The experimental "charge" in these experiments consisted of an accurately known amount of granulated rock sample (around 5 g) together with 200 ml of reactant solution. The tops of the HDPE bottles were securely tightened, the vessels were arranged symmetrically on the mixer, and the entire assembly was placed into a thermostatically-controlled fan-assisted oven. When

Table 2: Summary of experimental materials and conditions used.

Solvent	Deionised water			0.1 M acetic acid			0.01 M HCl, 0.003 M HNO3	0.1 M HCl, 0.03 M HNO3	
Sample ID	70°C, 1 bar batch	100°C, 200bar batch	200°C, 250 bar flow-through	70°C, 1 bar batch	150°C, 200 bar batch	250 °C, 250 bar flow-through	100°C, 200 bar batch	100°C, 200 bar batch	200 °C, 200 bar batch
HTLMix	✓			✓	✓	✓	✓	✓	✓
HTL315	✓	✓		✓		✓			
HTL319	✓			✓		✓			
HTL321			✓			✓	✓		
HTL322			✓			✓			
HTL324			✓			✓	✓		

running, the mixer turned at approximately six revolutions per minute—enough to ensure good mixing between solid and solution without causing too much mechanical damage to the solid grains.

Higher temperature and pressure experiments utilised titanium batch reactors inside thermostatically-controlled fan-assisted ovens [15, 16]. The basic layout of the batch reactors used is shown schematically in Figure 2. Viton O-rings are used between the vessel body and vessel head to prevent loss of pressure. A large retaining ring is screwed onto the top of the vessel to keep the vessel body and vessel head together when pressurised. This equipment was used for the experiments at 100°C, 150°C, and 200°C.

Loading the vessel consisted of adding accurately known amounts of granulated rock (approximately 8.75 g) and synthetic groundwater or other leaching solution (350 ml) plus a magnetic stirrer bead in the experiments carried out below 200°C. The head of the reaction vessel was then pushed on, and the retaining ring securely screwed down. The headspace of the vessel was flushed with nitrogen prior to pressurisation. A titanium dip tube (and associated valve), fitted with a PTFE filter assembly, was added to each vessel.

To minimise mechanical damage to the solid, the stirrer bead was both held in a small cage and only activated for approximately 2 minutes in every 4 hours. For the experiments conducted at 200°C, the stirrer assembly and stirrer bead, as well as the filter assembly, had to be removed, and instead, the vessels were periodically agitated by hand (on average about once per day). Nitrogen was used to pressurise these batch experiments with experimental pressure being controlled via an ISCO 360D syringe pump. The N_2 used was classified as "oxygen free" (99.998% pure).

At the end of each experiment, as much of the solution as possible was removed prior to cooling and depressurisation of the vessel. Once well below 100°C (i.e., the boiling point of the leachate being used), the vessel was slowly depressurised, dismantled, and reacted rock grains recovered for subsequent analysis. Batch experiments were run for around 600–1000 hours.

3.2. Flow-through Experiments. Leaching processes were also investigated under continuous flow conditions using a flow-through reactor (Figure 3). The reaction took place in a stainless steel high-pressure liquid chromatography (HPLC) column 250 mm in length and with an inner diameter of 21.2 mm. The pressure in the column was maintained by an Ecom Kappa 10 Single-Plunger HPLC pump. A 50 cm stainless steel capillary and a fluid back-pressure regulator were fitted at the outflow of the column. The length of this tubing was used to allow outflowing fluid to cool to below 90°C before being depressurised. Heating bands were attached to the column and controlled by a thermostat (WH-1435D PID digital thermostat with ±1°C control regulation). This high-pressure high-temperature device was loaded with approximately 150 g of the rock sample and operated at a temperature of approximately 250°C and a pressure of 250 bar. These parameters correspond to depths of around 2.5–3 km in an average geothermal field [9, 17]. During the experiments, the flow rate in the reactor was 0.5 ml per minute, which resulted in a contact time between the fluid and rock of 30–50 minutes, allowing the collection of sufficient sample volumes for chemical analyses.

3.3. Sampling and Analysis. For sampling, the experiments carried out using the rotating shaker setup; rotation was stopped, and the bottles were removed from the assembly one at a time to minimise any cooling following removal from the oven. Upon removal, each bottle was unsealed, and a sample was removed using a polyethylene syringe and subsequently filtered using a 0.2 μm nylon syringe filter prior to subsampling for analyses.

For experiments carried out using titanium vessels, a valve on top of the vessel (attached to an internal titanium sampling tube) was opened to a syringe attached to the valve via a length of polyetheretherketone (PEEK) tubing. An accurately known quantity (typically 1–5 ml) of fluid was allowed to flow into the syringe in order to flush the sample tube, valve, and tubing. This syringe was removed and discarded. A second syringe was then attached and used to withdraw an accurately known amount (approximately 10 ml) of fluid. This sample was subsequently filtered using a 0.2 μm nylon syringe filter.

Once a sample of filtered fluid was obtained, each was split into several sub-samples for ion chromatography (IC), inductively coupled mass spectrometry (ICP-MS), alkalinity (carried out by titration against sulphuric acid), and reduced iron (carried out colorimetrically using ultraviolet spectrometry) analyses as well as analysis of pH and Eh. Subsamples

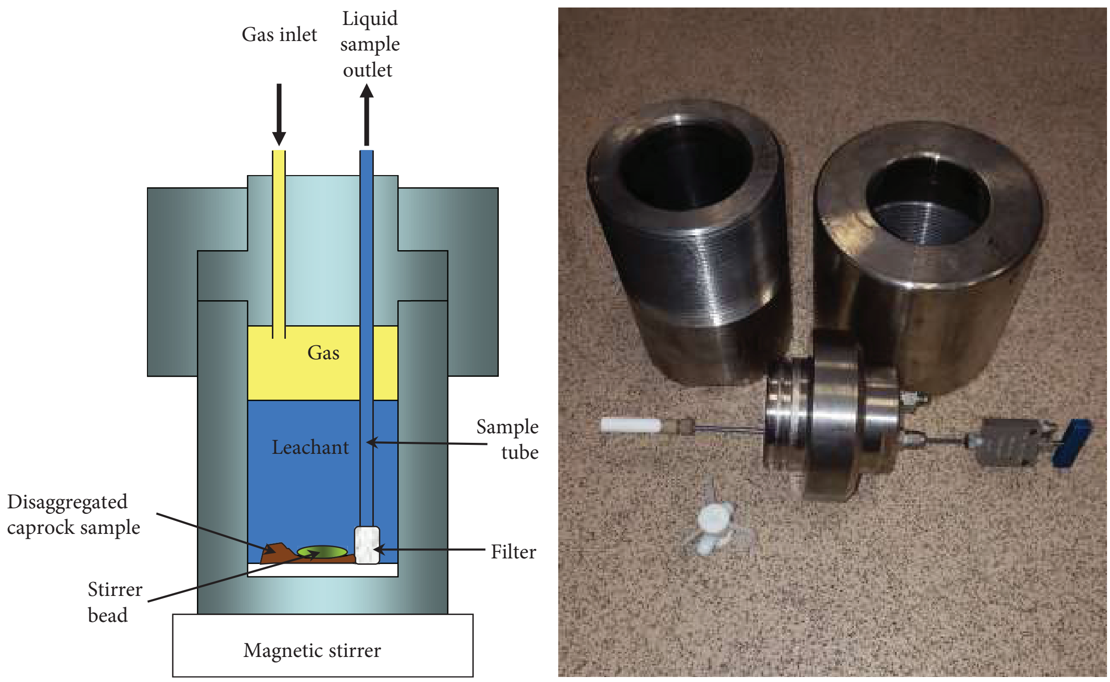

Figure 2: Schematic diagram and photograph of a titanium batch reactor.

(a) (b)

Figure 3: Flow-through reactor (a) and temperature control on top of the HPLC pump used (b).

Table 3: Physical properties of each fluid-rock interaction batch reactions.

Leachate ID	Rock sample ID	Rock sample origin	Rock sample type	Rock sample characteristics	Solvent	Pressure (bar)	Temperature (°C)	Residence time (h)
HTLMix + DI water	HTLMix	UK Herodsfoot	Baked sediments with mineralised veining	Mixture of various samples containing galena, sphalerite, and some chalcopyrite	Deionised water	1	70	670
HTLMix + 0.1 M acetic acid					0.1 M acetic acid			720
HTLMix + 0.1 M acetic acid						200	150	1000
HTLMix + 0.013 M mineral acid					0.01 M HCl + 0.003 M HNO_3		100	770
HTLMix + 0.13 M mineral acid					0.1 M HCl + 0.03 M HNO_3			770
HTLMix + 0.13 M mineral acid					0.1 M HCl + 0.03 M HNO_3		200	530
HTL315 + DI water	HTL315	UK South Caradon	Granite-hosted mineralisation	Mainstage mineralisation associated with granite bodies	Deionised water	1	70	670
HTL315+ 0.1 M acetic acid					0.1 M acetic acid			720
HTL319 + DI water	HTL319	UK Cligga Head	Granite-hosted mineralisation	Tin-tungsten mineralisation associated with granite bodies	Deionised water	1	70	670
HTL319 + 0.1 M acetic acid					0.1 M acetic acid			720
HTL321 + 0.013 M mineral acid	HTL321	RO Cacova Ierii	Skarn	Magnetite deposit enriched in sulphides with visible chalcopyrite	0.01 M HCl + 0.003 M HNO_3	200	100	770
HTL324 + 0.013 M mineral acid	HTL324	HU Recsk	Porphyry	Intrusion-related porphyry copper deposit	0.01 M HCl + 0.003 M HNO_3	200	100	650

Table 4: Concentration of the "at risk" elements in each leachate from the batch reaction.

Element Sample	Ag PPB	Co PPB	Ga PPB	Mo PPB	Sb PPB	Sr PPB	V PPB	W PPB	Total "at risk" PPB
HTLMix + DI water	*	*	*	*	116.41	51.30	*	*	167.71
HTLMix + 0.1 M acetic acid	*	77.29	17.15	*	20.41	92.04	*	67.67	274.56
HTLMix + 0.1 M acetic acid 200°C	*	26.48	4.00	1.04	656.28	141.60	*	*	829.40
HTLMix + 0.013 M mineral acid	*	3.76	*	2.64	32.10	84.80	*	0.24	123.54
HTLMix + 0.13 M mineral acid 100°C	*	159.07	12.00	17.48	3.49	149.20	*	0.28	341.52
HTLMix + 0.13 M mineral acid 200°C	*	979.95	8.00	176.00	7100.00	220.00	*	7.98	8491.92
HTL315 + DI water	*	1001.28	*	*	71.93	*	*	*	1073.21
HTL315 + 0.1 M acetic acid	*	1069.75	*	*	90.06	*	*	91.59	1251.40
HTL319 + DI water	*	*	*	*	2.41	*	*	181.83	184.24
HTL319 + 0.1 M acetic acid	*	*	*	*	*	*	*	128.04	128.04
HTL321 + 0.013 M mineral acid	*	11.64	*	2.60	43.51	101.20	*	*	158.95
HTL324 + 0.013 M mineral acid	*	5.52	*	0.44	0.16	58.40	*	*	64.52

*: concentration was under the detection limit.

for ICP-MS analysis were diluted using deionised water and acidified using HNO_3. Subsamples for alkalinity and ion chromatography (IC) analyses were diluted using deionised water. Subsamples for analysis of reduced iron were diluted and prepared for analysis using deionised water and 2,2-bipyridyl solution.

At the end of each experiment, as much of the fluid phase was removed as possible to minimise the formation of unwanted precipitates during cooling and depressurisation. The vessels were then cooled as rapidly as possible to below 80°C and then depressurised. After the opening of the reaction vessels, any residual fluid was sampled (and then subsampled and preserved as per samples described above) to allow characterisation of any chemical changes in the system during depressurisation and cooling. The reacted solids were removed from the vessel, a subsample of which was rinsed using acetone, and then oven dried at 30°C.

For quantitative whole-rock X-ray diffraction (XRD) analysis, >5 g samples of the starting solids were ball-milled and then micronized underwater to a fine powder (<10 μm). XRD analysis was carried out using a PANalytical X'Pert Pro series diffractometer equipped with a cobalt-target tube and operated at 45 kV and 40 mA. Derivation of quantitative mineralogical data was accomplished by using the least squares fitting process applying the Rietveld refinement technique [18]. A subsample of the crushed starting solids was also dissolved using hydrofluoric acid digestion, and the resulting liquid was analysed using ICP-MS as per the fluid samples from the experiments.

4. Results

4.1. Batch Experiments. Batch experiments were conducted using deionised water, acetic acid (in 0.1 M concentration), and mineral acid (a mixture of 0.13 M HCl and 0.013 M HNO_3) on the range of samples HTLMix, HTL315, HTL319, HTL321, and HTL 324 at 70°C, 100°C, 150°C, and 200°C under 1 bar (70°C experiments only) and 200 bar pressure (Table 3). In this study, the elements appearing in the highest concentration were Al, B, Ba, Ca, Cd, Cr, Cu, Fe, K, Mg, Mn, Na, Ni, Pb, Rb, S, Si, and Zn. The economic value of these elements is debatable, due to limited utility or wide availability, and these elements are here referred to as "common" elements. Elements with higher value but appearing in lower concentrations, such as Ag, Co, Ga, Mo, Sb, Sr, V, and W elements, were selected as desirable and referred to as "at risk" elements in this paper based on the evaluation by European Commission et al. [1]. Data about the composition of samples from batch reactions, on which the following figures are based, can be found in Tables 4 and 5. To illustrate results from analyses, spider plots were used, where individual elements are arranged in a ring around a central point representing zero concentration of all the elements. Thus, concentrations increase away from the centre of the plot (in this study on a logarithmic scale).

4.1.1. Leaching Tests Using Deionised Water as Solvent. Leaching experiments were carried out using deionised water on UK samples HTL315, HTL319, and HTLMix at 70°C. The total concentration of "common" elements found in the leachate shown in Figure 4 corresponds to approximately 70 ppm in the case of HTL315, 5.4 ppm in the case of HTL319, and 29 ppm in the case of HTLMix. In HTL315, Fe and Si were the elements detected in higher concentration, accounting for 58% and 24% of the total "common" elemental concentration, respectively. In HTL319, Si was the most abundant element, accounting for 96% of the total "common" elemental concentration. For the leachate produced by reaction with HTLMix, Mg was the most abundant element, with K and Si were also detected, accounting for 67%, 16%, and 15% of the total "common" elemental concentrations, respectively.

Reaction at 70°C temperature under 1 bar pressure with HTL315, HTL319, and HTLMix resulted in the mobilisation of approximately 1070 ppb, 180 ppb, and 170 ppb of the

Table 5: Concentration of the "common" elements in each leachate from the batch reaction.

Element Sample	Al PPB	B PPB	Ba PPB	Ca PPB	Cd PPB	Cr PPB	Cu PPB	Fe PPB	K PPB	Mg PPB	Mn PPB	Na PPB	Ni PPB	Pb PPB	Rb PPB	S PPB	Si PPB	Zn PPB
HTLMix + DI water	105	*	46	*	*	*	7	*	4684	19,343	*	*	*	418	12	*	4309	*
HTLMix + 0.1 M acetic acid	1642	*	*	91,652	17	*	15	*	3401	51,998	8309	*	117	871,112	22	*	14,277	3131
HTLMix + 0.1 M acetic acid 200°C	460	*	2162	112,006	22	*	12	13,059	5960	49,950	6996	12,000	71	18,499	15	*	75,692	6261
HTLMix + 0.013 M mineral acid	*	*	970	80,004	2	2	*	120	*	32,273	5679	4000	8	80	*	4001	*	120
HTLMix + 0.13 M mineral acid 100°C	76,984	*	958	124,006	1553	1094	34,406	12,103	15,601	112,961	8458	6400	1113	3,676,056	82	4001	81,044	323,065
HTLMix + 0.13 M mineral acid 200°C	29,722	*	1412	*	809	304	924	848,648	76,003	62,787	25,897	*	42,850	805,280	524	232,036	210,993,801	183,156
HTL315 + DI water	5287	*	*	*	*	*	3996	40,705	*	*	701	*	27	*	4	*	17,198	1922
HTL315 + 0.1 M acetic acid	7412	*	*	*	*	*	10,327	56,082	*	*	779	*	31	*	5	*	21,004	1115
HTL319 + DI water	*	*	*	*	*	*	11	*	*	*	206	*	*	*	8	*	5181	*
HTL319 + 0.1 M acetic acid	3079	*	*	*	*	36	132	4767	*	*	837	*	*	*	31	*	8822	*
HTL321 + 0.013 M mineral acid	*	*	866	92,005	23	2	*	8	1200	37,648	6726	3600	6	4	*	4001	*	760
HTL324 + 0.013 M mineral acid	26,623	*	1294	32,002	7	12	13	143,755	2400	22,871	1311	11,600	31	4	6	4001	*	1992

*: concentration was under the detection limit.

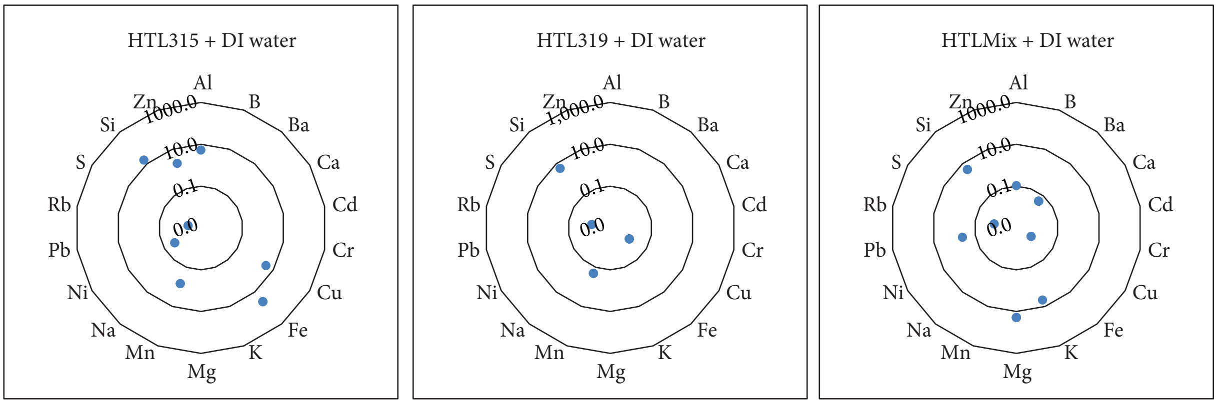

FIGURE 4: Common elemental composition (in ppm) of each leachate reacted with deionised water at 70°C temperature under 1 bar pressure in batch rotating shakers after 670 hours (absence of data points reflects concentrations below the limits of detection).

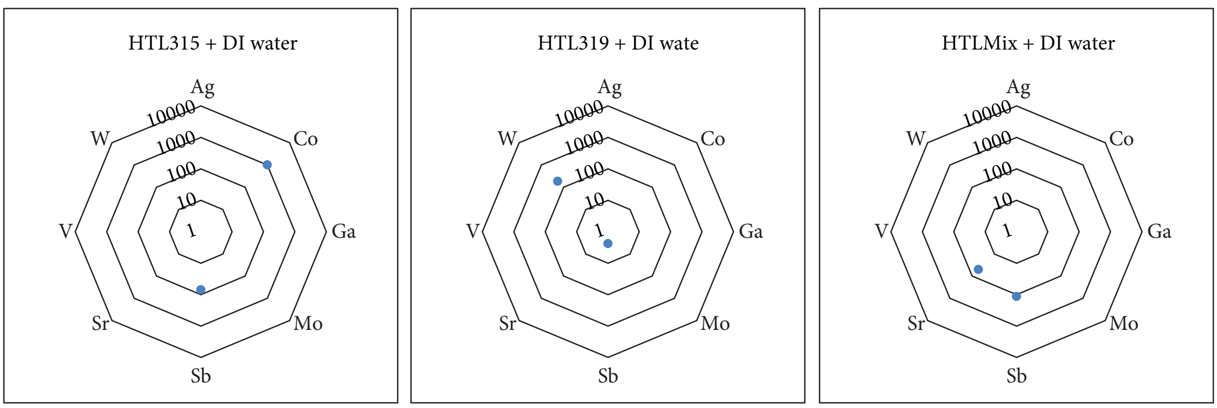

FIGURE 5: Concentration (in ppb) of the "at risk" elements in each sample reacted with deionised water at 70°C temperature under 1 bar pressure in batch rotating shakers after 670 hours (absence of data points reflects concentrations below the limits of detection).

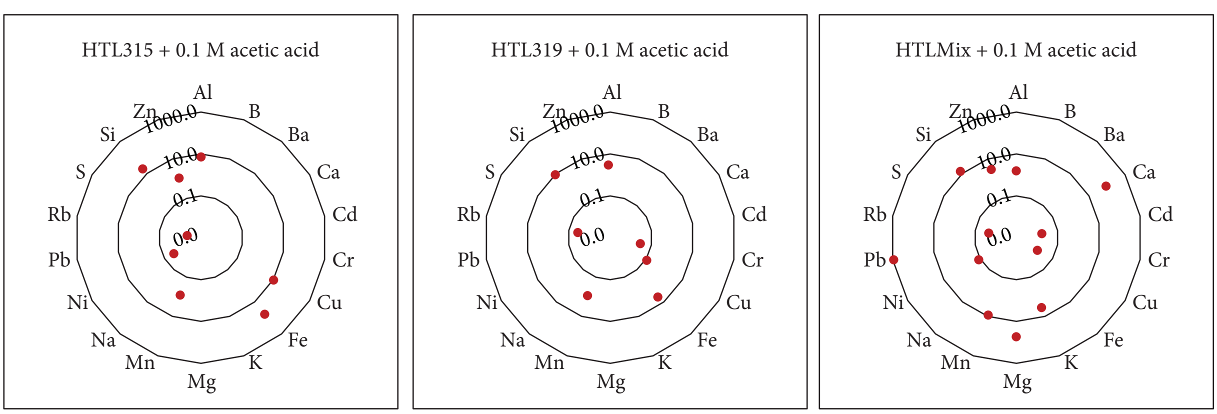

FIGURE 6: Elemental composition (in ppm) of each leachate reacted with 0.1 M acetic acid at 70°C temperature under 1 bar pressure in batch rotating shakers after 720 hours (absence of data points reflects concentrations below the limits of detection).

selected "at risk" elements, respectively. Of these elements, Co, W, and Sb were detected at the highest concentrations (Figure 5).

4.1.2. Leaching Tests Using Acetic Acid as Solvent. The total concentration of "common" elements in the final sample taken at 70°C, shown in Figure 6, corresponds to approximately 100 ppm in the case of HTL315, 18 ppm in the case of HTL319, and 1050 ppm in the case of HTLMix. In HTL315, Fe and Si were the elements with the highest concentration, yielding 58% and 22% of the total "common" elements. In HTL319, Si was the most dominant among the

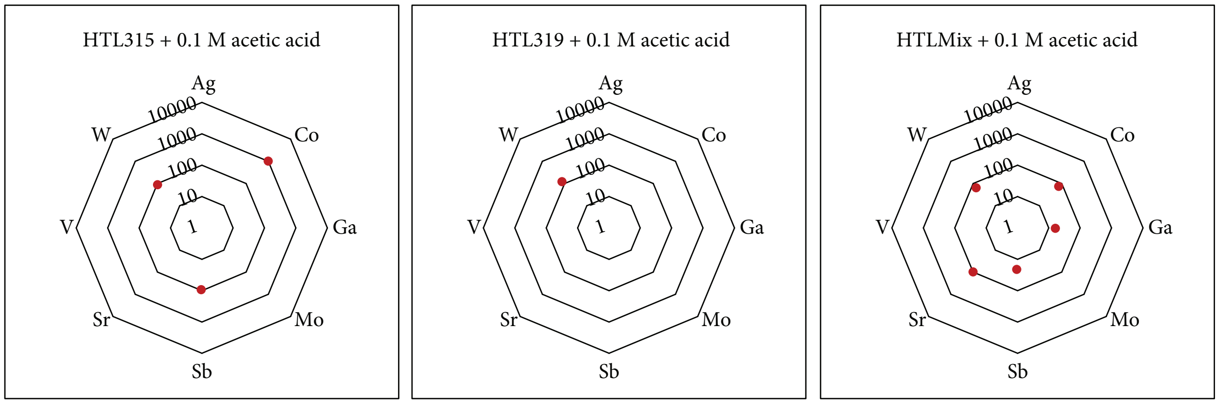

Figure 7: Concentration (in ppb) of the "at risk" elements in each sample reacted with 0.1 M acetic acid at 70°C temperature under 1 bar pressure in batch rotating shakers (absence of data points reflects concentrations below the limits of detection).

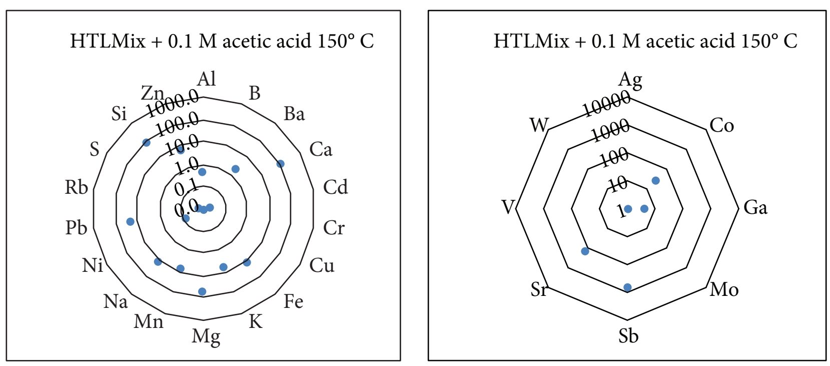

(a) (b)

Figure 8: Concentration of the "common" ((a) in ppm) and "at risk" ((b) in ppb) elements obtained from HTLMix at 150°C temperature under 200 bar pressure in Ti batch vessel after 1000 hours (absence of data points reflects concentrations below the limits of detection).

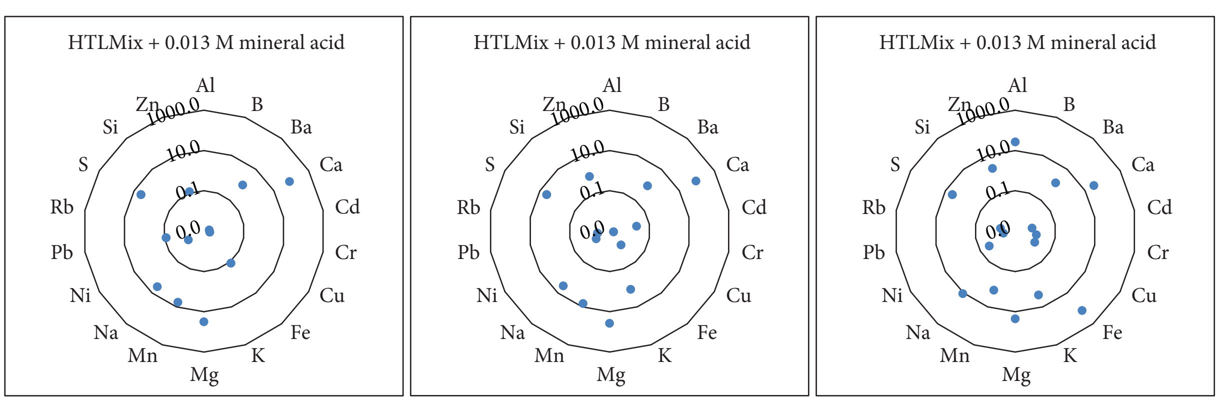

Figure 9: Elemental composition (in ppm) of each leachate reacted with the mixture of 0.01 M HCl and 0.003 M HNO_3 at 100°C temperature under 200 bar pressure in Ti batch reactors (absence of data points reflects concentrations below the limits of detection).

"common" elements, accounting for 50% of the total dissolved concentration. In the case of HTLMix, large amounts of lead were leached, with concentrations of 870 ppm Pb in the final sample, accounting for 83% of the total concentration of "common" elements observed.

Reaction with 0.1 M acetic acid at 70°C temperature under 1 bar pressure resulted in leached concentrations of approximately 1250 ppb of the selected "at risk" elements in the case of HTL315, 130 ppb in the case of HTL319, and 280 ppb in the case of HTLMix (Figure 7). The most efficient mobilisation was in the case of HTL315; in this sample, Co was leached at a concentration of up to 1070 ppb. Tungsten was also detected in every leachate though at lower concentrations.

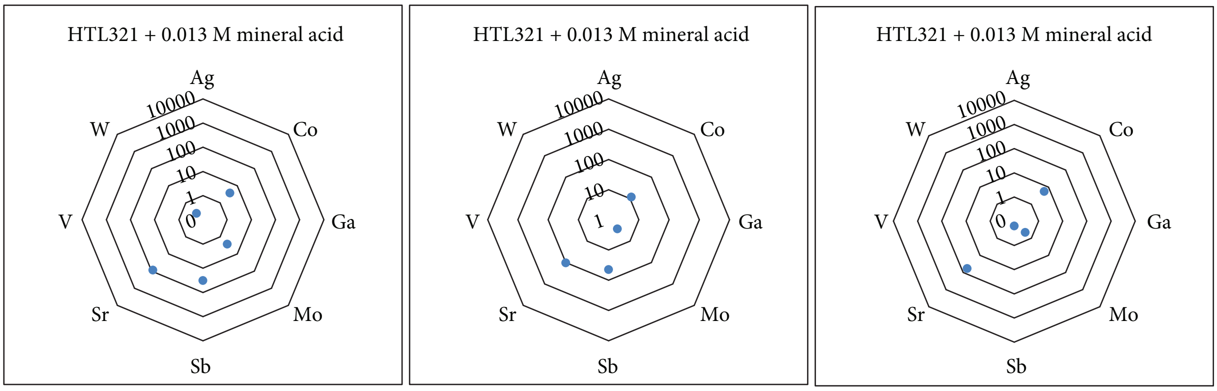

FIGURE 10: Concentration (in ppb) of the "at risk" elements in each sample reacted with the mixture of 0.01 M HCl and 0.003 M HNO_3 at 100°C temperature under 200 bar pressure in Ti batch reactors after 770 hours (absence of data points reflects concentrations below the limits of detection).

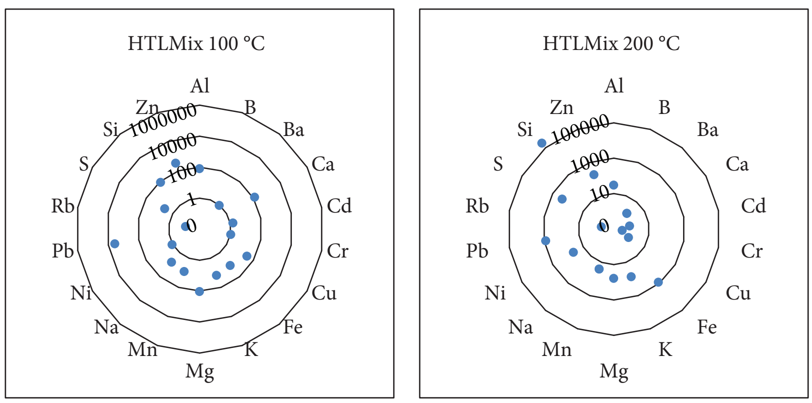

FIGURE 11: Elemental composition (in ppm) of HTLMix reacted with the mixture of 0.1 M HCl and 0.03 M HNO_3 at 100°C and 200°C temperature under 200 bar pressure in Ti batch reactors after 770 hours and 530 hours, respectively.

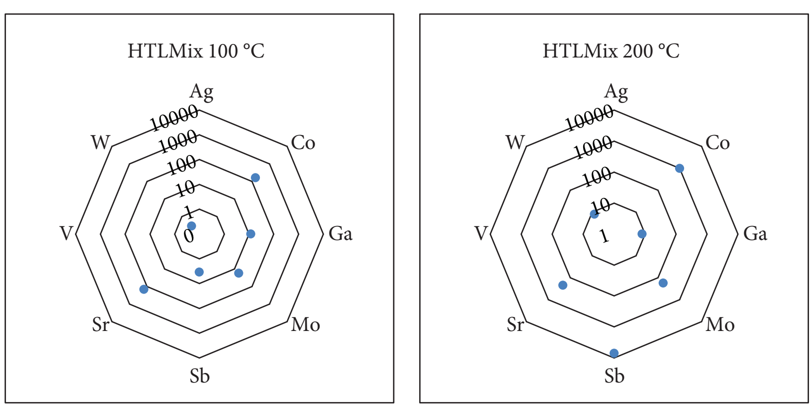

FIGURE 12: Concentration (in ppb) of the "at risk" elements in HTLMix reacted with the mixture of 0.1 M HCl and 0.03 M HNO^3 at 100°C and 200°C temperature under 200 bar pressure in Ti batch reactors after 770 hours and 530 hours, respectively (absence of data points reflects concentrations below the limits of detection).

HTLMix was also leached using 0.1 M acetic acid at 150°C temperature under 200 bar pressure. Figure 8 shows the concentrations of the selected "common" and "at risk" elements. The total concentrations of "common" and "at risk" elements mobilised were 300 ppm and 830 ppb, respectively. Ca, Si, and Pb had the highest abundance amongst the "common" elements, constituting 37%, 25%, and 6% of the total "common" elements leached, respectively. Sb, Sr, and Co were the most important "at risk" elements leached, constituting 79%, 17%, and 3% of the total, respectively.

4.1.3. Leaching Tests Using Mineral Acid as Solvent. Leaching in Ti batch reactors using the mixture of 0.01 M hydrochloric acid and 0.003 M nitric acid was conducted at 100°C

Table 6: Physical properties of each fluid-rock interaction in the flow-through reactor.

Leachate ID	Rock sample ID	Rock sample origin	Rock sample type	Rock sample characteristics	Solvent	Pressure minimum (bar)	Pressure maximum (bar)	Residence time (min)
HTL322 + DI water 1	HTL322	HU Rudabánya	MVT	Banded baritic lead ore from a metasomatic deposit hosted by limestone	Deionised water	225	290	36
HTL322 + DI water 2						250	257	48
HTL322 + DI water 3						250	285	35
HTL322 + 0.1 M acetic acid					0.1 M acetic acid	250	260	48
HTL324 + DI_water	HTL324	HU Recsk	Porphyry	Intrusion-related porphyry copper deposit	Deionised water	220	240	25
HTL324 + 0.1 M acetic acid					0.1 M acetic acid	250	250	38
HTL321 + DI_water	HTL321	RO Cacova Ierii	Skarn	Magnetite deposit enriched in sulphides with visible chalcopyrite	Deionised water	240	248	52
HTL321 + 0.1 M acetic acid					0.1 M acetic acid	250	270	27
HTL315 + 0.1 M acetic acid	HTL315	UK South Caradon	Granite-hosted mineralisation	Mainstage mineralisation associated with granite bodies	0.1 M acetic acid	250	281	37
HTL319 + 0.1 M acetic acid	HTL319	UK Cligga Head	Granite-hosted mineralisation	Tin-tungsten mineralisation associated with granite bodies	0.1 M acetic acid	218	265	42
HTLMix + 0.1 M acetic acid	HTLMix	UK Herodsfoot	Baked sediments with mineralised veining	Mixture of various samples containing galena, sphalerite, and some chalcopyrite	0.1 M acetic acid	250	289	36

Table 7: Concentration of the "at risk" elements in each leachate from the flow-through reaction.

Element Sample	Ag PPB	Co PPB	Ga PPB	Mo PPB	Sb PPB	Sr PPB	V PPB	W PPB	Total 'at risk' PPB
HTL322 + DI water 1	*	4.24	*	0.6	19.45	844.57	*	0.19	869.05
HTL322 + DI water 2	*	2.77	*	0.6	15.81	660.15	*	0.07	679.40
HTL322 + DI water 3	*	2.02	*	0.5	65.22	489.79	*	0.05	557.58
HTL322 + 0.1 M acetic acid	*	0.81	*	8.6	91.66	414.46	*	0.23	515.76
HTL324 + DI_water	0.09	0.28	*	3.8	18.75	377.31	0.3	1.06	401.59
HTL324 + 0.1 M acetic acid	*	*	*	*	*	2837.00	*	*	2837.00
HTL321 + DI_water	*	*	*	*	*	1526.00	*	*	1526.00
HTL321 + 0.1 M acetic acid	*	*	*	*	*	1094.00	*	*	1094.00
HTL315 + 0.1 M acetic acid	*	209.29	*	*	*	8.38	10	*	227.67
HTL319 + 0.1 M acetic acid	90	9.2927	*	*	440	95.15	*	470	1104.45
HTLMix + 0.1 M acetic acid	20	94.967	*	*	*	918.33	*	*	1033.30

*: concentration was under the detection limit.

temperature under 200 bar pressure. The total concentration of "common" elements leached in the final sample, shown in Figure 9, was approximately 130 ppm in the case of HTLMix, 150 ppm in the case of HTL321, and 250 ppm in the case of HTL324. In the HTLMix leachate, Ca and Mg were detected in the highest concentration, constituting 63% and 25% of the total "common" elements, respectively. In this sample, Mn, Na, and S were also found at notable concentrations. In the leachate reacted with HTL321, Ca and Mg were also the most abundant elements, constituting 63% and 26% of the total "common" elements leached, respectively. K, Mn, Ma, and S were also detected in lower but potentially recoverable concentrations in this sample. In the leachate reacted with HTL324, Fe was found in the highest concentration, constituting 58% of the total "common" elements leached. Al, Ca, Mg, and Zn were also found in concentrations of 27 ppm, 32 ppm, 23 ppm, and 2 ppm, respectively.

Reaction with the mixture of 0.01 M hydrochloric acid and 0.003 M nitric acid at 100°C under 200 bar pressure resulted in leachate concentrations of approximately 125 ppb of the selected "at risk" elements in the case of HTLMix, 160 ppb in the case of HTL321, and 65 ppb in the case of HTL324 (Figure 10). In these samples, Co, Mo, Sb, and Sr were detected, of which Sb had the highest concentrations in all three samples.

HTLMix was also leached using a higher concentration (0.1 M hydrochloric acid and 0.03 M nitric acid), at 100°C and 200°C, under 200 bar pressure. Figure 11 shows the concentrations of the "common" elements in each leachate. The total concentration of "common" elements leached was approximately 4480 ppm at 100°C (770 hours) and 213,000 ppm at 200°C (530 hours). In the case of reaction at 100°C, the most abundant element leached was Pb, which was found at a concentration of 3680 ppm in the leachate. At 200°C, Si, Fe, and Pb were the most abundant elements at 211000 ppm, 850 ppm, and 805 ppm concentration, respectively.

Reaction with the 0.13 M mineral acid solution at 100°C and 200°C temperature under 200 bar pressure resulted in concentrations of approximately 340 ppb and 8500 ppb of the selected "at risk" elements in the final samples taken, respectively. Figure 12 shows the measured Ag, Co, Ga, Mo, Sb, Sr, V, and W concentrations. In the case of reaction at 100°C, Co, Sr, and Ga were mobilised at concentrations of 160 ppb, 150 ppb, and 10 ppb, respectively. Reaction at 200°C resulted in the mobilisation of 7100 ppb Sb, 980 ppb Co, 220 ppb Sr, 180 ppb Mo, 8 ppb Ga, and 8 ppb W.

4.2. Flow-through Measurements. Experiments using the flow-through reactor described in the methods section were conducted using deionised (DI) water and 0.1 M acetic acid on samples HTL315, HTL139, HTL321, HTL322, HTL324, and HTLMix at 200 and 250°C temperature under 250°bar pressure. A summary of the actual physical properties during the flow-through tests is represented by Table 6. Leachate samples from each reaction were analysed using ICP-MS. Data about the composition of samples from the flow-through reaction, on which the following figures are based, can be found in Tables 7 and 8.

4.2.1. Leaching Tests Using Deionised Water. Flow-through leaching experiments were carried out using deionised water on samples HTL321, HTL322, and HTL324 at 200°C. The concentration of "common" elements leached can be seen in Figure 13, and the concentration of "at risk" elements mobilised from solid samples is presented in Figure 14.

The total concentration of the selected "common" elements in HTL321 is approximately 1000 ppm (of which 380 ppm is Ca and 380 ppm is S); for HTL322, the total leached is 90 ppm (of which 40 ppm is Ca and 27 ppm is S); for HTL324, the total is 940 ppm (of which 480 ppm is Ca and 360 ppm is S). Reaction with deionised water resulted in a total concentration of 400 ppb of the selected "at risk" elements in the case of HTL321, 700 ppb in the case of HTL322, and 520 ppb in the case of HTL324. The highest concentration element among the "at risk" elements was Sr, representing 94%, 94%, and 76% of the total amount of "at

Table 8: Concentration of the "common" elements in each leachate from the flow-through reaction.

Element Sample	Al PPB	B PPB	Ba PPB	Ca PPB	Cd PPB	Cr PPB	Cu PPB	Fe PPB	K PPB	Mg PPB	Mn PPB	Na PPB	Ni PPB	Pb PPB	Rb PPB	S PPB	Si PPB	Zn PPB
HTL322 + DI water 1	21	62	248	52,890	140	2	3	*	2940	4290	577	1530	42	1314	9	36,000	4576	5895
HTL322 + DI water 2	4	45	228	47,650	117	2	2	*	3430	3420	420	1830	25	1067	11	31,000	4237	5041
HTL322 + DI water 3	12	27	220	21,240	79	1	16	*	1390	1580	266	1690	7	17,008	4	14,000	1740	5768
HTL322 + 0.1 M acetic acid	4	289	107	477,120	*	1	9	*	10,820	26,190	960	8490	65	2	81	364,000	51,658	27
HTL324 + DI_water	76	7105	155	383,830	*	8	8	*	8180	126,020	286	18,800	3	19	60	379,000	74,144	16
HTL324 + 0.1 M acetic acid	*	479	1958	378,200	2577	*	*	*	54,000	44,000	645	10,000	*	537,892	*	22,000	*	98,738
HTL321 + DI_water	*	439	268	1,261,900	*	*	*	90,925	41,000	24,000	8896	63,000	*	5299	*	182,000	*	1702
HTL321 + 0.1 M acetic acid	*	12,906	153	1,314,300	*	*	*	29,330	7000	375,000	1904	17,000	*	22,190	*	375,000	*	934
HTL315 + 0.1 M acetic acid	2548	1718	26	36,719	*	145	45	12,812	21,313	11,997	*	6186	356	1145	*	*	*	6292
HTL319 + 0.1 M acetic acid	645	399	71	7793	*	201	13	54,192	7450	2344	*	4169	290	98	*	*	*	208
HTLMix + 0.1 M acetic acid	98	678	639	609,030	84	13	1	4805	49,918	117,900	*	29,278	154	243,620	*	*	*	7969

*: concentration was under the detection limit.

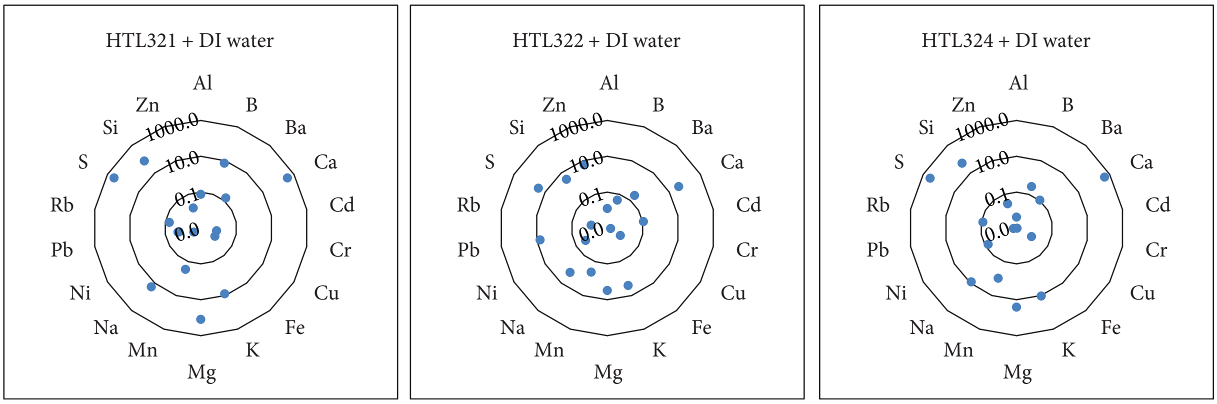

FIGURE 13: Elemental composition (in ppm) of each leachate from samples reacted with deionised water at 200°C temperature under 250 bar pressure in the flow-through reactor after 52 minutes, 48 minutes, and 25 minutes, respectively (absence of data points reflects concentrations below the limits of detection).

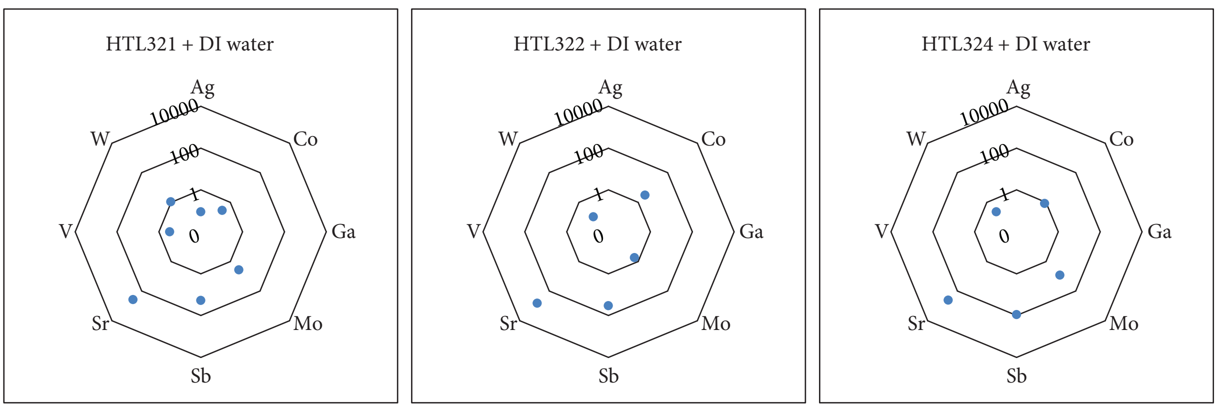

FIGURE 14: The amount of "at risk" elements in leachate from samples reacted with deionised water at 200°C temperature under 250 bar pressure in ppb after 52 minutes, 48 minutes, and 25 minutes, respectively (absence of data points reflects concentrations below the limits of detection).

risk" elements in the leachates, respectively. Sb and W were also detected amongst other potentially useful elements.

4.2.2. Leaching Tests Using Acetic Acid as Solvent. Flow-through leaching experiments were also carried out using 0.1 M acetic acid. Total dissolved solids (TDS) concentrations in the leachates from these experiments were too high to use the ICP-MS analysis previously employed; therefore, an instrument meant for midgrade concentrations, ICP-OES, was used. This method had a higher detection limits for some crucial elements; therefore, it was useful only in the determination of the concentrations of the most abundant elements. The concentrations of elements in the leachate as a result of the reaction can be seen in Figure 15.

The total concentrations of "common" elements leached, shown in Figure 15, correspond to approximately 1060 ppm in the case of HTLMix, 100 ppm in the case of HTL315, 80 ppm in the case of HTL319, 2150 ppm in the case of HTL321, 1150 ppm in the case of HTL322, and 1680 ppm in the case of HTL324. Generally, the most abundant element in the leachates was Ca, constituting 57%, 36%, 10%, 61%, 33%, and 75% of the total "common" elements in leachates from experiments using HTLMix, HTL315, HTL319, HTL321, HTL322, and HTL324, respectively. In the case of HTLMix and HTL322, enhanced Pb release was experienced with concentrations of 240 ppm and 540 ppm in the leachates from these samples, respectively.

Reaction with 0.1 M acetic acid at 250°C temperature under 250 bar pressure resulted in total concentrations of the selected "at risk" elements of 1030 ppb, 230 ppb, 1100 ppb, 1100 ppb, 2840 ppb, and 1530 ppb for leachates from experiments using HTLMix, HTL315, HTL 319, HTL321, HTL322, and HTL324, respectively. Figure 16 shows the concentrations of Ag, Co, Ga, Mo, Sb, Sr, V, and W in these samples.

In HTLMix, Ag was detected at a concentration of 20 ppb. In HTL315, 10 ppb of V was detected together with Sr and Co. The widest range of elements was mobilised from HTL319 with leachate concentrations of 440 ppb Sb, 95 ppb Sr, 90 ppb Ag, and 9 ppb Co; W was also detected in a notable amount at a concentration of 470 ppb. In the cases of HTL321, HTL322, and HTL324, only Sr was detected in one of the largest concentrations in the leachates at concentrations of 1090 ppb, 2840 ppb, and 1530 ppb, respectively.

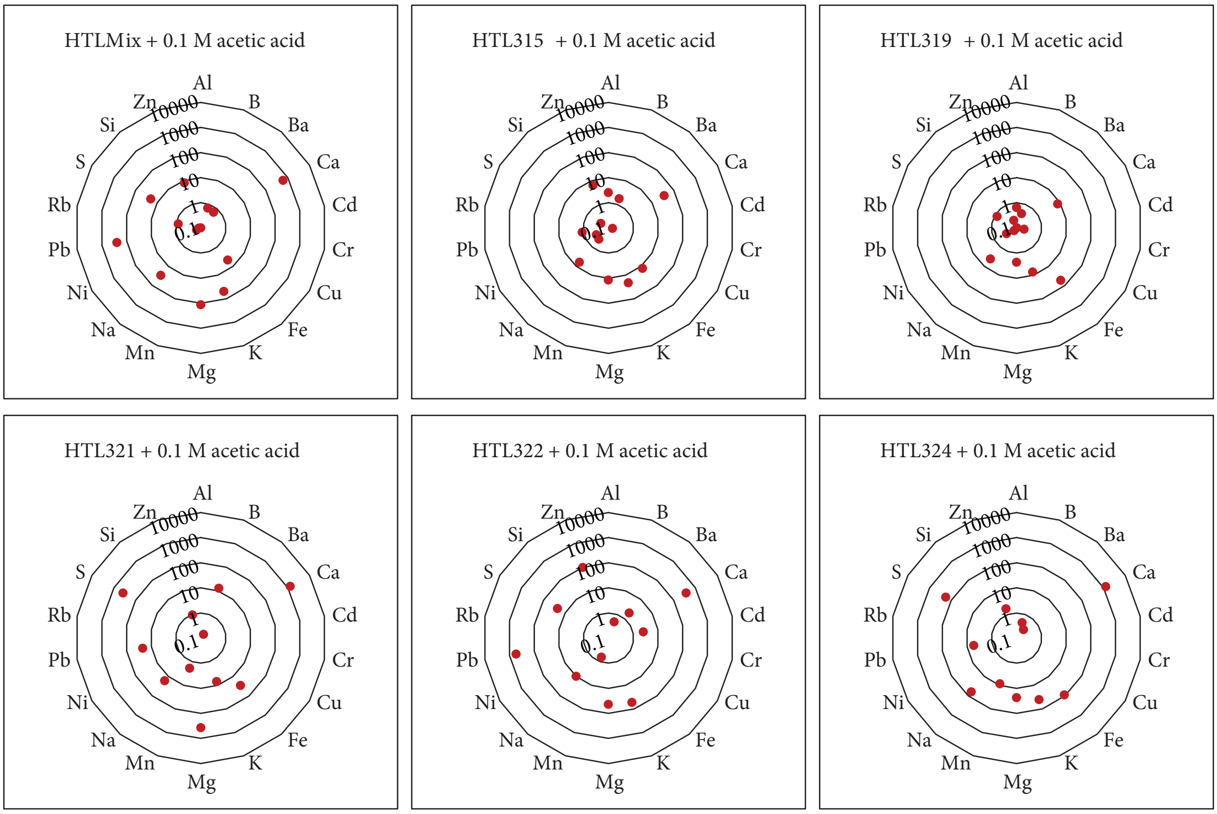

Figure 15: Elemental composition of each leachate reacted with 0.1 M acetic acid at 250°C temperature under 250 bar pressure in the flow-through reactor after 36, 37, 42, 27, 38, and 48 minutes, respectively (absence of data points reflects concentrations below the limits of detection).

5. Discussion

5.1. Comparison of Different Fluids. The tests in this study were designed largely to test the efficacy of different leaching agents. While aggressive fluids, such as mineral acids, clearly have more potential to dissolve rock and associated mineralisation, this is not the only consideration in such a system. Also, of primary concern are the environmental impact of the fluids used and the impact on the reservoir and infrastructure. While a mineral acid may leach larger concentrations of desirable elements, it is also likely to attack bulk rock, leaching less desirable elements. The latter may require consideration when it comes to reinjection or disposal or may cause problems of precipitation in the system (as commonly occurs for silica). Likewise, such fluids are likely to attack borehole and surface infrastructure materials and have a more environmental impact. More benign fluids, such as fresh water, mild acids, or organic leachants, are more likely to be publicly and environmentally acceptable but have the obvious trade-off of weaker leaching effects and potential instability at elevated temperatures (particularly in the case of organic leachants). Some investigation of the relative performance of potential leachants is therefore required and a comparison between our chosen leachants is provided below.

For each fluid studied (deionised water, 0.1 M acetic acid, and with 0.13 M mineral acid), one experiment was chosen from the batch tests to compare the dissolution properties of each fluid. Experimental runs which were conducted under very similar conditions were selected, and results from these are shown in Figure 17 for "common" elements and in Figure 18 for "at risk" elements. The figures include data from HTLMix reacted with deionised water at 200°C under 200 bar pressure for 670 hours with 0.1 M acetic acid at 150°C under 200 bar pressure for 1000 hours and with 0.13 M mineral acid at 200°C under 200 bar pressure for 530 hours.

The sum of mobilised "common" elements is approximately 80 ppm, 300 ppm, and 213,000 ppm in the case of deionised water, 0.1 M acetic acid, and 0.13 M mineral acid, respectively. The huge increase in total dissolved elements is largely due to the previously mentioned large amount of Si mobilised (approximately 211,000 ppm) in the case of the mineral acid experiment. This considerable attack on the silicates (largely quartz) present in the system by the more acidic fluids and such extremely high Si concentration indicates that the solution was highly effective at dissolving the matrix minerals. Such dissolution, leading to a reduction in solids volume and the associated increase in porosity, could expose more surfaces of metal-bearing minerals and also increase permeability and enhance fluid flow through the system. However, a higher dissolved load could also cause more precipitation on cooling. This highlights the duality of such fluids, enhancing reservoirs through increased

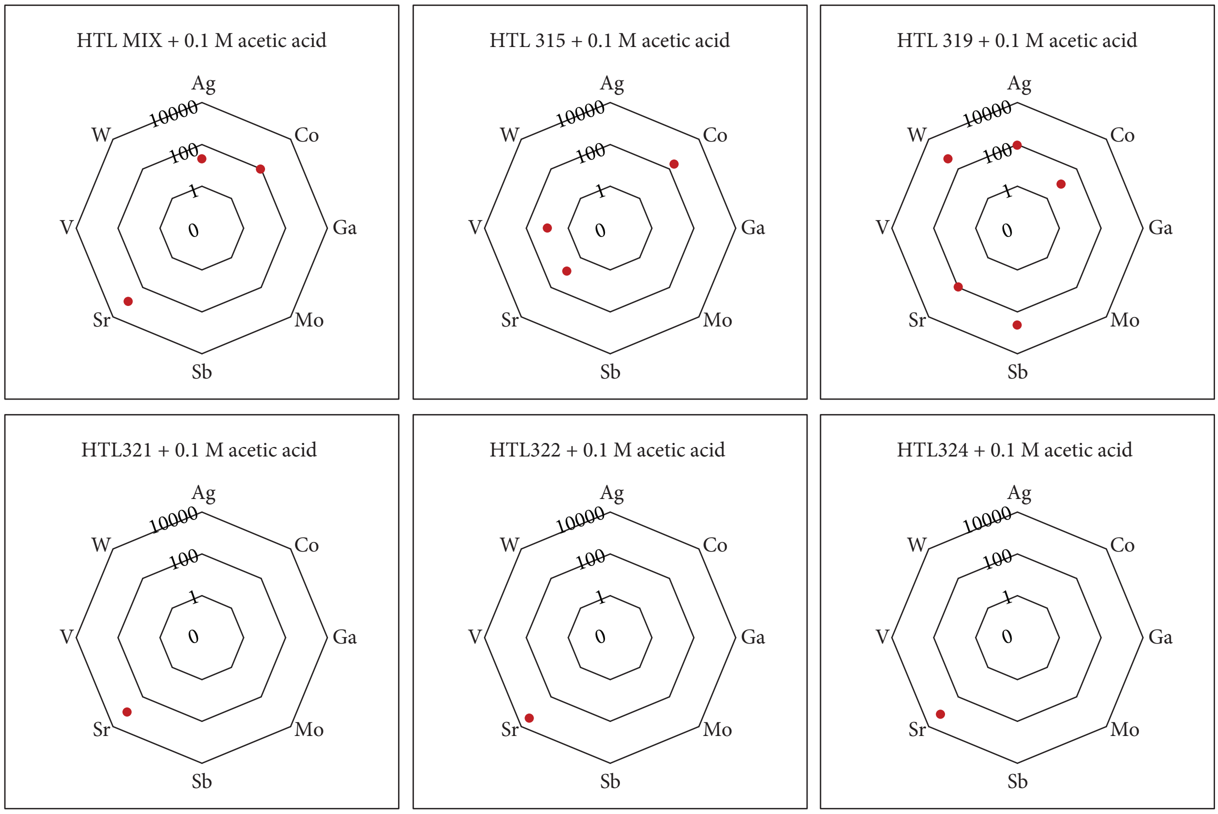

Figure 16: The amount of "at risk" elements in leachate samples reacted with 0.1 M acetic acid at 250°C temperature under 250 bar pressure in ppb after 36, 37, 42, 27, 38, and 48 minutes, respectively (absence of data points reflects concentrations below the limits of detection).

permeability but potentially also leading to issues with precipitation in surface infrastructure.

Total concentrations of "at risk elements" are approximately 50 ppb in the case of reaction with deionised water, 830 ppb in the case of reaction with acetic acid, and 8500 ppb when mineral acid was used. There is a strong relation between acidity and the total amount of mobilised elements. In our study, during batch experiments at higher temperatures, mineral acid was the best solvent, resulting in relatively high metal mobilisation and high concentration of Al and Si, which in practice would mean a higher risk for scaling. Leaching with acetic acid resulted in moderate metal concentration and significantly lower Al and Si concentrations, suggesting this as a viable leaching option and a good compromise between useable metal release and scaling risk. Also, it could be more challenging to use mineral acids as leaching solvent in geothermal systems due to difficulties around transportation, handling, storage, and environmental issues. In terms of mobilised "at risk" elements, acetic acid was more effective than deionised water but less so than mineral acid (both in terms of dissolved concentrations and the spread of elements leached in detectable concentrations). Even though it is difficult to quantify the environmental impact, the additional leaching potential of mineral acid is unlikely to make use of such an aggressive fluid, even when used at relatively dilute concentrations as here, acceptable. The results indicate, however, that even a relatively mild leachant, such as acetic acid, with which the public is familiar as an everyday substance, can substantially increase leaching potential. In this case, a switch from deionised water to acetic acid generates a nearly 20-fold increase in the dissolved load of the selected "at risk" elements. Naturally, acetic acid may not be suitable for use under all circumstances; organic acids have a tendency to break down at elevated temperatures for example (though the natural breakdown of an injectant may be seen as desirable in the long term), but these results highlight the potential of using such, relatively simple, fluids to enhance leaching in an EGS system.

5.1.1. Batch Experiments. A time series of elemental concentrations from HTLMix reacted with 0.13 M mineral acid at 100°C temperature under 200 bar pressure in a batch reactor is shown in Figure 19. Samples shown in the figure were collected after 70 hours, 290 hours, and 770 hours of reaction.

The total concentration of the selected elements in the first sample was approximately 4190 ppm, 4220 ppm in the second sample, and 4480 ppm in the third sample. The trend shows a slight, but steady, increase in leachate concentrations over time for most elements. The notable exception to this trend is iron, which after an initial increase can be seen to decrease over the course of the experiment, indicating some reprecipitation or scavenging of this element. Leaching efficiency is largest at the beginning of the experiment and decreases over time in the case of every element.

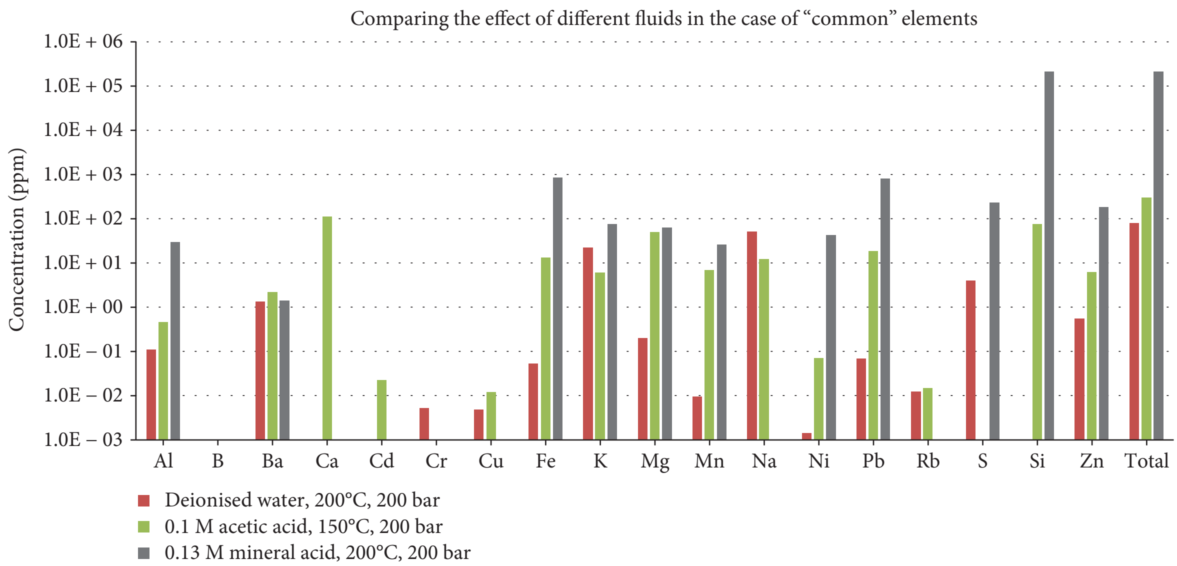

Figure 17: Comparison of the effectiveness of different fluids for "common" elements with concentrations in ppm.

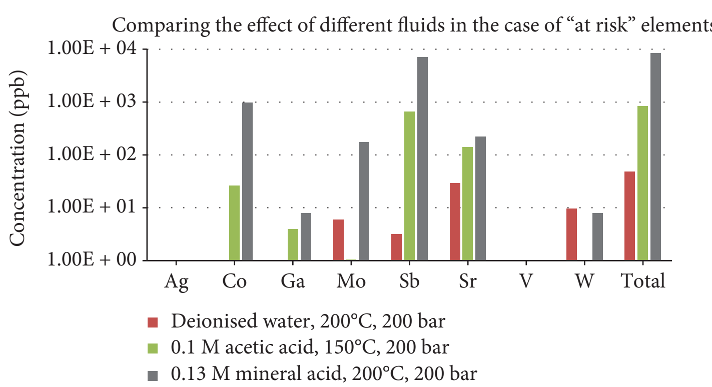

Figure 18: Comparison of the effectiveness of different fluids for "at risk" elements with concentrations in ppb.

Exceptionally high concentrations of Pb were detected at concentrations of approximately 3530 ppm, 3520 ppm, and 3680 ppm after 70 h, 290 h, and 770 h reaction, respectively. Leaching was most rapid in the first 70 hours, mobilising 3530 ppm Pb, and then decreased radically, only increasing Pb concentrations by 150 ppm over the remaining 700 hours of the experiment, as the system approached equilibrium.

Available surface area for a chemical reaction (and heat exchange) is crucial for raw material mobilisation, as mineralised rock formations dissolve quickly, suggesting that increasing available surface through stimulation might be more effective in increasing dissolved load rather than increasing the path length or residence time in the reservoir [19]. On a reservoir scale, this would mean that the targeted metal-rich ore formation is depletable and extraction would be most efficient early on in an extraction project with returns likely to decrease relatively rapidly over time [20]. The lifespan of such a metal extraction facility would be highly dependent on the size and grade of the geological formation but would likely be shorter than the plant life of a geothermal energy-producing facility without managing the reservoir in such a way that injected fluid could contact fresh surfaces regularly, i.e., through redirection of groundwater flow or through mechanical stimulation of the reservoir, creating fresh surfaces.

5.1.2. Flow-through Measurements. In addition to fresh surface area, another limiting factor in potential metal extraction will be the volume of "fresh" fluid that can be passed through the reservoir. In the batch experiments above, reactions can be seen slowing dramatically within a few 10s of hours as equilibrium is approached. Therefore, comparison with flow-through experiments can be instructive. A time series of elemental concentrations from one of the flow-through experiments is shown in Figure 20. Samples shown in the figure represent concentrations from reactions in the first 36 minutes, 37–84 minutes, and 85–119 minutes.

The total concentration of the shown elements in the first sample was approximately 110 ppm, 98 ppm in the second sample, and 65 ppm in the third sample. This trend in leachate concentrations is not element specific; the concentrations

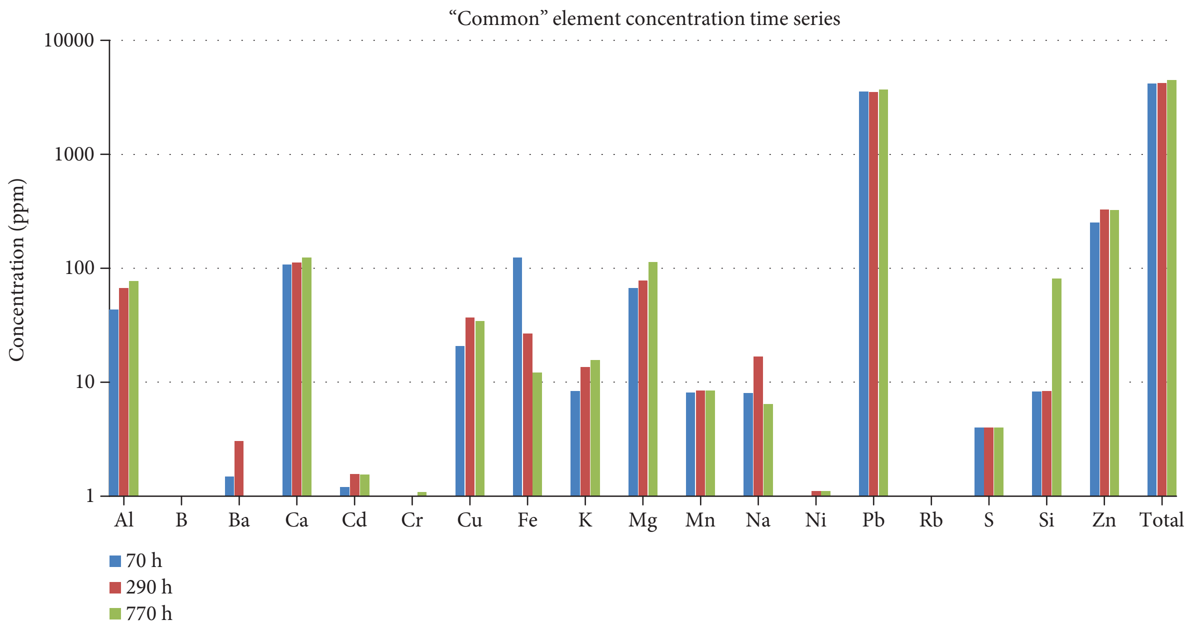

Figure 19: The kinetics of elemental composition over time in leachates from HTLMix sample reacted with 0.13 M mineral acid at 100°C temperature under 200 bar pressure in the batch reactor after 70, 290 and 770 hours, respectively.

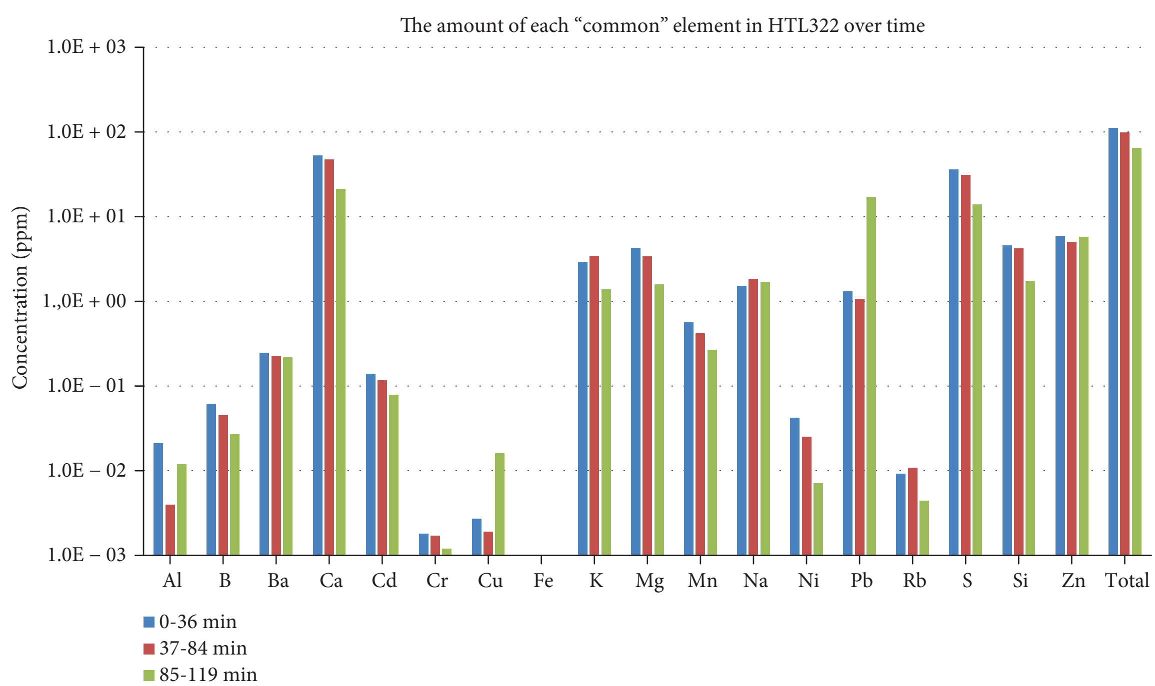

Figure 20: The kinetics of elemental composition over time in leachates from HTL322 sample reacted with deionised water at 200°C temperature under 250 bar pressure in the flow-through reactor after 36, 84, and 119 minutes, respectively.

of Ca (53 ppm, 47 ppm, and 21 ppm), Mg (4 ppm, 3 ppm, and 1.5 ppm), Mn (580 ppb, 420 ppb, and 270 ppb), S (35 ppm, 30 ppm, and 15 ppm), and Si (5 ppm, 4 ppm, and 1.5 ppm) amongst others show this trend, too. Even though the concentration of total dissolved "common" elements increased over time, the amount of increase decreased.

The tendency shown by these graphs indicates a rapid leaching reaction (for the first sample the contact time was 36 minutes). Dissolution of solid material occurs most rapidly during earlier times and then continues at lower dissolution rates. This is a key factor to consider when designing the circulation rate of an EGS system, which controls the residence time of the fluid in the reservoir. When combining metal leaching with the harnessing of geothermal energy, the rock dissolution processes for metal mobilisation would have longer contact times than those demonstrated here;

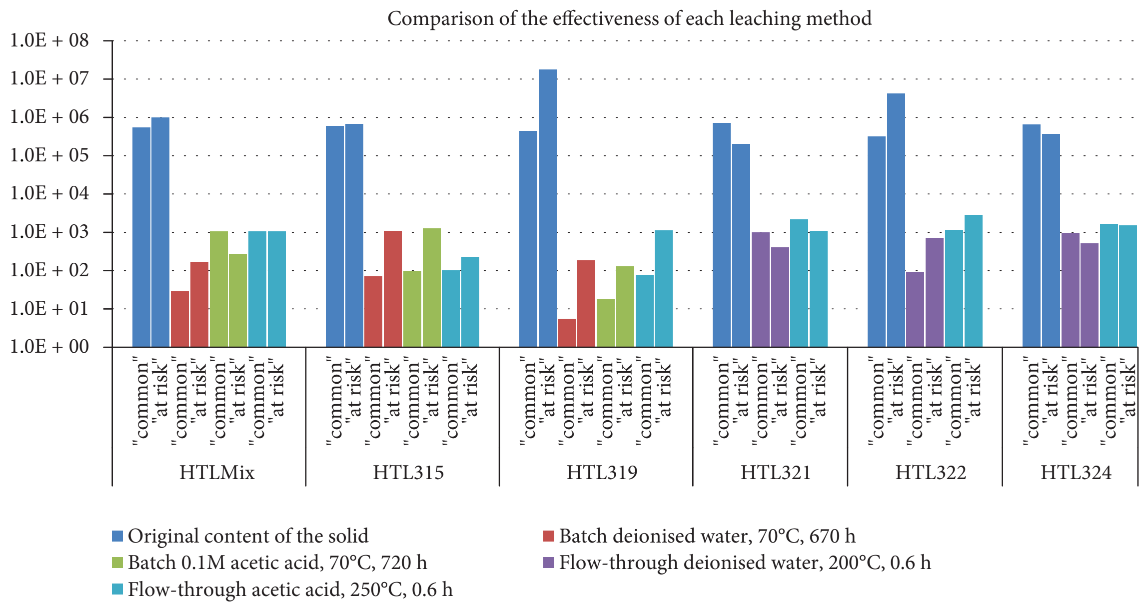

Figure 21: Comparison of rock sample composition to results from the batch and flow-through leaching experiments with deionised water and acetic acid as solvent. Important to note that the axis is logarithmic and the concentrations of "common" elements are in ppm and the concentrations of "at risk" elements are in ppb.

Table 9: Concentration of the "at risk" elements in each solid rock sample.

Element Sample	Ag PPB	Co PPB	Ga PPB	Mo PPB	Sb PPB	Sr PPB	V PPB	W PPB	Total 'at risk' PPB
HTLMix	45258.83	4169.87	4272.66	223.06	861478.98	16679.67	20292.37	42936.29	995311.73
HTL315	11973.44	249443.41	9746.84	780.91	145129.71	15440.17	7738.55	216446.11	656699.15
HTL319	639.66	430.16	1195.83	1533.93	5513.29	9968.94	718.91	17678896.30	17698897.02
HTL321	424.80	78783.79	1392.45	700.33	58165.19	15421.11	22437.25	25124.42	202449.34
HTL322	534398.93	4028.59	1282.41	2386.12	2497731.37	1156992.59	2913.91	9290.47	4209024.39
HTL324	3098.11	48344.41	17976.82	20344.31	694.81	5236.13	258590.19	6466.08	360750.86

therefore, results from this study could be considered as minimum thresholds.

In both experimental setups, the solid sample used was powdered rather than a whole rock. This form of material might have several high energy sites caused by the sample preparation, leading to relatively high dissolution rates over the course of the experiments. This might also be the case in a geothermal reservoir which has been stimulated. New fresh surfaces with which the fluid may react, leading to high initial loads, which will tail off with time. If no stimulation is being carried out, dissolution may be lower, but steady. The fresh surface area in a reservoir will be relatively low, but the contact time will be much longer than that shown here. Contact time for fluid-rock interactions in case of batch reactions was average 30 days maximum, while flow-through tests had less than 1 hour contact time (but much more solid material and hence available surface area). In an operating EGS plant in Europe, the average travel time of the fluid was 23 days, depending on the flow path [21, 22]. It will be important to consider these effects when looking at the whole life-cycle of a project, possibly resulting in high recovery initially, tailing off later on, without continued stimulation or exposure of new surfaces.

5.1.3. Summary. While batch experiments are useful in rapidly elucidating relative leaching potentials of various fluids, the results they produce are often difficult to compare to "real" systems due to very high fluid-rock ratios and the fact that they represent a closed system with no input of fresh fluid. As part of this work, therefore, flow-through experiments were also carried out, allowing a direct comparison between the two system types. Figure 21 is a summary of the experiments conducted with deionised water and acetic acid. It displays the total concentrations of "common" and "at risk" elements from all initial solid samples and next to it in each leachate. Data about the composition of solid rock samples, on which the following figures are based, can be found in Tables 9 and 10.

The data in Figure 21 has been broken down to Figure 22, which compares the total concentration of "common" elements in the final leachates, and Figure 23, which focuses on the more critical "at risk" elements.

TABLE 10: Concentration of the "common" elements in each solid rock sample.

Element Sample	Al PPM	B PPM	Ba PPM	Ca PPM	Cd PPM	Cr PPM	Cu PPM	Fe PPM	K PPM	Mg PPM	Mn PPM	Na PPM	Ni PPM	Pb PPM	Rb PPM	S PPM	Si PPM	Zn PPM
HTLMix	15530.48	*	46	4205	37	25	641	5993	5880	2974	350	551	9	83,238	40	14,437	408,010	6814
HTL315	16406.93	*	18	374	1	24	13,412	132,105	868	1927	765	510	8	28	8	91,747	330,518	249
HTL319	3438.966	*	11	109	0	28	74	16,407	1262	51	4656	104	1	27	26	59	412,250	68
HTL321	517.3251	*	8	51,541	0	10	1445	397,790	34	37,169	782	55	8	7	0	217,122	3290	142
HTL322	1292.076	*	2503	9029	1075	14	8	16,480	546	2013	301	62	7	59,105	2	2729	39,010	178,876
HTL324	11615.29	*	16	1485	1	5	11,585	186,533	1766	4374	561	851	33	12	8	75,251	345,450	189

*: concentration was under the detection limit.

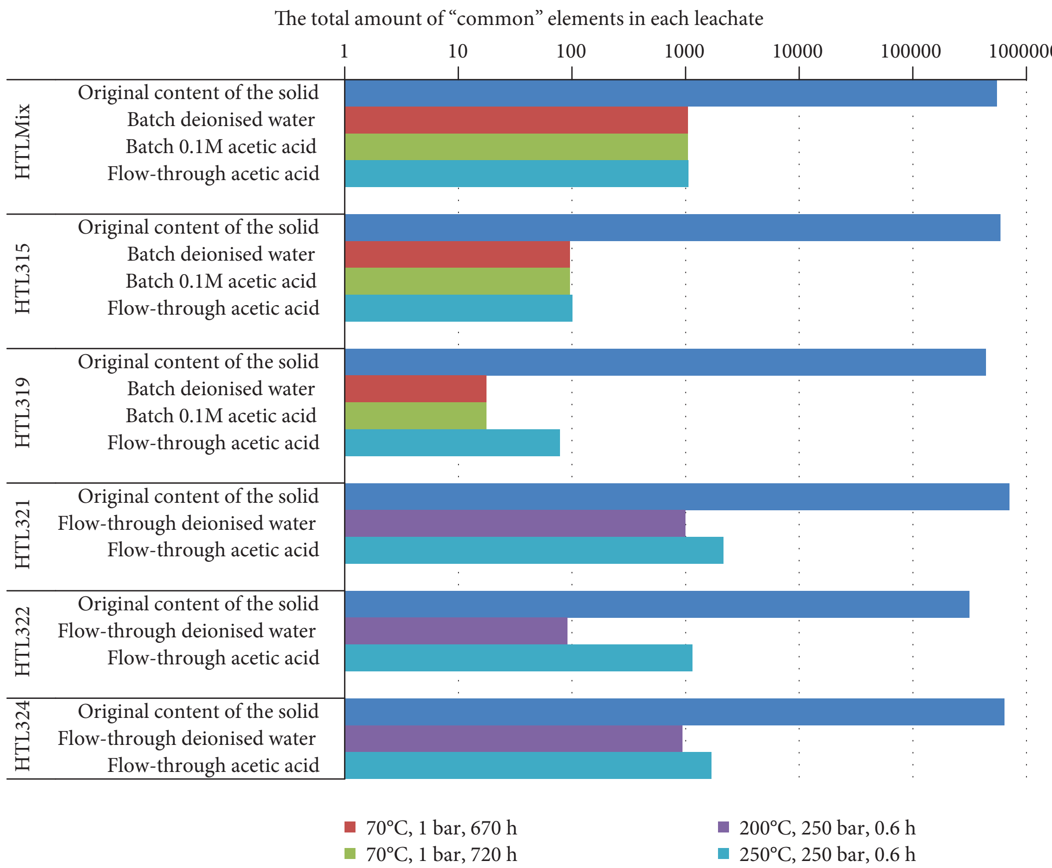

FIGURE 22: Summarising chart of detected "common" elements during each experiment with concentrations in ppm.

As shown in Figure 22, acetic acid has a much better potential to dissolve "common" elements relative to deionised water. The experiment carried out using HTL322 and different fluids is a good example for this; acetic acid (mobilising 0.368% of the original content) resulted in an almost 13 times increase in the concentration of "common" elements over deionised water (mobilising 0.029% of the original content). Based on these samples, however, flow-through reactions yielded in slightly higher total dissolved element concentrations than batch reactions, even over relatively short contact times. This in part was due to a considerably lower fluid to rock ratio used in the flow-through experiments, which also indicates that the availability of fresh surface area is an important factor in determining leaching rates. Given the rapidity of reaction in the flow-through experiments, these results indicate that even in a reservoir where fresh surface area is more limited than that used here, reasonably high dissolved loads should be achievable, especially given the much greater contact times between fluid and mineral in such systems. The spider plots of these reactions show similar patterns, in terms of leachate elemental compositions, in both experimental setups.

In some of the flow-through experiments (e.g., flow-through reaction with 0.1 M acetic acid and HTL321), elements are observed in the leachates at very elevated (>1000 ppm) concentrations. Generally, Ca, Fe, Mg, and S were the most abundant elements in the leachates, all of which are associated with scale formation. During laboratory tests, no scaling in the equipment or in the tubing was observed. Figure 23 shows only the concentration elements which we have defined as "at risk".

The trend of mobilisation of "at risk" elements correlates to that of "common" elements. Acetic acid proved to be far more effective than deionised water in all cases. One of the most effective dissolution of "at risk" elements was in the case of HTL321 reacted with 0.1 M acetic acid, where 0.54% of the original content could be mobilised. This is 1.5 times more effective than the best result at "common" elements. Sr, Co, W, and Mo elements were leached at the highest concentrations, indicating the potential for further investigations due to the criticality of tungsten and cobalt.

6. Conclusions

Laboratory batch and flow-through leaching tests were run in the range of 70–250°C under 1–300 bar pressure, conditions which include the properties of an average geothermal reservoir at 3 km depth. As a result of the reactions in the laboratory, reasonable concentrations of a wide range of elements could be mobilised. Detected elements were grouped as "common" and "at risk" elements. Selected "common" elements have less economic importance and higher occurrence (in both the solid samples used and the produced leachates),

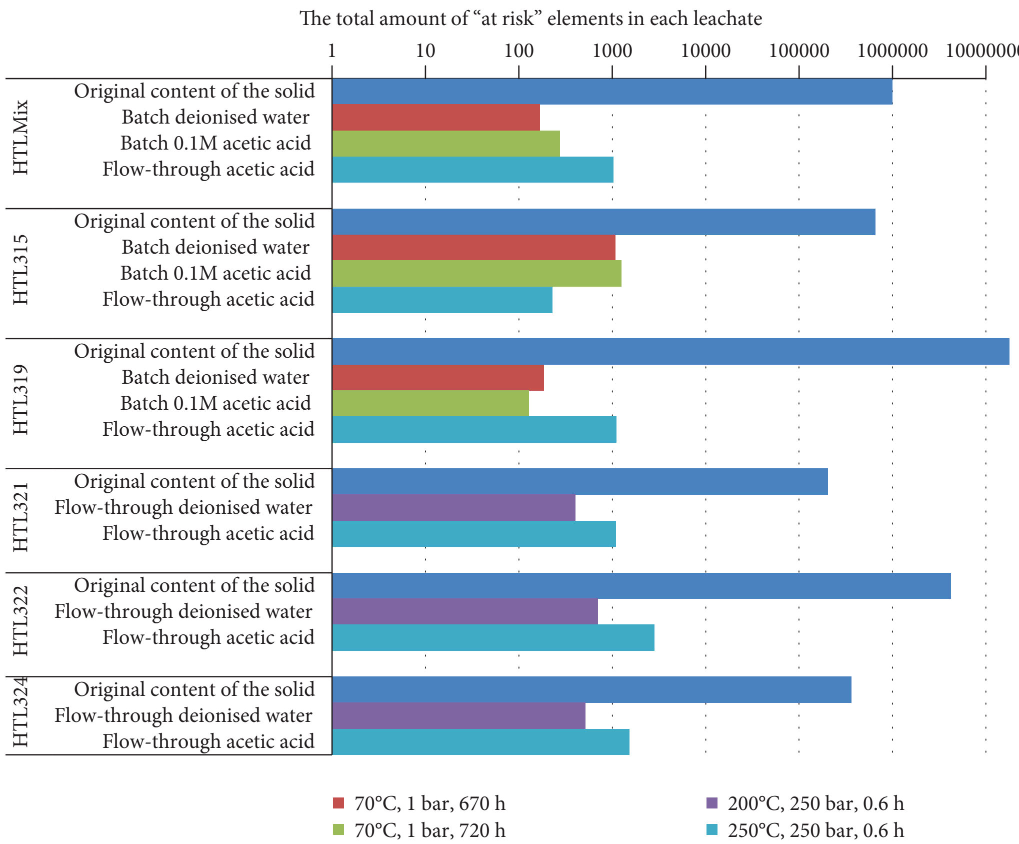

Figure 23: Summarising chart of detected "at risk" elements during each experiment with concentrations in ppb.

while our selected "at risk" elements have higher economic value, and lower supply security.

One of the highest concentrations of "common" elements occurred in the case of lead, which mobilised at concentrations of up to 870 ppm with acetic acid during the batch reaction and up to 540 ppm in the flow-through reactor. Notable concentrations of Zn are also present in leachates, which corroborates the enhanced dissolution progress. In laboratory tests, significant Al and Si were also found. Elevated concentrations of these elements indicate considerable dissolution of matrix silicates present in the samples. This could be desirable in terms of increasing reservoir permeability and opening flow paths, but if concentrations become too high, there is an increased risk of precipitation, which could clog fractures and inhibit fluid flow in a geothermal reservoir, and risk fouling boreholes or surface infrastructure. In a technologically optimised geothermal reservoir, where extraction would target metals but not necessarily in their pure forms (i.e., could include extraction of metals complexed with some of the scale-forming elements), therefore as they are removed from the fluid in a technological material extraction step, the risk of clogging would decrease in the reservoir and in the well. In this way, metal extraction would reduce natural scaling and therefore increase efficiency.

The highest concentration of a single element detected from the "at risk" group was 1070 ppb Co concentration in batch reactors with acetic acid and 2840 ppb Sr concentration in a flow-through setup with acetic acid. During all leaching tests, Sr, Co, W, and Mo were detected with the largest abundance, which is a good motivation towards further experiments as tungsten and cobalt have the highest economic risk rating for the EU, respectively.

In leaching reactions, even reasonably mild and environmentally acceptable fluids could be utilised to dissolve considerable amounts of silicate material as well as some elements of interest. Fast reaction rates given the right conditions (high temperature and pressure with good amount of available surface area) within the geothermal reservoir are promising in terms of potential to metal recovery. Future work and technological development is still needed to practically recover raw materials from geothermal fluids, as the desired concentrations for extraction tend to be higher than those achieved in this study. The results are intended to use for upscaling to reservoir scale and calculate likely dissolved loads achievable, given reaction rates and solubility of the various elements involved. In this study, the first steps were done to ensure the sustainability of the proposed technology, further investigations, advances in other technologies, and a full life cycle assessment study need to follow.

Data Availability

The ICP-MS and ICP-OES analysis data used to support the findings of this study are included within the article and within the appendices. All other previously reported (microscopic and XRD analyses) data used to support this study are available at http://www.chpm2030.eu. These prior studies (and datasets) are cited at relevant places within the text.

Conflicts of Interest

The authors declare that there is no conflict of interest regarding the publication of this paper.

Acknowledgments

The CHPM2030 project has received funding from the European Union's Horizon 2020 research and innovation programme under grant agreement No. 654100. The authors would like to express their gratitude to Richard Shaw, Jeremy Rushton, Alicja Lacinska, Dániel Fűzéri, Simon Chenery, Andrew Marriot, Elliott Hamilton, Michael Watts, Ian Mountney, and Simon Kemp for providing support and analysis for the BGS experimental program.

References

[1] European Commission Directorate-General for Internal Market, Industry, Entrepreneurship and SMEs, Deloitte Sustainability; British Geological Survey, Bureau de Recherches Géologiques et Minières, and Netherlands Organisation for Applied Scientific Research 2017, "Study on the review of the list of critical raw materials: critical raw materials factsheets," 2017, https://publications.europa.eu/en/publication-detail/-/publication/7345e3e8-98fc-11e7-b92d-01aa75ed71a1/language-en.

[2] V. D. Dang and M. Steinberg, "Preliminary design and analysis of recovery of lithium from brine with the use of a selective extractant," *Energy*, vol. 3, no. 3, pp. 325–336, 1978.

[3] W. P. C. Duyvesteyn, "Recovery of base metals from geothermal brines," *Geothermics*, vol. 21, no. 5-6, pp. 773–799, 1992.

[4] S. E. Kesler, P. W. Gruber, P. A. Medina, G. A. Keoleian, M. P. Everson, and T. J. Wallington, "Global lithium resources: relative importance of pegmatite, brine and other deposits," *Ore Geology Reviews*, vol. 48, pp. 55–69, 2012.

[5] R. G. Bloomquist, "Economic benefits of mineral extraction from geothermal brines," *Transactions - Geothermal Resources Council*, vol. 30, pp. 579–582, 2006.

[6] G. Neupane and D. S. Wendt, "Assessment of mineral resources in geothermal brines in the US," in *Proceedings of 42nd Workshop on Geothermal Reservoir Engineering Stanford University*, Stanford, CA, USA, 2017.

[7] P. Bajcsi, T. Bozsó, R. Bozsó et al., "New geothermal well-completion and rework technology by laser," *Central European Geology*, vol. 58, no. 1-2, pp. 88–99, 2015.

[8] J. A. Marshall, A. Bonchis, E. Nebot, and S. Scheding, "Robotics in mining," in *Springer Handbook of Robotics*, B. Siciliano and O. Khatib, Eds., pp. 1549–1576, Springer, Cham, 2016.

[9] K. Breede, K. Dzebisashvili, X. Liu, and G. Falcone, "A systematic review of enhanced (or engineered) geothermal systems: past, present and future," *Geothermal Energy*, vol. 1, no. 1, p. 4, 2013.

[10] É. Hartai, N. Németh, and J. Földessy, *CHPM2030 Deliverable D1.1: EGS-Relevant Review of Metallogenesis*, Zenodo, 2016.

[11] S. Mullens, E. Moens, R. Kemps et al., *Metal Content Mobilisation with Nanoparticles: CHPM2030 deliverable D2.3*, CHPM2030, 2018.

[12] J. Szanyi, T. Medgyes, B. Kóbor et al., *CHPM2030 Deliverable 5.1: Integrated Sustainability Assessment Framework*, Zenodo, 2017.

[13] A. Kilpatrick, C. Rochelle, J. Rushton et al., *Report on Metal Content Musing Mild Leaching, CHPM2030 Deliverable D2.2*, Zenodo, 2017.

[14] N. Németh, J. Földessy, É. Hartai et al., *EGS-Relevant Review of Orebody Structures: CHPM2030 Deliverable D1.3*, Zenodo, 2016.

[15] K. Bateman, C. A. Rochelle, G. Purser, S. J. Kemp, and D. Wagner, "Geochemical interactions between CO_2 and minerals within the Utsira caprock: a 5-year experimental study," *Energy Procedia*, vol. 37, pp. 5307–5314, 2013.

[16] C. A. Rochelle, A. E. Milodowski, K. Bateman, E. B. A. Moyce, and A. Kilpatrick, "A long-term experimental study of the reactivity of basement rock with highly alkaline cement waters: reactions over the first 15 months," *Mineralogical Magazine*, vol. 80, no. 6, pp. 1089–1113, 2016.

[17] Massachusetts Institute of Technology (MIT), *The Future of Geothermal Energy: Impact of Enhanced Geothermal System (EGS) on the United States in the 21st Century*, Idaho National Laboratory, Idaho Falls, ID, USA, 2006, https://energy.mit.edu/wp-content/uploads/2006/11/MITEI-The-Future-of-Geothermal-Energy.pdf.

[18] R. L. Snyder and D. L. Bish, "Quantitative analysis, *Modern Powder Diffraction*," in *Reviews in Mineralogy*, pp. 101–144, Mineralogical Society of America, Washington DC, USA, 1989.

[19] J. Szanyi, T. Medgyes, B. Kóbor, and M. Osvald, *Conceptual Framework for Orebody-EGS: CHPM2030 Deliverable D1.4*, Zenodo, 2016.

[20] J. Szanyi, M. Osvald, T. Medgyes et al., *CHPM2030 Deliverable 2.1: Recommendations for Integrated Reservoir Management*, Zenodo, 2017.

[21] A. Genter, N. Cuenot, B. Melchert et al., "Main achievements from the multi-well EGS Soultz project during geothermal exploitation from 2010 and 2012," in *Proceedings European Geothermal Energy Congress, EGC 2013*, Pisa, Italy, June 2013.

[22] E. Schill, A. Genter, N. Cuenot, and T. Kohl, "Hydraulic performance history at the Soultz EGS reservoirs from stimulation and long-term circulation tests," *Geothermics*, vol. 70, pp. 110–124, 2017.

Hindawi
Geofluids
Volume 2018, Article ID 6025038, 20 pages
https://doi.org/10.1155/2018/6025038

Research Article

Tectonic Evolution of the Southern Negros Geothermal Field and Implications for the Development of Fractured Geothermal Systems

Loraine R. Pastoriza[1,2] **Robert E. Holdsworth**[1] **Kenneth J. W. McCaffrey**[1] **and Edward Dempsey**[1,3]

[1]*Department of Earth Sciences, University of Durham, Durham DH1 3LE, UK*
[2]*Geosciences and Reservoir Engineering Group, Energy Development Corporation, Ortigas, Pasig City 1605, Philippines*
[3]*School of Environmental Sciences, University of Hull, Hull HU6 7RX, UK*

Correspondence should be addressed to Loraine R. Pastoriza; pastoriza.lr@energy.com.ph

Received 24 May 2018; Accepted 9 September 2018; Published 19 November 2018

Guest Editor: Domenico Montanari

Fluid flow pathway characterisation is critical to geothermal exploration and exploitation. In fractured geothermal reservoirs, it requires a good understanding of the structural evolution together with the fracture distribution and fluid flow properties. A fieldwork-based approach has been used to evaluate the potential fracture permeability characteristics of a typical high-temperature geothermal reservoir in the Southern Negros Geothermal Field, Philippines. This is a liquid-dominated resource hosted in the andesitic Quaternary Cuernos de Negros Volcano, Negros Island. Fieldwork reveals two main fracture groups based on fault rock characteristics, alteration type, relative age of deformation, and associated thermal manifestation, with the youngest fractures mainly related to the development of the current geothermal system. Fault kinematics, cross-cutting relationships, and palaeostress analysis suggest at least two distinct deformation events under changing stress fields since probably the Pliocene. We propose that this deformation history was influenced by the development of the Cuernos de Negros Volcano and the northward propagation of a major neotectonic structure located to the northwest, the Yupisan Fault. A combined slip and dilation tendency analysis of the mapped faults indicates that NW-SE structures should be particularly promising drilling targets under the inferred current stress regime, consistent with drilling results. However, existing boreholes also suggest that NE–SW structures can act as effective channels for geothermal fluids. Our observations suggest that these features were initiated as the dominant features in the older kinematic system and have then been reactivated at the present day.

1. Introduction

Permeability, heat source, fluid recharge, and capping mechanism are the vital elements to consider during the development of a geothermal reservoir [1, 2]. In a typical subduction-related geothermal system like those seen in the Philippines, the reservoir is mostly hosted in crystalline rocks in which permeability arises mainly from fractures, and less from the intrinsic permeability of the reservoir rocks [3]. It is therefore necessary to understand the type of fractures present, the fracture development history, and the nature of the transmissive present-day fracture networks developed at depth prior to tapping the reservoir through drilling. Ultimately, such understanding should allow geothermal production to be maximised through targeting optimal fractures in the subsurface.

However, the structural modelling of subsurface reservoirs in volcano-hosted geothermal systems has its own challenges. Subsurface analyses using seismic refraction and reflection data are difficult to use as thick volcanic rocks are usually opaque to seismic waves and geological structures are often difficult, or impossible, to image [4]. Resistivity data is commonly used to visualise the reservoir structure based on the implied fluid content and development of alteration zones [5]. Although this can highlight the presence of large-scale structures, it is still challenging to identify reservoir-scale fracture networks using this technique. Additionally, at the early stages of geothermal exploration, carrying out geophysical surveys (e.g., gravity, resistivity, and seismic) poses large financial risks to the developer. Thus, it is important to first maximise surface geological data before moving forward with the exploration stages. This work is aimed at illustrating how to better utilise surface geological data in understanding fractured geothermal systems using the Southern Negros Geothermal Field (SNGF) as a case study.

The SNGF lies in the municipality of Valencia in south Negros Oriental, Philippines. It is a volcano-hosted, high-temperature geothermal system, with temperatures ranging between 200 and 300°C, sitting on the northeastern flanks of the Cuernos de Negros (CDN) volcanic edifice (Figure 1). It is liquid-dominated with localised two-phase zones [6] containing fluids which are generally neutral in pH, moderately saline, and have low gas content [7]. The field was commissioned in 1983 with a total installed capacity of 192.5 MWe. However, despite its long history of geothermal exploration and development, its fracture systems are still poorly understood.

Here, we use field and thin-section observations to establish a deformation history for the SNGF particularly highlighting its role in influencing the development of the geothermal system. Given the limitations of outcrop quality and distribution that are typical in tropical countries (e.g., high rates of weathering and erosion and extensive vegetation cover) and the effects of volcanism (i.e., recent phreatic eruption of the volcanic centers may cover or erode exhumed structures), methodologies that optimise the field data are also examined. From the mapped structures, slip and dilation tendencies are evaluated and we show how these results could relate to and influence a drilling strategy for the SNGF.

2. Regional Geological Setting

The Philippine Archipelago is where four tectonic plates—SE Eurasia, Philippine Sea, Pacific, and Indo-Australia—meet [8]. The largely aseismic Palawan-Mindoro microcontinent lies to the west representing a fragment rifted from mainland Eurasia in the mid Cenozoic, and to the east lies the seismically active Philippine Mobile Belt on which the majority of the country is located (Figure 1(a)). The latter region is an actively deforming zone composed of terranes of various affinities (i.e., from the ancient Philippine Sea Plate and the Indo-Australian margin) [9] that are bordered by subduction zones of opposing polarities: the west-dipping Philippine Trench and East Luzon Trough to the east and the east-dipping Manila, Negros, Sulu, and Cotabato trenches to the west (Figure 1(a), [10–12]). Shallow earthquakes are dispersed across the Philippine Mobile Belt indicating its continued active deformation due to plate tectonic forces [8].

Traversing almost the entire length of the country, from northwest Luzon to southeast Mindanao, is the >1200 km long sinistral Philippine Fault (Figure 1(a)) which has formed due to the oblique convergence of the Philippine Sea Plate with the Philippine Mobile Belt [13]. It is suggested that the Philippine Fault formed 4 Mya after the plate convergence changed from north to NNW with respect to Eurasia, although its northern segment appears to have been initiated much earlier (10 Ma) [14]. GPS data show that the Philippine Fault has a slip rate of 2 to 3 cm/yr [14, 20] or 2.4 to 4 cm/yr [17] which represents a third of the oblique convergence of Philippine Sea Plate, whilst the two-thirds is accommodated along the Philippine Trench and other major structures across the country [14]. Maximum compression, σ_1, from recent studies is oriented between 90 and 110° in Luzon [17] and approximately east-northeast in Bicol region [16].

3. Geology of Negros

Negros Island is made up of three Cenozoic-Quaternary tectonostratigraphic terranes that represent part of the subduction arc system related to the Negros Trench (Figure 1(b)) and are underlain by oceanic volcaniclastic basement, which is thought to be Cretaceous in age [11, 21]. From west to east in Negros, two overlapping volcanic arcs of different ages, the Ancient and Recent Negros Arcs, and the sedimentary Visayan Sea Basin are present (Figure 1(b); [11, 22]).

The Ancient Negros Arc comprises Eocene to Oligocene andesitic to dacitic volcanic and clastic rocks intruded by a Miocene dacitic diatreme complex [22]. It is highly mineralised, hosting the Bulawan intermediate sulphidation gold deposit, the gold-poor Sipalay deposit, and the Hinobaan porphyry copper and molybdenum deposits [22], all of which are situated in the southwestern part of Negros. The Recent Negros Arc [11] or Negros Belt [23] is composed of Middle Miocene to Pliocene andesite flow breccias, volcaniclastics, and conglomerates that are overlain by Late Pliocene andesitic volcanics and Quaternary andesite and basalt stratovolcanoes [22]. Geomorphologically, the recent arc is represented by a 260 km chain of volcanoes, four of which are on Negros Island (from north to south): Mt. Silay, Mt. Mandalagan, Mt. Canlaon, and Cuernos de Negros (CDN) [23] (Figure 1(b)). Of these four, only Canlaon is active with the most recent volcanic activity (i.e., release of white plumes and volcanic earthquakes) occurring in January 2018 [24], whilst Mandalagan and Cuernos de Negros are considered to be in their fumarolic stage [23].

Towards the east, the Visayan Sea Basin, representing the back-arc region of the Negros arc system [25], underlies the eastern coast of Negros, the Tañon Strait, and the islands of Cebu and Bohol (Figure 1(b)). The basin is filled with up to 4 km thick carbonate and volcaniclastic sequences deposited from the Middle Oligocene to Middle Miocene [11]. These are generally folded, with fold axes oriented NNE-SSW on the average. Rangin et al. [25] proposed that the Visayan Basin comprises a series of NNE-SSW-trending horst and graben structures, with the Tañon Strait corresponding to a graben, which cuts the earlier folds. However, recent studies by Aurelio et al. [26] following the Mw 6.7 earthquake in February 2012 propose the existence of a northeast-striking and northwest-dipping reverse fault, the Negros Oriental

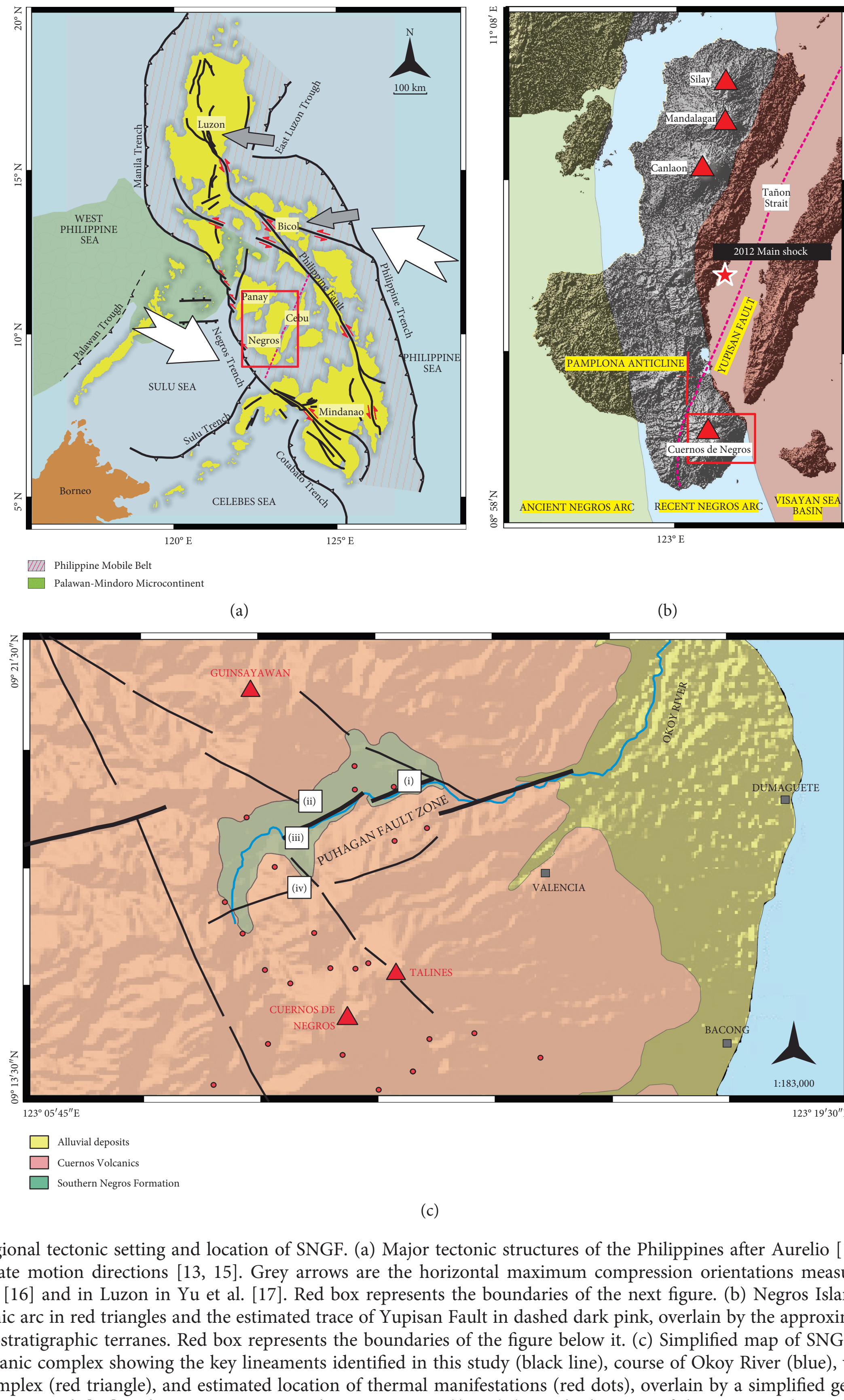

Figure 1: Regional tectonic setting and location of SNGF. (a) Major tectonic structures of the Philippines after Aurelio [14]. Large white arrows are plate motion directions [13, 15]. Grey arrows are the horizontal maximum compression orientations measured in Bicol in Lagmay et al. [16] and in Luzon in Yu et al. [17]. Red box represents the boundaries of the next figure. (b) Negros Island, showing the Negros volcanic arc in red triangles and the estimated trace of Yupisan Fault in dashed dark pink, overlain by the approximate boundaries of the tectonostratigraphic terranes. Red box represents the boundaries of the figure below it. (c) Simplified map of SNGF encompassing the CDN volcanic complex showing the key lineaments identified in this study (black line), course of Okoy River (blue), volcanic edifices within the complex (red triangle), and estimated location of thermal manifestations (red dots), overlain by a simplified geological map of the field from Rae et al. [18] and PNOC-EDC internal reports. Boxes (i) to (iv) are the location of the outcrops discussed in this paper. (b) and (c) overlay 90 m SRTM DEM data from Jarvis et al. [19].

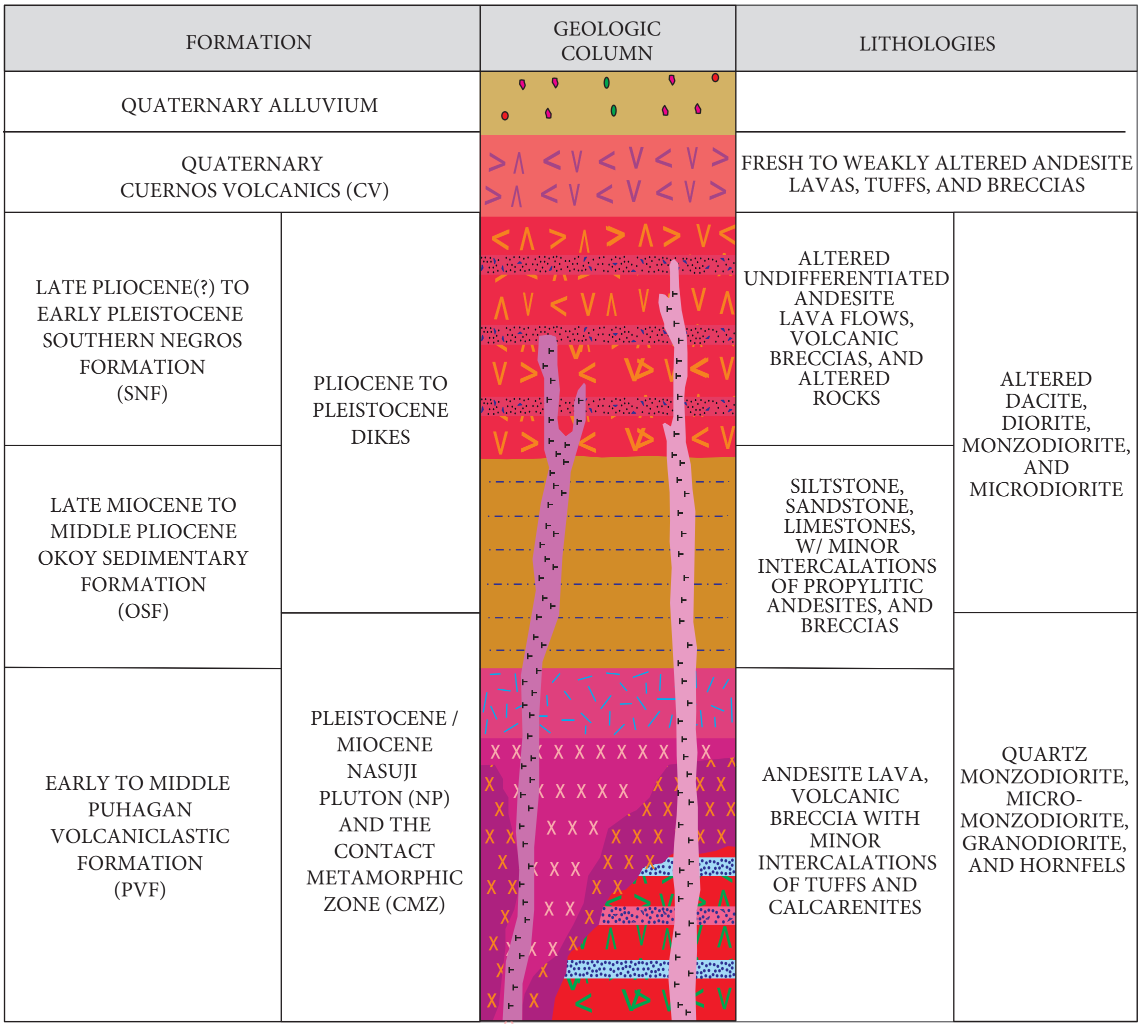

Figure 2: Geological column of the CDN volcano as encountered in the boreholes. Corresponding ages are in the first column, whilst their general lithologies are in the third column. Note that although there is a strong geochronological evidence that the Nasuji Pluton is younger, there is no clear evidence of its intrusion into the younger lithologies.

Thrust, that runs from west of CDN towards eastern offshore Negros.

Southern Negros is formed mainly by Quaternary volcanic rocks that are part of the Recent Negros Arc. Miocene to Early Pleistocene clastics have been locally exposed in the northwest part of CDN as part of the Pamplona Anticline—a result of the regional fault-propagation folding associated with the Negros Oriental Thrust, which is mapped onshore as the Yupisan Fault (Figure 1(b); [26, 27]).

4. Local Geology

Deep drilling to 3300 m depth over the last three decades reveals that the CDN volcanic complex was created by several volcanic and intrusive events ([26]; Figure 2). The oldest rocks drilled are thick, 990 m on average, Miocene volcanic sequences of altered andesites intercalated with tuffs and calcarenites with occasional volcanic and sedimentary breccias, known as the Puhagan Volcaniclastic Formation. These rocks are cross cut by the Nasuji quartz monzodiorite to micromonzodiorite pluton which led to the formation of a metamorphic aureole known as the Contact Metamorphic Zone. Geochronological studies of the pluton have yielded contradicting age of Miocene (10.5 Mya using K-Ar in [28, 29]) and Pleistocene (0.7 to 0.3 Mya using Ar-Ar in Rae et al. [18]). By the Early Pliocene, the Okoy Sedimentary Formation and overlying undifferentiated andesitic volcanics and pyroclastics of the Southern Negros Formation were deposited. All the above mentioned formations have been intruded by at least two dyke events during the Pliocene. Lateral and vertical variations of lithologies and facies within the Okoy Sedimentary and Southern Negros Formations have been detected during drilling of wells and indicate the presence of a palaeotopography within the SNGF in which the western sectors were uplifted in the Early Pliocene [28]. This is confirmed by fossil assemblages within the two formations in the western region which are characteristic of a shallow to subaerial environment, whilst those preserved in the eastern region are typical of a deep marine environment

Table 1: Summary of field characteristics of the two fracture groups mapped in SNGF.

	Group 1	Group 2
Fault rocks	Cohesive and cemented (cataclastic)	Generally noncohesive/poorly cemented Open fractures in some
Key alteration minerals	Abundant pyrite Amorphous silica Quartz Rare Cu sulfides	Abundant clays Quartz Native sulphur Zeolites, calcites, and gypsum
Kinematics	Mostly E-W (+/−) sinistral	Mostly NW-SE oblique dextral
Host rocks	Older Southern Negros Fm. Host has been completely altered previously	All lithologies Both altered and fresh rocks
Alteration pattern	Restricted to fractures	Diffuse or restricted to fractures
Other key observations		Usually related to recent (active/inactive) thermal activity

[28]. These rocks are overlain by the Quaternary-aged andesitic Cuernos Volcanics, which can be subdivided into different members depending on which volcanic edifice of the CDN volcanic complex they are associated with (i.e., main CDN peak, Talines, Guinsayawan, Figure 1(c)). Radiocarbon dating of charred wood within the Cuernos Volcanics suggests a youngest eruption age of 14,450 years [29]. These young volcanics cover much of the surface of the present-day CDN volcanic complex, with exposures of the older Southern Negros Formation limited to the downstream river valley area of the E-W Okoy River (Figure 1(c)).

Topographic lineament analysis using combined high- and low-resolution digital elevation models carried out indicates a dominance of ENE-WSW and NW-SE to NNW-SSE features (Figure 1(c)). The most conspicuous lineaments are the ENE-WSW-trending set that coincide with the Okoy River, and appear to be discontinuous and arranged as right-stepping *en echelon* features, representing the traces of a known fault network in SNGF, designated here as the Puhagan Fault Zone (Figure 1(c)). Geomorphological kinematic indicators such as push-up ridges observed along the trace of this fault zone suggest it has a dextral sense of movement.

5. Mapped Structures

The SNGF rocks exposed at the surface are exclusively deformed by brittle structures, including different types of fractures, such as faults, joints, and veins. The fractures observed in 84 out of the 135 outcrops that were studied can be sorted into two main groups, here termed group 1 and group 2. This two-fold classification is mainly based on the types of associated fault rocks, key alteration minerals, and the host rock which the fractures cut. The field characteristics are summarised in Table 1 and discussed in detail in the sections that follow.

5.1. Group 1 Fractures. Group 1 structures are restricted to the river exposures along the ENE-draining Okoy River gorge and one of its SE-draining tributaries (Figures 1(c), i and 3). This restricted region corresponds to the exposures of the Southern Negros Formation adjacent to the river, but it is most likely that these structures may be widely developed in the older rock strata that underlie much, if not all, of the Quaternary CDN edifice. Textures in the Southern Negros Formation in general are almost completely obliterated due to the effects of hydrothermal and supergene alteration, appearing as dark grey with yellowish to reddish patches due to iron oxide and sulphur deposition. Ghost phenocrysts are observed suggesting that the protoliths were porphyritic, but the crystals have been almost entirely replaced by clays.

Group 1 structures form as conspicuously grey fractures filled with abundant <1 mm to 2 mm grain-size pyrite crystals (Figure 3). Along the central part of the Okoy River gorge, these are E-W to WNW-ESE-striking (096°/62°-S) sinistral faults with slickenlines typically pitching <15° and which run subparallel to the trace of the main Puhagan Fault Zone. A fault core is recognised and is interpreted to correspond to the region where most shear displacement has been localised. A series of cm- to m-spaced ENE-WSW-trending subvertical faults here are filled with cataclasite comprising fine angular (rare 10 mm, mostly <5 mm grain-size) fragments of altered protolith, weakly foliated in some cases, set in a cemented dark grey matrix (almost clay-sized, <1 μm) (Figure 3(a)). Petrographic work on the fault rock samples suggests a dominance of pyrite mineralization within a generally cryptocrystalline matrix carrying identifiable fine crystals of pyrite, quartz, opaque minerals, and amorphous silica (Figure 4(a)). Sinistral senses of motion are indicated by microscopic kinematic indicators (i.e., *en echelon* features) (Figure 4(a)). Few offset markers are seen along the fault plane, so it is difficult to estimate total fault displacements.

The sinistral faults along the downstream part of Okoy River are associated with smaller NE-SW- to E-W-striking sinistral fractures based on millimeter-scale offsets, interpreted to be synthetic Riedel shears that are completely cemented and mineralised. Likewise, dense arrays of NE-SW-striking steeply dipping quartz- and pyrite-filled tensile fractures are observed (in i and ii in Figure 1(c)). Fine (~1 to 2 μm) gypsum crystals also occur within some mineral fills. The tensile fractures lie obliquely anticlockwise to the main sinistral faults or form as *en echelon* features (Figure 3(c)). Where the two key alteration minerals, pyrite and quartz, are present, they usually occur as anhedral crystals, but when pyrite occurs on its own, it is typically sub- to euhedral, with crystals that can be as large as 5 mm and usually oriented perpendicular to the fracture walls. Cockade

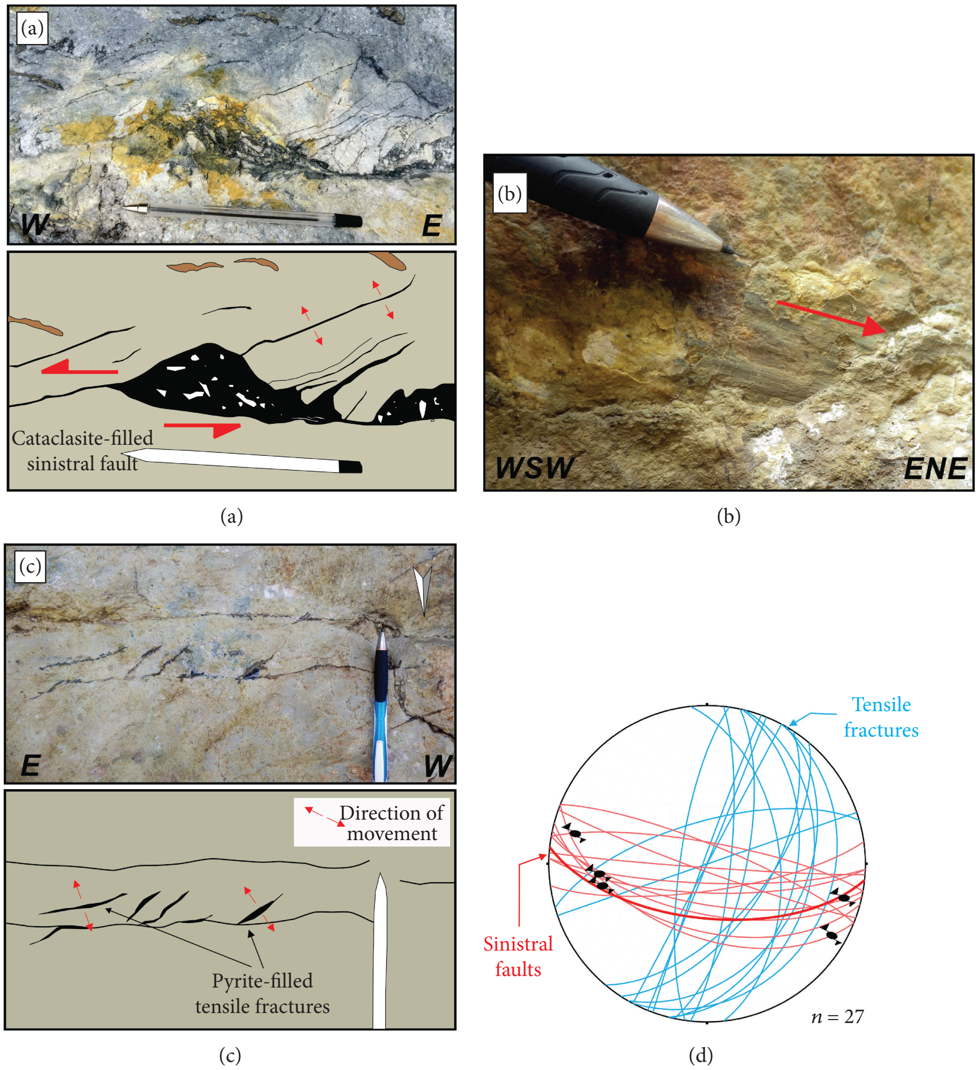

FIGURE 3: Group 1 fractures at the macroscale. (a) Close-up photo of the E-W to WNW-ESE sinistral faults showing the cataclastic core mapped along Okoy River (refer to Figure 1(c), i for the location). (b) Slickenlines preserved on the sinistral fault. (c) Pyrite-filled veins (located at Figure 1(c), i and ii). (d) Fault planes (red) and tensile fractures (blue) represented in an equal-area lower-hemisphere stereonet.

overgrowth textures [30] within some of the euhedral pyrite crystals are also observed in thin sections (Figure 4(b)).

5.2. Group 2 Fractures. Group 2 fractures are the dominant and ubiquitous features throughout the SNGF. Of the 84 outcrops mapped within the geothermal reservation, 90% expose faults classified under this group. The majority of large fractures are generally oriented WNW-ESE to NNW-SSE, usually steep to moderately dipping, exhibiting either normal, dextral, or normal-dextral oblique senses of movement, where kinematic indicators are preserved (Figure 5). Smaller, but poorly preserved and less frequent NE-SW and NNE-SSW-trending fractures have also been mapped. Where shear sense can be determined, it is often observed in normal faults and, more rarely, in sinistral structures.

Group 2 fractures generally contain incohesive fault rocks, typically fault gouges and fault breccias (Table 1). Occasionally, sharp slip planes or localised brittle shear zones occur. These structures cut both completely altered and fresh volcanic rocks. In some outcrops, the damage zones belonging to faults at least ten meters long have widths ranging a few centimeters to tens of meters. Most outcrops, however, preserve evidence that the brittle deformation is followed by intense clay alteration localised along the fault zone. Active and recently active thermal manifestations—such as hot springs, gas seepages, and hot ground—are often found along or adjacent to the traces of these group 2 fractures, implying the permeability present on these sets of structures that channel hydrothermal fluids. This further suggests that these faults play critical roles in the geothermal development and present-day fluid flow.

Two outcrops at localities 81 and 104 feature some of the best preserved group 2 structures and are discussed in detail below (more outcrop discussion can be found in Pastoriza [27]). These faults show the typical characteristics of the group, particularly the dominant NW-SE fractures. In

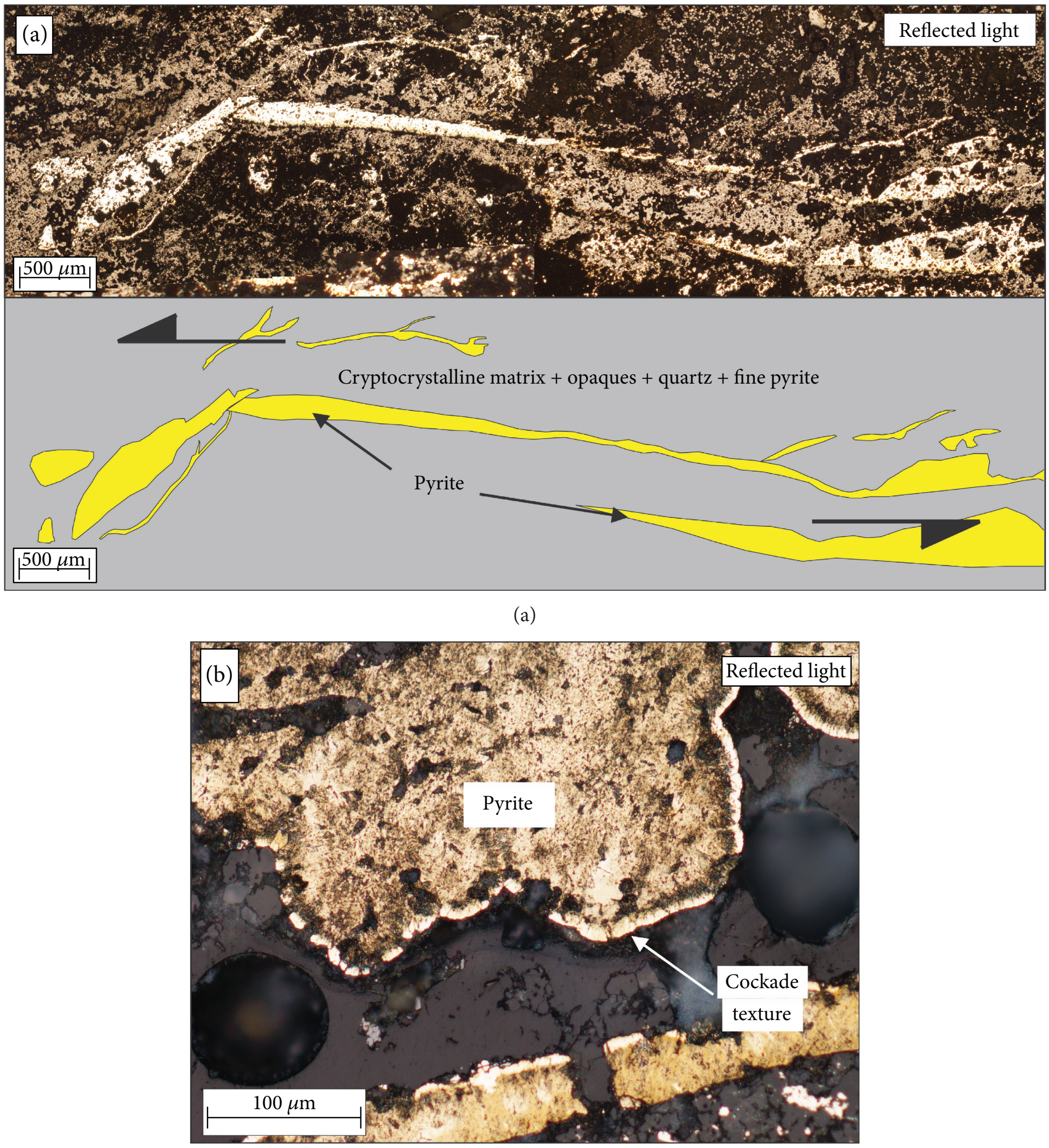

(a)

(b)

FIGURE 4: Group 1 fractures on a microscale. (a) Photomicrograph of the sinistral fault in Figure 3 shows consistent sinistral sense of motion. (b) A pyrite-filled vein from the same outcrop with cockade overgrowths.

locality 81, this fault is a large dextral-oblique structure, whilst at locality 104, the fault has a dip-slip normal sense of movement.

5.2.1. Locality 81. This WNW-ESE-oriented dextral-oblique fault (mean orientation of 118°/80°-S) cuts moderately to intensely altered porphyritic andesite (fault A in Figure 6; refer to box iv in Figure 1(c) for the location). Narrow 40 to 60 cm wide fault cores, with a wider 150 cm intensely damaged zone, are flanked by a still broader 600 cm wide moderately damaged zone. Background fracturing is present outside the damaged zones on both sides of the fault zone (Figure 6(b)). The fault preserves a crudely banded, variably altered pale gouge, formed by moderately to completely pulverised host rocks. In most parts, the fault is clay-altered and lined with fine-grained, hematite-filled and coarse-grained fibrous gypsum veinlets. Some less altered clasts of the porphyritic andesite protolith up to 15 cm in diameter are preserved within the fault core. Fault kinematics are gleaned from slickenlines and slickenfibres, varying between a purely dextral to less common dip-slip normal sense of motion (Figure 6(d)). Offset markers are poorly preserved, but are most likely minimal, suggesting generally small finite strains. One to two centimeter thick gypsum veins have crystallised along the walls of the fault planes and are oriented oblique to the wall (Figure 6(d)) suggesting that crystallization is contemporaneous with fault movements. Generally NW-SE-trending unfilled tensile fractures are observed to have formed adjacent to the fault plane, which are kinematically consistent with the main dextral shear sense inferred for the faults.

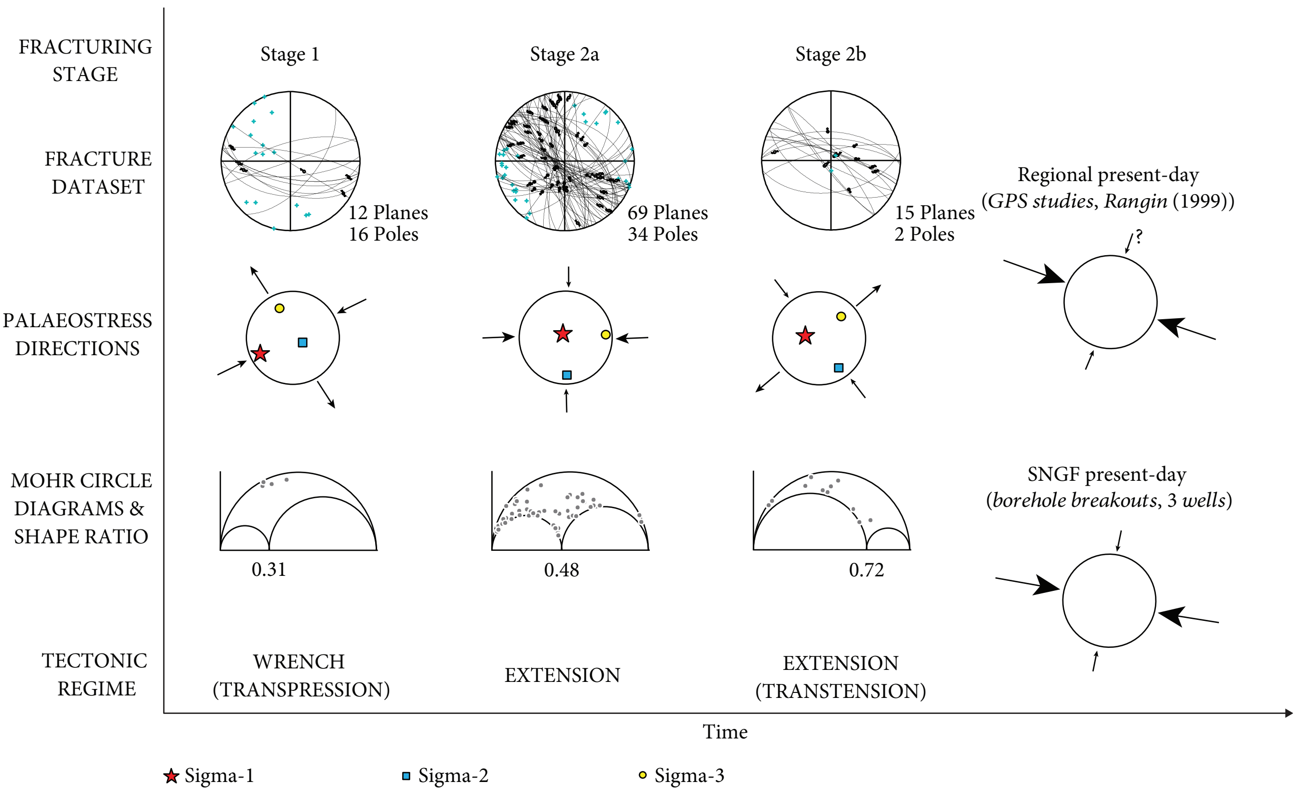

FIGURE 5: Summary of the palaeostress analysis results calculated per stage. Top row shows the stereographic projections of faults per stage with their corresponding slickenlines. Hollow symbols indicate a component of reverse sense of motion. Cyan stars represent poles of the tensile fractures. The stage 2a and stage 2b results are from the data which have been weighted by both the fault thickness and length. The smaller compression arrows in stage 2a and 2b suggest that the event is mainly extensional, and thus, the magnitude of compression may be minimal. The question mark in the regional present-day direction indicates that only the maximum compression direction is given in the cited study. The smaller arrows are thus assumed.

A left-stepping, generally E-W-striking dextral-normal fault occurs immediately to the south of the dextral fault (fault B in Figure 6). A 25 to 50 cm fault core here is filled with intensely oxidised fault rock (Figure 6(e)). Gypsum precipitation is preserved around some of the sheared margins of trapped protolith fragments. At the southern end of the outcrop, a network of associated smaller normal faults are generally oriented ENE-WSE to WNW-ESE with discrete slip planes (Figures 6(a) and 6(b)). Fault cores are not as well developed here compared to the two structures described above, but there is a strong indication that they channel hydrothermal fluids based on the formation of diffuse alteration haloes around most fractures. The network of smaller normal faults also appears to connect with the larger ones. Where they join, evidence of enhanced permeability is noted, such as the presence of empty vugs and suspected recent open fractures marking the sites of recently inactive gas seepage fissures, and preservation of increased deposition of secondary minerals (e.g., gypsum, travertine; Figure 6(e), ii).

5.2.2. Locality 104. A NW-SE-trending moderately north-dipping fault (131°/58°-N on average) runs perpendicular to the Okoy River (Figure 7; located at box iii in Figure 1(c)). It cuts an intensely silicified andesite outcrop that can be traced through both sides of the ravine, forming cave-like features on either side (Figure 7(a)). Preserved slickenlines and steps in the hanging wall suggest dip-slip normal senses of shear. The magnitude of displacement is difficult to assess due to the limits of exposure and lack of discernible offset markers in the wall rocks. The hanging wall is clearly exposed whilst the footwall is less distinct (Figure 7(b)). The fault core for this structure is a 12 to 15 cm thick gouge in which several fractured lensoid slivers of the host rock are entrained. The gouge-filled fault core is only exposed by hammering and has a thin film of what appears to be amorphous silica on its surface. Thin-section studies indicate intense silica-replacement and fracture infill of both the host rock and the fault rock (Figure 7(e)). Smaller fractures within the fault zone are oriented mostly WNW-ESE and are interpreted to be conjugate fractures to the main normal faults (Figure 7(d)). Where these smaller fractures join, local pull-apart structures or dilational jogs are observed (Figure 7(c)). In many cases, uncharacterised fine white crystals have precipitated around these structures which strongly suggest a recent outflow of mineral-rich fluids and/or gas. NNW-SSE sealed quartz veins and NW-SE unfilled tensile fractures are observed throughout the exposure which is consistent with the inferred direction of extension for this normal fault (Figure 7(d)).

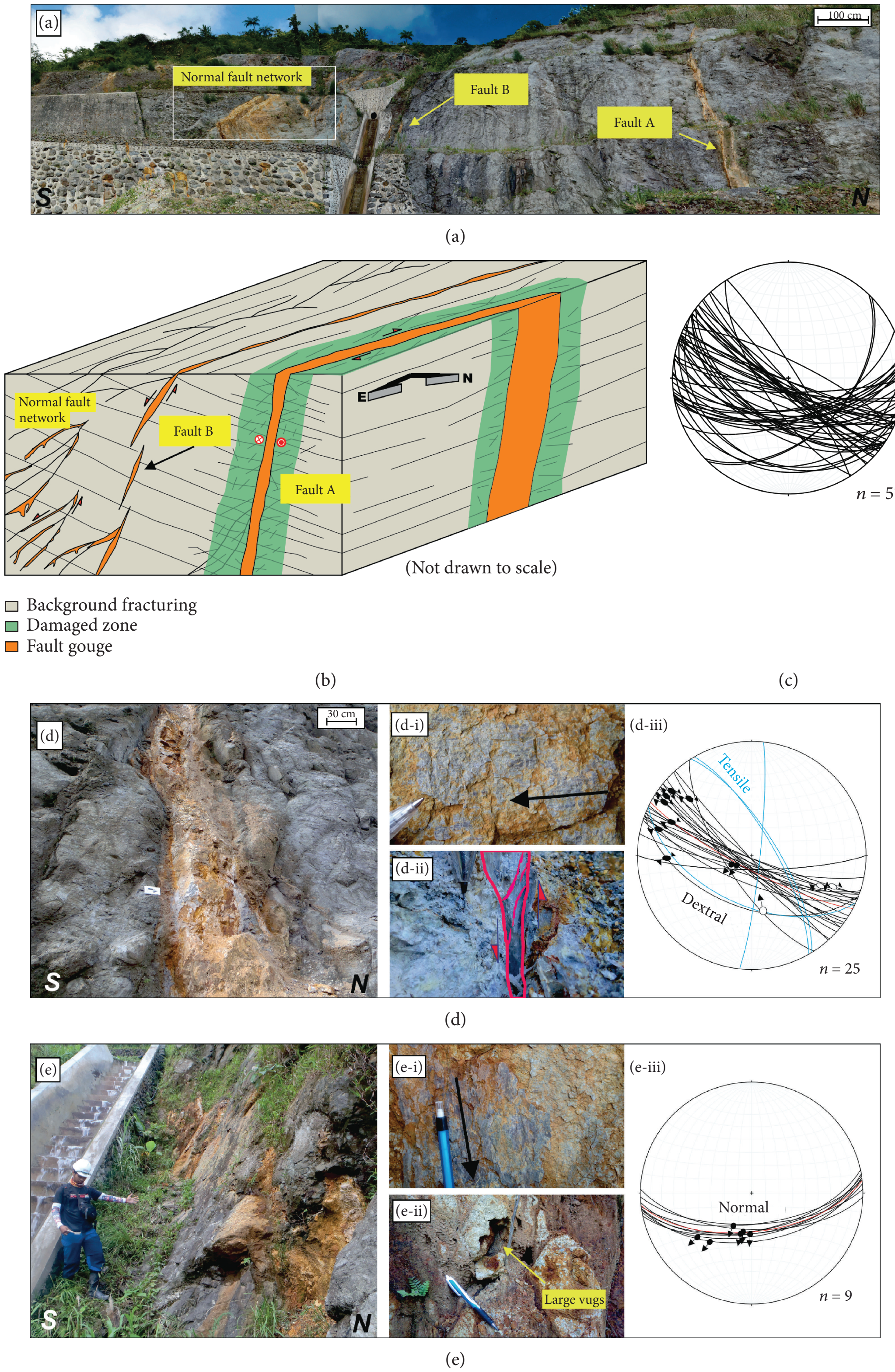

Figure 6: Group 2 NW-SE dextral and normal faults. (a) Panorama of the entire outcrop (refer to Figure 1(c), iv, for the location). (b) 3D sketch of the faults showing the location of the two large faults discussed in-text, and their subparallelism and potential linkage by an array of smaller normal faults. (c) Stereographic projection of all the fractures mapped in the locality. (d) The main dextral fault, fault A, showing the horizontal slickenlines (i), oblique gypsum crystals (ii), and the stereoplot (iii) which has tensile fractures in blue and average orientation of the fault plane in red. (e) The large normal fault, fault B, and its subvertical slickenlines (i), portions of suspected enhanced permeability (ii), and stereoplot (iii).

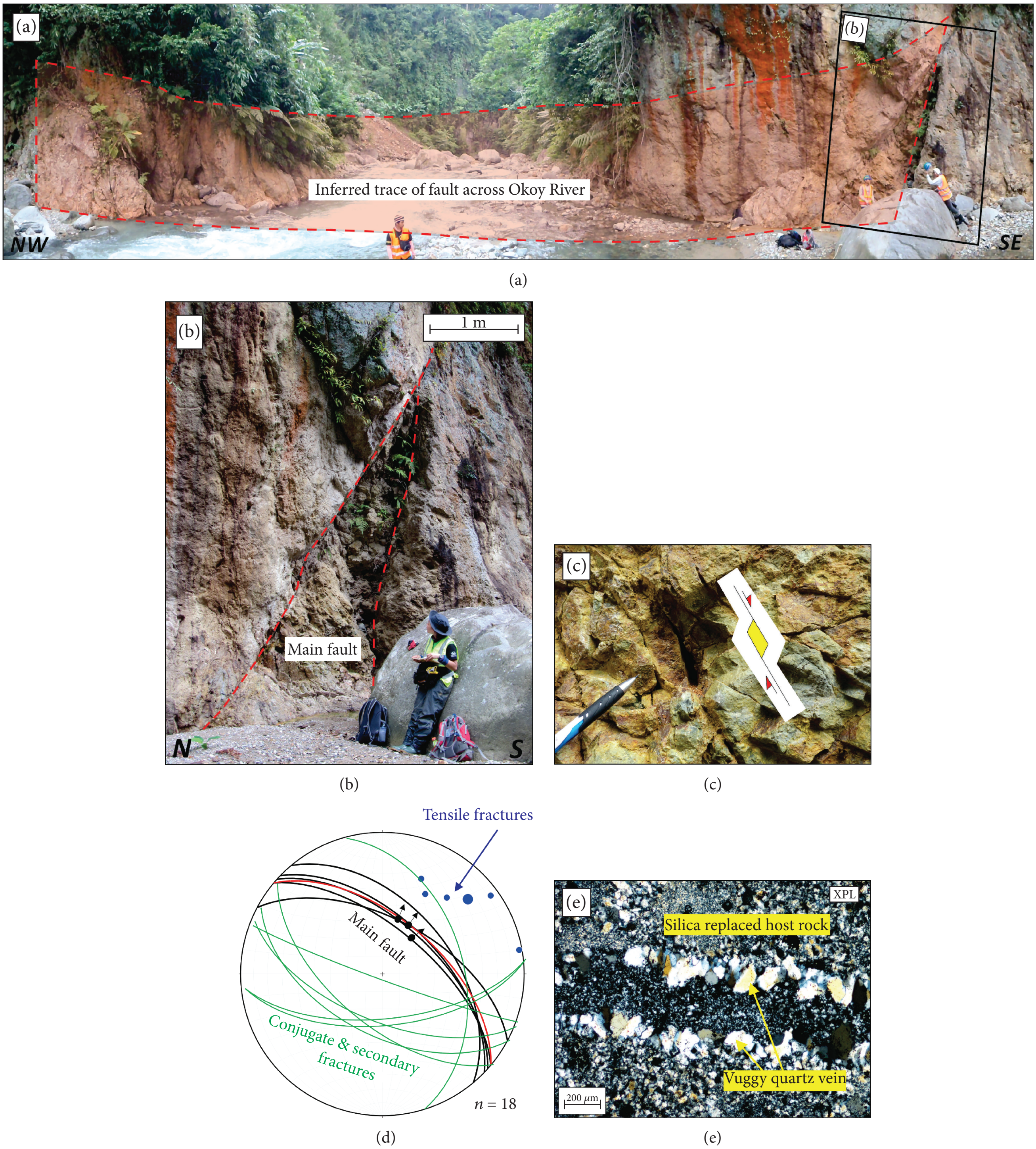

Figure 7: Group 2 NW-SE normal fault. (a) The structure at the midstream of Okoy River with the estimated fault trace projected as a red plane (see Figure 1(c), iii, for the location). (b) Section view of the SE side of the ravine showing the main structure. (c) Close-up photo of the small-scale dilational jogs which are common in the damage zone. (d) Stereonet showing the main fault planes in black, the average plane in red, and secondary and likely conjugate structures in green. Poles to the tensile fractures and veins are represented as blue dots. (e) Photomicrograph of the host rock, completely replaced by silica and also cut by a quartz vein.

5.3. Cross-Cutting Relationships. Group 1 structures are limited to the older Late Pliocene to Pleistocene Southern Negros Formation and are not observed in the younger lava flows and pyroclastics belonging to the Quaternary Cuernos Volcanics. Group 2 structures, on the other hand, are observed in both lithological formations. Given the older age of the lithological formation where group 1 fractures are found, this suggests that they are most likely to have

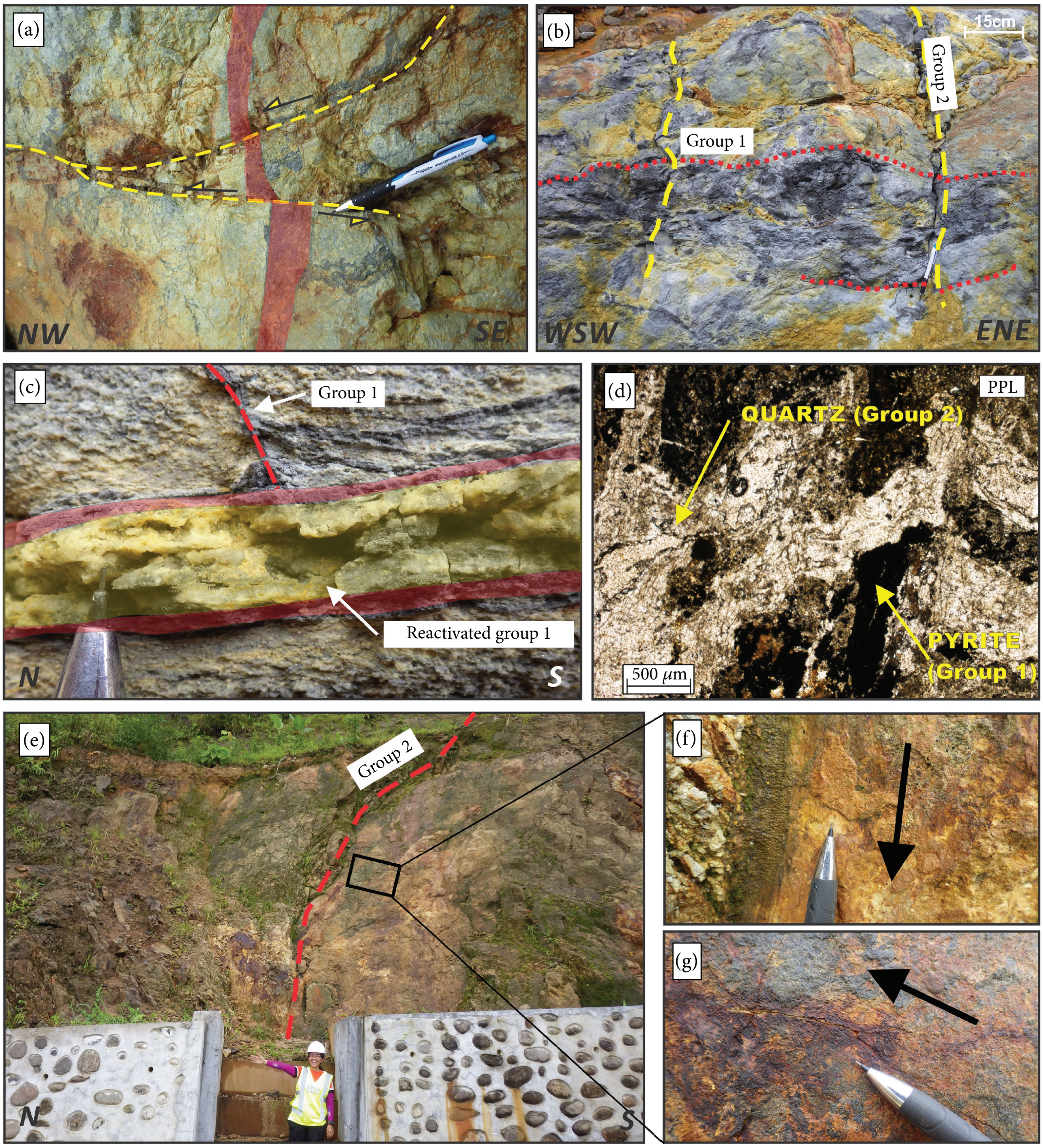

Figure 8: Cross-cutting observations. (a) NE–SW sinistral group 2 fault (in yellow broken line) offsets a WNW-ESE sinistral group 1 fault zone (in red). (b) Group 2 tensile fractures (yellow broken lines) also cut group 1 tensile fractures (red broken lines). (c) Group 1 pyrite-filled (in red) tensile fracture is reactivated and filled with quartz with sulphur precipitates (in yellow). (d) Cross-cutting pyrite (group 1) and quartz vein (group 2) in thin section. (e) An E-W moderately dipping group 2 fault (red line) has preserved two sets of overlapping slickenlines—(f) near vertical and (g) subhorizontal, suggesting two directions of movement along one fault.

formed earlier than group 2 and prior to the deposition of the Quaternary and Recent rocks (i.e., Cuernos Volcanics). The distinct characteristics of the associated fault rocks from the group 1 and group 2 fractures (Table 1) also suggest that the two groups of fractures have formed under different deformational conditions at different times.

Cross-cutting relationships observed in the field support the relative age hypothesis. In the downstream regions of the Okoy River valley, sinistral NE-SW-trending fractures interpreted as group 2 faults based on the development of millimeter-scale gouges with sulphur and oxides formed along exposed surfaces, everywhere offset group 1 WNW-ESE sinistral pyrite-filled fractures by up to 4 cm (Figure 8(a)). Offsetting relationships are also observed for two sets of tensile fractures trending ENE-WSW and NNW-SSE, interpreted to belonging to group 1 and group 2, respectively. Here,

Table 2: Palaeostress inversion results of all the fracture sets by fracturing events. Data were weighted based on the thickness of the deformation zone alone or together with the length of the lineament to minimise biases due to poor field exposures.

Stage	Weighting parameter	Number of data	Trend (plunge) of the principal axes, degree			Shape factor, δ	Mean slip misfit angle, degree
			σ_1	σ_2	σ_3		
Stage 1	N/A	5	243 (6)	138 (66)	336 (23)	0.31	18
Stage 2a	Thickness	57	314 (82)	185 (5)	95 (6)	0.44	28
Stage 2a	Thickness & length	57	269 (87)	1 (0)	91 (3)	0.48	37
Stage 2b	Thickness	11	269 (55)	153 (17)	53 (29)	0.71	24
Stage 2b	Thickness & length	11	275 (54)	155 (20)	54 (29)	0.72	23

the NNW-SSE fractures cut through the ENE-WSW ones (Figure 8(b)), suggesting that group 1 structures are older than group 2 structures.

Quartz- and occasionally sulphur-filled group 2 fractures offset the pyrite-dominated tensile fractures of group 1 (Figures 8(c) and 8(d)). In some cases, group 1 tensile fractures here have reopened, either as pure mode I or as hybrid fractures (Figure 8(c)). Based on this evidence, the fracturing event that formed the group 1 fractures is referred to as *stage 1*.

There is also some field evidence that the group 2 fractures may have accommodated more than one phase of deformation. This is based on several instances of group 2 fractures being offset by other group 2 faults with a different sense of slip which are inferred to have been reactivated. For example, in the northeast area of SNGF, a NW-SE-trending, gently dipping sinistral-reverse group 2 structure offsets a steeply dipping group 2 fault of similar trend by approximately one meter. An ENE-WSW- to E-W-trending group 2 fault in the northern area of SNGF preserves both near vertical (pitch 84°) and subhorizontal (pitch 20°) slickenlines (Figures 8(e) and 8(g)). These are related to normal and dextral senses of motion, respectively, based on slickenline stepping relationships. The steep lineations overprint the subhorizontal slickenlines suggesting that the fault initiated as a dextral structure and was then reactivated with a dip-slip sense of motion.

More generally, a distinct group of NW-SE-oriented dip-slip faults are seen to consistently offset all other fractures. In many cases, these structures show evidence of overprinting slickenlines, and in all cases, they reactivate as dip-slip structures rather than strike-slip features. It is therefore proposed that the group 2 fractures, identified on textural and alteration assemblage grounds, show evidence for at least two deformation events, herein termed as *stage 2a* and *stage 2b*.

Figure 5 summarises the key kinematic features of faulting during each of the stages. Stage 1 includes all the group 1-classified fractures, which are mostly E-W-trending sinistral faults and NE-SW-oriented (rare NW-SE) tensile fractures. Approximately 70% of the group 2 fractures are interpreted to have formed during stage 2a. This is dominated by NW-SE-oriented normal and dextral faults and NW-SE tensile fractures, and some N-S-striking normal and tensile fractures (Figure 5). Lastly, some NW-SE and E-W faults show evidence of later dip-slip normal movements and are considered to have formed during stage 2b.

6. Palaeostress Analysis

Following the classification of the mapped fractures into two stages based on field and microscopic characteristics, a stress inversion analysis was conducted to evaluate the possible stress conditions at the time of their formation. The inversion relies on the assumption that the faults and the blocks of rock they bound have not rotated significantly since their formation. This is a reasonably safe assumption given that the observed and inferred displacements of the key SNGF faults are minimal, suggesting that finite strains are overall low. The stress inversion was carried out in the Windows-based application, MyFault version 1.05, using the Minimised Shear Stress Variation inversion method which assumes that the magnitude of the shear stress on the fault is similar for all the fault planes at the time of rupture [31–33] (see the Supplementary Material for details of the methods (available here)). Amongst the various methods of stress inversions considered, this yielded the minimum misfit angles and thus is considered to be the most appropriate for the SNGF dataset. A weighting scheme was further applied in the inversion based on the thickness and length of the mapped faults to give more significance to larger structures over smaller ones.

For stage 1, σ_2 is calculated to be steeply plunging (66°/138°), whilst both σ_1 and σ_3 are horizontal to shallowly plunging, trending ENE and NNW-SSE, respectively (Table 2 and Figure 5). The calculated extensional direction, σ_3, is consistent with the poles to the majority of associated tensile fracture planes (Figure 5). With a shape factor of 0.31, the stress configuration suggests a strike-slip to transpressional tectonic setting.

During stage 2a, the implied tectonic setting has changed to a strongly extensional or normal-faulting regime. The calculated σ_1 is vertical whilst the principal extension direction, σ_3, is E-W, which coincides with the poles to the mapped N-S tensile fracture planes (Figure 5).

During stage 2b, σ_1 remained steeply plunging (55°/269°, Table 2) during a generally extensional or transtensional tectonic regime with a shape ratio of 0.71. The S_{Hmax} is now oriented NW-SE.

The *orientations* of the principal stresses in stage 2b appear to be similar to the present-day configuration but with a swapped σ_1 and σ_2. The World Stress Map [15] reports, based on limited data for Negros, a modern WNW-ESE and less common ENE-WSW-oriented S_{Hmax} in the southwest of Negros and Tañon Strait. The focal mechanism of the 2012 earthquake generator as discussed in Aurelio et al. [26] suggests that $S_{\mathrm{Hmax}} = \sigma_1$ is oriented NW-SE. GPS studies by Rangin et al. [34] likewise suggest a NW-oriented (315°) convergence direction, similar in direction to that reported by Kreemer et al. [35], which is parallel to the overall convergence direction estimated for the Philippine Sea Plate [13]. Finally, restricted borehole breakout data from SNGF wells indicate that S_{Hmax} is WNW-ESE. Overall, these present-day data suggest that S_{Hmax} is generally oriented NW-SE to WNW-ESE, consistent with the principal stress orientations determined for stage 2b, except that $S_{\mathrm{Hmax}} = \sigma_{2.}$ Thus, the youngest fractures in SNGF have probably formed in a stress field where the principal stress axis orientations were similar to the present day, but σ_1 and σ_2 may have switched due to the perturbing effect of the volcanic edifice in the region of the SNGF as discussed below.

7. Slip and Dilation Tendency Analysis

An attempt to identify which of the mapped structures might be the most favorable drilling targets is now presented, using a slip and dilation tendency analysis. The rationale here is that when a structure has a higher tendency to slip under the present-day stress conditions, there is a greater chance of increased fracture density and enhanced permeability [36]. Higher capacity to transport fluids is also probable when a structure is more prone to dilate, since fault aperture is most likely to readily enlarge. These concepts have been effectively applied, for example, in assessing fault reactivation potential in deep enhanced geothermal systems in Germany [37] and in understanding anisotropic transmissivity of the groundwater in the Yucca Mountain in Nevada [36].

All the analyses were carried out using 3DStress® version 5 software developed by the Southwest Research Institute. Present-day principal stress directions applied were based on the regional GPS studies of Negros Island (i.e., [34, 38]). Stress magnitudes were estimated from the lithological overburden pressure (for the vertical stress, S_v), borehole leak-off tests (for the minimum horizontal stress, S_{Hmin}), and the derived shape ratios from the palaeostress analysis (which allows calculation of the maximum horizontal stress, S_{Hmax}).

Overall, slip tendency values are quite low (<0.20) suggesting that in general, the structures in the SNGF are not prone to slip under the proposed present-day stress conditions. This contrasts with the strongly dilational tendency with widespread values approaching 1.0. The mapped steeply dipping to vertical NW-SE faults have the highest slip and dilation tendency followed by moderately dipping structures of similar orientations. The most stable faults are those striking NNE-SSW to NE-SW. These are the structures whose poles lie around the maximum principal stress (Figure 9).

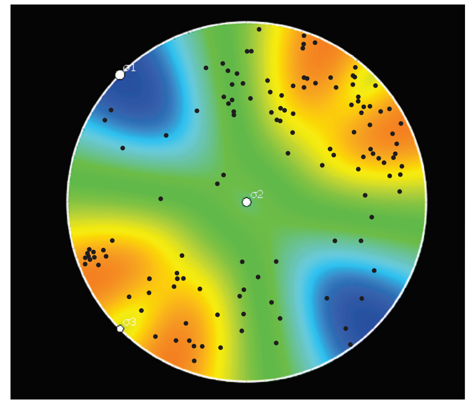

Figure 9: Stereonet of the combined slip and dilation tendencies. Fracture planes are represented as poles. Regions of higher slip and dilation tendencies are shown in warm colors whilst areas with the lowest tendencies are in cold colours. Present-day stress conditions are based on the orientations in Rangin et al. [34]. For complete results on the various scenarios, refer to Pastoriza [27].

8. Discussion

The fieldwork reveals the presence of two characteristically different groups of structures (groups 1 and 2) which accommodate three movement stages (stages 1, 2a, and 2b) in the SNGF. These, correspond to three brittle deformation events, with the most recent (stage 2b) mostly being limited to reactivation of pre-existing structures rather than involving new fracture formation. Palaeostress inversion analysis suggests a transition between a strike-slip to an extensional to transtensional tectonic regime. Stage 1 likely occurred under a strike-slip to transpressive tectonic regime where S_{Hmax} is oriented NE-SW. This formed mainly WNW-ESE-trending sinistral faults and NE-SW tensile fractures. Based on the reported age of the Southern Negros Formation in which these fractures were observed exclusively, the stage 1 fracturing event occurred no earlier than the Pliocene. The main sinistral faults run subparallel to the trace of the Puhagan Fault Zone which may suggest that it formed during stage 1, but was initiated as a sinistral structure, contrary to its observed present-day kinematics.

The stress conditions then changed to a strongly extensional regime when most of the group 2 fractures formed. New structures formed including WNW-ESE- to NNW-SSE-trending normal, dextral, and oblique (normal/reverse) faults together with less common ENE-WSW-oriented normal faults. Associated NNW-SSE tensile fractures and smaller faults offset earlier stage 1 fractures. The calculated principal extension direction is E-W for stage 2a whilst principal compression is steep to vertical. Horizontal compression is probably minor given the nature of the suggested tectonic regime, but could conceivably be oriented N-S. There is a perceived counterclockwise rotation of the compression direction around the vertical from stage 1 to stage 2a, which may have persisted to the present day, with a likely transitional phase captured by the stage 2b deformation reactivating mainly pre-existing group 2 fractures formed during stage 2a. The overall tectonic setting during stage 2b is also dominated by extension, with the principal extension direction, σ_3, now being NE-SW.

It is important to note here that the SNGF stress inversions have high misfit angles which imply that although the apparent *directions* of rotation are clear, the *amount* of rotation is rather less well-constrained. In the following subsections, we discuss geological processes that could potentially explain the directions of the interpreted local stress rotations within SNGF.

The possibility of block rotations is partially constrained by a palaeomagnetic study by McCabe et al. [39] that involved sampling and measurements at 86 sites across the Philippine Archipelago. Two key rotation events were suggested: first in the Early to Middle Miocene where it was suggested that the islands of Panay, Cebu, and Mindanao rotated clockwise, whilst Marinduque rotated counterclockwise. This, it was suggested, was related to the collision of the northern Palawan Block with the Philippine Mobile Belt. Since Negros Island is bordered by Panay, Cebu, and Mindanao, it may have also rotated clockwise at this time, but no Early to Middle Miocene samples were collected from Negros to determine this. In the Late Miocene to Pliocene, McCabe et al. [39] suggested that the central and northern parts of Luzon rotated clockwise potentially related to the collision of the Luzon Arc with Taiwan. No rotation was observed in other parts of Philippines during this period. Since then, it is suggested that the entire Philippine Arc has behaved as a single unit with no discernible rotations based on the available palaeomagnetic data [39]. It is possible, however, that the magnitude of any rotation that occurred close to the present-day may have been too small for the study to capture.

Thus, these studies suggest that since the Pliocene, there is no strong palaeomagnetic evidence to suggest that significant regional-scale block rotations have occurred in the island of Negros. This seems consistent with the generally low displacements inferred along the major fault structures in the SNGF, which suggests that the regional finite strain is low, meaning that significant fault-induced block rotations related to these faults are unlikely. Thus, it seems most likely that apparent changes in stress orientations due to block rotation are unlikely to have occurred in the last 5 Myr since the last plate reorganization happened [11, 40, 41]. Further, the direction of the observed rotations is also not consistent even if a "domino-style" rotation is considered (i.e., clockwise rotation of stress axes due to the movement of two large sinistral faults). Therefore, it is most likely that the observed stress rotations in the SNGF area are related to a smaller-scale heterogeneity in the regional stress field. We now go on to consider two possible geological processes which might account for such a locally controlled stress perturbation.

8.1. Possible Influences of the Philippine Fault and the Propagation of the Yupisan Fault. The observed stress rotation may reflect a smaller-scale disturbance that is related to the local lateral propagation of displacement along the Yupisan Fault. The Yupisan Fault is a NNE-SSW sinistral-reverse fault traversing the eastern coast of Negros in the north and passes through to the west of the CDN volcano in the southern part of the island (Figure 1(b); [26]). Stress rotation related to the Yupisan Fault is explored by looking at the displacement vectors of the Yupisan Fault as it continues to slip during the time of its formation (proposed to be during the Late Pliocene) and how the displacement could affect the surrounding blocks, including the area where the CDN volcano is located (details in Pastoriza [27]). Coulomb® 3.3 was used, which is a MatLab-based calculation and visualisation program designed for the determination of static displacements, strains, and stresses at any depth caused by a fault slip, magmatic intrusion, or dike expansion/contraction [42] following the concepts in Toda et al. [43] and Lin and Stein [44].

For this analysis, the southern inland trace of the Yupisan Fault was divided into five segments based on the curvature of the lineament observed on satellite imagery. The strike azimuth for each fault segment was extracted from the digital elevation models whilst the dip angle is taken from the earthquake focal mechanism data of the February 2012 Negros earthquake and was assumed to be the same for all five segments. Using the USGS-calculated 6.7 earthquake magnitude along Yupisan Fault in 2012, the amount of total co-seismic slip along the fault is estimated to be 0.524 m (calculation after Wells and Coppersmith [45]). This net slip was then broken down into dip and strike-slip components for each fault segment based on the estimated rake on that fault segment using geometrical rules. The geometrical rake was approximated with the aid of stereographical projections using the compression axis direction proposed by Rangin et al. [34].

A propagating Yupisan Fault was then modelled using Coulomb® 3.3 for two scenarios—one where the fault propagates northwards and another where it propagates southwards. The key assumption here is that every time a new segment slips, the older segments slip with it. This basically confers a cumulative displacement for each segment. Additionally, it is assumed that each time the Yupisan Fault slips, an earthquake with the same magnitude of 6.7 is generated.

Figure 10 illustrates that the total amount of slip for each segment gradually increases as the Yupisan Fault propagates. In a northward propagating model, at the first onset of the structure *Time 1*, the southernmost segment slips 0.43 and 0.30 m along the strike and the dip, respectively (Figure 10). By *Time 5,* it has slipped a total of 2.15 m sinistrally and 1.50 m along its dip. In a northward propagating Yupisan Fault, this configuration induced a progressive clockwise block rotation on both sides of the fault (Figure 10). The directions are the other way around for the stress rotations which would be counterclockwise. These observations are opposite if a southward growing Yupisan Fault is considered [27]. From stage 2a to the present day, an apparent counterclockwise rotation of the stresses around the horizontal is observed (Figure 5). This observation therefore fits a northward-propagating Yupisan Fault model, where the footwall, in which the CDN and SNGF are situated, appears to have rotated progressively clockwise, as the fault continued to move.

The model suggests that after five slip increments along the Yupisan Fault (*Time 5*), the southern part of the footwall

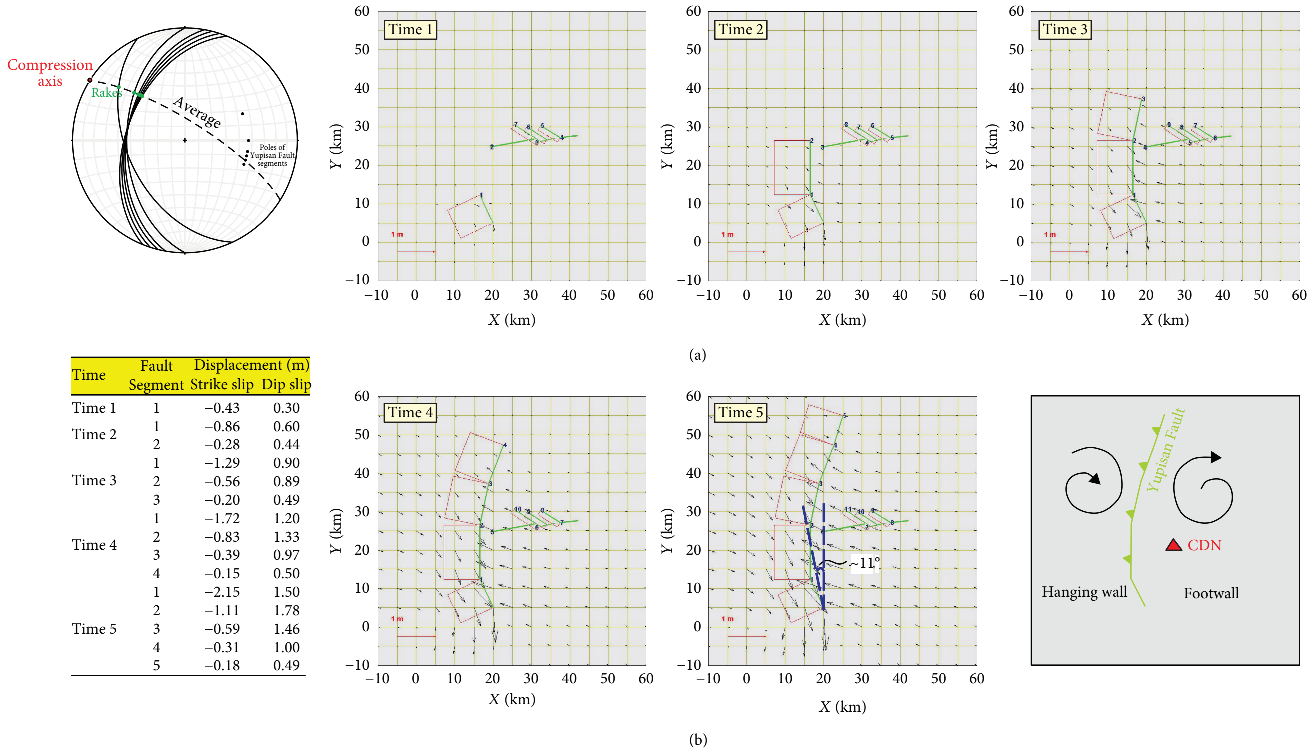

Time	Fault Segment	Displacement (m) Strike slip	Dip slip
Time 1	1	−0.43	0.30
Time 2	1	−0.86	0.60
	2	−0.28	0.44
Time 3	1	−1.29	0.90
	2	−0.56	0.89
	3	−0.20	0.49
Time 4	1	−1.72	1.20
	2	−0.83	1.33
	3	−0.39	0.97
	4	−0.15	0.50
Time 5	1	−2.15	1.50
	2	−1.11	1.78
	3	−0.59	1.46
	4	−0.31	1.00
	5	−0.18	0.49

Figure 10: Displacement vector model of a northward propagating Yupisan Fault. Stereonet in the upper left shows the orientation of the Yupisan Fault segments discussed in-text. The table below it lists the amount of cumulative displacement per time for each fault segment, where a negative strike-slip displacement refers to sinistral movement along that fault segment. The boxes on the right show the propagation of the Yupisan Fault from time 1 to time 5. Each fault segment is represented in green whilst the red boxes connected to it are the projected subsurface plane. Displacement vectors are shown as the black arrows. The green E-W and NW-SE lines at the centre of each box represent the Puhagan Fault and some of the key structures within SNGF. Shown in the final box is the general rotation of the blocks for the footwall and hanging wall of the Yupisan Fault, where the CDN volcano and SNGF are on the footwall.

has rotated roughly 11° (Figure 10). This is close to the 9° rotation along the horizontal from stage 2b (144°) to the present day (135° in [34]) (Figure 5) suggesting a potentially good fit with the northward-propagating Yupisan Fault as a potential trigger of the observed rotation of the stresses within the SNGF. Further, considering that this modelling utilised the present-day compression direction of 315°/135°, the consistency of the degree of rotation with the stress inversion results suggest that the present-day stress conditions may have actually remained relatively constant throughout stage 2a and that the growing Yupisan Fault has triggered local block rotations within its immediate vicinity resulting in an *apparent* rotation of the local stress fields. Potentially, the observed change in tectonic regime between stage 1 and stage 2a could be due to changes in the stress magnitudes, leading to a "flipping" of the stress axes, which does not necessarily require a drastic change in the far-field stress orientations. This illustrates how the growth of large-scale regional deformation structures may potentially affect smaller-scale stress fields.

Although we have initially eliminated the possibility of block rotation in Negros Island given that no palaeomagnetic data can support it, the smaller-scale rotation proposed herein is possible at low finite strains. A local palaeomagnetic study could help to test and refine this model, provided that a minimal rotation of 11° can be captured.

8.2. Changes in Tectonic Regime and the Development of the CDN Volcanic Activity. Given the presence of an active subduction zone (Negros Trench) located to the southwest of the SNGF and a large reverse fault (Yupisan Fault) on its western flank (Figure 1(a)), a dominant horizontal compression direction might be expected for the study area. Although this is true for stage 1, it does not seem to be the case during stage 2a and stage 2b which are both predominantly extensional based on the results of the palaeostress inversions and the observed dominance of normal faults.

The spatial and temporal effects of volcanism on the stress fields in the summit region of a volcano have been explored by a number of authors, e.g., [46–48]. Being centrally located in a volcanic complex, the potential influence of the CDN volcanic activity on the stress fields over time and the style of fracturing within the SNGF should not be disregarded. The CDN volcano is characterised by several episodes of volcanism and intrusion marked by thick sequences of volcanic deposits seen in the subsurface, with three distinct volcanic centers of varying ages exposed at the surface. Terakawa et al. [47] have shown that volcanic activity can induce temporal stress changes in the summit regions of erupting volcanoes. Thus, during the 2014 eruption of Mount Ontake in Japan, focal mechanisms indicate that normal-faulting dominated pre-eruption whilst reverse faulting prevailed thereafter. Further, it was demonstrated that the average misfit angle of the focal mechanisms around and in the periphery of the edifice significantly increased prior to the eruption. An inflation under the volcano, which was driven by magmatic or hydrothermal fluids, was identified as the cause of the stress perturbation, particularly resulting in the rotation of the maximum and minimum principal stresses [47]. The results of this study and that of Vargas-Bracamontes and Neuberg [49], amongst others, clearly illustrate how magma pressures can locally perturb and even overpower the regional stress field in an area of active volcanism. This potentially results in local stress fields being different from the prevailing large-scale conditions.

The dominance of mostly normal faults in the group 2 fractures during both stages 2a and 2b may potentially be related to the inflation and gravity spreading of the CDN volcano and associated intrusive emplacements. Formation of grabens along the flanks and *en echelon* strike-slip faults, folds, and reverse structures at the base are typically observed on gravitational spreading volcanoes based on analogue modelling [50] and field observations [51]. Similar structures are also observed when the spreading is associated with magmatic intrusion. The abundance of extensional structures in the SNGF may be associated with this type of spreading behaviour. With continued dyke emplacements underneath the CDN, the volcano would continue to grow, requiring the surface to expand. Such expansion is most easily accommodated by fracturing. This is consistent with the observation that the southwest area of the geothermal field is most dissected by normal faults, which is the closest to the main edifice (highest elevation mapped) and where the Nasuji Pluton is laterally situated in the subsurface. Rae et al. [52] have illustrated that the intrusive events underneath the CDN have influenced the alteration type and the propagation of heat below the SNGF. It is perhaps not surprising then that during the several intrusion events, hydrofractures have formed and are later reactivated as shear or as tensile structures.

Thus, volcanism, spreading, intrusion, and the geothermal processes, are likely to have independently or altogether influenced the observed dominant normal-faulting regime within the SNGF since stage 2a.

9. Synthesis and Conclusion

Remote sensing studies and surface-based geological fieldwork conducted within the SNGF reveal that the region is dominated by brittle deformation. Age indicators and cross-cutting relationships suggest that at least two fracture-forming events occurred and have been locally reactivated under evolving stress fields. The changes are most likely driven by regional and local tectonic and volcanic processes within Southern Negros. Although limited by the age of the oldest rocks exposed at the surface, the deformation history proposed is constrained from the Middle Pliocene to the present day. This assumes that the reported age of Late Pliocene to Early Pleistocene of the Southern Negros Formation, which is purely based on field stratigraphic position, is correct. A regional structural evolution with time is illustrated in Figure 11(a) whilst a more detailed and localised view is shown in Figure 11(b).

By the Pliocene, the Philippine Fault had started to propagate in the eastern part of the Philippines and the present-day plate vectors were already in place. Southern Negros at this time was still partly submerged underwater and the Southern Negros Formation, which formed as a result of the volcanic activity of the palaeo-CDN, was deposited underwater in Puhagan (central part of the field) but subaerially in the west [28]. An emergent volcanic edifice in the western part of the present-day CDN may have existed at this time (Figure 11(a), i). An early phase of brittle deformation, stage 1, occurred, affecting the SNF and, presumably, older lithologies. Stress inversion analyses of the rather limited field data suggest a NE-SW-oriented horizontal maximum compression under a strike-slip or transpressional regime, which is also consistent with the equivalent-age structures observed in the country rocks to the northwest of SNGF in the Pamplona-Sta. Catalina area [27]. In southern Negros, a sinistral ENE-WSW-trending *en echelon* palaeo-Puhagan Fault is thought to have been present, running across the northern flanks of the palaeo-CDN edifice (Figure 11(b)). Associated with this major structure were a series of E-W sinistral faults and NE-SW tensile fractures cutting the early SNF and older rocks (Figure 11(b)). During this time, a smaller hydrothermal system may have existed which may be related to early intrusions (e.g., Puhagan dykes in [28]). The SNF rocks experienced intense preliminary alteration whilst fractures were channeling sulphide-rich fluids. A dominantly reducing environment, maybe because of less interaction with surface waters, prevailed, meaning that these fluids deposited widespread pyrite along the fractures. Cockade structures within the pyrite veins suggest episodic influxes of sulphide-rich fluids into open-fracture systems over significant timescales [30].

By the end of the Pliocene, it is suggested that the Yupisan Fault had started to propagate northwards from the SSW coast of Southern Negros towards the eastern coast of the island, under a stress regime similar to the present day, i.e., NW-SE horizontal compression ([34]; Figure 11(a), ii). The palaeo-CDN continued its activity, and deposition of SNF was maintained. In the Early to Middle Pleistocene, emplacement of the main Nasuji Pluton [18] and associated intrusions occurred, particularly in the western part of the SNGF. This intrusion triggered significant steam-heated argillic alteration in the western area of the geothermal field which is one of the earliest dated hydrothermal alteration episodes (0.7 Mya in Rae et al. [52] and 0.81 Mya in Takashima and Reyes [53]) in the SNGF. Leach and Bogie [54] concluded that this process may have introduced a barren porphyry-copper-type deposit, which they considered to be the relict alteration suite observed in the SNGF boreholes today. An overpressured magma chamber resulting from the intrusion may have induced hydrofracturing in the immediate vicinity of the pluton. This drastically increased the degree of fracturing in the western sector, which is exhumed today.

The Pleistocene marked the peak of the volcanic activity of the CDN complex which led to the deposition of lava flows

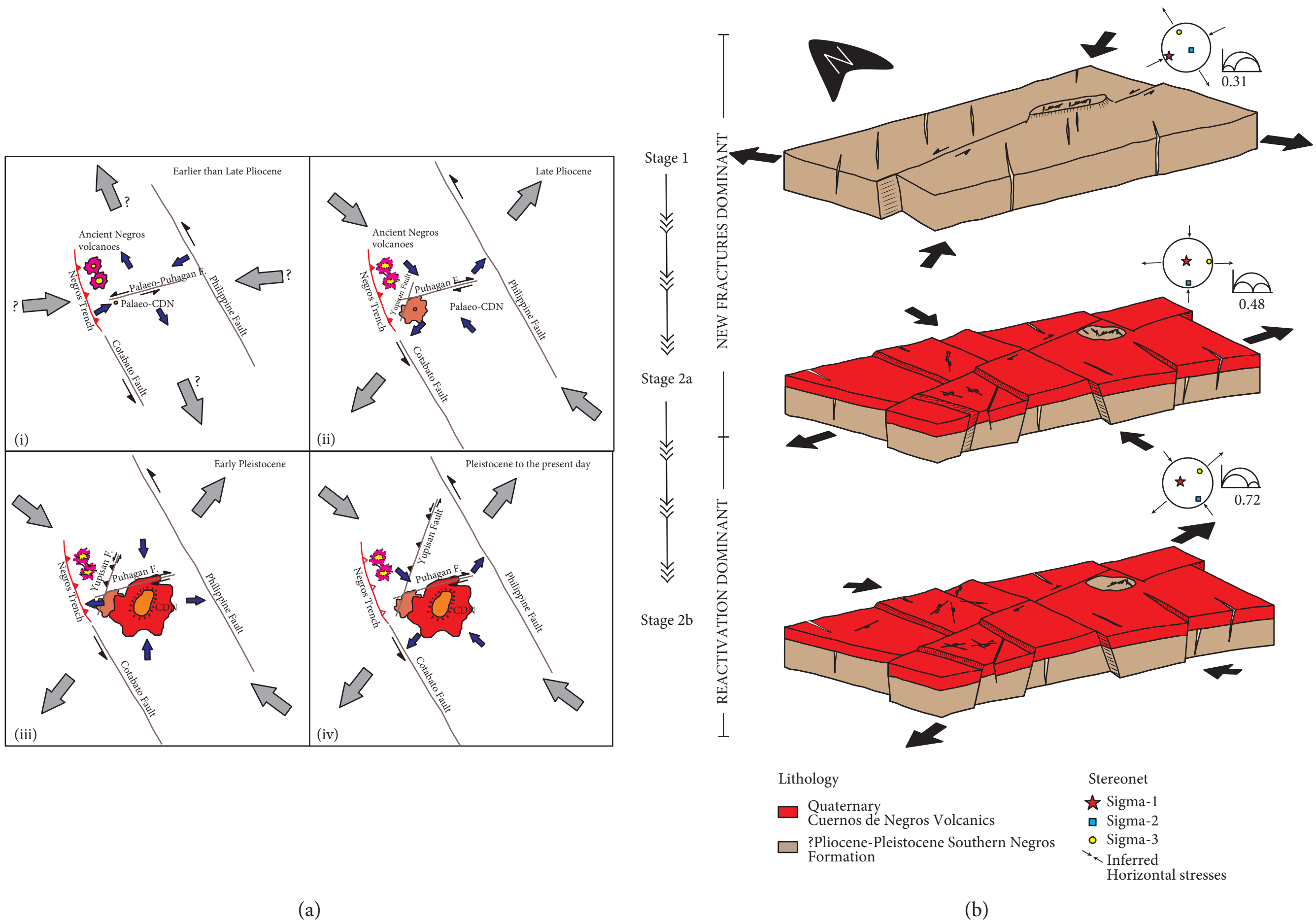

FIGURE 11: Structural evolution of the Southern Negros and the SNGF. (a) Simplified diagram of the tectonic evolution of the Cuernos de Negros volcanic complex and its relationship with the key regional structures in the Philippines (i.e., Philippine and Cotabato Faults). (i) to (iv) represent a progressive evolution with increasing time. (b) For SNGF, the model focuses on the three stages of fracturing. Apparent changes in stress directions suggested in the palaeostress inversion which could be a function of small-scale block rotation are indicated. Note that the sketches are not drawn to scale. The stereonets and the Mohr circles are generated in MyFault. Stage 1 at the local scale is contemporaneous with (i) at the regional scale, whilst stages 2a and 2b occurred during (iii) and (iv) at the regional scale, respectively.

and pyroclastics. It is suggested that a regional NW-SE compressional stress regime dominated in the SNGF and reactivated the palaeo-Puhagan Fault with dextral-strike slip kinematics (Figures 11(a) and 11(b)). Its kinematics is clearly observed today based on the modern geomorphology, offsetting the CDN complex and the Yupisan Fault right-laterally. This formed NW-SE dextral Riedel structures related to the Puhagan Fault in the northern part of SNGF. Locally, with a more active volcano formation, a localised extensional setting prevailed under stage 2a, with the dominant extension somewhat consistent with the regional extension direction (Figure 11(a), iii), where WNW-ESE to NNW-SSE normal, dextral, and oblique (normal/reverse) and rare ENE-WSW normal faults propagated. NNW-SSE-trending tensile fractures clearly offset the earlier tensile and sinistral structures. In the northern area of the field, the earlier hydrofractures were reactivated as shear fractures. The heat in the subsurface particularly shifted towards the central part of the SNGF (central Okoy) following the conduction-convection model of Takashima and Reyes [53]. With the now crystallised dykes and/or pluton, Rae et al. [52] suggested that the circulation became more diluted, being affected by meteoric water, and less influenced by hydrothermal sources. This led to a propylitic and illite-rich alteration, affecting the immediate country rock. Consequently, stage 2a fractures are in most cases host to thick clay alteration and iron-oxide formation.

During the Holocene, the volcanic activity in the CDN waned, thus the regional stress fields became more prevalent within the SNGF, but still under a local extensional/transtensional setting (Figure 11(a), iv and Figure 11(b)). The final fracturing transpired during stage 2b formed mostly NW-SE-oriented normal faults. Reactivation of the stage 2a fractures, mostly as dip-slip structures was also common. By this time, the heat was now centered in Puhagan as a result of either shifting due to convection-conduction [53] or because a younger intrusion event occurred underneath the area as proposed by Rae et al. [18]. Many of these young structures served as channels in the present-day hydrothermal system towards the surface, appearing as a result of the concentration of active thermal manifestations around Puhagan today. This suggests that a majority have remained open and active in the present-day stress configuration.

The results of the slip and dilation tendency analysis suggesting that NW-SE-oriented fractures should in theory be the best and most permeable drilling targets. This agrees with actual drilling results in SNGF [55]. However, the slip and dilation tendencies indicate that NE-SW and NNE-SSW-oriented structures should be the least permeable as they are likely presently stable; they are, however, also known to be important in the fluid flow regime of the SNGF based on actual boreholes [55]. These large-scale NE-SW faults could have been original tensile fractures formed during stage 1 and could have been reactivated during succeeding fracturing events. Such reactivation may have re-opened these structures at depth as tensile fractures in the predominantly extensional regime of stage 2a +/− a component of shearing. As the geothermal system was already developing during stages 2a and 2b, temperatures at the fracturing depths may well have been much higher, making rapid cementation/sealing of the fracture planes less likely. This reactivation model may explain why some larger NE-SW faults have remained opened until the present day and consequently are proven to be permeable channels of geothermal fluids in the SNGF [55].

This work is by far the most comprehensive geological analysis and the first microtectonic work on the SNGF surface geological data. Several structural field campaigns and studies have been done in the field over the last 30 years [56–62] as part of its exploration and development works. However, geological interpretations were limitedly based on orientation analysis (i.e., the orientation of the fractures with the highest frequency correlated to the orientation of the regional structure) with very minimal attempts to rank or prioritize structures with varying characteristics. There was a significant lack of the appreciation of the kinematics of mapped faults and their implication to potential subsurface permeability, and consequently the drilling strategy.

The work presented here addresses that gap by illustrating a more comprehensive approach to surface geological data analysis. From a thorough characterisation of the mapped faults (e.g., fracture fills and kinematics), their cross-cutting relationships, and a stress inversion, one can build the deformation history of the field. With a refined geological history and the information on the associated fluid alteration for each phase, a better understanding on which structures related to the geothermal development can be provided. Further, the utilization of the slip and dilation tendency analysis is a useful tool in the identification of the potential interaction of the mapped faults with the present-day stresses and how this may influence fluid flow. This could help to delineate structures which are currently stressed and thus may be potential drilling targets given the likely increased fracture intensity and widening of the fracture aperture.

This work illustrates how a strongly field-based geological approach can inform exploration and eventual development strategies for drilling, even at the early stages of the field exploration (i.e., even prior to drilling) and can be further enhanced by incorporating a multiscale fracture attribute and topology analysis as presented in Pastoriza [27]. This geological workflow should supplement existing workflows for building conceptual models at the exploration stage (e.g., Cumming [63]) and, when integrated with geochemical, geophysical, and hydrological data, be usefully employed for field-scale development of geothermal resources.

Data Availability

The data that support the findings of this study are available from the Durham University E-Theses Repository, but restrictions apply to the availability of these data, under a confidentiality agreement between the Energy Development Corporation and Durham University. Data are however available from the authors upon reasonable request and with permission to the Energy Development Corporation.

Disclosure

This work is part of the PhD thesis of the main author at Durham University.

Conflicts of Interest

The authors declare that there is no conflict of interest regarding the publication of this paper. Energy Development Corporation has reviewed and granted permission to publish this work.

Acknowledgments

Due acknowledgment is to the Energy Development Corporation for granting access to internal reports and well data; to Jonathan Kit Reyes and Ferdie Castillejo for the assistance in the field campaigns in Negros; to Mario Aurelio, Jon Gluyas, and Richard Walker for their contributions in the entire project, and to Nick Primaleon and the two anonymous reviewers for their constructive criticisms to improve this paper. This work is funded by the Energy Development Corporation.

Supplementary Materials

The supplementary material details the stress inversion methods applied in the paper. It highlights the assumptions considered and how the minimum shear stress variation method was selected amongst other methods available in the literature. *(Supplementary Materials)*

References

[1] E. Huenges, Ed., *Geothermal Energy Systems: Exploration, Development, and Utilization*, Wiley-VCH, Weinheim, Germany, 2010.

[2] L. Ochieng, "Overview of geothermal surface exploration methods," in *Short Course VIII on Exploration for Geothermal Resources*, pp. 1–13, Kenya, 2013.

[3] P. F. Dobson, T. J. Kneafsey, J. Hulen, and A. Simmons, "*Porosity, permeability, and fluid flow in the Yellowstone geothermal system, Wyoming*," *Journal of Volcanology and Geothermal Research*, vol. 123, no. 3-4, pp. 313–324, 2003.

[4] S. R. Schutter, "*Hydrocarbon occurrence and exploration in and around igneous rocks*," *Geological Society, London, Special Publications*, vol. 214, no. 1, pp. 7–33, 2003.

[5] N. Coppo, J. M. Baltassat, J. F. Girard et al., "3-D magnetotelluric investigations for geothermal exploration in Martinique (Lesser Antilles). Characteristic deep resistivity structures, and shallow resistivity distribution matching heliborne TEM results," in *Proceedings World Geothermal Congress*, Melbourne, Australia, 2015.

[6] A. E. Ciriaco and M. O'Sullivan, "3D dual porosity modeling of tracer transport in Palinpinon 1 Geothermal Field, Philippines," in *Proceedings World Geothermal Congress*, Melbourne, Australia, 2015.

[7] G. Magro, F. Gherardi, and F. E. B. Bayon, "*Noble and reactive gases of Palinpinon geothermal field (Philippines): origin, reservoir processes and geodynamic implications*," *Chemical Geology*, vol. 339, pp. 4–15, 2013.

[8] R. K. Cardwell, B. L. Isacks, and D. E. Karig, "The spatial distribution of earthquakes, focal mechanism solutions, and subducted lithosphere in the Philippine and Northeastern Indonesian Islands," in *The tectonic and geologic evolution of Southeast Asian seas and islands*, D. E. Hayes, Ed., pp. 1–35, American Geophysical Union, 1980.

[9] G. P. Yumul, C. B. Dimalanta, and R. A. Tamayo, "Indenter-tectonics in the Philippines: example from the Palawan Microcontinental Block - Philippine Mobile Belt Collision," *Resource Geology*, vol. 55, no. 3, pp. 189–198, 2005.

[10] F. C. Gervasio, "The age and nature of orogenesis in the Philippines," *The Philippine Geologist*, vol. 20, no. 4, pp. 121–140, 1966.

[11] Mines and Geosciences Bureau, *Geology of the Philippines*, M. A. Aurelio and R. E. Pena, Eds., Department of the Environment and Natural Resources, Quezon City, 2010.

[12] D. R. Sarewitz and D. E. Karig, "Geologic evolution of Western Mindoro Island and the Mindoro Suture Zone, Philippines," *Journal of Southeast Asian Earth Sciences*, vol. 1, no. 2, pp. 117–141, 1986.

[13] C. DeMets, R. G. Gordon, and D. F. Argus, "Geologically current plate motions," *Geophysical Journal International*, vol. 181, no. 1, pp. 1–80, 2010.

[14] M. A. Aurelio, "Shear partitioning in the Philippines: constraints from Philippine fault and global positioning system data," *The Island Arc*, vol. 9, no. 4, pp. 584–597, 2000.

[15] O. Heidbach, J. Reinecker, M. Tingay et al., "Plate boundary forces are not enough: second- and third-order stress patterns highlighted in the World Stress Map database," *Tectonics*, vol. 26, no. 6, 2007.

[16] A. M. F. Lagmay, A. M. P. Tengonciang, and H. S. Uy, "Structural setting of the Bicol Basin and kinematic analysis of fractures on Mayon Volcano, Philippines," *Journal of Volcanology and Geothermal Research*, vol. 144, no. 1–4, pp. 23–36, 2005.

[17] S.-B. Yu, Y. J. Hsu, T. Bacolcol, C. C. Yang, Y. C. Tsai, and R. Solidum, "Present-day crustal deformation along the Philippine Fault in Luzon, Philippines," *Journal of Asian Earth Sciences*, vol. 65, pp. 64–74, 2013.

[18] A. J. Rae, D. R. Cooke, D. Phillips, and M. Zaide-Delfin, "The nature of magmatism at Palinpinon geothermal field, Negros Island, Philippines: implications for geothermal activity and regional tectonics," *Journal of Volcanology and Geothermal Research*, vol. 129, no. 4, pp. 321–342, 2004.

[19] A. Jarvis, H. I. Reuter, A. Nelson, and E. Guevara, *Hole-filled SRTM for globe Version 4*, CGIAR-CSI SRTM 90m Database, 2008.

[20] E. Barrier, P. Huchon, and M. Aurelio, "Philippine fault: a key for Philippine kinematics," *Geology*, vol. 19, no. 1, pp. 32–35, 1991.

[21] R. U. Solidum, P. R. Castillo, and J. W. Hawkins, "Geochemistry of lavas from Negros Arc, west central Philippines: Insights into the contribution from the subducting slab," *Geochemistry, Geophysics, Geosystems*, vol. 4, no. 10, p. 9008, 2003.

[22] S. Garwin, R. Hall, and Y. Watanabe, "Tectonic setting, geology, and gold and copper mineralization in Cenozoic magmatic arcs of Southeast Asia and the West Pacific Appendix 1. Society of Economic Geologists, Inc.," *Economic Geology*, vol. 100, pp. 891–930, 2005.

[23] H. von Biedersee and H. Pichler, "The Canlaon and its neighbouring volcanoes in the Negros Belt, Philippines," *Journal of Southeast Asian Earth Sciences*, vol. 11, no. 2, pp. 111–123, 1995.

[24] GVP, "Kanlaon: eruptive history," 2018, http://www.volcano.si.edu/volcano.cfm?vn=272020#bgvn_3202.

[25] C. Rangin, C. Muller, and H. Porth, "Neogene geodynamic evolution of the Visayan Region," in *On the Geology and Hydrocarbon Prospects of the Visayan Basin, Philippines*, H. Porth and C. H. Daniels, Eds., pp. 7–28, Geologisches Jahrbuch, 1989.

[26] M. A. Aurelio, J. D. B. Dianala, K. J. L. Taguibao et al., "Seismotectonics of the 6 February 2012 Mw 6.7 Negros Earthquake, central Philippines," *Journal of Asian Earth Sciences*, vol. 142, pp. 93–108, 2017.

[27] L. R. Pastoriza, *The Geological Characterisation and Permeability Evaluation of Fractures in the Southern Negros Geothermal Field, Negros Island, Philippines, in Earth Sciences*, University of Durham, 2017.

[28] H. G. Ariceto-Villarosa, E. L. Bueza, A. G. Reyes, and M. C. Zaide-Delfin, *The Subsurface Geology and Alteration Mineralogy of Nasuji-Sogongon Sector, Southern Negros Geothermal Field*, PNOC-Energy Development Corporation Internal Report, 1988.

[29] M. Zaide, *Interpretation of Rock-Dating Results in the Southern Negros Geothermal Field*, PNOC-EDC Internal Report, 1984.

[30] M. Frenzel and N. H. Woodcock, "Cockade breccia: product of mineralisation along dilational faults," *Journal of Structural Geology*, vol. 68, Part A, pp. 194–206, 2014.

[31] A. J. Michael, "Use of focal mechanisms to determine stress: a control study," *Journal of Geophysical Research*, vol. 92, no. B1, pp. 357–368, 1987.

[32] A. J. Michael, "Determination of stress from slip data: faults and folds," *Journal of Geophysical Research: Solid Earth*, vol. 89, no. B13, pp. 11517–11526, 1984.

[33] A. M. Dichiarante, *A Reappraisal and 3D Characterisation of Fracture Systems within the Devonian Orcadian Basin and Its Underlying Basement: an Onshore Analogue for the Clair Group, Earth Sciences*, University of Durham, Durham, UK, 2017.

[34] C. Rangin, X. le Pichon, S. Mazzotti et al., "Plate convergence measured by GPS across the Sundaland/Philippine Sea Plate deformed boundary: the Philippines and eastern Indonesia," *Geophysical Journal International*, vol. 139, no. 2, pp. 296–316, 1999.

[35] C. Kreemer, W. E. Holt, S. Goes, and R. Govers, "Active deformation in eastern Indonesia and the Philippines from GPS and seismicity data," *Journal of Geophysical Research: Solid Earth*, vol. 105, no. B1, pp. 663–680, 2000.

[36] D. A. Ferrill, J. Winterle, G. Wittmeyer et al., "Stressed rock strains groundwater at Yucca Mountain, Nevada," *GSA Today*, vol. 9, no. 5, pp. 2–7, 1999.

[37] I. Moeck, G. Kwiatek, and G. Zimmermann, "Slip tendency analysis, fault reactivation potential and induced seismicity in a deep geothermal reservoir," *Journal of Structural Geology*, vol. 31, no. 10, pp. 1174–1182, 2009.

[38] C. Rangin, "Rigid and non-rigid micro-plates: Philippines and Myanmar-Andaman case studies," *Comptes Rendus Geoscience*, vol. 348, no. 1, pp. 33–41, 2016.

[39] R. McCabe, E. Kikawa, J. T. Cole et al., "Paleomagnetic results from Luzon and the central Philippines," *Journal of Geophysical Research*, vol. 92, no. B1, pp. 555–580, 1987.

[40] M. Aurelio, "*Tectonics of the Philippines Revisited*," *Journal of the Geological Society of the Philippines*, vol. 55, no. 3/4, pp. 119–183, 2000.

[41] M. A. Aurelio, R. E. Peña, and K. J. L. Taguibao, "Sculpting the Philippine archipelago since the Cretaceous through rifting, oceanic spreading, subduction, obduction, collision and strike-slip faulting: contribution to IGMA5000," *Journal of Asian Earth Sciences*, vol. 72, pp. 102–107, 2013.

[42] S. Toda, R. S. Stein, V. Sevilgen, and J. Lin, *Coulomb 3.3. Graphic-Rich Deformation and Stress-Change Software for Earthquake, Tectonics, and Volcano Reserach and Teaching-User Guide*, U.S. Geological Survey open-file report 2011-1060, Reston, Virginia, 2011.

[43] S. Toda, R. S. Stein, K. Richards-Dinger, and S. B. Bozkurt, "Forecasting the evolution of seismicity in southern California: animations built on earthquake stress transfer," *Journal of Geophysical Research B: Solid Earth*, vol. 110, no. B5, 2005.

[44] J. Lin and R. S. Stein, "Stress triggering in thrust and subduction earthquakes and stress interaction between the southern San Andreas and nearby thrust and strike-slip faults," *Journal of Geophysical Research: Solid Earth*, vol. 109, no. B2, 2004.

[45] D. L. Wells and K. J. Coppersmith, "New empirical relationships among magnitude, rupture length, rupture width, rupture area, and surface displacement," *Bulletin of the Seismological Society of America*, vol. 84, no. 4, 1994.

[46] D. C. Roman, "Temporal and spatial variation of local stress fields before and after the 1992 eruptions of Crater Peak vent, Mount Spurr volcano, Alaska," *Bulletin of the Seismological Society of America*, vol. 94, no. 6, pp. 2366–2379, 2004.

[47] T. Terakawa, A. Kato, Y. Yamanaka et al., "Monitoring eruption activity using temporal stress changes at Mount Ontake volcano," *Nature Communications*, vol. 7, 2016.

[48] J. J. Sánchez, M. Wyss, and S. R. McNutt, "Temporal-spatial variations of stress at Redoubt volcano, Alaska, inferred from inversion of fault plane solutions," *Journal of Volcanology and Geothermal Research*, vol. 130, no. 1-2, pp. 1–30, 2004.

[49] D. M. Vargas-Bracamontes and J. W. Neuberg, "Interaction between regional and magma-induced stresses and their impact on volcano-tectonic seismicity," *Journal of Volcanology and Geothermal Research*, vol. 243-244, pp. 91–96, 2012.

[50] A. Delcamp, B. van Wyk de Vries, M. R. James, L. S. Gailler, and E. Lebas, "Relationships between volcano gravitational spreading and magma intrusion," *Bulletin of Volcanology*, vol. 74, no. 3, pp. 743–765, 2012.

[51] A. Borgia and B. van Wyk de Vries, "The volcano-tectonic evolution of Concepción, Nicaragua," *Bulletin of Volcanology*, vol. 65, no. 4, pp. 248–266, 2003.

[52] A. J. Rae, D. R. Cooke, D. Phillips, C. Yeats, C. Ryan, and D. Hermoso, *Spatial and Temporal Relationships between Hydrothermal Alteration Assemblages at the Palinpinon Geothermal Field, Philippines: Implications for Porphyry and Epithermal Ore Deposits*, Society of Economic Geologists, Special Publication, 2003.

[53] I. Takashima and A. G. Reyes, "Alteration and TL age of the Palinpinon geothermal area, Negros Island, southern Philippines," *Journal of the Geothermal Research Society of Japan*, vol. 12, no. 4, pp. 315–325, 1990.

[54] T. M. Leach and I. Bogie, "Overprinting of hydrothermal regimes in the Palinpinon geothermal field, Southern Negros, Philippines," in *4th New Zealand Geothermal Workshop*, Auckland, New Zealand, 1982.

[55] F. E. B. Bayon and M. S. Ogena, "Handling the problem of rapid reinjection returns in Palinpinon-I and Tongonan, Philippines," in *Proceedings World Geothermal Congress*, Antalya, Turkey, 2005.

[56] J. B. Pornuevo and R. O. Obusan, *Structural Mapping at Nasuji-Sogongon and Puhagan Sectors, Southern Negros Geothermal Field, Negros Oriental*, PNOC-EDC Internal Report, 1983.

[57] H. J. Tebar, *Structural Mapping at West Nasuji-Sogongon Sector, Southern Negros Geothermal Field, Negros Oriental*, PNOC-EDC Internal Report, 1984.

[58] J. R. Batolbatol and M. R. D. Fermin, "Surface structures of Nasuji-Sogongon Sector, Southern Negros Geothermal Field," Energy Development Corporation Internal Report, 2014.

[59] N. D. Salonga, *Surface Structures of Okoy Sector, Southern Negros Geothermal Field*, PNOC-EDC Internal Report, 1989.

[60] M. Cerio and F. Tosco, *Dauin Geothermal Prospect - Geology*, Energy Development Corporation Internal Report, 2014.

[61] R. S. Alincastre, *Geology of Baslay-Dauin Prospect*, PNOC-EDC Internal Report, 1982.

[62] H. J. Tebar, D. Z. Hermoso, and R. G. Lapuz, *Geology of North Okoy Geothermal Prosposect, Southern Negros Geothermal Field, Negros Oriental*, PNOC-Energy Development Corporation Internal Report, 1984.

[63] W. Cumming, "Geothermal resource conceptual models using exploration data," in *Thirty-Fourth Workshop on Geothermal Reservoir Engineering*, Stanford, California, 2009.